I. R. IRAN

ISSN: 1728-144X
e-ISSN: 1735-9244

International Journal of Engineering

Journal Homepage: www.ije.ir

MERC

TRANSACTIONS B: Applications

Volume 34, Number 02, February 2021

Materials and Energy Research Center

In the Name of God

INTERNATIONAL JOURNAL OF ENGINEERING
Transactions B: Applications

International **J**ournal of **E**ngineering *Transactions A: Basics* (ISSN 1728-1431) (EISSN 1735-9244)
International **J**ournal of **E**ngineering *Transactions B: Applications* (ISSN 1728-144X) (EISSN 1735-9244)
International **J**ournal of **E**ngineering *Transactions C: Aspects* (ISSN 2423-7167) (EISSN 1735-9244)
Web Sites: www.ije.ir & www.ijeir.info E-mails: ije.editor8@gmail.com, Tel: (+9821) 88771578, Fax: (+9821) 88773352
Materials and Energy Research Center (MERC)

ISSN: 1728-144X, e-ISSN: 1735-9244

International Journal of Engineering, Volume 34, Number 2, February 2021

CONTENTS:

Transactions B: Applications

ISSN: 1728-144X, e-ISSN: 1735-9244

International Journal of Engineering, Volume 34, Number 2, February 2021

Electrical & Computer Engineering

Industrial Engineering

Mechanical Engineering

ISSN: 1728-144X, e-ISSN: 1735-9244

International Journal of Engineering, Volume 34, Number 2, February 2021

International Journal of Engineering

Journal Homepage: www.ije.ir

Efficient Removal of Copper Ion from Aqueous Solution using Crosslinked Chitosan Grafted with Polyaniline

H. Zare*[a], H. G. Taleghani[b], J. Khanjani[a]

[a] *Department of Chemical, Materials and Polymer Engineering, Buein Zahra Technical University, Qazvin, Iran*
[b] *Faculty of Chemical Engineering, University of Mazandaran, Babolsar, Iran*

PAPER INFO

Paper history:
Received 17 October 2020
Received in revised form 25 November 2020
Accepted 03 December 2020

Keywords:
Copper Ions
Chitosan
Polyaniline
Removal Efficiency
Adsorption Isotherms
Kinetic Models

ABSTRACT

A high-performance adsorbent was produced by grafting polyaniline onto biopolymer chitosan. The morphological structure of cross-linked chitosan grafted with polyaniline was studied by scanning electron microscopy. Functional groups of the synthesized adsorbent were identified by Fourier-transform infrared. The performance of the prepared adsorbent was examined by batch adsorption experiments. The adsorption studies were performed with different operating parameters such as contact time, initial pH, adsorbent dosage and temperature. To evaluate adsorption isotherms, Freundlich, Langmuir and Dubinin-Radushkevich models were fitted to obtained data and the isotherm parameters were determined. Kinetics of the adsorption was studied by pseudo-first-order and pseudo-second-order models. It was observed that the obtained data were fitted more accurately with the pseudo-second-order model than the pseudo-first-order model. At optimum conditions, the maximum capacity and the removal efficiency of copper ions adsorption were obtained 131.58 mg/g and 92.5%, respectively. The regeneration efficiency and the removal efficiency of regenerated adsorbent were 97.7 and 90.4%, respectively. The results revealed the adsorbent has a great potential for adsorption of Cu (II) from aqueous solution.

***doi**: 10.5829/ije.2021.34.02b.01*

1. INTRODUCTION

Heavy metals removal from wastewater is a global issue since they are the most dangerous environmental pollutants. Various industries, especially metal finishing, electroplating, plastics, battery, and etching are continuously releasing copper in their discharges [1-4]. Copper is an essential trace element but its concentration in air, water, and food should be below the tolerance limits; otherwise, it would be harmful to humans and animals. Intake of copper can lead to health complications such as causes irritation, mucosal, hepatic, lung cancer and capillary damage [3, 5, 6].

In recent years, various treatment procedures have been established for the removal of heavy metal ions. Currently, treatment processes include precipitation, oxidation-reduction, ion exchange, membrane filtration-osmosis, coagulation-flocculation, and adsorption. Each technique has its advantages and disadvantages, but the adsorption method has been widely employed due to its simplicity of design and operation, low cost, high removal efficiency, and ease of adsorbent regeneration [7, 8].

Chitosan is a biopolymer with the linear structure of β-(1-4)-2amino-2-dexy-D-glucopyranose. Chitosan is generally produced by the deacetylation of chitin found in fungal cell walls and the exoskeleton of arthropods including insects, arachnids, and crustaceans (lobsters, crabs, and shrimps) [9-11]. Chitosan has potential to be employed in a diversity of fields, particularly in wastewater treatment. Chitosan is an appropriate adsorbent for the removal of heavy metals owing to the hydroxyl and amine functional groups [12, 13]. Chitosan has low mechanical strength and thermal stability and also it is soluble in acidic conditions [14, 15]. Several chemical and physical procedures have been applied to improve chitosan properties. Chemical modifications such as crosslinking and grafting improved porosity,

*Corresponding Author Institutional Email: *hv.zare@bzte.ac.ir* (H. Zare)

Please cite this article as: H. Zare, H. G. Taleghani, J. Khanjani, Efficient Removal of Copper Ion from Aqueous Solution using Crosslinked Chitosan Grafted with Polyaniline, International Journal of Engineering, Transactions B: Applications, Vol. 34, No.2, (2021) 305-312

surface area, and mechanical properties of chitosan [16, 17].

In the current research, an appropriate adsorbent was made for removing Cu (II) from aqueous phase. In order to modify chitosan properties, chitosan was crosslinked by glutaraldehyde. Then crosslinked chitosan was grafted with polyaniline. The impact of initial pH, contact time, temperature, and adsorbent dosage were investigated. The resulted data were assessed by Freundlich and Langmuir isotherm models. Also, the adsorption kinetics were studied by pseudo-first-order (PFO) and pseudo-second-order (PSO) models.

2. MATERIALS AND METHODS

2. 1. Materials Aniline, ammonium persulfate, acetic acid, citric acid, $CuSO_4.5H_2O$, and glutaraldehyde (50 wt% in H_2O) were purchased from Merck (Darmstadt, Germany). chitosan (85% deacetylated) were purchased from Sigma-Aldrich (St. Louis, Mo., USA). Stock solution of 1 g/l of Cu (II) was prepared using analytical grade $CuSO_4.5H_2O$ and kept at ambient temperature. Desired concentrations of Cu ions were prepared by diluting the stock solution with double distilled water.

2. 2. Adsorbent Preparation Chitosan was firstly dissolved in a solution of 2.5% acetic acid. Then 1.5% glutaraldehyde was poured into the chitosan solution and the obtained mixture stirred at 150 rpm for 5 h. Glutaraldehyde crosslinks chitosan chains by connecting amine groups. 2% aniline monomer in 50 ml of 1 M citric acid was added to the crosslinked chitosan solution. Then 5 ml of 10% ammonium persulfate was added to the solution drop by drop and stirred at 150 rpm for 10 h. In order to remove oligomers and impurities, cross-linked chitosan grafted with polyaniline (CCGP) was filtered and washed with acetone and double-distilled water. Finally, the resulted composite was completely dried in an oven at 60 °C for about 24 h.

2. 3. Batch Adsorption Experiments To investigate the impact of operating conditions on Cu (II) adsorption, experiments were conducted in batch mode. Adsorption isotherm and kinetic evaluations were conducted for the adsorption process. Adsorption experiments were carried out with an initial concentration of 100 mg/l Cu (II) on a heater stirrer (IKA, Germany) at 300 rpm. Batch experiments for the elimination of Cu (II) from aqueous solution were conducted in a pH range of 2-6, adsorbent dosage of 1-5 g/l, and at various temperature in the range of 20 to 40 °C. The initial pH of the solution was set with addition of HCl solution for the required pH value. The initial pH of the solution was determined with a pH meter (AZ 86502, Taiwan). Sampling was performed at specified time intervals, and Cu (II) concentration was determined by inductively coupled plasma optical emission spectrometry (ICP-OES, Varian 730-ES, USA). The Cu (II) removal efficiency, Re (%), was determined according to the following relation:

$$\mathrm{Re} = \frac{C_i - C_t}{C_i} \times 100 \quad (1)$$

where C_i is the initial Cu (II) concentration (mg/l), and C_t is the concentrations of Cu (II) at a given time (mg/l). q is the adsorption capacity, which is the Cu (II) amount adsorbed per unit mass of the adsorbent (mg/g). At a certain contact time of t, q_t (mg/g) was obtained by means of the equation below:

$$q_t = (C_i - C_t) \times \frac{V}{m} \quad (2)$$

where V and m were the solution volume (1) and the adsorbent dosage (g), respectively.

2. 4. Characterization Fourier-transform infrared (FTIR) spectra were acquired with a FTIR spectrometer (Bruker Tensor, Germany). The dried samples were milled into powder. One mg of each sample was blended with 100 mg of spectrophotometric grade KBr in an agate mortar and pressed into a tablet. FTIR spectra were recorded in the wavelength range of 400 to 4000 cm^{-1}. In order to study the surface morphology, the prepared CCGP was gold-coated with a sputtering coater (Emitech K575X, England), and the CCGP surface was observed by scanning electron microscope (SEM) (Phenom-ProX Sem, Netherlands).

3. RESULTS AND DISCUSSION

3. 1. FTIR Analysis Functional groups of prepared CCGP were studied using FTIR (Figure 1). The IR spectra of CCGP showed an absorption band at 3439 cm^{-1} due overlapping the stretching vibration bands of both hydroxyl (–OH) and amine (–NH) groups [18]. The peaks at 2847 and 2923 cm^{-1} were attributed to the asymmetric and symmetric stretching vibrations of $–CH_2$ groups [19]. The peak at 1642 cm^{-1} corresponds to the stretching vibration of the C=O band of acetyl groups of chitosan remained in the adsorbent [3, 20]. The peak appearing at 1553 cm^{-1} associated with the nitrogen quinone, and the peak at 1456 cm^{-1} attributed to the benzene ring confirms the formation of polyaniline [21, 22]. The absorption band at 1310 cm^{-1} is due to the C–N stretching vibration of the benzenoid unit [23].

3. 2. SEM and EDAX Analysis In order to investigate surface morphology of CCGP, scanning electron microscopy (SEM) image was taken at a magnification of 27500x (Figure 2). According to the

SEM image, CCGP contains particles smaller than 500 nm and has a high specific surface area. The large contact surface area between adsorbent and metal ions allows a large amount of adsorption relative to the weight of the adsorbent. EADX analysis of CCGP were performed before and after adsorption of copper ions (Figure 3). The presence of copper peak after adsorption indicates that copper ions were successfully adsorbed onto the CCGP.

3. 3. Effect of Contact Time One of the effective parameters in the adsorption experiments is the contact time. Effect of contact time was studied with Cu (II) concentration of 100 mg/l, adsorbent dosage of 5 g/l, initial pH of 6 and at temperature of 20 °C for 180 min. Figure 4 presents the impact of time on the elimination of Cu (II) from the aqueous phase by the CCGP. The adsorption process reached to equilibrium after 100 min of contact time. At equilibrium time of 100 min, removal efficiency of 84.1% achieved and then remained almost constant.

3. 4. Effect of pH The pH of the solution is recognized as the greatest significant parameter affecting

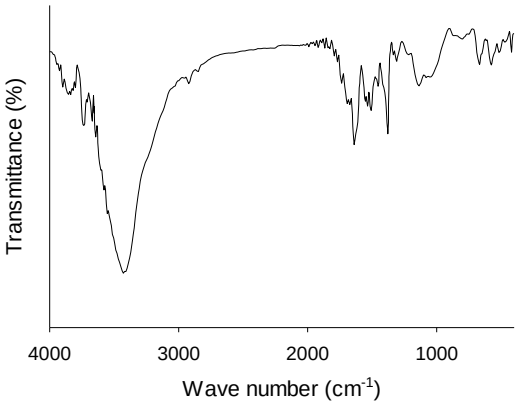

Figure 1. FTIR spectra of the CCGP

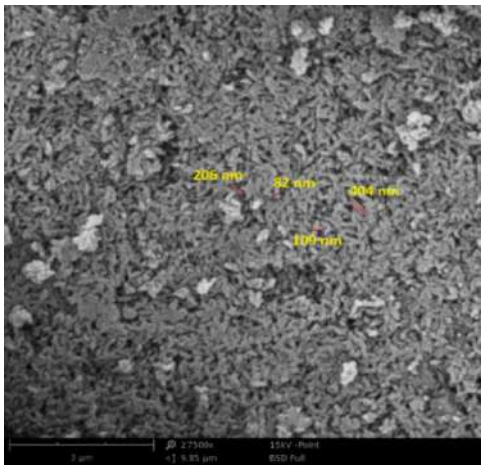

Figure 2. SEM image of CCGP with magnification of 27500x

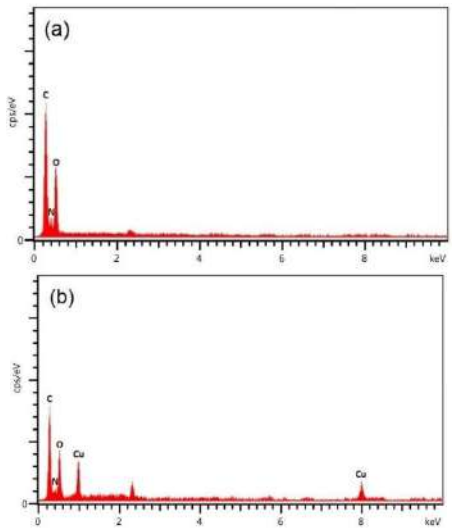

Figure 3. EADX analysis (a) before and (b) after adsorption of copper ions onto the CCGP

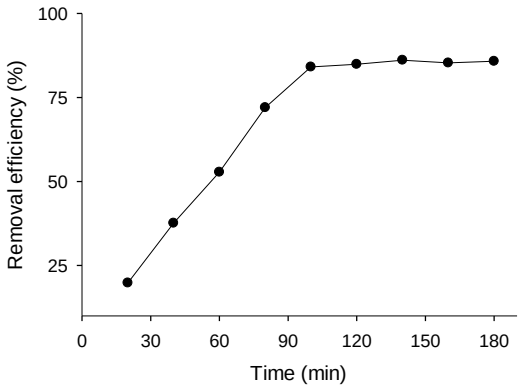

Figure 4. The removal efficiency of Cu (II) ions by CCGP versus contact time, (Cu (II) concentration=100 mg/l, adsorbent dosage=5 g/l, initial pH=6, T=20 °C)

metal ions adsorption. To investigate the effect of pH on the adsorption process, the experiments were conducted at initial pH range of 2 to 6. At pH above 6, hydrate structures of copper are formed and the Cu (II) ions precipitate in the solution. Figure 5 presents the impact of pH on the removal of Cu (II) from solution by the CCGP. It can be perceived that the adsorbed amount of metal ions decreased with decreasing pH of solution. This is because at low pH values the amount of H^+ ions is high and therefore protons can contend with the copper cations for surface sites of the adsorbent. The removal efficiency was reached to maximum value at pH=6; therefore, further experiments were performed with an initial pH of 6.

3. 5. Effect of Temperature and Dosage of Adsorbent The impact of adsorbent dose was investigated within the range of 1 to 5 g/l of the

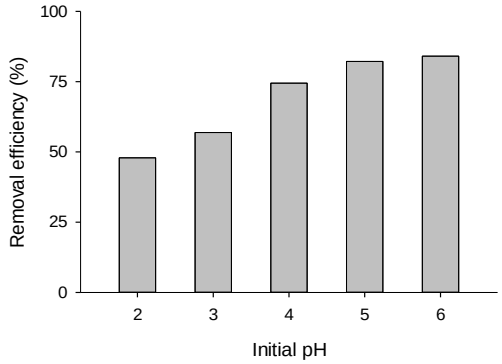

Figure 5. Impact of initial pH on the removal efficiency, (contact time=100 min, T=20 °C and adsorbent dosage=5 g/l)

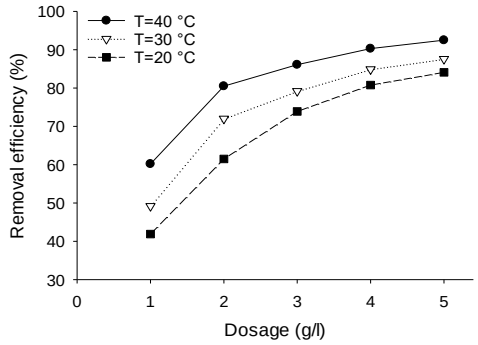

Figure 6. Removal efficiency of Cu (II) at the adsorbent dosage of 1–5 g/L and temperature of 20–40 °C

adsorbent. The adsorption experiment was conducted at an optimum pH of 6 with the Cu (II) concentration of 100 mg/l. The experiments were carried out under isothermal conditions at various temperatures of 20, 30, and 40 °C. According to curves depicted in Figure 6, as the CCGP dosage increased, the Cu (II) adsorption onto the CCGP rapidly increased. When the adsorbent dose increases, the amount of available surface area increases, resulting in enhanced absorption of copper ions. Also, with increasing adsorbent dosage, the removal efficiency of Cu (II) increased. Maximum removal efficiency (92.5%) was obtained at an adsorbent dosage of 5 g/l and a temperature of 40°C.

3. 6. The Isotherm Models Isotherms study the association between metal ions concentration in aqueous phase and the metal ions adsorbed onto the adsorbent at a constant temperature. The Langmuir model, a widely used isotherm, is suitable for investigating the adsorption of a monolayer on a surface containing a limited number of adsorption sites, which is given in the equation as follows [24]:

$$\mathrm{Re} = \frac{q_{max} K_L C_e}{1 + K_L C_e} \quad (3)$$

The linear form of the Langmuir equation can be rearranged as shown below [25]:

$$\frac{C_e}{q_e} = \frac{1}{(K_L q_{max})} + \frac{C_e}{q_{max}} \quad (4)$$

where C_e (mg/l) is the equilibrium concentration of Cu (II) in the aqueous phase, q_e (mg/g) is the Cu (II) amount adsorbed per unit mass of the adsorbent at equilibrium, q_{max} (mg/g) is the maximum capacity of adsorption at a given temperature, and K_L (L/mg) is the Langmuir constant. The plots of the adsorption isotherm fitted by the Langmuir equation are presented in Figure 7. The values of maximum capacity of the adsorption, q_{max}, and the Langmuir isotherm constants, K_L, were determined from the linear plots (Table 1).

The empirical Freundlich isotherm model was extensively used to define the equilibrium adsorption data for a heterogeneous surface. The nonlinear form of the Freundlich model is expressed by the following equation [26]:

$$q_e = K_F (C_e)^{(1/n)} \quad (5)$$

when the Freundlich equation is rearranged in logarithmic form, a linear equation of log (q_e) versus log (C_e) is obtained as follows [27]:

$$\log (q_e) = \log (K_F) + \left(\frac{1}{n}\right) \log (C_e \quad (6)$$

where K_F is the Freundlich isotherm constant ((mg/g)/(mg/L) ^{n}) which is associated to the adsorption capacity, and n is the adsorption intensity parameter. The plot of log (q_e) against log (C_e) is drawn according to the experimental adsorption data (Figure 8). Freundlich isotherm parameters were determined, which are summarized in Table 1. Depending on the results of adsorption isotherms, the maximum capacity of adsorption was obtained 131.58 mg/g at temperature of 40 °C. Also, the comparison of isotherm models showed that the experimental data were fitted better with Freundlich model than the Langmuir model.

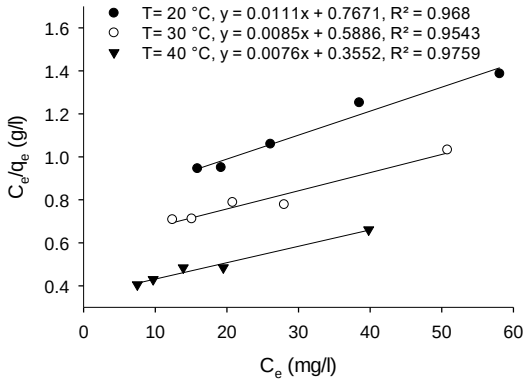

Figure 7. The Cu (II) adsorption isotherm data fitted by Langmuir model at various temperatures of 20–40 °C, (Cu (II) concentration=100 mg/l, initial pH=6, contact time=100 min)

To investigate the mechanism of the adsorption of Cu (II) ions on the CCGP, Dubinin-Radushkevich (D-R) model was applied. The D-R model is given in linear form as follows [28]:

$$\ln(q_e) = \ln(q_s) - \beta\varepsilon^2 \quad (7)$$

In above equation, q_e is the mol of copper ions adsorbed per unit mass of the adsorbent at equilibrium (mol/g), q_s is the isotherm saturation capacity (mol/g), β is the D-R isotherm constant related to adsorption energy (mol^2/J^2), and ε is the Polanyi potential that can be calculated by the following equation:

$$\varepsilon = RT \ln\left[1 + \frac{1}{C_e}\right] \quad (8)$$

The mean free energy E (J/mol) of the adsorption process depends on β, which is calculated by the following equation:

$$E = \frac{1}{\sqrt{2\beta}} \quad (9)$$

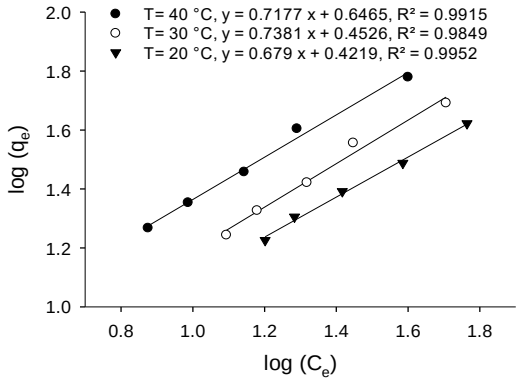

Figure 8. The Cu (II) adsorption isotherm data fitted by Freundlich model at various temperatures of 20–40 °C, (Cu (II) concentration=100 mg/l, initial pH=6, contact time=100 min)

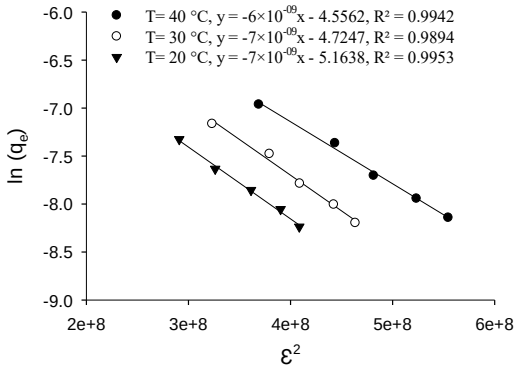

Figure 9. The Cu (II) adsorption isotherm data fitted by D-R model at various temperatures of 20–40 °C, (Cu (II) concentration=100 mg/l, initial pH=6, contact time=100 min)

The amount of E value is useful to determine the mechanism of the adsorption process. The E values between 8 and 16 kJ/mol indicate that chemical interaction is the mechanism of the adsorption. If the value of E is less than 1, physical absorption is the dominant mechanism [29]. The plot of ln (q_e) versus ε^2 is depicted in Figure 9. The D-R isotherm parameters are listed in Table 1. The E values obtained from D-R isotherm model showed that chemical adsorption is the dominant mechanism of the copper ions adsorption onto the CCGP.

3. 7. Adsorption Kinetics Adsorption kinetics was employed to investigate the diffusion of adsorbate into the adsorbent by measuring the adsorption uptake regarding the time at a constant concentration. In order to study the adsorption kinetics, the batch experiment was carried out at a pH of 6, a temperature of 40 °C and an adsorbent dosage of 5 g/l for 180 min (Figure 10a). PFO and PSO models were applied to study adsorption kinetics of Cu (II) by the adsorbent.

The PFO kinetic model for Cu (II) adsorption on the adsorbent was evaluated by incorporating the experimental adsorption data into the following equation [30]:

$$\log(q_e - q_t) = \log q_e - \frac{k.t}{2.303} \quad (10)$$

where q_e (mg/g) is the equilibrium amount Cu (II) adsorbed per unit mass of the adsorbent, and k (min^{-1}) is the PFO rate constant. The rate constant value, k, is determined from the linear plot (Figure 10b). The values of the PFO rate constant and the correlation coefficient were k = 0.042 min^{-1} and 0.882, respectively.

The differential equation of PSO kinetic model is represented as follows [31]:

$$\frac{dq_t}{dt} = K(q_e - q_t)^2 \quad (11)$$

TABLE 1. Isotherm specifications of the Freundlich and Langmuir models for the adsorption of Cu (II) ions on the CCGP

Isotherm models	Parameters	Temperature (ºC)		
		20	30	40
Langmuir	K_L (L/mg)	0.0145	0.0161	0.0214
	q_m (mg/g)	90.09	108.70	131.58
	R^2	0.968	0.954	0.976
Freundlich	K_F ((mg/g)/(mg/L)^n)	2.64	2.84	4.43
	n	1.47	1.35	1.39
	R^2	0.995	0.985	0.992
D-R	E (kJ/mol)	8.452	8.452	9.129
	R^2	0.995	0.989	0.994

PSO model can be written to linear form for the convenience of plotting and determining rate constant as following equation [32]:

$$\frac{t}{q_t} = \frac{1}{Kq_e^{\ 2}} + \frac{t}{q_e} \quad (12)$$

where q_t (mg/g) is the Cu (II) amount adsorbed per the mass of the adsorbent at a contact time of t (min). K (g mg^{-1} min^{-1}) represents the kinetic rate constant that depends on the conditions of the copper adsorption process on the adsorbent. The adsorption kinetics plot fitted by PSO is shown in Figure 10c. The PSO rate constant, k = 6.06×10^{-5} g mg^{-1} min^{-1} was determined from the linear plot with the correlation coefficient of0.983. Based on the results, for the absorption of copper ions onto CCGP, PSO kinetic model was more suitable than PFO model.

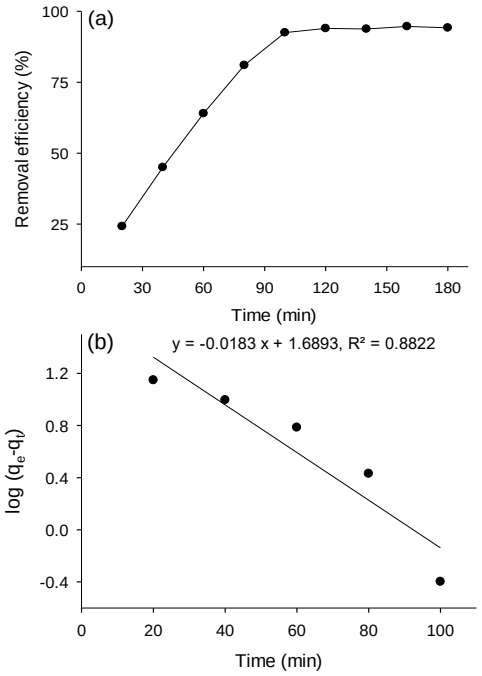

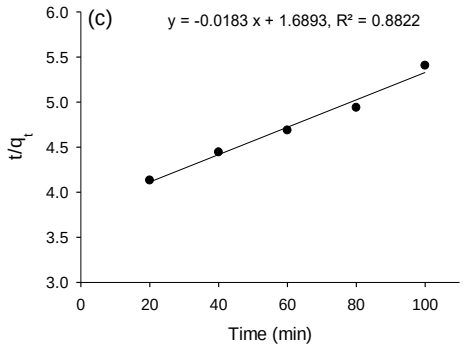

Figure 10. (a) Removal efficiency of Cu (II) (initial concentration = 100 mg/l, pH = 6, adsorbent dosage = 5 g/L, T = 40 °C, t = 180 min), (b) PFO kinetic model, and (c) PSO kinetic model for Cu (II) adsorption onto CCGP

3. 8. Regeneration and Reusability of the Adsorbent Regeneration and reusability of the CCGP saturated with copper ions was studied after five consecutive adsorption-desorption cycles. For each adsorption-desorption cycle, CCGP was soaked three times in succession in 0.5 ml HCl solution for 2 hours at 300 rpm. The CCGP was filtered and washed with double-distilled water after each soak. The adsorption experiments were done again using the regenerated CCGP at optimum conditions. After one cycle of adsorption-desorption, the efficiency of CCGP regeneration and the removal efficiency of Cu (II) ions were 97.7 and 90.4%, respectively. After five adsorption-desorption cycles, the regeneration efficiency and the removal efficiency were 81.7 and 75.6%, respectively. Results showed that CCGP has good performance for regeneration and reusability.

Adsorption of Cu (II) ions from aqueous solution using CCGP was investigated. Maximum adsorption capacity (mg of metal ion adsorbed per gram of adsorbent) of CCGP for Cu (II) ions was 131.58 mg g^{-1}. The results were compared with other adsorbents reported in literature (see Table 2). It can be seen that the synthesized CCGP had the highest potential to remove heavy metals from aqueous solutions.

TABLE 2. Comparison of the maximum adsorption capacities of CCGP with other adsorbents

Adsorbent	Maximum adsorption capacity, mg/g	Reference
Chlamydomonas microsphaera collected by polyaluminium chloride flocculation	79.4	[33]
Magnetic chitosan	104	[34]
Carboxylated cellulose cryogel beads crosslinked by maleic anhydride	84.12	[35]
Functionalized graphene nanosheets	103.22	[36]
Chitosan-modified magnetic Mn ferrite nanoparticles	65.1	[37]
Calcium alginate with encapsulated graphene oxide	60.2	[38]
Epichlorohydrin cross-linked xanthate chitosan	43.47	[39]
Powdered activated carbon-magnetite nanoparticles	23.61	[40]
Spherical polystyrene-supported chitosan	99.8	[41]
CCGP	131.58	This study

4. CONCLUSION

Preparation of an efficient adsorbent by grafting polyaniline onto cross-linked chitosan was reported in this paper. The synthesized composite material CCGP has a high specific surface area with different functional groups, such as amine and hydroxyl, which can enhance the adsorption capacity for heavy metals. The removal efficiency of Cu (II) was dependent on the contact time, initial pH, temperature, and adsorbent dosage. The experimental data were appropriately fitted to Freundlich isotherm model and PSO model with good correlation coefficients. It was concluded that the synthesized adsorbent can effectively remove the copper ions from aqueous solutions.

5. ACKNOWLEDGMENT

The authors wish to acknowledge Buein Zahra Technical University and the University of Mazandaran for the facilities provided to accomplish this research.

6. REFERENCES

1. Al-Saydeh, S.A., El-Naas, M.H. and Zaidi, S.J., "Copper removal from industrial wastewater: a comprehensive review", ***Journal of Industrial and Engineering Chemistry***, Vol. 56, (2017), 35-44. doi: 10.1016/j.jiec.2017.07.026
2. Karim, N., "Copper and human health-a review", ***Journal of Bahria University Medical & Dental College***, Vol. 8, No. 2, (2018), 117-122.
3. Krstić, V., Urošević, T. and Pešovski, B., "A review on adsorbents for treatment of water and wastewaters containing copper ions", ***Chemical Engineering Science***, Vol. 192, (2018), 273-287. doi: 10.1016/j.ces.2018.07.022
4. Mohamadi, S., Saeedi, M. and Mollahosseini, A., "Desorption kinetics of heavy metals (lead, zinc, and nickel) coexisted with phenanthrene from a natural high buffering soil", ***International Journal of Engineering***, Vol. 32, No. 12, (2019), 1716-1725. doi: 10.5829/IJE.2019.32.12C.04
5. Shahrin, S., Lau, W.J., Goh, P.S., Jaafar, J. and Ismail, A.F., "Adsorptive removal of Cr(VI) and Cu(II) ions from water solution using graphene oxide-manganese ferrite (Gmf) nanomaterials", ***International Journal of Engineering***, Vol. 31, No. 8, (2018), 1341-1346. doi: 10.5829/ije.2018.31.08b.24
6. Yao, Z.Y., Qi, J.H. and Wang, L.H., "Equilibrium, kinetic and thermodynamic studies on the biosorption of Cu (II) onto chestnut shell", ***Journal of Hazardous Materials***, Vol. 174, No. 1-3, (2010), 137-143. doi: 10.1016/j.jhazmat.2009.09.027
7. Peng, W., Li, H., Liu, Y. and Song, S., "A review on heavy metal ions adsorption from water by graphene oxide and its composites", ***Journal of Molecular Liquids***, Vol. 230, (2017), 496-504. doi: 10.1016/j.molliq.2017.01.064
8. Zhang, L., Zeng, Y. and Cheng, Z., "Removal of heavy metal ions using chitosan and modified chitosan: a review", ***Journal of Molecular Liquids***, Vol. 214, (2016), 175-191. doi: 10.1016/j.molliq.2015.12.013
9. Rolandi, M. and Rolandi, R., "Self-assembled chitin nanofibers and applications", ***Advances in Colloid and Interface Science***, Vol. 207, (2014), 216-222. doi: 10.1016/j.cis.2014.01.019
10. Roseman, S., Li, X. and Comb, D., "Conversion of chitin into N-acetylglucosamine, glucosamine and bioethanol", (2016), Google Patents.
11. Varalakshmi, V. and Mala, R., "Effect of herbal extract on antimicrobial susceptibility profile of drug resistant burn wound isolates", ***International Journal of Agriculture, Environment and Biotechnology***, Vol. 6, No. 4S, (2013), 815.
12. Fan, C., Li, K., He, Y., Wang, Y., Qian, X. and Jia, J., "Evaluation of magnetic chitosan beads for adsorption of heavy metal ions", ***Science of the Total Environment***, Vol. 627, (2018), 1396-1403. doi: 10.1016/j.scitotenv.2018.02.033
13. Gokila, S., Gomathi, T., Sudha, P. and Anil, S., "Removal of the heavy metal ion chromiuim (VI) using chitosan and alginate nanocomposites", ***International Journal of Biological Macromolecules***, Vol. 104, (2017), 1459-1468. doi: 10.1016/j.ijbiomac.2017.05.117
14. Abraham, A., Soloman, P. and Rejini, V., "Preparation of chitosan-polyvinyl alcohol blends and studies on thermal and mechanical properties", ***Procedia Technology***, Vol. 24, (2016), 741-748. doi: 10.1016/j.protcy.2016.05.206
15. Silina, N., Morozov, A., Gornostaeva, E., Smirnova, L. and Zaytsev, S., "Ultrasound-assisted synthesis of block copolymers of chitosan and D, L-lactide: structure and properties", ***Polymer Science, Series B***, Vol. 59, No. 5, (2017), 551-559. doi: 10.1134/S1560090417050116
16. Acharyulu, S.R., Gomathi, T. and Sudha, P., "Physico-chemical characterization of cross linked chitosan-polyacrylonitrile polymer blends", ***Der Pharmacia Lettre***, Vol. 5, No. 2, (2013), 354-363.
17. Mochalova, A. and Smirnova, L., "State of the art in the targeted modification of chitosan", ***Polymer Science, Series B***, Vol. 60, No. 2, (2018), 131-161. doi: 10.1134/S1560090418020045
18. Moussout, H., Ahlafi, H., Aazza, M. and Bourakhouadar, M., "Kinetics and mechanism of the thermal degradation of biopolymers chitin and chitosan using thermogravimetric analysis", ***Polymer Degradation and Stability***, Vol. 130, (2016), 1-9. doi: 10.1016/j.polymdegradstab.2016.05.016
19. Arumugam, T., Krishnamoorthy, P., Rajagopalan, N., Nanthini, S. and Vasudevan, D., "Removal of malachite green from aqueous solutions using a modified chitosan composite", ***International Journal of Biological Macromolecules***, Vol. 128, (2019), 655-664. doi: 10.1016/j.ijbiomac.2019.01.185
20. Pires, C.T., Vilela, J.A. and Airoldi, C., "The effect of chitin alkaline deacetylation at different condition on particle properties", ***Procedia Chem***, Vol. 9, (2014), 220-225. doi: 10.1016/j.proche.2014.05.026
21. Deng, J., Ding, X., Zhang, W., Peng, Y., Wang, J., Long, X., Li, P. and Chan, A.S., "Carbon nanotube–polyaniline hybrid materials", ***European Polymer Journal***, Vol. 38, No. 12, (2002), 2497-2501. doi: 10.1016/S0014-3057(02)00165-9
22. Zhang, H., Zhao, Q., Zhou, S., Liu, N., Wang, X., Li, J. and Wang, F., "Aqueous dispersed conducting polyaniline nanofibers: promising high specific capacity electrode materials for supercapacitor", ***Journal of Power Sources***, Vol. 196, No. 23, (2011), 10484-10489. doi: 10.1016/j.jpowsour.2011.08.066
23. Liu, W., Kumar, J., Tripathy, S., Senecal, K.J. and Samuelson, L., "Enzymatically synthesized conducting polyaniline", ***Journal of the American Chemical Society***, Vol. 121, No. 1, (1999), 71-78. doi: 10.1021/ja982270b

24. Langmuir, I., "The adsorption of gases on plane surfaces of glass, mica and platinum", ***Journal of the American Chemical society***, Vol. 40, No. 9, (1918), 1361-1403. doi: 10.1021/ja02242a004
25. Sasikala, S. and Muthuraman, G., "Removal of heavy metals from wastewater using tribulus terrestris herbal plants powder", ***Iranica Journal of Energy and Environment***, Vol. 7, No. 1, (2016), 39-47. doi: 10.5829/idosi.ijee.2016.07.01.06
26 Freundlich, H., "Over the adsorption in solution", ***The Journal of Physical Chemistry***, Vol. 57, (1906), 1100-1107.
27. Yavuz, A.G., Dincturk-Atalay, E., Uygun, A., Gode, F. and Aslan, E., "A comparison study of adsorption of Cr (VI) from aqueous solutions onto alkyl-substituted polyaniline/chitosan composites", ***Desalination***, Vol. 279, No. 1-3, (2011), 325-331. doi: 10.1016/j.desal.2011.06.034
28. Dubinin, M.M., Zaverina, E. and Radushkevich, L., "Sorption and structure of active carbons. I. adsorption of organic vapors", ***Zhurnal Fizicheskoi Khimii***, Vol. 21, No. 3, (1947), 151-162.
29. Sarı, A. and Tuzen, M., "Biosorption of cadmium (II) from aqueous solution by red algae (*Ceramium virgatum*): equilibrium, kinetic and thermodynamic studies", ***Journal of Hazardous Materials***, Vol. 157, No. 2-3, (2008), 448-454. doi: 10.1016/j.jhazmat.2008.01.008
30. Rodrigues, L.A., Maschio, L.J., da Silva, R.E. and da Silva, M.L.C.P., "Adsorption of Cr (VI) from aqueous solution by hydrous zirconium oxide", ***Journal of Hazardous Materials***, Vol. 173, No. 1-3, (2010), 630-636. doi: 10.1016/j.jhazmat.2009.08.131
31. Satapathy, M. and Das, P., "Assessment on the modelling of the kinetic parameter for the removal of crystal violet dye using Ag-soil nanocomposite: linear and non-linear analysis", ***Desalination and Water Treatment***, Vol. 57, No. 9, (2016), 4073-4080. doi: 10.1080/19443994.2014.987179
32. Gao, A., Xie, K., Song, X., Zhang, K. and Hou, A., "Removal of the heavy metal ions from aqueous solution using modified natural biomaterial membrane based on silk fibroin", ***Ecological Engineering***, Vol. 99, (2017), 343-348. doi: 10.1016/j.ecoleng.2016.11.008
33. Jiang, X., Zhou, X., Li, C., Wan, Z., Yao, L. and Gao, P., "Adsorption of copper by flocculated *Chlamydomonas microsphaera* microalgae and polyaluminium chloride in heavy metal-contaminated water", ***Journal of Applied Phycology***, Vol. 31, No. 2, (2019), 1143-1151. doi: 10.1007/s10811-018-1636-6
34. Zhang, S., Zhou, Y., Nie, W., Song, L. and Zhang, T., "Preparation of uniform magnetic chitosan microcapsules and their application in adsorbing copper ion (II) and chromium ion (III)", ***Industrial & Engineering Chemistry Research***, Vol. 51, No. 43, (2012), 14099-14106. doi: 10.1021/ie301942j
35. Tang, C., Brodie, P., Brunsting, M. and Tam, K.C., "Carboxylated cellulose cryogel beads via a one-step ester crosslinking of maleic anhydride for copper ions removal", ***Carbohydrate Polymers***, Vol. No. (2020), 116397. doi: 10.1016/j.carbpol.2020.116397
36. Cao, M.-l., Li, Y., Yin, H. and Shen, S., "Functionalized graphene nanosheets as absorbent for copper (II) removal from water", ***Ecotoxicology and Environmental Safety***, Vol. 173, No. (2019), 28-36. doi: 10.1016/j.ecoenv.2019.02.011
37. Meng, Y., Chen, D., Sun, Y., Jiao, D., Zeng, D. and Liu, Z., "Adsorption of Cu^{2+} ions using chitosan-modified magnetic Mn ferrite nanoparticles synthesized by microwave-assisted hydrothermal method", ***Applied Surface Science***, Vol. 324, No. (2015), 745-750. doi: 10.1016/j.apsusc.2014.11.028
38. Algothmi, W.M., Bandaru, N.M., Yu, Y., Shapter, J.G. and Ellis, A.V., "Alginate–graphene oxide hybrid gel beads: An efficient copper adsorbent material", ***Journal of Colloid and Interface Science***, Vol. 397, No. (2013), 32-38. doi: 10.1016/j.jcis.2013.01.051
39. Kannamba, B., Reddy, K.L. and AppaRao, B., "Removal of Cu (II) from aqueous solutions using chemically modified chitosan", ***Journal of Hazardous Materials***, Vol. 175, No. 1-3, (2010), 939-948. doi: 10.1016/j.jhazmat.2009.10.098
40. Shahrashoub, M. and Bakhtiari, S., "The efficiency of activated carbon/iron oxide nanoparticles composites in copper removal: Industrial waste recovery, green synthesis, characterization, and adsorption-desorption studies", ***Microporous and Mesoporous Materials***, Vol. No. (2020), 110692. doi: 10.1016/j.micromeso.2020.110692
41. Jiang, W., Chen, X., Pan, B., Zhang, Q., Teng, L., Chen, Y. and Liu, L., "Spherical polystyrene-supported chitosan thin film of fast kinetics and high capacity for copper removal", ***Journal of Hazardous Materials***, Vol. 276, No. (2014), 295-301. doi: 10.1016/j.jhazmat.2014.05.032

Persian Abstract

چکیده

جاذبی با کارایی بالا با استفاده از پیوند دادن پلی آنیلین به بیوپلیمر کیتوسان تولید شد. ساختار مورفولوژی کیتوسان متصل شده عرضی و پیونده زده شده با پلی آنیلین توسط میکروسکوپ الکترونی روبشی بررسی شد. گروه‌های عاملی جاذب سنتز شده با استفاده از طیف سنجی مادون قرمز تبدیل فوریه شناسایی شد. عملکرد جاذب تهیه شده برای حذف یون‌های مس از محلول آبی با استفاده از روش ناپیوسته مورد تحقیق قرار گرفت. مطالعات جذب به عنوان تابعی از زمان تماس، pH اولیه، دما و میزان جاذب انجام شد. جهت ارزیابی ایزوترم جذب، مدل‌های لانگمویر، فروندلیچ و دوبینین رادوشکویچ برای داده‌های آزمایشگاهی برازش شد و پارامترهای ایزوترم تعیین گردید. سینتیک جذب توسط مدل‌های شبه درجه اول و شبه درجه دوم مورد مطالعه قرار گرفت. مشاهده شد که داده‌های آزمایشگاهی با مدل شبه درجه دوم بهتر از مدل شبه درجه اول برازش می‌شود. در شرایط بهینه حداکثر ظرفیت جذب و حداکثر راندمان حذف جاذب برای جذب Cu (II) به ترتیب ۱۳۱/۵۸ میلی گرم بر گرم و ۹۲/۵ درصد به دست آمد. راندمان احیای جاذب و راندمان حذف برای جاذب احیا شده به ترتیب ۹۷/۷ و ۹۰/۴ درصد شد. نتایج نشان داد جاذب سنتز شده پتانسیل بالایی برای حذف یون‌های مس از محلول آبی دارد.

International Journal of Engineering

Journal Homepage: www.ije.ir

Analytical Stress Analysis in Single-lap Adhesive Joints under Buckling Loads

F. Marchione*

Dipartimento di Ingegneria Civile, Edile e Architettura (DICEA), Università Politecnica delle Marche, via B. Bianche, Ancona, Italy

P A P E R I N F O

Paper history:
Received 04 September 2020
Received in revised form 29 September 2020
Accepted 26 October 2020

Keywords:
Buckling Load
Single-lap Adhesive Joint
Adhesively Bonded Joints
Stress Distribution

A B S T R A C T

Adhesive joints find numerous applications in various industrial fields. They represent a valid alternative to traditional joining methods. Much of the available scientific literature has focused on the study of adhesive joints subjected to tensile loads. There have also been numerous studies concerning the stresses distributions in the adhesive layer. However, in real case applications, adhesive joints could also be subject to cyclic tensile-compression loads and therefore could be subject to buckling phenomena. The objective of the present paper is to investigate the numerical study of the stress distribution in the adhesive layer under buckling condition. The study presented develops with the analysis of a single-lap joint with a combination of steel adherends and three different structural adhesives with different thickness and Young's modulus. The joints are modeled using FE ANSYS©19 software. Through numerical analyzes, it is possible to predict the value of the critical load for each single analyzed combination. Once the critical load is determined, the stresses in the middle plane of the adhesive layer are determined. The results obtained show that for small adhesive thicknesses (i.e. 0.30 mm) it is possible to reduce the stress peaks - with the same critical load value - by using structural adhesives with low elastic modulus (e.g. silicones).

***doi**: 10.5829/ije.2021.34.02b.02*

NOMENCLATURE

EPX1	First epoxy adhesive	ρ	Density (kg/m^3)
EPX2	Second epoxy adhesive	ν	Poisson ratio
SIL	Silicone adhesive	E	Young Modulus

1. INTRODUCTION

Adhesive bonding nowadays represents a joining technique widely used in numerous applications [1-3] (e.g. automotive, naval, footwear and civil engineering applications). This type of joint provides considerable advantages over traditional joining techniques, such as a more uniform stresses distribution obtained without adding weight to the structure.

Among the most studied joints in the literature, there is the Single-lap joint (SLJ) [4-6]. Most studies focus on assessing its mechanical properties for shear and bending stresses.

Adams and Peppiatt's [7] studies were among the first in deepening the knowledge about the mechanical behaviour of the adhesive joint under tensile loads. The main result was that the stress distribution is characterized by stress peaks at the edges of the bonded region. Hamdan [8] analysed the effects of non-dimensional geometric parameters on stress concentration factors of circular hollow section brace-to-H-shaped section T-connections under axial compression. Rastegarian et al. [9] studied the dependency of structural performance level and its corresponding inter-story drift in conventional RC moment frames. Specimens were studied by pushover analysis and equations were proposed to predict inter-story drift. Rahman et al. [10] studied the improvement in stress distribution of flexible pavement due to the application of geo-jute at three specific positions. Results showed that the inclusion of geo-jute on flexible pavement significantly improves its mechanical

*Corresponding Author Institutional Email: f.marchione@pm.univpm.it (F. Marchione)

Please cite this article as: F. Marchione, Analytical Stress Analysis in Single-lap Adhesive Joints under Buckling Loads, International Journal of Engineering, Transactions B: Applications Vol. 34, No. 02, (2021) 313-318

performance. Ferdinand et al. [11] analysed the application of BRB in strengthening of RC frame structures to meet Chinese seismic design code. The results show that buckling restrained braces demonstrated better performance of strengthening the structure and make it meet the requirement of code. Haghollahi [12] presented a numerical study on the behavior of connection between steel I-beam and H-column affected by cyclic loading. The results showed that welded flange plate (WFP) connection which did not satisfy the criteria of AISC seismic provisions for special moment frames, can be upgraded by a vertical triangular rib plate in order to be used in special moment frames.

Mohammed et al. [13] presented a numerical analysis using FE method to investigate the effect of semi-rigid connections on post-buckling behaviour of two-dimensional frames with different supporting types and different lateral loading cases. Abdolvahab [14] investigated local buckling of sinusoidal corrugated plates under uniform uniaxial loading on the transverse edges of the plate using the Galerkin method. The results obtained for the critical buckling load of sinusoidal corrugated metal plates and the results relating to the metal homogeneous flat plates were compared using the same supporting conditions and loading. Selahi et al. [15] presented a solution for stress distribution using the energy method, considering the effect of adhesive thickness. Further studies [16] investigated a numerical 3D stress distribution in a composite single-lap adhesive joint, determining also the location of the damage initiation. Bai et al. [17] studied a method for interfacial stress analysis of composite single-lap joint based on full-field deformation. Li et al. [18] modeled a 2D FE analysis to determine the stress in the adhesive thickness of composite single-lap joints. The results showed that the stress peaks increase with adhesive thickness and Young's modulus.

Although numerous studies have been carried out on adhesive joints under tensile loads, those on other loading conditions are still relatively scarce. In fact, in several real applications, adhesive joints are subjected to different types of loads (e.g. bending, cyclical tensile and compression loads, pure compression). In the case of axial compression stresses, instability phenomena may occur. As with other structural elements, compression loads can lead to the buckling condition of the adhesive joint and then can cause its failure. This failure mode may lead to the failure of the structure for stress values much lower than the ones related to the characteristic strengths of the materials. The innovation of the present paper is that it focuses on the stress distribution in the SLJ taking into account the compression loads in buckling condition.

Holston [19] provided a closed-form solution for buckling loads based on potential energy for a rectangular composite plate. Kim and Kwon [20] determined a closed-form solution for one-edge-free composite plates under buckling loads.

Since the problem of instability is quite common in the various applications of structural adhesives, the study and verification of structural performance under axial load conditions is fundamental in the design phase. Figure 1 illustrates the research methodology.

The present paper focuses on different combinations of structural adhesives (i.e. two epoxy adhesives and a silicone) in a single-lap adhesive joint and their stress distribution as the thickness of the adhesive layer varies (0.30, 0.60, 1.00 mm) in the buckling load condition.

The following section reports on the materials and methods considered for the consequent FE analysis. In particular, all geometrical and physical characteristics of the joint are illustrated, as well as the FE analysis settings. The results obtained are detailed and discussed in the following.

2. FINITE ELEMENT ANALYSIS

A configuration of a typical single-lap joint, used as a model for the FE following analysis is depicted in Figure 2.

The dimensions of the adherends are 140×25×5 mm, representing its length, width and thickness, respectively. The bonding area is 25×25 mm; the thickness of the adhesives varies in relation to the configuration considered (0.30, 0.60 and 1.00 mm).

The same boundary conditions have been applied to all the configurations considered. The surfaces of the clamping areas on the adherends are shown in Figure 2. Tables. 1-2 show the mechanical properties of the materials and the adhesives considered.

A plane strain condition is used for FE analysis by specifying the width in the definition of the elements. The numerical modeling is carried out with the software ANSYS©19. The model is meshed with PLANE 182, a 4-node structural solid and a base element size of 0.10 mm. The analysed joints are made of S235JR steel adherends and different adhesives (two epoxies and one silicone).

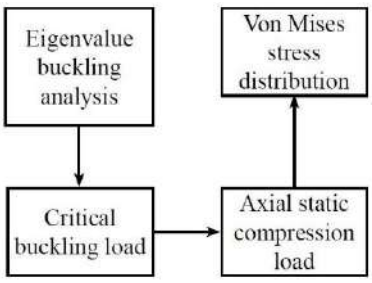

Figure 1. Research methodology

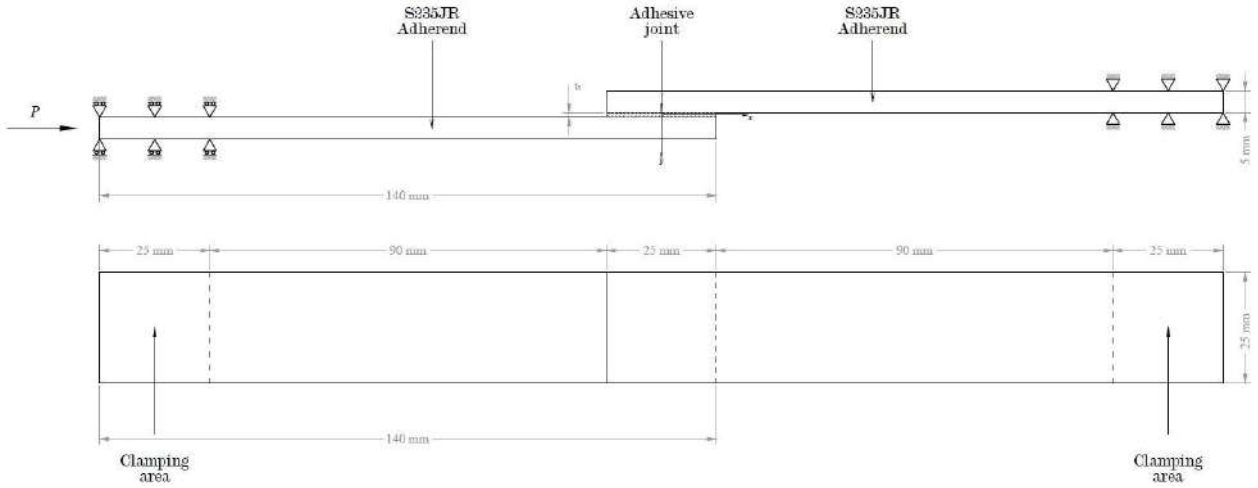

Figure 2. Geometry of Single lap adhesive joint: lateral and top view

The FE analysis here presented is a "Linear Eigenvalue Buckling Analysis" which returns the buckling load for the first buckling mode for each configuration. Once the buckling load is determined, the structure is axially statically loaded with the critical load in order to determine the stress distribution in the middle plane of the adhesive layer. The results are detailed in the following.

3. RESULTS AND DISCUSSION

This section reports on the buckling analysis of the single-lap adhesive joint illustrated in section 2.

TABLE 1. Materials' characteristics for the FEA model

STEEL S235JR		
E_t [GPa]	ρ [N/m^3]	$\boldsymbol{\nu}$ [-]
69	78000	0.30

TABLE 2. Adhesive's characteristics for the FEA model

EPX 1	
E [GPa]	$\boldsymbol{\nu}$ [-]
17.50	0.30
EPX 2	
E [GPa]	$\boldsymbol{\nu}$ [-]
3.25	0.40
SIL	
E [MPa]	$\boldsymbol{\nu}$ [-]
1.00	0.30

Different combinations of adhesives (i.e. epoxy and silicone adhesives) with various thicknesses (0.30 mm, 0.60 mm, 1.00 mm) are considered and analysed.
The eigenvalue analysis is carried out with the FE software ANSYS©19.

The buckling load condition, and hence its value is determined through the linear eigenvalue analysis. Once the critical load is known, the joint is statically loaded with the buckling load. Therefore, the stress distribution (Von Mises criterion) is determined along the adhesive layer midplane.

Figures 3-5 show the stress distribution obtained for each configuration. Figure 3 shows the stress distribution for EPX1 configuration: stresses values are almost constant and equal to the peaks for the adhesive thickness of 0.30 and 0.60 mm. It could be observed that the 1.00 mm thickness of the adhesive influences the stress distribution. In fact, it is characterized by two lower peaks at the edges of the bonding region and almost a parabolic trend in the middle area.

Figure 4 shows the stress distribution for EPX2 configuration: stresses values are almost constant for the first two configurations (0.30 and 0.60 mm adhesive thickness). Also in this case, it could be observed that the 1.00 mm thickness of the adhesive presents two peaks at the edges of the bonding region and almost a parabolic trend in the middle area. In this case, the highest stress peaks are observed in the 1.00 mm thick adhesive.

Figure 5 shows the stress distribution for SIL configuration: stresses values are very low if compared to other configurations (0.03 MPa) and almost constant for the first two thickness values. In this case, the 1.00 mm thick adhesive presents a higher stress value (0.61 MPa).

Tables 3-5 show the buckling load and stress peaks values obtained for each configuration. It could be

observed that every combination, except for SIL with 1.00 adhesive thickness, shows almost the same buckling load value (always between 813-854 N).

On the other hand, stress peaks are very different in relation to the adhesive considered. In fact, EPX 1 shows high values of stresses; EPX 2 shows lower values, almost half compared to the previous adhesive. SIL adhesive configurations show always very low-stress peaks values (between 0.03 and 0.61 MPa) since the adhesive is the less stiff among all the adhesives considered. In particular, considering the stress values, the first two SIL configurations are optimal since at the same buckling load they allow to reach very load value in the adhesive layer. This mechanical behaviour of the joint is due to the ductility typical of silicone adhesives.

The last configuration for SIL adhesive (1.00 adhesive thick) shows the effect of the adhesive thickness: buckling occurs for very low axial compressive load (8.36 N).

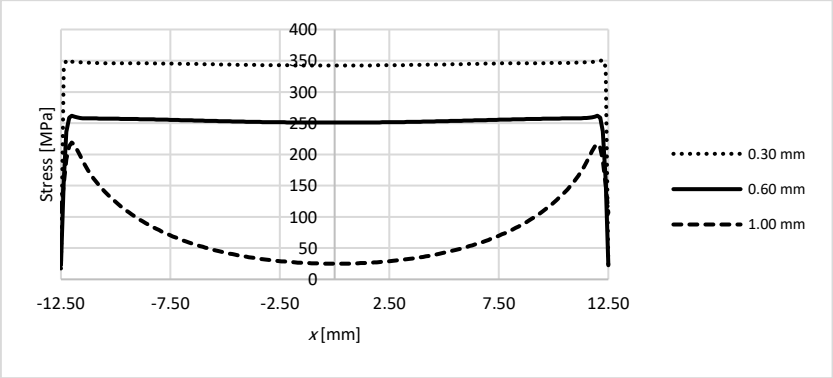

Figure 3. Stress distribution for EPX1 adhesive configurations

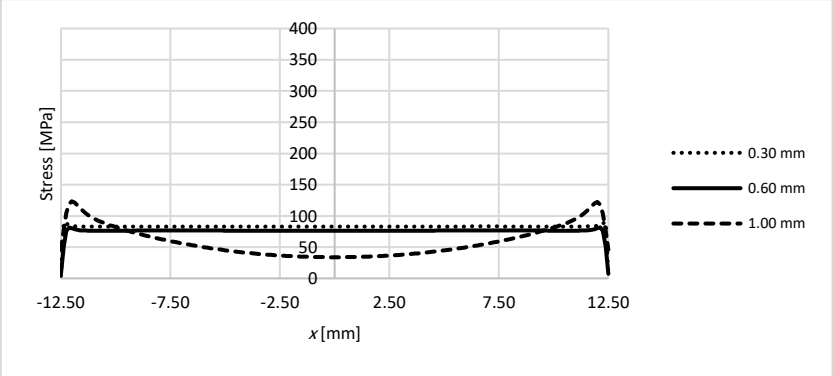

Figure 4. Stress distribution for EPX2 adhesive configurations

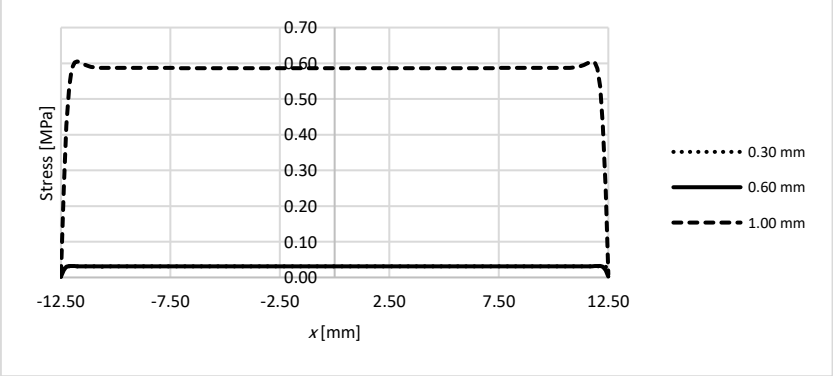

Figure 5. Stress distribution for silicone (SIL) adhesive configurations

TABLE 3. Buckling load and stress peaks – EPX1

Adhesive thickness [mm]	Buckling load [N]	Stress peak [MPa]
0.30	852.13	351.54
0.60	853.14	261.91
1.00	841.74	219.06

TABLE 4. Buckling load and stress peaks – EPX2

Adhesive thickness [mm]	Buckling load [N]	Stress peak [MPa]
0.30	850.97	90.30
0.60	851.29	81.65
1.00	813.50	123.45

TABLE 5. Buckling load and stress peaks - SIL

Adhesive thickness [mm]	Buckling load [N]	Stress peak [MPa]
0.30	850.57	0.03
0.60	850.56	0.03
1.00	8.36	0.61

4. CONCLUSIONS

The majority of the scientific literature about structural adhesives dealt with both numerical and experimental studies of adhesive joints subjected to tensile loads. Since in the real application cases adhesive joints could be subject also to compression loads, such as cyclic tensile-compression loading conditions, therefore the adhesive joints may undergo buckling.

This paper investigates the buckling phaenomena with a numerical study of the stress distribution in the adhesive layer under the buckling condition. In particular, a S235JR steel-steel single-lap joint is considered. In this study, three different adhesives with different mechanical and geometrical properties are analysed and compared. The study therefore deals with the influence of the thickness and stiffness of the adhesive on the global mechanical performance of the joint.

The main outcomes are:

- the adhesive thickness and stiffness influence the stress distribution and the buckling load value. In fact, the choice of an adhesive should consider these points to prevent undesired failure modes;
- the choice of a ductile adhesive (e.g. SIL adhesive) with an appropriate thickness could allow to provide the same mechanical performance of a more stiff adhesive (e.g. EPX2 or EPX1) with much lower stress distribution;
- the design phase of a structural element involving the use of structural adhesive should properly consider the buckling analysis (buckling load and stress distribution).

In conclusion, the study of the stability of the adhesive joint is necessary to predict the real behaviour of the structural system, in order to prevent premature failures.

The study of buckling phaenomena allows to provide the correct indications about the correct choice of the adhesive joint. This analysis allows to avoid sudden and undesired failure phenomena.

5. REFERENCES

1. Van Lancker, B., Dispersyn, J., De Corte, W. and Belis, J., "Durability of adhesive glass-metal connections for structural applications", ***Engineering Structures***, Vol. 126, (2016), 237-251. doi:10.1016/j.engstruct.2016.07.024
2. Hara, D. and Özgen, G.O., "Investigation of weight reduction of automotive body structures with the use of sandwich materials", ***Transportation Research Procedia***, Vol. 14, (2016), 1013-1020. doi:10.1016/j.trpro.2016.05.081
3. Vogelesang, L. and Vlot, A., "Development of fibre metal laminates for advanced aerospace structures", ***Journal of Materials Processing Technology***, Vol. 103, No. 1, (2000), 1-5. doi:10.1016/S0924-0136(00)00411-8
4. Ramezani, F., Ayatollahi, M., Akhavan-Safar, A. and da Silva, L., "A comprehensive experimental study on bi-adhesive single lap joints using dic technique", ***International Journal of Adhesion and Adhesives***, Vol. 102, (2020), 102674. doi:10.1016/j.ijadhadh.2020.102674
5. Demir, K., Bayramoglu, S. and Akpinar, S., "The fracture load analysis of different support patches in adhesively bonded single-lap joints", ***Theoretical and Applied Fracture Mechanics***, Vol. 108, (2020), 102653. doi:10.1016/j.tafmec.2020.102653
6. Kanani, A.Y., Hou, X. and Ye, J., "The influence of notching and mixed-adhesives at the bonding area on the strength and stress distribution of dissimilar single-lap joints", ***Composite Structures***, Vol. 241, (2020), 112136. doi:10.1016/j.compstruct.2020.112136
7. Adams, R. and Peppiatt, N., "Effect of poisson's ratio strains in adherends on stresses of an idealized lap joint", ***Journal of Strain Analysis***, Vol. 8, No. 2, (1973), 134-139. doi:10.1243/03093247V082134
8. Hamdan, A.I., "Stress concentration factors (scfs) in circular hollow section chs-to-h-shaped section welded t-joints under axial compression", ***Civil Engineering Journal***, Vol. 5, No. 1, (2019), 33-47. doi:10.28991/cej-2019-03091223
9. Rastegarian, S. and Sharifi, A., "An investigation on the correlation of inter-story drift and performance objectives in conventional rc frames", ***Emerging Science Journal***, Vol. 2, No. 3, (2018), 140-147. doi:10.28991/esj-2018-01137
10. Rahman, M.M., Saha, S., Hamdi, A.S.A. and Alam, M.J.B., "Development of 3-d finite element models for geo-jute reinforced flexible pavement", ***Civil Engineering Journal,*** Vol. 5, No. 2, (2019), 437-446. doi:10.28991/cej-2019-03091258

11. Ferdinand, N., Jianchang, Z., Qiangqiang, Y., Wang, G. and Junjie, X., "Research on application of buckling restrained braces in strengthening of concrete frame structures", ***Civil Engineering Journal***, Vol. 6, No. 2, (2020), 344-362. doi:10.28991/cej-2020-03091475
12. Haghollahi, A. and Ahmadi, H., "Cyclic behavior of steel beam-to-column moment connections using different sizes of flange plates and reinforced by a single rib plate", ***Civil Engineering Journal***, Vol. 4, No. 1, (2018), 138-150. doi:10.28991/cej-030975
13. Mohammed, D.R. and Ismael, M.A., "Effect of semi-rigid connection on post-buckling behaviour of frames using finite element method", ***Civil Engineering Journal***, Vol. 5, No. 7, (2019), 1619-1630. doi:10.28991/cej-2019-03091358
14. Abdolvahab, V., "Investigating the local buckling of rectangular corrugated plates", ***Civil Engineering Journal***, Vol. 2, No. 8, (2016), 389-397. doi:10.28991/cej-2016-00000043
15. Yousefsani, S.A., Tahani, M. and Selahi, E., "Analytical solution of stress field in adhesively bonded composite single-lap joints under mechanical loadings", ***International Journal of Engineering***, Vol. 27, No. 3, (2014), 475-486. doi:10.5829/idosi.ije.2014.27.03c.16
16. Behera, R.K., Parida, S. and Das, R., "3-d interfacial stress analysis of adhesively bonded curved laminated frp composite single lap joint", ***Materials Today: Proceedings***, Vol. 26, (2020), 1948-1952. doi:10.1016/j.matpr.2020.02.426
17. Bai, R., Bao, S., Lei, Z., Yan, C. and Han, X., "Finite element inversion method for interfacial stress analysis of composite single-lap adhesively bonded joint based on full-field deformation", ***International Journal of Adhesion and Adhesives***, Vol. 81, (2018), 48-55. doi:10.1016/j.ijadhadh.2017.11.011
18. Li, G., Lee-Sullivan, P. and Thring, R.W., "Nonlinear finite element analysis of stress and strain distributions across the adhesive thickness in composite single-lap joints", ***Composite Structures***, Vol. 46, No. 4, (1999), 395-403. doi:10.1016/S0263-8223(99)00106-3
19. Holston Jr, A., "Buckling of orthotropic plates with one free edge", ***AIAA Journal***, Vol. 8, No. 7, (1970), 1352-1354. doi:10.2514/3.5900
20. Kim, H. and Kwon, H., "Buckling of composite flanges in partially disbonded adhesive joints", ***Journal of Composite Materials***, Vol. 38, No. 24, (2004), 2213-2230. doi:10.1177/0021998304045592

Persian Abstract

اتصالات چسبنده کاربردهای بی شماری را در زمینه های مختلف صنعتی پیدا می کنند .آنها جایگزین معتبری برای روشهای پیوستن سنتی هستند .بیشتر ادبیات علمی موجود به مطالعه اتصالات چسبی تحت بارهای کششی متمرکز شده است .همچنین مطالعات زیادی در مورد توزیع تنش در لایه چسب انجام شده است .با این حال ، در موارد واقعی ، اتصالات چسبنده نیز می توانند تحت فشارهای فشاری کششی حلقوی قرار گیرند و بنابراین می توانند تحت پدیده های کمانش قرار بگیرند .در این مقاله مطالعه عددی توزیع تنش در لایه چسب تحت شرایط کمانش بررسی می شود .به طور خاص ، یک اتصال تک دور با ترکیبی از چسبنده های فولادی و سه چسب ساختاری با ضخامت و مدول مختلف یانگ در نظر گرفته می شود .مفاصل با استفاده از نرم افزار FE ANSYS © 19 مدل سازی شدند .از طریق تجزیه و تحلیل عددی ، پیش بینی مقدار بار بحرانی برای هر ترکیب تجزیه و تحلیل شده واحد امکان پذیر بود .پس از تعیین بار بحرانی ، تنش ها در صفحه میانی لایه چسب تعیین شد .می توان مشاهده کرد که برای ضخامت های کوچک چسب) یعنی 0.30 میلی متر (می توان با استفاده از چسب های ساختاری با مدول الاستیک کم) به عنوان مثال سیلیکون ها (، قله های تنش را کاهش داد - با همان مقدار بار بحرانی.

International Journal of Engineering

Journal Homepage: www.ije.ir

Essential Improvements in Gypsum Mortar Characteristics

M. Hashempour*[a], A. Asaad Samani[b], A. Heidari[c]

[a] *Department of Civil and Environmental Engineering, Amirkabir University of Technology, Tehran, Iran*
[b] *Department of Civil Engineering, University of Qom, Qom, Iran*
[c] *Department of Civil Engineering, Shahrekord University, Shahrekord, Iran*

PAPER INFO

Paper history:
Received 02 October 2020
Received in revised form 29 October 2020
Accepted 04 November 2020

Keywords:
Cement
Compressive Strength
Gypsum
Mortar
Nano Silica
Water Absorption

ABSTRACT

Gypsum mortar is a common building material that can be used especially for plastering the walls. This mortar has three important weaknesses which can limit the gypsum mortar for building and statue construction. First; it has low compressive strength. Second; it has high water absorption, and third; it has low setting time. In the current study, cement, Nano silica, and a superplasticizer with polycarboxylate ether were used for solving the problems. The results showed that using cement with providing C-S-H can improve the mortar strength trend line. The results showed significant growth of 28th day compressive strength (from 9 MPa to 45 MPa). Using Nano silica increases the compressive strength by making C-S-H dense and decreases the water absorption to 1/3 of the control sample. Consuming polycarboxylate ether causes the uniform dispersion of Nanoparticles through mortar. This even diffusion blocks the pores and reduces their mean dimensions. The ANOVA test was used to find the main effective parameters on the 28th day compressive strength, water absorption, and setting time. In this regard, Nano silica (49.82% contribution), cement content (56.68% contribution), and superplasticizer (73.10% contribution) have the main roles in compressive strength, water absorption, and setting time, respectively.

doi: *10.5829/ije.2021.34.02b.03*

NOMENCLATURE

Subscripts			
C	Abbreviation of cement	*MS*	Mean squares
P	Plasticizer	*DF*	Degree of freedom
N	Nano silica	*PCS*	Polycarboxylate ether superplasticizer
W	Water	*SEM*	Scanning electron microscopy
SS	Sum of squares	*TEM*	Transmission electron microscopy

1. INTRODUCTION

Mortars are the main building materials [1, 2] consisting of cement, water, gypsum, additives, etc. [3, 4]. Gypsum mortar with a special function in the building industry has its users [4]. Working with this material has its intricacy and delicate. So, it needs special skills and tricks. It is used to cover different surfaces and make them decorative. Researchers have investigated many methods or additives to provide a more stable mortar. For example, Morsy et al. [5] investigated the properties of a cementless mortar. They used gypsum with different percentages. Their results indicated that gypsum's addition in a certain amount had a remarkable effect on flexural and compressive strengths. In another study, removing cement was conducted using Flyash, Nano silica, and glass powder. This work enhances the mechanical properties and can help prevent the CO_2 from releases to the atmosphere [6]. In another case, Alexandra et al. [7] studied interactions between the hydration of alite and gypsum in cement compounds. They concluded that the interaction of gypsum with

*Corresponding Author Institutional Email: m.hashempour@aut.ac.ir (M. Hashempour)

Please cite this article as: M. Hashempour, A. Asaad Samani, A. Heidari, Essential Improvements in Gypsum Mortar Characteristics, International Journal of Engineering, Transactions B: Applications, Vol. 34, No.2, (2021) 319-325

Aluminium accelerates the reaction of alite. In fact, gypsum has a positive effect on the composition of cement.

Naik et al. [8] replaced Fly Ash with conventional bricks. These bricks used cement and gypsum in their composition. This new brick can be used for constructing low-cost houses in the vicinity of the thermal power plant. Taha et al. [9] produced a new natural building material consisting of soil, cement, gypsum, and straw fibers. Their product can decrease the thermal conductivity; increasing fiber, cement, and gypsum are the reason for this phenomenon. They also demonstrated that barley straw fiber-reinforced bricks could have the highest values of thermal insulation. Frank et al. [10] evaluated gypsum's effects on the hydration of calcium sulfoaluminate cement. In this research, the amount of anhydrite was replaced by gypsum. Eventually, they found that the replacement of a part of the anhydrite by gypsum can improve hydration kinetics and compressive strength of mortar. Jeong et al. [11] examined the effectiveness of different gypsum and water quantity on the strength of the cement paste consisting of calcium sulfoaluminate belite. The results showed that the amount of gypsum controls the hydration of ye' elimite and belite in the cement composition. In another study conducted by Magdalena et al. [12], the rheology of gypsum compounds at high temperatures was investigated. In this study, the results demonstrated that pure gypsum has significant resistance at high temperatures. During a research Fernandez et al. [13] added nano-silica (NSI) and polycarboxylate ether superplasticizer (PCS) to aerial lime mortars. The addition of PCS could enhance the flowability of lime mortar. Besides, the setting time accelerated. The existence of either NSI or PCS in lime mortar can improve mechanical strengths. As a result of combining two materials, the microstructural of lime mortar modified and leads to the optimized mix design. Suleyman et al. [14] implemented the production of the mix design with polycarboxylate ether. It was proved that polycarboxylate ether with main chain length has specific actions on compressive strength, ultrasonic pulse velocity, and water absorption capacity. The results also indicated that the increase in main chain length can improve the mixtures' time-dependent flow performance. Changes in length also have significant effects on adsorption behavior. In another research conducted by Shengnan et al. [15], the chemical structure of polycarboxylate superplasticizer (PCS) in cement-based materials was investigated. The main chain length of PCS provides procrastination for the hydration of cement. Gypsum mortars have many defects that limited their functions. Low strength and setting time besides high water absorption are their main weaknesses. The authors' searches showed that enough efforts to improve the gypsum mortar characteristics have not been made. In this regard, with the combination of white cement, polycarboxylate ether, and nano silica, some successful attempts were made. "The current study is organized into three main sections. Section (2) is designated the experimental program described as materials, mix design, and test procedures. Section (3) is the result and discussion which discussed the achievements and mechanical and statistical results."

2. EXPERIMENTAL PROGRAM

Four main tests such as compressive strength, water absorption, setting time, and scanning electron microscope (SEM), were done for evaluating the mechanical properties of the Gypsum mortar. Also, for finding the main significant parameter, the ANOVA test was done by XLSTAT V. 2016. The details of the experimental program are as follows.

2. 1. Materials Introduction For producing the mortar, gypsum, white cement, superplasticizer, water, and nano silica were used. The gypsum was from the Semnan gypsum factory by the Aeineh trademark. After transferring gypsum stone to the factory, it crushed and entered the cooking kiln for about one hour. Then, it has been grinded as special particle sizes. Cement was manufactured by the Semnan cement factory. The superplasticizer was Polycarboxylate Ether from LG (White Damavand) factory. It has a light brown color, less than 0.01 chloride ion, pH of 7, and 1.08 density. It is necessary to use a kind of water that has no harmful material for mortar making. In this regard, the potable water of Shahrekord was used. Silicon oxide nanoparticles were Aerosil®200 with white color, 200 m^2/g specific surface area, purity of +99%, and 11-13nm particle dimension. Figure 1 shows the TEM of utilized nano SiO_2.

2. 2. Mix Design First gypsum and cement were mixed by 50:50 ratios for 3 minutes in a 5L drum. After making a solution with superplasticizer (1% and 1.5% of the total weight of mixture), water, and nano silica (0.5, 0.75, and 1% of cement weight) was added. The stirring of solution continued until complete dispersion of

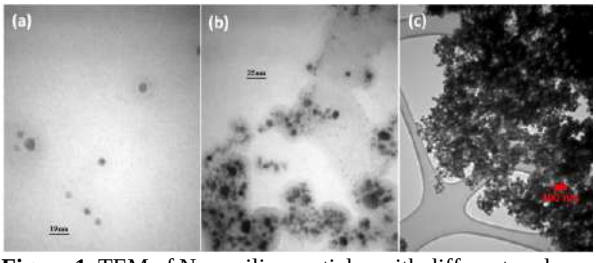

Figure 1. TEM of Nano silica particles with different scales; a) 19 nm, b) 35nm, c)100nm

particles in it. The solution poured into the drum. The mixing procedure was sustained for 5 minutes with average speed. It should be noted that the three end minutes were done by the higher speed of the drum. Table 1 shows the mix design of the current study, and the methodology is as Figure 2. It is important to save a sequence. First, the desirable flowability should be seen. After gaining a sample with enough setting time, the other steps, such as compressive strength and water absorption, can be done. Finally, samples with the highest compressive strength will be the gypsum mortar, problem solvers. Table 1 summarized, C the abbreviation of cement, N is used as nano silica, and P is the plasticizer. For compressive strength, water absorption 5 cm cubic molds were poured by mortar. The molds were opened after 1st, 7th, and 28th days after water curing at 25°C (ASTM C 109). The setting time test was done on the first day of mortar production. Section 2.3 explains the experimental test procedures.

2. 3. Test Procedures

2. 3. 1. Compressive Strength After curing, samples were broken by using a 2000 KN underload hydraulic jack. Since the samples had relatively small dimensions, they were stand in the special flexible encasement. With increasing the load, the case's ceil is coming down and distributing the uniform pressure in each direction. The samples were broken after 1st, 7th, and 28th days.

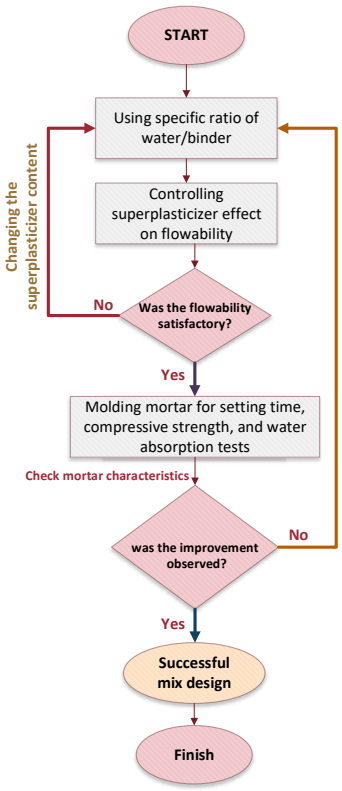

Figure 2. Methodology flowchart

TABLE 1. Mix design

Mix label	Nano SiO_2* (%)	Superplasticizer* (%)	W/C
C5P1	0	1	0.4
C5P1.5	0	1.5	0.4
C5P1N0.5	0.5	1	0.5
C5P1N0.75	0.75	1	0.5
C5P1N1.0	1	1	0.5
C5P1.5N0.5	0.5	1.5	0.5
C5P1.5N0.75	0.75	1.5	0.5
C5P1.5N1.0	1	1.5	0.5

*weight ratio of cement

2. 3. 2. Water Absorption The water absorption test was implemented after 28 days of curing. Based on ASTM C 642, the saturated surface dry (SSD) samples were weighed. Then samples were kept in an oven for 24 h at 110 ± 5ºC. Finally, samples were weighed again.

2. 3. 3. Setting Time The test was done based on ASTM C 191 by Vicat needle experiment. In this regard, a needle with 1.13 mm diameter and 300g weight was released on the mortar surface during some special periods (Figure 3, shows the Vicat instrument). The ruler instrument measured penetration. The initial and final time of the setting was measured to determine the hardening time of the mortar.

2. 3. 4. Scanning Electron Microscope (SEM) SEM was conducted by AIS 2100 from Seron

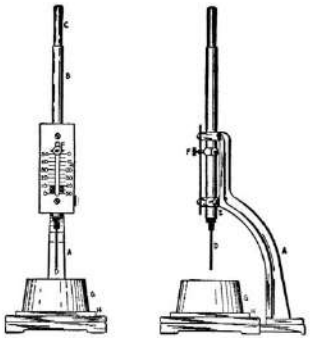

Figure 3. Vicat instrument (ASTM C 191); A) frame, B) movable rod, C) plunger end, D) removable steel needle, E) setscrew, F) adjustable indicator, G) cone frustum as mortar holder, H) glass slide

technology. For preparing samples first, a section was taken out from the 28th day crushed specimen after breaking by a hydraulic jack. It was sieved through a 125 µm mesh and prepared for gold coating. Pictures were detected with 1 and 10 µm scales.

3. RESULTS AND DISCUSSION

3. 1. Compressive Strength Figure 4, illustrates the compressive strength test results. After adding cement with 50% of the mortar's total weight, the compressive strength shows the improvement trend, especially after 28 days. Subsequently adding the Nano silica particles to the mortar, the compressive strength improves significantly.

For example, C5P1.5N1 (with 42MPa) compared to the control sample (with 7.2 MPa) proves the new mix design's good performance. Using cement provides an opportunity for strength progresses. So as time passes and cement hydration completion, the mortar microstructure becomes denser [16]. The development of C-S-H is the main reason for strength enhancement. Nanomaterials have various behavior. In almost all of them, they can fill the nanopores of mortar or cement, decrease the porosity, and develop the strength. But nano silica with a silicate base can improve the C-S-H purity and make it denser [17]. It is interesting to pay attention to the C5P1N0.75 and C5P1N1 strength differences with C5P1.5N0.75 and C5P1.5N1. The superplasticizer with polycarboxylate Ether base provides a particular property. It is clear that by rises the Nanoparticles, the water demand increases [18, 19]. Providing higher amounts of water can prevent gaining strength by causes the pores due to the higher W/C ratio. So superplasticizer maintains the workability and reduces the need for water [20]. The longer chain of polycarboxylate can increase the hydration level. Moreover, it disperses nanoparticles uniformly through mortar. This uniform diffusion blocks the pores and reduces their mean dimensions [13]. Doleželová et al. [21] improved the strength of the mortar by using slag. Slag can increase strength, but it raises the weight significantly. Nano silica has a superior effect. It enhances the strength and does not change the weight of samples. It is worth attention that micro-silica (silica fume) can not provide acceptable strength results compared to nano silica [22].

3. 2. Water Absorption Figure 5 shows that the control sample has the highest water absorption rate (approximately 27%). Based on what Krejsová et al. [23] showed, the high water absorption is due to large, primarily pores of gypsum (1µ-3µm). The gypsum, without any processing, can absorb water and moisture from the air. So for humid countries, the gypsum should not be used as plasters or other products. Since it absorbs water, expands, and collapses.

In some situations, it shows the yellow stain and becomes dirty. In this regard, a distinctive process should be done. Using cement reduces the water absorption to around 20%. It is not satisfactory. The water absorption index is high enough to cause the gypsum crash. Using silicate Nanoparticles as additive besides polycarboxylate ether can solve this problem. Nanoparticles fill the pores, help the generation of C-S-H [23], and increase the mortar density. Nevertheless, they have a high specific area that can grow water demand and negatively affect mortar water absorption. Using polycarboxylate can inhibit the water addition and make W/C constant [24]. Besides, it disperses nano SiO_2 through cement particles and makes an agglomeration by bonding bridges between them [13, 14, 25]. Figure 6 shows the polycarboxylate effects on dispersion and bonding of cement and Nanoparticles. A sample such as C5P1N1 has 10% water absorption, nearly 1/3 of gypsum mortar absorption (Control sample).

3. 3. Setting Time Figure 7 shows the results of the final setting time by the Vicat experiment. For gypsum mortar without any processing, the setting time happens immediately (5 min). This prevents amateur workers from appropriate working with gypsum. Adding

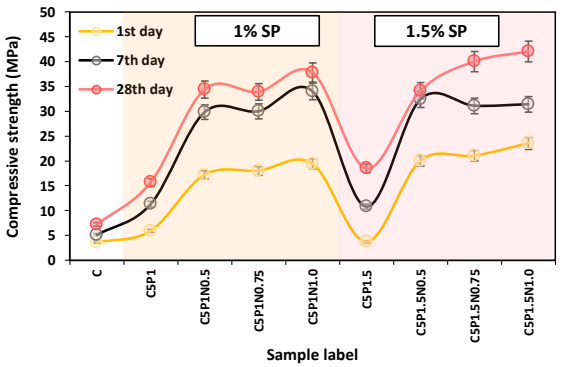

Figure 4. Compressive strength of samples

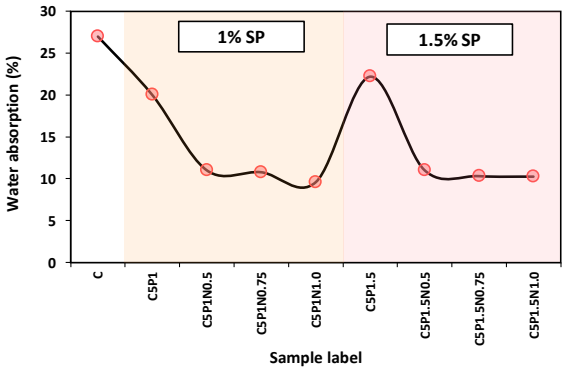

Figure 5. Water absorption of samples

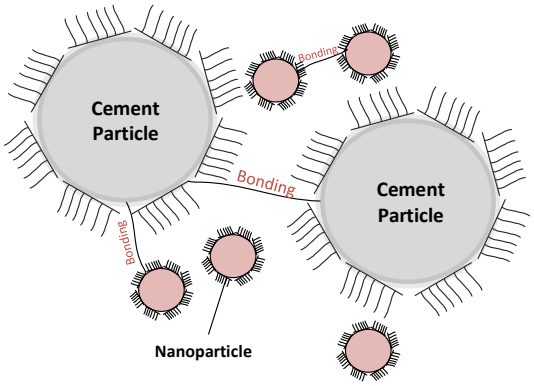

Figure 6. Long chains and bonding bridges in processed gypsum mortar with Nanoparticles, cement, and polycarboxylate ether

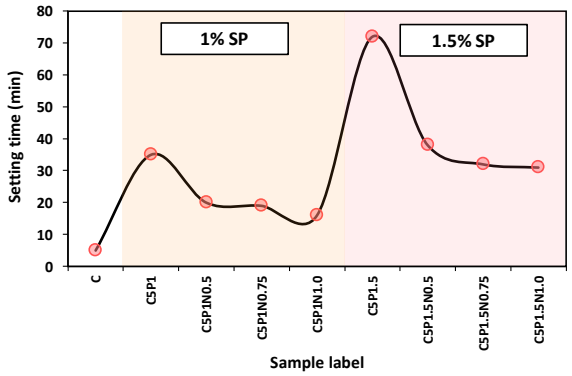

Figure 7. Results of setting time of gypsum mortar

superplasticizer causes a longer time of setting. Increasing the superplasticizer from 1 to 1.5% makes mortar retarder. For example, C5P1.5N0.5 need 70 minutes for the setting. It is ideal for the sculptors and plastering of walls.

It should be noted that using Nano silicate with a high specific area can cause lowering the setting time. So for controlling the hardening of mortar and providing flowability, adjusting the superplasticizer content is necessary.

3.4. SEM Analysis As evident in Figure 8, the mortar has a homogenous and dense shape (a), and C-S-H can be obvious by flat hexagonal shape (b). The presence of pseudohexagonal, flat surfaces, and blade shapes are evidence of gypsum crystals (c). They were also detected at [26].

3.5. ANOVA

3. 5. 1. ANOVA for 28th Day Compressive Strength For providing a better index of finding the most influential parameter on mortar strength, the ANOVA test was utilized. With a dataset of some samples with different cement and superplasticizer contents, the ANOVA was done. Table 2 shows the degree of freedom (DF), Sum of squares (SS), Mean squares (MS), and contribution of each parameter on compressive strength.

As expected, Nano silica, with an approximate 50% contribution, has the leading role on 28th day compressive strength. Although, the effects of cement content on mortar strength property can not be ignored. The superplasticizer, with a 1.2% contribution, has no significant effects on mortar strength characteristics.

3. 5. 2. ANOVA for Water Absorption The ANOVA test for a setting time showed that cement content with about 57% contribution has the most crucial part in the mortar's water absorption behavior. Table 3 demonstrates the ANOVA results for water absorption effective parameters. Besides, superplasticizer with nearly under 1% contribution, has no active role. So for adjusting the gypsum mortar water absorption paying attention to cement content is crucial.

3. 5. 3. ANOVA for Final Setting Time The ANOVA test also was used for setting time. With a dataset of some samples with different cement and superplasticizer contents, the ANOVA was done. Table 4 shows the contribution of each parameter in the final setting time.

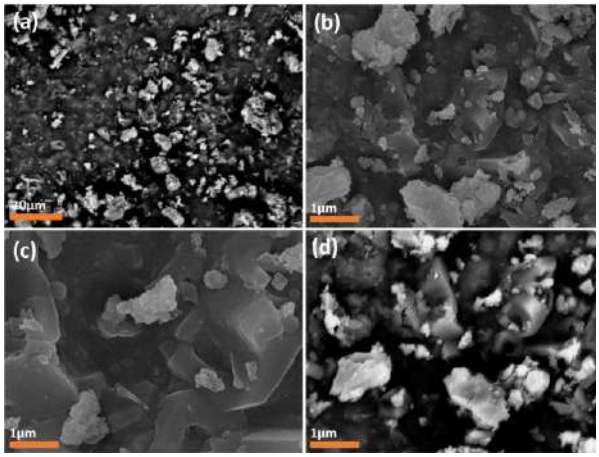

Figure 8. SEM analysis of gypsum mortar (C50S1.5N1 sample)

TABLE 2. ANOVA for 28th day compressive strength

Source	DF	SS	MS	contribution (%)
Cement	4	574.13	143.534	46.210
Nano silica	3	619.01	206.338	49.822
Superplasticizer	2	15.42	7.7130	1.241
Error	8	33.87	4.234	2.726
Total	17	1242.44	361.820	100

TABLE 3. ANOVA for water absorption

Source	DF	SS	MS	contribution (%)
Cement	1	342.60	342.60	56.68
Nano silica	1	228.49	228.49	37.80
Superplasticizer	1	0.81	0.81	0.13
Error	14	32.56	2.32	5.39
Total	17	604.47	574.23	100

TABLE 4. ANOVA for final setting time

Source	DF	SS	MS	contribution (%)
Cement	4	681.29	170.323	8.90
Nano silica	3	544.37	181.458	7.11
Superplasticizer	2	5597.0	2798.508	73.10
Error	8	833.81	104.227	10.89
Total	17	7656.5	3254.516	100

With an approximate 73% contribution, superplasticizer was the most influential parameter in setting time. This verifies the experimental results (section 3.3).

4. CONCLUSION

Gypsum mortar is a common building material that can mostly be used for plastering the walls. This mortar has three important weaknesses, which can limit the gypsum mortar for building and statue construction. First, it has a low compressive strength. Second, it has high water absorption, and third, it has a short setting time. In the current study, the authors focus on solving the mentioned problems. In this regard, cement, Nano silica, and a superplasticizer with polycarboxylate ether base have been chosen. The results of mechanical tests are as follows:

- The compressive strength with using white cement shows the improvement trend. Cement generates tobermorite and changes the microstructure of mortar. Then, C-S-H by traping the gypsum crystals can increase the density. It is the main reason for reaching 45MPa (C50P1.5N1) from 9 MPa (Control sample).
- Adding Nano silica increases the compressive strength by making C-S-H dense. It reduces the capillary pores and the water absorption to 1/3 of the control sample. For C5P1.5N1, the water absorption showed about 10%, nearly 1/3 of the control sample water absorption.
- Using polycarboxylate ether causes the uniform dispersion of Nanoparticles through mortar. This even diffusion blocks the pores and reduces their mean dimensions.
- The results also proved that polycarboxylate ether increases the setting time without extra water to the mixture. So it can help the compressive strength and water absorption properties by keeping the W/C ratio constant.
- The samples with 1.5% superplasticizer have longer setting times. C5P1.5, with about 70 min, is the most retarder sample.
- Using Nanosilica with a high specific area can develop the C-S-H and reduce the setting time. So for Nano modified samples such as C5P1.5N1 (30 min), although the setting time reduced from 70 to 30 min, it is acceptable compared to the control sample with about 5 min.
- SEM pictures showed the C-S-H hexagonal microstructures, which are dispersed through mortar. Also, they showed pseudohexagonal, flat surfaces, and bladed shapes of gypsum crystals. In these pictures, the ettringite did not detect.
- The results of ANOVA for finding the main effective parameter on 28th day compressive strength showed that Nano silica has the leading role in compressive strength (49.82% contribution) and cement content (46.21% contribution) has the second important character on mortar strength property.
- The contribution of cement, Nano silica, and superplasticizer proved that cement content (56.68% contribution) significantly affected mortar water absorption. The superplasticizer with about under 1% contribution has not active participation in water absorption of mortar.
- ANOVA also proved that superplasticizer (73.10% contribution) is the most influential parameter on mortar setting time, and Nano silica can not play a major role in it (7.11% contribution).

5. REFERENCES

1. Heidari, A., Hashempour, M., Javdanian, H. and Nilforoushan, M.R., "The effects of reactive mgo on the mechanical properties of rock flour mortar", ***Iranian Journal of Science and Technology, Transactions of Civil Engineering***, Vol. 43, No. 3, (2019), 589-598. doi: 10.1007/s40996-018-0204-2.
2. Heidari, A., Hashempour, M., Javdanian, H. and Karimian, M., "Investigation of mechanical properties of mortar with mixed recycled aggregates", ***Asian Journal of Civil Engineering***, Vol., No., (2018). doi: 10.1007/s42107-018-0044-1.
3. Chikouche Hamina, M. and Naceri, A., "Effects of pozzolanic admixture (waste bricks) on mechanical response of mortar", ***International Journal of Engineering, Transactions B: Applications,*** Vol. 21, No. 1, (2008), 1-8.
4. Fakhri, B., Sadr Karimi, J. and Kiyani, M., "Gypsum dissolution effects on the performance of a large dam (technical note)", ***International Journal of Engineering, Transactions B: Applications***, Vol. 21, No. 2, (2008), 143-150.

5. Morsy, M., Alsayed, S. and Salloum, Y., "Development of eco-friendly binder using metakaolin-fly ash–lime-anhydrous gypsum", ***Construction and Building Materials***, Vol. 35, No., (2012), 772-777. doi: https://doi.org/10.1016/j.conbuildmat.2012.04.142.
6. Jawad, Z., Ghayyib, R. and Salman, A., "Microstructural and compressive strength analysis for cement mortar with industrial waste materials", ***Civil Engineering Journal***, Vol. 6, No. 5, (2020). doi: 10.28991/cej-2020-03091524.
7. Quennoz, A. and Scrivener, K.L., "Interactions between alite and c3a-gypsum hydrations in model cements", ***Cement and Concrete Research***, Vol. 44, No., (2013), 46-54. doi: https://doi.org/10.1016/j.cemconres.2012.10.018.
8. Naik, N., Bahadure, B. and Jejurkar, C., "Strength and durability of fly ash, cement and gypsum bricks", ***International Journal of Computational Engineering Research***, Vol. 4, No. 5, (2014), 48-51.
9. Ashour, T., Korjenic, A., Korjenic, S. and Wu, W., "Thermal conductivity of unfired earth bricks reinforced by agricultural wastes with cement and gypsum", ***Energy and Buildings***, Vol. 104, (2015), 139-146. doi: https://doi.org/10.1016/j.enbuild.2015.07.016
10. Winnefeld, F., Martin, L.H.J., Müller, C.J. and Lothenbach, B., "Using gypsum to control hydration kinetics of csa cements", ***Construction and Building Materials***, Vol. 155, No., (2017), 154-163. doi: https://doi.org/10.1016/j.conbuildmat.2017.07.217.
11. Jeong, Y., Hargis, C.W., Chun, S.-C. and Moon, J., "The effect of water and gypsum content on strätlingite formation in calcium sulfoaluminate-belite cement pastes", ***Construction and Building Materials***, Vol. 166, (2018), 712-722. doi: https://doi.org/10.1016/j.conbuildmat.2018.01.153.
12. Doleželová, M., Scheinherrová, L., Krejsová, J. and Vimmrová, A., "Effect of high temperatures on gypsum-based composites", ***Construction and Building Materials***, Vol. 168, (2018), 82-90. doi: https://doi.org/10.1016/j.conbuildmat.2018.02.101.
13. Fernández, J.M., Duran, A., Navarro-Blasco, I., Lanas, J., Sirera, R. and Alvarez, J.I., "Influence of nanosilica and a polycarboxylate ether superplasticizer on the performance of lime mortars", ***Cement and Concrete Research***, Vol. 43, (2013), 12-24. doi: https://doi.org/10.1016/j.cemconres.2012.10.007.
14. Özen, S., Altun, M.G. and Mardani-Aghabaglou, A., "Effect of the polycarboxylate based water reducing admixture structure on self-compacting concrete properties: Main chain length", ***Construction and Building Materials***, Vol. 255, (2020), 119360. doi: https://doi.org/10.1016/j.conbuildmat.2020.119360.
15. Sha, S., Wang, M., Shi, C. and Xiao, Y., "Influence of the structures of polycarboxylate superplasticizer on its performance in cement-based materials-a review", ***Construction and Building Materials***, Vol. 233, (2020), 117257. doi: https://doi.org/10.1016/j.conbuildmat.2019.117257.
16. Hashempour, M., Heidari, A. and Jounaghani, M.S., "The evaluation of the stress-strain characteristics of mcc concrete", ***Materials Today Communications***, Vol. 23, (2020), 101133. doi: https://doi.org/10.1016/j.mtcomm.2020.101133.
17. Tavakoli, D., Hashempour, M. and Heidari, A., "Use of waste materials in concrete: A review", ***Pertanika Journal of Science and Technology***, Vol. 26, No. 2, (2018), 499-522.
18. Senff, L., Labrincha, J.A., Ferreira, V.M., Hotza, D. and Repette, W.L., "Effect of nano-silica on rheology and fresh properties of cement pastes and mortars", ***Construction and Building Materials***, Vol. 23, No. 7, (2009), 2487-2491. doi: https://doi.org/10.1016/j.conbuildmat.2009.02.005.
19. Quercia, G., Hüsken, G. and Brouwers, H.J.H., "Water demand of amorphous nano silica and its impact on the workability of cement paste", ***Cement and Concrete Research***, Vol. 42, No. 2, (2012), 344-357. doi: https://doi.org/10.1016/j.cemconres.2011.10.008.
20. Adjoudj, M.h., Ezziane, K., Kadri, E.H., Ngo, T.-T. and Kaci, A., "Evaluation of rheological parameters of mortar containing various amounts of mineral addition with polycarboxylate superplasticizer", ***Construction and Building Materials***, Vol. 70, (2014), 549-559. doi: https://doi.org/10.1016/j.conbuildmat.2014.07.111.
21. Doleželová, M., Krejsová, J. and Vimmrova, A., "Influence of fine aggregate on some properties of gypsum mortars", ***IOP Conference Series: Materials Science and Engineering***, Vol. 379, (2018), 012005. doi: 10.1088/1757-899X/379/1/012005.
22. Kovler, K., "Strength and water absorption for gypsum—cement—silica fume blends of improved performance", ***Advances in Cement Research***, Vol. 10, No. 2, (1998), 81-92. doi: 10.1680/adcr.1998.10.2.81.
23. Krejsová, J. and Doleželová, M., "Resistance of mortars with gypsum, lime and composite binders against molds", ***Acta Polytechnica CTU Proceedings***, Vol. 21, (2019), 16-20. doi: 10.14311/APP.2019.21.0016.
24. Toledano-Prados, M., Lorenzo-Pesqueira, M., González-Fonteboa, B. and Seara-Paz, S., "Effect of polycarboxylate superplasticizers on large amounts of fly ash cements", ***Construction and Building Materials***, Vol. 48, (2013), 628-635. doi: https://doi.org/10.1016/j.conbuildmat.2013.07.069.
25. Ren, C., Hou, L., Li, J., Lu, Z. and Niu, Y., "Preparation and properties of nanosilica-doped polycarboxylate superplasticizer", ***Construction and Building Materials***, Vol. 252, (2020), 119037. doi: https://doi.org/10.1016/j.conbuildmat.2020.119037.
26. Buck, B., Wolff, K., Merkler, D. and McMillan, N., "Salt mineralogy of las vegas wash, nevada: Morphology and subsurface evaporation", ***Soil Science Society of America Journal***, Vol. 70, (2006), 1639-1651. doi: https://doi.org/10.2136/sssaj2005.0276.

Persian Abstract

چکیده

ملات گچی دارای سه ضعف مهم است که می‌تواند آن را برای ساخت مجسمه و ساختمان‌ها محدود کند؛ دارای مقاومت فشاری پایین ، جذب آب زیاد و زمان گیرش کم است. در مطالعه حاضر، از سیمان، نانو سیلیس و یک ابر روان‌کننده با پایه‌ی پلی کربوکسیلات اتر برای حل مشکلات استفاده شد. نتایج نشان داد که استفاده از سیمان با ایجاد C-S-H می‌تواند روند رشد مقاومت را بهبود بخشد. نتایج مقاومت فشاری ۲۸ روزه نشان داد (از ۹ مگاپاسکال به ۴۵ مگاپاسکال) استفاده از نانو سیلیس نه تنها با ایجاد تراکم C-S-H باعث افزایش مقاومت فشاری می‌شود، بلکه باعث کاهش جذب آب به نسبت یک سوم نمونه شاهد می‌گردد. مصرف پلی کربوکسیلات اتر باعث پراکندگی یکنواخت ذرات نانو در ملات شده که این امر حتی حفرات را مسدود کرده و ابعاد متوسط آنها را کاهش می‌دهد. همچنین، از آزمون ANOVA برای یافتن پارامترهای اصلی موثر در مقاومت فشاری ۲۸ روزه، جذب آب و زمان گیرش استفاده شد. در این راستا، نانو سیلیس (۴۹/۸۲ درصد مشارکت)، سیمان (۵۶/۶۸ درصد) و فوق روان کننده (۷۳/۱۰ درصد) به ترتیب نقش‌های اصلی در مقاومت فشاری، جذب آب و زمان گیرش دارند.

International Journal of Engineering

Journal Homepage: www.ije.ir

Study of Bond Strength of Plain Surface Wave Type Configuration Rebars with Concrete: A Comparative Study

S. B. Wani*, M. S. Haji Sheik Mohammed

Department of Civil Engineering, B. S. Abdur Rahman Crescent Institute of Science & Technology, Chennai, India

P A P E R I N F O

Paper history:
Received 19 September 2020
Received in revised form 26 October 2020
Accepted 29 October 2020

Keywords:
Reinforced Concrete
Bond Strength
Mild Steel Rebar
Plain Surface Wave Type Configuration Rebar
High Yield Strength Def Rebar
Durability
Rib Configuration

A B S T R A C T

This study investigates the bond strength behaviour of plain surface wave type configuration (PSWC) rebars in comparison to mild steel (MS) and high yield strength deformed (HYSD) rebars of varied rib configuration as per BIS and ASTM standards. The variables in the rebar include plain surface, curved surface, parallel rib, diamond rib and Nano modified cement polymer anticorrosive coating (CPAC). Total of 30 pull-out specimens and 12 beam-end specimens were put to a pull-out test following BIS and ASTM standard respectively. The load corresponding to 0.025mm free end (FE) slip and 0.25mm loaded end (LE) slip were carefully observed. The load-deflection behaviour, appearance of the first crack in the specimens and ultimate failure load was recorded. The experimental results showed that as compared to MS rebars, HYSD rebars offer an approximately threefold increase in ultimate bond strength and 1.5 times increase in usable bond strength irrespective of varied rib configuration. PSWC rebars with 4mm offset and 80mm pitch offered 2.4 times increase in ultimate strength and 76.2% increase in usable bond strength as compared to MS rebars. The ultimate pull-out load of PSWC rebars was around 25% and the usable bond strength was only 8.6% lesser than HYSD rebars with parallel ribs. The adopted coating enhanced the corrosion resistance and the reduction in bond strength with any surface configuration was less than the permissible maximum reduction of 20% as specified in IS 13620-1993. Hence it can be concluded that PSWC rebars offered promising bond strength results and upon further optimization and study in other aspects, PSWC rebars can be a way to replace HYSD rebars in future for enhancing concrete durability at zero added cost.

***doi**: 10.5829/ije.2021.34.02b.01*

1. INTRODUCTION

The durability problem of concrete structures reinforced with HYSD rebars is worldwide resulting in early age failures and renovation costs add a large amount in annual expenditures [1, 2]. Neville [3] suggests reasons as "poor understanding of deterioration processes, inadequate acceptance criteria of concrete at site, and changes in cement properties and construction practices". The major prominent threat unquestionably is corrosion of reinforcing steel, causing cracking, staining, and spalling of the cover of RC elements [4, 5]. This can result in unserviceable structures which can be unsafe for the occupants. Alekseev, et al. [6] commented on the above scenario as "the durability of reinforcement specimens with a stepped (deformed) profile may be roughly an order less than that of smooth specimens since the former have stress concentrators on the surface at the bases of projections, which represent sites of preferential formation of cracks".

Anil [7] reported the yield strength as well as the bond strength of HYSD rebars is higher in comparisons to plain round MS rebars and concluded that there are certain durability issues concerning HYSD rebars in reinforced concrete structures like problems of early distress and associated failures of reinforced concrete structures built using HYSD rebars due to early corrosion. The observations by CPWD [8], Swamy [9], and Papadakis, et al. [10] are evidence of old concrete structures which were reinforced with MS rebars, performing much better than more recent structures reinforced with ribbed CTD and TMT rebars when such structures were subjected to the same environment.

*Corresponding Author Email:shoibbwani@gmail.com (S. B. Wani)

Please cite this article as: S. B. Wani, M. S. Haji Sheik, Study of Bond Strength of Plain Surface Wave Type Rebars with Concrete: A Comparative Study, International Journal of Engineering, Transactions B: Applications Vol. 34, No. 02, (2021) 326-335

To attain a substitute and economical solution for overcoming the early corrosion problem in using HYSD rebars in reinforced concrete structures, an innovative type of reinforcing steel rebar named as PSWC rebar with a normal plain round surface having slightly curved axis has been proposed [7]. The offset (excursion from the original straight axis) is merely 4-8 millimetres as shown in Figure 1.

The PSWC rebar having offset-length of 4mm was selected for the study. The selection of the parameters was done based on the literature study [11-14].

In plain rebars, the ultimate pull-out force is not unlike as the load at which initial noticeable slip occurs, but in ribbed rebars, the ultimate pull-out load may resemble a greater slip which may not be obtained practically before other major failures occur. Thus in the study, the ultimate pull-out/failure load and complete load-slip behaviour of the selected rebars was observed and compared.

2. SCOPE AND OBJECTIVE OF THE STUDY

The strength aspect of PSWC rebar has to be tested to prove its viability of replacing the conventional rebars in concrete structures. Hence the bond strength of PSWC rebars in comparison with MS and HYSD rebar with varied rib configuration was presented in the study. Also, the influence of Nano modified CPAC on bond strength development has been included and compared following BIS guidelines.

3. MATERIAL PROPERTIES & MIX DESIGN

3. 1. Concrete Mix Proportioning The M30 concrete mix was formulated as per IS 10262-2009 [15]. "Ordinary Portland Cement, 53-grade approved by IS 12269-1987" [16], fine aggregate (FA) of zone II as specified in IS 383-1970 [17] and 20 mm downgraded blue granite coarse aggregate (CA) was used. The proportioning of ingredients per m^3 of concrete are presented in Table 1 with w/c ratio obtained as 0.45.

3. 2. Reinforcing Rebars To maintain quality throughout the study samples of selected 16mm diameter of MS of Fe250 grade, HYSD parallel ribs and HYSD diamond ribs rebars of Fe500 grade conforming to IS 1786-2008 [18] were tested to study the mechanical properties and chemical composition. The tension test outcomes as per IS 1608:2005 [19] are stated in Table 2.

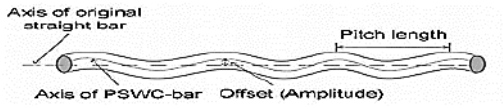

Figure 1. Representation of PSWC rebar

TABLE 1. Mix proportion

Cement (kg/m^3)		FA (kg/m^3)	CA (kg/m^3)
438		588.74	1044.22
Mix ratio:	1:	1.344:	2.384

Table 3 includes the chemical composition of rebars used in pullout tests. The tests were conducted in 'Chennai Mettex Laboratory'. The test results were compared with standard values set by major steel-producing industries and other premier research centres. The outcomes were found in the optimum range confirming the use of quality steel in the study.

3. 3. Development of Cement Polymer Anticorrosive Coating System The Nano modified CPAC on the rebars was applied following IS 13620-1993 [20] guidelines. The "site oriented CPAC (passivating type) was composed of nitrite, styrene-butadiene polymer and other additives" [21]. The polymer solution was milky white, basic pH of 12.5 and a density of 1.035g/cm^3. This anticorrosive polymer solution was compatible with concrete or cement paste

TABLE 2. Tension test results

Category of Rebar	Yield Strength (MPa)	Ultimate Strength (MPa)	Percentage Elongation in Length (mm)	Percentage Reduction in Area (mm^2)
MS R	466.72	583.40	27.5	54.23
HYSD PR R	498.36	622.96	22.5	55.45
HYSD DR R	547.77	684.72	26.2	54.90

R: Rebar, PR: Parallel Ribs, DR: Diamond Ribs

TABLE 3. Chemical composition of steel

Chemical Component (%)	MS R	HYSD PR R	HYSD DR R
Carbon	0.284	0.203	0.222
Manganese	0.553	0.696	0.567
Silicon	0.157	0.208	0.104
Sulphur	0.028	0.024	0.024
Phosphorous	0.036	0.033	0.032
Chromium	0.190	0.092	0.186
Nickel	0.099	0.068	0.069
Molybdenum	0.017	0.013	0.016

R: Rebar, PR: Parallel Ribs, DR: Diamond Ribs

when uniformly mixed with fresh OPC. The procedure involved the removal of loose rust and scales from the steel rebars by hard wire brush before brush coating [21]. The Nano modification in the CPAC was done by incorporating 5gram of Nano Titanium Dioxide (Nano TiO_2) in 1litre of CPAC. The thickness of the coating ranges from 150±25µm for 1 coat and 225±25µm for 2 coat measured by pull-off type thickness gauge. The treatment duration was 12hours.

4. EXPERIMENTAL PROGRAM

The Universal Testing Machine (UTM) of capacity 1000 kN and capable of load increment at the rate of 2250kg/minute was used for testing. The load cell of 500kN (Model: ELC-30S) was used in the test setup. Dial micrometres were used at both FE and LE of the rebars to measure corresponding slip. A 20mm rebar length from the rear face of the concrete specimen was provided with proper facing done to measure the FE slip and also the sufficient rebar from the front face was provided to safeguard the rebar in the UTM. "Polyvinyl Chloride (PVC) pipes were used as a bond breaker to restrict the bonded length of the rebars and to avoid a localized cone-type of failure of concrete at the LE of the specimen" [22, 23]. The standard procedure followed was as per IS 2770 (Part I)–1967 [23] and ASTM A944-10 [24]. The minimum load corresponding to 0.025mm FE and 0.25 mm LE slip was considered for calculating the usable bond strength throughout the study. Equation (1) is recommended to calculate bond stresses.

$$u = F/\pi\, d_r\, l_r \quad (1)$$

where F is the force in rebar, dr is the diameter and lr is the bond length of the rebar.

4. 1. BIS Pull-out Specimens Pullout specimens of dimensions '150×150×150mm' were cast with centrally embedded test rebar. At the FE, dial micrometre with least count of 2.5×10^{-3} mm with a range of 2·5mm was used. At the LE, dial micrometre with least count of 2.5×10^{-2} mm and a range of 12.5mm was used. The bonded length was restricted to 80mm in all the test rebars. The mould, mixing and curing of specimens conform to the requirements as specified in IS 516-1959 [25]. In the LE, the concrete cube was placed on a bearing arrangement of similar dimensions with 18mm hole in the centre to accommodate the test rebar. A helical of 6mm diameter, MS rebar conforming to Grade I of IS 432 (Part 1)-1982 at 25 mm pitch [23] was provided as reinforcement.

Totally 30 BIS pull-out specimens were cast and tested. Figure 2 shows the different types of rebars that were tested for bond strength as per the procedure.

Figure 3 shows the reinforcement and arrangement of mould for casting pull-out specimens.

After 28 days of curing a thin and neat layer of good strength, gypsum plaster was applied on the specimens before 2 hours of testing to assure proper seating of the specimens in the test setup. Figure 4 shows the view of casted BIS pull-out specimens and Figure 5 illustrates the pull-out test setup.

(a) Uncoated rebars

(b) Coated rebars

(c) PSWC rebars

Figure 2. (a), (b) and (c) Type of rebars

Figure 3. Arrangement of mould for casting pull-out specimen

4. 2. ASTM Beam End Specimens As per ASTM A944-10 [24], the specimen shall consist of the test rebar cast in a block of RC with dimensions as follows:

i. [600 + 25mm] length
ii. [db+200+13mm] width
iii. Minimum [db+cb+le+60mm] height

Notations:
cb = concrete cover in mm
db = nominal diameter of test rebar in mm
le = embedment length in mm

Four stirrups were provided on the two flexural reinforcing rebars on either side of the test rebar and placed inline to the length of a specimen. Figure 6 shows the reinforcement and arrangement of mould for casting beam-end specimens.

4. 2. 1. Modifications Done in Beam End Specimens The specimen was scaled down to suit the testing facility. The beam–end specimens were scaled down to 75% of the recommended size that is 25% of the length was reduced. To the scaled-down length of the specimen, the reinforcement was also scaled down.

Figure 4. Casted BIS pull-out specimens

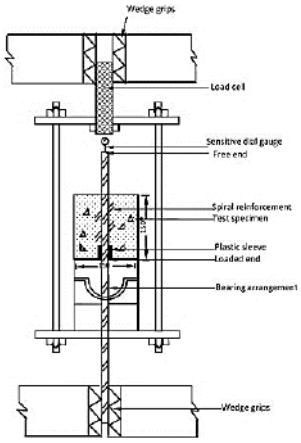

Figure 5. Schematic diagram of pull-out test setup

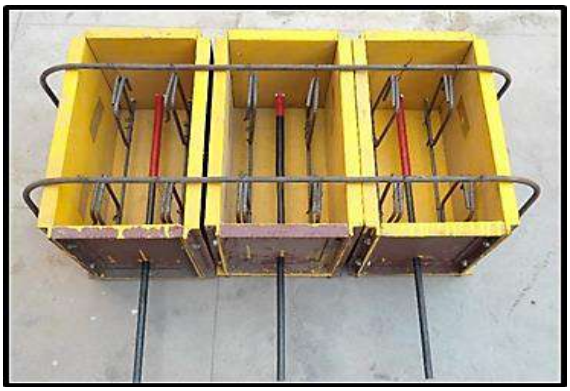

Figure 6. Arrangement of mould for casting beam-end specimens

Table 4 shows the details of the original and scaled-down specimen.

The bonded length was restricted to 200mm in all the test rebars. PSWC rebar of 4mm offset and 200mm pitch length was used to compare with conventional rebars. The flexural reinforcement having 0.5 times the cross-sectional area of the test rebar was provided with 4 rings of size '200mm×110mm' as side face reinforcement in which each flexural rebar was provided with 2 rings. Figure 7 shows the PSWC rebar of 4mm offset and 200mm pitch length.

Subsequent 28days of curing, the specimens were tested in the UTM with fabricated testing apparatus. Two dial gauges of accuracy 0.001 mm and 0.01 mm were used to measure the slip of the rebars at the FE and LE. Figure 8 shows the casted beam-end specimens and Figure 9 shows the test setup.

5. RESULTS AND DISCUSSION

5. 1. Summary of BIS Pull-out Test Results Table 5 shows the test observation in BIS pull-out specimens. The variation in the usable bond strength has

TABLE 4. Original and scaled-down test specimens

Description	Original Dimensions	Scaled Down Dimensions
Length	600 mm	450 mm
Breadth	230 mm	230 mm
Height	300 mm	300 mm

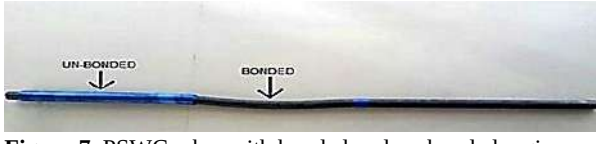

Figure 7. PSWC rebar with bonded and un-bonded regions

been calculated with respect to MS uncoated rebar. The coating thickness mention was a mean of a minimum of five readings that were taken throughout the length of rebar.

Figure 8. Casted beam-end specimens

Figure 10 shows the modes of failure in BIS pull-out specimens. From left to right it represents yielding of steel, pullout failure and pullout associated with splitting of concrete.

Figure 9. Pull-out test in progress

TABLE 5. Observations on pullout test

No.	Type of Rebar	Load (kN)		Usable Bond Strength (MPa)	Mean Variation (%)	Coating Thickness (µm)	Mean cube compressive strength of concrete (MPa)	Inclination of Ribs (Degrees)	Ultimate Pullout Load (kN)	Average Ultimate Pullout Load (MPa)	Variation (%)	Type of Failure
		0.025 mm FE slip	0.25 mm LE slip									
1	S1MS UR	17.91	16.89	4.20		-			32			Pullout
2	S2MS UR	20.71	18.72	4.65	-	-	32.91	0	34	32	-	Pullout
3	S3MS UR	15.11	15.06	3.75		-			30			Pullout
4	S1HYSD PR UR	37.80	32.60	8.10		-			102			Splitting
5	S2HYSD PR UR	42.67	33.46	8.32	+92.86%	-	31.47	78	105.7	102	+218.75%	Splitting
6	S3HYSD PR UR	32.93	31.74	7.89		-			98.3			Splitting
7	S1HYSD DR UR	39.00	35.37	8.80		-			112.61			Yield
8	S2HYSD DR UR	44.87	38.07	9.47	+109.52%	-	29.66	83	115.77	112.61	+251.90%	Yield
9	S3HYSD DR UR	33.13	32.67	8.12		-			109.45			Yield
10	S1HYSD PR 1C	40.06	25	6.21		150.5			97.60			Splitting
11	S2HYSD PR IC	34.96	23	5.71	+47.86%	151	30.98	78	101.6	97.60	+205%	Splitting
12	S3HYSD PR 1C	45.16	27	6.71		150			93.6			Splitting
13	S1HYSD PR 2C	24.2	25	6.01		250			90.20			Splitting
14	S2HYSD PR 2C	23.7	21.91	5.45	+39.52%	253	31.65	78	84.78	90.20	+181.88%	Splitting

15	S3HYSD PR 2C	24.7	28.09	6.14		247			95.62			Splitting
16	S1HYSD DR 1C	37.22	26.74	6.65		150			105.32			Yield
17	S2HYSD DR 1C	36.56	27.62	6.87	+60.95%	148	31.09	83	101.99	105.32	+229.125	Splitting
18	S3HYSD DR 1C	37.88	27.18	6.76		152			108.65			Yield
19	S1HYSD DR 2C	34	25.70	6.40		250.5			100			Yield
20	S2HYSD DR 2C	33	23.12	5.75	+47.61%	246	29.21	83	100.76	100.66	+214.56	Splitting
21	S3 HYSD DR 2C	35	25.90	6.44		255			101.24			Splitting
22	S1MS R 1C	23.5	17.50	4.35		150			26			Pullout
23	S2MS R 1C	25	16.57	4.12	-4.76%	147	32.43	0	23	26	-18.75%	Pullout
24	S2MS R 1C	22	14.07	3.50		153			29			Pullout
25	S1MS R 2C	19	16.20	4.03		250			25			Pullout
26	S2MS R 2C	17	12.62	3.14	-11.90%	260	31.17	0	27.72	25	-21.88%	Pullout
27	S3MS R 2C	21	15.80	3.92		240			22.28			Pullout
28	S1PSWC UR	33.5	29.75	7.40		-			76.40			Pullout
29	S2PSWC UR	34.67	30.37	7.55	+76.20%	-	30.91	0	72.96	76.40	+138.75%	Pullout
30	S3PSWC UR	32.33	29.13	7.24		-			79.84			Pullout

S: Specimen, R: Rebar, UR: Uncoated Rebar, C: Coat

Figure 10. Modes of failure

The following observations were noted in the load-slip behaviour of rebars in BIS pull-out specimens:

(a) From the load-slip behaviour of MS UR, HYSD PR UR and HYSD DR UR revealed that at 0.025mm FE slip value, the load values observed for HYSD PR were in line with HYSD DR configuration. However, the MS R shows some initial resistance to slip with load increment but once the initial slip in the rebar occurs there was further huge slip observed on an increment of load in both FE and LE. The average ultimate load in MS UR was observed as 32kN with a usable bond strength of 4.20MPa. Similarly, the ultimate load for HYSD PR UR and HYSD DR UR was observed as 102kN and 112.61kN respectively. The usable bond strength value of HYSD PR UR and HYSD DR UR was observed as 8.10MPa and 8.80MPa respectively.

(b) From the load-slip behaviour of HYSD PR UR, HYSD PR 1C and HYSD PR 2C revealed that the peak load sustained by one and two coated rebars was 97.60kN and 90.20kN respectively. However, for uncoated rebar

the ultimate pull-out load was 102kN. The single coated rebars carried 4.31% and two coated rebars carried 11.57% lesser load than uncoated rebars. Usable bond strength of single coated rebars was 23.33% and for double-coated rebars was 27.65% lesser than uncoated rebars.

(c) From the load-slip behaviour of HYSD DR UR, HYSD DR 1C and HYSD DR 2C.It was observed that single and double coated rebar withstands 6.47% and 10.61% lesser ultimate load respectively than uncoated rebar. Usable bond strength of single coated rebars was 23.18% and for double-coated rebar was 29.55% lesser than uncoated rebars.

(d) From the load-slip behaviour of MS UR, MS R 1C and MS R 2C. The ultimate load-carrying capacity of single and double-coated rebars was less by 18.75% and 21.88% respectively when compared to uncoated rebars. The usable bond strength for single coated rebars was 4.76% and for double-coated rebars was 11.90% lesser when compared to uncoated rebars.

(e) From the load-slip behaviour of MS UR, HYSD PR UR and PSWC UR with 4 mm deformation and 80 mm pitch length. It was observed that MS rebar carries 138.75% lesser load than PSWC rebar. HYSD PR UR showed 33.50% greater ultimate load carrying capacity and usable bond strength of just 9.46% greater than PSWC rebars.

5. 1. 1. Evaluation of Initial Crack and Ultimate Load of MS Rebars, HYSD Rebars and PSWC Rebars Figure 11 shows the evaluation of loads at which the first crack was visible and the ultimate load at which specimens failed in the pull-out test. PSWC rebars perform better than MS rebars. In HYSD rebar with parallel and diamond rib configuration, there was an appreciable difference between the first visible crack load and ultimate load. The corresponding difference between load at which first visible crack in HYSD PR UR and PSWC rebar was comparatively low.

5. 2. Summary of ASTM Beam-end Specimens Table 6 shows the observation of the pull-out test in beam-end specimens. The variation in usable bond strength has been calculated with respect to MS uncoated rebar. Figure 12 shows the crack pattern observed in the specimens during the test.

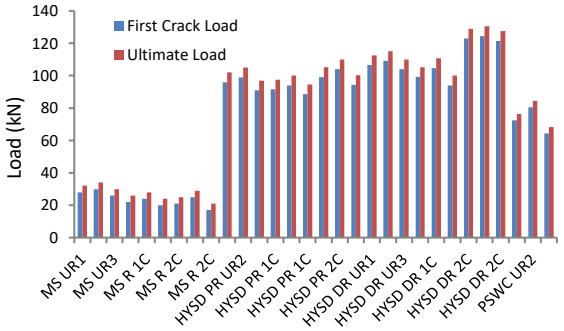

Figure 11. Evaluation of initial crack load and ultimate load

Figure 12. Crack pattern in beam-end specimens

TABLE 6. Observations on pull-out test

No.	Type of Rebar	Load (kN)		Usable Bond Strength (MPa)	Mean Variation (%)	Mean cube compressive strength of concrete (MPa)	Inclination of Ribs	Ultimate Pullout Load (kN)	Mean Ultimate Pullout Load (MPa)	Variation (%)	Crack Pattern	Type of Failure
		0.025 mm FE slip	0.25 mm LE slip									
1	S1 MS UR	25.19	24.89	2.48				35.7			Linear	Pullout
2	S2 MS UR	24.47	22.64	2.25	-	32.91	0	32	35.70	-	Linear	Pullout
3	S3 MS UR	25.91	27.14	2.58				39.4			Linear	Pullout
4	S1 PSWC UR	37.52	36.75	3.66	+48.36%	31.77	0	78.40	78.40	+119.60%	Linear	Pullout

5	S2 PSWC UR	38.44	35.76	3.56				84			Linear	Pullout
6	S3 PSWC UR	36.6	37.74	3.64				72.8			Linear	Pullout
7	S1 HYSD PR UR	39.81	38.61	3.84				114			Y shape	Splitting
8	S2 HYSD PR UR	38.42	37.90	3.77	+57.38%	29.89	78	118	114	+219.33%	Y shape	Pullout
9	S3 HYSD PR UR	41.20	39.31	3.91				110			Y shape	Splitting
10	S1 HYSD DR UR	43.86	41.5	4.12				120			Y shape	Splitting / Yield
11	S2 HYSD DR UR	41.78	39.53	3.93	+68.85%	32.43	83	126.7	120	+236.13%	Y shape	Splitting
12	S3 HYSD DR UR	45.94	43.47	4.32				113.3			Y shape	Pullout

S: Specimen, UR: Uncoated Rebar

The following observations were noted in the load-slip behaviour of beam-end specimens:

(a) From the load-slip behaviour of MS UR, HYSD PR UR and HYSD DR UR. The average ultimate load-carrying capacity of HYSD PR UR and HYSD DR UR was 219.32 and 236.13% greater than MS UR respectively. The usable bond strength of HYSD PR UR and HYSD DR UR was 57.37 and 68.85% greater than MS UR respectively.

(b) From the load-slip behaviour of MS rebar and PSWC rebar with 4mm profile deformation and 200mm pitch length, the PSWC rebar offered significantly improved resistance against slip in the initial stage as compared to MS rebar. PSWC rebar offered appreciably higher ultimate bond strength, 119.60% greater than MS rebar due to the presence of offset (ridge) and pitch (valley) of the steel-concrete interface. PSWC rebar showed significantly higher usable bond strength of the order of 48.0% greater as compared to MS rebar.

5. 2. 1. Evaluation of Initial Crack Load and Ultimate Load of MS Rebars, HYSD Rebars and PSWC Rebars Figure 13 shows the evaluation of loads at which the first crack was visible in the specimen and the ultimate load at which the specimen fails in the pull-out test. It was evident that PSWC rebars perform better than MS rebar in the pull-out test. In HYSD rebar with parallel and diamond ribs, there is an appreciable difference between first crack load and ultimate load. The corresponding difference between the load at which the first crack is visible in HYSD PR UR and PSWC rebar was less.

Figure 14 shows the embedded coated rebars and the concrete at the end of the test. It was observed that the

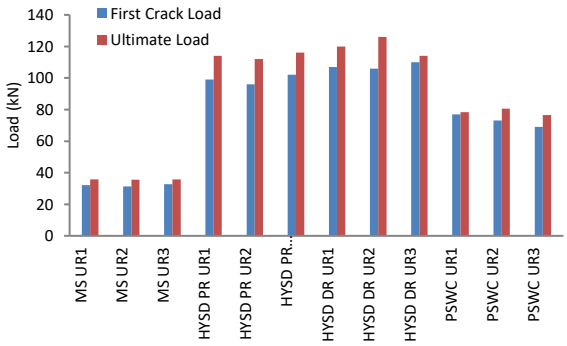

Figure 13. Evaluation of first crack and ultimate load

Figure 14. Condition of concrete and coated rebar at the end of the test

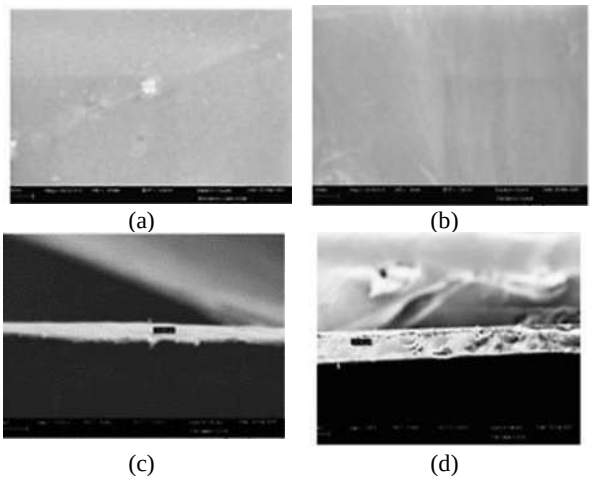

Figure 15. SEM Images of a) Plain CPAC b) TiO_2 Modified CPAC c) Cross-sectional View of 1coat Coating d) Cross-sectional View of 2-coat Coating; All images have a magnification level of approximately 100,000 times

uncoated rebars were corroded more and the coating is more adhesive to the concrete than rebar. Figure 15 shows the scanning electron microscope (SEM) images of Nano modified CPAC adopted in the study.

6. CONCLUSIONS

The experimental and comparative study on bond strength of plain surface wave type configuration rebars (PSWC) with concrete was carried out as per BIS and ASTM procedure. In addition to this, a Nano TiO_2 altered cement polymer anti-corrosive coating (CPAC) was included in the study to access its mechanical and durability properties. The following conclusions were noted.

(a) Irrespective of surface configuration, the bond strength of uncoated rebars was found more than that of coated rebars.

(b) There is a marginal rise in usable bond strength and the peak pull-out load of HYSD DR rebars as compared to HYSD PR rebars by 5-11%.

(c) As compared to MS rebars, HYSD rebars offered an approximately threefold increase in ultimate bond strength and 1.5 times increase in usable bond strength irrespective of rib configuration. The ultimate load-carrying capacity of coated HYSD diamond rib rebars surpassed mild steel rebars by four times in few cases.

(d) In BIS pull out test, PSWC rebars with 4mm offset and 80mm pitch offered ultimate load-carrying capacity of 76.40kN that is 2.4 times more than MS rebars. Also, there was a rise in usable bond strength by 76.20% compared to MS rebars.

(e) In ASTM beam-end specimens, PSWC rebars with 4mm offset and 200mm pitch offered ultimate load-carrying capacity of 78.4kN that is 2.2 times more than MS rebars. Also, there was a rise in usable bond strength by 48.36% compared to MS rebars.

(f) PSWC rebars exhibit an improved slip resistance and well-established load-slip behaviour as compared to MS rebars.

(g) In BIS pull-out test the ultimate bond strength of PSWC rebars was around 33.5% less as compared to uncoated HYSD rebars and the usable bond strength was about 9.5% less than for HYSD rebars with parallel ribs.

(h) The reduction in bond strength of coated rebars with any rib configuration was less than the maximum reduction of 20% specified by IS 13620-1993. Both 1coat and 2coated rebars satisfied IS code provisions.

(i) PSWC rebars with 4mm offset and 80 mm pitch offered promising bond strength. Upon further optimization and testing of the rebar in other aspects, PSWC rebar can be future rebar to replace HYSD rebars for durable concrete construction at zero additional cost.

7. REFERENCES

1. Koch, G.H., Brongers, M.P., Thompson, N.G., Virmani, Y.P. and Payer, J.H., Cost of corrosion in the united states, in Handbook of environmental degradation of materials. 2005, Elsevier.3-24. doi: 10.1016/b978-081551500-5.50003-3
2. Hansson, C., "The impact of corrosion on society", ***Metallurgical and Materials Transactions A***, Vol. 42, No. 10, (2011), 2952-2962. doi:10.1007/s11661-011-0703-2.
3. Neville, A., "Why we have concrete durability problems", ***Special Publication***, Vol. 100, (1987), 21-30. doi.
4. Association, B.C., "Development of an holistic approach to ensure the durability of new concrete construction", ***British Cement Association***, (1997). doi.
5. Gehlen, C., Matthews, S., Osterminski, K., Straub, D., Kessler, S., Mayer, T., Greve-Dierfeld, V. and Zintel, M., "Condition control and assessment of reinforced concrete structures exposed to corrosive environments (carbonation/chlorides)", (2011). doi:10.35789/fib.bull.0059.
6. Alekseev, S., "Durability of reinforced concrete in aggressive media, AA Balkema Publishers, Vol. 96, (1993).
7. Kar, A.K., "A rebar for durable concrete construction", ***The Masterbuilder***, Vol. 13, No. 7224-236.
8. Bharti, B.K. and Thakkar, J.J., "Swot of central public works department india: A case study", ***Journal of Advances in Management Research***, (2013).
9. Swamy, R., "Infrastructure regeneration: The challenge of climate change and sustainability-design for strength or durability?", ***Indian Concrete Journal***, Vol. 81, No. 7, (2007), 7-13.
10. Papadakis, V.G., Vayenas, C.G. and Fardis, M.N., "Physical and chemical characteristics affecting the durability of concrete", ***Materials Journal***, Vol. 88, No. 2, (1991), 186-196. doi:10.14359/1993.
11. Kar, A.K., Dave, U.V. and Ritesh S. Varu, "Performances of columns reinforced with pswc-bars and other rebars", ***The Indian Concrete Journal***, Vol. 92, No. 7, (2018), 12-17.

12. Kar, A.K., "A theory on the performance of reinforced-concrete elements", ***Proceedings of the Institution of Civil Engineers-Construction Materials***, Vol. 172, No. 4, (2019), 213-221. doi:10.1680/jcoma.18.00019
13. Kar, A., "Improved rebar for durable concrete constructions", ***New Building Materials & Construction World***, Vol. 16, No. 1, (2010), 180-199.
14. Kar, A.K., Dave, U.V. and Patel, N.A., "Performances of beams reinforced with pswc-bars and other rebars", ***Journal of Structural Engineering, CSIR-Structural Engineering Research Centre***, Vol. 46, No. 1, (2019), 29-38. doi.
15. 10262-, I., *Recommended guidelines for concrete mix design*, Bureau of Indian Standards New Delhi, India.
16. BIS, I., *12269-1987: Specifications for 53 grade ordinary portland cement*. 1987, Bureau of Indian Standards, New Delhi.
17. BIS, I., "Is 383-1970: Specification for coarse and fine aggregate from natural sources for concrete (second rev.)", ***Bureau of Indian Standards, New Delhi***, (1970).
18. Steel, I.S.H.S.D., *Bars and wires for concrete reinforcement-specification*. 1786, IS.
19. Standard-IS, I., "Is 1608: 2005: Metallic materials-tensile testing at ambient temperature. 3rd revision", ***New Delhi: Bureau of Indian Standards***, (2005).
20. Standard-IS, I., "Is 13620-1993, specification for fusion bonded epoxy-coated reinforcing bars," ***New Delhi: Bureau of Indian Standards***, (1993).
21. Mohammed, M.H.S., Raghavan, R.S., Knight, G.S. and Murugesan, V., "Macrocell corrosion studies of coated rebars", ***Arabian Journal for Science and Engineering***, Vol. 39, No. 5, (2014), 3535-3543. doi:10.1007/s13369-014-1006-x
22. Fathifazl, G., Razaqpur, A.G., Isgor, O.B., Abbas, A., Fournier, B. and Foo, S., "Bond performance of deformed steel bars in concrete produced with coarse recycled concrete aggregate", ***Canadian Journal of Civil Engineering***, Vol. 39, No. 2, (2012), 128-139. doi:10.1139/l11-120
23. Standard-IS, I., "Is 2770-1997, method of testing bond in reinforced concrete part-i- pullout test is 2770-1997", ***Bureau of Indian Standards, New Delhi, India***, (1997).
24. "Astm a944-10, "standard test method for comparing bond strength of steel reinforcing bars to concrete using beam-end specimens", ***ASTM International***, doi: 10.1520/a0944-10
25. Standard, I., "Method of tests for strength of concrete", ***Bureau of Indian Standards, Manak Bhavan***, Vol. 9, (1959).

Persian Abstract

چکیده

این مطالعه رفتار استحکام پیوند میلگردهای پیکربندی نوع موج سطح ساده (PSWC) را در مقایسه با میلگردهای فولاد خفیف (MS) و تغییر شکل مقاومت عملکرد عملکرد بالا (HYSD) با پیکربندی دنده متنوع مطابق با استاندارد BIS و ASTM بررسی می کند. متغیرهای موجود در میلگرد شامل سطح ساده ، سطح منحنی ، دنده موازی ، دنده الماس و پوشش ضد خوردگی پلیمر سیمان اصلاح شده نانو (CPAC) است. در مجموع ۳۰ نمونه کششی و ۱۲ نمونه انتهای پرتو به ترتیب با استاندارد BIS و ASTM در آزمون کشش قرار گرفتند. بار مربوط به لغزش انتهای آزاد ۰.۰۲۵ میلی متر (FE) و لغزش انتهای بارگذاری شده ۰.۲۵ میلی متر (LE) با دقت مشاهده شد. رفتار انحراف بار ، ظاهر اولین ترک در نمونه ها و بار شکست نهایی ثبت شد. نتایج تجربی نشان داد که در مقایسه با میلگردهای MS ، میلگردهای HYSD تقریباً سه برابر در افزایش مقاومت پیوند نهایی و ۱.۵ برابر در مقاومت پیوند قابل استفاده بدون توجه به پیکربندی دنده متنوع ، افزایش می یابد. میلگردهای PSWC با افست ۴ میلی متر و گام ۸۰ میلی متر در مقایسه با میلگردهای MS 2.4 برابر افزایش مقاومت نهایی و ۷۶.۲۰٪ افزایش مقاومت باند قابل استفاده دارند. بار نهایی کششی میلگردهای PSWC حدود ۲۵٪ است و مقاومت باند قابل استفاده تنها ۸.۶٪ کمتر از میلگردهای HYSD با دنده های موازی است. پوشش پذیرفته شده مقاومت در برابر خوردگی را افزایش داده و کاهش مقاومت پیوند با هر نوع پیکربندی سطحی کمتر از حداکثر کاهش مجاز ۲۰٪ است که در ۱۳۶۲۰: ۱۹۹۳ مشخص شده است. از این رو می توان نتیجه گرفت که میلگردهای PSWC نتایج امیدوار کننده استحکام باند را ارائه می دهند و با بهینه سازی و مطالعه بیشتر در سایر جنبه ها ، میلگردهای PSWC می توانند راهی برای جایگزینی میلگردهای HYSD در آینده برای افزایش دوام بتن با هزینه اضافه شده صفر باشند.

International Journal of Engineering

Journal Homepage: www.ije.ir

Planned Special Event Travel Demand Model Development

M. E. Ergin*, H. O. Tezcan

Istanbul Technical University, Faculty of Civil Engineering, Department of Transportation Engineering, Istanbul, Turkey

P A P E R I N F O

Paper history:
Received 27 August 2020
Received in revised form 30 October 2020
Accepted 04 November 2020

Keywords:
Choice Model
Planned Special Event
Survey Methodology
Traditional 4-step Model
Travel Demand Analysis

A B S T R A C T

When a planned special event (PSE) is mentioned, large and international organizations are considered. These organizations attract so many people all around the world to local points. However, relatively small scale PSEs such as ordinary league games that are organized once every two weeks that impact the daily traffic of the cities especially metropolitans, are neglected. This paper focuses on the travel demand modelling of the ordinary super league games in Istanbul. As a purpose of this paper, in order to obtain a customizable and standalone PSE model, survey design and data collection procedures, a new methodology for trip generation, trip distribution, and modal split steps of the traditional 4-step demand modelling are considered. With the opportunity provided by the newly proposed methodology, unlike most previous studies in literature, all trips and activities in the same day with the PSE are taken into the modelling process. Because of the nature of the PSEs, participants prefer to perform additional (derived) activities in the time between leaving the origin and joining the PSE. Accordingly, 1, 2, and 3-step groups are defined, and the shape of trip length distributions are different not only from the peak hours but also from each other. At the end, the model estimation and development of the PSE travel demand model are presented with conclusions and suggestions.

***doi**: 10.5829/ije.2021.34.02b.05*

NOMENCLATURE

U	Utility of an alternative
X	Vector of attributes
S	Vector that specifies the characteristics of the individual
C	Choice set
V	Deterministic component of the equation (deterministic part)
Pr	Probability of a chosen alternative
e	Exponential form of formula
T_{ij}	Future trips made from zone i to zone j
t_{ij}	Current trips made from zone i to zone j
P_{ij}	Future trip production of zone i
O_{ij}	Current trip production of zone i
A_{ij}	Future trip attraction of zone j
D_{ij}	Current trip attraction of zone j
k	Number of zones
A_i	Balance factor
B_j	Balance factor
f(cij)	Deterrence function of the trips between zone i and zone j.
cij	Travel costs from zone i and zone j
Greek Symbols	
ε	Stochastic component of the equation (stochastic part)
B, n	Unknown parameters
∑	Sum operator
θ	Constraint function
Subscripts	
i,j	Alternatives, zones
t,	Individual

1. INTRODUCTION

Rapid increase in the world's population has contributed to a huge need for new transport demand strategies [1] and one of the current transportation demands is the planned special event travel demand. A planned special event (PSE) is a public activity with a predetermined date, venue, and duration that may affect the regular service of the surface transport network due to enhanced traffic demand and/or decreased capability related to event planning [2]. PSE impacts transportation network with its known location and scheduled time as a result of increases in travel demand or decreases in the

*Corresponding Author Institutional Email: eergin@itu.edu.tr (M. E. Ergin)

Please cite this article as: M. E. Ergin, H. O. Tezcan, Planned Special Event Travel Demand Model Development, International Journal of Engineering, Transactions B: Applications Vol. 34, No. 02, (2021) 336-347

capacity of road segments [3]. Even though PSEs are planned occurrences, they raise the travel demand abnormally and temporarily while their impact on traffic could be significant [4]. For example in a study by Kwon et al. [5] PSEs effect on total daily travel delay is found to be 4.5% in San Francisco Bay Area (USA). Furthermore, according to Federal Highway Administration Office (FHWA) report [6], an estimated 5 percent of congestion is caused by special events.

Special events can be classified in different ways in terms of their size (number of participants), form, content, location and impact area [7]. While the peak hour demand found by reducing from daily travel demand is used in traditional models, temporary and short period of time travel demand is modelled by event based modelling. Kuppam et al. [8] claims that travel demand models were designed to understand traveling to unique special events. Generally, the literature on PSE studies is dominated by large-scale events such as Olympic Games, World Cup Tournaments, Winter Games, etc. [9-11]. Kuppam et al. [8] try for defining special events in the area that have an effect on travel demand, especially transit riding, gathering travel relevant data associated with the PSEs, and creating an exclusive model for special events (SEM) which is also the aim of this study as well.

In the literature, PSE models generally consider the travel demand for the main activity by directly focusing on the trips between origin of the individual and the activity venue. Travel demand from other zones to the event venues is solely forecasted [8, 11-13]. The main activity approach leads to various analyses considering traffic management [2, 3, 9, 10, 14] or spectator (customer) satisfaction [15] while the interim trips (and derived activities) are disregarded. However, due to the nature of the PSEs, most of the time, participants prefer to perform additional (derived) activities in the time between leaving the origin and joining the PSE. While some studies in the literature consider the origin of the special event trips as only home or hotel with some assumptions [16], some others, such as Florez et al. [17] stated that especially the guest travelers in the area may choose walking mode in order to perform some activity in the surrounding area before the game. Moreover, Yan et al. [16] grouped the spectators with regard to their origins, and stated the possibility of the performing other type of activities before or after the main activity which is PSE. Bowman and Ben-Akiva [18] defined activities into groups and named the most important activity of the day as the primary activity, and the other activities defined as secondary activities.

The aim of this study is to establish a custom PSE model for Istanbul (Turkey). For this aim a number of soccer games in three different stadiums in the city is considered. By using the data collected from attendees to these games, conventional 4-step model is retrofitted to PSEs with various modifications in the first three steps of the model. These modifications account for the constraints (such as stadium capacity) arise from the event itself while new additions (such as the derived activities/trips) are also integrated. The paper is structured as follows: firstly survey methodology will be explained, and then data results will be given afterward. Following part, the modelling methodology is presented briefly with the detailed case study and the custom PSE model for soccer games in Istanbul and then the results of the model are presented. At the end, the paper is finished by the discussion and conclusion part by giving recommendations for future studies and new policy decisions.

2. SURVEY METHODOLOGY

The data used in this study were collected from three venues that belong to the three biggest soccer clubs in Istanbul and Turkey which are Besiktas, Fenerbahce and Galatasaray through face-to-face surveys. For each team, seven game days were selected. Seven games were included in the survey study for Besiktas and Fenerbahce, and six games were included for Galatasaray. At each game day, the surveys started about three hours before the games and completed before the game started because the road segments were started to be closed three hours before the game. Also, according to the study of Chang and Lu [19], around 30% of attendees reached to the immediate vicinity of the venue three hours before the PSE. The surveys were conducted to the fans waiting in the area that is closed to traffic and fully secured by police while only the fans who were going to enter the stadium were inquired. All the participants were home team fans. The key obstacles encountered by the survey team and the steps taken to mitigate the related issues are described below:

- Permission (Having permits to execute surveys from the stadium managers): The clubs were contacted to get permission to perform the surveys inside the stadiums. Due to having no permission, surveys were conducted in the immediate vicinity of the stadiums. Also, Kuppam et al. [8] tried the same way in their study.
- Different profiles (Conflicts in attendance profiles): Every game draws essentially the same socio-demographic profile but the profile varies with respect to the various ticket prices that makes it very difficult to get a representative sample. Thus, broad enough surveys were designed to obtain the required statistical meaning at a relatively small marginal error.

The surveys were conducted only for ordinary league games. In order to avoid any difference in the fan profiles, local derbies and European cup games were

omitted. The socio-economic structures and seniority of the fans who participated in the surveyed games are similar and it does not change from game to game. In Table 1, information about stadiums as well the surveys are provided.

3. DATA DESCRIPTION

The number of the valid surveys in Besiktas Vodafone Park, Fenerbahce Ulker and Galatasaray Turk Telekom venues is 1168. The general descriptive statistics of the data are presented in Table 2. According to Table 2, the average age of the fans is 30 and only 6% are women. At most, the 25 - 34 age group of fans follow the game in the stadium (38%). Generally, fans not only come from any districts of Istanbul, but also from out of Istanbul and even abroad. According to the data, 24% (n=277) of the respondents are from out of the city and 3% (n = 39) from abroad. 26% of the participants stated that they have a monthly income of 3,501-5,000 Turkish Liras (TL) while the average monthly income is around 3.200 TL. People attend to soccer games mostly with a friend (n = 704; 60%). Moreover, 35% and above of Fenerbahce and Galatasaray fans follow all home games inside the stadium during one season.

TABLE 1. Information about the venues and the surveys

Teams	Name of the Venues	Venue Capacity	Average Number of Attendance	Survey		
				Sample Size	Confidence Level	Sample Size/Average Number of Attendance
Besiktas	Vodafone Park	41,903	31,245	386	95%	0.01
Fenerbahce	Ulker	50,530	36,677	399	95%	0.01
Galatasaray	Turk Telekom	52,280	34,481	383	95%	0.01

TABLE 2. Descriptive statistics (N=1168)

Criteria	Classification	N	Percentage	Criteria	Classification	N	Percentage
Age Groups	15-24	361	31%	Private Car Ownership	No	648	55%
	25-34	446	38%		Yes	520	45%
	35-44	265	23%	Who Does the Activity with?	Alone	259	22%
	45-54	79	7%		Friends	704	60%
	55 +	17	1%		Older Family Member	71	6%
Gender	Woman	68	6%		Adult Family Member	100	9%
	Man	1100	94%		Young Family Member	34	3%
Residential Status	Out-of-town	277	24%	Ticket Types	Gift Match Ticket	113	9.7%
	Abroad	39	3%		Gift Seasonal Ticket	18	1.5%
	Istanbul	852	73%		Match Ticket	620	53.1%
Income Groups	< 1.800	289	25%		Seasonal Ticket	417	35.7%
	1.800 - 3.500	249	21%	Seasonal Ticket	No	733	63%
	3.501 - 5.000	307	26%		Yes	435	37%
	5.001 - 6.500	140	12%	How Often Do You Participate in Matches?	0 - 4	382	33%
	6.501 - 8.000	58	5%		5 - 8	248	21%
	8.000 +	125	11%		9 - 13	139	12%
Top 5 Job/Task	Student	285	24%		14 +	399	34%
	Tradesman	117	10%	How Do You Watch the Matches outside the Venue?	Do Not Watch	79	7%
	Engineer	58	5%		Paid Channel	664	57%
	Civil Servant	42	4%		Cafe	223	19%
	Teacher	39	3%		Internet	202	17%
	Others	627	54%				

4. PLANNED SPECIAL EVENTS MODELS

In this section, the proposed PSE model is presented. The structure of this model is strongly linked to traditional 4-step model which is well-known and widely used for the aggregate trip-based modelling [20]. However, based on various properties of PSEs a number of modifications are introduced where necessary. The proposed methodology presented in this paper covers the first three steps of the 4-step model while traffic assignment is left out. It should be noted that regardless of the modelling purpose, the assignment procedure is well known, widely applied and straightforward. In addition, the inherent nature of PSEs does not bring in any constraints or necessitates any changes in the assignment procedure.

Eventually, the proposed model will extend to the mode choice step (3rd step) and it should be assumed that a standard traffic assignment calculation will complete the model.

The proposed methodology presented in this paper covers the first three steps of the 4-step model while traffic assignment is left out. It should be noted that regardless of the modelling purpose, the assignment procedure is well known, widely applied and straightforward. In addition, the inherent nature of PSEs does not bring in any constraints or necessitates any changes in the assignment procedure. Eventually, the proposed model will extend to the mode choice step (3rd step) and it should be assumed that a standard traffic assignment calculation will complete the model.

4. 1. Trip Generation Trip generation is used for prediction of the number of trips produced from a particular zone and trips attracted to a particular zone. Factors affecting trip production and attraction can be specified as household size, household income, residential density, employment, retail floor space area, hospital capacity, school capacity, etc. Different modelling methods are used for trip generation step such as category analysis, trip rates based on activity participation, and regression analysis. The regression analysis is the mostly used method of the trip generation step.

Due to the characteristics of selected PSE, in this study, the trip generation step carried out by only considering the trip attractions. Consequently, in trip matrices, venues are considered only attraction zones. In this study, the districts of the Istanbul were determined as production zones.

Especially in metropolitan cities such as Istanbul, PSE should be considered together with all activities and trips on the event day. Therefore, in this study, daily activities and trips starting from leaving home and up to the PSE are considered. As a result, the trips made on the days of PSE were divided into three groups. These are:

- 1-Step Group (n=742): who reach the stadium directly and without extra activity,
- 2-Step Group (n=376): who reach the stadium after performing one interim activity and makes two trips,
- 3-Step Group (n=50): who reach the stadium after performing two interim activities and makes three trips.

As a well-known fact, transportation demand is derived from activity demand. Consequently, for each individual, all the activities occurring at different locations in a day generate trips by different transport means. Therefore, the individuals in 1-step group make a single trip to reach PSE while each additional step generate an additional trip.

4. 1. 1. Trip Production Methodology for PSEs in Trip Generation According to Kuppam et al. [8], the capacity of the stadium constraints the generation of trips for special events. Yan et al. [16] used the 2005 HITS data where the group-specific activity chain probability is specified, in order to obtain the total number of trips generated by traffic analysis zone (TAZ) by multiplying the activity chain probability with the number of group population in trip generation step of the modelling.

No matter how much the population of the analysis area increases, the number of people entering the stadium will not change unless the stadium capacity is increased. For this reason, the following procedure has been applied to each stadium separately. First of all, trips to the stadium are divided into trip groups as above and the number of people in each travel group is determined. Depending on the capacity of the stadium, those who came by 1 trip, those who came by two trips and those who came by 3 trips were enlarged according to the number of people in the group. In this approach, additional trip matrices are generated. The total number of the generated trip matrices is 6 (one trip matrix is for 1-step group, 2 trip matrices are for 2-step group and 3 trip matrices are for 3-step group). For example, those who came by 2 trips must have a travel matrix for their first trip, and the growth constraint for this trip matrix should not exceed the total capacity of those who arrived by 2 trips in total. Moreover, those who come with 3 trips must have trip matrices of their first and second trips, and so on. For this group, the growth constraint of their second trip is the capacity of the last trip, and the growth constraint of their first trip is the capacity of the second trip. The constraints are illustrated in Figure 1. These constraints are not only for the total number of trips, especially for the first step of 2-step group and the first and the second step of the 3-

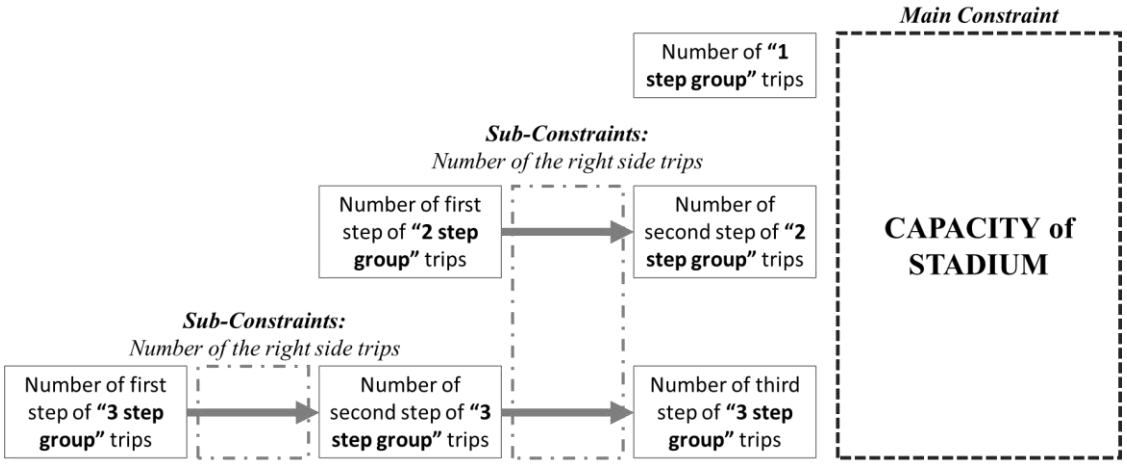

Figure 1. Illustration of the constraints of the growth of the trips

step group. If these constraints does not apply, there may be inconsistency with the number of the trips and some of the trips may be lost in the model. At the end, the trips are enlarged by the origin and destination accordingly.

Istanbul has 39 districts and all of them are included into the model as separate zones. Moreover, out-of-town arrivals are represented by an independent zone. In addition to this, the three venues are defined as different zones. In the 1-step group and the last steps of 2-step and 3-step trip group matrices, the venue zones are defined as only the attraction zones.

4. 2. Trip Distribution Trip productions and attractions is not adequate for modelling and decision making. In order to get a better idea for decision making trip distribution step uses the trips obtained from previous step. Trip distribution presents the distribution of trips from/to particular zones. Generally, a trip matrix is used which shows the origin and destination of the trips between particular zones and this matrix is called origin-destination (O-D) trip matrix. Ortuzar and Willumsen [21] stated that this representation is needed for all assignment models. After having the last version of the O-D trip matrix, the total number of the generated trips should be equal to the number of the attracted trips. If it is not, the balancing process should be performed.

In the study of Kuppam et al. [8] only the last trips were taken into consideration and trips were classified as home-based, work-based, hotel-based, and other-based trips. Moreover, as it was emphasized before, other trips and activities on the PSE day were considered as activities unrelated to PSE. However, derived activities and trips on the day of PSE mostly related with the PSE as it is stated in the Bowman and Ben-Akiva [18] study. It is not only this connection but also the location of the derived activity may affect the chosen transportation mode to reach the venue of PSE. Therefore, in this study, the trips before PSE are also included in the model. By this way, it is aimed to account for all trips from the starting time of the day to the starting time of the PSE.

Trip distribution step was implemented for each 6 different trip matrices which were created in the previous step, separately. However, it is clear that the characteristics of the matrices are very different from each other. In this regard, two types of distribution modelling was used: The growth factor model and the gravity model. Shortly, Figure 2 shows the specific place of which model is used.

Different models were used at this step due to the fact that the gravity model distributes the trips to the places where there is no trip demand. In this case, due to the calculation procedure, even when there are no trips between two observed zones, a certain number of trips are distributed between these zones. This approach can be accepted to be valid in classical 4-step model approach context for daily home-based travel demand. Because in these models, the production of the trips are related with household size, number of student, and number of workers. On the other hand, the attraction of the trips are related with socio-economic indicators such as school capacity, hospital capacity, and employment.

However, this does not apply to the special events travel demand model, due to the fact that all zones do not contain venues which are the main attraction points. For example, in this study, we could lose some of the trips between specific zones to venues in our last trip matrices if we would use the gravity model instead of the growth factor, because, the gravity model distributes the trips with regards to their population and distance. So, the traveler would be stunned by the purpose and lost in the model. For this reason, the Fratar method from the growth factor family was used in the first leg

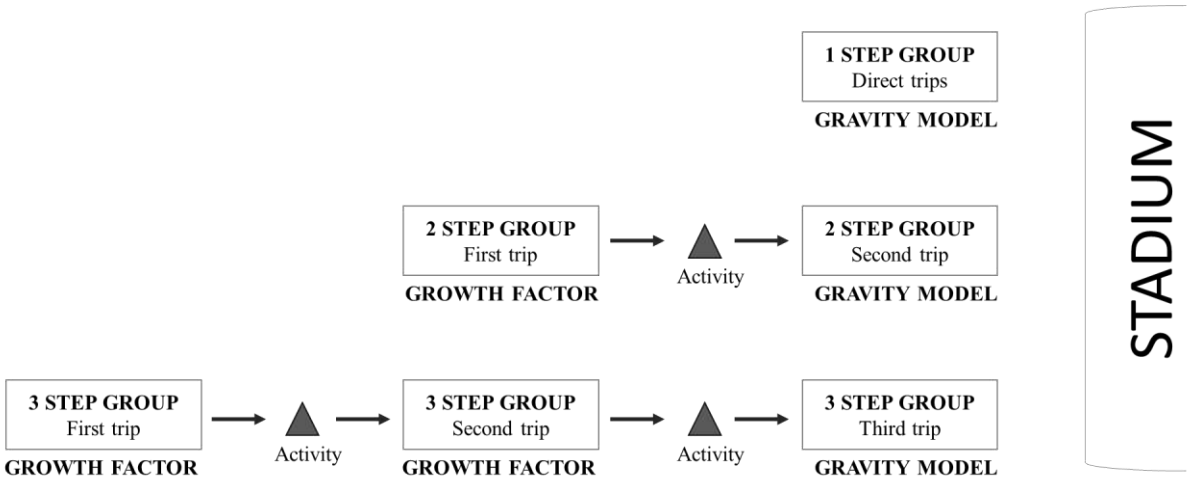

Figure 2. Distribution methodology of the trip groups

of the 2-step group matrix and the first two legs of the 3-step group matrix. Moreover, the gravity model is used in the 1-step group matrix, the last steps of the 2 and 3-step groups' matrices.

Estimation of the number of future trips in each of them matrix cells, the base data is used by various methods such as the growth factor method and the gravity model.

4. 2. 1. The Growth-Factor Method Where the data is only available with regards to the future trip rates of factors which are defined as growth factor, the growth factor methods can be used. The uniform growth factor, single constrained growth factor, the doubly constrained growth factor, the Fratar method are members of the growth factor family.

4. 2. 2. The Fratar Model This method was introduced by Fratar and this modelling approach makes the assumptions that the existing trips *tij* would increase proportionally to (P_i/O_i) and proportionally to (A_j/D_j). The multiplication by two growth factors of the current flow would result in projected trips occurring in zone i being greater than the future forecasts. Therefore, a normalizing expression is presented which is proportion of the total of all the existing trips out of zone i, and multiplication of the total of all the existing trips out of zone i and the growth factor at the end of the trip. The Fratar model is given by Salter and Hounsell [22]:

$$T_{ij} = t_{ij} \times \frac{P_i}{O_i} \times \frac{A_j}{D_j} \times \frac{\sum^k t_{ik}}{\sum^k \left[\frac{A_i}{a_i}\right] \times t_{ik}} \quad (1)$$

With this approach, the distribution of future trips is made by defining a separate coefficient for each zone. In the Fratar model, the trip distribution rate of each zone within all zones and the future production and attraction rates are included, and is calculated separately for each zone. This calculation model has some disadvantages like other growth factor models. For example, as Salter and Hounsell [22] stated that the growth factor methods are strongly dependent on the growth factor itself and the growth factor should be calculated precisely, and this can be defined as the source of error. Since the Fratar method is a member of the growth factor family, no calibration is required.

In the context of the proposed methodology, this method is used for the trips of people who attended a certain activity (eating, drinking, meeting, sightseeing, shopping, etc.) which are their previous trip/trips before coming to the venue. Moreover, within the scope of this study, the possible maximum number of trips are defined by the limitations of the known capacities of the stadiums.

The reasons for applying the Fratar method can be listed as follows:

- The trips whose only purposes are to participate in the planned special event, are made to different zones with different purposes by using the gravity model,
- Because of the nature of the gravity model, as the size of the zones increases the number of trips increases. As a result, mostly attracted zones obtain high number of trips and it increases during the calibration of the gravity model. Even, at the end of the second iteration, some of the zones which produced low rate of trips are seemed almost zero travel demand,
- As in the traditional four-step model, the capacity of the hospital, school, or the number of employment is very important however, it can be deducted that the travel demand for planned special events are not related to them.

4. 2. 3. The Gravity Model As it is known, in the two restricted gravity models, the whole trips are separated to all zones by weighting according to the number of trip productions and attractions.

$$T_{ij} = A_i \times B_j \times O_i \times D_j \times f(c_{ij}) \quad (2)$$

The given *f(cij)* function generally is chosen among following forms. The sum of the trips made to a region in the below forms is distributed to all zones that are linked to the origin zone.

$$1)\ f(c_{ij}) = e^{(-\beta \times c_{ij})}$$

$$2)\ f(c_{ij}) = c_{ij}^{-n} \quad (3)$$

$$3)\ f(c_{ij}) = c_{ij}^{n} \times \exp(-\beta c_{ij})$$

The calibration of the unknown parameters in Equation 3 (β and/or n) is performed by an iterative procedure that looks for convergence to the actual trip length distribution (TLD) at each iteration. In the general practice, for trips during morning or evening peak hours the TLD follows a right-skewed distribution that represents less numbers of short and long trips. However, for PSEs the distributional shape of the TLDs should be expected to be very much different than the TLDs for peak hours.

In the proposed methodology, the gravity model was used for the last steps of the trip groups. The last step of each group only contains trips between various districts and the venues while no trips exist between other zones.

In the traditional 4-step model, in order to obtain the trip distribution matrix, Equation (2) is generally used and the third form of the $f(c_{ij})$ is preferred. In this calculation, when there are no trips between zones, the c_{ij} values are equal to zero. However, based on the selected deterrence function these zero values could be converted into a non-zero deterrence value (*since* $e^0=1$) and in turn, these non-zero deterrence values would lead to the distribution of trips between zones that do not have any observed trips. Obviously, this is a quite problematic issue when modelling PSEs because the final step of the PSE trip distribution should strictly assign the trips only to the venues. In an effort to overcome this problem, a dummy variable that takes the value of 1 if the destination is the venue and 0 otherwise is incorporated into the deterrence function. By this way, it becomes possible to assure that the trips are assigned only to the venues. Equation (4) presents the new deterrence function that contains the abovementioned dummy variable. In the equation, j = 41, 42 and 43 are the zone numbers of the venues:

$$f(c_{ij}) = e^{(-\beta \times c_{ij})} \times \theta_{ij}$$

$$subject\ to\ \theta_{ij} = \begin{cases} 1; if\ i \leq 40\ and\ j = 41,42,43 \\ 1; if\ i > 40\ and\ j < 40 \\ 0; otherwise \end{cases} \quad (4)$$

Figures 3, 4 and 5 present the results of the gravity model calculations in this study. Figure 3 is for direct trips from origins to the venues while Figures 4 and 5 are for the last steps of 2-step and 3-step trips, respectively. As it can be seen from the figures the TLDs are converged after 3 iterations for all cases. Note that the shape of TLDs are different not only from the peak hours but also from each other for 1, 2 and 3-step trip groups. For the last step of 2 and 3-step trips the TLDs have a decreasing form that indicates the trips to be concentrated at short distances (or travel times) to the venues. However, for 1-step (direct) trips short distances are less frequently observed. The distribution still resembles a left skewed distribution whereas very long distances are also present.

4. 3. Modal Split The third stage of the classical 4-step travel demand model is the modal split. At this stage, the probability of selecting each transportation mode is calculated and split is made accordingly.

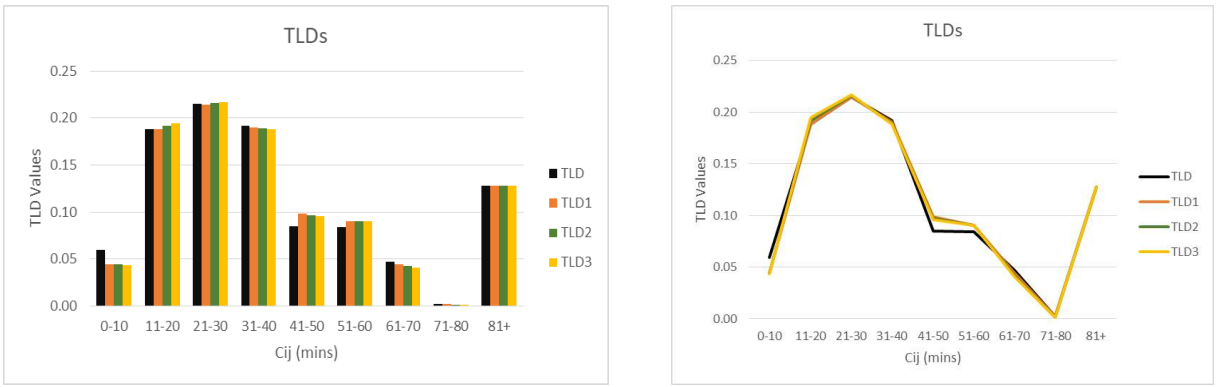

Figure 3. Trip Length Distribution Results (1-Step Trips)

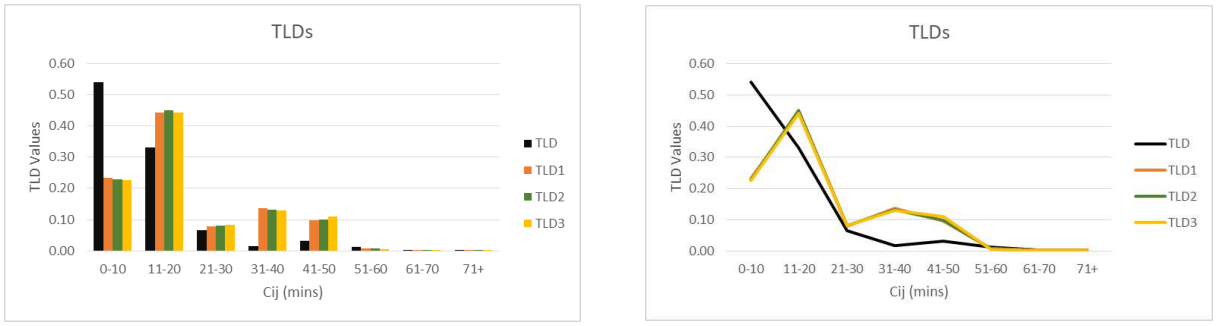

Figure 4. Trip Length Distribution Results (Last step of 2-Step Group)

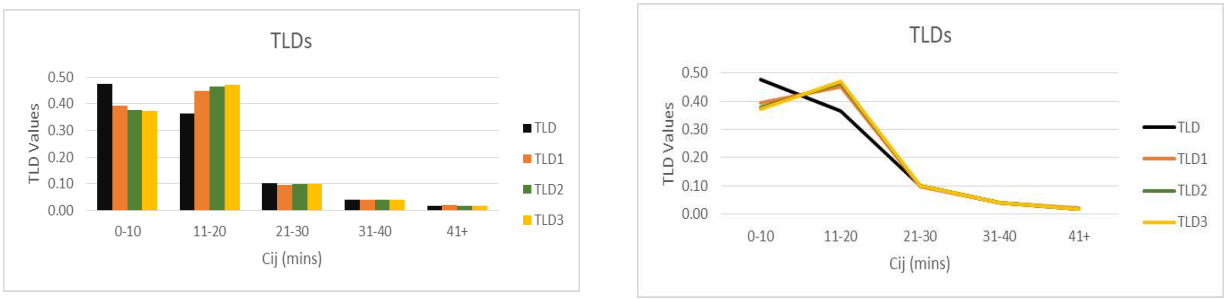

Figure 5. Trip Length Distribution Results (Last step of 3-Step Group)

First of all, the probability of selecting a transportation mode is calculated according to the assumptions within the scope of random utility theory which states that each user makes logical choices in the phase of split, has an information about each mode of transportation, and knows which one will provide the most benefit. In the 4-step model, which is generally used in home-based compulsory trips and is more effective in revealing the demand for transportation during peak hours, the benefits of the transportation modes are expressed by variables such as travel time and travel cost. In this case, the assumption is made that the user prefers the least costly and earliest mode. A widely used modelling approach for choice modelling is the multinomial logit model (MNL) which is convenient to apply and understand.

The framework of MNL is based on the utility theory. This theory assumes that an individual always selects the alternative that maximizes his/her utility from a set of alternatives. Koppelman and Bhat [23] used the utility theory general rule as:

$$U(X_i,s) > U(X_j,s) \quad (6)$$

Equation (6) specifies that when the options (alternative set includes) are only i and j, the individual will select the alternative *i* instead of *j*. To generalize the formula, it is assumed that in a case where there are *j* options, *J* will show the set of options and *J* has 2 or more elements. Thus, the probability of choosing alternative *i* is calculated by the following equation [24]:

$$P_r(i) = \frac{e^{V_i}}{\sum_{j=1}^{J} e^{V_j}} \quad (7)$$

In the literature, some of studies utilized the MNL for modelling the PSEs [8, 9, 13, 19], some others used the activity based modelling approach [16, 25] and some others tried different approaches such as the mesoscopic simulation model; an approach also containing the MNL [10], the category based modelling approach [26], etc. In this study, the MNL approach was used to calculate the probabilities of modes in the stage of modal split.

In this study, 4 transportation modes are defined: public transportation (PT), private vehicle (PV), private vehicle + public transportation (PVPT), and walking (W). The PVPT mode is used to represent the trips that are made by private vehicles at least in some part of the trip.

As it was mentioned before, the assumption is made due to the random utility theory that the user prefers the least costly and earliest mode for his/her trip. However, in this study, the choice of modes in PSEs travel demand model is thought to depend not only on travel time and travel cost but also on different variables specific to special events. For this reason, the modelling study was carried out by deriving new variables based on special events in the selection of the mode from the questionnaires.

4. 4. Variables of the Models Since the special events travel demand is different from the demand for

transportation to daily home-based work trips, new variables must be defined in addition to the travel time and travel costs that are the basis for that particular type of trips. Because, the special event participants do not have the behavior to catch up with the special event as soon as possible and with the least cost based on the data obtained from the surveys. Instead, spectators tends to go to the special event area much earlier, to experience the pre-event atmosphere. Therefore, the variables to be used in the mode choice model should be defined accordingly. As a result, "Arrival time" in minutes (ARRVT) will show how much time individuals allocate coming to the venue and its surroundings before the start of the match, and ANTICI (Annual average ticket price, which shows how much of their annual earnings are reserved for a season ticket to follow their matches from the venue / Annual average income, TL) variables were defined. Unlike the traditional 4-stage model, these new variables of planned special events were defined. The rest of the variables are travel time and travel cost which are commonly used in general. Finally, "ASC" presents the alternative specific constant of the modes.

In the previous steps, trip production and trip distribution operations were carried out on 6 different travel matrices in total: 1-Step, 2_1-Step, 2_2-Step, 3_1-Step, 3_2-Step and 3_3-Step. During the modal split step of the approach, modal segregation was made for each travel matrix separately. Furthermore, PVPT mode is considered as the reference mode in the modelling process. As a result, the model estimation results are given in Table 3.

The observation modal split of each trip matrix and the model results accordingly are given in the Table 4 above.

5. DISCUSSION AND CONCLUSION

This paper offers a very detailed description of the travel demand analysis of the planned special events from the beginning to the end. This analysis consists of survey methodology and model development with the dataset obtained by travel surveys. One of the aspects of this paper that is different from other similar studies in the literature, daily activity and trips are considered as they are related to the PSE. Because, as it is shown in the results, individuals do not take any risk to miss the game, so they plan their daily activities and trips according to PSE starting time. Dai et al. [27] claimed that participants of the PSE generally arrive in a short time before the start. On the contrary, according to the survey data, the spectators arrive to the vicinity of the stadium on average 140 minutes before the start of the game, although this games are organized every two

TABLE 3. Model estimation results

Variables	1-STEP GROUP		2-STEP GROUP				3-STEP GROUP					
			2_1-STEP		2_2-STEP		3_1-STEP		3_2-STEP		3_3-STEP	
CHO	**Coefficient**	**z**	**Coefficient**	**z**	**Coefficient**	**z**	**Coefficient**	**z**	**Coefficient**	**z**	**Coefficient**	**z**
ASC_PT	3.071*	5.89	4.917*	5.69	5.175*	4.03	0.087	0.01	1.090	1.55	4.377*	1.67
Travel time	-0.004	-0.91	-.015*	-2.24	-0.005	-0.27	-.061*	-1.80	-0.003	-0.19	-0.027	-0.63
Travel cost	-0.098	-1.44	-.200*	-1.94	-.334*	-1.88	-0.122	-0.35	-153.559	-0.81	-0.491	-0.87
ANTICI_PT	0.428	0.11	-0.002	-0.01	-6.009	-0.55	11.994	0.45	1.580	0.98	-	-
ARRVT_PT	0.002	0.64	0.001	0.30	-0.000	-0.05	0.021	1.03	-	-	-0.000	-0.09
ASC_PV	2.216*	4.12	3.459*	3.91	2.336*	1.85	-0.553	-0.09	-	-	-	-
Travel time	-0.007	-0.73	-.033*	-1.78	-0.001	-0.04	-0.068	-0.70	-	-	-	-
Travel cost	-.038*	-1.83	-.064*	-2.15	-0.136	-1.38	-0.167	-1.38	-	-	-	-
ANTICI_PV	-5.671	-1.20	0.028	0.13	-21.104	-1.40	9.603	0.36	-	-	-	-
ARRVT_PV	-0.000	-0.08	0.001	0.52	0.004	0.71	0.019	0.94	-	-	-	-
ASC_W	4.171*	6.04	5.250*	4.60	8.641*	7.53	3.196	0.37	2.958*	2.15	7.488*	3.50
Travel time	-.041*	-5.67	-.048*	-3.90	-.0571*	-9.60	-0.050	-1.00	-.037*	-1.91	-.064*	-3.59
ANTICI_W	-6.320	-0.91	-1.202	-0.73	-0.983	-0.09	-259.887	-0.37	-3.178	-0.84	-	-
ARRVT_W	-0.000	-0.06	0.002	0.61	-0.006	-1.02	0.0179	0.85	-	-	-0.002	-0.22

* ==> *Significance at 10% level.*

TABLE 4. Comparison of the modal split of the trip matrices of observations and model results

	1-STEP GROUP		2-STEP GROUP				3-STEP GROUP					
	1-Step Trips - Obs.	1-Step Trips Model	2_1-Step Trips - Obs.	2_1-Step Trips Model	2_2-Step Trips - Obs.	2_2-Step Trips Model	3_1-Step Trips - Obs.	3_1-Step Trips Model	3_2-Step Trips - Obs.	3_2-Step Trips Model	3_3-Step Trips - Obs.	3_3-Step Trips Model
PT	69%	71%	65%	65%	33%	57%	58%	58%	58%	59%	32%	34%
PV	20%	20%	27%	26%	5%	7%	32%	32%	26%	25%	8%	9%
PVPT	5%	5%	4%	4%	1%	2%	3%	3%	0%	0%	0%	0%
W	6%	4%	4%	5%	61%	33%	6%	7%	16%	16%	60%	56%

weeks. According to Chang and Lu [19], 39.5% of respondents consider about traffic congestion, 17.3% of willing to shop, some of them worry about parking space, so respondents come over the venues about three hours before the PSE. Finally, it can easily be said that the relationship between previous activities which can be defined as derived activities, and main activity (PSE) is very obvious.

As a result, the conclusions of the overall study can be emphasized as follows:

1. The new methodology of the modelling can be implied to any special event in any city,
2. The results of the modelling can be assigned easily to the current transport network. Also, the trip matrices can be added to the transportation master plan model of the metropolitan.
3. The model may be used to forecast travel demand for every potential PSE.
4. The results of the model can be used as input of the other macro planning studies such as transportation master plan, urban planning, etc.
5. In order to analyze travel behavior of the spectators, it is better to separate trips into the step groups. As it was presented in Figures 3, 4 and 5, trip length distributions of the various step groups are different from each other. Modelling PSE travel demand by combining all the trips at once decreases the resolution of the model.
6. In future studies, the traffic in the vicinity of the stadiums can be modelled at the micro-level and integrated into this macro-level PSE model in order to develop short-term, micro-scale traffic management and control policies.
7. On the other hand, the economic and fiscal feasibility of the projects may use the results of the PSE travel demand in some special cases. Generally, transportation master plan studies consider only the weekday peak hour traffic for modelling, and the projects and policies are developed according to the modelling results of the specific days and time. Due to some of the PSEs are organized on weekdays and weekend days, the effect of the travel demand for PSE can be ignored. However, it should be included travel demand forecasting process. The forecasting of travel demand brings out a very important grade which directly affects the selection of various management policies [28]. In order to follow an appropriate way to establish a policy or project to obtain a better-served transport network in the city, travel demand for PSE should be taken into consideration.
8. In this study football is considered as PSE. However, in some other countries, the PSE can be basketball, volleyball, etc. Cities of different sizes or cultures may have different orientations to a single sport, but in general sports activities are the ones that are followed with interest by everyone in all countries from east to west. For instance, in this study, no impact of age, gender, and level of income on mode choice preferences was observed. The participation patterns to these activities are similar around the world that lead to the use of models having a similar approach to the one used in this paper.
9. PSEs are extra activities that people choose for having a good time and pay for them in order to raise their happiness and satisfaction. Better transport network services support their purposes. As a result, these events have an important role for citizens to come together, to be one, and a sense of possession of the city.

6. ACKNOWLEDGMENT

The authors wish to thank Istanbul Technical University Scientific Research Projects Coordination Unit (ITU BAP) for their support.

7. REFERENCES

1. Sumi, L. and Ranga, V., "Intelligent traffic management system for prioritizing emergency vehiclesin a smart city", ***International Journal of Engineering- Transaction A: Basics,*** Vol. 31, No. 2, (2018), 278-283. https://doi.org/10.5829/ije.2018.31.02b.11
2. Federal Highway Administration (FHWA). "Managing Travel for Planned Special Events Handbook: Executive Summary", FHWA-HOP-07-108. Department of Transportation, (2007), Washington D.C, USA. https://ops.fhwa.dot.gov/publications/fhwahop07108/plnd_spcl_evnts.pdf
3. Latoski S P, Dunn W M, Wagenblast B, Randall J, Walker M D. "Managing travel for planned special events." Department of Transportation, (2003), USA. https://ops.fhwa.dot.gov/program_areas/sp-events-mgmt/handbook/handbook.pdf
4. Federal Highway Administration (FHWA). "Planned Special Events – Economic Role and Congestion Effects", FHWA-HOP-08-022. Department of Transportation, (2008), Washington D.C, USA. https://ops.fhwa.dot.gov/publications/fhwahop08022/fhwa_hop_08_022.pdf
5. Kwon, J., Mauch, M. and Varaiya, P. "Components of Congestion: Delay from Incidents, Special Events, Lane Closures, Weather, Potential Ramp Metering Gain, and Excess Demand." ***Transportation Research Record: Journal of the Transportation Research Board,*** No. 1959, Transportation Research Board of the National Academies, (2006), 84-91. https://doi.org/10.1177/0361198106195900110
6. Federal Highway Administration, "An Initial Assessment of Freight Bottlenecks on Highways" (2005). https://www.fhwa.dot.gov/policy/otps/bottlenecks/bottlenecks.pdf
7. Getz D. "Event Tourism: Definition, evolution, and research." ***Tourism Management.*** Vol. 29, No. 3, (1997), 403-428. https://doi.org/10.1016/j.tourman.2007.07.017
8. Kuppam A, Copperman R, Lemp J, Rossi T, Livshits V, Vallabhaneni L, Jeon K and Brown E. "Special events travel surveys and model development", ***Transportation Letters,*** Vol. 5, No. 2, (2013), 67-82, DOI: 10.1179/1942786713Z.0000000007. https://doi.org/10.1179/1942786713Z.0000000007
9. Frantzeskakis J, Frantzeskakis M. "Athens 2004 Olympic Games: Transportation Planning, Simulation and Traffic Management", ***ITE Journal,*** Vol. 76, No. 10, (2006), 26-32. https://trid.trb.org/view/795755
10. Lin, Y.-Z and Chen, W. –H. "A simulation-based multiclass, multimodal traffic assignment model with departure time for evaluating traffic control plans of planned special events". ***Transport. Res. Procedia,*** Vol. 25, (2017), 1352-1379. https://doi.org/10.1016/j.trpro.2017.05.161
11. Frawley S, Hoven P V. "Football participation legacy and Australia's qualification for the 2006 Football World Cup". ***Soccer & Society***. (2015), Vol. 16, No. 4, 482-492. https://doi.org/10.1080/14660970.2014.882817
12. Li Y, Wang X, Sun S, Ma X, Lu G. "Forecasting short-term subway passenger flow under special events scenarios using multiscale radial basis function networks", ***Transportation Research Part C.*** Vol. 77, (2017), 306-328. https://doi.org/10.1016/j.trc.2017.02.005
13. Shakibaei S, Tezcan O H, Ogut S. "Evaluating Transportation Preferences for Special Events: A Case Study for a Megacity, Istanbul." EWGT2013 - 16th Meeting of the EURO Working Group on ***Transportation. Procedia - Social and Behavioral Sciences***; Vol. 111, (2014), 98-106. https://doi.org/10.1016/j.sbspro.2014.01.042
14. Zagidullin R. "Model of Road Traffic Management in the City during Major Sporting Events", ***Transportation Research Procedia***. Vol. 20, (2017), 709-716. https://doi.org/10.1016/j.trpro.2017.01.115
15. Shin J, Lyu S O. "Using a discrete choice experiment to estimate spectators' willingness to pay for professional baseball park sportscape", ***Sport Management Review***, Vol. 22, (2019), 502-512. https://doi.org/10.1016/j.smr.2018.06.009
16. Yan, L. C., Yang, S. S. and Fu, G. J. "Travel Demand Model for Beijing 2008 Olympic Games", ***Journal of Transportation Engineering***, Vol. 136, No. 6, (2010), 537-544. https://ascelibrary.org/doi/10.1061/%28ASCE%29TE.1943-5436.0000105
17. Florez, J., Muniz, J., and Portugal, L. "Pedestrian quality of service: Lessons from Maracanã Stadium", ***Procedia - Social and Behavioral Sciences,*** Vol. 160, (2014), 130-139. https://doi.org/10.1016/j.sbspro.2014.12.124
18. Bowman, J.L., and Ben-Akiva M.E. "Activity-based disaggregate travel demand model system with activity schedules", ***Transportation Research Part A***, Vol. 35, (2000), 1–28. https://doi.org/10.1016/S0965-8564(99)00043-9
19. Chang, M. and Lu, P. "A Multinomial Logit Model of Mode and Arrival Time Choices for Planned Special Events", ***Journal of the Eastern Asia Society for Trans. Studies,*** Vol. 10, (2013). https://doi.org/10.11175/easts.10.710
20. M. Elmorssy and T.H. Onur, "Modelling Departure Time, Destination and Travel Mode Choices by Using Generalized Nested Logit Model: Discretionary Trips", ***International Journal of Engineering, Transactions B: Applications,*** Vol. 33, No. 2, (2020), 186-197. https://doi.org/10.5829/IJE.2020.33.02B.02
21. Ortuzar, J. D., and Willumsen, L. G. "Modelling Transport (4th Edition)". A John Wiley and Sons, Ltd., Publication, (2011). ISBN: 978-0-470-76039-0.
22. Salter, RJ and Hounsell, NB. Highway traffic analysis and design. New York: Palgrave Macmillan, 1996. https://doi.org/10.1007/978-1-349-13423-6
23. Koppelman F S, Bhat C. "A Self Instructing Course in Mode Choice Modelling: Multinomial and Nested Logit Models." U.S. Department of Transportation Federal Transit Administration, (2006), 18-19. https://www.ce.utexas.edu/prof/bhat/COURSES/LM_Draft_060131Final-060630.pdf
24. Kamboozia, N., Ameri, M., and Hosseinian, S.M. "Statistical analysis and accident prediction models leading to pedestrian injuries and deaths on rural roads in Iran". ***International Journal of Injury Control and Safety Promotion***, (2020). https://doi.org/10.1080/17457300.2020.1812670
25. Milkovits, M., Kuppam, A., Kurth, D. and Rossi, T. "Comprehensive Validation Of An Activity-Based Model - Experiences from Houston-Galveston Area Council's Activity-Based Model Development", Prepared for presentation and possible publication ***Transportation Research Board 94th Annual Meeting*** Washington, D.C. Submitted: August 1, 2014. https://trid.trb.org/view/1338527
26. Kwoczek, S., Di Martino, S. and Nejd, W. "Predicting and visualizing traffic congestion in the presence of planned special events." ***Journal of Visual Languages and Computing,*** Vol. 25, (2014), 973-980. https://doi.org/10.1016/j.jvlc.2014.10.028
27. Dai, L., Gu, J., Sun, Z., and Qiu, H., "Study on Traffic Organization and Management Strategies for Large Special Events", ***International Conference on System Science and Engineering***, (2012), Dalian, China. https://doi.org/10.1109/ICSSE.2012.6257222
28. Ghasemi, J. and Rasekhi, J., "Traffic Signal Prediction Using Elman Neural Network and Particle Swarm Optimization", ***International Journal of Engineering, Transactions B: Applications***, Vol. 29, No. 11, (2016), 1558-1564. https://doi.org/10.5829/idosi.ije.2016.29.11b.09

Persian Abstract

چکیده

وقتی یک رویداد ویژه برنامه ریزی شده (PSE) ذکر می شود ، سازمان های بزرگ و بین المللی در نظر گرفته می شوند. این سازمان ها افراد زیادی را در سراسر جهان به نقاط محلی جذب می کنند. با این حال ، PSE های مقیاس نسبتاً کوچک مانند بازی های لیگ معمولی که هر دو هفته یک بار برگزار می شوند و بر ترافیک روزانه شهرها به ویژه کلانشهرها تأثیر می گذارند ، نادیده گرفته می شوند. این مقاله بر مدل سازی تقاضای سفر از بازیهای سوپرلیگ معمولی در استانبول تمرکز دارد. به عنوان یک هدف از این مقاله ، به منظور دستیابی به یک مدل PSE قابل تنظیم و مستقل ، طراحی نظر سنجی و روش های جمع آوری داده ها ، روش جدیدی برای تولید سفر ، توزیع سفر و مراحل تقسیم معین مدل سنتی تقاضای ۴ مرحله ای در نظر گرفته شده است. با فرضتی که روش پیشنهادی تازه ارائه داده است ، برخلاف بیشتر مطالعات قبلی در زمینه ادبیات ، همه سفرها و فعالیت ها در همان روز با PSE به فرآیند مدل سازی اختصاص می یابد ، زیرا به دلیل ماهیت PSE ها ، شرکت کنندگان ترجیح می دهند کارهای اضافی (فعالیت های مشتق شده) در فاصله بین ترک مبدا و پیوستن بهPSE . بر این اساس ، گروه های ۱ ، ۲ و ۳ مرحله ای تعریف می شوند و شکل توزیع طول سفر نه تنها از ساعات اوج مصرف بلکه با یکدیگر متفاوت است. در پایان ، برآورد مدل و توسعه مدل تقاضای سفر PSE با نتیجه گیری و پیشنهادات ارائه شده است.

International Journal of Engineering

Journal Homepage: www.ije.ir

The Post-disaster House: Simple Instant House using Lightweight Steel Structure, Bracing, and Local Wood Wall

I. N. Sutarja[a], M. D. W. Ardana[a], I. D. G. A. D. Putra*[b]

[a] *Department of Civil Engineering, Faculty of Engineering, Udayana University, Bali Indonesia*
[b] *Department of Architecture, Faculty of Engineering, Udayana University, Bali Indonesia*

PAPER INFO

Paper history:
Received 3 November 2020
Received in revised form 20 November 2020
Accepted 10 December 2020

Keywords:
Ergonomic
Earthquakes
Natural Hazard
Safety
Comfort

ABSTRACT

Losing a house is the biggest threat to people during natural disasters, such as earthquakes that are frequent natural hazards in Indonesia. Post-disaster housing reconstruction becomes a construction challenge to build adequate houses contributing to personal safety, health and comfort. The invention of a simple ergonomic instant house using lightweight steel structure, bracing, and the local wood walls is urgently needed. This invention is proposed to provide quick and low-cost mass construction house which meet safety and comfort requirements. The house is designed in 6 meters by 3.5 meters while the height of the ceiling is 2.8 meters. The house's front side is equipped with a door and a window, while at the back is equipped with a window. The six criteria for appropriate technology are considered in the construction method. The criteria include technical, ergonomic, social and cultural, energy-saving systems, and environmentally friendly. The scheme of systemic, holistic, interdisciplinary and participatory (SHIP) is considered at stages of design, construction and maintenance. The structure system is analyzed with a 3D model of the finite element method using SAP-2000. The given questionnaires' feedback assesses the satisfaction of the residents living in the house. The conclusions are included in five substances: (1) The house materials are lightweight steels, bracings, and local wood; (2) The structure should meet the safety requirement; (3) The house satisfies the requirement of safety and health; (4) The residents are satisfied and positively improve their living conditions following the disaster; (5) The house satisfies a simple ergonomic house.

***doi**: 10.5829/ije.2021.34.02b.06*

1. INTRODUCTION

A nation ravaged by earthquakes has significant reconstruction problems after disasters [1, 2]. The damages of buildings, including houses, have been the most severe risk in the aftermath of natural disasters and earthquakes in Indonesia's archipelago, including Bali. After disasters, reconstruction of housing is becoming a challenge to create suitable houses for the community [3–6]. This obstacle is an important aspect of the rebuilding process after the earthquake [7]. The other task of providing an appropriate post-disaster house is to manufacture housing units for construction after an earthquake within a certain period and in mass numbers [1]. Many ring of fire areas, like Bali, are also facing this threat, located in the tropical region and the fire ring, Bali is at high risk for natural hazards, including earthquakes [8]. Bali's earthquakes in 1815 and 1917, well known as "*gejer* Bali," caused numerous casualties of 10.253 people and 1500 people to lose their lives [9]. The other earthquakes in Bali that caused casualties and buildings' damage, including houses, were in Buleleng in 1862, known as the Buleleng earthquake; Seririt in 1976, called Seririt earthquake [10]; and Negara in 1890, called Negara earthquake [11]. Several other earthquakes also led to material loss. The earthquakes taking place outside Bali can also impact Bali. The earthquake with magnitude of 6.4 on the Richter scale on 29 July 2018 and the other one with a magnitude of 7 on the Richter

*Corresponding Author Institutional Email: diasanaputra@unud.ac.id (I. D. G. A. D. Putra)

Please cite this article as: I. N. Sutarja, M. D. W. Ardana, I. D. G. A. D. Putra, The Post-disaster House: Simple Instant House using Lightweight Steel Structure, Bracing, and Local Wood Wall, International Journal of Engineering, Transactions B: Applications Vol. 34, No. 02, (2021) 348-354

scale in Lombok on 5 August 2018 [12] destroyed many buildings in Bali.

This paper then argues that instant houses need to be constructed for those whose areas are seriously affected by the earthquake as shelters and a temporary residence for the victims. A simple house with the structural system of lightweight steel structure, bracing and local wooden walls, which is sheltered but resistant to absolute earthquake magnitude and still endow with comfortable, are needed. A lightweight steel structure has strong seismic impact properties in an earthquake-prone environment [13]. This structure's benefits are economical, weight decline, excellent moisture type stability, fast site installation, easy prefabrication, good reusable recycling, and possible reuse [14]. This system can also be constructed within a short period, relatively inexpensive, environmentally friendly, secure, comfortable and accessible.

2. METHOD

To examine this system, a lightweight weight steel structure, bracing and local wooden walls house as a mockup structure was constructed in Selemadeg Bali. The building applied six criteria of efficient technology (technical, ergonomic, socio-cultural, energy-saving and environmentally friendly). These criteria were combined with the SHIP approach (systemic, holistic, interdisciplinary and participatory). This approach aims to produce appropriate, environmentally friendly and energy-preserving technology that matches local wisdom [15]. Both approaches are applied from the design, construction and maintenance stages [16].

To evaluate the building's performance as a post-disaster building, this paper then investigated three aspects: building structure performances, physical comfort, and people's perception. The building structure's performances were analyzed using the Finite Element Method (FEM) and based on IBC 2009 to determine their safety level. The Finite Element Method is one of the most widely used numerical methods in engineering. This method attempts to solve partial differential equations and other integration equations that result in the discretization of continuum objects. This method is known to be quite effective in solving a structure analysis. In this method, the simulation of the structure was analysed using the SAP-2000 computer program. In this structural examination, some elements were investigated, including static and live loads that were the main components to analyze building structured. Since the building is located in the ring of fire and tropical regions, the earthquake and wind loads were also important in analyzing the structure's stability.

On the other hand, the house's physical comfort, including humidity, temperature, wind speed, noise and lighting, was measured in the built-up structure. This physical comfort is related to the ergonomic components that are associated with the occupants' satisfaction. People's expectations of safety, subjective comfort and satisfaction were then analyzed using questionnaires after the respondents used the structure for daily activities. These components are evaluated because they were related to the perception of people that used the structure.

3. RESULTS AND DISCUSSIONS

3. 1. The Characteristics of the Sample House

The house mockup was constructed as shown in Figure 1. Steel bracing was used since the method is easy to be applied and has low weight [17]. The construction took one week and one week for finishing such as painting and floor tiling. The construction was started from preparing the land (Figure 1a) and followed by constructing the concrate brick foundation (Figure 1b).

The lightweight steels and the concrete bricks were then built (Figure 1c) on the foundation. The final step was the installation of wooden walls on the concrete brick walls, floor tiling and painting the wall (Figure 1d.). The system used the structure's honesty, like the Balinese building when structural elements reveal and exhibit their purposes and materials [18, 19]. The Characteristics are presented in Table 1

3. 2. The Performance of the Building Structure

Structure performance is defined as the horizontal deviation ratio of the building peak divided by the total building height (Hsx). The building's performance was analyzed on three dimensions that evaluated the working earthquake weight before the maximum horizontal deviation was determined using SAP-2000 (Figure 2).

According to the loading characteristics and the post-disaster house design's actual working conditions, the structure's load could be analyzed. The paper analyzed the loads modeling, including static load, which consists of the weight of the structure, walls, floors and roofs, and live load, which is the external loads acting on the structure such as the weight of users, occupants or movable furniture (Figure 3). Since the environmental conditions are important and influence the structure, the temporary loads, including earthquake and wind load, were also analyzed (Figure 4). This figure shows the earthquake response spectrum for the Bali region to determine the earthquake load received by the structure.

Based on the three-dimensional analysis of SAP-2000, the maximum horizontal deviation of the building was 21 mm in the transverse direction (x) and 15 mm in the longitudinal direction (y). Meanwhile, the building's height from the floor to the peak (Hsx) was 4200 mm.

The structure performance was evaluated by multiplying 0.02 with Hsx (0.02 x Hsx), in which, based

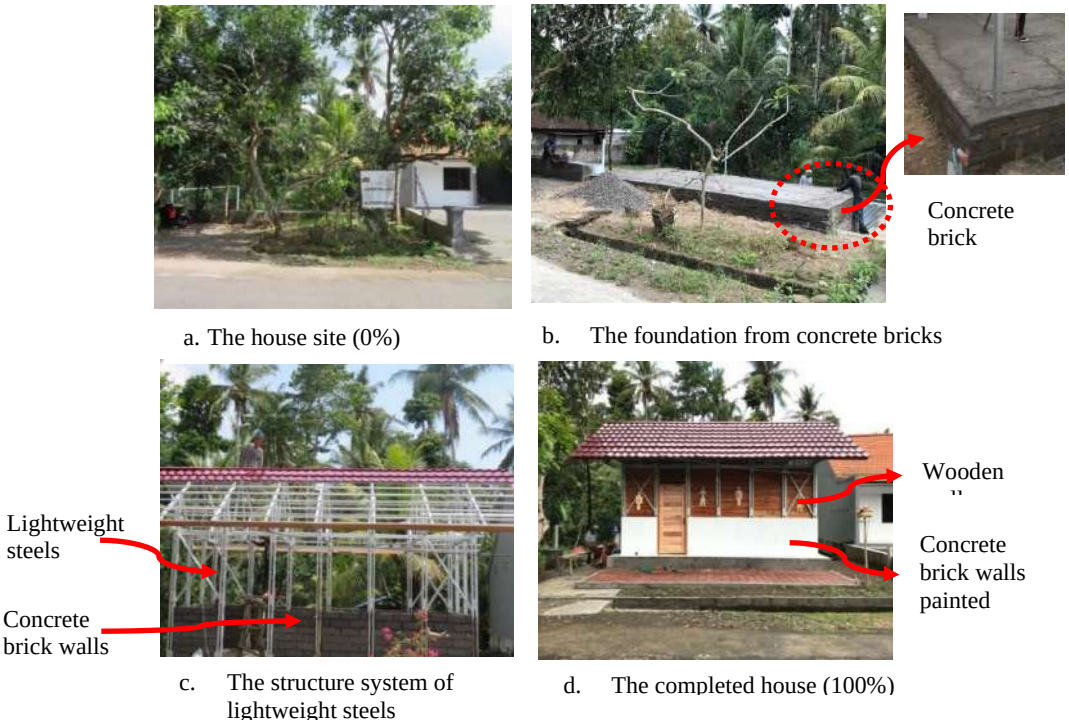

a. The house site (0%) b. The foundation from concrete bricks

c. The structure system of lightweight steels d. The completed house (100%)

Figure 1. The construction stages of the instant simple house with the structural system of lightweight steels, bracing and local wooden walls

TABLE 1. Characteristics of the instant simple house

No.	Specification	Value	Unit
1	The length of the building	6	m
2	The width of the building	3.5	m
3	The height of the building	4.2	m
4	The structural system of lightweight steels	40	m2
5	Metal tile roofs	51.2	m2
6	Local wooden walls	23.5	m2
7	Concrete walls covered with plaster	18	m2
8	A door	1.6	m2
9	Windows	0.8	m2
10	The ceramic floor	20	m2
11	Concrete foundation	18	m

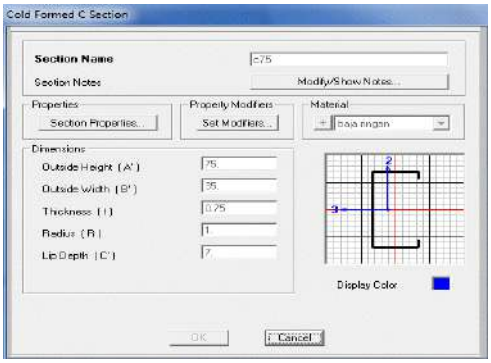

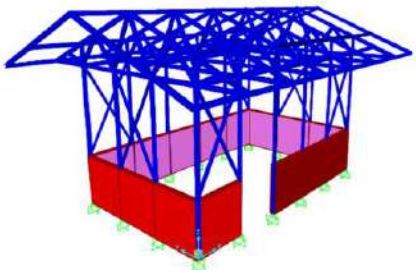

Figure 2. Dimensional modeling of the structural system of the house

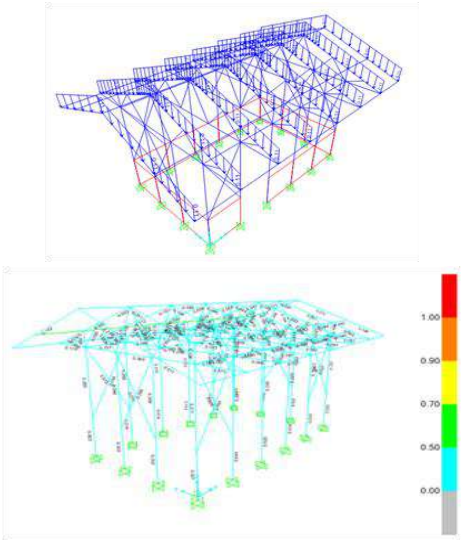

Figure 3. Static and live load

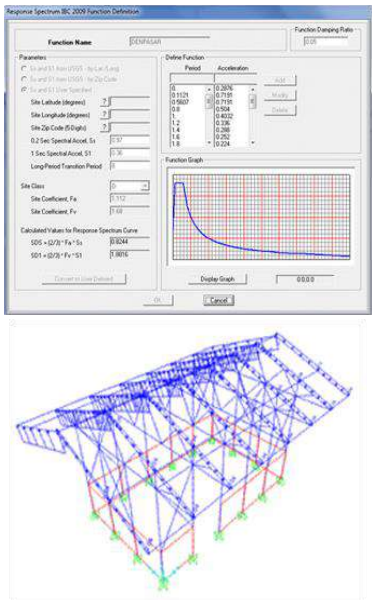

Figure 4. Earthquake and wind load

on the data, the structure is in good condition. This good performance can be analyzed since the result is 84 mm in which the result was less than the allowable value.

The stress ratio for all structural components resulting from peak, wind and earthquake loads can be described by colors in which green means under 70% and light blue means under 50%. Based on the SAP-2000 analysis, the post-disaster house structure's stress ratio was less than 50% in the lightweight steels and less than 70% on the foundation (Figure 5).

3. 3. The Physical Comfort The aspects of measuring the physical comfort consist of the humidity,

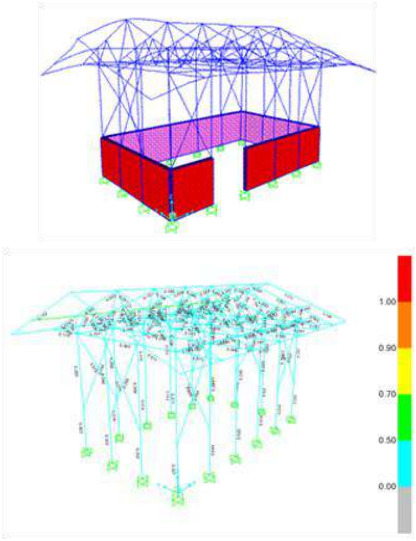

Figure 5. Deflection and the stress ratio

air temperature, wind velocity [20], natural illumination and noise. These parameters were measured at 6 AM, 8 AM, noon, 2 PM, 4 PM and 6 PM. The higher humidity was at 6.00 AM (82.1%), while the lowest (63.2 %) was at noon. The results contrasted with the temperature where the higher temperatures were at noon and 2.00 PM (30.6 ° C and 31.5° C). These results parallel to the natural illumination in which the highest was at noon (260 lux) and the lowest was at 6.00 PM (135 lux). The detail of the results is presented in Table 2.

3. 4. The People's Perception The information on the people's perception of the instant simple house was obtained through questionnaires. The perception, which was measured, included security, subjective comfort, adaptive comfort, and satisfaction. Mostly, the respondents thought that the structure was secure, comfortable and satisfied (Table 3).

TABLE 2. Physical comfort of the house

No	Descreption	The time when it was measured (Bali Time)						
		6:00 AM	8:00 AM	10:00 AM	12:00 AM (noon)	2:00 PM	4:00 PM	6:00 PM
1	Temperature (^{0}C)	15.2	26.8	28.8	30.6	31.5	29.5	29.2
2	Humidity (%)	82.1	84.1	75.6	63.2	68.5	72.8	77.6
3	Noise (dBA)	44	41	43	38	45	43	44
4	Natural Illumination (lux)	150	185	230	260	255	225	135
5	The wind velocity (m/second)	0.1	0.15	0.1	0.2	0.2	0.1	0.1

TABLE 3. People's perception

No.	Number of Samples	Description of Perception	People's Perception
1	11	Security	Secure
2	11	Subjective comfort	Comfortable
3	11	Thermal comfort	Comfortable and acceptable
4	11	Satisfaction	Highly satisfied

3. 5. Discussion

3. 5. 1. Performance and Security of the Structural System

The structural system showed a highly good performance based on the deviation to the building's height towards both the house's width and length. The structure performance value that was 84 mm means that the value was less than the allowable value. This value presented that the structure was in a good performance. The stress ratio under 70% demonstrated that the structure could address the loads on the structure.

The analysis of the earthquake load on this structure was necessary. Many researchers such as Yosafat [21], and Almeida et al. [22] suggested that the structure resistance to the earthquake loads was highly prominently evaluated since most parts of Indonesia's earthquake intensity, including Bali, ranges from being moderate to high. Based on the Indonesian National Standard, the stress ratio smaller than 70% means that the house was satisfied and secure to be used, based on the requirement.

3. 5. 2. The Physical Comfort

The house's physical comfort is affected by temperature, relative humidity, wind velocity, lighting, and noise. The house's temperature ranged from 25.2ºC to 31.5ºC (Table 2). These data demonstrated that the average temperature was 28.8ºC. This temperature level produced thermal comfort for the occupants or users based on the requirement of thermal comfort level in the equator (22.5ºC to 29.5ºC [23] or 22.8ºC to 30.2ºC [24]).

The comfortable temperature was also parallel to the humidity in which relative humidity (RH) of the outdoor and indoor was almost similar, between 62.3% and 84.1%. It is better and safer if the RH is higher than 20% all year, 60% during the dry season, and under 80% in the winter [24]. RH more than 80% may cause less comfortable, disrupt the health of the inhabitant, and cause fungus on the skin.

The wind speed influences the percentage of RH. The wind movement influences the velocity of lost heat through evaporation and convection. The wind speed requirement for human comfort ranges from 0.1 to 0.3 m/s [23, 24]. It would be better if the wind speed is higher than 0.2 m/s [25]. These requirements have been fulfilled by the sample house in which the room's wind velocity ranged from 0.1to 0.2 m/s during day time. However, at night it was 0 m/s as the ventilation and window were closed. When the window and door closed, the fresh outdoor air could not enter inside, so that the air velocity was 0 m/s. This condition presents that the room still needs ventilations open all day to maintain the room's air circulation.

The outside wind is a potential air motion to reduce high temperatures, humidity and solar radiation in the room. The move also plays a role in air movement in the building through the ventilation. The house components, including a window installed on the front side and ventilation installed on the backside, have caused air motion and cross circulation inside the room. The fresh cooling air enters the room and pushing the hot air to the outside. This air circulation has produced indoor thermal comfort. Therefore, the thermal comfort created by this cooling air motion eliminates the need for artificial devices. This inside air circulation has impacted human healthiness and has increased the occupants' comfort [26, 27].

The natural illumination within the room during day time ranged from 135 Lux to 260 Lux. These data demonstrated that the natural illumination in the room still addressed the requirements (115 Lux) [28]. The natural illumination intensity was highly influenced by the width, position and type of the windows and door. In this structure, a window was installed at the front side, and another window was installed at the back. This position has produced cross air circulation from the front to the back and vice versa. In this term, the fresh air circulation and natural illumination were interrelated. According to Hindarto [29], the natural illumination from the window spreads into the room, and the air circulation in the room has caused not only comfortable but also energy efficiency [30] in which the house does not need another illumination device.

The natural illumination makes the room brighter and healthier. The sun's daylight penetrated the house so that the use of artificial illumination could be reduced. This condition influenced the maintenance and operational cost of the house [31]. The natural illumination could also kill any germs or bacteria that can grow well in a humid environment. The natural daylight is also related to Vitamin D, which is useful for the bone and skin [28].

Moreover, the maximum noise within a room during daytime is 45 dBA, which is still under the noise standard in Bali in which the standar is 50 dBA during day time and 45 dBA at night [32].

3. 5. 3. People's Perception

The people's perception of the building, which was already constructed, was positive in which the people feel secure and comfortable. In these terms, construction solutions have been proposed to improve human comfort, including the building's thermal performance [30]. The

environmental condition, which includes the temperature, humidity, noise, natural lighting and the wind velocity, made the people feel comfortable.

They were also satisfied with the building materials used, the construction process and the final result of the house. The instant simple house construction satisfied what is required to be healthy, secure, and ergonomic. This condition contributed to the living quality of its dwellers. If a house can fulfill its dwellers' needs and desires, it acts as a facility capable of improving the quality of life of its dwellers.

4. CONCLUSSIONS

Located in the tropical region and the ring of fire, the Bali's construction practices and analysis are influenced by natural hazards, including earthquakes and environmental conditions such as wind, humidity, temperature, natural illumination and noise. In order to investigate the safety, the computer modeling of the structure was analyzed with the finite element method using SAP-2000. This method was an effective way to analyzed the stress and stability of the structure. On the other hand, the satisfaction and comfort of the occupants were investigated through questionnaires.

The instant simple house using lightweight steel structure, bracing and local wooden wall has fulfilled the requirement. The structure has produced the structural system that has met the safety requirements in terms of static, live, earthquake and wind loads. Through analizing these four aspects, the house could be safely used by occupants.

In terms of comfortable and perseption of the occupants, the house designed was also to fulfill the requirements to safety and positively improve their living conditions after the disaster. Since the house produced comfortable and satisfying to the occupants, the house also addressed the ergonomic requirements.

However, the house designed should be installed ventilation so that at night, where a door and windows were closed, the fresh air can effectively enter the house and produce thermal comfort for the occupants.

5. ACKNOWLEDGMENTS

Thank God Almighty, as it is His blessing, which enabled this article to be completed on time. A word of appreciation should also go to Udayana University for funding this study.

6. REFERENCES

1. Tas, M., Tas, N., and Cosgun, N. "Study on permanent housing production after 1999 earthquake in Kocaeli (Turkey)," ***Disaster Prevention and Management***, Vol. 19, No. 1, (2010), 6-19, doi: 10.1108/09653561011022108.
2. Biswas, R. "Evaluating seismic effects on a water supply network and quantifying post-earthquake recovery," ***International Journal of Engineering, Transactions. B Application.,*** Vol. 32, No. 5, (2019), 654-660, doi:10.5829/ije.2019.32.05b.05.
3. Jigyasu, R. "From Marathwada to Gujarat – Emerging Challenges in Post-Earthquake Rehabilitation for Sustainable Eco-Development in South Asia," Proceedings of the First Society's resilience to disasters 21 International Conference on Post-disaster Reconstruction: Improving Post-disaster Reconstruction in Developing Countries, 23-25 May, Universite de Montreal, Montreal, Canada, (2002), 1-22, http://www.grif.umontreal.ca/pages/i-rec papers/rohit.PDF(Accessed 23rd Noveber 2012).
4. Wu, T.Y. and Lindell, M. K. "Housing reconstruction after two major earthquakes: The 1994 northridge earthquake in the United States and the 1999 Chi-chi earthquake in Taiwan," ***Disasters***, Vol. 28, No. 1, (2004), 63-81, doi:10.1111/j.0361-3666.2004.00243.x.
5. Chang, Y., Wilkinson, S., Potangaroa, R. and Seville, E. "Resourcing challenges for post-disaster housing reconstruction: A comparative analysis," ***Building Research and Information***, Vol. 38, No. 3, (2010), 247-264, doi:10.1080/09613211003693945.
6. Johnson, C. "Strategic planning for post-disaster temporary housing," ***Disasters***, Vol. 31, No. 4, (2007), 435-458, doi:10.1111/j.1467-7717.2007.01018.x.
7. Tas, N., Cosgun, N. and Tas, M., "A qualitative evaluation of the after earthquake permanent housings in Turkey in terms of user satisfaction—Kocaeli, Gundogdu Permanent Housing model," ***Building Environment***, Vol 42, No. 9, (2007), 3418-3431. doi.org/10.1016/j.buildenv.2006.09.002.
8. Bencana, M., "Mitigasi bencana berbasis potensi wisata: Studi kasus pantai pandawa, Desa Kutuh, Kecamatan Kutu Selatan, Kabupaten Badung, Provinsi Bali", (2016), 261-266, https://www.researchgate.net/publication/309555791.
9. Hidayatunnisak, S., Susilo, A. and Anshori, M. "Studi tomografi seismik untuk menentukan model kecepatan gelombang p daerah Bali," ***Brawijaya Physics Student Journal***, Vol. 2, No.1. (2014), 1-5, https://www.neliti.com/publications/159723/ studi-tomografi-seismik-untuk-menentukan-model-kecepatan-gelombang-p-daerah-bali.
10. Sabrianto L. and Awali, A. "Seismic Microzonation Using Microtremor Measurement for Natural Disasters Mitigation of Earthquake at Regions Singaraja City the Province of Bali Indonesia," ***ARPN Journal of Earth Sciences,*** Vol. 6, No. 1, (2017), 1-6, http://www.arpnjournals.org/jes/ research_papers/rp_2017/jes_0617_59.pdf.
11. Sulaeman, C., Hidayati, S., Omang, A.and Priambodo, I. C. "Tectonic model of Bali Island inferred from GPS data," ***Indonesian Journal of Geoscience***, Vol. 5, No. 1, (2018), 81-91, doi: 10.17014/ijog.5.1.81-91.
12. Salim, M. A., Siswanto, A. B. and Ardhani, M. S., "Recovery civil construction buildings due to the Earthquake Lombok," ***International Journal of Scientific and Technology Ressearch***, Vol. 8, No. 11, (2019), 814-817
13. Li, X., Wang, J., Meng, X., and Wang, J., "Comparison and Analysis of Lightweight Steel Structure Residential Housing," International Conference on Mechatronics, Control and Electronic Engineering (MCE-14), (2014), 718-722, doi:10.2991/mce-14.2014.146.
14. Santos, P., Martins, C., and Da Silva, L. S. "Thermal performance of lightweight steel-framed construction systems," ***Metallurgical Research and Technology***, Vol. 111, No. 6, (2014), 329-338, doi: 10.1051/metal/2014035.

15. Sudiajeng, L., Wiraga, I. W., Parwita, I. G. L. and Santosa, G. "Domestic recharge wells for rainwater-harvesting in Denpasar City, Bali - Indonesia," ***International Journal of Geomate***, vol. 13, No. 36, (2017), 50-57, doi: 10.21660/2017.36.2828.
16. Sutarja, I.N., Wirawibawa, I.B.G. and Yana A.A.G.A., Simple House with Brick Walls and Structure System of Bamboo Reinforced Concrete , Safe and Comfortable," ***Journal of Civil Engineering, Architecture and Built Environment***, Vol. 1 No. 1, (2017), 1-5, retrieved from https://ocs.unud.ac.id/index.php/JCABE/article/view/59936
17. Kafi, M. A., Kheyroddin, A., and Omrani, R."New Steel Divergent Braced Frame Systems for Strengthening of Reinforced Concrete Frames," ***International Journal of Engineering, Transactions A: Basics***, Vol. 33, No. 10, (2020), 1886-1896, doi:10.5829/ije.2020.33.10a.07.
18. Putra, I. D. G. A. D., Lozanovska, M. and Fuller, R. J. "A methodology to evaluate the transformation of traditional balinese houses as a consequence of Tourism," ***Archnet-IJAR***, Vol. 11, No. 1, 2017. 83-100, doi: 10.26687/archnet-ijar.v11i1.1134.
19. Dwijendra, N. K. A. "Meru as a hindu sacred building architecture with a high roof and resistant to earthquakes in Bali, Indonesia," ***Civil Engineering and Architecture,*** Vol. 8, No. 3, 350-358, 2020, doi: 10.13189/cea.2020.080319.
20. Rahim M. and Hamzah, B. "Land surface effects and thermal performance in hot-humid climate area," ***International Journal of Geomate,*** Vol. 17, No. 62, (2019), 237-243, doi:10.21660/2019.62.ICEE5.
21. Yosafat, A. P. "Evaluas Kinerja Gedung Beton Bertulang Tahan Gempa dengan Pushover Analysis (Sesuai ATC-40, FEMA 356 dan FEMA 440)," ***Jurnal Teknik Sipil***, Vol. 3, No. 1, (2006), 4-52, retrieved from http://sipil-uph.tripod.com/vol3.1.5.pdf.
22. De Almeida, N. M., Sousa, V., Dias, L. A. and Branco, F. A. "Managing the technical risk of performance-based building structures," ***Journal of Civil Engineering Management***, Vol. 21, No. 3, (2015), pp. 384–394, doi:10.3846/13923730.2014.893921.
23. Rahim, M.R, "*Fisika Bangunan untuk Area Tropis*." Bogor: PT Penerbit IPB Press, 2012, retrieved from https://books.google.co.id/books/about/Fisika_Bangunan_untuk_Area_Tropis.html?id=FKz5DwAAQBAJ&redir_esc=y
24. Latifah N L, "Fisika Bangunan 1" Jakarta: Griya Kreasi (2015)
25. Grandjean E. and Kroemer, K. H. E. "Fitting the task to the human: a textbook of occupational ergonomics." London: Taylor and Francis, (2009)
26. Szokolay, S. V. "Introduction to architectural science: the basis of sustainable design." Routledge, (2014).
27. Zheng, M. Li, S. and Liu, H. "Study on outdoor thermal environment of campus based on GIS," ***International Journal of Geomate***, Vol. 14, No. 46, (2018), 102-106, doi:10.21660/2018.46.7364.
28. Wibisono, M. "Pencahayaan Dalam Desain Rumah Tinggal, Tren Arsitektur 2010." mtmdesign.wordpress.com, (2010), retrieved from http://mtmdesign.wordpress.com/2010/08/10/ (2011).
29. Hindarto, P. "Memaksimalkan Pencahayaan Alami Dalam Rumah Kita.," *2011*, retrieved from http://astudioarchitect.com/2011/04/memaksimalkan-pencahayaan-alami-dalam.html (accessed Jan. 01, 2012).
30. Kulkarni, P. and Muthadhi, A. "Improving Thermal and Mechanical Property of Lightweight Concrete Using N-Butyl Stearate/Expanded Clay Aggregate with Alccofine1203," ***International Journal of Engineering, Transactions A: Basics***, Vol. 33, No. 10, (2020), 1842-1851, doi:10.5829/IJE.2020.33.10A.03
31. Indra, Z. P. "Pencahayaan Alami Solusi Utama Mendapatkan Kenyamanan dan Penghematan Listrik," (2011).
32. Sutarja, I. N. and Putra, I.D.G.A.D. "The Traditional Balinese Compound Walls as A Barrier of Traffic Noise," ***International Journal of Civil Engineering and Technology***, Vol. 10, No. 11, (2019), 323-332.

Persian Abstract

چکیده

از دست دادن خانه بزرگترین تهدید برای مردم در هنگام بلایای طبیعی مانند زمین لرزه هایی است که مکرراً خطرات طبیعی در اندونزی است. بازسازی مسکن پس از فاجعه به یک چالش ساختمانی برای ساخت خانه های مناسب تبدیل می شود که به ایمنی ، سلامتی و آسایش شخصی کمک می کند. اختراع یک خانه فوری ارگونومیک ساده با استفاده از ساختار فولادی سبک ، مهاربند و دیوارهای چوبی محلی به شدت مورد نیاز است. این اختراع برای تهیه سریع و کم هزینه ساخت وساز خانه ای ارائه می شود که شرایط ایمنی و آسایش را داشته باشند. این خانه در ۶ متر در ۳.۵ متر طراحی شده در حالی که ارتفاع سقف ۲.۸ متر است. قسمت جلویی خانه به در و پنجره مجهز است ، در حالی که در پشت به پنجره مجهز شده است. شش معیار برای فن آوری مناسب در روش ساخت در نظر گرفته شده است. این معیارها شامل فنی ، ارگونومیک ، اجتماعی و فرهنگی ، سیستم های کم مصرف و سازگار با محیط زیست است. طرح سیستماتیک ، جامع ، میان رشته ای و مشارکتی (SHIP) در مراحل طراحی ، ساخت و نگهداری در نظر گرفته شده است. سیستم سازه با استفاده ازنرم افزار SAP-2000 با مدل سه بعدی از روش اجزای محدود تجزیه و تحلیل می شود. بازخور پرسشنامه های ارائه شده رضایت ساکنان ساکن خانه را ارزیابی می کند. نتیجه گیری در پنج ماده گنجانده شده است: (۱) مواد خانه فولادهای سبک ، مهاربندها و چوب های محلی هستند. (۲) ساختار باید الزامات ایمنی را برآورده کند. (۳) خانه نیازهای ایمنی و بهداشت را برآورده می کند. (۴) ساکنان راضی هستند و به طور مثبت شرایط زندگی خود را پس از فاجعه بهبود می بخشند. (۵) خانه یک خانه ارگونومیک ساده را ارضا می کند.

IJE TRANSACTIONS B: Applications Vol. 34, No. 02, (February 2021) 355-366

International Journal of Engineering

Journal Homepage: www.ije.ir

Earthquake Prediction Modeling using Dynamic Changes Case Study: Alborz Region

T. Sadeghian*, M. Emamgholi Babadi

Department of Civil Engineering, Research Institute of ShakhesPajouh, Isfahan, Iran

P A P E R I N F O

Paper history:
Received 03 November 2020
Received in revised form 28 December 2020
Accepted 28 December 2020

Keywords:
Coulomb Stress
Dynamic Changes
Earth Viscosity
Earthquake Prediction
Rudbar Earthquake

A B S T R A C T

This study aims to investigate the computational effect of Earth's viscosity on the Coulomb stress changes. Therefore, several large earthquakes in the Alborz region are selected and Coulomb stress changes are calculated in them, then the Coulomb stress temporal changes are shown by assuming the earth as an elastic layer on a viscous- elastic half-space. The spatial and temporal changes of the crustal deformation process associated with earthquakes depend on several parameters including the thickness of the lithosphere, viscosity of the asthenosphere, and dip angle of fault. The findings of this study are presented by determining the impact of modeling results on each of the input parameters through the sensitivity analysis of co-seismic and post-seismic deformation due to the dip-slip and strike-slip faulting. In addition to the useful results reported for the impact of parameters, the obtained results indicate the occurrence of numerous aftershocks in a region with increased Coulomb stress from 0.1 to 0.8 bar and the non-occurrence or low-occurrence of aftershocks in a region with reduced Coulomb stress. In addition to the predicted locations of aftershocks, it is also possible to determine the location of the next major earthquake using Coulomb stress change calculations.

***doi**: 10. 5829/ije.2021.34.02b.07*

1. INTRODUCTION

Crustal deformation measurement by modern methods has an important impact on current tectonic studies. Even though these measurements provide valuable information about the way of current earth deformation for researchers, they have no answer for the causes of these deformations. Furthermore, these measurements cannot determine and justify the future or past tectonic earth behavior [1]. Therefore, different branches of earth sciences apply the mathematics and physics-based models. In crustal deformation studies, the fault models based on the geological, geodetic and seismic information provide valuable information about the properties and behavior of a fault during the time. Based on the previous observations, the models provide estimates of future deformations and seismic risks for researchers and are so valuable for neighboring big cities of active seismic zones [2]. For example, some studies have been done using an artificial neural networks (ANN) [3] or a machine learning [4].

Crustal deformation occurs locally at long-term intervals (Quaternary and Miocene) due to the earthquakes and landslides in major fault systems. Considering this fact, the collision boundary of Arabian and Eurasian planes are expanded in a large zone (almost within the political borders of Iran) and it is in fact like a soft wide boundary between two moving and colliding Arabian and Eurasian planes. Deformation resulting from this collision is distributed in a wide range of different faulting systems in Iran.

This study seeks to indicate the computational impact of Earth's viscosity on Coulomb stress changes. Thus, several large earthquakes in the Alborz zone are selected and their Coulomb stress changes are calculated. The Coulomb stress changes are shown assuming the earth as an elastic layer on a viscous-elastic half-space.

Modeling makes the temporal prediction of earthquakes possible. By modeling the Coulomb stress dynamic changes, the fault movements can be typically stimulated by the movement of tectonic plates and the

*Corresponding Author Email: *tadbirtara@gmail.com* (T. Sadeghian)

Please cite this article as: T. Sadeghian, M. Emamgholi Babadi, Earthquake Prediction Modeling using Dynamic Changes Case Study: Alborz Region, International Journal of Engineering, B: Applications Vol. 34, No. 02, (2021) 355-366

position parameters on these planes in target periods. Different points on the planes, typically around the fault and created coverage networks around it are modeled by changes in the horizontal and vertical positions. These points are simulated at defined time intervals. The displacement of points over time can be investigated and expanded through these tools and models.

The research on the 1999 Marmara Earthquake Sequence in Turkey and the effects of Coulomb stress on it can be considered as the studies in this regard [5, 6] or also the first research on San Andreas Fault and the static stress changes [7]. Furthermore, research was done by Freed and Lin [8] on the Viscoelastic Stress Transfer over time in the 1999 Hector Mine Earthquake. Another study in this regard was conducted by Wang in 2008 on delay and triggering of an earthquake by a dynamic interaction between faults in the Xianshuihe fault zone in southwest China [9]. Paolucci et al. [10] also used a physics-based numerical approach to a model of earthquake ground motion due to induced seismicity in the Groningen gas field.

2. PROBLEM STATEMENT

2. 1. A Three-dimensional Semi-analytical Viscoelastic Model for Temporal Analysis of Earthquake Cycles The earthquake cycle analysis for large complex tectonic boundaries, which are deformed during thousands of years, needs the development of effective and complex models. In this study, Maxwell three-dimensional linear elastic semi-analytical model is introduced and developed for utilizing the computational benefits of convolution theory in Fourier Theorem [11]. (According to convolution theory, the convolutive integrals can be solved by Fourier integral method). The new aspect of this model is the analytical solution for surface loading of an elastic plane on a viscoelastic half-space. When the model is fully implemented, the following cases will be simulated [12]

1. Inter-seismic stress accumulation in the upper locked section of the fault
2. Repeated earthquakes in pre-existing fault planes
3. The response of elastic viscosity under-plane asthenosphere after rupture.

According to the proposed approach, it is possible to investigate the thousand years of earthquake cycle along with the fault systems with complex three-dimensional geometry.

The long-term tectonic loading, sudden fault rupture and post-seismic transient return are among the key factors of the earthquake cycle and represent the important spatial and temporal characteristics of crustal deformation. Understanding these dynamics for complex continental borders needs temporal three-dimensional models that can simulate deformation at the large scale of time and space. These models should include both the real three-dimensional geometry of fault systems and the viscoelastic response of repeated earthquakes [13]. Even by limiting the quasi-static mode (no seismic waves), these models should include the time period from rupture (about 100 seconds) to return which takes about 1000 years as well as the longitudinal range from the fault thickness (about 500 m) to deformation boundary (about 1000 km) [14].

The pure numerical algorithms, which even can be run in the most powerful computers, cannot sufficiently solve this wide range of length and time. Therefore, there is a need for improved analytical methods to reduce the numerical range of issues.

This study provides a semi-analytical solution for the response of an elastic plane overlying a viscoelastic half-space due to the time-dependent volumetric point forces (Figure 1). Although the presented method expands an analytical method [15], it has the computational advantages compared to the numerical methods and has a qualitative agreement with most of the numerical pure studies. The three-dimensional issue is analytically solved both in vertical (z) and time (t) dimensions. While, a solution is expanded in two horizontal dimensions (x, y) in Fourier Transform space to utilize the advantages of convolution theory. Using this method, the fault horizontal pattern and distribution of slip can be without an increase in complex computational load. The three-dimensional model shown here can be easily run in a computer through a network that covers a spatial zone from 1 km to 2048 km; this model can also be implemented for broader networks.

The viscoelastic half-space has the viscosity coefficient of η. d_1 and d_2 are the low and high locking depth, respectively. The velocity vectors are applied in opposite directions to the fault plane.

Here, the semi-analytical solution to the three-dimensional viscoelastic issue is expanded for the vertical strike-slip fault model and it compares the

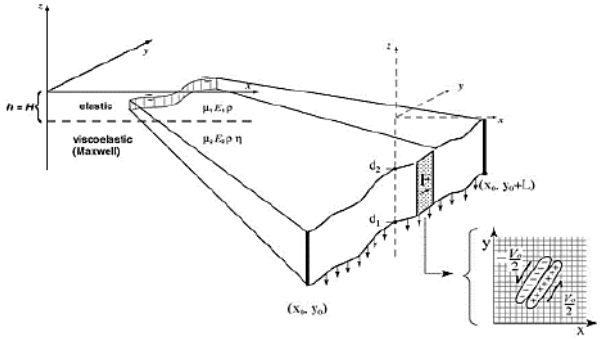

Figure 1. Three-dimensional fault Fourier model which simulates an elastic layer on a viscoelastic linear half-space

numerical results compared to the known analytical solutions to assess the accuracy and efficiency of the technique. These models are necessary because the seismic and geodetic measurements only record a small part of the earthquake cycle on the main parts of the fault, thus the viscoelastic asthenosphere response which involves a long-term fault-fault connection remains with a weak bound. Furthermore, the mechanical post-seismic deformations leave numerous unanswered questions that are associated with the rheological parameters and ground time-dependent relaxation process.

Several post-seismic models have been developed with adaption to the surface geodetic velocities. These models include the poroelastic flow of fluids in the upper crust, deep aftershocks and fault zone collapse. However, numerous efforts are taken to investigate these models from the post-seismic behavior. A model based on the viscoelastic connection between the upper elastic plane and a viscoelastic linear half-space is investigated in this study [16, 17].

Furthermore, the effect of gravity is considered in a viscoelastic model to ensure the results of vertical strikes.

In addition to understanding the post-seismic deformation, numerous studies have focused on the three-dimensional development of the stress field. Coulomb stress changes caused by major earthquakes are utilized to explain the triggering of subsequent earthquakes and aftershocks [18–20].

Several stress transfer calculations are only based on the pure elastic models because the analytical solutions Okada [21] can be effectively measured in three dimensions for actual geometry of fault and rupture history. However, the viscoelastic models are needed to investigate the temporal deformation and earthquake triggering at the time scales comparable with return periods. As a result, several models of actual elasticity are developed and applied for stress triggering after major earthquakes.

However, due to the limitations in computer speed and memory, most of these numerical models are limited with a relatively simple return interval and fault geometry. Therefore, the current models do not sufficiently show the three-dimensional interaction of multiple fault intersection branches covering several earthquake cycles. A complete model is combined from two concepts which can improve the seismic hazard analyses and provide a better understanding of the physics of the earthquake cycle [22].

2. 2. Coulomb Stress Coulomb stress is a criterion of shear stress loading on a fault with a particular azimuth. Positive Coulomb stress indicates the tendency towards the fault plane rupture and the negative stress indicates the non-tendency towards the fault plane rupture. This thesis uses the method by King et al. [7] and defined the Coulomb rupture criterion as follows:

$$\sigma_f = \tau - \mu_f \sigma_n \quad (1)$$

In this regard, σ_n and τ are normal and shear stresses on the rupture plane respectively and μ_f is the effective coefficient of friction. The model used in this study produces the three-dimensional displacement field vector from which the stress tensor is calculated. The shear stress and tension are assumed right-handed and positive because Coulomb stress is zero at the surface and becomes singular in locking depth. Coulomb stress is calculated at half locking depth and μ_f is assumed equal to 0.6. The main objective is to detect Coulomb stress accumulation both before and after the earthquake.

2. 3. Coulomb Stress Change Modelling To perform the calculations, a variety of parameters especially the parameters describing the reference fault (the fault model which is built by optimal input geometric and physical parameters and based on which the faults are compared) and receiver fault are introduced into the model. Reference fault is determined with rupture parameters (slip, depth, length and Rake angle) and fault geometry (strike and dip angles). The receiver plane of fault, on which the Coulomb stress change is determined, is described by geometry and mechanism of faulting (strike, dip and Rake angles) [23].

Furthermore, the friction coefficient of the receiver fault and the half-space elastic parameters should be determined. The friction coefficient is determined from 0.6 to 0.8 using the experimental samples, but it seems that it is possible to change it at the interval from zero to 0.8 in stress triggering studies. The calculated results show a high sensitivity to the friction coefficient. In performing the calculations, the coefficient of friction is selected equal to 0.6. Therefore, Poisson's ratio is selected equal to 0.25, $8\times10^5 bar$ for Young's modulus and $3.3\times10^{10} Pascal$ for shear modulus [24].

Rupture parameters are the empirical parameters that connect the rupture length, width and average to the intensity of earthquakes.

3. REFERENCE MODEL

According to Figure 2 for the thickness of the elastic layer, the reference value of 41 km is used in this regard. Fault plane dip angle is selected equal to 20 degrees and locking depth above the rupture plane equal to 6 km.

TABLE 1. Geometry of reference faults considers the Coulomb stress changes modeling due to an earthquake.

Fault	Length (km)	Width (km)	Locking depth (km)	Dip (deg.)	Rake angle (deg.)	Slip	
						Strike	Dip
Reference Fault 1	80	40	6.0	20.0	0.0	5.0	5.0
Reference Fault 2	80	40	6.0	20.0	90.0	5.0	5.0

Furthermore, according to Table 1, the rupture plane is considered as the dip and strike-slip rate with a slip of 5 m and an area of 40×80 square kilometers. Dimensions in Figure 2 are selected according to the similar geometric values in previous studies [25, 26].
In addition to the geometry and location of reference faulting, the physical environment of the upper elastic layer should be described with other values. For these parameters, the average international values are selected according to Table 2

The applied half-space utilizes an elastic layer with a thickness of 41 km and a viscoelastic half-space. The coordinate system origin is at the top of the fault plane center and its x-axis is parallel to the longitudinal direction of the fault plane. The upper reference fault plane limit is at a depth of about 6 km from the ground. The fault plane is 80 km in length and 40 km in width and has a dip angle of 20 degrees to the horizontal level.

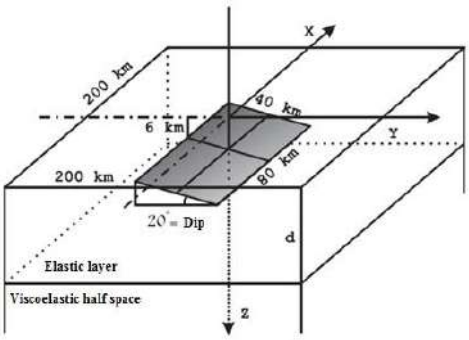

Figure 2. The geometry of fault and reference environment used in modeling the sensitivity analysis

TABLE 2. Physical properties of the elastic layer

Depth (km)	Wave velocity, P, (km/s)	Wave velocity, S, (km/s)	Density (kg/m^3)	Viscosity (Pa.s)
41	6.7	3.87	2900	0.0

4. DATA ANALYSIS

4. 1. Rupture Parameters The data of earthquake Mw= 7.4 (20.6.1990) in the Rudbar area was used for doing the calculations. Characteristics of this earthquake are extracted from the CMT catalog which gives us information such as the depth and magnitude of earthquakes as well as the spatial and temporal.

4. 2. Dynamic Modelling of Coulomb Stress Changes in the Alborz Mountains It is essential to know about the time and place of the severe earthquake and possible aftershocks due to the alarm before the earthquake and aftershocks to reduce the financial and human losses. Therefore, this question should be answered how the occurrence of an earthquake can cause another earthquake? This fact should be taken into account that an earthquake is along with faulting or rupture in the elastic crust of Earth. Therefore, the rupture criterion should be investigated in the elastic crust of Earth (Coulomb rupture criterion). According to the Coulomb rupture criterion, the tendency of rock to the elastic rupture is subject to normal and shear stresses imposed to the assumed rupture plane, and if the rate of Coulomb stress is higher than the critical limit, the elastic rupture or earthquakes will occur. Thus, the time-dependent modeling of Coulomb stress changes in the earth's crust caused by the tectonic co-seismic, post-seismic and pre-seismic activities, can be used as a criterion for estimating the time and place of earthquake hazard. This research

Wells Experimental relations provide the slip rate; and we obtain the direction of fault movement, which is the boundary condition in this section, through the Focal mechanism for a strike-slip fault, for instance, the left-handed Strike-Slip.

The experimental relations [27] between the intensity of earthquake and rupture parameters are utilized to calculate the length and width of rupture as well as the detachment due to the earthquake as follows.

$$\log(RLD) = -2.44 + 0.59 \times M_w \quad (2)$$

$$\log(RW) = -1.01 + 0.32 \times M_w \quad (3)$$

$$\log(AD) = -4.80 + 0.69 \times M_w \quad (4)$$

In the above equations, *Mw* is the earthquake moment rate, RLD is the subsurface rupture length in kilometer, RW is the width of rupture along the fault dip in kilometer and *AD* is the average rupture in meter.

4. 3. Three-dimensional Modelling of Displacement Field and Coulomb Stress Changes The model introduced by Okada [28] is utilized for modeling the three-dimensional displacement field of this earthquake, the results of the calculation are shown in Figures 3 and 4.

4. 4. Investigating Coulomb Stress Time Changes for Selected Earthquakes Afterward, Coulomb stress changes are measured for nine major mechanical and historical earthquakes with magnitudes greater than 6 in the Alborz region at the intervals of 5 years assuming the strike and dip slip receiver faults (the faults in these regions are more from these two types). The characteristics of selected earthquakes are presented in Table 3. Figure 4 to Figure 7 show the Coulomb stress time changes at intervals of 5 years assuming the strike-slip receiver faults. Figure 8 to Figure 11 shows the Coulomb stress time changes at intervals of 5 years assuming the dip-slip receiver faults. Coulomb stress time changes at intervals of 5 years can be seen in sequential forms.

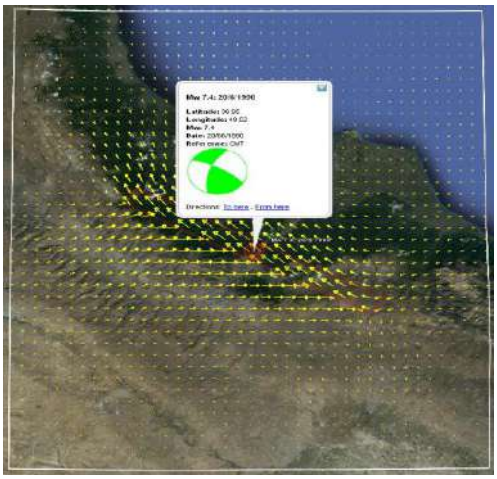

Figure 3. Horizontal displacement model due to the earthquake of Mw = 7.4 (20.6.1990) in Rudbar area in meter

For calculations, an elastic layer with a thickness of 41 km and a Lame coefficient of 40 GPa on the viscoelastic half-space with a Lame coefficient of 70 GPa and a viscosity of 1.0×10^{20} Pas. To achieve more accurate results, the fault planes are divided into smaller pieces. The results of calculations indicate the Coulomb stress changes at different time intervals affected by the viscosity of the viscoelastic half-space.

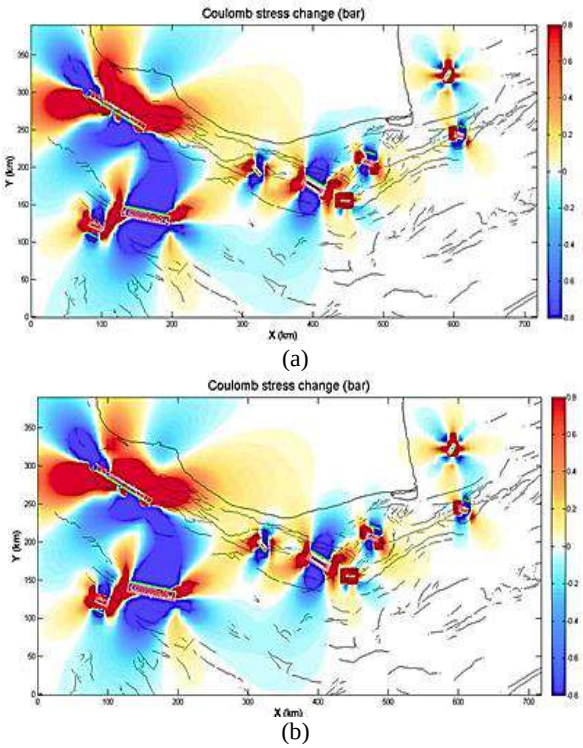

Figure 4. Coulomb stress time changes at 5-year time intervals assuming the Strike-slip receiver faults, a- Coulomb stress changes during an earthquake, b- Coulomb stress changes 5 years after the earthquake.

TABLE 3. Characteristics of selected earthquake for a dynamic study of Coulomb stress changes

Faults name	rake	dip	strike	Mag.	Depth (km)	lon (deg)	lat (deg)	Date (mm/dd/yyyy)
North Alborz F.	126	30	106	Ms:6.3	12	53.32	36.36	4/11/1935
North Alborz F.	90	45	120	Ms:6.8	13	52.47	36.07	7/2/1957
Ipak F.	70	52	101	Ms:7.2	15	49.81	35.71	9/1/1962
Khazar F.	126	30	106	Mw:6.1	15	54.77	36.68	10/29/1985
North Alborz F.	24	83	91	Mw:6	30	52.97	35.9	1/20/1990
Rudbar F.	32	73	300	Mw:7.4	18	49.35	36.99	6/20/1990
Ipak F.	99	29	295	Mw:6.5	11	49.02	35.6	6/22/2002
Kandevan F.	98	67	319	Ms:6.4	27	51.57	36.26	5/28/2004
Khazar F.	-156	67	211	ML:6.2	17	54.58	37.4	10/7/2004

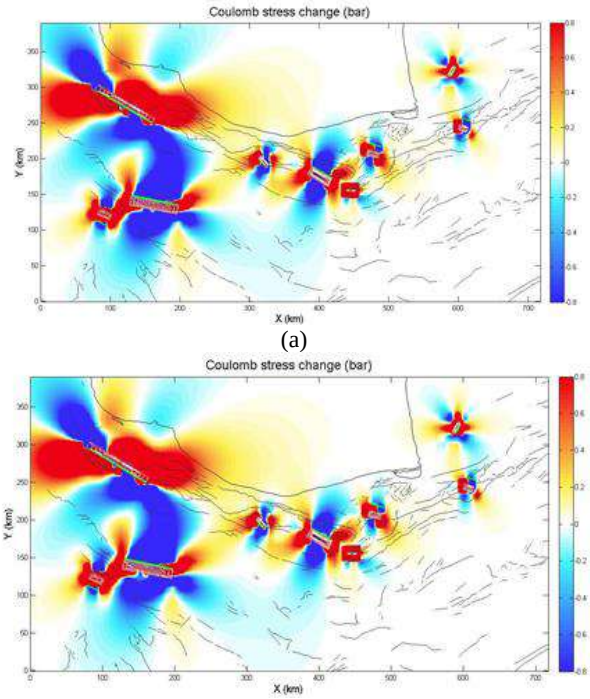

Figure 5. Coulomb stress changes at 5-year time intervals assuming the strike-slip receiver faults: a - Coulomb stress changes 10 years after the earthquake, b - Coulomb stress changes 15 years after the earthquake

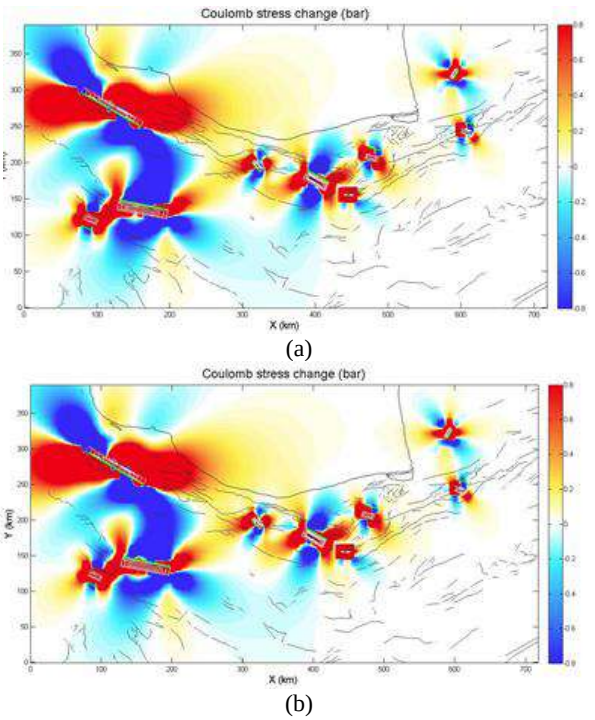

Figure 6. Coulomb stress changes at 5-year time intervals assuming the strike-slip receiver faults a - Coulomb stress changes 20 years after the earthquake, b – Coulomb stress changes 25 years after the earthquake

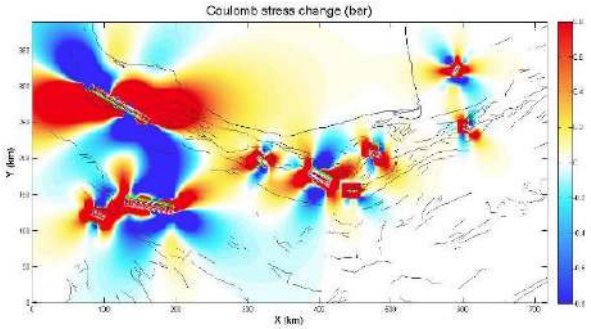

Figure 7. Coulomb stress changes at 5-year time intervals assuming the strike-slip receiver faults: Coulomb stress changes 30 years after the earthquake.

4. 5. Numerical Results of Dynamic Changes in Coulomb Stress of Rudbar Zone Assuming the Strike-Slip Fault The numerical value of the dynamic range for Coulomb stress in the Rudbar zone is investigated according to Table 4 for strike-slip faults.

According to this assessment for strike-slip faults, the zones, which have had the increase and reduction in Coulomb stress over time, are identified and the numerical values of this increased Coulomb stress are determined in the North - North East - East – and West of Rudbar zone. Furthermore, they have had reduced

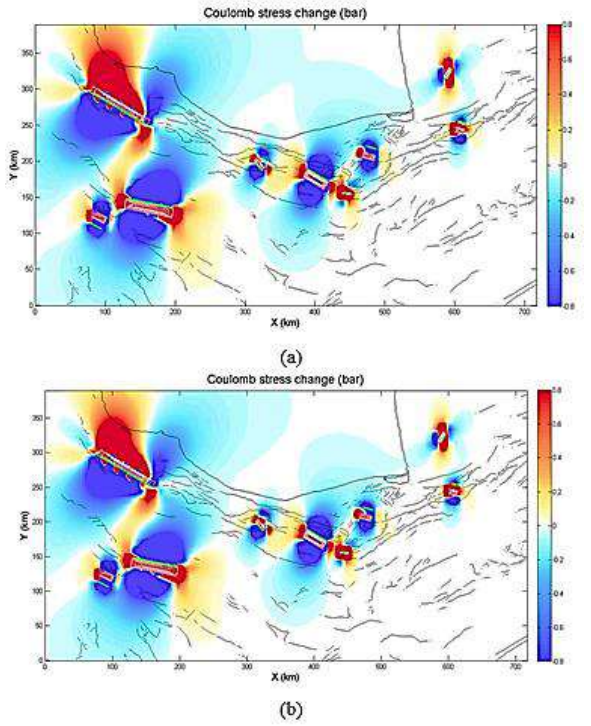

Figure 8. Coulomb stress changes at 5-year time intervals assuming the dip slip receiver faults; a - Coulomb stress changes during the earthquake, b - Coulomb stress changes 5 years after the earthquake

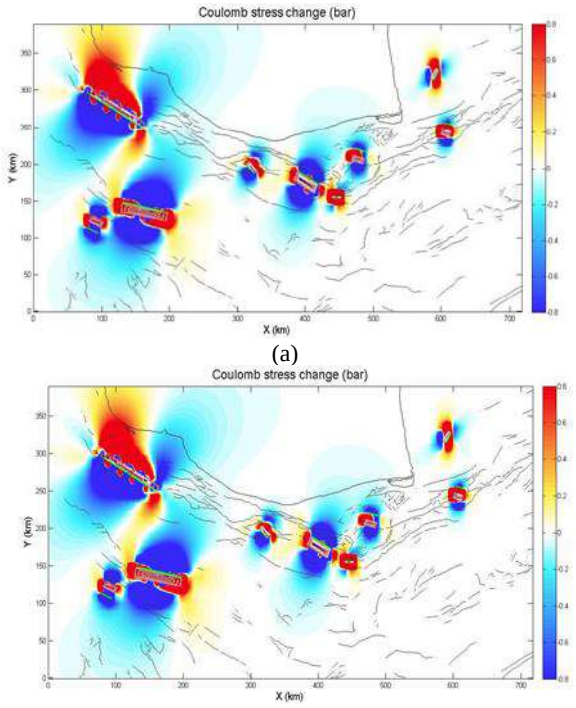

Figure 9. Coulomb stress changes at 5-year time intervals assuming the dip-slip receiver faults a - Coulomb stress changes 10 years after the earthquake, b - Coulomb stress changes 15 years after the earthquake

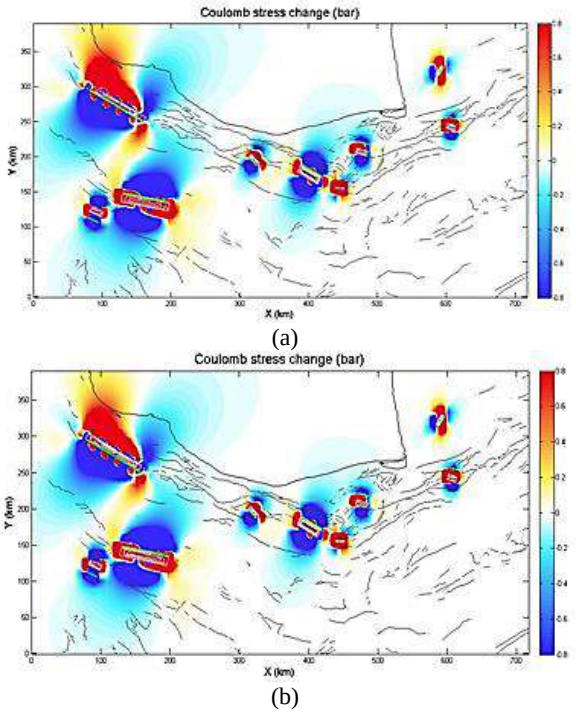

Figure 10. Coulomb stress changes at 5-year time intervals assuming the dip-slip receiver faults: a - Coulomb stress changes 20 years after the earthquake, b - Coulomb stress changes 25 years after the earthquake

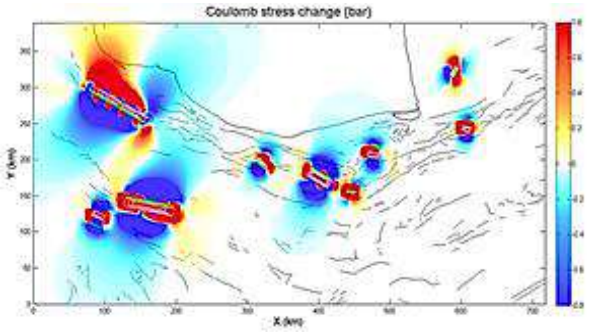

Figure 11. Coulomb stress changes at 5-year time intervals assuming the dip-slip receiver faults Coulomb stress changes 30 years after the earthquake

Coulomb stress in North West - South East - South and Southwest directions. According to Table 4, the farther from the center of the faulting plane zone (during a constant time), the more the Coulomb stress is reduced. Furthermore, this stress is also enhanced both in spatial and time dimensions by imposing the 5-year intervals in some directions and reduced in other dimensions. Furthermore, the rate of changes has been positive in the enhanced Coulomb stress zone and negative in the reduced Coulomb stress zone.

According to Figures 12 to 14, it is observed that most of the aftershocks occurred in an increased Coulomb stress zone. According to the number and location of an earthquake that occurred in the 5-year intervals, it can be concluded that in zones with high Coulomb stress, the earthquakes and subsequent aftershocks have been increased. For instance, the center of earthquakes in the Rudbar zone increased the Coulomb stress zone in 1995.

As considered, the number of earthquakes that occurred in increased Coulomb stress in 2005 was greater than 1995 and 2000 and this indicates that the number and possibility of earthquakes in these regions has been higher over time and by increased Coulomb stress. Accordingly, this possibility can be higher for the regions with increased Coulomb stress during 2015 and 2020.

4. 6. Numerical Results of Dynamic Changes in Coulomb Stress of Rudbar Zone Assuming the Dip-Slip Fault According to this assessment for dip-slip faults, the zones, which have had the increase and reduction in Coulomb stress over time, are identified and the numerical values of this increased Coulomb stress on dip-slip faults are determined in the North - North West- and South East of Rudbar zone. Furthermore, they have had reduced Coulomb stress in North East – South- and Southwest directions. According to Tables 5-8, the farther from the center of the faulting plane zone (during a constant time), the more the Coulomb stress is reduced. Contrary to strike-

TABLE 4. Numerical results of dynamic changes in Coulomb stress of Rudbar zone in 5-year intervals assuming

Time	Coulomb stress	Distance from fault center (km)	Intervals of stress levels in Bar
During an earthquake	Increase	0-50	0.6-0.8
		50-100	0.4-0.6
		100-200	0-0.4
	Reduction	0-50	-0.6
		50-100	(-0.4)-(-0.6)
		100-200	0-(-0.2)
5 years later	Increase	0-75	0.6-0.8
		75-120	0.4-0.6
		120-280	0-0.4
	Reduction	0-140	(-0.6)-(-0.8)
		140-180	(-0.4)-(-0.6)
		180-350	0-(-0.4)
10 years later	Increase	0-100	0.6-0.8
		100-130	0.4-0.6
		130-300	0-0.4
	Reduction	0-150	(-0.6)-(-0.8)
		150-210	(-0.4)-(-0.6)
		210-350	0-(-0.4)
15 years later	Increase	0-120	0.6-0.8
		120-200	0.4-0.6
		220-320	0-0.4
	Reduction	0-100	(-0.6)-(-0.8)
		100-150	(-0.4)-(-0.6)
		150-250	0-(-0.4)
20 years later	Increase	0-130	0.6-0.8
		130-180	0.4-0.6
		180-390	0-0.4
	Reduction	0-80	(-0.6)-(-0.8)
		80-110	(-0.4)-(-0.8)
		100-110	0-(-0.4)
25 years later	Increase	0-150	0.6-0.8
		150-200	0.4-0.6
		200-410	0-0.4
	Reduction	0-70	(-0.6)-(-0.8)
		70-100	(-0.4)-(-0.6)
		100-170	0-(-0.4)
30 years later	Increase	0-160	0.6-0.8
		160-180	0.4-0.6
		180-430	0-0.4
	Reduction	0-60	(-0.6)-(-0.8)
		60-90	(-0.4)-(-0.6)
		90-150	0-(-0.4)

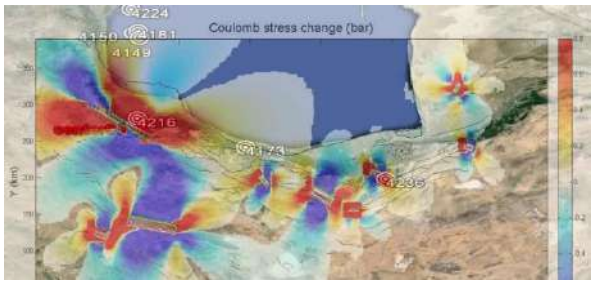

Figure 12. Earthquakes occurred in increased Coulomb stress zone in 1995

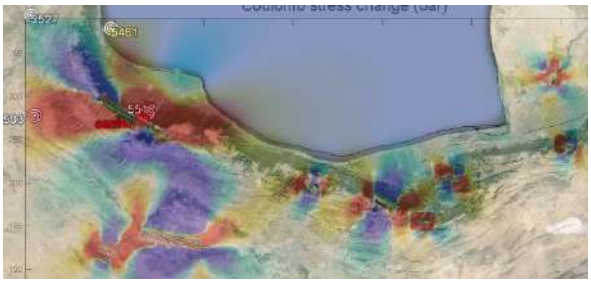

Figure 13. Earthquakes occurred in increased Coulomb stress zone in 2000

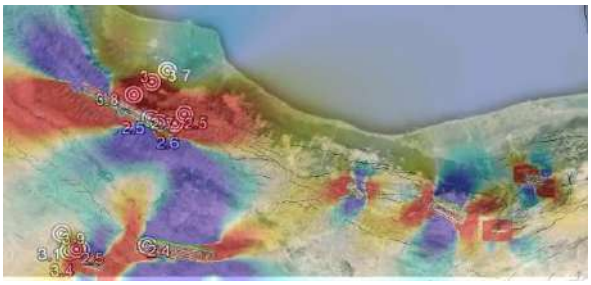

Figure 14. Earthquakes occurred in increased Coulomb stress zone in 2005

slip faulting, this stress is reduced both in spatial and time dimensions by imposing the 5-year intervals in some directions. Furthermore, the rate of changes has been negative-positive in the enhanced Coulomb stress zone and positive in the reduced Coulomb stress zone.

TABLE 5. Properties of earthquakes created in Central Alborz and Rudbar zones in 1995

Magnitude	Depth	Longitude	Latitude	Occurrence Time	Date
4.6	48	49.43	38.48	16:54	15/05/1995
4.4	33	49.33	38.56	21:54	15/05/1995
4.2	33	46.29	32.57	16:46:13	17/06/1995
4.1	45	49.4	38.6	16:45:11	06/07/1995
4.9	63	49.46	37.07	06:56:37	15/10/1995
3.9	10	49.27	38.98	23:23:47	04/11/1995

TABLE 6. Properties of earthquakes created in Central Alborz and Rudbar zones in 2000

Magnitude	Depth	Longitude	Latitude	Occurrence Time	Date
3.5	114	45.92	34.3	12:26:50	15/03/2000
4.2	33	48.17	36.96	3:42:40	10/04/2000
4.1	40	49.57	37.02	20:32:51	28/04/2000
3.9	33	48.05	37.95	5:31:17	19/05/2000

TABLE 7. Properties of earthquakes created in Central Alborz and Rudbar zones in 2005 (from CMT in Catalog)

Magnitude	Depth	Longitude	Latitude	Occurrence Time	Date
3.7	14	49.74	37.06	11:31:38	01/01/2005
2.6	14	49.83	36.64	7:02:27	02/01/2005
2.5	49.68	49.68	36.64	0:0:34	09/03/2005
3.7	48.83	48.83	35.63	5:41:13	10/03/2005
3.4	48.85	48.85	35.59	12:3:23	08/04/2005
3.8	43	49.42	36.86	8:44:13	14/04/2005
2.4	45	49.60	35.66	20:39:2	17/05/2005
2.5	14	48.96	35.61	7:48:6	03/06/2005
3.9	14.1	48.75	35.73	3:50:45	24/07/2005
3	15	49.60	36.97	10:42:22	24/08/2005
2.5	15.4	49.921	36.72	23:37:42	02/11/2005
2.7	24.9	49.60	36.68	16:20:55	29/11/2005

TABLE 8. Numerical results of dynamic changes in Coulomb stress of Rudbar zone in 5-year intervals assuming the dip-slip fault

Time	Coulomb stress	Distance from fault center (Km)	Intervals of stress levels in Bar
During an earthquake	Increase	0-75	0.6-0.8
		70-100	0.4-0.6
		100-130	0-0.4
	Reduction	0-75	(-0.6)-(-0.8)
		75-130	(-0.4)-(-0.6)
		130-300	0-(-0.4)
5 years later	Increase	0-60	0.6-0.8
		60-80	0.4-0.6
		80-115	0-0.4
	Reduction	0-70	(-0.6)-(-0.8)
		70-120	(-0.4)-(-0.6)
		120-260	0-(-0.4)
10 years later	Increase	0-50	0.6-0.8
		50-65	0.4-0.6
		65-100	0-0.4
	Reduction	0-50	(-0.6)-(-0.8)
		50-85	(-0.4)-(-0.6)
		85-220	0-(-0.4)
15 years later	Increase	0-45	0.6-0.8
		45-60	0.4-0.6
		60-80	0-0.4
	Reduction	0-45	(-0.6)-(-0.8)
		45-80	(-0.4)-(-0.6)
		80-200	0-(-0.4)
20 years later	Increase	0-43	0.6-0.8
		43-55	0.4-0.6
		55-70	0-0.4
	Reduction	0-45	(-0.6)-(-0.8)
		45-70	(-0.4)-(-0.6)
		70-170	0-(-0.4)
25 years later	Increase	0-30	0.6-0.8
		30-40	0.4-0.6
		40-80	0-0.4
	Reduction	0-35	(-0.6)-(-0.8)
		35-50	(-0.4)-(-0.6)
		50-140	0-(-0.4)
30 years later	Increase	0-30	0.6-0.8
		30-40	0.4-0.8
		40-80	0-0.4
	Reduction	0-30	(-0.6)-(-0.8)
		30-40	(-0.4)-(-0.6)
		40-140	0-(-0.4)

5. CONCLUSIONS AND SUGGESTIONS

Spatial and temporal changes in the crustal deformation process associated with the earthquakes depend on several parameters; doing the sensitivity analysis on these parameters is very important. Three different variables, namely, lithosphere thickness, asthenosphere viscosity and dip angle of fault, are some of these parameters [29–32].

The following results are obtained by doing the sensitivity analysis in co-seismic and post-seismic deformation due to dip-slip and strike-slip faulting:
The viscoelastic model sensitivity to input parameters is not correlated with the type of faulting.

Co-seismic and post-seismic displacement analysis is highly dependent on the fault slip rate especially at the top of the rupture plane.

The co-seismic displacement analysis is highly dependent on the fault plane dip angle. The surface measurements in rupture plane are the most appropriate information for determining the probable value of the fault dip angle.

Co-seismic and post-seismic displacement analysis is a little dependent on the fault length.

Co-seismic and post-seismic displacement analysis is highly dependent on the fault width especially at the top of the rupture plane.

Co-seismic and post-seismic displacement analysis is highly dependent on the fault locking width especially at the top of the rupture plane and this dependence is higher for co-seismic displacement.

The co-seismic displacement analysis has no sensitivity to the viscosity coefficient of the viscoelastic half-space, but the deviations from the reference model are high at the top of the rupture plane by changing the viscosity and elastic layer thickness according to the deformation analysis after the earthquake. A little farther, where the horizontal displacement reaches the maximum level of another one, the viscosity and thickness of the elastic layer have again more impact than the dip angle of rupture level. Thus it is suggested to measure the viscosity in the zones with large post-seismic displacement. Furthermore, this zone can provide information that is useful for determining the thickness of the elastic layer.

In a general state, the fault dip angle can be obtained using the post-seismic deformation information. The best place for finding the value of this parameter is where the direction of post-seismic displacement is changed.

The co-seismic displacement analysis shows no sensitivity to the density of elastic layer or viscoelastic half-space; in contrast, the post-seismic displacement analysis shows a little sensitivity to the density of elastic layer or viscoelastic half-space, thus it is no suggested determining the density of elastic layer or viscoelastic half-space by this model.

The occurrence of an earthquake can change the Coulomb stress distribution in the region and this leads to moving Coulomb stress changes, moving stress, even small, can lead to the rupture of surrounding faults even after a long time. This issue indicates the basic needs for modeling the Coulomb stress which refers to the future seismic hazards in the Iranian earthquake-prone plateau.

If the change in Coulomb stress is modeled considering the inter-seismic properties of faults for an inter-seismic period and calibrated according to the Coulomb stress changes due to the co-seismic and post-seismic movements, the obtained model can be utilized as a tool for warning before an earthquake or for predicting the earthquakes. The accuracy of a model is highly dependent on the accuracy of its input parameters. The biggest problem in this regard is the lack of accurate data on active faults or very little accurate information in this regard.

According to various cases in selecting the reference fault geometry and physical properties of a reference environment, it is suggested choosing their value according to the physical and geometrical characteristics of a studied site and concerning the approximate and less-accurate values of non-geodetic methods for input parameters and their changes in the estimated error range of less-accurate methods.

The distribution of GPS stations is in a way that they are not so appropriate for determining the fault locking depth. To achieve better results especially in the case of locking depth, it is suggested utilizing the denser GPS networks especially in areas close to the faults.

6. REFERENCES

1. Sarlis, N. V., Skordas, E. S., and Varotsos, P. A., "Natural Time Analysis: Results Related to Two Earthquakes in Greece during 2019", ***Proceedings***, Vol. 24, No. 1, (2019), 20. doi:10.3390/iecg2019-06194
2. Sharma, S., Venkateswarlu, H., and Hegde, A., "Application of Machine Learning Techniques for Predicting the Dynamic Response of Geogrid Reinforced Foundation Beds", ***Geotechnical and Geological Engineering***, Vol. 37, No. 6, (2019), 4845–4864. doi:10.1007/s10706-019-00945-7
3. Sivandi-Pour, A., and Noroozinejad Farsangi, E., "Statistical Prediction of Probable Seismic Hazard Zonation of Iran Using Self-organized Artificial Intelligence Model", ***International Journal of Engineering, Transactions A: Basics***, Vol. 32, No. 4, (2019), 467–473. doi:10.5829/ije.2019.32.04a.02
4. Sharma, N., Chakrabarti, A., Balas, V. E., and Martinovic, J., .Data Management, Analytics and Innovation, Vol. 1175, (2021) Singapore, Springer Singapore. doi:10.1007/978-981-15-5619-7
5. Çakir, Z., Barka, A. A., and Evren, E., "Coulomb Stress Interactions and the 1999 Marmara Earthquakes", ***Turkish Journal of Earth Sciences***, Vol. 12, No. 1, (2003), 91–103
6. Ozturk, B. M., "Seismic drift response of building structures in seismically active and near -fault regions", Ph.D. Dissertations, Purdue University, (2003).

7. King, G. C., Stein, R. S., and Lin, J., "Some characteristic features of the Anatolian fault zone", ***Bulletin of the Seismological Society of America***, Vol. 84, No. 3, (1994), 935–953.
8. Freed, A. M., and Lin, J., "Delayed triggering of the 1999 Hector Mine earthquake by viscoelastic stress transfer", ***Nature***, Vol. 411, No. 6834, (2001), 180–183. doi:10.1038/35075548
9. Wang, H., Liu, J., Shi, Y. L., Zhang, H., and Zhang, G. M., "Dynamic simulation of interactions between major earthquakes on the Xianshuihe fault zone", ***Science in China, Series D: Earth Sciences***, Vol. 51, No. 10, (2008), 1388–1400. doi:10.1007/s11430-008-0110-8
10. Paolucci, R., Mazzieri, I., Piunno, G., Smerzini, C., Vanini, M., and Özcebe, A. G., "Earthquake ground motion modeling of induced seismicity in the Groningen gas field", ***Earthquake Engineering & Structural Dynamics***, Vol. 50, No. 1, (2021), 135–154. doi:10.1002/eqe.3367
11. Al-Najjar, H. A. H., Kalantar, B., Pradhan, B., and Saeidi, V., "Conditioning factor determination for mapping and prediction of landslide susceptibility using machine learning algorithms", Earth Resources and Environmental Remote Sensing/GIS Applications X, Vol. 11156, (2019), 19. doi:10.1117/12.2532687
12. Galkina, A., and Grafeeva, N., "Machine learning methods for earthquake prediction: a Survey: A survey", Proceedings of the FourthConference on Software Engineering and Information Management (SEIM 2019), (2019), 25–32, RWTH Aahen University, 25–32
13. Zhou, Z., Lin, Y., Zhang, Z., Wu, Y., and Johnson, P., "Earthquake detection in 1D time-series data with feature selection and dictionary learning", ***Seismological Research Letters***, Vol. 90, No. 2 A, (2019), 563–572. doi:10.1785/0220180315
14. Vasti, M., and Dev, A., "Classification and analysis of real-world earthquake data using various machine learning algorithms", ***Lecture Notes in Electrical Engineering***, Vol. 612, (2020), 1–14. doi:10.1007/978-981-15-0372-6_1
15. Hossain, M. S., Al Hasan, A., Guha, S., and Andersson, K., "A belief rule based expert system to predict earthquake under uncertainty", ***Journal of Wireless Mobile Networks, Ubiquitous Computing, and Dependable Applications***, Vol. 9, No. 2, (2018), 26–41. doi:10.22667/JOWUA.2018.06.30.026
16. Rundle, J. B., "Viscoelastic-gravitational deformation by a rectangular thrust fault in a layered Earth", ***Journal of Geophysical Research***, Vol. 87, No. B9, (1982), 7787. doi:10.1029/JB087iB09p07787
17. Smith, B., and Sandwell, D., "Coulomb stress accumulation along the San Andreas Fault system", ***Journal of Geophysical Research: Solid Earth***, Vol. 108, No. B6, (2003). doi:10.1029/2002jb002136
18. Thatcher, W., Matsuda, T., Kato, T., and Rundle, J. B., "Lithospheric loading by the 1896 Riku-u earthquake, northern Japan: implications for plate flexure and asthenospheric rheology.", ***Journal of Geophysical Research***, Vol. 85, No. B11, (1980), 6429–6435. doi:10.1029/JB085iB11p06429
19. Deng, J., and Sykes, L. R., "Evolution of the stress field in southern California and triggering of moderate-size earthquakes: A 200-year perspective", ***Journal of Geophysical Research: Solid Earth***, Vol. 102, No. B5, (1997), 9859–9886. doi:10.1029/96jb03897
20. Stein, S., and Wysession, M., An Introduction to Seismology, Earthquakes, and Earth Structure, (2009) John Wiley & Sons.
21. Okada, Y., "Internal deformation due to shear and tensile faults in a half-space", ***Bulletin of the Seismological Society of America***, Vol. 82, No. 2, (1992), 1018–1040.
22. Gitis, V. G., and Derendyaev, A. B., "Web-based GIS platform for automatic prediction of earthquakes", ***Lecture Notes in Computer Science (Including Subseries Lecture Notes in Artificial Intelligence and Lecture Notes in Bioinformatics)***, Vol. 10962 LNCS, (2018), 268–283. doi:10.1007/978-3-319-95168-3_18
23. Asim, K. M., Idris, A., Iqbal, T., and Martínez-Álvarez, F., "Earthquake prediction model using support vector regressor and hybrid neural networks", ***PLoS ONE***, Vol. 13, No. 7, (2018), 1–22. doi:10.1371/journal.pone.0199004
24. Zhang, L., Si, L., Yang, H., Hu, Y., and Qiu, J., "Precursory Pattern Based Feature Extraction Techniques for Earthquake Prediction", ***IEEE Access***, Vol. 7, (2019), 30991–31001. doi:10.1109/ACCESS.2019.2902224
25. Fernández, J., Yu, T. T., and Rundle, J. B., "Horizontal viscoelastic-gravitational displacement due to a rectangular dipping thrust fault in a layered Earth model", ***Journal of Geophysical Research B: Solid Earth***, Vol. 101, No. 6, (1996), 13581–13594. doi:10.1029/96jb00525
26. Thatcher, W., and Rundle, J. B., "A viscoelastic coupling model for the cyclic deformation due to periodically repeated earthquakes at subduction zones.", ***Journal of Geophysical Research***, Vol. 89, No. B9, (1984), 7631–7640. doi:10.1029/JB089iB09p07631
27. Wells, D. L., and Coppersmith, K. J., "New empirical relationships among magnitude, rupture length, rupture width, rupture area, and surface displacement", ***Bulletin of the Seismological Society of America***, Vol. 84, No. 4, (1994), 974–1002
28. Okada, Y., "Surface deformation due to shear and tensile faults in a half-space", ***Bulletin of the Seismological Society of America***, Vol. 75, No. 4, (1985), 1135–1154
29. Mignan, A., "A preliminary text classification of the precursory accelerating seismicity corpus: inference on some theoretical trends in earthquake predictability research from 1988 to 2018", ***Journal of Seismology***, Vol. 23, No. 4, (2019), 771–785. doi:10.1007/s10950-019-09833-2
30. Razifard, M., Shoaei, G., and Zare, M., "Application of fuzzy logic in the preparation of hazard maps of landslides triggered by the twin Ahar-Varzeghan earthquakes (2012)", ***Bulletin of Engineering Geology and the Environment***, Vol. 78, No. 1, (2019), 223–245. doi:10.1007/s10064-018-1235-4
31. Pandit, A., and Biswal, K. C., "Prediction of earthquake magnitude using adaptive neuro fuzzy inference system", ***Earth Science Informatics***, Vol. 12, No. 4, (2019), 513–524. doi:10.1007/s12145-019-00397-w
32. Asim, K. M., Idris, A., Martinez-Alvarez, F., and Iqbal, T., "Short Term Earthquake Prediction in Hindukush Region Using Tree Based Ensemble Learning", Proceedings - 14th International Conference on Frontiers of Information Technology, FIT 2016, (2017), 365–370. doi:10.1109/FIT.2016.073

Persian Abstract

چکیده

در این تحقیق، هدف بررسی تاثیر گرانروی زمین در تغییرات تنش کولمب به‌صورت محاسباتی می باشد. بدین منظور تعداد چند زمین‌لرزه بزرگ در منطقه البرز انتخاب و تغییرات تنش کولمب ناشی از آنها محاسبه شده است، سپس با فرض زمین به‌صورت یک لایه کشسان روی یک نیم‌فضای گرانرو- کشسان، تغییرات زمانی تنش کولمب نشان داده شده است. تغییرات مکانی و زمانی فرآیند تغییرشکل پوسته‌ای مرتبط با زلزله، تابع چندین پارامتر است از جمله آنها می توان به ضخامت سنگ‌کره، گرانروی سست‌کره و زاویه شیب گسل اشاره نمود. به منظور تعیین میزان تأثیر نتایج مدل‌سازی به هر یک از پارامترهای ورودی با انجام آنالیز حساسیت در تغییرشکل هم‌لرزه و بعدلرزه ناشی از گسلش شیب‌لغز و امتدادلغز نتایج این پژوهش ارائه شده است. علاوه بر نتایج مفیدی که در ارتباط با تاثیر پارامترها گزارش شده است، نتایج حاصل نشان دهنده وقوع اکثر پس-لرزه‌ها در منطقه افزایش تنش کولمب از ۰/۱ تا ۰/۸ بار و عدم وقوع یا وقوع تعداد کم پس‌لرزه‌ها در مناطق کاهش تنش کولمب است. علاوه‌بر پیش‌بینی مکان پس‌لرزه‌ها می‌توان مکان زمین‌لرزه‌های اصلی بعدی را نیز با استفاده از محاسبات تغییر تنش کولمب تعیین نمود.

International Journal of Engineering

Journal Homepage: www.ije.ir

Influence of Plastic Fiber on the Geotechnical Properties of Gypseous Soil

S. M. Abdulrahman*, M. Y. Fattah, E. A. Ihsan

Department of Civil Engineering, University of Technology, Baghdad, Iraq

P A P E R I N F O

Paper history:
Received 5 September 2020
Received in revised form 26 October 2020
Accepted 29 October 2020

Keywords:
Fiber Plastic
Collapse
Gypseous Soil
Direct Shear Strength

A B S T R A C T

In the last five decades, the rise of the plastic industry led to increase in the waste of plastic in the environment, therefore the scientists were thinking to reduce plastic waste by recycling the plastic. On the other hand, there is a problem of collapse of gypseous collapsible soil upon wetting. In this paper, one of the methods to recycling plastic is adopted to improve the gypseous soil by mixing with 1% plastic fiber to increase the shear strength and improve collapsibility of soil at the state of saturation or soil wetting. The soil used is classified as SW-SM, the gypsum content is 39% and the relative density is equal to 73%. Fiber plastic is made from plastic waste in the environment of investigation. Several tests were conducted on the soil such as collapse test, direct shear test, also model loading test on the soil before and after mixing with fiber plastic. The worst case of gypsum soil is at saturation by rain or groundwater rise which was simulated during the loading test. It was concluded that the value of soil cohesion gradually increases from 2 MPa at the state of the natural soil to 11 MPa after mixing with 1% of plastic fibers. From the three model loading tests, the load carrying capacity of a model footing on submerged gypseous soil increased from 2.66 MPa for untreated soil to 4.8 MPa when the soil is mixed with 1% plastic fiber and extended to a depth of 0.5 B. The earing capacity also increased to 6.8 MPa when the soil is mixed with 1% plastic fiber and extended to a depth of B.

***doi**: 10.5829/ije.2021.34.02b.08*

NOMENCLATURE

USCS	Unified Soil Classification System	CP	Collapse potential %
Cu	Coefficient of uniformity	$D_{15(B)}$	The particle diameter through which (15% of soil) will pass
Cc	Coefficient of curvature	$D_{15(F)}$	The particle diameter through which (15% of filter material) will pass
Gs	Specific gravity	$D_{85(B)}$	The particle diameter through which (85% of the soil) will pass
E	Void ratio	ϕ	Internal friction angle
Δe	Change in void ratio	c	Cohesion, (kPa)
ΔH	Change in the cell height	**Greek Symbols**	
H_o	Cell height	$\frac{D15(F)}{D85(F)} \leq 4-5$	Filter equalization, The first part
τ	Maximum shear stress,(kPa)	$\frac{D15(F)}{D85(F)} \geq 4-5$	Filter equalization, The second part
B	Width of model bace	$Cp = \frac{\Delta H}{H_o} \times 100 = \frac{\Delta e}{1+e_o} \times 100$	(Collapse potential %) equalization

1. INTRODUCTION

Scientists pointed out to estimate in the year 2012 alone, that about 280 million tonnes of plastic have been used worldwide. But about 130 million tonnes of plastics were waste on earth. Therefore, 150 million tonnes of plastic are remaining due to use in the daily lives of human beings.

The growing use resulted in a massive upsurge in the quantity of plastic waste. These wastes have highlights impacts on the environment such as maculation and sapping of resources. Restoring plastic dumps and reusing it helps in alleviating environmental degradation. The recycled plastic waste in U.S.A get

* Corresponding Aurthor Email: 40336@uotechnology.edu.iq (S. M. Abdulrahman)

Please cite this article as: S. M. Abdulrahman, M. Y. Fattah, E. A. Ihsan, Influence of Plastic Fiber on the Geotechnical Properties of Gypseous Soil, International Journal of Engineering, Transactions B: Applications Vol. 34, No. 02, (2021) 367-374

was 5.7% of the total plastics waste, while Europe recycled 39% of the total plastics waste [1].

Studies have shown that gypseous soil is improved using waste materials such as fiber plastic that is content is available at low cost. Polypropylene that is one of the kinds of plastic waste is used to improve the soil shear strength. When the plastic fiber is added to the soil, this leads to help in mitigating the volume change behaviour [2].

Collapse or unstable soil structure can produce vital problems for construction. Because the super layer of plastic fiber is tensile strength, its price is cheap, and it is widely available as waste material. Some scientists have suggested using it as improved soil mechanical properties [3]. For many causes such as home appearance, durability, ease of installation and energy efficiency, lead to vinyl siding to use in the building and construction industry besides using plastics have a variety of benefits, but the effects are noxious to the environment.

Tang et al. [4] used plastic fiber to improve soil such as clay, life of fibers depends on the percentage temperature as (5, 10, 20) years at a temperature of (121, 110, 99)° C. The temperature of 120°C is stable and approved in the laboratory [5]. The method the fibers interact with soil particles was investigated using sensitive devices such as an optical microscope and a scanning electron microscope, of their studies it appears that the fiber feature that occurs during shearing does not rupture, but the defects of the fibbers are expanded, and some damage may occur in Figure 1. The damage is the beginning of the distance of the plastic fiber with any cutting style.

Researchers pointed out that damage occurs most often when fiber is pressed by a high energy effect. The fibers lose their straightness become many bends (angles) at the end. Figure 1 shows what it interaction steps between the fiber and the particles of soil as hereunder: (a) Particles of soil being curb by fiber from packing tightly. (b) Also, particles of soil are triggering fiber stretch and imprints on the fiber allowing adhesion to develop [4].

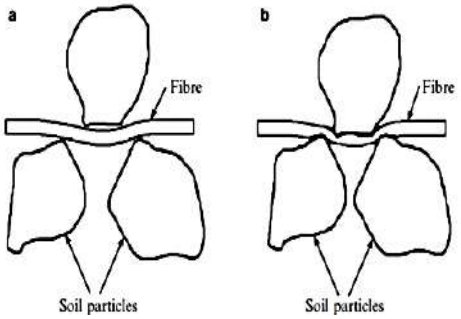

Figure 1. Behavior of the plastic fiber in soil

Previous research that studied the problems of gypseous soil showed that the behavior of this soil refers to strong soil in its dry state, but it collapses when exposed to groundwater or rain due to the dissolution of gypsum in the water. Therefore, some researchers have undertaken studies to solve this problem, as follows:

Injection of gypseous soil with acrylate liquid reduces collapse by more than 50-60% [6].

Improving the properties of gypseous soil by using materials that increase the cohesion property between gypsum soil particles, for example (cement, kaolin, lime, calcium chloride, [7].

Using silicon oil was found to increase the parameters of shear strength of the soil by increasing the cohesion between the grains of soil [8].

Long-term soaking and leaching effects on the strength and stability properties of the gypseous soils stabilized by lime were studied by Aldaood et al., [9]. The stabilized soaked soil specimens showed that the collapsibility properties were decreased as compared to un-soaked specimens.

Hydro-mechanical behavior of unsaturated collapsible soils can be drastically affected by saline infiltrations. Garakani et al. [10], investigated hydro-mechanical characteristics of an unsaturated collapsible loessial soil diluted with saturated solutions of three different salts that are frequently involved in transportation infrastructure (namely NaCl, CaCl2 and KCl) by conducting scanning electron microscopy (SEM), filter paper, uniaxial compression and oedometer tests. Results implied that there is a critical saline degree of saturation (corresponded to each loading path and each mixing salt type), at which the magnitude and modality of the osmotic and matric suctions within the soil fabric are changed. In addition to experimental studies, empirical constitutive models are presented in this paper to predict the changes in strength, stiffness and yield stress of the tested collapsible soil subjected to different road salts. Comparisons show very good agreement between the laboratory test results and the model predictions.

Collapse problem treatment of gypseous soil by nanomaterials was also studied. Hayal et al. [11] added Nano-silica to the soil. the collapse potential (CP) decreased whenever the Nano-silica increases until 1%, the percent of decrease in CP is about 91%.

Zakaria [12] tried to improve soil strength properties and intrusion of reinforcing sorces into soil. The footing was modeled by a square steel plate 0.1 by 0.1 m. The footing is loaded as to have a stress of 40 kPa and settlement was receded in dry and in soaking conditions. Two depths of the geo-mesh reinforcement are used, one B (B is width of footing) and 0.5B. Results revealed that the best improvement obtained is the case of a square geo-mesh width of 7.5B and located at depth of B/2 under footing, with an improvement in terms of

collapse settlement of 35%, and a settlement reduction in dry condition of 50%. The least improvement is the case of square geo-mesh with a width of 4B and depth of one B, and it was really negligible, about 4% decrease in collapse settlement.

The objective of the present study is improving the collapsible soil characteristics through reducing the phenomenon of collapse of soaked gypseous soil by mixing the soil with plastic fiber. The study methodology includes tracing the changes in collapse potential investigated in the soaked gypseous soil before and after treatment by carrying out laboratory experiments including collapse test and direct shear strength test.

2. MATERIALS AND MODEL PART TEST

2. 1. Soil The soil sample used is incurred from Iraq with a gypsum content of 39%. The soil used can be categorized as (SW-SM) according to the Unified Soil Classification System (USCS). Figure 2 explains the grain size distribution of the soil used and Table 1 explains the properties of soil that include percent of soil constituents, specific gravity, maximum and minimum dry unit weights and relative density.

2. 2. Plastic Fibers Additives The plastic fiber used is cheap and available in the market and is known as polypropylene (fiber plastic). The specifications of the polypropylene fiber are listed in Table 2 including the physical properties. Figure 3 shows the fiber plastic used.

2. 3. Model Loading Tests

2. 3. 1. Model Parts The model consists of the following parts as shown in Figure 4.

1. A steel container containing saturated gypsum soil prepared with dimensions (350 x 500 x 300) mm.

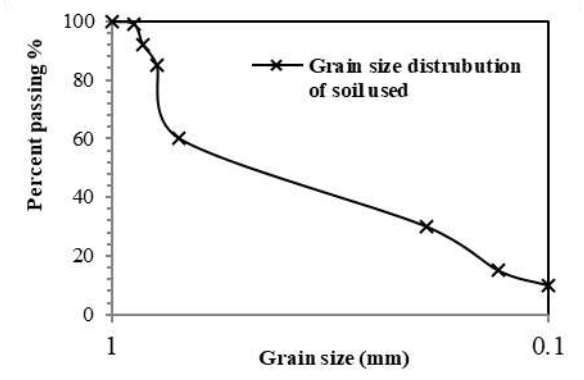

Figure 2. Soil grain size distribution

TABLE 1. The Soil of physicals properties

Index property s	Index value	Specification
Gypsum content (%)	39	
Sand %	94	
Silt & clay %	4	
D_{10}	0.1	
D_{30}	0.19	
D_{60}	0.7	ASTM D422-2001 [13]
Coefficient of uniformity, Cu	7	
Coefficient of curvature, Cc	1.39	
Soil classification, (USCS)	SW-SM	
Specific gravity, (Gs)	2.6	ASTM D854-2005 [14]
Optimum moisture content (%)	11.0	ASTM D-698 [15]
Maximum dry weight, (kN/m^3)	16.8	ASTM D4253-2000 [16]
Minimum dry weight, (kN/m^3)	11.5	ASTM D4254-2000 [17]
Angle of internal friction, θ°	36	ASTM D3080-1998 [18]
Dry unit weight, (kN/m^3)	15.2	
Void ratio, e	0.625	
Relative density (%)	73 %	

Figure 3. Fiber plastic

2. Frame element structure used to carry the exenrual static load to the footing as increments.
3. Dead weights used were (7.5 , 12.5 , 17.5 , 22.5, 27.5 , 32.5) N.
4. Dial gauges to read the settlement of the footing under external load.
5. Square steel footing with dimensions (60 x 60) mm.

TABLE 2. Specification for polypropylene fibers (fiber plastic) [19]

Fiber properties	Values
Fiber type	Single fiber
Length, (mm)	6
Diameter, (mm)	0.034
Density, (g/cm^3)	0.91
Tensile strength, (MPa)	350
Young's modulus, (MPa)	3500
Fusion point , °C	165
Burning point, °C	590° C
Surface area, (m^2/kg)	250
Elongation, %	24.4
Water absorption	Nil
Dispensability	Excellent
Acid & alkali resistance	Very good

Figure 4. Model loading test.

A filter material was placed at the bed of the model to block the soil flow. The filter material was selected based on the following criteria in Equations (1) and (2) [20]:

$$\frac{D15(F)}{D85(F)} \leq 4-5 \quad (1)$$

$$\frac{D15(F)}{D85(F)} \geq 4-5 \quad (2)$$

Figure 5, explains the grain-size distribution of the filter material.

2. 4. Soil Bed Preparation for the Model A water drainage network has been established at the bottom of the container to represent the reality of groundwater. This network is connected to a water tank at a height of 15 m. Through its faucets water is drained from the tank to the water drainage network to feed the

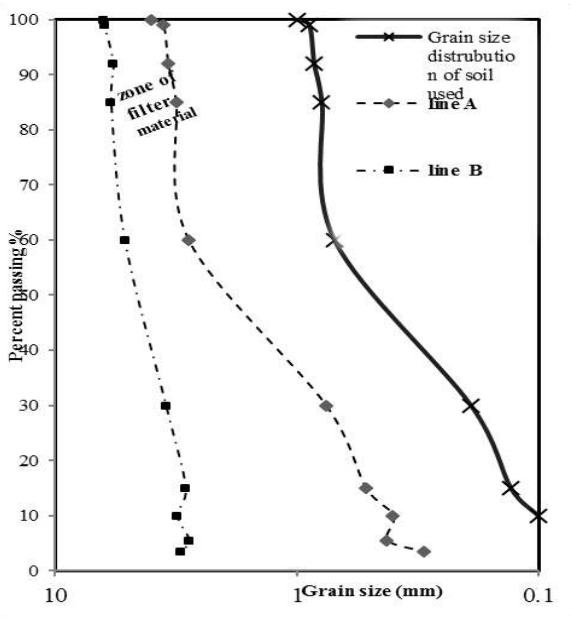

Figure 5. The grain-size distribution of the filter material

container with a water until the water reaches the surface of the model to ensure the representation of the reality of gypsum soil exposure. For groundwater rise saturation with rain together, a new system to make as a soil filter bed preparation is adopted to ensure that all specimens will be equally extremely wetted. The procedure consists of the following steps:

1. A gravel layer was placed at the bed of the container to make the water able to dissipate as shown in Figure (6-a).
2. The hollow plastic tubes have holes to allow the water to rise and pass through a uniform flow, Figures (6-b), (6-c).
3. Fly mesh layer was put at the upper of the hollow plastic tubes to prevent and avert soil drop through the holes to the gravel layer and make an empty space within the filter layer, Figure (6-d).
4. A soil filter was constructed from two layers 50 mm each compacted at relative density of (73%).
5. A double layer of fly-mesh was put over the layers mentioned above to prevent mixing between the filter and soil. Figure (6-e) illustrates the filter material installation.

2. 5. Soil Saturation in the Model The actual state of soil subjected to groundwater or rain is idealized by thoroughly soaking the sample with water. Soaking the soil with water was made for a period of one day to simulate the situation under the footing. The tested soil is supplied with water through the. The flow of water was through a plastic mesh below the filtered soil layer, the tank was closed off and the water flow to the model was stopped.

Figure 6. Steps of preparation of soil model loading test

2. 6. Model Tests Three model tests were established: In the first model, a model foundation was tested on gypseous soil before treatment. The second and third models were tested for the foundation on gypseous soil after treatment by mixing with 1% of the plastic fibers. The mixed soil was extended to depths of (0.5B and 1B), respectively where B is the footing width. The testing procedure is illustrated in Figure 7.

3. DATA ANALYSIS AND TESTING RESULTS

3. 1. Shear Strength Test Results To investigate the effect of mixing the soil with fiber on the parameters of shear strength of the gypseous soil, direct shear test was carried out on the soil in its natural state and after treatment with plastic fiber. In this test, the time of sample soaking in water was 24 hours. Figure 8 explains the relationship between shear stress and normal stress for the soil at its natural soil state and also the soil after treatment by mixing with 1% fiber plastic material. It is observed that both the cohesion and angle of internal friction increase. Table 3 summarizes the increase in the shear strength parameters (c and ϕ) after mixing the soil with 0.1% fiber plastic. From the direct shear test, it is found that the soaked gypseous soil exhibits very high shear strength after treatment by mixing with 1% fiber plastic percent to be more than 5.5 times from soil without treatment. Therefore, fiber plastic is considered a substance that contributes to improve the engineering properties, as it works as a reinforcement to bond the soaked gypseous soil particles and protect it from degradation.

Figure 7. Performing loading on gypseous soil pressure

Nareeman and Fattah (2012) [21] found that the shear stress increased for soil reinforced by horizontal geonet layer, while the vertical displacement decreased. This is because the geonet layer works as a reinforcement layer that strengthens the soil and tends to increase shear strength of the soil. It can be seen that both compression and dilation of the soil are decreased by adding reinforcement layers.

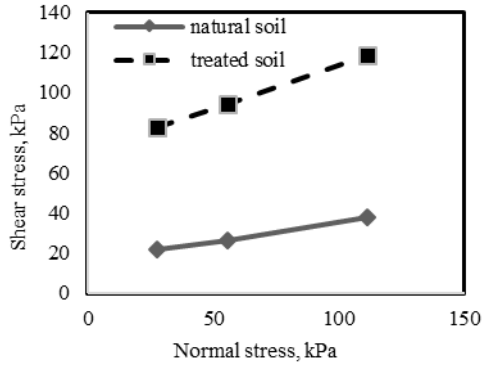

Figure 8. Relationship between shear stress and normal stress in the direct shear test

TABLE 3. Results of direct shear test

Percentage of fiber		**0**	**1**
Cohesion, c (kPa)		2	11
Internal friction angle, ϕ°		36	44
Maximum shear stress (kPa)	τ_1	22.1	82.7
	τ_2	26.5	93.9
	τ_3	37.8	118.3

3. 2. Collapse Test Results The results of the odometer test are described for the gypseous soil after mixing with polypropylene fiber (plastic fiber). The collapse potential is calculated as in Equation (3) [22]:

$$Cp = \frac{\Delta H}{H_o} \times 100 = \frac{\Delta e}{1 + e_o} \times 100 \quad (3)$$

Figure 9 shows that linear decrease of settlement and the void ratio for the soil can occur under 0.21 to 0.006 MPa pressure. The figure shows a comparison of the results between the gypseous soil tested without treatment, and the gypseous soil after mixing with 1% plastic fibers. Moreover, Table 4 explains the decrease in the collapse of gypseous soil from 12.9 to 0.96 at 1% percentage of fiber plastic where the collapse potential is presented for each case.

Fattah et al. (2013) [23] concluded that the gypseous soil exhibited similar behavior for all unsoaked specimens. The soil showed a clear peak value of shear stress at each normal stress. All soils have a cohesion component; this may be due to the cementing action of gypsum for untreated soil and the cementing action of gypsum and acrylate liquid for the treated soil. In addition, the soil samples exhibited dilation under all normal stresses. The results of specimens sheared after soaking show that the behavior of the stress-strain relationship is changed from dense state to lose state. The curves do not show a clear peak, so the tests were continued until the sample reached a 20% strain. All the samples revealed compression when sheared under all normal stresses.

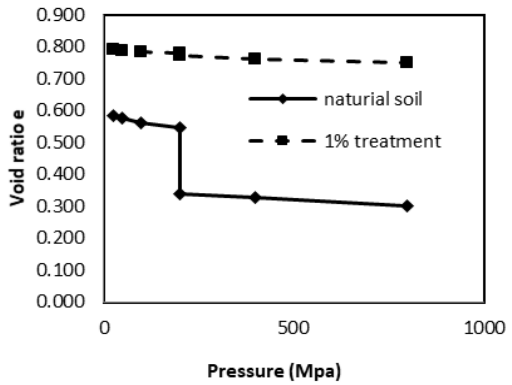

Figure 9. Pressure – void ratio relation for gypseous soil before and after mixing with plastic fiber

TABLE 4. Collapse potential and problem severity type

Severity of the problem	Collapse potential, Cp (%)	Condition
Severely trouble	12.9	Before treatment
No problem	0.96	After treatment

3. 3. Model Loading Test Results In the present study, the failure load is considered the load causing a settlement that represents 10% of the footing width. Figure 10 illustrates the model loading test results on saturated gypseous soils until failure occurs. At 10% of the footing width, the footing failure pressure is (2.66 MPa). Figure 11 shows the result of the pressure – settlement relation for the gypseous soil mixed with 1% plastic fibers extended to a depth equal to half the width of the footing.

At 10% of the footing width, the value of failure pressure is (4.8 MPa). Figure 12 illustrates the pressure – settlement relation for a footing model on gypseous soil mixed with 1% of plastic fibers and extended to a depth equalize to the width of the footing, failure occurs at a settlement of 10% of the footing width, the value of failure pressure is (6.8 MPa). After full inundation of collapsible soil, the bonds of cementing between particles get broken, and the remaining shear strength is derived from the inter-granular frictional forces. Consequently, the angle of internal friction can be utilized as an adequate parameters measure [24].

In addition, fiber plastics provide another type of bond that resists inundation of collapsible soil, it is added to cohesion of soil particles. This treatment is considered economical, as it is used in a very small percentage, and it is an available material that can be obtained from the waste of plastic factories or consumed plastic water bottles or as polypropylene fibers material.

The present action of fiber mixed gypseous soil can be compared with the results of Zakaria (2020) [12] who found that all reinforcement cases for the depth of 0.5B show higher improvement ratios than the similar cases for depth one B, indicating that the majority of collapse potential is taking place in the zone of soil almost directly beneath footing. In addition that the sizes of the geo-mesh in the first case are smaller than that for the latters.

After full inundation of collapsible soil, the cementing bonds between particles get broken, and the

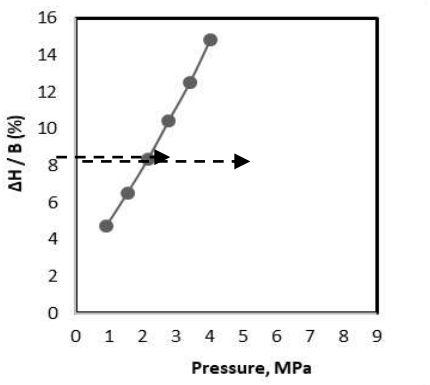

Figure 10. Relation between pressure and settlement for gypseous without treatment

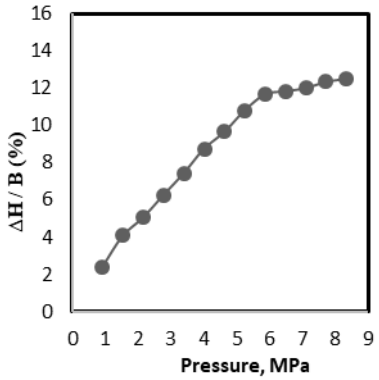

Figure 11. Relation between pressure and settlement for gypseous with mixing with 1% plastic fiber extended to a depth of 0.5 B

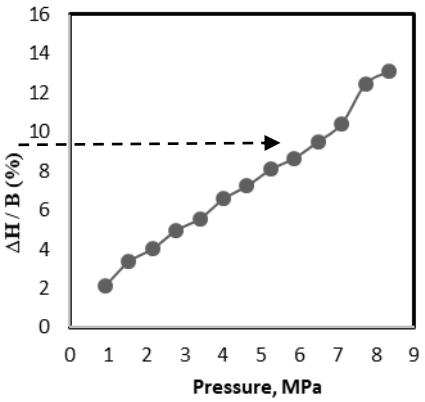

Figure 12. Relation between pressure and settlement for gypseous with mixing with 1% plastic fiber extended to a depth of B

remaining shear strength is derived from the intergranular frictional forces. Consequently, the angle of internal friction can be utilized as an adequate measure of shear strength [25].

4. CONCLUSION

It was noted through previous studies that no study had ever been done regarding the addition of plastic fibers to gypseous soil. Through this paper, the possibility of adding this material as an attempt to improve the soil has been made. In the light of experimental model tests and tests resultant, and also the following conclusions can be drawn:

1. From the direct shear test, the soaked gypseous soil exhibits very high shear strength after treatment by mixing with 1% fiber plastic percent to be more than 5.5 times from soil without treatment.
2. From collapse test results, the collapse potential of gypseous soil with gypsum content was 39% was 12.9% and classified as (severely trouble). After treatment using 1% of fiber plastic, the collapse potential decreased to 0.96% only with a classification of (no problem) which indicates the interesting role of fibers in treatment of collapse problem.
3. From the three model loading tests, the load carrying capacity of a model footing on submerged gypseous soil increased from 2.66 MPa for untreated soil to 4.8 MPa when the soil is mixed with 1% plastic fiber and extended to a depth of 0.5 B. The earing capacity also increased to 6.8 MPa when the soil is mixed with 1% plastic fiber and extended to a depth of B. This means that mixing the soil to a limited depth below the footing with fiber could reveal a beneficial effect in decreasing the soil collapse.

5. REFERENCES

1. Adhikary, B., Shusheng, P., and Mark, S. "Dimensional stability and mechanical behavior of plastic composites based on recycled and virgin LDPE.", ***Composites: Part B***, No. 39. (2008).
2. Gowthami, D., and Sumathi, R. "Expansive soil stabilization using plastic fiber waste polypropylene", ***International Journal of Latest Research in Engineering and Technology***, Vol. 3, No. 7, (2017), 24-30.
3. Sahil R. "Review on improvement in strength of soil by adding waste fly-ash and polypropylene fiber.", ***International Research Journal of Engineering and Technology***, Vol. 5, No. 3, (2018), 4001-4005. https://irjet.net/archives/V5/i3/IRJET-V5I3938
4. Tang, C., Shi, B., Gao, W., Chen, F., and Cai, Y."Strength and mechanical behavior of short polypropylene fiber reinforced and cement stabilized clayey soil.", Geotextiles and Geomembranes, Vol. 25, No. 3, (2007), 194-202. DOI: 10.1016/j.geotexmem.2006.11.002
5. Jasim, Y.H. (2019). Geotechnical properties of different soils reinforced by polypropylene fiber. MSc. Thesis. Civil Engineering Department, University of Technology, Baghdad, Iraq, (2019).
6. Fattah, M.Y., Al-Ani, M.M., and Al-Lamy, M.T. "Treatment of collapse of gypseous soils by grouting.", Proceedings of the Institution of Civil Engineers, Ground Improvement Journal, UK, Vol. 166, No. GI1, (2013), 32-43. DOI: 10.1680/grim.11.00020
7. Ibrahim S.F., Dalaly N. K., AlAbaby M. "Studies on improvement of properties of gypseous soils.", Proceedings of the 15th Asian Regional Conference on Soil Mechanics and Geotechnical Engineering, Japanese Geotechnical Society Special Publication, (2016), 570-575.
8. Ibrahim, A. N., and Schanz, T. "Improvement of gysiferous soil strength by silicone oil.", ***Soil Mechanics and Foundation Engineering***, Vol. 54, No. 2, (2017), 117-121. DOI: 10.1007/s11204-017-9443-7
9. Aldaood, A., Bouasker, M., and Al-Mukhtar, M. "Free swell potential of lime-treated gypseous soil.", ***Applied Clay Science***, Vol. 102, (2014), 93-103. DOI: 10.1016/j.clay.2014.10.015.

10. Garakania, A. A., Haerib, S. M., Cheratib, D. Y., Givib, F. A., Tadib, M. K., Hashemib, A. H., Chitib, N., Qahremani, F., "Effect of road salts on the hydro-mechanical behavior of unsaturated collapsible soils", ***Transportation Geotechnics***, Vol. 17, (2018), 77-90. https://doi.org/10.1016/j.trgeo.2018.09.005.
11. Hayal, A. L., Al-Gharrawi, A. M. B., and Fattah, M. Y., "Collapse problem treatment of gypseous soil by nanomaterials.", ***International Journal of Engineering, Transactions C: Aspects,*** Vol. 33, No. 9, (2020), 1737-1742. DOI: 10.5829/ije.2020.33.09c.06.
12. Zakaria, W. A., "Intrusion of Geomesh in Gypseous Soil Under Single Footing", ***International Journal of Engineering, Transactions C: Aspects,*** Vol. 33, No. 9, (2020), https://10.5829/IJE.2020.33.09C.05.
13. American Society of Testing and Materials ASTM D422-2001-ASTM D854-2005-ASTM D4254-2000, Standard test method for measurement of sieve analysis of soils. (1998).
14. American Society of Testing and Materials ASTM D854-2005. ASTM D4254-2000, Standard test method for measurement of specific gravity of soils. (1998).
15. American Society of Testing and Materials ASTM D-698 ASTM D854-2005. ASTM D4254-2000, Test method for measurement of optimum moisture content of soils. (1998).
16. American Society of Testing and Materials ASTM D4253-2000. ASTM D4254-2000, Standard test method for measurement of maximum dry weight of soils. (1998).
17. American Society of Testing and Materials ASTM D4254-2000, Standard test method for measurement of minimum dry weight of soils. (1998).
18. American Society of Testing and Materials ASTM D3080, Standard test method for measurement of direct shear of soils. (1998).
19. Falorca, I., and Pinto, M. "Effect of short randomly distributed polypropylene microfibers on shear strength behavior of soils.", ***Geosynthetics International,*** Vol. 18, No. 1, (2011), 2-11.
20. Das, B. M. and Sobhan, K., Principles of geotechnical engineering. eighth edition, Cengage Learning, (2014).
21. Nareeman, B. J., Fattah, M. Y., "Effect of Soil Reinforcement on Shear Strength and Settlement of Cohesive-Frictional Soil", ***International Journal of Geomate***, Vol. 3, No. 1 (Sl. No. 5), pp. 308-313 Geotec., Const. Mat. & Env., ISSN:2186-2982(P), 2186-2990(O), Japan (2012).
22. American Society of Testing and Materials ASTM D5333 (2018), Standard test method for measurement of collapse potential of soils. Annual Book of ASTM Standards, Vol.04.08, Philadelphia, PA, ASTM, USA. Copyright, ASTM International, 100 Barr Harbor Drive, P&O Box C700, West Conshohocken, P&A 19428-2959, United States. (2018).
23. Fattah, M. Y., Al-Ani, M. M., Al-Lamy, M. T. A., "Treatment of Collapse of Gypseous Soils by Grouting", ***Proceedings of the Institution of Civil Engineers, Ground Improvement Journal***, UK, DOI: 10.1680/grim.11.00020, Vol. 166, Issue GI1, pp. 32-43 (2013).
24. Ashour, M., Abbas, A., Altahrany, A., Alaaeldin, A. "Modelling the behavior of inundated collapsible soils.", Engineering Reports.2020;e12156. Wiley online library.com/journal/eng2 1of14. Retrieved from https://doi.org/10.1002/eng2.12156.
25. Hayal, A. L., Al-Gharrawi, A. M. B., Fattah, M. Y., " Collapse Problem Treatment of Gypseous Soil by Nanomaterials", ***International Journal of Engineering, Transactions C: Aspects*** Vol. 33, No. 9, 1737-1742 (2020)

Persian Abstract

در پنج دهه گذشته ، ظهور صنعت پلاستیک منجر به افزایش ضایعات پلاستیک در محیط شد ، بنابراین دانشمندان در فکر کاهش ضایعات پلاستیک با بازیافت پلاستیک بودند. در این مقاله ، یکی از روشهای بازیافت پلاستیک برای بهبود خاک گچی با مخلوط شدن با ۱٪ الیاف پلاستیک جهت افزایش مقاومت برشی و بهبود قابلیت جمع شدن در حالت اشباع یا خیس شدن خاک در نظر گرفته شده است. خاک مورد استفاده به عنوان SW-SM طبقه بندی می شود ، محتوای گچ ۳۹٪ و چگالی نسبی برابر با ۷۳٪ است. پلاستیک الیافی در محیط تحقیق از ضایعات پلاستیکی ساخته می شود. چندین آزمایش روی خاک انجام شد مانند آزمایش ریزش ، آزمون برش مستقیم ، همچنین آزمون بارگذاری مدل روی خاک قبل و بعد از اختلاط با پلاستیک الیاف. بدترین حالت خاک گچ در اشباع شدن باران یا بالا آمدن آب زیرزمینی است که در هنگام آزمایش بارگیری شبیه سازی شده است. نتیجه گیری شد که مقدار انسجام خاک پس از مخلوط شدن با ۱٪ الیاف پلاستیک به تدریج از ۲ MPa در حالت خاک طبیعی به ۱۱ MPa افزایش می یابد.

International Journal of Engineering

Journal Homepage: www.ije.ir

Orthotropic Coefficients and Continuity Factors of Reinforced Concrete Slabs Supported on 3-sides

S. Gupta*[a], H. Singh[b]

[a] *D.A.V. Institute of Engineering & Technology, Punjab, India*
[b] *Guru Nanak Dev Engineering College, Punjab, India*

PAPER INFO

Paper history:
Received 12 July 2020
Received in revised form 11 September2020
Accepted 26 October2020

Keywords:
Concrete
Moment-field
Analysis
Finite Element Analysis

ABSTRACT

The analysis and design of reinforced concrete slabs supported on 3-sides in masonry or reinforced concrete construction involve analytical formulations. In published analytical formulations, orthotropic coefficients and continuity factors are unknown parameters. To obtain moment carrying capacity of the slabs using available formulations, these factors must be required. In this research work, these orthotropic coefficients and continuity factors are presented for transverse loaded RC rectangular slabs supported on three sides under uniform area loading at top face of the slab. These coefficients were obtained using FEA (Finite element Analysis) based Structural Analysis Program (SAP) software. It is also validated with FEA (Finite element Analysis) based SCIA Engineer software and published formulations. It have been observed that obtained results are well comparable with published literature and FEM based software. Results presented in this research paper are conducive to predict the moment-field of the reinforced concrete rectangular slabs supported on three sides having one edge is unsupported. These coefficients will be very helpful for structural designers dealing with reinforced concrete slabs supported on three sides.

***doi**: 10.5829/ije.2021.34.02b.09*

1. INTRODUCTION

The Slab is one of the integral parts of the construction practices, integrity of the same affects the analysis and design of the structures. Due to different support conditions, like discontinuous and continuous edges and various aspect ratios, moment field of the slabs may vary. While analyzing, the slabs haaving variation in moment-field (bending moment) in orthogonal directions are considered to be non-isotropic slabs. In general practice of reinforced concrete construction, tensile steel is placed parallel to the edges due to which these slabs were also considered as orthotropic slabs. Moment-field develops at the continuous edges of the slab arise a need to calculate continuity factors and difference in moment field in orthogonal directions arise a need to calculate orthotropic coefficients.

Nowadays, finite element method (FEM) analysis is adopted worldwide and researchers are also using FEM in conjunction with yield line theory for analyzing slabs. Ingerslev [1] firstly came with the concept of yield line theory. Johansen [2-4] contributes a lot in this field and proceeds the Ingerslev work by introducing geometrical unknown variables to predict the failure mechanisms. After that several researchers [5-10] worked in the field of yield line analysis of reinforced concrete slabs and their work was accepted by world community.

With the increase in use of FEM in engineering several researchers start using this technique in analyzing slabs. Al-Sabah and Falter [11, 12] presented a non-iterative lower bound finite element method using rotation free elements to analyze the isotropic and non-isotropic slabs which is safer than yield line theory due to lower bound approach. Gohnert [13] presented the yield-line elements with the help of FEA to calculate the load carrying capacity of the slabs using both elastic and inelastic analysis. The theory proposed is called an over-shoot method. Firstly, an elastic theory was used to

*Corresponding Author Email: sushantgupta1994@gmail.com (S. Gupta)

Please cite this article as: S. Gupta, H. Singh, Orthotropic Coefficients and Continuity Factors of Reinforced Concrete Slabs supported on 3-sides, International Journal of Engineering (IJE), IJE TRANSACTIONS A: Basic 375-381

formulate the flexibility matrix in the form of compatibility equations using principle of virtual work. After that elastic analysis was transformed into an in-elastic analysis by adapting the elastic flexibility matrix. Obtained results were validated within a maximum percentage difference of 10 percent with johansen yield line theory and within 20 percent with experimental data.

Famiyesin et al [14] incorporate the membrane effect in the conventional yield line theory to mobilize the results obtained by the conventional yield line theory by using available test results. By using parametric study of FE based analysis, charts have been developed which are helpful to determine collapse load of the slab with different percentage of steel. Kwan [15] presented a new method for defining or predicting the yield line patterns of the slabs. In this method, yield line patterns were attained in terms of dip (rotation) and strike (orientation of axis of rotation) of slab surface using work method. Based on the above methodology, a new computer program was produced in which users no longer need to input any assumed yield line pattern however, program automatically adjusts the yield line pattern to obtain critical load factor. The limitation of this method is that it is not applicable to convex polygonal slabs.

Singh and Kumar [16] presented a simplified approach using yield line theory for analyzing the three sides supported slabs by using equations of four sides supported slabs. Gupta and Singh [17] formulated the design aids for the analyzing of the three-side supported RC rectangular slabs for different support conditions which were obtained with the help of yield line theory and FEA. Gupta and Naval [18] presented a simplified approach to analyze the slabs supported on two adjacent edges with the help of yield line theory.

Abdul-Razzaq et al. [19] studied the behavior of post-tensioned two way slab under flexure. Parametric study carried out by the author reveals that moment carrying capacity of the slabs having tendons placed in two directions is more than slabs having tendons in one direction. Wenjiao et al. [20] studied the crack response of reinforced concrete two way slab subjected to dynamic loading using finite element analysis. Authors observed that existence of initial cracks in slabs damage more than normal slabs under same loading condition. Colombo et al. [21] presented a new strip method considering tensile membrane action of the slabs when large deflections reached, where tensile membrane action plays a key role. This method was used to obtain ultimate load carrying capacity of reinforced concrete two way slabs. The analytical model was validated for laterally restrained strips and slabs supported on four laterally unrestrained edges with experimental data.

If we want to determine the moment-field of RC slabs correspond to any value of load, we have to know the orthotropic coefficients and continuity factors which we can't obtain directly from the yield line theory. Singh et al. [16] stated that it is desirable to use orthotropic coefficients and continuity factors correspond to elastic distribution to determine bending moment for better performance under service conditions. Detailed literature reveals that many mathematical equations are available to obtain the moment-field of reinforced concrete slabs having different boundary conditions. However, in these formulations these parameters are still unknown. To encounter this problem, authors proposed the orthotropic coefficients and continuity factors of reinforced concrete slabs supported on 3-sides with one edge is unsupported carrying uniform area loading to obtain moment field of the RC slabs under service conditions. The proposed coefficients are very helpful for structural designers to analyze and design the slabs supported on three sides.

2. NUMERICAL MODELLING

Numerical modelling of the RC rectangular slabs supported on three sides was carried out using FEM based SAP software. SAP is useful for analyzing and designing the structural and non-structural elements. In this research work, SAP was used to obtain the moment field of the slabs which is helpful to procure the orthotropic coefficients and continuity factors. The whole methodology is shown by means of flow chart in Figure 1.

Let us consider a slab having span L_x in x direction and L_y in y direction giving an aspect ratio r equals to L_y/L_x. L_x is parallel to free edge and is taken as 3m which is freeze for all cases whereas L_y is variable depending on the aspect ratio. The negative moment of resistance of the slabs was observed at continuous edges in both directions i.e. m'_x in x direction and m'_y in y direction as shown in Figure 2. Similarly, the positive moment of resistance was observed in both directions i.e. m_x in x direction and m_y in y direction. From these moments of resistance, orthotropic coefficients which is defined as the ratio of m_y/m_x and continuity factors i_1 and i_2

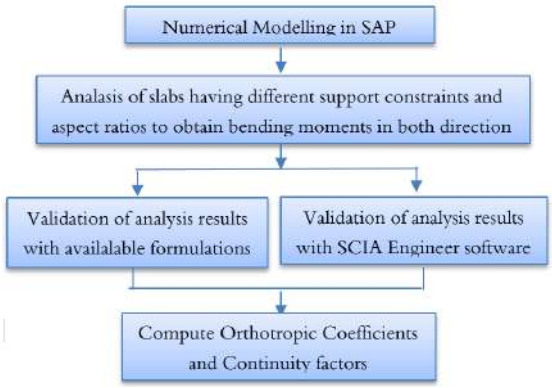

Figure 1. Flow chart of research methodology

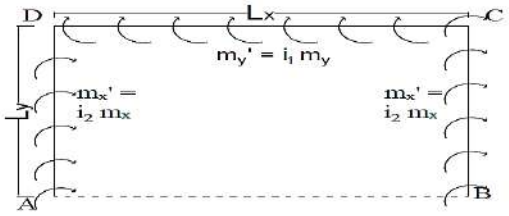

Figure 2. Moment field acting on slab

which are the ratio of m'_y/m_y and m'_x/m_x respectively were determined.

2. 1. Description of Models Slabs having different support conditions (Three sides discontinuous, three sides continuous, parallel sides discontinuous, parallel sides continuous and two adjacent sides discontinuous) and different aspect ratios (1.0, 1.1, 1.2, 1.3, 1.4, 1.5, 1.6, 1.7, 1.8, 1.9 and 2.0) were modelled. For modelling, four node shell type section was used and thickness of the slab was taken as 130mm. Mesh size is very critical while analyzing so, to get the precise results, sensitivity analysis was carried out to obtain an optimum mesh size which comes out to be 0.05 meter equally in both directions. This was obtained by reducing the size of mesh till it does not affect the results after further reducing the mesh size.

2. 2. Material Properties For modelling of the slabs, concrete material was used having compressive strength 20 MPa, Modulus of elasticity was obtained from the equation given in design code BIS: 456 [22] i.e.

$$\text{Modulus of elasticity} = 5000\sqrt{fck} \quad (1)$$

where, fck is compressive strength of concrete which is taken as 20 MPa. Using equation (1) we get modulus of elasticity as 22360.67 MPa. Other properties of concrete such as Poisson ratio was taken as 0.15 and density of concrete as 25 KN/m^3.

3. SAP RESULTS

Let us consider a transverse loaded slab carrying uniform area loading 10 KN/m^2 on the top face of the slab to obtain the moment-field of the slab. Figure 3 shows moment-field in x direction for the 3-sides supported continuous slab and Figure 4 shows moment-field in y direction for the 3-sides supported continuous slab. Results for different boundary conditions and different aspect ratios were presented in Table 1.

4. VALIDATION OF SAP RESULTS

Results obtained from SAP were validated with available formulations and FEM based SCIA Engineer software.

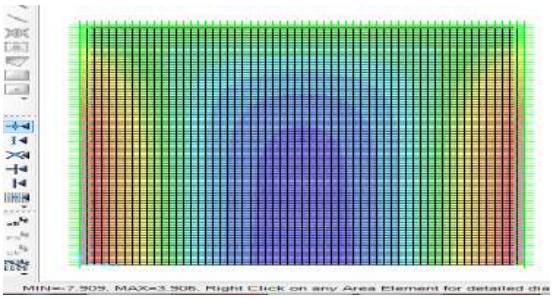

Figure 3. Moment field in x direction for the 3-sides continuous slab for aspect ratio 1.5 from SAP

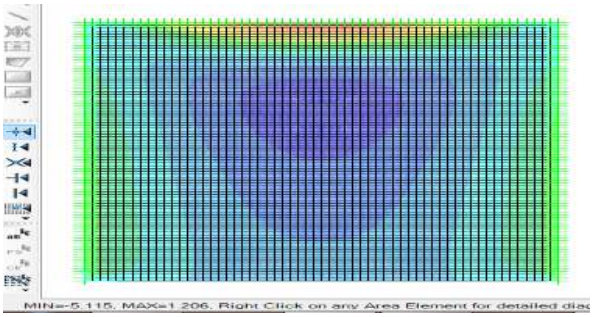

Figure 4. Moment field in y direction for the 3-sides continuous slab for aspect ratio 1.5 from SAP

4. 1. Validation with Timoshenko and Krieger Results obtained from SAP were validated with results published by Timoshenko and Krieger [23] for the case of 3-sides continuous slab having one edge is free for aspect ratio 1.0. The moment in x and y direction can be obtained from moment coefficients given in Table 2 which were proposed in published literature.

4. 2. Validation with SCIA Engineer In SCIA Engineer, orthotropic RC rectangular slab supported on three sides was modelled having aspect ratio 1.5 i.e. L_x was taken as 3m and L_y was taken as 4.5m with five different support conditions. For validation of results, different material properties like compressive strength, modulus of elasticity, poisson's ratio and density of concrete and mesh size were kept same as used in SAP software. For analysis, uniform area load of 10 KN/m^2 was applied at the top surface of the slab. Figure 5 depicts the moment field for the 3-sides supported continuous slab in x direction and Figure 6 shows the moment field for the 3-sides supported continuous slab in y direction.

Comparative analysis given in Table 3 shows that results obtained from numerical simulation are well validated with available formulations given in the literature. This shows that results obtained from SAP can be used to obtain the orthotropic coefficients and continuity factors. The case of 3-sides continuous slab is only validated because the other cases like 3-sides Discontinuous, Parallel Supported sides Continuous and

Parallel Supported sides Discontinuous are related to the case of 3-sides continuous slab by varying the continuity factors. The case of slab supported on two adjacent discontinuous sides is not available in literature so this case is validated with SCIA Engineer software.

Comparative analysis given in Table 4 shows that results obtainerd from SAP are well comparable with SCIA Engineer software.

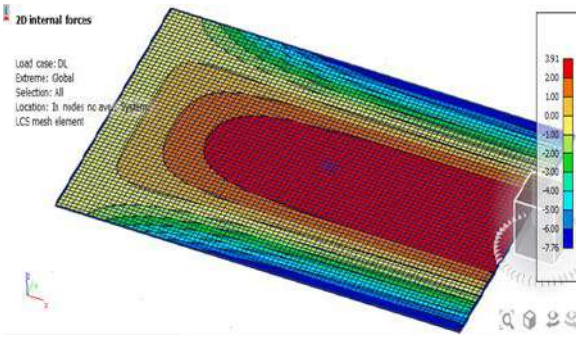

Figure 5. Moment field in x direction for the 3-sides continuous slab for aspect ratio 1.5 from SCIA Engineer

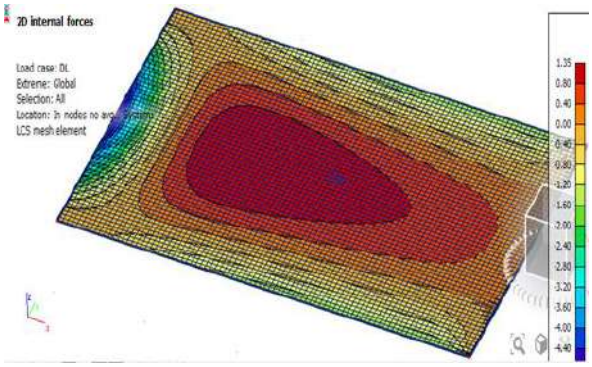

Figure 6. Moment field in y direction for the 3-sides continuous slab for aspect ratio 1.5 from SCIA Engineer

TABLE 1. Results obtained from finite element method (FEM) based SAP Software

S. No.	moment field	Aspect ratio, r										
		1.0	1.1	1.2	1.3	1.4	1.5	1.6	1.7	1.8	1.9	2.0
1	**3-sides Discontinuous**											
	Positive moment in x	9.70	10.17	10.53	10.81	11.02	11.18	11.31	11.41	11.48	11.53	11.58
	Positive moment in y	2.85	2.90	2.92	2.94	2.95	2.95	2.96	2.96	2.96	2.96	2.96
2	**3-sides Continuous**											
	Positive moment in x	3.85	3.90	3.91	3.92	3.91	3.91	3.90	3.90	3.89	3.89	3.89
	Moment in x at continuous edge	8.08	8.05	8.00	7.96	7.93	7.91	7.89	7.88	7.87	7.87	7.86
	Positive moment in y	1.17	1.19	1.20	1.20	1.21	1.21	1.21	1.21	1.21	1.21	1.21
	Moment in y at continuous edge	5.09	5.10	5.11	5.11	5.11	5.12	5.12	5.12	5.12	5.12	5.12
3	**Parallel Supported sides Continuous**											
	Positive moment in x	3.93	3.93	3.92	3.91	3.91	3.90	3.89	3.89	3.89	3.89	3.89
	Moment in x at continuous edge	8.06	8.00	7.96	7.92	7.90	7.88	7.87	7.87	7.86	7.86	7.86
	Positive moment in y	1.46	1.47	1.47	1.47	1.47	1.47	1.47	1.47	1.47	1.47	1.47
	Moment in y at continuous edge	-	-	-	-	-	-	-	-	-	-	-
4	**Parallel Supported sides Discontinuous**											
	Positive moment in x	8.39	9.12	9.70	10.16	10.52	10.80	11.01	11.18	11.30	11.40	11.47
	Moment in x at continuous edge	-	-	-	-	-	-	-	-	-	-	-
	Positive moment in y	2.23	2.37	2.46	2.53	2.57	2.59	2.61	2.62	2.63	2.63	2.63
	Moment in y at continuous edge	10.58	10.80	10.95	11.04	11.11	11.15	11.18	11.20	11.21	11.22	11.23
5	**Two adjacent sides Discontinuous**											
	Positive moment in x	6.28	6.39	6.47	6.51	6.54	6.56	6.57	6.57	6.57	6.57	6.57
	Moment in x at continuous edge	11.92	11.93	11.93	11.93	11.92	11.91	11.90	11.89	11.88	11.87	11.87
	Positive moment in y	1.98	2.00	2.01	2.01	2.01	2.01	2.01	2.01	2.01	2.01	2.01
	Moment in y at continuous edge	-	-	-	-	-	-	-	-	-	-	-

TABLE 2. Moment coefficients given in Timoshenko and Krieger [23]

b/a	$M_x = \beta_1 qa^2$ β_1	$M_y = \beta_2 qa^2$ β_2	$M_x = \beta_3 qa^2$ β_3	$M_y = \beta_4 qa^2$ β_4
1	0.0444	0.0138	-0.0853	-0.0510

TABLE 3. Validation of Results with published literature

S. No.	Support Conditions and moment field	Aspect Ratio, r 1.0	
1	**3-sides Continuous slab**	Results from SAP	Results from literature [23]
	Positive moment in x	3.85	3.99
	Negative moment in x at continuous edge	8.08	7.67
	Positive moment in y	1.17	1.24
	Negative moment in y at continuous edge	5.09	4.59

TABLE 4. Validation of Results with SCIA Engineer

S. No	Moment-Field and Boundary Condition	SAP	SCIA
1	**3-sides Discontinuous**		
	Positive moment in x	11.18	11.33
	Positive moment in y	2.95	3.36
2	**3-sides Continuous**		
	Positive moment in x	3.91	3.91
	Moment in x at continuous edge	7.91	7.76
	Positive moment in y	1.21	1.35
	Moment in y at continuous edge	5.12	4.40
3	**Parallel Supported sides Continuous**		
	Positive moment in x	3.90	3.90
	Moment in x at continuous edge	7.88	7.74
	Positive moment in y	1.47	1.63
	Moment in y at continuous edge	-	-
4	**Parallel Supported sides Discontinuous**		
	Positive moment in x	10.80	10.94
	Moment in x at continuous edge	-	-
	Positive moment in y	2.59	2.96
	Moment in y at continuous edge	11.15	10.95
5	**Two adjacent sides Discontinuous**		
	Positive moment in x	6.56	6.61
	Moment in x at continuous edge	11.91	11.74
	Positive moment in y	2.01	2.27
	Moment in y at continuous edge	-	-

5. RESULTS AND DISCUSSION

Numerical simulation of the three sides supported reinforced concrete rectangular slabs for different boundary conditions and different aspect ratios carrying uniform area load was carried out with the help of SAP and results are presented by the authors in Table 1. Results presented in Table 1 were validated with available literature and with SCIA Engineer software and those results were presented in Tables 3 and 4 respectively.

Results obtained from SAP were used to discover orthotropic coefficients and continuity factors and results are given in Table 5. The moment distribution across the slab varies with boundary constraints, aspect ratio and loading condition. However, the orthotropic coefficients and continuity factors are function of bending moment itself. And, results presented in Table 5 shows that these coefficients change with boundary constraints and aspect ratio.

These factors will be helpful for designers dealing in the slabs supported on 3-sides to calculate moment-field of the slabs using available analytical formulations in which these parameters are unknown.

TABLE 5. Orthotropic coefficients and continuity factors

S. No	Support Conditions and moment field	Aspect ratio, r 1.0	1.1	1.2	1.3	1.4	1.5	1.6	1.7	1.8	1.9	2.0
1	**3-sides Discontinuous**											
	Value of μ	0.293	0.285	0.278	0.272	0.268	0.264	0.261	0.260	0.258	0.256	0.255
2	**3-sides Continuous**											
	Value of μ	0.303	0.305	0.306	0.307	0.308	0.309	0.309	0.309	0.310	0.310	0.310
	Value of i_1	4.358	4.290	4.258	4.244	4.240	4.241	4.242	4.246	4.246	4.250	4.250
	Value of i_2	2.097	2.065	2.045	2.033	2.027	2.025	2.023	2.023	2.023	2.023	2.023
3	**Parallel Supported sides Continuous**											

	Value of μ	0.372	0.373	0.374	0.376	0.376	0.377	0.377	0.377	0.378	0.378	0.378
	Value of i_1	-	-	-	-	-	-	-	-	-	-	-
	Value of i_2	2.051	2.035	2.028	2.024	2.023	2.022	2.022	2.022	2.023	2.023	2.023
4	**Parallel Supported sides Discontinuous**											
	Value of μ	0.265	0.259	0.254	0.249	0.244	0.240	0.237	0.234	0.232	0.231	0.229
	Value of i_1	4.752	4.564	4.446	4.373	4.326	4.298	4.282	4.273	4.270	4.269	4.268
	Value of i_2	-	-	-	-	-	-	-	-	-	-	-
5	**Two adjacent sides Discontinuous**											
	Value of μ	0.316	0.312	0.310	0.309	0.308	0.307	0.307	0.307	0.306	0.306	0.306
	Value of i_1	-	-	-	-	-	-	-	-	-	-	-
	Value of i_2	1.898	1.866	1.845	1.831	1.823	1.816	1.812	1.809	1.808	1.806	1.806

6. CONCLUSION

In this research work, the orthotropic coefficients and continuity factors have been presented by the authors for the transverse loaded reinforced concrete rectangular slabs supported on 3-sides having one edge is unsupported for different boundary conditions carrying uniform area loading with the help of numerical simulation of FEM based Structural Analysis Program (SAP) software. It is possible to find these factors from published literature but all cases were not mentioned and if anyone wants to use the theory of plates, the equations used in these concepts are very cumbersome so it is not feasible to use these in daily routine. Yield line analysis is also a widely accepted tool for analysis of the slabs but it is not feasible to obtain orthotropic coefficients and continuity factors from yield line theory. The factors proposed by the authors can be used by the designers dealing with slabs supported on 3-sides to obtain the moment field of the slab.

Results obtained from Structural Analysis Program (SAP) software were validated with available literature with a maximum percentage difference of 9.82 percent. Results obtained from SAP were also validated with FEM based SCIA Engineer software and results are in favour with a maximum percentage difference of 14.06 percent.

The results presented in table 5 are simple to apply in equations of yield line theory in routine flow of calculations for determining moment carrying capacity, and would save computational time for analyzing and designing of the slabs.

7. REFERENCES

1. Ingerslev, A., Om en elementaer beregningsmetode af krydsarmerede plader. [The strength of rectangular slabs], [In Danish] (also printed in English), The Institution of Structural Engineers 1, No. 1, (1923), 3-14
2. Johansen, K.W., "Beregning af krydsarmerede jernbetonpladers brudmoment", In Bygningsstatiske Meddelelser, (In Danish), Vol. 3, No. 1, (1931), 1-18
3. Johansen, K.W., "Yield-line theory", Cement and Concrete Association, London, (1943)
4. Johansen, K.W., "Yield-line formulae for slabs", Cement and Concrete Association, London, (1972)
5. Kemp, K.O., "The Yield Criterion for Orthotropically Reinforced Concrete Slabs", ***International Journal of Mechanical Sciences Press Ltd***., Britain, 7, (1965), 737-746. doi; 10.1016/0020-7403(65)90002-0
6. Jones, L.L. and Wood, R.H., "Yield line analysis of slabs", James & Hudson, London, (1967).
7. Park, W.L. Gamble., "Reinforced Concrete Slabs", JohnWiley and Sons, New York, (2000).
8. Kennedy, G.C., "Practical yield line design", British cement Association, U.K, (2003).
9. Megson, T.H.G. "Structural and Stress Analysis", Elsevier Chapter 19, (2005), 625-639 doi: 10.1016/b978-0-7506-6221-5.x5000-0
10. Pillai, U. and Menon D., "Reinforced Concrete Design", Tata Mc Graw Hill Education, New Delhi, (2011).
11. Al-Sabah, A. S., and Falter, H., "Finite element lower bound "yield line" analysis of isotropic slabs using rotation-free elements", ***Engineering Structures Elsevier***, Vol. 53, (2013), 38-51. Doi: 10.1016/j.engstruct.2013.03.005
12. Al-Sabah, A. S., and Falter, H., "Rotation free finite element 'yield line' analysis of non isotropic slabs", ***Australian Journal of Structural Engineering, Taylor & Francis***, Vol. 16, No. 4, (2015), 273-282. Doi: 10.1080/13287982.2015.1092689
13. Gohnert, M., "Collapse load analysis of yield-line elements", ***Engineering Structures Elsevier***, Vol. 22, No. 8, (2000), 1048-1054. Doi: 10.1016/S0141-0296(99)00012-7
14. Famiyesin, O.O.R., K.M.A., Y.H, Chia and P.A. Slade., "Numerical and Analytical predictions of the Limit Load of Rectangular Two Way Slabs", ***Computers and Structures Elsevier***, Vol. 79, No. 1, (2001), 43-52. Doi: 10.1016/S0045-7949(00)00113-9
15. Kwan., "Dip and strike angles method for yield line analysis of reinforced slabs", ***Magazine of Concrete Research ICE***, Vol. 56, No. 8, (2004), 487-498. Doi: 10.1680/macr.2004.56.8.487
16. Singh, N.K., and M. Kumar, "Prediction of collapse load of three-side-supported RC rectangular slabs: A simplified approach", ***The Indian Concrete Journal***, Vol. 85, No. 7, (2011), 21-29

17. Gupta, S., Singh, H., 'Analysis of reinforced concrete rectangular slabs with three-sides supported under uniformly distributed load", ***Asian Journal of Civil Engineering, Springer***, Vol. 21, No. 1, (2020), 81-90 doi: 10.1007/s42107-019-00182-6

18. Gupta, S., Naval, S., 'Analysis of Orthotropic RC Rectangular Slabs Supported on Two Adjacent Edges-A Simplistic Approach' ***Civil Engineering Journal***, Vol. 6, No. 10, (2020), 1992-2001. Doi: 10.28991/cej-2020-03091598

19. Abdul-Razzaq et al. "Finite Element Modelling of Post-Tensioned Two Way Concrete Slabs under Flexural Loading", ***Civil Engineering Journal,*** Vol. 4, No. 1, (2018), 1-10 doi: 10.28991/cej-030964

20. Wenjiao, Z., et al. "Numerical Simulation of Cracked Reinforced Concrete Slabs Subjected to Blast Loading", ***Civil Engineering Journal***, Vol. 4, No. 2, 320-333 doi: 10.28991/cej-030994

21. Colombo, M. et al. "A Design Approach to Evaluate the Load-Carrying Capacity of Reinforced Concrete Slabs Considering Tensile Membrane Action", ***Structrural Engineering International***, (2020): doi: 10.1080/10168664.2020.1747957

22. BIS: IS 456 - 4th Rev. Plain and reinforced concrete-code of practice. Bureau of Indian Standards, India, (2000).

23. Timoshenko, S.P. and Krieger, S.W., "Theory of Plates and Shells", Mc Graw Hill Education, Indian Edition, (2015).

Persian Abstract

چکیده

تجزیه و تحلیل و طراحی صفحات بتن آرمه که از ۳ طرف در ساخت و سازهای بتونی یا بتن مسلح پشتیبانی می شوند ، شامل فرمول های تحلیلی است. در فرمولهای تحلیلی منتشر شده ، ضرایب ارتوتروپی و عوامل تداوم پارامترهای ناشناخته ای هستند. برای بدست آوردن ظرفیت حمل لحظه ای اسلبها با استفاده از فرمولاسیون های موجود ، این عوامل باید مورد نیاز باشد. در این کار تحقیقاتی ، این ضرایب ارتوتروپیک و فاکتورهای تداوم برای اسلبهای مستطیلی RC بارگذاری عرضی که از سه طرف تحت بارگذاری منطقه یکنواخت در بالای صفحه دال پشتیبانی می شوند ، ارائه شده است. این ضرایب با استفاده از نرم افزار (FEA) تحلیل اجزای محدود مبتنی بر برنامه تحلیل ساختاری (SAP)بدست آمد. همچنین با نرم افزار مهندس SCIA و فرمولهای منتشر شده) FEAتحلیل اجزا محدود) تأیید می شود. مشاهده شده است که نتایج به دست آمده با ادبیات منتشر شده و نرم افزار مبتنی بر FEM قابل مقایسه است. نتایج ارائه شده در این مقاله تحقیقاتی برای پیش بینی میدان گشتاور دالهای مستطیل بتونی مسلح که از سه طرف دارای یک لبه پشتیبانی می شوند ، پشتیبانی نمی شود. این ضرایب برای طراحان سازه ای که با دال های بتونی تقویت شده از سه طرف پشتیبانی می شوند بسیار مفید خواهد بود.

IJE TRANSACTIONS B: Applications Vol. 34, No. 02, (February 2021) 382-392

International Journal of Engineering

Journal Homepage: www.ije.ir

Behavior and Strength of Steel Fiber Reinforced Self-compacting Concrete Columns Wrapped by Carbon Fiber Reinforced Polymers Strips

S. A. Abbas*[a], I. F. Ali[b], A. A. Abdulridha[a]

[a] *Department of Civil Engineering, University of Technology, Baghdad, Iraq*
[b] *The Ministry of Transport and Communications, Baghdad, Iraq*

P A P E R I N F O

Paper history:
Received 17 August 2020
Received in revised form 27 October 2020
Accepted 29 October 2020

Keywords:
Carbon Fiber Reinforced Polymers
Finite Element
Mechanical Properties
RC Columns
Self-compacted Concrete
Steel Fibers

A B S T R A C T

Strength capacity of reinforced concrete columns is very important to resists and transmit the external loadings. For Architects the engineerings requirements to use small cross section of reinforced concrete columns or in case of poor control quality we need to increase the compressive strength of concrete or use a strengthening technique of the structural elements such as column. In the present paper, the behavior and strength of four steel fiber reinforced self-compact concrete columns reinforced by one layer of CFRP that is wrapped around a square of reinforced concrete columns subjected to static loads is investigated. Self-compacting concrete by using limestone powder is adopted and is mixed with different percentages of steel fiber such as 1%, 1.5% and 2%. Different tests are adopted to investigate the mechanical properties of self-compacted concrete mixed with different steel fiber percentages. Test results show that there is an increase in concrete mechanical properties such as compressive strength, splitting tensile strength and modulus of rupture that reflects on the increase in load capacity of column; specimens when wrapped by CFRP. The increment in columns strength capacity is more than 50% as compared with the control column. All the test specimens are modeled using finite element analysis by ANSYS and the numerical results are compared with tested specimens.

***doi**: 10.5829/ije.2021.34.02b.10*

NOMENCLATURE

A_g	Gross area of section (mm^2)	h	Overall thickness or height of a member (mm)
A_{st}	Total area of longitudinal reinforcement (mm^2)	n_f	Number of plies of FRP reinforcement
b	Width of rectangular cross section (mm)	P_n	Nominal axial load strength at given eccentricity(N)
E_f	Tensile modulus of elasticity of CFRP (MPa)	r	Radius of the edges of a square or rectangular section confined with CFRP (mm)
$f_c^{`}$	Specified compressive strength of concrete (MPa)	**Greek Symbols**	
$f_{cc}^{`}$	Apparent compressive strength of confined concrete (MPa)	φ	Strength reduction factor (0.85)
f_{fe}	Effective stress in the FRP; stress level attained at section failure (MPa)	ε_{fe}	Effective strain level in FRP reinforcement; strain level attained at section failure (mm/mm)
f_y	Specified yield strength of non-prestress steel reinforcement (MPa)	φ_f	CFRP strength reduction factor (0.95)
f_l	Confining pressure due to CFRP jacket (MPa)	ρ f	CFRP reinforcement ratio
t	Nominal thickness of one ply of the FRP reinforcement (mm)	ρ g	Ratio of the area of longitudinal steel reinforcement to the cross-sectional area of a compression member
k_a	Efficiency factor for CFRP reinforcement (based on the section geometry)		

Corresponding Author Institutional Email: *40348@uotechnology.edu.iq* (S. A. Abbas)

Please cite this article as: S. A. Abbas, I. F. Ali, A. A. Abdulridha, Behavior and Strength of Steel Fiber Reinforced Self-compacting Concrete Columns Wrapped by Carbon Fiber Reinforced Polymers Strips, International Journal of Engineering, B: Applications Vol. 34, No. 02, (2021) 382-392

1. INTRODUCTION

Reinforced concrete columns are vertical structural elements that the main bearing transfer loads to the foundation. The column stability relies on the Euler formula is that based on the elastic analysis. The column stability depends on the column stiffness and the slenderness ratio. Short columns are classified based on the slenderness ratio. Axially loaded columns are those where the loads lie with the center of gravity of the column cross-section. An increase in compressive strength by adding steel fiber provides the column more strength and reduces the buckling for long term effects. Fibers are planned to advance flexural strength, tensile strength and toughness [1]. The presence of steel fibers makes the concrete matrix less workable such that usage of self-compact concrete is the best solution. Mixing of steel fiber with self-compact concrete as additives material producing a new concrete with special specifications. Self-compact concrete (SCC) is the concrete compacted under its self-weight without use of a mechanical vibrator to stirring the concrete mix.

Many studies concluded that the self-compact concrete is very useful to fill the spaces for heavy structural elements such as columns. Many advantages for self-compact concrete that made the structural engineering adapt for example reduction in time of constructions, no noise, improved the capacity of the structural member by filling the spacing's and giving excellent structural behavior. Superplasticizer is also used in concrete mix to avoid segregations and increase concrete workability. Different methodologies were adapted to strengthen if smaller cross section of concrete and re-strength were used when there is a damage in concrete. Fiber reinforced polymers (FRP) family such as Glass fiber reinforced polymers (GFRP), Armed fiber reinforced polymers (AFRP), Carbon Fiber reinforced polymers (CFRP) and Basalt fiber reinforced polymers (BFRP) has become increasingly popular for structural civil engineering applications. The advantages of FRP family are their high ratio of strength for the weight with corrosion resistance and their ease of use. Many researchers investigated the concrete mechanical properties that are mixed with steel fiber and explored a different structural member with and without wrapped by FRP family. Abdel-Hay [2], investigated the behavior and strength of reinforced concrete columns strengthened by CFRP. Then, test results showed that the ultimate load of the wrapped column increases due to the confinement.

Karbhari and Eckel [3] tested reinforced concrete columns strength by jacket steel section concluded that the main reasons why the designers have not used jackets are low corrosion resistance, increase in dead load and expensive cost. Mirmiran et al. [4] tested concrete columns reinforced by fiber polymer bars in which test results indicated that the large deformation capacity with low corrosion to environmental gave more attention to use CFRP as an excellent option as an alternative and extremely efficient re-strength technique. Bogdanovic [5] studied the performance of reinforced concrete columns strengthened by FRP strips. Based on the test observations and recorded results, he indicated that the confinement effectiveness of CFRP relies on the concrete type, reinforcement, number and stiffness of FRP layers and loading status. Olivova and Bilcik [6] investigated reinforced concrete circular columns wrapped by FRP, and concluded that when the load was applied as eccentrically; not at the center of the column cross section, the mode of failure of the unconfined columns by CFRP was due to the crushing of the concrete on the compression side. Ou and Truong [7] studied the retrofitted damaged columns, and test results showed that the ductile failure mode occurs when the column was wrapped by CFRP. That means there was an enhancement in lateral strength of reinforced concrete columns. Abdel-Mooty et al. [8] looked out on the behavior of damaged reinforced columns wrapped by FRP columns and concluded that the electiveness of FRP improvement depends on the level of damage experienced. Ghosh and Sheikh [9] studied reinforced concrete columns wrapped by FRP and concluded that the influence of wrapping in the case of square section columns is more effective than rectangular columns.

Ali et al. [10] investigated the effect of steel fibers on the mechanical concrete properties and the column capacity and found that the presence of steel fiber was adopted in concrete to reduce the cracks due to performing of a plastic hinge in the concrete. Ozturk et al. [11] studied the seismic analysis on the existing building and the methodology that it was adopted as retrofitted by CFRP in which the analysis results indicated that the presence of CFRP decreased the drift that came from lateral loadings. Ozturk et al. [12] studied the retrofit methodology by adopted FRP material on the existing building, analysis results showed that there are improvements in stable maximum drift due to apply of FRP as compared with the control building. Kianoush and Esfahani [13] investigated the axial compressive strength of reinforced concrete columns strengthened by FRP. Test results, the FRP wrap did not increase the strength of square columns with sharp corners. However, the square column with rounded corners exhibited higher strength and ductility compared to those with the sharp corners.

2. AIM AND SIGNIFICANT OF RESEARCH

Different tests for circular columns that were wrapped by CFRP but there were a few researchers that focused on the behavior and strength of square steel fiber reinforced concrete column was using wrapped by CFRP. The aims

and the significance of the present study are to evaluate the mechanical properties of new concrete as steel fiber self compacting concrete and the behavior and strength of wrapped reinforced concrete columns by CFRP sheets under the effect of axial static loadings. Different percentages of steel finer are adopted such as 1%, 1.5% and 2% added with self-compacting limestone powder to produce a new concrete of steel fiber self compacting concrete (SFSCC). The SFSCC is adapted to cast four short columns wrapped by CFRP to have the same scheme and then tested. Columns capacity, lateral and longitudinal displacement with full behavior for all tested columns are recorded and discussed. Finite element models are simulated for all tested specimens to checkouts the performance of composite columns.

3. THEORETICAL ANALYSIS

Wrapping of CFRP around compression structural members such as reinforced concrete columns will confine the column leading to an increase the strength axial compression load capacity. The presence of FRP strips around compression members also increases the tensile strength of column; also improves the ductility of concrete. The non-prestress concrete with tie reinforcements, the axial load capacity is [14]:

$$\emptyset P_n = 0.8\emptyset[0.85\varphi_f \hat{f_{cc}} \left(A_g - A_{st}\right) + f_y A_{st} \quad (1)$$

The modified compressive strength of confinement concrete by applies Equation (2) as follows:

$$\hat{f_{cc}} = \hat{f_c}\,[2.25\sqrt{1 + 7.9\frac{f_i}{\hat{f_c}}} - 2\frac{f_i}{\hat{f_c}} - 1.25 \quad (2)$$

$$f_i = \frac{k_a\,\rho_f\,f_{fe}}{2} = \frac{k_a\,\rho_f \varepsilon_{fe}\,E_f}{2} \quad (3)$$

The reinforcement ratio for adopted square sections calculated as follows:

$$\rho_f = \frac{2t\,n_f\,(b+h)}{bh} \quad (4)$$

$$K_a = 1 - \frac{(b-2r)^2+(h-2r)^2}{3bh(1-\rho_g)} \quad (5)$$

4. EXPERIMENTAL PROGRAM–MATERIALS USED

All raw materials that used to cast the short column specimens were tested using cement, aggregates, limestone powder (LSP) as a filler material for self-compacting concrete and steel fiber as follows:

4. 1. Cement Ordinary Portland cement-Type I was used, the test results complying with Iraqi standards specifications IQS No.5-1984 [15]. Tables 1 and 2 list the chemical composition and physical properties of cement.

TABLE 1. Portland cement physical properties

Properties	Results	Iraqi specification, Limits [15]
Specific surface area, m^2/kg	310	> 230.0
Time of sitting by Vicat′s apparatus		
Initial, hour: minute	1:41	≥ 0.75 hours
Final, hour: minute	3:45	≤ 10.0 hours
"Compressive strength, MPa"		
3 days	22.6	> 15
7 days	30	> 23
Soundness		
Autoclave, (%)	0.5	< 0.8

TABLE 2. Portland cement chemical composition

Oxide composition	Content (%)	Iraqi specification Limit [15]
Silica dioxide, SiO_2	21.71	-
Lime, Cao	61.81	-
Iron oxide, Fe_2O_3	3.32	-
Alumina trioxide, $Al2O_3$	4.62	-
Sulphates, SO_3	2.53	< 2.8 %
Magnesia oxide, MgO	3.03	< 5.0 %
Insoluble residue	0.86	< 1.5 %
Loss on ignition	2.14	< 4.0 %
Lime saturation factor	0.84	0.66 to1.02

4. 2. Aggregates Coarse aggregate with maximum size of 12 mm and fine aggregate with maximum size of 4.75 mm were used. The utilized fine and coarse aggregate properties are employed with the Iraqi specification No.45/1984 [16] as publicized in Tables 3 and 4 correspondingly.

4. 3. Limestone Powder Limestone powder (LSP) was used as a filler material for the concrete mix as self-compacting concrete with fineness 315 m^2/kg that is classified as fine aggregate gradation zone (2). Tables 5 and 6 list the physical and chemical composition of LSP.

TABLE 3. Grading of fine aggregate

Sieve Size (mm)	% Passing by weight	Limits of the IQS. No.45-1984 zone (2) [16]
4.75	100	90-100
2.36	89	75-100
1.18	70.1	55-90
0.60	58	35-59
0.30	24.2	8-30
0.15	3.1	0-10

TABLE 4. Grading of coarse aggregate

Sieve size (mm)	% Passing by weight	Limits of the IQS. No.45-1984 [16]
20	100	100
14	94	90-100
10	61	50 – 85
5	5	0-10
2.36	0	0

TABLE 5. Physical composition of Limestone powder

Physical form	Fine aggregate gradation zone (2)
Color	White
Fineness (Blain) (m^2/kg)	315

TABLE 6. Chemical composition of Limestone dust

Oxide	% Content
Al_2O_3	0.61
SiO_2	1.22
SO_3	0.1
Fe_2O_3	0.2
MgO	0.32
CaO	60.1
L.O.I	36.5

4. 4. Super-plasticizer A chemical admixture based on modified polycarboxylic (Glenium 51) was used as a high range water reducing agent plus that matching the requirements of ASTM C-494 [17].

4. 5. Micro Steel Fiber Steel fiber with 15 mm in length, 0.25 mm in diameter and tensile strength (2000 MPa) was adopted.

4. 6. Carbon Fiber Reinforced Polymers (CFRP) Sika - Wrap - 300C woven carbon fiber fabric is used to strengthen specimens.

The roll of carbon fiber was 500 mm in width and 50 m in length (standard roll). Table 7 lists the product description of the (CFRP) as per Sika Company and Figure 1 shows the typical CFRP roll.

4. 7. Adhesive Materials Sikadur-330 was adapted to bonded CFRP sheets with concrete column. Table 8 lists the properties of the used adhesive material.

The Sikadur-330 contained two containers, as A (1 kg) and B (2 kg) mixed with uniform stirring to produce the final bond material with total weight (3 kg).

TABLE 7. Technical properties of CFRP

Properties	Sika Warp-300 C/60
Tensile strength, (MPa)	3900
% Elongation at break, (strain)	1.5%
Areal weight, (g/m^2)	300±15
E-modulus, (MPa)	230000
Density, (g/cm^3)	1.79
Thickness, (mm)	0.166

Figure 1. CFRP standard roll

TABLE 8. Properties of the adhesive material

Density at+23°C (kg/l)	E-Modulus (MPa)	Tensile strength (MPa)	Setting time (Minute) at 35°C	% Elongation
Parts (A+B) mixed: 1.31	Flexural: 3800 Tensile : 4500	30	Part A:part B ratio: 4:1	0.9

5. STEEL REINFORCEMENTS

All columns specimens were reinforced by four rebars as main reinforcements with 10 mm in diameter that were tied by nine 4 mm in diameter. The distribution of tied reinforcements at 115 mm center to center started from 50 mm from each end in addition to two stirrups at each end that was shown in Figure 2. The column was designed based on the ACI-318-2014 [18] in which the concrete column is (415 kN) as ultimate strength capacity without CFRP. The mechanical properties for column reinforcement that tested based on ASTM A996M-05 [19].

6. CONCRETE MIXES

Theoretical mix design was calculated for required compressive strength of concrete with practical trail mix as normal and with additives materials. Slump flow, T50, L-box and V-funnel tests were performed to ensure the concrete working as self-compacting. Furthermore, the results listed in Table 9 were compared with the limitation of EFNARC- 2002 [20] and ACI 237R-07 [21], the SC mix is conforming to specifications.

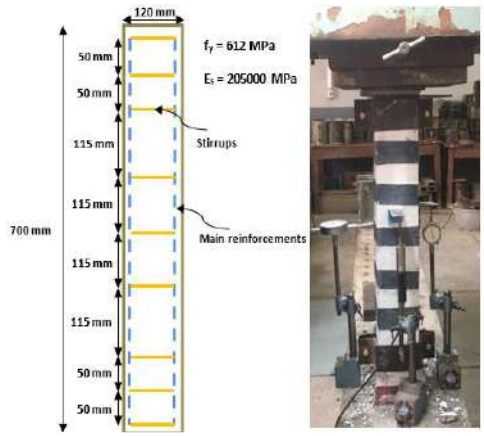

Figure 2. Column dimensions and test setup layout

TABLE 9. Fresh SCC test results [10]

Test method	Results	Range of the EFNARC- 2002 [20]
Slump flow(mm)	710	650-800
T500 (sec)	2	2-5
V-funnel (sec)	9	6-12
L-box (H2/H1)	0.8	0.8-1

7. EXPERIMENTAL PROGRAM

A total of four RC square column specimens were cast and wrapped by CFRP sheets that surrounded the circumference of column and then tested to investigate the effect of steel fiber ratio on the behavior of SCC warped reinforced concrete columns by CFRP sheets. Twenty-four cubes and prisms with dimensions as (150x150x150) mm and (100x100x400) mm respectively were cast and then tested to measure the compressive strength and flexural strength respectively. Cylinders with 150 mm in diameter and 300 mm in height were tested to measure the concrete compressive strength. The characteristics of tested specimens were presented in Table 10. C0%, C1%, C1.5% and C2% represent column specimen with (0, 1, 1.5 and 2)% steel fiber percentages respectively.

TABLE 10. Characteristics of tested specimens

Specimens	Compressive strength ($f_c^{'}$) (MPa)	% Steel fiber ratio	% CFRP by area	CFRP width (mm)
C0%	30	0.0	50	50
C1%	30	1.0	50	50
C1.5%	30	1.5	50	50
C2%	30	2.0	50	50

8. COLUMN SPECIMENS AND TEST PROCEDURE DESCRIPTION

Four tested specimens as a square in cross-section (120x120) mm with column height 700 mm with cover 20 mm are cast in laboratory at the University of Technology in Iraq. The main reinforcements are 4ϕ10 mm, and are tied by 9ϕ4 mm uniformly distributed with layout. All specimens as short columns are tested by a hydraulic machine capacity of 2500 kN.

Thick steel plates with 7 mm thickness are fixed at top and bottom of each specimen during test to avoid stress concentration and to ensure uniform applied load. The applied load is recorded by a calibrated load and by LVDT-dial gages are used to measure the vertical and horizontal displacement at the top of specimen. The applied vertical load increased incrementally with 10 kN.

9. TEST RESULTS AND DISCUSSIONS

Mechanical properties of a new concrete as SFSCC are investigated for all mechanical properties. The main parameters that were observed during tests are the ultimate capacity of the columns, longitudinal displacements and lateral (buckling) displacements for all columns that wrapped by CFRP assuming that there are full interactions between the CFRP and concrete column and there are no slips.

9. 1. Mechanical Properties Mechanical properties for SFSCC are obtained by testing cubes, cylinders and prisms to find out the compressive strength, splitting tensile strength and modulus of rupture. The compressive strength of cubes was tested based on the BS1881-116 [22]. Test results showed that there is increment in compressive strength as compared with normal concrete. The increase in compressive strength relies on the steel fiber percentage. When there is increase in the steel fiber percentage that led to an increase in compressive concrete strength because of the steel fiber producing connections between the matrix components and prevent early failure due to reduce the cracks propagations that lead to increase in strength capacity for cubes, cylinders and the columns specimens. Indirect tensile test of SFSCC was carried out based on ASTM C496 [23]. Test results showed that there are increases in splitting tensile strength as compared to normal concrete.

These increased in mechanical properties of SFSCC due to increase in inside tension resistance because increase in ductility and become more strength to prevent internal stresses. Modulus of ruptures test of SFSCC based on ASTM C78 / C78M-16 [24] was performed. It was found that there were increases in modulus of rupture as compared with normal concrete. The presence of steel

fiber within the concrete matrix makes the concrete prism more ductile and resistant due to applied load that means the concrete is not still as brittle so that the SFSCC becomes more flexible. Table 11 lists the test results for all specimens and their comparison with normal concrete.

9. 2. Structural Composite Columns The ultimate capacities of the composite columns are listed in Table 12 increase in load capacities of composite column specimens. Table 12 lists the maximum axial and lateral displacement, and the percentage decrease in deformations.

TABLE 11. Test results for all specimens and their comparisons with normal concrete

Cube		
% Steel fiber	**Average compressive strength at 28 days (MPa)**	**% Increase in compressive strength**
0	30	-
1	35	16.67
1.5	38	26.67
2	42	4.00
Cylinder		
% Steel fiber	**Average tensile strength at 28 days (MPa)**	**% Increase in tensile strength**
0	3.0	-
1	3.2	6.67
1.5	3.3	10.00
2	3.5	16.67
Prism		
% Steel fiber	**Average modulus of rupture at 28 days (MPa)**	**% Increase in modulus of rupture**
0	4.2	-
1	4.5	7.14
1.5	4.6	9.50
2	4.8	14.29

10. MODE OF FAILURE

Figure 3 shows the failure modes for all composite column specimens. The failure modes of composite columns occur in concrete and no pullout or spalling of CFRP at the end for each specimen's tests except specimen C0% in which the CFRP spall from the concrete column. The column C0% crushed at the central height that is mean in the compression face in addition to appears high cracks that propagated near the center of the specimen. Column C1%, crushed at middle with less crack, while composite columns C1.5% and C2% less crush and no CFRP are spalling occurs in middle due to increase in applied load.

Figures. 4 and 5 show the behavior of load versus the longitudinal and lateral displacement up to ultimate loads for all composite column specimens. Initially, the load – displacements behavior starts linear for all specimens. The slope of linear behavior represents the initial stiffness of the composite column is high due to the higher stiffness of composite column specimens that make the displacements small concerning applied load (increase in moment of inertial and equivalent of modulus of elasticity) because of composite action. When the load increases, the deformation becomes high and the slope of the curve becomes toward the horizontal direction due to decreased column stiffness up to ultimate loads. The inflection point becomes high when the steel fiber percentage increases and presences of CFRP that means there is enhancement in ductility in the range of elastic deformation (elastic load). The relationships between applied loads and displacements are 52%, 63%, 67% and 72% from the ultimate loads that represent the inflections points for all columns are approximately linear and then after that become nonlinear for columns C0%, C1%, C1.5% and C2% respectively. The presence of CFRP that surrounded all specimens makes the concrete more confinements that help and work such as tie reinforcement so that the amounts of lateral displacements become less. No slip developed between the interface of CFRP and concrete at the interfaces between these two materials due to the amount of epoxy more than enough to work as full interaction. The strengthening technique (CFRP distributions along with the height of the specimen) that adopted gave and

TABLE 12. Maximum axial and lateral displacements of composite columns

Column mark	Ultimate load (kN)	Maximum longitudinal displacement (mm)	Maximum lateral displacement (mm)	% load capacity	% Decrease of longitudinal displacement	% Decrease of lateral displacement
C0%	670	7.2	1.2	-	-	-
C1%	710	6.8	1.1	5.97	5.55	8.33
C1.5%	760	5.8	0.99	13.43	19.44	17.50
C2%	810	5.2	0.94	20.9	27.77	21.67

Figure 3. Mode of failure for all specimens

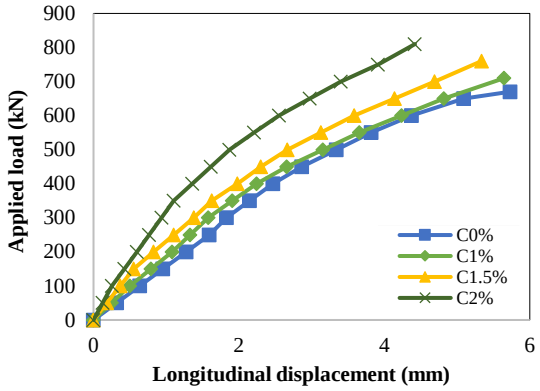

Figure 4. load-longitudinal displacement for all columns

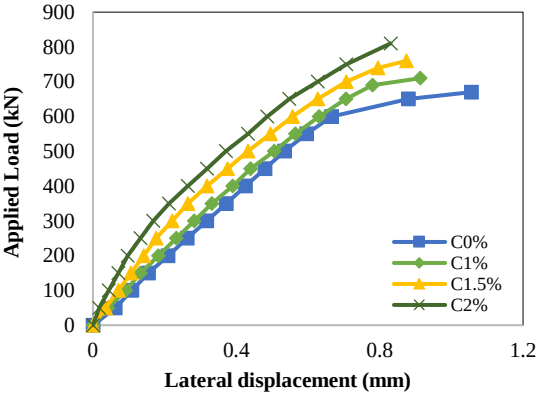

Figure 5. load- lateral displacement for all columns

provides significant concrete confinement due to an increase in strength column capacity. Project the ultimate load of 0% steel fiber on all other specimens gave less longitudinal and lateral displacement.

11. COLUMNS STRENGTH CAPACITY – ACI-440-2R-2002

Based on the ACI-318-2014 [18] as reinforced concrete column and ACI-440-2R-2002 [14] equations as compression members strengthening by FRP strips by the CFRP properties mentioned above, Table 13 lists the columns strength capacities and the comparisons between theoretical and experimental works. An increase in column capacity and reduction in longitudinal and lateral displacement rely on the increase in steel fiber percentage.

12. COLUMNS MODELING - FINITE ELEMENT ANALYSIS

Finite element analysis was performed in ANSYS software to simulate all column specimens that were strengthened by CFRP. Different elements are adopted for this purpose such as SOLID65 element for concrete material, LINK180 element for main reinforcement and stirrups, SHELL181 element to simulate CFRP layer [25]. The main assumptions considered in the numerical analysis were the plane section remains plane before and after applied loads, the concrete is homogeneous, full bounds between concrete and reinforcements, full interactions between the concrete and CFRP layers and the material nonlinearity of CFRP is linear up to failure. The support conditions and the applied loading were the same as experimental tests. Dimensions and mechanical properties that were adopted in numerical analysis to checkouts the performance of the tested specimens were the same as the experimental tests. Figure 6 shows the three-dimensional model of the element, main reinforce ments and stirrups, and CFRP layers simulations/ column model meshes. Figures 7 to 14 show the longitudinal and

TABLE 13. Compressions between experimental and theoretical columns strength capacities

Column mark	Ultimate load (experimental test) (kN)	ACI-318-2014 [18] without CFRP	% Increase in capacity compare RC column (415 kN)	% Increase in capacity compare with ACI-318-2014 [18] Without CFRP	ACI-440-2R-2002 [14]	(Experimental/ Theoretical) capacity	% Difference in capacity
RC Column	-	415	-	-	-	-	-
C0%	670	415	61.45	61.45	500	1.34	34
C1%	710	456	71.08	55.70	550	1.29	29
C1.5%	760	481	83.13	58.00	575	1.32	32
C2%	810	515	95.18	57.28	602	1.34	34

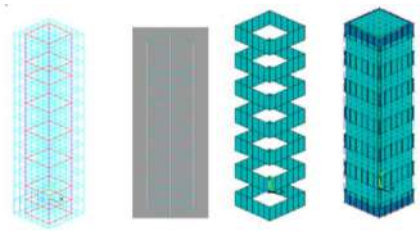

Figure 6. Three-dimensional wireframe model, main and stirrups reinforcements, CFRP layers and the full model

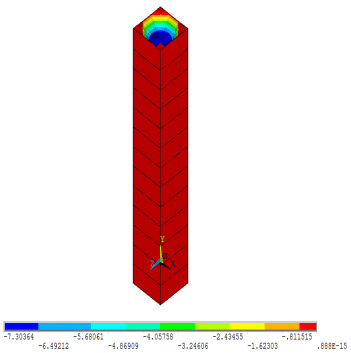

Figure 7. Longitudinal displacemnts along the C0% column model (mm)

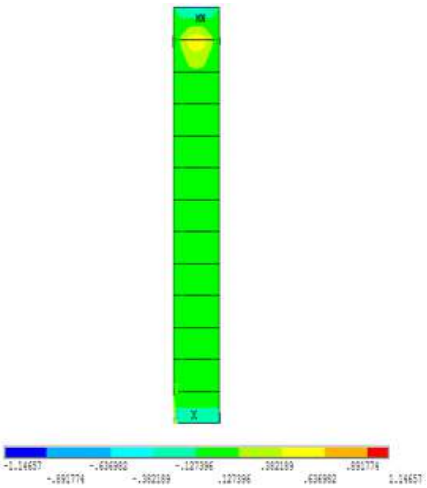

Figure 8. Lateral displacements along the C0% column model (mm)

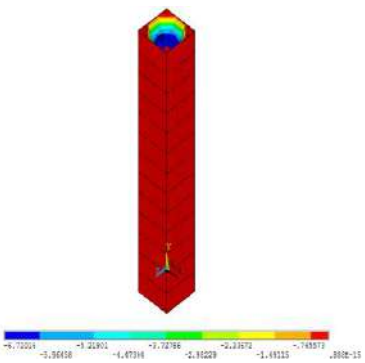

Figure 9. Longitudinal displacements along the C1% column model (mm)

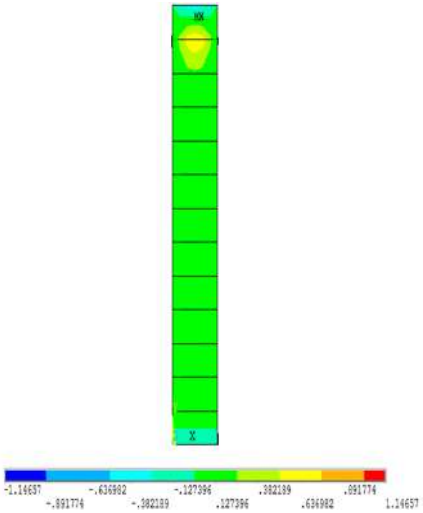

Figure 10. Lateral displacements along the C1% column model (mm)

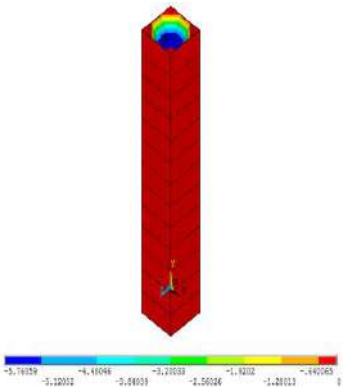

Figure 11. Longitudinal displacements along the C1.5% column model (mm)

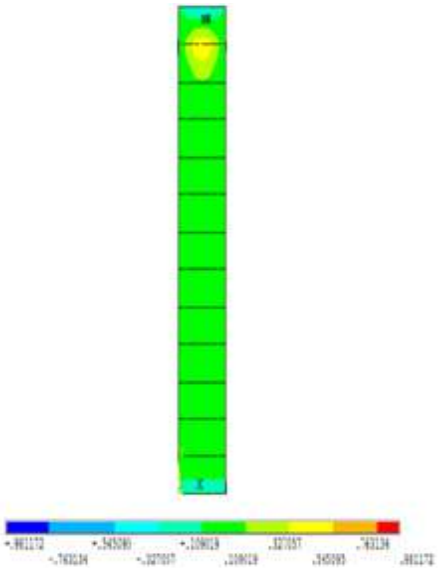

Figure 12. Lateral displacements along the C1.5% column model (mm)

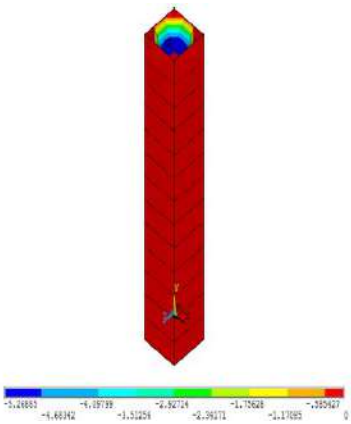

Figuer 13. Longitudinal displacements along the C2% column model (mm)

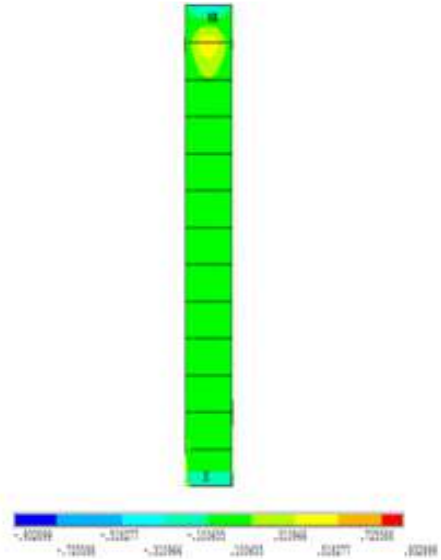

Figure 14. Lateral displacements along the C2% column model (mm)

lateral displacements numerical results for all the models. Table 14 lists comparison between experimental and numerical results. Figures 15 and 16 show the comparison results between experimental and numerical analysis with 45° line for longitudinal and lateral displacement. All the points lie rounded the 45° line, which means that the numerical solution is conservative. The meaning of the comparison results is rounded to unity and the standard deviation value along with the variance are found were very so small.

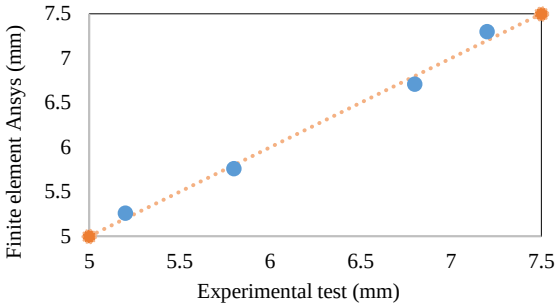

Figure 15. Comparison between finite element analysis and experimental test results for longitudinal displacements

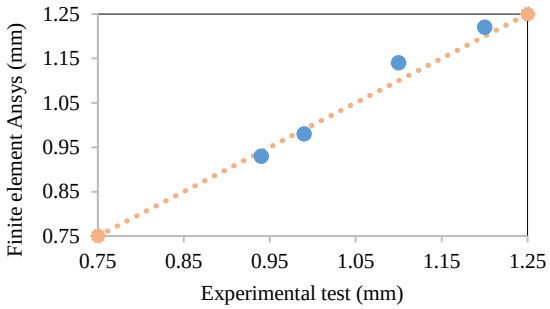

Figure 16. Comparison between finite element analysis and experimental test results for lateral displacements

TABLE 14. Compressions between experimental tests with columns simulated by ANSYS

Column mark	Maximum longitudinal displacement experimental (mm)	Maximum lateral displacement experimental (mm)	Maximum longitudinal displacement ANSYS (mm)	Maximum lateral displacement ANSYS (mm)	%longitudinal displacement ANSYS/experimental	%lateral displacement ANSYS/experimental
C0%	7.2	1.2	7.30	1.22	101.01	101.66
C1%	6.8	1.1	6.71	1.14	98.67	103.63
C1.5%	5.8	0.99	5.76	0.98	99.31	99.98
C2%	5.2	0.94	5.26	0.93	101.15	98.93
Mean					1.0004	1.0105
Standard division					0.0123	0.0205
Variance					0.000153	0.00042

13. CONCLUSION

Based on the experimental investigations, evaluations of the behavior and strength of SFSCC short composite columns subjected to static axial loads are examined. The following are the most important notices for observing and recording results:

1. Increase in SFSCC mechanical properties due to a reduction in the voids between concrete mixes.
2. Presences of steel fibers within the concrete mix increase the column capacity.
3. Increase in steel fibers ratio that reduces longitudinal and lateral displacement
4. Delay on the first crack loads on steel fiber concrete due to improvement in elastic displacement within the elastic zone of column specimens.
5. The wrapped CFRP around the concrete columns increases the concrete strength and resistance due to concrete confinements that reflect an increase in concrete compressive strength.
6. The column capacity as compared with the column capacity based on ACI-code, is increased due to the presence of steel fibers and CFRP strips.
7. Enhancement for strength and ductility due to composite action of composite columns that increases the stiffness due to increment in the moment of inertia and transform modulus of elasticity. In practice as experimental tests, the full composite action between CFRP and concrete column gave an increase in column strength and resistance to applied load.
8. The experimental strength capacity for each column is more than the theoretical analysis calculations that gave more safety in design, and there is an increase in column capacity as well as compared with the RC column only without strengthening.
9. Numerical results for all models by ANSYS showed close matching results with the experimental tests.
10. More specimens need to gate more information by taking more parameters such as CFRP laters and layouts, type of loading such as biaxial loadings.

14. REFERENCES

1. Kazemi, M. T., Zakeri, I., and Shahvari, F. V., "Mixed Mode Fracture in Reinforced Concrete with Low Volume Fraction of Steel Fibers", ***International Journal of Engineering, Transactions B: Applications***, Vol. 24, No. 1, (2011), 1–18. Retrieved from http://www.ije.ir/article_71877.html
2. Abdel-Hay, A. S., "Partial strengthening of R.C square columns using CFRP", ***HBRC Journal***, Vol. 10, No. 3, (2014), 279–286. doi:10.1016/j.hbrcj.2014.01.001
3. Karbhari, V., and Eckel, D., "Effects of Short-Term Environmental Exposure on Axial Strengthening Capacity of Composite Jacketed Concrete", ***Journal of Composites Technology and Research***, Vol. 17, No. 2, (1995), 99-106. doi:10.1520/CTR10472J
4. Mirmiran, A., Yuan, W., and Chen, X., "Design for slenderness in concrete columns internally reinforced with fiber-reinforced polymer bars", ***Structural Journal***, Vol. 98, No. 1, (2001), 116–125. Retrieved from https://trid.trb.org/view/676209
5. Bogdanovic, A. N. D. I., Strengthening Circular Concrete Columns Using FRP Sheets-Applications, Thesis, Composite Materials in Civil Engineering, University of Manitoba, Canada, (2002). Retrieved from https://scholar.google.com/scholar?hl=en&as_sdt=0%2C5&q=Strengthening+circular+concrete+columns+using+FRP+sheets-applications&btnG=
6. Olivova, K., and Bilcik, J., "Strengthening of concrete columns with CFRP", ***Slovak Journal of Civil Engineering***, Vol. 1, (2009), 1–9. Retrieved from https://www.researchgate.net/publication/303248946
7. Ou, Y. C., and Truong, A. N., "Cyclic behavior of reinforced concrete L- and T-columns retrofitted from rectangular columns", ***Engineering Structures***, Vol. 177, (2018), 147–159. doi:10.1016/j.engstruct.2018.09.012
8. Abdel-Mooty, M. A. N., Issa, M. E., Farag, H. M., and Bitar, M. A., "Seismic upgrading of square and rectangular RC columns using FRP wrapping", ***WIT Transactions on The Built Environment***, Vol. 85, (2006), 1–10. doi:10.2495/HPSM06041
9. Ghosh, K. K., and Sheikh, S. A., "Seismic Upgrade with Carbon Fiber-Reinforced Polymer of Columns Containing Lap-Spliced Reinforcing Bars", ***ACI Structural Journal***, Vol. 104, No. 2, (2007), 227–236. https://doi.org/10.14359/18535
10. Ali, I. F., Abdulridha, A. A., and Abbas, S. A., "Behavior and strength properties of steel fiber reinforced self-compacting concrete columns", ***Journal of Engineering Science and Technology***, Vol. 15, No. 5, (2020), 3204–3217. Retrieved from http://jestec.taylors.edu.my/Vol%2015%20issue%205%20October%202020/15_5_25.pdf
11. Ozturk, B., Senturk, T., and Yilmaz, C., "Analytical investigation of effect of retrofit application using CFRP on seismic behavior of a monumental building at historical Cappadocia region of Turkey", In Proceedings of the 9th U.S. National and 10th Canadian Conference on Earthquake Engineering, Toronto, Canada, (2010). Retrieved from https://www.researchgate.net/publication/282186105_
12. Ozturk, B., Yilmaz, C., and Senturk, T., "Effect of FRP retrofitting application on seismic behavior of a historical building at Nigde, Turkey", In Proceedings of the 14th European Conference on Earthquake Engineering, Ohrid, (2010). Retrieved from https://www.researchgate.net/publication/282186102_
13. Kianoush, M. R., and Esfahani, M. R., "Axial Compressive Strength of Reinforced Concrete Columns Wrapped with Fiber Reinforced Polymers (FRP)", ***International Journal of Engineering, Transactions B: Applications***, Vol. 18, No. 1, (2005), 9–19. Retrieved from http://www.ije.ir/article_71563.html
14. American Concrete Institute, Guide for the design and construction of externally bonded FRP systems for strengthening concrete structures. Reported by ACI Committee 440440.2R-02, (2002).
15. Iraqi Standard Specification IQS, Ordinary Portland cement. No. 5, Iraq, (1984).
16. Iraqi Standard Specification IQS, Natural aggregate using in concrete and building. No. 45, Iraq, (1984)
17. American Society of Testing and Materials ASTM C494M–17, Standard specification for chemical admixtures for concrete, (2005).
18. American Concrete Institute ACI 318, Building code requirements for concrete and commentary. Farmington Hills, MI 48331, USA, 503, (2014).

19. American Society of Testing and Materials ASTM-A996M, Standard specification for rail-steel and axle-steel deformed bars for concrete reinforcement, (2005).
20. European Federation for Specialist Construction Chemicals and Concrete Systems EFNARC, Specification and guidelines for self-compacting concrete, (2002).
21. American Concrete Institute ACI 237R-07, Self-consolidating concrete, (2007).
22. British Standard Institution BS .1881, Part 116, Method for determination of compressive strength of concrete cubes, (1989).
23. American Society of Testing and Materials ASTM C496-96, Standard test method for splitting tensile of cylindrical concrete specimens. Book of Standards, Vol. 04-02, (1996).
24. American Society of Testing and Materials ASTM C78M – 16, Standard test method for flexural strength of concrete (using simple beam with third-point loading), (2002).
25. ANSYS manual reference help Version 18.2, ANSYS Multiphasic, ANSYS, Inc. is a UL registered ISO 9001:2000 Company.

Persian Abstract

چکیده

ظرفیت مقاومت ستون‌های بتن آرمه برای مقاومت در برابر بارهای خارجی و انتقال آن‌ها بسیار مهم است. برای معماران، الزامات موتور برای استفاده از مقطع کوچک ستون‌های بتن مسلح یا در صورت عدم کنترل کیفیت، ما باید مقاومت فشاری بتن را افزایش دهیم یا از تکنیک تقویت عناصر سازه‌ای مانند ستون استفاده کنیم. در مقاله حاضر، رفتار و مقاومت چهار ستون بتونی خود متراکم تقویت شده با الیاف فولادی تقویت شده توسط یک لایه CFRP که به دور یک مربع از ستون‌های بتن مسلح تحت بارهای استاتیک قرار گرفته است، بررسی شده است. بتن خود متراکم با استفاده از پودر سنگ آهک اتخاذ می‌شود و با درصدهای مختلف فیبر فولاد مانند ۱٪، ۱/۵٪ و ۲٪ مخلوط می‌شود. آزمون‌های مختلفی برای بررسی خصوصیات مکانیکی بتن خود متراکم مخلوط با درصد فیبرهای مختلف فولاد انجام شده است. نتایج آزمایش نشان می‌دهد که در خصوصیات مکانیکی بتن مانند مقاومت فشاری، مقاومت کششی تقسیم شده و مدول پارگی افزایش یافته است که منعکس‌کننده افزایش ظرفیت بار ستون است. نمونه‌ها هنگامی که توسط CFRP بسته‌بندی می‌شوند. افزایش ظرفیت مقاومت ستون‌ها در مقایسه با ستون کنترل بیش از ۵۰٪ است. تمام نمونه‌های آزمایش با استفاده از تجزیه و تحلیل عناصر محدود توسط ANSYS مدل‌سازی شده و نتایج عددی با نمونه‌های آزمایش شده مقایسه می‌شود.

IJE TRANSACTIONS B: Applications Vol. 34, No. 02, (February 2021) 393-402

International Journal of Engineering

Journal Homepage: www.ije.ir

Utilizing the Modified Popovics Model in Study of Effect of Water to Cement Ratio, Size and Shape of Aggregate in Concrete Behavior

H. R. Darvishvand[a], S. A. Haj Seiyed Taghia*[a], M. Ebrahimi[b]

[a] *Department of Civil Engineering, Qazvin Branch, Islamic Azad University, Qazvin, Iran*
[b] *Engineering Technology Department, South Carolina State University, SC, USA*

PAPER INFO

Paper history:
Received 29 September 2020
Received in revised form 30 October 2020
Accepted 04 November 2020

Keywords:
Aggregate
Correlation Coefficient
Percentage of Change in Energy Absorption
Stress-Strain Test
Variation Coefficient
Water to Cement Ratio

ABSTRACT

Three parameters, size, shape of aggregate, and water to cement ratio, play important role on concrete behavior. To study the effect of these parameters, two types of aggregates were used, rounded (river) and sharped corners (broken). The maximum sizes of aggregates were chosen to be 9.5, 12.5, 19 and 25 mm for water to cement ratio were 0.35, 0.42, 0.54 and 0.76. In this investigation, the total of 32 mixed designs were made. The stress-strain tests were performed on the entire samples, and the results were compared with the Popovics model. To further evaluate the analysis, three criteria, correlation coefficient, variation coefficient, and percentage of change in energy absorption were demonstarted. Analysis showed that there is significant differences between the Popovics model and our experimental results. The Modified Popovics model was introduced for better understanding the concrete behavior in compression. The proposed model covered a wide range of the parameters concerned in this investigation. The Modified Popovics model was comapred with several models such as the Popovics, Hognestad, Thorenfeldt, and Tsai and the results showed that modified approach has a better clarification for behavior of concrete in compression. Moreover, the results indicated that these models were more accurate for prediction of concrete behavior with rounded aggregates in comparison to sharped aggregates.

doi: *10. 5829/ije.2021.34.02b.11*

1. INTRODUCTION

Concrete is a mixture of cementitious material, aggregate, and water. Variety of gravel shapes and water to cement ratio affect the behavior of concrete.

The aggregate geometry influences required cement paste, placement factors (workability and pumpability), mechanical properties, and seismic parameters. Rounded aggregates are desirable because they joggle in the mixing and handling process. Aggregate can also contain flat or elongated shapes, and it is possible a thin, flat particle is oriented in the hardened concrete due to external stress and change in concrete strength [1–9]. Many researchers were trying to investigate the effect of gravel's size and shape on concrete behavior [10, 11]. Ogundipe et al. [12] and Yu et al. [13] studied the role of coarse aggregate size on concrete behavior in compression. The results of their experimental work were stated that compressive strength increases by raising of coarse aggregate size up to the specified limit.

The water to cement ratio of concrete is important from the aspect of durability, impermeability and strength. Too high water to cement ratio, may cause inadequate structural capability and not provide a durable protective environment for the steel reinforcement, permitting rapid carbonation and subsequent loss of the protective alkaline environment for the steel [14].

Rational analysis and the design of reinforced concrete structures are based on the prediction of stress–strain concrete relationship. Hognestad [15], Smith and Young [16], Desayi and Krishnan [17], Kent and Park [18], Sargin et al. [19], Popovics [20], Wang et al. [21], Carreira and Chu [22], Thorenfeldt et al. [23], Tsai [24], Hsu and Hsu [25], Almusallam and Alsayed [26], Attard

*Corresponding Author Institutional Email: *ali.taghia@qiau.ac.ir* (S. A. Haj Seiyed Taghia)

Please cite this article as: H. R. Darvishvand, S. A. Haj Seiyed Taghia, M. Ebrahimi, Utilizing the Modified Popovics Model in Study of Effect of Water to Cement Ratio, Size and Shape of Aggregate in Concrete Behavior, International Journal of Engineering, B: Applications Vol. 34, No. 02, (2021) 393-402

and Setunge [27], Kumar [28], Lokuge et al. [29], Tasnimi [30], and Lokuge et al. [31], Nematzadeh and Hasan-Nattaj [32], Al-Tikrite et al. [33], and Peng et al. [34] have proposed a number of empirical expressions for the stress–strain curve of concrete in the past.

The accuracy and reliability of stress–strain curve of concrete are dependent on two main parameters: testing circumstance and concrete properties. Testing circumstance includes reliability of the instruments, shape and size of the specimen, strain rate, and the type of strain gauge. Concrete characteristics depend on many interrelated variables such as water to cement ratio, the mechanical and physical properties of cement and aggregate, and the age of specimen when is tested.

The Popovics model [20] is one of the model which is used to study concrete behavior in compression. This model will be explained in the following section.

1. 1. Popovics Stress-Strain Model of Unconfined Concrete Figure 1 represents the Popovics model [20] which proposes a single equation, is used to describe unconfined concrete stress-strain behavior as given by Equation (1).

A major appeal of this model is that, it only requires three parameters to control the entire pre and post peak behavior.

The parameters define the curve are: ε_c, concrete strain, f_c, concrete stress, f'_c, concrete compressive strength, and ε'_c, concrete strain at f'_c.

$$\frac{f_c}{f'_c} = \frac{n(\frac{\varepsilon_c}{\varepsilon'_c})}{(n-1)+(\frac{\varepsilon_c}{\varepsilon'_c})^n} \quad (1)$$

In the equation, n, can be expressed as an approximate function of the compressive strength of normal weight concrete as:

$$n = 0.4 \times 10^{-3} f'_c(psi) + 1 \quad (2)$$

The Popovics equation works well for most normal strength concrete (f'c<55 MPa), but for higher strength concrete, it lacks the necessary control over the slope of the post-peak branch.

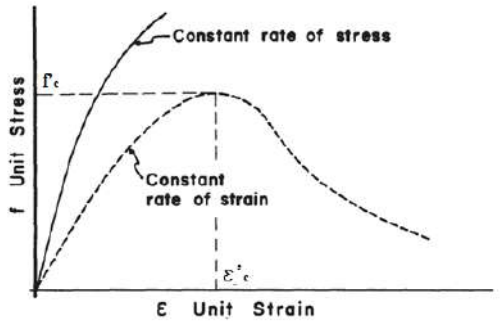

Figure 1. Popovics stress-strain model for unconfined concrete behavior

Besides the Popovics model, there are the other models, Hognestad [15], Thorenfeldt et al. [23] and Tsai [24] which are used for concrete behavior estimation. In this research, these models are used for validation of proposed stress-strain model and explained in the following sections.

1. 2. Hognestad Stress-Strain Model of Unconfined Concrete Hognestad [15] sugessted a stress-strain relation for unconfined concrete as followed:

$$f_c = f'_c\left[\frac{2\varepsilon_c}{\varepsilon'_c} - \left(\frac{\varepsilon_c}{\varepsilon'_c}\right)^2\right] \quad (3)$$

The definition of ε_c, f_c, ε'_c, f'_c parameters are similar to the Popovics models explained in section 1.1.

1. 3. Thorenfeldt Stress-Strain Model of Unconfined Concrete Thorenfeldt et al. [23] modified the Popovics [20] equation to adjust the descending branch of the concrete stress-strain equation. The Thorenfeldt et al. [23] sugessted the following relation for the unconfined concrete:

$$\frac{f_c}{f'_c} = \frac{n(\frac{\varepsilon_c}{\varepsilon'_c})}{(n-1)+(\frac{\varepsilon_c}{\varepsilon'_c})^{nk}} \quad (4)$$

In Equation (4) 'k', takes a value of 1 for values of (ε_c/ ε'_c)<1 and values greater than 1 for (ε_c/ ε'_c)>1. Thus by adjusting the value of 'k' the post-peak branch of the stress-strain equation can be made steeper. This method can be illustrated for high-strength concrete where the post-peak branch becomes steeper with a raise in the concrete strength.

1. 4. Tsai Stress-Strain Model of Unconfined Concrete Tsai [24] presented a generalized form of the Popovics [20] relation, which has greater control over the post-peak branch of the stress-strain equation. Tsai's relation includes two additional parameters, one to control the ascending and a second to control the post-peak behavior of the stress-strain curve. The sugessted stress-strain equation for unconfined concrete by Tsai is shown below:

$$y = \frac{mx}{1+\left(m-\frac{n}{n-1}\right)x+\frac{x^n}{n-1}} \quad (5)$$

where $y=f_c/f'_c$= the ratio of the concrete stress to the ultimate strength, $x=\varepsilon_c/\varepsilon'_c$= the ratio of concrete strain to the strain at y=1, $m=E_0/E_c$= the ratio of initial tangent modulus to secant modulus at y=1, ′n′=a factor to control the steepness rate of the descending portion of the stress-strain equation. The following expressions were expressed for the factors ′m′ and ′n′.

$$m = 1 + \frac{17.9}{f'_c} \quad (6)$$

$$n = \frac{f'_c}{6.68} - 1.85 > 1 \quad (7)$$

For assessment, 32 mix designs are considered to check the compatibility of the Popovics model with the stress-strain experimental data in compression. The samples cover a wide range of size and shape of aggregate, and water to cement ratio.

The following section explains the outline of experimental programs.

2. EXPERIMENTAL PROGRAM

In this section, the material types, mix design, preparation and curing are described, respectively.

2. 1. Material Types The ordinary Portland cement is used in the specimens. They are made according to ASTM C150 [35] standard. The gravel and sand aggregates are of river type in accordance with ASTM C33 [36] standard. The sand sizes range from 0 to 4.75 mm with apparent weight of 2650 kg/m^3 in SSD (Saturated Surface Dry) state with 24-hour water absorption of 1.5%, and additionally, the super-plasticizer of P10-3R type is used based on ASTM C494 [37]. Gravels, rounded and sharped types, are in four different sizes with maximum diameters of 9.5, 12.5, 19, and 25 mm, as shown in Figure 2.

2. 2. Mix Design In this study, 32 mix designs are used and summarized in Table 1. Three samples are built for each mix design and as a result, three stress-strain plots are obtained from three experiments, the plots are averaged out to a single stress-strain curve and it is considered as an averaged plot.

In Table 1, the codes designate the following:

Character WC followed by the numbers 1-4 are: water to cement ratio (W/C) with 0.76, 0.54, 0.42 and 0.35, respectively, GN and GB followed by the numbers 1-4 stand for Gravel of Natural (rounded corners), Gravel of Broken (sharped corners), and the maximum size of coarse aggregate 9.5, 12.5, 19, and 25 mm, respectively.

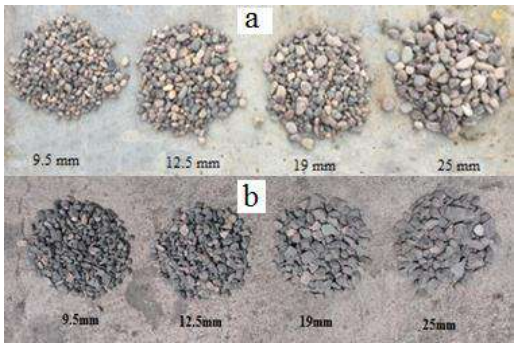

Figure 2. Images demonstrate the size of sieved aggregates; (a): Rounded type; (b): Sharped type

TABLE 1. Mix designs used in the different samples

NO.	Code	Maximum Gravel Size (mm)	Gravel (kg/m^3)	Sand (kg/m^3)	Cement (kg/m^3)	W/C
1	WC1GN1	9.5	1290	898	250	0.76
2	WC1GN2	12.5	1290	898	250	0.76
3	WC1GN3	19	1290	898	250	0.76
4	WC1GN4	25	1290	898	250	0.76
5	WC1GB1	9.5	1290	898	250	0.76
6	WC1GB2	12.5	1290	898	250	0.76
7	WC1GB3	19	1290	898	250	0.76
8	WC1GB4	25	1290	898	250	0.76
9	WC2GN1	9.5	1170	820	350	0.54
10	WC2GN2	12.5	1170	820	350	0.54
11	WC2GN3	19	1170	820	350	0.54
12	WC2GN4	25	1170	820	350	0.54
13	WC2GB1	9.5	1170	820	350	0.54
14	WC2GB2	12.5	1170	820	350	0.54
15	WC2GB3	19	1170	820	350	0.54
16	WC2GB4	25	1170	820	350	0.54
17	WC3GN1	9.5	1090	762	450	0.42
18	WC3GN2	12.5	1090	762	450	0.42
19	WC3GN3	19	1090	762	450	0.42
20	WC3GN4	25	1090	762	450	0.42
21	WC3GB1	9.5	1090	762	450	0.42
22	WC3GB2	12.5	1090	762	450	0.42
23	WC3GB3	19	1090	762	450	0.42
24	WC3GB4	25	1090	762	450	0.42
25	WC4GN1	9.5	947	663	550	0.35
26	WC4GN2	12.5	947	663	550	0.35
27	WC4GN3	19	947	663	550	0.35
28	WC4GN4	25	947	663	550	0.35
29	WC4GB1	9.5	947	663	550	0.35
30	WC4GB2	12.5	947	663	550	0.35
31	WC4GB3	19	947	663	550	0.35
32	WC4GB4	25	947	663	550	0.35

2. 3. Preparation and Curing of Specimens First, concrete is constructed and then inserted into pre-prepared cylindrical molds (with dimensions of 15 cm × 30 cm). They are kept in constant temperature and humidity for 24 hours in order to harden. After 24 hours, the specimens are removed from the molds and are placed into a water pond with temperature of 20 ± 2 °C for curing. The curing time of the samples is equal to 28 days in order to do stress-strain tests.

3. RESULTS AND DISCUSSION

3. 1. Plots of Stress-Strain for Experiment and Popovics Model The stress-strain tests are performed on all 32 mix design samples. All the plots are analyzed but since there are too many results to be explained, authors discuss only two representative of mix designs, WC2GN1 and WC2GB1. Figures 3a and 3b demonstrate the stress-strain plots according to the tests and Popovics models [20] for two mix designs, WC2GN1 and WC2GB1, respectively.

The following section describes three criteria to evaluate the capability of Popovics model [20] to explain the stress-strain data obtained through experiments.

3. 2. Definition of Criteria for Comparing the Stress-Strain Testing Results with the Popovics Model These criteria are defined separately, in the next sections which provide the possibility of comparing stresses between behavioral models and the experimental results within the limit of concrete strain.

3. 2. 1. Criterion 1: Correlation Coefficient Correlation coefficient is a numerical measure, meaning a statistical relationship between two variables (X, Y). These variables (here stresses) are obtained from corresponding strains of the two curves, test and model. These variables (here stresses) are obtained from corresponding strains of the two curves, test and model. The equation for the correlation coefficient [38] can be written as:

$$\rho_{X,Y} = \frac{\sum(X-\bar{X})(Y-\bar{Y})}{\sqrt{\sum(X-\bar{X})^2 \sum(Y-\bar{Y})^2}} \quad (8)$$

where, $\bar{X}$ and $\bar{Y}$ are the means of two variables.

All values assume in the range from −1 to +1, where +1 indicates the strongest possible agreement and −1 the strongest possible disagreement. If the value of correlation coefficient is close to zero, it is indication of no or weak correlation.

The correlation coefficients between experimental data and the Popovics model for the whole samples (Table 1) are evaluated. These coefficients are reported for rounded and sharped aggregates, separately. The estimated average correlation coefficients between the Popovics model and the experimental data are equal to 0.985 and 0.971 for rounded and sharped aggregates, respectively. They indicate a fairly acceptable correlations, specially for rounded aggregates.

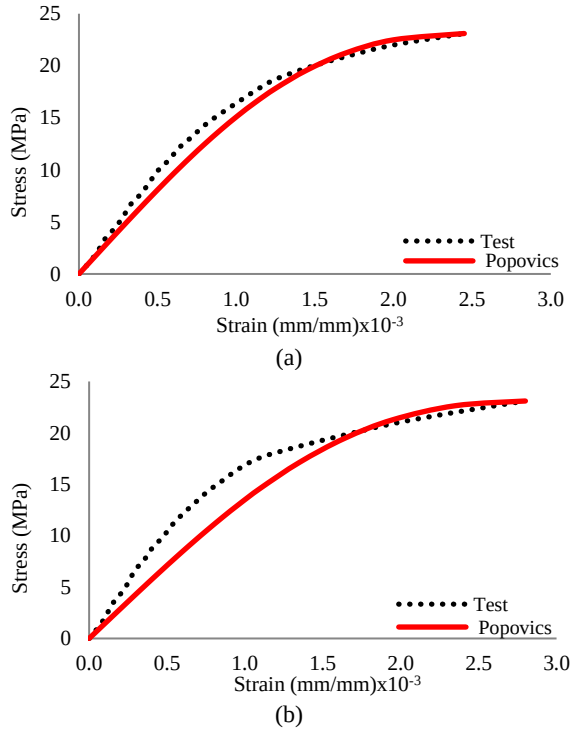

Figure 3. Plots of stress-strain for the test and Popovics model; (a): Mix design, WC2GN1; (b): Mix design, WC2GB1

3. 2. 2. Criterion 2: Variation Coefficient The coefficient of variation (CV) is a statistical measure of the dispersion of data points in a data series around the mean. The coefficient of variation represents the ratio of the standard deviation to the mean. In this research, data points are stresses for corresponding strains. The coefficient of variations are evaluated between experimental data and the Popovics model [20] for the whole samples (Table 1). These coefficients are reported for rounded and sharped aggregates, separately.

The average results show that there are limitations of 1.08% and 1.68% for rounded and sharped aggregates, respectively, in difference between the variation coefficient in the Popovics model [20] and the experimental data which are negligible.

3. 2. 3. Criterion 3: Percentage of Change in Energy Absorption The percentage of change in energy absorption is defined by the following expression:

$$p = \left|\frac{Area_{exp} - Area_{Popovics}}{Area_{exp}}\right| \times 100 \quad (9)$$

In which: P is percentage of change in energy absorption, $Area_{exp}$ represents area under the stress-strain curve of experimental data, and $Area_{Popovics}$ is area under the Popovics stress-strain curve.

It should be noted that the area under the stress-strain curve implies the absorbed energy in stress-strain behavior. MATLAB software [39] is used for calculating this area for each specified curve. The percentages of change in energy absorption are estimated based on Equation (9) for the entire samples (Table 1). These percentages are reported for rounded and sharped aggregates, separately. The average changes in energy absorption are equal to 7.8% and 11.5%, for rounded and

sharped aggregates, respectively which are fairly significant values.

To overcome this difference, a modified relation is proposed regarding Popovics model in the next section.

3. 3. The Modified Popovics Model The drift among the data in two stress-strain plots, experiments and Popovics model [20], is attributed to the lack of parameters (i.e. size, shape of aggregate, and water to cement ratio) in mathematical formulation of Popovics model [20]. Popivics model only considers compressive strength in establishing the stress-strain curve, whereas parameters such as shape and size of aggregate are effective on integrity of concrete matrix. Moreover, water to cement ratio parameter specifies the effectiveness of cement paste and its cohesion in mixtures. As a result, these parameters are determinative on failure strain and the trend of stress-strain curve.

The Popovics model with new coefficients, is introduced, and is called Modified Popovics model in order to distinguish from the Popovics model.

The modified model is similar to the Popovics model; just the parameter ‘’m’’ is added. The Modified Popovics model is suggested as follows:

$$\frac{f_c}{f_c'} = \frac{nm(\frac{\varepsilon_c}{\varepsilon_c'})}{(n-1)+(\frac{\varepsilon_c}{\varepsilon_c'})^{nm}} \quad (10)$$

“m” is the minor modification coefficient obtained from the following equation:

$$m = s\,.\,F(d_r).\ F(wc_r) \quad (11)$$

In Equation (11), s is representative for the effect of aggregate geometry (Table 2) and $F(d_r)$ is the aggregate size function in which the independent variable dr is defined as:

$$d_r = \frac{d_i}{d_0} \quad (12)$$

where in, d_i is maximum size of aggregates in mm (i.e. 9.5, 12.5, 19 and 25 mm), d_0: is the base size of aggregate (assumed here 12.5 mm), and $F(wc_r)$ is the water to cement ratio function in which the independent variable wc_r is defined as:

$$wc_r = \frac{wc_0}{wc_i} \quad (13)$$

where in, wc_i is water to cement ratio (i.e. 0.76, 0.54, 0.42 and 0.35) and wc_0 is the base water to cement ratio (assumed here 0.76).

$F(d_r)$ and $F(wc_r)$ functions as well as “s” are obtained by the curve fitting of stress-strain tests data with the Modified Popovics model. This regression is based on the three mentioned criteria in section 3.2. The functions $F(d_r)$, $F(wc_r)$ and the coefficient “s” are obtained as follows:

$$F(d_r) = 0.12\ d_r + 0.63 \quad (14)$$

$$F(wc_r) = -0.25\ wc_r + 1.25 \quad (15)$$

TABLE 2. Calculation of "s" coefficient based on curve fitting

	Rounded corners	Sharped corners
“s” value	1.2	1

In the following section, the equation of Modified Popovics model, Equation (10) is plotted for only two mix designs.

3. 4. Comparison of Stress-Strain Experimental Data with Popovics and Modified Popovics Models In order to better understand the trend of Equation (10), stress-strain plots are drawn for two representative mix designs, WC2GN1 and WC2GB1 (See Figure 4).

This section focuses on compatibility of stress-strain experimental data with Popovics and Modified Popovics models aided by three criteria, defined in section 3.2 “*Definition of criteria for comparing the stress-strain testing results with the Popovics model*”. The data from stress-strain tests are used to support plotting the Figures 5-7 and 9-11.

3. 4. 1. Correlation Coefficient Criterion for Comparison In Figure 5, the average correlation coefficients of experimental data are compared with

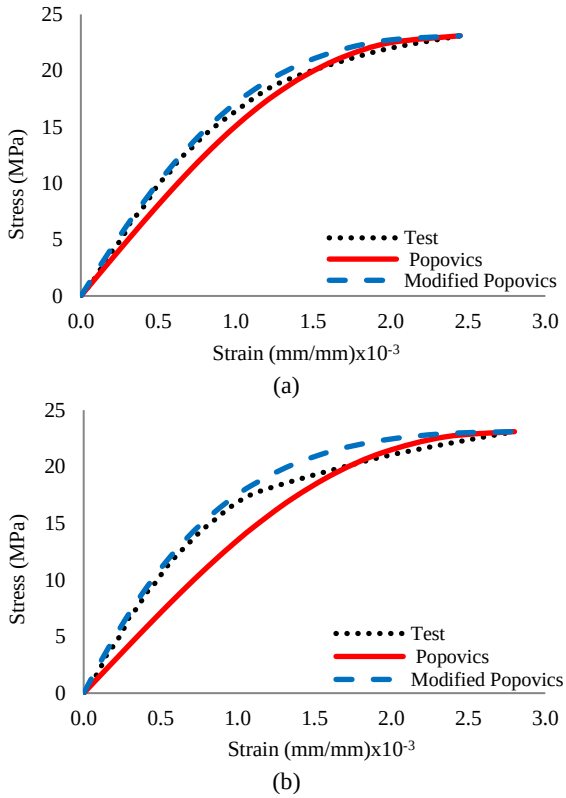

Figure 4. Plots of stress-strain for the test, Popovics and Modified Popovics models; (a): Mix design, WC2GN1; (b): Mix design, WC2GB1

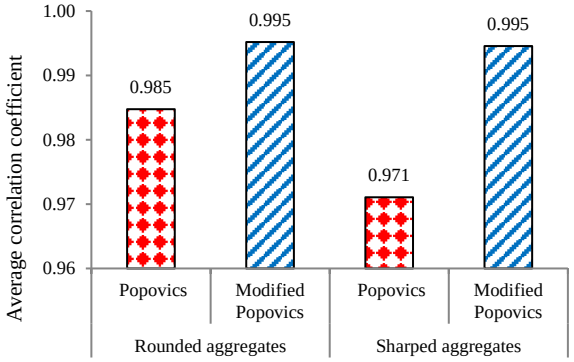

Figure 5. Comparison of average correlation coefficients from experimental data with Popovics and Modified Popovics models

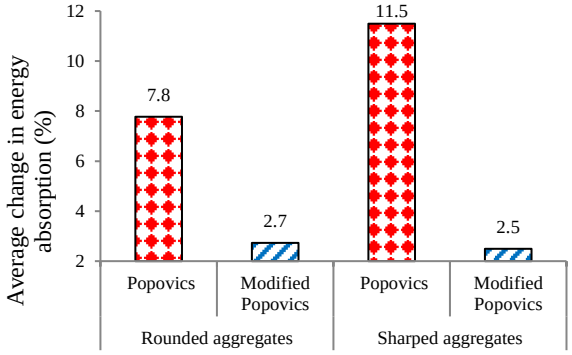

Figure 7. Average changes in energy absorption from experimental data with Popovics and Modified Popovics models

the Popovics and Modified Popovics models for rounded and sharped aggregates, separately.

From this figure, the average correlation coefficients of the Popovics model [20] are equal to 0.985 and 0.971 for rounded and sharped aggregates, respectively, but the coefficient in Modified Popovics model, increases to 0.995 for both types of aggregates. These improvements are not tangible.

3. 4. 2. Variation Coefficient Criterion for Comparison Figure 6 shows the comparison of average variation coefficients of experimental data with Popovics and Modified Popovics models for rounded and sharped aggregates, separately.

Figure illustrates the average variation coefficients of the Popovics model are equal to 1.08 % and 1.68%, but the coefficients in Modified Popovics model, reduce to 0.36% and 0.30% for rounded and sharped aggregates, respectively, which are not a significant differences.

3. 4. 3. Percentage of Change in Energy Absorption Criterion for Comparison In Figure 7, the average changes in energy absorption of experimental data are compared with the Popovics and Modified Popovics models for rounded and sharped aggregates, separately.

As demonstrated in Figure 7, the average changes in energy absorption of the Popovics model are equal to 7.8% and 11.5% for rounded and sharped aggregates, respectively, but these values decline to 2.7% and 2.5% for the Modified Popovics model, which shows a significant decrease and indicates that the Modified Popovics model has a better acceptable performance in modeling of concrete behavior.

The proposed model leads to more accurate results in comparison to the Popovics model. That is because, the proposed model was extracted and pulled out from the experimental data and the curve fitting. In the following sections, in order to reach an overall approach, the capability of the other models mentioned in "*Introduction*" section is plotted and compared with the Modified Popovics model.

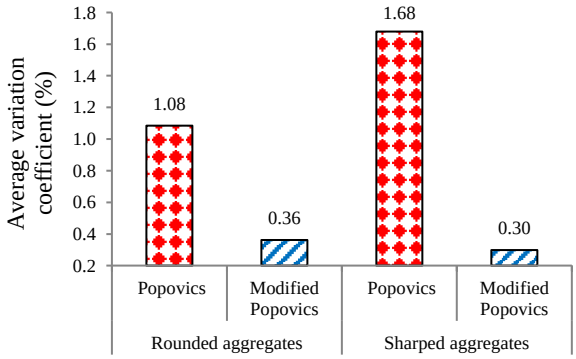

Figure 6. Average variation coefficients from experimental data with Popovics and Modified Popovics models

3. 5. The Plots of the Other Models in Comparison with the Modified Popovics Model The Modified Popovics model is plotted with other models described in the "*Introduction*" section. These models are Hognestad, Thorenfeldt, and Tsai. In Figure 8, for instance, the strain-strain experimental data for two representative mix designs WC2GN1 and WC2GB1 along with the other models, are presented.

3. 6. Validation of the Other Models with the Modified Popovics Model This section concentrates on comparative study of the Modified Popovics model with the models mentioned in section 1, aided by three criteria as defined in section 3.2, "*Definition of criteria for comparing the stress-strain testing results with the Popovics model*".

3. 6. 1. Correlation Coefficient Criterion for Validation Experimental data are used to calculate correlation coefficients of Modified Popovics, Hognestad, Thorenfeldt, and Tsai models for rounded

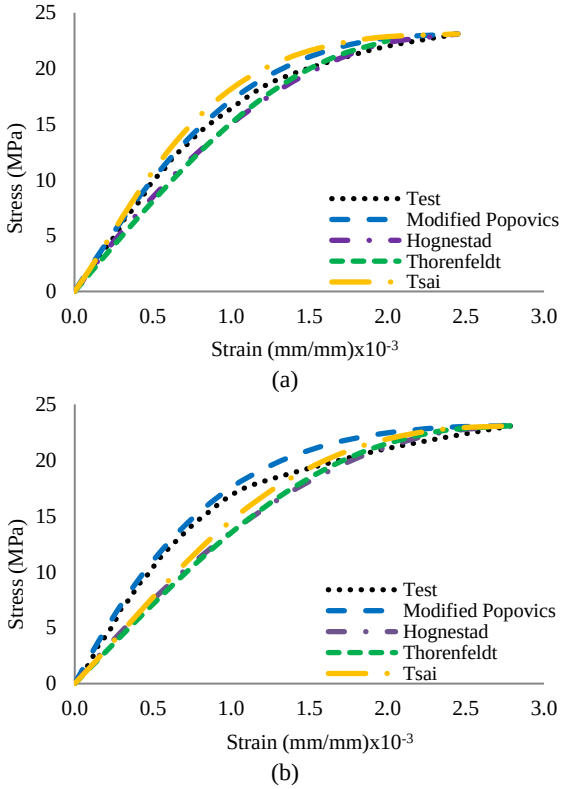

Figure 8. Plots of stress-strain for the test, Modified Popovics, Hognestad, Thorenfeldt, and Tsai models; (a): Mix design, WC2GN1; (b): Mix design, WC2GB1.

and sharped aggregates, separately. The coefficients are averaged out and demonstrated in Figure 9.

The maximum value among those values belongs to the Modified Popovics Model, which implies the better estimation of concrete behavior with respect to the other models.

Also, according to this criterion, the figure indicates that the prediction of concrete behavior with rounded aggregates is more precise compared to sharped aggregates for all the models duscussed in this article.

3. 6. 2. Variation Coefficient Criterion for Validation Similarly, in Figure 10, the average variation coefficients of Modified Popovics, Hognestad [15], Thorenfeldt et al. [23] and Tsai [24] models are reported for rounded and sharped aggregates, separately. The minimum value among those values belongs to the Modified Popovics model which shows the better estimation of concrete behavior with respect to the other models.

Once again, this figure illustrates that by considering the entire models, the prediction of concrete behavior with rounded aggregates is more accurate relative to sharped aggregates.

3. 6. 3. Percentage of Change in Energy Absorption Criterion for Validation With the similar method, in Figure 11, the average changes in energy absorption of Modified Popovics, Hognestad, Thorenfeldt and Tsai models are reported for rounded and sharped aggregates, separately. The minimum value among those values belongs to Modified Popovics model that displays the better estimation of concrete behavior with respect to the other models. Lastly, according to this criterion, this figure confirms that considering the entire models, the prediction of concrete behavior with rounded aggregates is more accurate relative to sharped aggregates.

The utilization of the other models, Hognestad, Thorenfeldt, and Tsai, for verification of proposed model illustrates that parameters such as water to cement ratio, shape and size of aggregate have ability to affect the behavior of stress-strain in concrete. This shows that proposed model is accurate regarding to the description of concrete behavior in comparison to the other models used in this research.

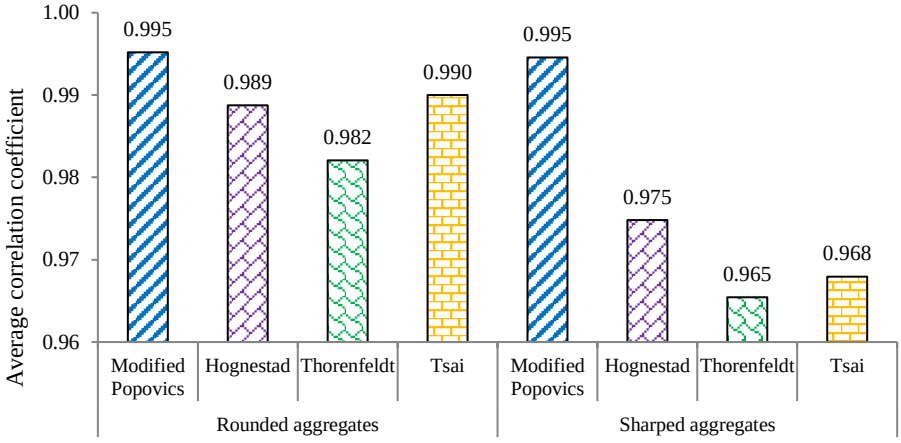

Figure 9. Average correlation coefficients from experimental data with Modified Popovics, Hognestad, Thorenfeldt, and Tsai models

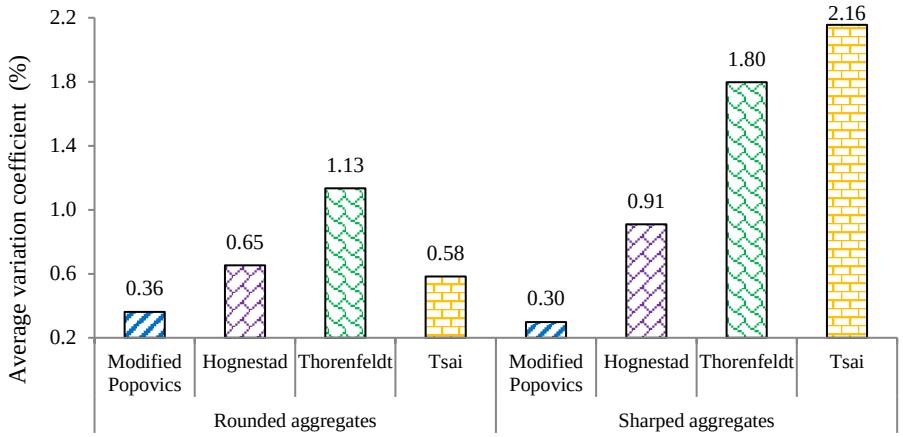

Figure 10. Average variation coefficients from experimental data with Modified Popovics, Hognestad, Thorenfeldt, and Tsai models

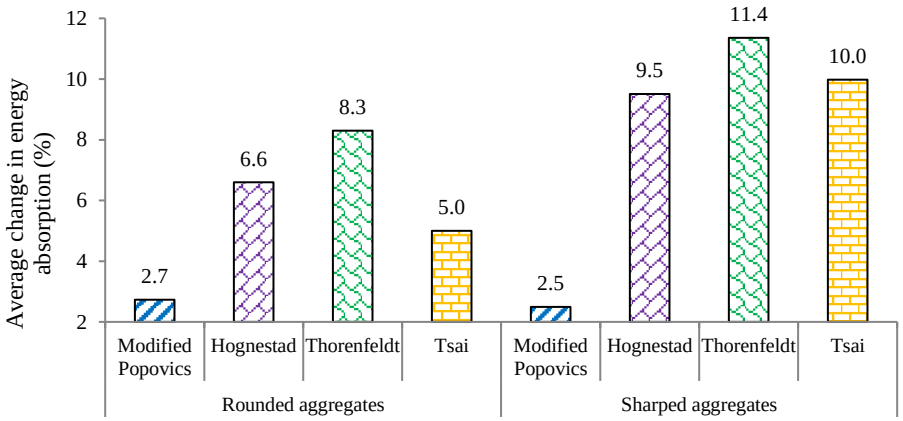

Figure 11. Average changes in energy absorption from experimental data with Modified Popovics, Hognestad, Thorenfeldt, and Tsai models

4. CONCLUSION

In this paper, at first, the Popovics model was compared with the experimental results. The tests considered the effects of concrete characteristics such as size and shape of aggregate, and water to cement ratio.

Then, the Popovics model was modified to have a good fit with the results obtained through experimental tests. For comparison and validation of modified model, three criteria were chosen, correlation coefficient, variation coefficient, and percentage of change in energy absorption.

The following are the summary of the conclusion:

1. The average correlation coefficient between Popovics model and experimental data were 0.985 and 0.971 for rounded and sharped aggregates, respectively, but these values increased to 0.995 for both aggregate types with the Modified model, which did not show any significant improvement with respect to the old values.
2. The average variation coefficient between Popovics model and experimental data were 1.08% and 1.68% but then, these values reduced by 0.36% and 0.30% for rounded and sharped aggregates, respectively regarding the Modified model, which did not apparently indicate any tangible differences.
3. The average change in energy absorption for Popovics model with respect to experimental data were 7.8% and 11.5% but then, these values significantly declined regarding the Modified model by 2.7%, and 2.5% for rounded and sharped aggregates, respectively, which clearly reflected the capability of Modified model.
4. The three criteria confirmed that the prediction of concrete behavior with rounded aggregates is more reliable in comparison to the sharped aggregates for all the models discussed in this article.
5. It was reasonable to conclude that Modified Popovics model expressed clearly the behavior of concrete in compression in comparison to Hognestad, Thorenfeldt, and Tsai models.

5. ACKNOWLEDGMENTS

The authors would like to thank Mr. Borjali Darvishvand for his collaboration in editing the article and Mr. Mir Shahab Sayyafi for providing us his mechanical testing facilities at Pey Azma Beton Kouhestan Laboratory in Rasht, Iran.

6. REFERENCES

1. Kaplan, M., "Flexural and compressive strength of concrete as affected by the properties of coarse aggregates", ***Journal Proceedings***, Vol. 55, No. 5, (1959), 1193–1208.
2. Walker, S., and Bloem, D., "Effects of aggregate size on properties of concrete", ***Journal Proceedings***, Vol. 57, No. 9, (1960), 283–298.
3. Bloem, D., and Gaynor, R., "Effects of aggregate properties on strength of concrete", ***Journal Proceedings***, Vol. 60, No. 10, (1963), 1429–1456.
4. Cordon, W., and Gillespie, H., "Variables in concrete aggregates and Portland cement paste which influence the strength of concrete", ***Journal Proceedings***, Vol. 60, No. 8, (1963), 1029–1052.
5. Ruiz, W. ., Effect of volume of aggregate on the elastic and inelastic properties of concrete, M.S. Thesis, Cornell University, (1966).
6. Brzezicki, J. M., and Kasperkiewicz, J., "Automatic Image Analysis in Evaluation of Aggregate Shape", ***Journal of Computing in Civil Engineering***, Vol. 13, No. 2, (1999), 123–128. doi:10.1061/(asce)0887-3801(1999)13:2(123)
7. Mehta, P., and Monteiro, P., Concrete: Microstructure, Properties, and Materials, McGraw-Hill Education, (2014).
8. Li, Z., Advanced Concrete Technology, John Wiley & Sons, (2011).
9. ASTM C125., Standard Terminology Relating to Concrete and Concrete Aggregates. West Conshohocken, PA: ASTM, (2019).
10. Ede, A. N., Olofinnade, O. M., Bamigboye, G. O., Shittu, K. K., and Ugwu, E. I., "Prediction of fresh and hardened properties of normal concrete via choice of aggregate sizes, concrete mix-ratios and cement", ***International Journal of Civil Engineering and Technology (IJCIET)***, Vol. 8, No. 10, (2017), 288–301 http://eprints.covenantuniversity.edu.ng/id/eprint/9581
11. Neetu, N., and Rabbani, A., "Influence of size of aggregates on the Compressive strength of concrete", ***International Journal of Engineering Development and Research***, Vol. 5, (2017), 27–30.
12. Ogundipe, O. M., Olanike, A. O., Nnochiri, E. S., and Ale, P. O., "Development of Soil Distribution and Liquefaction Potential Maps for Downtown Area in Yangon, Myanmar", ***Civil Engineering Journal***, Vol. 4, No. 4, (2018), 836. doi:10.28991/cej-0309137
13. Yu, F., Sun, D., Wang, J., and Hu, M., "Influence of aggregate size on compressive strength of pervious concrete", ***Construction and Building Materials***, Vol. 209, (2019), 463–475. doi:10.1016/j.conbuildmat.2019.03.140
14. Mehta, P. K., "Studies on blended Portland cements containing Santorin earth", ***Cement and Concrete Research***, Vol. 11, No. 4, (1981), 507–518. doi:10.1016/0008-8846(81)90080-6
15. Hognestad, E., Study of Combined Bending and Axial Load in Reinforced Concrete Members, University of Illinois, Urbana, (1951).
16. Smith, G., and Young, L., "Ultimate flexural analysis based on stress-strain curves of cylinders", ***Journal Proceedings***, Vol. 53, No. 12, (1956), 597–609.
17. Desayi, P., and Krishnan, S., "Equation for the stress-strain curve of concrete", ***Journal Proceedings***, Vol. 61, No. 3, (1964), 345–350.
18. Kent, D., and Park, R., "Flexural members with confined concrete", ***Journal of the Structural Division***, Vol. 97, No. 7, (1971), 1969–1990.
19. Sargin, M., Ghosh, S. K., and Handa, V. K., "Effects of lateral reinforcement upon the strength and deformation properties of concrete", ***Magazine of Concrete Research***, Vol. 23, Nos. 75–76, (1971), 99–110. doi:10.1680/macr.1971.23.76.99
20. Popovics, S., "A numerical approach to the complete stress-strain curve of concrete", ***Cement and Concrete Research***, Vol. 3, No. 5, (1973), 583–599. doi:10.1016/0008-8846(73)90096-3
21. Wang, P., Shah, S., and Naaman, A., "Stress-strain curves of normal and lightweight concrete in compression", ***Journal Proceedings***, Vol. 75, No. 11, (1978), 603–611.
22. Carreira, D. J., and Chu, K.-H., "Stress-Strain Relationship for Plain Concrete in Compression", ***Journal Proceedings***, Vol. 82, No. 6, (1985), 797–804.
23. Thorenfeldt, E., "Mechanical properties of high-strength concrete and applications in design", Symposium Proceedings, Utilization of High-Strength Concrete, Norway, (1987).
24. Tsai, W. T., "Uniaxial Compressional Stress-Strain Relation of Concrete", ***Journal of Structural Engineering***, Vol. 114, No. 9, (1988), 2133–2136. doi:10.1061/(asce)0733-9445(1988)114:9(2133)
25. Hsu, L. S., and Hsu, C.-T. T., "Complete stress — strain behaviour of high-strength concrete under compression", ***Magazine of Concrete Research***, Vol. 46, No. 169, (1994), 301–312. doi:10.1680/macr.1994.46.169.301
26. Almusallam, T. H., and Alsayed, S. H., "Stress–strain relationship of normal, high-strength and lightweight concrete", ***Magazine of Concrete Research***, Vol. 47, No. 170, (1995), 39–44. doi:10.1680/macr.1995.47.170.39
27. Attard, M., and Setunge, S., "Stress-strain relationship of confined and unconfined concrete", ***Materials Journal***, Vol. 93, No. 5, (1996), 432–442.
28. Kumar, P., "A compact analytical material model for unconfined concrete under uni-axial compression", ***Materials and Structures***, Vol. 37, No. 9, (2004), 585–590. doi:10.1007/bf02483287
29. Lokuge, W. P., Sanjayan, J. G., and Setunge, S., "Constitutive Model for Confined High Strength Concrete Subjected to Cyclic Loading", ***Journal of Materials in Civil Engineering***, Vol. 16, No. 4, (2004), 297–305. doi:10.1061/(asce)0899-1561(2004)16:4(297)
30. Tasnimi, A. A., "Mathematical model for complete stress–strain curve prediction of normal, light-weight and high-strength concretes", ***Magazine of Concrete Research***, Vol. 56, No. 1, (2004), 23–34. doi:10.1680/macr.2004.56.1.23
31. Lokuge, W. P., Sanjayan, J. G., and Setunge, S., "Stress–Strain Model for Laterally Confined Concrete", ***Journal of Materials in Civil Engineering***, Vol. 17, No. 6, (2005), 607–616. doi:10.1061/(asce)0899-1561(2005)17:6(607)
32. Nematzadeh, M., and Hasan-Nattaj, F., "Compressive Stress-Strain Model for High-Strength Concrete Reinforced with Forta-Ferro and Steel Fibers", ***Journal of Materials in Civil Engineering***, Vol. 29, No. 10, (2017), 04017152. doi:10.1061/(asce)mt.1943-5533.0001990
33. Al-Tikrite, A., and Hadi, M. N. S., "Stress–Strain Relationship of Unconfined RPC Reinforced with Steel Fibers under Compression", ***Journal of Materials in Civil Engineering***, Vol. 30, No. 10, (2018), 04018234. doi:10.1061/(asce)mt.1943-

5533.0002445

34. Peng, J.-L., Du, T., Zhao, T.-S., Song, X., and Tang, J.-J., "Stress–Strain Relationship Model of Recycled Concrete Based on Strength and Replacement Rate of Recycled Coarse Aggregate", ***Journal of Materials in Civil Engineering***, Vol. 31, No. 9, (2019), 04019189. doi:10.1061/(asce)mt.1943-5533.0002847
35. ASTM C150. Standard Specification for Portland Cement, West Conshohocken, PA: ASTM, (2005).
36. ASTM C33. Standard Specification for Concrete Aggregates, West Conshohocken, PA: ASTM, (2018).
37. ASTM C494. Standard specification for chemical admixtures for concrete, West Conshohocken, PA: ASTM, (2005).
38. Kim, B. S., Park, S. G., You, Y. K., and Jung, S. I., Probability & Statistics for Engineers & Scientists, Pearson education-Korea Inc, (2011).
39. MATLAB, The MathWorks Inc. Natick, MA, USA, (2017).

Persian Abstract

چکیده

سه پارامتر، اندازه، شکل سنگدانه و نسبت آب به سیمان، نقش مهمی بر رفتار بتن ایفا می‌کنند. برای مطالعه اثر این پارامترها، دو نوع سنگدانه گردگوشه (رودخانه‌ای) و تیزگوشه (شکسته) استفاده شد. حداکثر اندازه سنگدانه ها ۹/۵، ۱۲/۵، ۱۹ و ۲۵ میلیمتر برای نسبت آب به سیمان ۰/۳۵، ۰/۴۲، ۰/۵۴ و ۰/۷۶ انتخاب شدند. در این بررسی، در مجموع ۳۲ طرح اختلاط ساخته شدند. آزمایش‌های تنش-کرنش بر روی تمام نمونه ها انجام شد و نتایج با مدل پوپوویچ مقایسه شد. برای ارزیابی بیشتر تحلیل انجام شده، سه معیار ضریب همبستگی، ضریب تغییرات و درصد تغییر در جذب انرژی بکار رفت. تحلیل نتایج، اختلاف قابل توجهی بین مدل پوپوویچ و نتایج آزمایشگاهی را نشان داد. مدل پوپوویچ اصلاح شده برای درک بهتر رفتار بتن در فشار معرفی شد. مدل پیشنهادی، طیف گسترده‌ای از پارامترهای مورد بررسی در این تحقیق را پوشش داد. مدل پوپوویچ اصلاح شده با چندین مدل مانند پوپوویچ، هاگنستاد، تورنفلد و سای، مقایسه شد و نتایج نشان داد که رویکرد اصلاحی، وضوح بهتری برای رفتار بتن در فشار دارد. علاوه بر این، نتایج نشان داد که این مدل‌ها برای پیش‌بینی رفتار بتن با سنگدانه‌های گردگوشه در مقایسه با سنگدانه‌های تیزگوشه دقت بهتری دارند.

International Journal of Engineering

Journal Homepage: www.ije.ir

Evaluation of Linear Permanent Magnet Vernier Machine Topologies for Wave Energy Converters

N. Arish[a], F. Marignetti[*b]

[a] Faculty of Electrical and Computer Engineering, Semnan University, Semnan, Iran
[b] Department of Electrical and Information Engineering the University of Cassino and South Lazio, Cassino, Italy

PAPER INFO

Paper history:
Received 29 September 2020
Received in revised form 26 November 2020
Accepted 09 December 2020

Keywords:
Wave Energy
Energy Converter
Permanent Magnet Shape
Vernier Machine
Halbach Array
Linear Machine
Finite Element Method

ABSTRACT

Today, the importance of using vernier machines in wave energy converters has increased because of its simple structure and ability to generate a lot of thrust force at low speeds due to the magnetic gear effect. The linear vernier permanent magnet machine has been designed in various structures. Proper design and selection of the main parameters of the machine will improve performance and increase the efficiency of the linear vernier machine. One of these parameters is the shape of the permanent magnets and how they are magnetically oriented. The novelty of this paper is the reduction of leakage flux, achieved by changing the shape and orientation of the permanent magnet. Three types of linear permanent magnet vernier machines with different permanent magnet structures and orientation, including V-shape, Halbach array and consequent-pole are presented. The considered machines have been compared to each other and to the existing machine in terms of airgap flux density, back EMF, PM flux, Inductance, thrust force, detent force, loss, efficiency, power factor, flux density and flux line, using the finite element method in the same conditions and with the same volume of permanent magnets. The results show that the magnetic orientation and shape of the permanent magnet have a considerable effect on the leakage flux, and all the proposed models have a lower leakage flux and better performance compared to the existing model.

doi: *10.5829/ije.2021.34.02b.12*

1. INTRODUCTION

The belief that non-renewable energies will run out one day has always been the best motivation for researchers and scientists to think about how to take advantage of clean energy as well as replacing non-renewable energy [1, 2]. Wave energy and wind energy is one of the most important renewable energies due to its relatively high energy density and high predictability, which requires electric converters to exploit it [3, 4]. Linear Permanent Magnet Vernier Machine (LPMVM) is one of these converters, which has been used widely in several structures and operated base on the magnetic gear effect [5]. Magnetic gear effect is a phenomenon that magnetic field in the air gap with a small movement of translator changes remarkably, which provides the ability to produce high thrust force at low speeds. The reason for this feature is the existence of a large number of magnetic pole pairs. Each structure of LPMVM has advantages and disadvantages that are used based on constraints, location and circumstances. The Vernier machine, in addition to advantages such as high torque production at low speeds and a robust and simple structure, has one main drawback. High leakage flux due to the presence of several pairs of magnetic poles causes low power factor (PF) that is an inherent fundamental weakness among all the vernier machines [6]. Over time, various methods have been proposed to improve the PF and performance of LPMVM, each one reducing leakage flux. One of the most important factors influencing leakage flux and

*Corresponding Author Email: marignetti@unicas.it (F. Marignetti)

Please cite this article as: N. Arish, F. Marignetti, Evaluation of Linear Permanent Magnet Vernier Machine Topologies for Wave Energy Converters, International Journal of Engineering, Transactions B: Applications Vol. 34, No. 02, (2021) 403-413

power factor is the structure of magnets and their magnetic orientation [7]. Shi et al. [8] and Almoraya et al. [9], changing the shape and orientation of the permanent magnets from simple to skew, were able to diminish leakage flux in the air gap and increase the electromagnetic performance of the proposed machines. Huo et al. [10] by adding smaller magnets with a horizontal magnetic orientation to larger magnets with vertical magnetic orientation, created an integrated Halbach array that reduces leakage flux and increases machine efficiency. Zhao et al. [11] and shi et al. [12] improved thrust force, flux density and back EMF in the presented machines by dividing the magnet into smaller magnets in different magnetic directions and converting the magnet with a simple array to Halbach array. Nematsaberi et al. [13], by using the spoke array permanent magnet instead of a simple permanent magnet and adding non-magnetic material decreased the leakage flux remarkably which raised the thrust force and PF. Arish et al. [14] have improved the performance of the proposed machine by reducing leakage flux and increasing generation of the magnetic field by hybrid structure and the simultaneous use of two different permanent magnet structures, skew and Halbach [15]. Khaliq et al. [16] have reduced the leakage flux in the proposed machine by using a spoke array permanent magnet in the dual stator structure. Arish et al. [17] by using high-temperature superconductor (HTS) material as bulk between the slot of stator reduced leakage flux and improved electromagnetic performance of the proposed machine. Almoraya et al. [18] by changing the magnetic circuit, not only reduced the volume of PM but also increased the performance of the proposed machine. The purpose and novelty of this paper are to improve the performance of the existing LPMVM and reducing leakage flux by changing the magnetic orientation and shape of the permanent magnets. Therefore, three models are presented with the same volume of PM, but different geometry and orientation. All PMs are located on the stator as a Halbach array, V-shape, Consequent-pole, and base-line (existing) which are shown in Figure 1. The structure of this article is as follows: all the models are examined in section 2. The main function of the presented machines is analyzed section 3. The electromagnetic characteristics in all models are analyzed by FEM and compared with each other in section 4, and finally, the conclusion is given in the last part. The research methodology is also summarized in Figure 2 as a flowchart.

2. MACHINE STRUCTURE

The operation of all the proposed models is in the form of wave energy converters installed on shallow shores so that the stator is fixed on the shore and there is a mechanical arm in the water that transmits the wave energy to the translator and moves it which is shown in Figure 3. The energy of wave with variable speeds is captured by a mechanical arm and changed to the standard range by mechanical gear. A power electronic converter is used for the network connection of the wave energy converter which links the voltage of the wave energy converter with a changing frequency and amplitude to the network with a fixed frequency and amplitude, because of the irregular movement of continuously varying speed. All models have been made of laminated iron translator and stator which 3-phase concentrated winding and NdFeB rare earth magnet are located on the stator. All models have a total of six coils which each phase has two coils. The stator contains six major teeth in which each of them is divided into smaller teeth which are known as flux modulation teeth. All models have been designed at a constant permanent span and the same condition such as materials, geometry, speed, armature current, number of turn per coil and frequency. The key design parameters of the Baseline model are depicted in Figure 4 and written in Table 1.

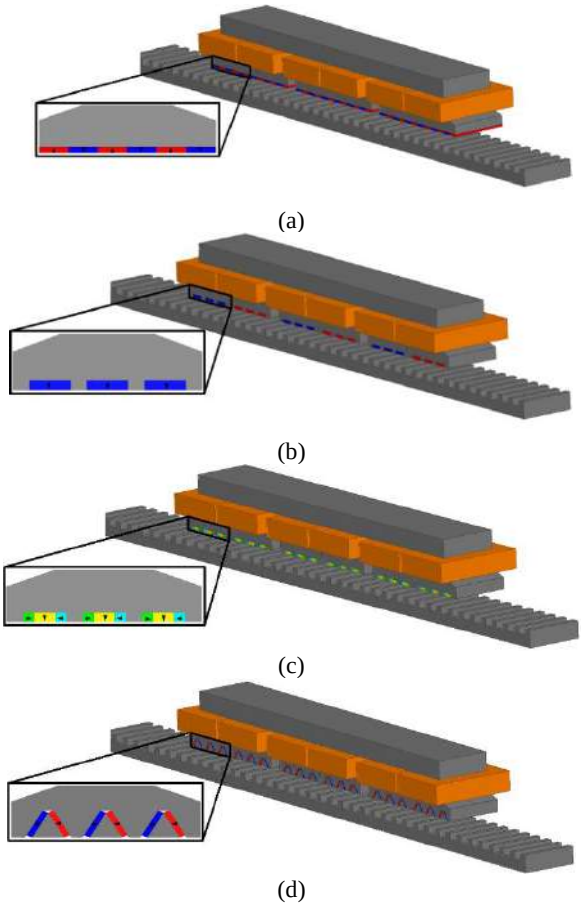

Figure 1. Machines structure. (a) Baseline model (existing), (b) Consequent-pole model, (c) Halbach model, (d) V-shape model

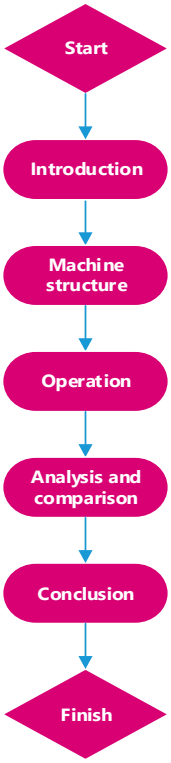

Figure 2. The flowchart of the research methodology

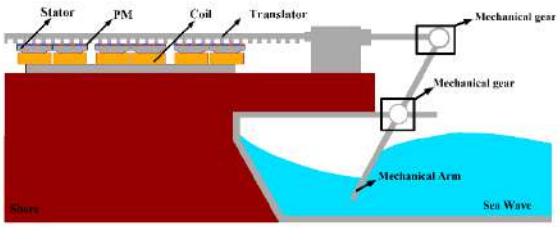

Figure 3. Operation of the linear permanent magnet vernier machine as a wave energy converter

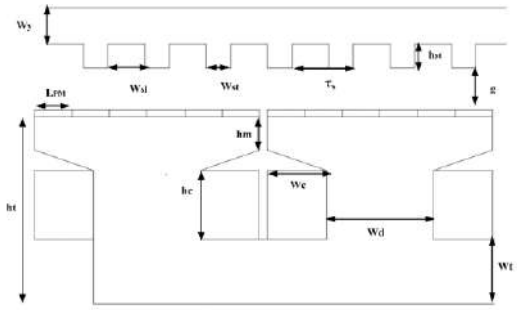

Figure 4. The key design parameters of the Baseline model

2. 1. Baseline Model The Baseline model is known as a simple and rigid structure with high thrust force and force density [19]. In this structure, permanent magnets are mounted on the surface of the stator as tandem and without any space. All PMs are magnetized in two vertical magnetic orientations (upward and downward) one after another.

TABLE 1. The key design parameters of the Baseline model

Items	Unit	Proposed machine
Rate current	A	7
Speed	m/s	1.5
Thickness of PM	mm	3
g	mm	2
w_y	mm	10
w_t	mm	16
w_{st}	mm	6
w_{sl}	mm	9
h_{st}	mm	6
h_m	mm	8.25
h_t	mm	46.25
w_c	mm	14
h_c	mm	17
τ_s	mm	15
l_{PM}	mm	9
w_d	mm	26

2. 2. Consequent-pole Model The Consequent-pole model is as same as the Baseline model in terms of structure and operation [20]. The only difference between them is the thickness of PMs, which, in the Consequent-pole pole model, is twice the Baseline model. Also, orientation in the major teeth is in one direction and changes by every major tooth. So that, if the magnetic orientation of all magnets on the first major teeth is upward, the magnetic orientation of all magnets in the consequent major teeth is downward.

2. 3. Halbach Model In this structure, permanent magnets are divided into three segments in which a vertical magnetized magnet is located between two horizontal magnetized magnets. The middle part generates the main flux, while two other parts operate as a flux barrier and reduce leakage flux at the edge of the magnets. Thickness and width of the Halbach array PMs have a remarkable effect on the performance of the machine and, with the correct selection of the width of segments based on Equations (1) and (2), both back EMF and PM flux can be sinusoidal and symmetrical [11].

$$w_v + 2w_h < \tau_s \quad (1)$$

$$w_h \leq w_v \quad (2)$$

2. 4. V-Shape Model In this structure, simple permanent magnets are divided into two segments as V-shape which are magnetized in two different horizontal orientations that guide the flux into the teeth of the stator and the translator. Skewing of permanent magnet reduces leakage flux, detent force, and ripple force [21].

3. OPERATION

The pole pitch and teeth pitch of the Vernier machine play a prominent role in its operation. The pole pitch of the translator is given by Rostami et al. [22]:

$$\tau_s = \frac{n_s}{l_a} \tag{3}$$

where n_s and l_a are the active teeth number of the stator and active length of the linear permanent magnet vernier machine, respectively. The frequency of a linear permanent magnet Vernier machine is related to the translator's speed (v) and translator pole pitch (τ_s) , as:

$$f = \frac{v}{\tau_s} \tag{4}$$

The relationship between the number of pole pairs of the air gap (P_w) and the permanent magnet field (P_{pm}) and stator teeth (P_s) can be expressed as follows :

$$P_w = \frac{P_s - P_{pm}}{P_s} \tag{5}$$

The gear ratio (*Gr*) has been known as the ratio of the number of stator's teeth and pole pairs of the air gap [12]:

$$G_r = \frac{P_s}{P_w} \tag{6}$$

The speed of the magnetic field generated by the permanent magnet is directly related to the gear ratio and, increasing gear ratio, the speed of the magnetic field increases. This expresses that the speed of magnetic field (V_{eff}) is much larger than the speed of the translator:

$$G_r = \frac{P_s}{P_w} = \frac{V_{eff}}{v} \tag{7}$$

Magnetic gear effect in Vernier machine is a unique feature, and a considerable change in the magnetic field causes all models to be capable of generating high thrust force at low-speed with small displacement. The magnetic gear effect operates at one pole pitch in four main steps. In all models, when the permanent magnet is aligned with the translator's teeth, which is defined as the initial position (X=0), linkage flux is at the maximum value. By moving the translator at the right hand as a quarter of the translator's pole pitch (X= 1/4 τ_s), the linkage flux drops to zero. In the next positions (X= 1/2 τ_s) and (X= 3/4 τ_s), the flux linkage reaches the minimum value and zero, respectively. This cycle is repeated by moving the translator for all models. The effect of the magnetic gear ratio has been depicted for the Baseline model in Figure 5 for four main positions. As can be seen, the low change of the mechanical position of the translator leads to a significant change of linkage flux. Waveforms of back EMF and PM flux have been depicted in four main positions for phase B in Figure 6.

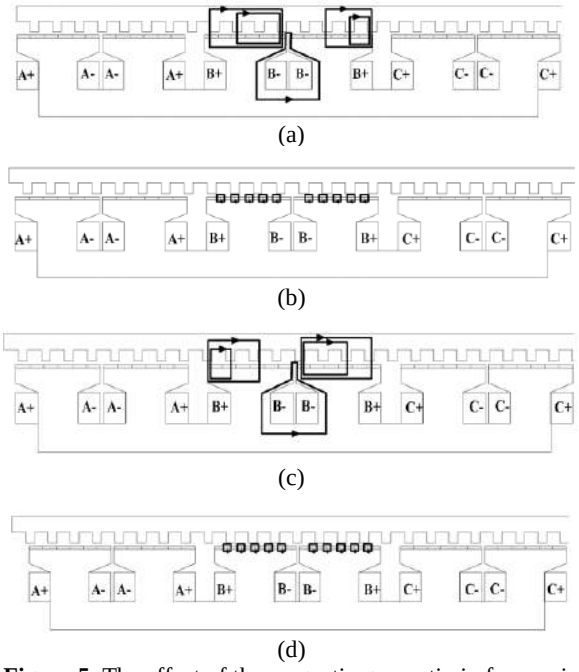

Figure 5. The effect of the magnetic gear ratio in four main positions

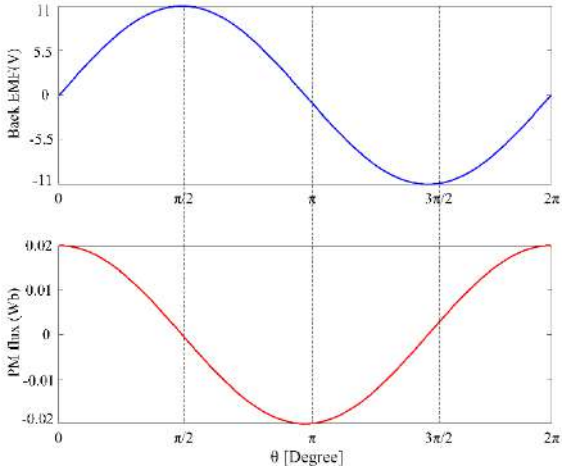

Figure 6. Waveforms of back EMF and PM flux in four main positions for phase B

4. ANALYSIS AND COMPARISON

Basically, the analysis of electric machines in two-dimensional and three-dimensional space is done by the FEM by solving the partial differential equations governing meshing. There are different ways to solve these equations that eventually all come to the same answer [23, 24].

To increase the accuracy of the analysis, the number of mesh elements can be increased and the mesh size can be minimized. These actions may result in an increase in the computation time, although with a little improvement of the results accuracy. Therefore, in order to increase the accuracy of the results and decrease the computation time, in some areas like the air gap, where the flux lines change more, the size of the mesh can be selectively decreased and the number of mesh elements can be raised. To find the best number of meshes, analyses have been done for the baseline model with the various number of the mesh by step of 2000 meshes ie: (4000, 6000, 8000, 10000, 12000, 14000, 16000 and 18000). For a better comprehension, all electromagnetic characteristics of the baseline model have been written in Table 2 for various range of mesh. It is evident that 12000 number of meshes which were created on the surface of the electrical machine is the best step for analyses, because after that not only the results don't change considerably but also it is time-consuming. The meshing method for the Baseline model is shown in Figure 7. For an accurate and fair comparison, performance analysis of all models has been carried out at the transient (full-load) and magnetostatic (no-load) states at the same geometry, materials, speed, current, frequency, turn per coil, magnet pitch and volume. The only variable are the shape and orientation of PM. All analyses have been done in terms of back EMF, PM flux, inductance, thrust force, loss, PF, efficiency and detent force. The conditions of sea wave are very different and consequently, the translator's speed changes continually during its performance. All analyses for all models have been done for a wide range of speeds (0.5 to 3 m/s). Results of electromagnetic analyses of all models respected to the speed have been depicted in Figure. 8. As can be seen, speed of translator does not have considerable impact on the inductance and inductance in all speeds is constant. On the other hand, by increasing speed of the translator, PM flux and back EFM increased too.

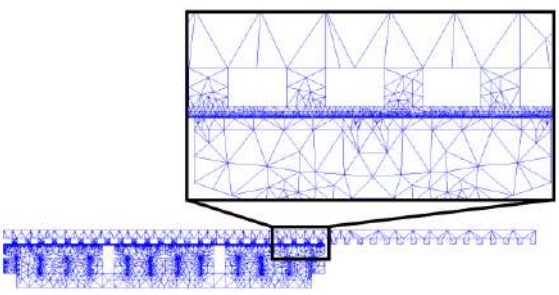

Figure 7. The meshing method of the Baseline model

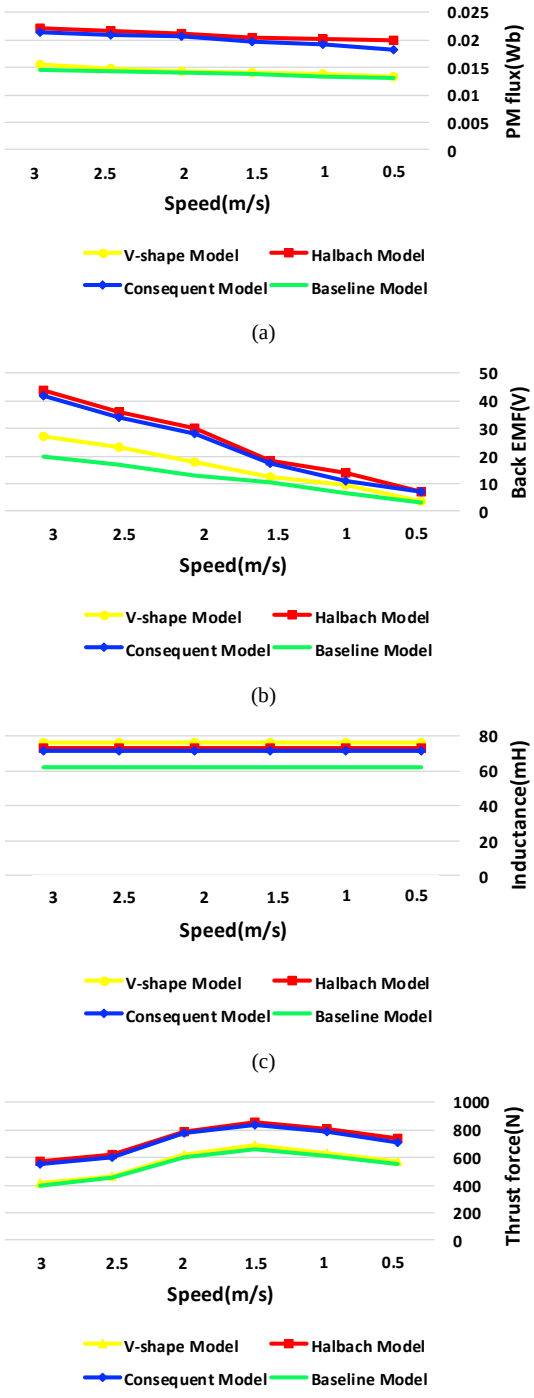

Figure 8. Electromagnetic charictristics of all models respect to speed. a)PM flux, b) Back EMF, c) Inductance, d) Thrust force

TABLE 2. The electromagnetic characteristic of baseline model for various number of meshes

Number of meshes	PM flux (Wb)	Back EMF (V)	Inductance (mH)	Detent force (N)	Thrust force (N)
4000	0.0135	10.4	61.3	39	680
6000	0.0136	10.45	61.5	39.8	684
8000	0.0137	10.5	61.9	40.3	686
10000	0.0137.5	10.55	62.1	40.6	688
12000	0.0138	10.6	62.21	41	690
14000	0.01383	10.63	62.26	41.1	691
16000	0.013835	10.68	62.28	41.3	691.2
18000	0.013839	10.69	62.29	41.5	691.5

However, by raising the speed of translator, thrust force in all models at first increases and then reduces. It shows that linear vernier machine is able to generate high thrust force at the low speed (0.5 -1.5 m/s). It should be noted that by increasing the speed of translator, ripple of thrust force increases and waveforms of PM flux and back EMF lose their pure sine. Following that, best performance of all models is at the range speed of (0.5 to 1.5 m/s).

4. 1. No-load Performance Analysis No-load analysis has been done at the open circuit position while just PM generate a magnetic field. Analysis of the air gap flux density, PM flux, back EMF, detent force, and flux line distribution have been carried out in this state. Since in all models, magnet volume and magnet span are constant, the flux line generated by PMs is also constant. The reduction of leakage flux increases the magnetic field in the core and improves electrical machine performance. Figure 9 shows flux line distribution for all models which according to this figure, the flux path of flux linkage and leakage flux are at the same position (x=0). As can be seen, leakage flux in the air gap is various in all models and is higher in the Baseline model compared to other models. It is evident that the shape and magnetic orientation of the permanent magnet have a considerable impact on the leakage flux. Figure 10 depicts the air gap flux density of all models. The interaction of teeth of the translator and magnetic field generated by PM results in magnetic flux in the air-gap. Peak values of air-gap flux density for the Baseline model, Consequent-pole model, Halbach model and V-shape model are 0.510 T, 523 T, 0.543 T and 0.310 T, respectively. Halbach array and Consequent-pole model have higher air-gap flux density compared to other models indicating that these two models have the lowest flux leakage. The back EMF is a derivative of PM flux over time, which means that these parameters are interdependent and change accordingly. The reduction of leakage flux increases the effective flux and magnetic field which accordingly increases the PM flux and then back EMF.

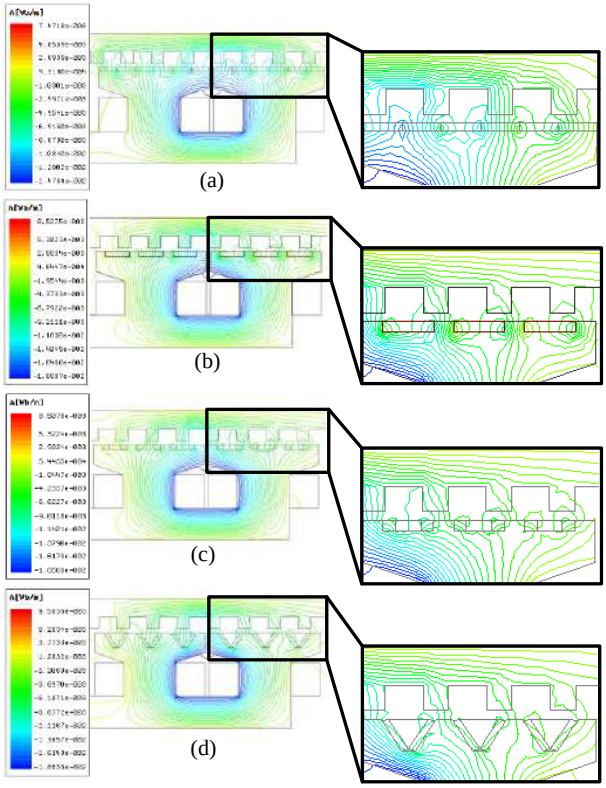

Figure 9. Flux line distribution for all models. (a) Baseline model, (b) Consequent-pole model, (c) Halbach model, (d) V-shape model

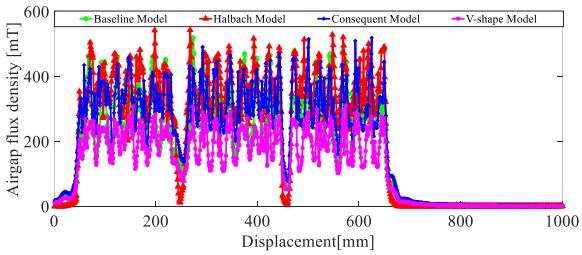

Figure 10. Comparison of air gap flux density

By changing the flux path in the core of the machine, the value and the orientation of the PM flux in the winding will change simultaneously, which makes inducing the back-EMF [11].

$$EMF = \frac{d\psi_m}{dt} = \frac{d\psi_m}{dx}.\frac{dx}{dt} = \frac{d\psi_m}{dx}.v \quad (8)$$

where, x, v and ψ are translator movement, translator speed and PM flux. Figures 11 and 12 show back EMF and PM flux for all models at the same speed and condition. It is evident that Halbch and Consequent-pole models generate higher PM flux and back EMF compared to other models, due to the low leakage flux. RMS values of PM flux for Baseline model, Consequent-pole model, Halbach model and V-shape model are 0.0138 Wb, 0.0196 Wb, 0.0204 Wb and 0.0141 Wb, respectively. Also, maximum values of back EMF for Baseline model, Consequent-pole model, Halbach model and V-shape model are 10.6 V, 17.5 V, 18.4 V and 12.2 V, respectively. In the Halbach model, the flux is finely distributed in the air gap in comparison to the near-constant flux density above the inset magnet, because the flux spreads uniformly through the pole piece, so the waveform in this model is more sinusoidal than other models. Detent force is a detrimental factor in the performance of electric machines, causing vibration and noise and reducing machine efficiency [25, 26]. Detent force consists of two main factors, slot effect and end effect. In linear vernier machines, end effect has a great impact on the detent force. The detent force for all models is shown in Figure 13. The peak 2 peak values of the detent force for Baseline model, Consequent-pole model, Halbach model and V-shape model are 41 N, 53 N, 17 N and 28 N, respectively.

4. 2. Full-load Performance Analysis Full-load analysis has been done while winding and PM generate magnetic field simultaneously. Analysis of flux density distribution, inductance, thrust force, PF, loss and efficiency has been carried out in this state. The flux-density distribution for all models is depicted in Figure 14. As can be seen, magnetic field in all models in the teeth of the stator and translator is higher than in other parts of the machine.The maximum value of the magnetic field is in the standard range and lower than *2T*, which clarifies that all machines operate properly and are not saturated. Inductance for each phase in Vernier machine are obtained at the full load state. For example, for phase-A, self-inductance can be calculated when DC current (i_a=7A) is applied to phase-A, while other phases are at the no-load state (Ib=Ic=0) [25].

$$L_{aa} = \frac{\phi_a(I_b = I_c = 0, I_a = I) - \phi_a(I_a = I_b = I_c = 0)}{I} \quad (9)$$

Figure 15 depicts the Inductance for all models. The average values of inductance for Baseline model, Consequent-pole model, Halbach model and V-shape model are 62.21 mH, 72.67 mH, 72.85 mH and 76.38 mH, respectively. The equivalent circuit of phase-A has been drawn in Figure 16. The terminal voltage for phase-A for the vernier machine can be obtained by Equation (10):

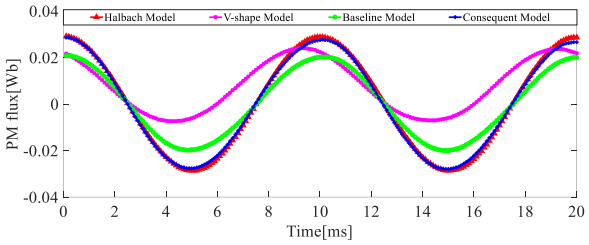

Figure 11. Comparison of PM flux

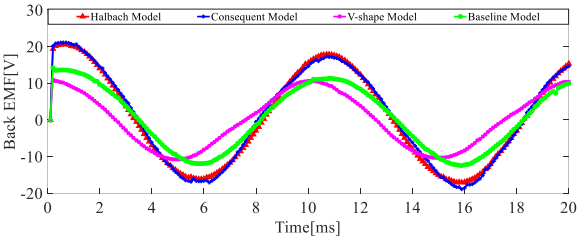

Figure 12. Comparison of back EMF

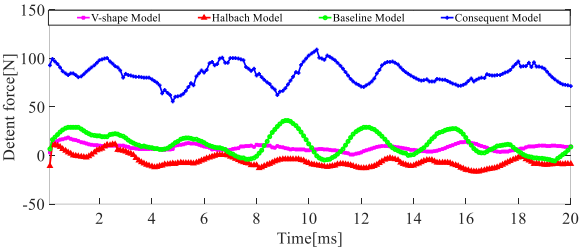

Figure 13. Comparison of detent force

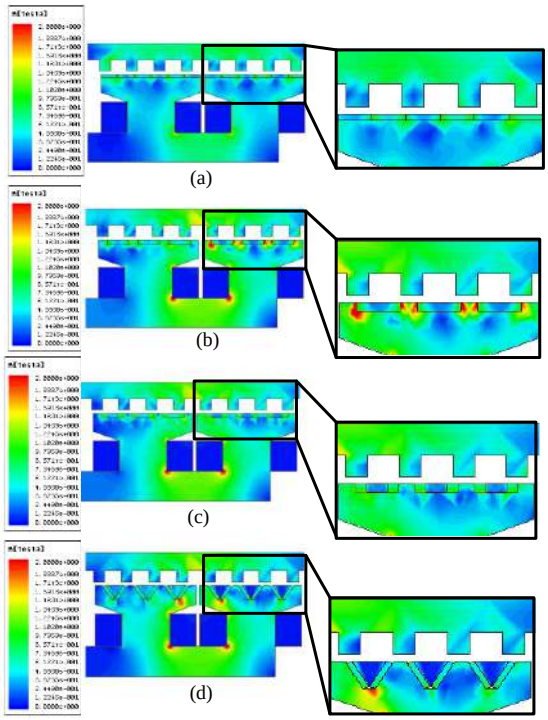

Figure 14. Flux density distribution for all models. (a) Base line model, (b) Consequent-pole model, (c) Halbach model, (d) V-shape model

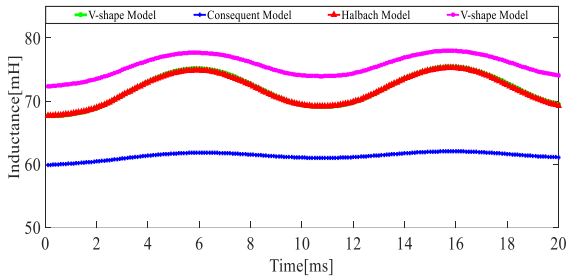

Figure 15. Comparison of inductance

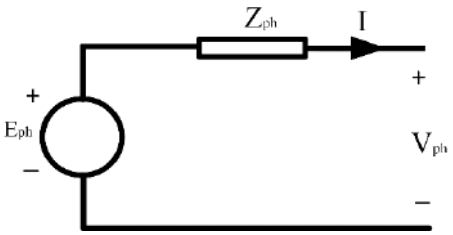

Figure 16. The equivalent circuit of phase-A

$$V_{ph} = R_a I_a + L_s \frac{di_a}{dt} + E_{ph} \quad (10)$$

The terminal voltage of phase-A is obtained by adding the no-load back EMF with voltage drop of the armature resistance and armature inductance.

The power factor in linear Vernier permanent magnet machine is low as shown in the phasor diagram. The phasor diagram has been depicted in Figure 17 by neglecting stator resistance. Because of the insignificant internal resistance, the voltage drop can be neglected for simple computation [13].

$$\cos\theta = \frac{E_{ph}}{V_{ph}} \approx \frac{E_{ph}}{\sqrt{E_{ph}^2 + (I_q X_q)^2}} \quad (11)$$

where, E_{ph} is no-load back EMF, V_{ph} is the terminal voltage, Iq is the q-axis current and Xq is the q-axis inductance. For constant terminal voltage, by diminishing current and average of inductance, PF can be improved. Figure 18 shows the variation of thrust force for all models with respect to the current. The Halbach model has the best overload capability than the Consequent-pole model because of the magnetic orientation. In fact, the saturation range in the halbach PM is larger than using a simple PMs disposition. Increasing the current value from 1 A to 7 A, the thrust force increases dramatically and, increasing further, all models saturate and the thrust force does not change considerably, which clarifies that 7 A is the best selection for the current. The thrust force for all models is in Figure 19. The average values of the thrust force for Baseline model, Consequent-pole model, Halbach model and V-shape model are 690 N, 860 N, 840 N and 660 N, respectively. The ratio of the peak-to-peak value of the thrust force to the average of the thrust force is defined as the ripple force. This index may be used to reduce the ripple force noise and diminish vibrations, so to improve performances of the electrical machine:

$$Ripple - Force = \frac{Force_{\max} - Force_{\min}}{Force_{avg}} \times 100 \quad (12)$$

Ripple force is caused by several reasons: asymmetrical three-phase windings and high amount of detent force, higher harmonics in the waveform of back-EMF and non-sinusoidal stator current waveforms and air gap flux-density. In order to reduce the value ripple force using concentrated winding, skewing slot of the translator and PM, and selecting suitable magnetic gear ratio are effective solutions [26-28]. The ripple force for Baseline model, Consequent-pole model, Halbach model and V-shape model is 24, 16, 14, 29%, respectively. In order to determine the cost-effectiveness in terms of the generation of thrust force for all models, the average thrust density of the machines can be calculated according to literature [29, 30]. Where, F,

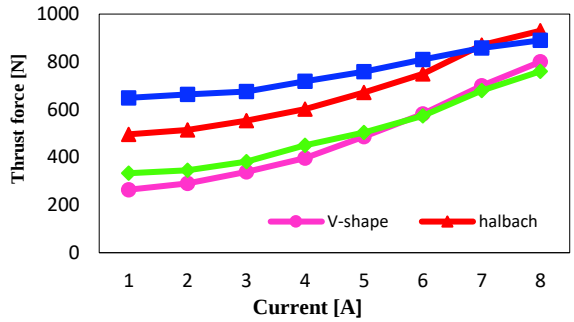

Figure 18. Thrust force of all models respect to the current

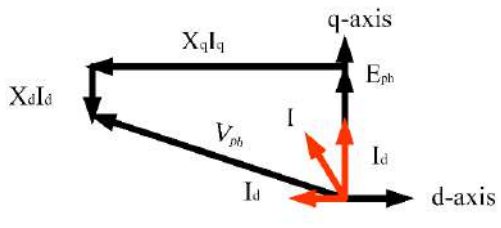

Figure 17. Phasor diagram

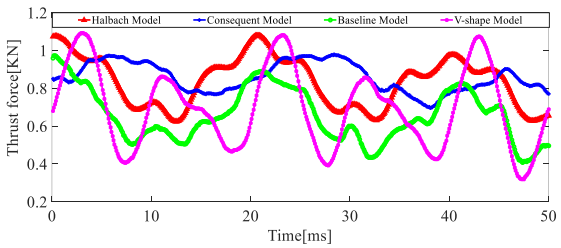

Figure 19. Thrust force waveforms for all models at 7 A

V and F_d are the average of thrust force, active volume of machine and force density, respectively. The values of force density for Baseline model, Consequent-pole model, Halbach model and V-shape model are 34055 N/m^3, 42446 N/m^3, 41458 N/m^3 and 32574 N/m^3, respectively. The shear stress for all models can be obtained by the following formula [9]:

$$F_d = \frac{F}{V} \tag{13}$$

$$\sigma = \frac{F}{A_{airgap}} \tag{14}$$

where σ is the shear stress and A_{airgap} is the air gap area. The values of shear stress for Halbach array, V-shape, Consequent-pole and Bbase-line are 953 KN/m^2, 1187 KN/m^2, 1160 KN/m^2 and 911 KN/m^2, respectively. The PF is one of the most critical parameters in Vernier machines, because it is normally low due to high leakage flux. PF can be calculated as follows [6]:

$$PF = \frac{1}{\sqrt{\frac{LI}{\phi}+1}} \tag{15}$$

where, ϕ, I and L are the PM flux, phase current and inductance in the LPMVM, respectively. Clearly, reducing inductance and phase current and increasing PM flux, the power factor will increase. PF for Baseline model, Consequent-pole model, Halbach model and V-shape model is 0.21 , 0.23, 0.22, 0.19, respectively. Core losses are created by the alternating magnetic field in the iron parts. The major components of the core losses are the hysteresis and the eddy current losses. Eddy current loss is created as a coil is wrapped around a core and an alternating AC supply is applied. The flux produced in the coil is alternating as long as the supply to the coil is alternating. Altering the flux by the core causes an induced emf inside the core, based on the Faraday's law of electromagnetic induction. The current starts to flow in the core by the emf induction. Hysteresis loss is generated by the magnetization and demagnetization of the core caused by the flow of the current in the forward and reverse directions, that laminating the core can decrease the eddy current losses and hysteresis losses.

The total loss and efficiency for all models at fixed current density and coil area are calculated and compared. Total loss for the Baseline model, Consequent-pole model, Halbach model and V-shape model are 21 W, 20.7 W, 20.5 W, 20.3 W, respectively. Efficiency for all models can be calculated as follows:

$$\eta = \frac{P_{out} - loss}{P_{out}} \times 100 \tag{16}$$

Efficiency for the Baseline model, Consequent model, Halbach model and V-shape model are 75, 86, 85 and 80%, respectively. The main electromagnetic parameters of all models have been written in Table 3. Also, For better comprehension, the performance of similar structures of the vernier machine which were explained in the introduction has been compared to all the presented models in Table 4.

TABLE 3. The comparison of electromagnetic characteristics

	Unit	Baseline Model	Consequent-pole Model	Halbach Model	V-shape Model
Airgap flux	T	0.510	0.523	0.543	0.310
PM flux	Wb	0.0138	0.0196	0.0204	0.0141
Back EMF	V	10.6	17.5	18.4	12.2
Inductance	mH	62.21	72.67	72.85	76.38
Detent force	N	41	53	17	28
Thrust force	N	690	860	840	660
Ripple force	%	24	16	14	29
Force density	N/m^3	34055	42446	41458	32574
Shear stress	KN/m^2	953	1187	1160	911
Loss	W	21	20	20.5	20.3
Efficiency	%	75	86	85	80
PF	-	0.21	0.22	0.23	0.19

TABLE 4. Performance comparison of similar structures

	PM flux (RMS)	Induced voltage (Max)	Inductance (Avg)	Thrust force (Avg)	PF
Unit	Wb	V	mH	N	
A model [6]	0.036	9.4	-	599	0.74
B model [7]	-	59	16.3	818	0.65
C model [8]	-	40	-	2332	0.51
D model [9]	0.057	65	-	1087	-
E model [10]	-	21.4	-	1650	0.47
F model [11]	0.18	86	-	2200	0.28
G model [12]	0.081	23	18.1	1860	-
H model [13]	0.049	34	16	2300	-
I model [14]	0.49	167	-	4950	-
J model [15]	0.141	60	43	1860	-

Basline model	0.0138	10.6	62.21	690	0.21
Halbach model	0.0204	18.4	72.85	840	0.23
V-Shape model	0.0141	12.2	76.38	660	0.19
Consequent-pole model	0.0196	17.5	76.67	860	0.22

5. CONCLUSION

In this article, three structures of LPMVM have been proposed. All structures have a concentrated winding mounted on the stator and PM on the translator as Halbach array, V-shape array, and Consequent-pole array. The purpose of this paper is to analyze the effect of magnetic orientation and shape of the PM on the flux leakage and performance of LPMVM, operating as a wave energy converter. For a fair comparison, all models are compared to each other using the FEM method using the same condition and geometry in terms of airgap flux density, back EMF, PM flux, Inductance, thrust force, detent force, loss, efficiency, power factor, flux density, and flux lines. The highest value of the air gap flux density belongs to the Halbach model, which indicates that this model has the lowest flux leakage. Also, the maximum RMS of the PM flux, power factor, and peak values of the back EMF belongs to the Halbach model. Moreover, the lowest peak-to-peak value of the detent force belongs to the Halbach model which shows that the Halbach model has the lowest ripple force. Minimum and maximum of total loss and efficiency belong to Consequent-pole model, respectively. Also, the maximum value of force density, shear stress, and average thrust force belongs to the Consequent-pole model. It should be noted that the minimum of the average value of the inductance belongs to the Halbach model and the V-shape model. The results show that changing the shape and orientation of PM has a considerable effect on the performance of LPMVM which is used for wave energy converters.

6. REFERENCES

1. Kibaara, Samuel Kariuki, et al. “Comparative Analysis of Implementation of Solar PV Systems Using the Advanced SPECA Modelling Tool and HOMER Software: Kenyan Scenario.” ***HighTech and Innovation Journal***, Vol. 1, No. 1, (2020), doi.10.28991/hij-2020-01-01-02.
2. Aminoroayaie Yamini O, Mousavi SH, Kavianpour MR, Movahedi A "Numerical modeling of sediment scouring phenomenon around the offshore wind turbine pile in marine environment". ***Environmental Earth Sciences***, Vol. 77, No. 23, (2018) doi.org/10.1007/s12665-018-7967-4.
3. Ha, K., "Innovative Blade Trailing Edge Flap Design Concept using Flexible Torsion Bar and Worm Drive". ***HighTech Innovation Journal,*** Vol. 1, No. 3, (2020). doi.org/10.28991/hij-2020-01-03-01.
4. Yamini, O. A., et al. “Wave Run-up and Rundown on ACB Mats under Granular and Geotextile Filters’ Condition.” ***Marine Georesources and Geotechnology***, Vol. 36, No. 8, (2018), 895-906, doi.10.1080/1064119X.2017.1397068.
5. Arish, N., "Electromagnetic performace analysis of linear vernier machine with PM and HTS-Bulk", ***Physica C: Superconductivity and its Applications,*** Vol. 579, (2020). doi.org/10.1016/j.physc.2020.1353751.
6. Li, D., Qu, R and Lipo, TA., " High-Power-Factor Vernier Permanent-Magnet Machines", ***IEEE Transactions on Industry Applications,*** Vol. 50, No. 6, (2013). doi. 10.1109/TIA.2014.2315443.
7. Raihan, M.A.H., Baker, N., Smith, K andAlmoraya, A., "Linear consequent pole Halbach array flux reversal machine" ***TheJournal of Engineering,*** Vol. 2019, No. 17, (2019). doi. 10.1049/joe.2018.8110.
8. Shi, C., Qu, R., Gao, Y., Li, D., Jing, L and Zhou, Y. "Design and Analysis of an Interior Permanent Magnet Linear Vernier Machine" ***IEEE Transactions on Magnetics,*** Vol. 54, No. 11, (2018). doi.org/10.1109/TMAG.2018.2840832.
9. Almoraya, A.A., Baker, N.J., Smith, K.J., and Raihan, M.A.H., "Design and Analysis of a Flux-Concentrated Linear Vernier Hybrid Machine with Consequent Poles", ***IEEE Transactions on Industry Applications,*** Vol. 55, No. 5, (2019), 4595-4604. doi.org/10.1109/TIA.2019.2918499.
10. Huo, Y., Qu, R., Gao, Y., Jia, S and Fan, X., "Design of a linear vernier permanent magnet machine with high thrust force density and low thrust force ripple" IEEE International Electric Machines and Drives Conference, (2017). doi.10.1109/IEMDC.2017.8002234
11. Zhao, W., Zheng, J., Wang, J., Liu, G., Zhao, J. and Fang, Z., "Design and analysis of a linear permanent- magnet vernier machine with improved force density", ***IEEE Transactions Industrial Electronics,*** Vol. 63, No. 4, (2016), 2072–2082. doi.10.1109/TIE.2015.2499165
12. Shi, C., Li, D., Qu, R., Zhang, H., Gao, Y and Huo, Y., "A Novel Linear Permanent Magnet Vernier Machine with Consequent-Pole Permanent Magnets and Halbach Permanent Magnet Arrays" ***IEEE Transactions on Magnetics,*** Vol. 53, No. 11, (2017), 1-4. doi.10.1109/TIE.2015.2499165.
13. Nematsaberi, A. and Faiz, J., "A Novel Linear Stator-PM Vernier Machine With Spoke- Type Magnets", ***IEEE Transactions on Magnetics***, Vol. 54, No. 11, (2018), 1–5. doi.org/10.1109/iraniancee.2019.878640.
14. Arish, N., Teymoori, V., Yaghobi, H. and Moradi, M., " Design of New Linear Vernier Machine with Skew and Halbach Permanent Magnet for Wave Energy Converter", 34 th P ower System Conference (PSC), (2019). doi.10.1109/PSC49016.2019.9081549.
15. Arish, N and Teymoori, V., "Development of Linear Vernier Hybrid Permanent Magnet Machine for Wave Energy Converter" ***International Journal of Engineering, Transaction B:*** **Applications,** Vol. 33, No. 5, (2020), 805-813. doi.org/10.5829/ije.2020.33.05b.12.
16. Khaliq, S., Zhao, F and Kwon, B., "Design and analysis of a dual stator spoke type linear vernier machine for wave energy extraction," IEEE International Magnetics Conference (INTERMAG), Beijing, (2015), doi.10.1109/INTMAG.2015.7157480.
17. Ardestani, M., Arish, N. and Yaghobi, H., "A new HTS dual stator linear permanent magnet Vernier machine with Halbach array for wave energy conversion", ***Physica C:***

Superconductivity and its Applications, Vol. 567, (2020). doi.10.1016/j.physc.2019.1353593.

18. Almoraya, A.A., Baker, N.J., Smith, K.J and Raihan, M.A.H.: "Development of a double-sided consequent pole linear vernier hybrid permanent-magnet machine for wave energy converters", in '2017 IEEE International Electric Machines and Drives Conference, IEMDC 2017' (2017). doi:10.1109/IEMDC.2017.8002157.
19. Zhao, W., Liu, X., Chau, K.T., Xiao, F., Cheng, M and Du, Y.: 'Linear primary permanent magnet vernier machine for wave energy conversion*'IET Electric Power Applications*, Vol. 9, No. 3, (2015). doi.org/10.1049/iet-epa.2014.0138 .
20. Almoraya, A.A., Baker, N.J., Smith, K.J and Raihan, M.A.H, "An investigation of a linear flux switching machine with tapered ferromagnetic poles", in '2017 20th International Conference on Electrical Machines and Systems, ICEMS 2017' (2017) doi.org/10.1109/ICEMS.2017.8056083.
21. Baker, N.J., Raihan, M.A.H., Almoraya, A.A., Burchell, J.W., Mueller, M.A., "Evaluating Alternative Linear Vernier Hybrid Machine Topologies for Integration into Wave Energy Converters" ***IEEE Transactions on Energy Conversion***, Vol. 33, No. 4 (2018). doi.org/10.1109/TEC.2018.2873913.
22. Rostami, M., Nadery, P and Shiri, A., " Analysis of Linear Primary Permanent Magnet Vernier Machine Using Finite element method" in '2020 11th Power Electronics, Drive Systems, and Technologies Conference, PEDSTC 2020' (2020). doi: 10.1109/PEDSTC49159.2020.9088394.
23. Arish, N., Ardestani, M., and Hekmati, A., " Study on the optimum structure of the rotor slot shape for a 20-kW HTS", ***Physica C: Superconductivity and its Applications,*** Vol. 567, No. 12, (2020).
24. Movahedi, A., Kavianpour, M and Yamini, O., "Experimental and Numerical Analysis of the Scour Profile Downstream of Flip Bucket with Change in Bed Material Size." ***ISH Journal of Hydraulic Engineering***, Vol. 25, No. 8, (2019), doi.10.1080/09715010.2017.1398111.
25. A. N. Patel and B. N. Suthar, "Cogging torque reduction of sandwiched stator axial flux permanent magnet brushless dc motor using magnet notching technique", ***International Journal of Engineering Transaction A: Basics***, Vol. 32, No. 7, (2019), 940-946. doi.10.5829/ije.2019.32.07a.06.
26. Botha, C.D., Kamper, M.J., Wang, R.-J., Sorgdrager, A.J., "Force Ripple and Cogging Force Minimisation Criteria of Single-Sided Consequent-Pole Linear Vernier Hybrid Machines", (2020), 469-475, doi: 10.1109/ICEM49940.2020.9270845.
27. Sorgdrager, A.J., Wang, R.J., Grobler, A.J "Robust Torque Ripple Mitigation of a Line-Start PMSM by Means of the Taguchi Method," 2019 Southern African Universities Power Engineering Conference/Robotics and Mechatronics/Pattern Recognition Association of South Africa (SAUPEC/RobMech/PRASA), Bloemfontein, South Africa, 2019, 259-264, doi: 10.1109/RoboMech.2019.8704771.
28. Liu, Y., Zhu, Z.Q., " Influence of gear ratio on electromagnetic performance and geometries of Vernier permanent magnet synchronous machines", IEEE Energy Conversion Congress and Exposition, ECCE 2017. (2017). doi.org/10.1109/ECCE.2017.8096471.
29. Moradi Cheshmeh Beigi, H., "Design,. optimization and FEM analysis of a surface-mounted permanent-magnet brushless DC motor", ***International Journal of Engineering, Transaction B: Applications,*** Vol. 31, No. 2, (2018), 339-345. doi.10.5829/ije.2018.31.02b.19.
30. Arish, N., Ardestani, M., Teymoori, V., "Comparison of Dual Stator Consequent-pole Linear Permanent Magnet Vernier Machine with Toroidal and Concentrated Winding", in '2020 11th Power Electronics, Drive Systems, and Technologies Conference, PEDSTC 2020' (2020). doi: 10.1109/PEDSTC49159.2020.9088384.

Persian Abstract

چکیده

امروزه، اهمیت استفاده از ماشین های ورنیر در مبدلهای انرژی موج به دلیل ساختار ساده و توانایی آن در ایجاد نیروی رانش زیاد در سرعتهای پایین افزایش یافته است که به دلیل اثر دنده ای مغناطیسی است. ماشین خطی ورنیر با آهنربا دایمی در ساختار های مختلفی طراحی شده است. طراحی و انتخاب مناسب پارامترهای اصلی دستگاه باعث بهبود عملکرد و افزایش کارایی ماشین های ورنیر خطی می شود. یکی از این پارامترها شکل آهن ربا و نحوه جهت گیری مغناطیسی آنهاست. نوآوری این مقاله کاهش شار نشتی با تغییر شکل و تغییر جهتگیری مغناطیسی آهنرباهای دایمی است. به طوری که ، سه نوع ماشین خطی ورنیر با جهتگیری مغناطیسی و ساختار آهنربای مختلف از جمله V شکل ، آرایه هالباخ و قطب متعاقب ارائه شده است. ماشین های در نظر گرفته شده از نظر تراکم شار شکاف هوا ، EMF برگشتی ، شار PM ، اندوکتانس ، نیروی رانش ، نیروی بازدارندگی، تلفات، راندمان، ضریب قدرت، چگالی شار و خطوط شار با استفاده از روش المان محدود با نرم افزار مکسول تحت شرایط یکسان و حجم آهنربا یکسان با یکدیگر و ماشین موجود مقایسه شده اند. نتایج نشان میدهند که جهت گیری مغناطیسی و شکل آهن ربا های دایمی بر روی شار نشتی تاثیر قابل توجهی دارد و همه ی مدل های ارایه شده نسبت به مدل موجود شار نشتی کمتر و عملکرد بهتری دارند.

International Journal of Engineering

Journal Homepage: www.ije.ir

A Novel Method for Forecasting Surface Wind Speed using Wind-direction based on Hierarchical Markov Model

N. Chiniforoush*, G. Latif Shabgahi

Department of Electrical Engineering, Shahid Beheshti University, Tehran, Iran

PAPER INFO

Paper history:
Received 13 April 2020
Received in revised form 14 November 2020
Accepted 18 December 2020

Keywords:
Hidden Markov Model
Temporal Stationary
Weather Forecasting
Wind Regime
Wind Speed

ABSTRACT

This article presents a new method for detecting heterogeneities in wind data set to predict wind speed based on the well-known Hidden Markov Model (HMM). In the proposed method, the HMM categorizes the wind time series into some groups in which each group represents a wind regime. Each regime uses an internal first-order Markov Chain (MC) for forecasting, and the combination of all regimes outputs generates the final wind speed forecast. The model proposed in this study is called "Hierarchical Markov Model ". The first layer detects and separates wind regimes as heterogenic groups of wind data by the use of wind direction data, based on HMM, and the second layer forecasts the wind speed using MC. The proposed model is implemented and tested using real data. Its effectiveness in terms of temporal stationary index is compared with that of a first-order MC-based method. The results showed that more than 70% improvement can be achieved in wind speed prediction by the proposed method. Moreover, it gives a probability distribution function of wind speed prediction, which is sharper than the one obtained with the first-order MC; means that more precise prediction.

***doi**: 10. 5829/ije.2021.34.02b.13*

NOMENCLATURE

Γ	Transition probability matrix	α	Initial distribution
P_r	Probability value	x_t	Number of successes
M_t	The sequence of random variables	n_t	Number of experiments at time t
$\gamma_{i,j}$	Probability of transition from state i to state j	π_i	Probability of success
$n_{i,j}$	Number of transitions from state i to state j	m	Number of multinomial-HMM states
w_t	Wind speed (m/s)	q	Number of quantized levels of HMM
v_t	Quantized wind speed	D_j	Quantized wind direction
β	Temporal stationary	R	Wind regime
T	Number of time intervals	d_t	Wind direction
k	Number of Markov states	V_t	Wind speed state vector
L_T	Likelihood		

1. INTRODUCTION

The wind is one of the most important atmospheric phenomena due to its influence on many aspects of human life. Decision-making, in many ways, is directly dependent on the wind. Examples include urban air pollution management, wind-power-plant generation, maritime and air transport, tourism, and sports. Wind speed forecasting has an essential role in wind-power-plant generation and operation because the generated power depends directly on wind speed if it is between two upper and lower thresholds [1]. So, this issue has been the subject of intense research. For example, comprehensive studies have been conducted on the wind by Keyhani et al. [2] to investigate wind energy potential as a power generation source.

*Corresponding Author Email: *navid.ch@gmail.com* (N. Chiniforoush)

Please cite this article as: N. Chiniforoush, G. Latif Shabgahi, A Novel Method for Forecasting Surface Wind Speed using Wind-direction based on Hierarchical Markov Model, International Journal of Engineering, B: Applications Vol. 34, No. 02, (2021) 414-426

In meteorology, using numerical weather prediction (NWP) models is a common method of wind forecasting. NWP models use physical models of the atmosphere and oceans to predict the weather based on current weather conditions. These models, which are mainly used for large-scale phenomena, provide accurate results in long-term forecasts [3]. As discussed by Han et al. [4], statistical post-processing of NWP ensembles improved the results. They compared and analyzed the statistical post-processing methods, including bias-corrected and probabilistic forecasts of wind speed to provide more accurate weather information. However, NWPs are not efficient in terms of high computational volume in short-term and very short-term forecasts. In such cases, statistical models are preferred [5].

Short-term wind speed models are built upon either probability distribution theory or time series analysis approach. In probability distribution models, it is assumed that the wind speed follows a specific probability distribution such as Weibull. In these methods, the parameters of the probability distribution function are estimated, usually based on historical data. Since these historical data do not always obey one type of distribution, considering a particular distribution may cause a significant error in these conditions. Autoregressive Moving Average (ARMA) and Markov Chain (MC) are two methods in the time series analysis group. MCs have been used in many applications for wind speed modelling. The main feature of these models is their ability to incorporate both statistical and temporal characteristics of wind speed. In contrast to ARMA, MCs (despite their simplicity) can model time-dependent wind characteristics. Recent studies have shown that the simplicity of MCs makes them a valuable tool in modelling. However, MCs are not capable of modelling wind characteristics at high frequencies [6]. Wind speed time series had been found as long-term correlated statistics [7]. Therefore, Statistical methods have been used comprehensively to improve wind field simulation and wind forecasting. Liu et al. [8] presented an improved wind field simulations by the non-Gaussian Least Square model by precisely and stably simulating velocity skewness and kurtosis .

Based on Markov Model, several studies have been carried out for forecasting weather parameters like temperature and wind. Shamshad et al. [9] compared the results of the first and second-order MC for wind forecasting and showed that the second-order MC does not improve the results so much.

Tagliaferi et al. [6] showed the Nested Markov Chain (NMC) for wind modelling improves MC's accuracy and temporal correlation without excessively increasing computational time. The NMC can be considered as an extended MC such that each state itself is a standalone MC process. In this model, the time series is generated using an internal MC. Here, non-Markovian models can also be used to generate the inner layer time series in this process. In some studies, the semi-Markov model has been used to improve the accuracy and autocorrelation of standard MCs [10]. This is because of the model's ability to save past transitions through an auxiliary random process. The characteristics of this model are as follows. First, the time step is not constant; second, the random variable may have any distribution; and third, the duration of being in each state affects the transition probability.

The wind is affected by other meteorological parameters such as air temperature, air pressure and relative humidity. These parameters have cyclic change over a day and a season. As a result, wind changes have a daily periodic regularity [11, 12] or a seasonal period [13]. Xie et al. [14] presented a non-homogeneous Markov Chain (NHMC) wind speed model to develop a more accurate method for modelling wind speed time series by considering seasonal and daily changes for wind speed.

Ailliot and Monbet [15] used the Markov Switching Auto-Regressive (MSAR) model to describe the time series of the wind. In this method, some self-recursive models were used to describe the temporal behaviour of wind speed. Switching between these models is controlled by HMM. Also, non-homogeneous hidden Markov-switching models for wind time series were used by Ailliot et al. [16].

Generally, the aforementioned researches did not separate the behaviour of different wind regimes in order to achieve better forecasting results. Most of Markov-based methods use the MC only for predicting wind speed. In reality, detecting and separation of wind regimes is an important issue. This issue cannot be achieved through MCs.

Major efforts have been invested in finding a way to accommodate heterogeneous groups with distinct probability distribution function in wind direction time-series to produce a sharper and more accurate probabilistic wind speed forecast. For this aim, HMM can be utilized as a powerful tool. The aim of this article is to take the hidden Markov model to detect heterogeneities in wind data set from which wind regimes can be extracted. States of the model are in fact wind regimes, and the subsystems of each regime (HMM state) is a six-state MC denoting the specific wind speed interval. This hierarchal model gives us the probability of having a wind speed within a specific interval in a specific regime in the near future

This paper is structured as follows. Following this introduction, the first-order MC and its stationary evaluation are briefly explained in section 2. The theoretical concept of mixed models is described, and HMM is introduced. Based on the described features, a new method for predicting wind speed is proposed based on HMM, and an evaluation method is developed based

on temporal stationary test. Having applied this method to real data, the results are compared with those of the first-order MC in section 3 and the advantages of the proposed model are described. Considerations for real-time applications are also discussed in this section. Section 4 concludes the paper with a summary and gives an outlook on future works.

2. MATERIAL AND METHODS

2. 1. Markov Theory The various versions of Markov models have been used in different engineering fields. MCs are used for short-term predictions. Semi-Markov models have been commonly used where state transition probabilities in systems are time-dependant. HMMs are used to find heterogeneities in data sequences and time-series, i.e., for behaviour recognition [17].

In this article, HMM is taken to detect and separate wind regimes as heterogenic groups of wind data. Each regime is, in fact, a state of this HMM. Members of each group are then modelled with an MC for wind prediction. In the following, the Markov chain and hidden Markov theorems are briefly explained.

2. 1. 1. First Order Markov Chain A sequence of random variables (time-series) $\{M_t: t \in \mathrm{N}\}$ is an MC if for all $t \in \mathrm{N}$ it satisfies the property $P_r(M_{t+1}|M_t, \dots, M_1) = P_r(M_{t+1}|M_t)$. It means that considering the history of the process up to time t is equivalent to considering the most recent value M_t.

In a first-order k-state MC, the transition probability matrix $\boldsymbol{\Gamma}$ has a size of k × k represented as Equation (1):

$$\boldsymbol{\Gamma} = \begin{bmatrix} \gamma_{1,1} & \gamma_{1,2} & \cdots & \gamma_{1,k} \\ \gamma_{2,1} & \gamma_{2,2} & \cdots & \gamma_{2,k} \\ \vdots & \vdots & \vdots & \vdots \\ \gamma_{k,1} & \gamma_{k,2} & \cdots & \gamma_{k,k} \end{bmatrix} \quad (1)$$

where $\gamma_{i,j}$ represents the probability of transition from state i to state j. This probability is calculated as Equation (2):

$$\gamma_{i,j} = \frac{n_{i,j}}{\sum_j n_{i,j}} \quad (2)$$

where $n_{i,j}$ is the number of transitions from state i to state j in the whole time–series. Partitioning the whole range of wind speed to several equal or unequal levels gives the states of the representing MC of the system. A simple way is to take all partitions equal, except the last one, and to partition the whole range into some levels (here, for example, 6) as Equation (3):

$$\begin{aligned} &v_t = i \quad if \quad 5(i-1) \le w_t < 5i \ , \ i = 1,2,3,4,5 \\ &v_t = 6 \quad if \quad 5i \le w_t \ , \quad i = 6 \end{aligned} \quad (3)$$

where w_t is wind speed (m/s) and v_t is the quantized wind speed. Probabilistic wind speed prediction in the next step can be declared easily using Equation (4).

$$V_1 = V_0 \,.\, \boldsymbol{\Gamma} \quad (4)$$

where V_0 is the initial condition vector, indicating the current wind state. For example, if six levels are considered for wind speed, the vector $V_0 = [\,0\ 1\ 0\ 0\ 0\ 0\,]$ shows that the system is currently in state 2. In this case, according to Equation (4), V_1 shows the probability of each state in the next step. This method is only valid when the Markov process is not time-dependent (i.e. it is stationary).

A common way to test the temporal stationary attribute of an MC of a time-series is dividing the time-series into two or more parts and designing an MC for each part. The primary Markov chain is stationary if the transition probability matrices of each part's MC are nearly equal. One way for evaluation of the temporal stationary conditions, parameter β is defined by Equation (5) [9].

$$\beta = 2\sum_1^T \sum_{i,j}^k n_{i,j}(t) \ln\left(\frac{\gamma_{i,j}(t)}{\gamma_{i,j}}\right), \quad \mathrm{t} = 1,2,\dots,\mathrm{T} \quad (5)$$

where T is the number of time intervals, k is the total number of states, and $n_{i,j}(t)$ and $\gamma_{i,j}(t)$ are the numbers of occurrence and probability of transitions from state i to state j, respectively.

Such an MC is stationary if β has a χ^2 distribution with $k(k-1)(T-1)$ degrees of freedom. It is stationary in a 5% confidence interval if $\beta < \chi^2\,(5\%\,, \mathrm{Degrees\ of\ Freedom})$.

2. 1. 2. Hidden Markov Model Hidden Markov model is a well-known model for univariate or multi-variable time series and is specially used for modelling discrete series such as group series or counting series.

Hidden Markov Model $\{X_t : t \in \mathbb{N}\}$ is a special kind of dependent mixed models. Considering $\boldsymbol{M}^{(t)}$ and $\boldsymbol{X}^{(t)}$ as histories from 1 to t, this model is expressed as Equation (6).

$$\begin{aligned} &P_r\left(M_t \middle| \boldsymbol{M}^{(t-1)}\right) = P_r(M_t|M_{t-1}),\ t = 2,3,\dots \\ &P_r\left(X_t \middle| \boldsymbol{X}^{(t-1)}, \boldsymbol{M}^{(t)}\right) = P_r(X_t|M_t),\ t \in N \end{aligned} \quad (6)$$

The model has two parts. One is 'parameter process' $\{M_t : t = 1,2,\dots\}$ which is unobserved and satisfies Markov property. The other is 'state-dependent process' $\{X_t : t = 1,2,\dots\}$, where the distribution of X_t depends only on the current state M_t and is not dependent on previous states or observations. $\{X_t\}$ is an m-state HMM, if the Markov chain $\{M_t\}$ has m states. Whenever the model stays in one of these states, the distribution of the model will be its corresponding X_t; i.e., $\{X_t : t = 1,2,\dots\}$. This structure is expressed with the directional graph of Figure 1.

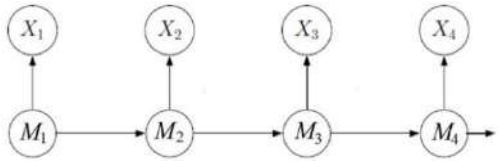

Figure 1. Directional graph of HMM model structure. In this model, the parameter process selects one of M_1, M_2, M_3, M_4 and its corresponding distribution (X_1, X_2, X_3, X_4) is determined.

Likelihood of an m states HMM (L_T) for the data sequence $(x_1, x_2, \dots, x_T)$ with initial distribution $\boldsymbol{\alpha}$ and transition probability matrix $\boldsymbol{\Gamma}$, is expressed by Equation (7) where $\boldsymbol{P}(x_T)$ is the probability of occurrence of x_T and $\mathbf{1}$ is a row vector of ones.

$$L_T = \boldsymbol{\alpha P}(x_1)\boldsymbol{\Gamma P}(x_2)\boldsymbol{\Gamma P}(x_3) \dots \boldsymbol{\Gamma P}(x_T)\mathbf{1}' \quad (7)$$

2. 1. 3. Multinomial-HMM When the output of an experiment is binary (success or failure), the binomial model is used to calculate the probability of success in a certain number of experiments. Binomial probabilities are expressed by Equation (8).

$$p_i(x_t) = \binom{n_t}{x_t} {\pi_i}^{x_t}(1-\pi_i)^{n_t - x_t} \quad (8)$$

where x_t is the number of successes, n_t the number of experiments at time t and π_i is the probability of success. For instance, if "Tails" is the success in tossing a coin, and in the first experiment there are five times toss with two "Tails" outcome, then n_1=5 and x_1=2.

"Binomial-HMM" Model is a type of HMM in which the observed values $\{x_t : t = 1, \dots, T\}$, are the number of successes in $n_1, n_2, \dots, n_T$ independent Bernoulli experiments. A model with *m* states has *m* values for success probability π_i (i indicates each of the states).

A "multinomial-HMM" is the extended model of binomial-HMM. In this case, it is assumed that there are *q* possible outcomes in each experiment, where $q > 2$. Therefore, the number of observed results is q times the previous case and is: $\{x_{tj} : t = 1, \dots, T; j = 1, \dots, q\}$ and $x_{t1} + x_{t2} + \cdots + x_{tq} = n_t$ (n_t is the number of experiments at time *t*). For example, in a 6-state dice throw, if the dice is thrown seven times in the first experiment and the number "3" comes twice, then $n_1 = 7$ and $x_{13} = 2$. The vector X_t, which contains all observations at time *t*, can be written as Equation (9).

$$X_t = (x_{t1}, x_{t2}, \dots, x_{tq}) \quad (9)$$

For an *m*-state "multinomial-HMM" model, there is a $m \times m$ transition probability matrix Γ. Each of the *m* states is associated with a multinomial distribution, and each of these multinomial distributions has q unknown probabilities (emission), which for state i, denoted by $\pi_{i1}, \pi_{i2} \dots, \pi_{iq}$.

An important case of the multinomial–HMM is obtained by considering $n_t = 1$ for all t. In this case, as $\sum_{k=1}^{q} x_{tk} = 1$, in the vector X_t with dimension q, one of the elements is "1", and the rest is "0". Considering:

$$X_t = (\underbrace{0, \dots, 0}_{j-1}, 1, \underbrace{0, \dots, 0}_{q-j})$$

Defining $\boldsymbol{\pi}(j) = diag(\pi_{1j}, \dots, \pi_{mj})$, the likelihood of observed groups $j_1, j_2, \dots, j_T$ at times $1, 2, \dots, T$ is expressed as Equation (10) [18].

$$L_T = \boldsymbol{\alpha\pi}(j_1)\boldsymbol{\Gamma\pi}(j_2)\boldsymbol{\Gamma} \dots \boldsymbol{\pi}(j_T)\mathbf{1}' \quad (10)$$

2. 2. A Novel Method for Wind Forecasting In this section, a novel wind speed forecasting method is presented based on a hierarchical Markov model. This is a two-layer model, in which the top layer is a Multinomial-HMM. In this layer, each state, representing a particular wind regime, is a firs-order MC for which each state represents a specific wind speed interval. Figure 2 shows the basic structure of the proposed model.

The proposed method is suitable for very short-term wind forecasting (from a few seconds up to a few hours). Hourly forecasts of wind direction and speed are widely used for daily public planning. Meanwhile, shorter times are usually employed, for example, in wind turbine management to maximize the receivable power and prevent damage to equipment [19-21].

This kind of forecasting also is useful for aircraft landing and take-off processes.

2. 2. 1. Method Implementation The implementation of the proposed method, results in predicting probability values for wind speed, leading to improved results of the well-known first-order MC.

Figure 3 illustrates the proposed method. The method includes the following three phases.

- Phase A: HMM definition and parameter estimation
- Phase B: Regime separation
- Phase C: Online forecasting

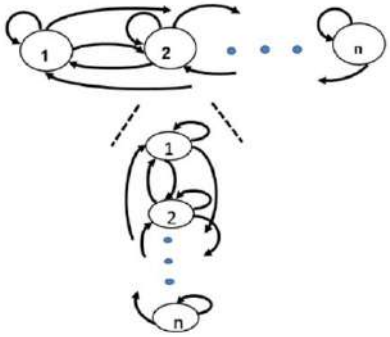

Figure 2. Structure of the proposed hierarchical Markov model

Each phase has some steps as the following:

Phase A:

a. In this step, wind speed and direction time series at a given interval is gathered and pre-processed to produce training data for estimating model parameters. Like other data-driven methods, the completeness and proper sequence of collected data must be checked. The purpose of this step is to ensure the validity of the wind time series. For better consistency, data series should be examined and, in case of missing, should be recovered based on an interpolation algorithm. When the wind speed is zero, the wind direction is assumed invalid and deleted from the data set. The observed wind direction data should be treated in a way that any single observed wind direction is coded from 1 to 16, depending on lying in one of the 16 conventional directions N, NNE, …, NNW. Thus, there are 16 possible outcomes for any single direction value i.e. $D_1, D_2, \dots, D_{16}$.

b. In this step, the maximum likelihood problem for the "multinomial-HMM" model problem based on the well-known Baum-welch algorithm on wind direction time series is solved such that to determine the model parameters to maximize Equation (10). These parameters are the transition probability matrix between m states ($\Gamma_{m\times m}$) and the probability corresponding to each of $D_1, D_2, \dots, D_{16}$ in each state (emissions). Considering m=2, each direction D_j is associated with two probability values: the probability of occurrence in state one π_{1j} and the probability of occurrence in state two π_{2j}.

Phase B:

c. In this step, the wind time series is separated into two parts according to probability corresponding to each of 16 directions. Any direction that is more likely to occur in the first state falls into the first part, and any direction that is more likely to occur in the second state falls into the second one. Equation (11) shows the procedure.

$$\begin{aligned} &if \quad \pi_{1j} > \pi_{2j} \quad then \\ &\quad D_j \in R_1 \\ &\quad else \quad D_j \in R_2 , \\ &i = 1, \dots, q \end{aligned} \tag{11}$$

This is used to separate wind time series into two groups R_1 and R_2 according to wind direction, which is named them as "wind regime" from now on.

d. In this step, the transition probability matrix of the first-order MC is calculated.

According to Equations (1) and (2) represent wind speed time series in each regime.

Phase C:

e. In this step, online wind speed and direction are measured, and the most probable regime is chosen according to the direction.

f. In the last step, wind speed is predicted based on current wind speed and the first-order MC corresponding to the dominant regime and also considering transition probability between regimes.

The above six steps can also be carried out for more numbers of regimes.

2. 2. 2. Method Evaluation Approach Generally, the most important criterion to evaluate Markov models is to compare the transition probability matrix obtained from the test data with the transient probability matrix obtained from the training data. The more the similarity between these two transition probability matrices is, the more successful the forecasting model will be. "Temporal Stationary" is one of the most practical comparison tools.

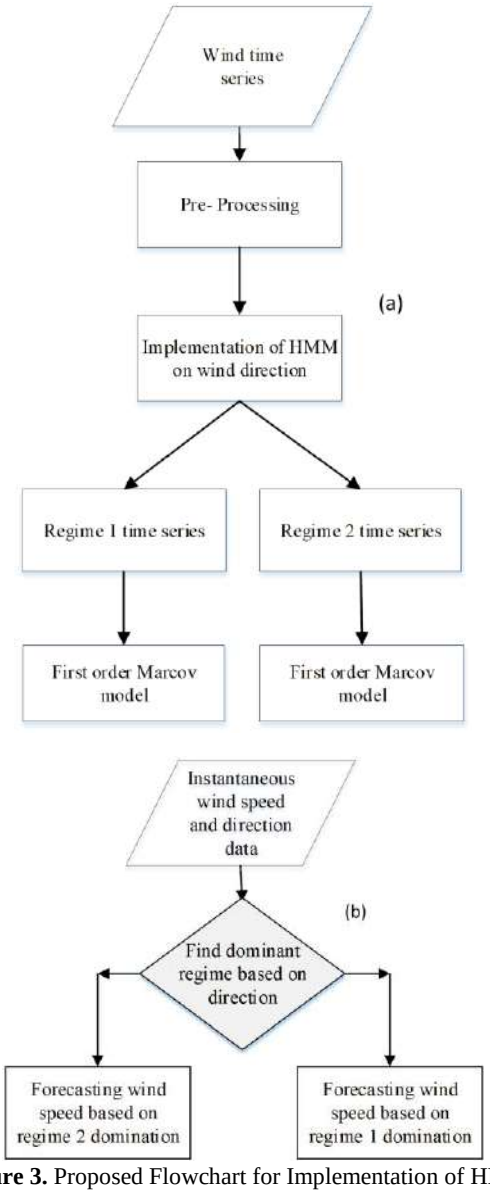

Figure 3. Proposed Flowchart for Implementation of HMM Model, **a.** Flowchart Part I (Modeling), **b.** Flowchart Part II (Forecast)

Using the proposed method, the temporal stationary value for the whole model is calculated as follows. By choosing T=2, the Equation (5) is simplified as Equation (12), and the degree of freedom is equal to $k(k-1)$.

$$\beta = 2\sum_{i,j}^{k}(n_{i,j}(1)ln\left(\frac{\gamma_{i,j}(1)}{\gamma_{i,j}}\right) + n_{i,j}(2)ln\left(\frac{\gamma_{i,j}(2)}{\gamma_{i,j}}\right)) \quad (12)$$

As the wind time series has been partitioned into two regimes, according to step C of the proposed method, temporal stationary of each regime is calculated by Equation (12). The value of $\beta_{Extended}$ can then be computed from the expanding Equation (13).

$$\beta_{Extended} = \frac{n^{(1)}\beta_1 + n^{(2)}\beta_2}{n^{(1)}+n^{(2)}}, \quad (13)$$

where β_1 and β_2 are the temporal stationary values of the first and the second groups, respectively, and $n^{(r)}$ is the number of the existing elements in regime r, $r = 1,2$.

To compare the performance of the proposed model against the first-order MC, it is necessary to calculate and compare their β values for wind time-series data. The smaller value indicates a better (near to reality) forecast.

To calculate the temporal stationary index of first-order MC for two-time series $\{M_1, M_2, \dots, M_n\}$ and $\{N_1, N_2, \dots, N_n\}$, it is enough to find $\gamma_{i,j}(1)$ for the first time-series and $\gamma_{i,j}(2)$ for the second time-series according to Equation (2). The $\gamma_{i,j}$ is then calculated according to Equation (2) for the time-series $\{M_1, M_2, \dots, M_n, N_1, N_2, \dots, N_n\}$. Now the value of β can be calculated cording to Equation (12). To calculate temporal stationary of the proposed method, each of the time-series $\{M_1, M_2, \dots, M_n\}$ and $\{N_1, N_2, \dots, N_n\}$ should be split into groups according to the defined HMM regiems. Group one of the first time-series and group one of the second time-series are used to calculate β_1 and send groups of them are used to calculate β_2. Then having the number of elements each group, it is easy to calculate the temporal stationary of the proposed method by Equation (12).

2. 3. Implementation of The Proposed Forecasting Method

In this section, the proposed method is implemented and examined by real wind time series. The results are compared to the first-order MC. It is assumed that the inner layer of each regime is a first-order MC. The states are defined as described in Equation (3).

2. 3. 1. Field Data

The measured values of wind speed and direction near the runway 29 of Imam Khomeini International Airport (IKIA) were taken as test data. Direction and speed of wind in this site are measured and saved every 30 seconds by an anemometer that is installed at the top of a 10 meters length mast. The installed anemometer is of WMT700 type with a measuring range of 0.01 to 75 m/s and accuracy of ±0.1 m/s or 2 % of reading, whichever is greater. Ultrasonic sensors provide reliable data due to their extremely low measuring threshold, good stability, accuracy and their ability to operate in harsh and cold climates [22].

The mast is placed at coordinates 35° 24' 54" N, 51° 9' 46" E close to the runway as shown in Figure 4. Statistical data for four years (2013 to 2016) was gathered. It was seen that the ratio of missing data to all data is less than 0.1% in the entire collection period in our data set. The collected data are used by the proposed method, and the results are gathered to study. Previous studies on the wind in Tehran was carried out based on a 3-hour period measured long-term wind speed data of meteorological station in Mehrabad airport in Tehran [2]. An Alternative data source would be remote sensing systems that gather the data remotely over a wide area as reported in literature [23, 24] for precipitation.

2. 3. 2. Parameters Estimation

The two-state HMM is fed with eight sets of monthly test data (The wind speed of March and July of the year 2013 to the year 2016). Eight sets of parameters are presented in in Tables 1 and 2, which correspond to the eight sets of these monthly data.

Table 1 shows that the transition probability matrices for the same month of different years are more similar than the values of the other months.

From Table 2, it is observed that 16 probabilities associated with each state in March 2013 ($\boldsymbol{\pi_{1j}}$ and $\boldsymbol{\pi_{2j}}$) are almost similar to other March months, while they differ from values of July months. Also, those values are approximately similar in all July months.

Figure 4. Position of runway anemometer of IKIA

TABLE 1. Transition probability matrix for each of eight data sets (March and July of four consecutive years from 2013 to 2016).

	July	March
2013	$\boldsymbol{\Gamma} = \begin{bmatrix} 0.9935 & 0.0065 \\ 0.0085 & 0.9915 \end{bmatrix}$	$\boldsymbol{\Gamma} = \begin{bmatrix} 0.9883 & 0.0117 \\ 0.0281 & 0.9719 \end{bmatrix}$
2014	$\boldsymbol{\Gamma} = \begin{bmatrix} 0.9950 & 0.0044 \\ 0.0055 & 0.9945 \end{bmatrix}$	$\boldsymbol{\Gamma} = \begin{bmatrix} 0.9844 & 0.0156 \\ 0.0291 & 0.9709 \end{bmatrix}$
2015	$\boldsymbol{\Gamma} = \begin{bmatrix} 0.9930 & 0.0070 \\ 0.0095 & 0.9905 \end{bmatrix}$	$\boldsymbol{\Gamma} = \begin{bmatrix} 0.9896 & 0.0104 \\ 0.0217 & 0.9783 \end{bmatrix}$
2016	$\boldsymbol{\Gamma} = \begin{bmatrix} 0.9941 & 0.0059 \\ 0.0066 & 0.9934 \end{bmatrix}$	$\boldsymbol{\Gamma} = \begin{bmatrix} 0.9861 & 0.0139 \\ 0.0202 & 0.9798 \end{bmatrix}$

TABLE 2. 16 probabilities associated with each state in two groups of identical months in four consecutive years. All of the probabilities multiplied by 1000.

		March 2013		**March 2014**		**March 2015**		**March 2016**	
Direction		π_{1j}	π_{2j}	π_{1j}	π_{2j}	π_{1j}	π_{2j}	π_{1j}	π_{2j}
1	N	0	40	0	64	0	79	0	59
2	NNE	0	36	0	66	39	6	50	16
3	NE	0	14	0	64	58	0	60	10
4	ENE	21	88	1	58	36	0	34	0
5	E	48	3	48	3	51	0	40	0
6	ESE	127	0	117	0	100	0	109	0
7	SE	81	0	91	0	82	0	73	0
8	SSE	30	0	40	0	35	0	37	0
9	S	29	0	29	0	22	0	20	0
10	SSW	36	0	26	0	17	0	21	0
11	SW	30	0	33	0	21	0	17	0
12	WSW	93	0	113	0	68	0	78	0
13	W	219	0	216	0	207	0	195	0
14	WN	284	68	280	48	257	101	247	121
15	NW	2	594	6	544	1	647	3	677
16	NNW	0	166	0	162	0	165	0	155
		July 2013		**July 2014**		**July 2015**		**July 2016**	
Direction		π_{1j}	π_{2j}	π_{1j}	π_{2j}	π_{1j}	π_{2j}	π_{1j}	π_{2j}
1	N	1	93	0	62	3	77	5	73
2	NNE	3	31	2	62	74	4	2	28
3	NE	50	2	53	5	98	0	48	0
4	ENE	61	0	62	0	85	0	55	0
5	E	177	0	200	0	155	0	165	0
6	ESE	395	0	464	0	329	0	380	0
7	SE	170	0	161	0	153	0	168	0
8	SSE	65	0	33	0	51	0	81	0
9	S	53	0	13	0	32	0	76	0
10	SSW	12	2	10	2	16	2	11	2
11	SW	13	19	1	10	4	14	9	24
12	WSW	0	19	0	15	0	24	0	14
13	W	0	38	0	28	0	74	0	54
14	WN	0	186	0	206	0	191	0	201
15	NW	0	480	0	492	0	470	0	480
16	NNW	0	129	0	117	0	143	0	123

In Table 2, the probability values are shown by factor × 1000 for readability. For instance, in the first row, the numbers 0 and 40 in columns "March 2013" show that the north wind has a probability of 0 in regime 1 (i.e., in regime 1 northern wind does not exist) and 0.04 in regime 2. It can be concluded that every northern wind belongs to regime 2.

The results of Table 2 also are presented in Figures 5 and 6 in a bar graph form. As expected, the probability values for the same two months are not quite the same. But they are much closer than two months apart.

2. 3. 3. Regime Separation Using Equation (11), in March 2013, directions 1, 2, 3, 4, 15 and 16 are assigned to regime 2. The remaining directions are assigned to regime one as Equation (14).

$$R_1 = \{5,6,7,8,9,10,11,12,13,14\}, \quad R_2 = \{1,2,3,4,15,16\}, \tag{14}$$

The sets R_1 and R_2 are used to separate March 2013 wind speed time series into two groups according to the corresponding direction. A first-order MC now can be used to forecast wind speed in each of the two separated groups. The transition between pre-quantized levels of wind speed is now modelled as a first-order MC. Moreover, the transition probability matrix for each group (Γ_1 and Γ_2) is calculated as Equation (2). These matrices will be used later for wind forecasting.

2. 3. 4. Online Forecasting Now, as the wind time series of March 2013 has been used for parameter estimation, wind forecasting for March is feasible.

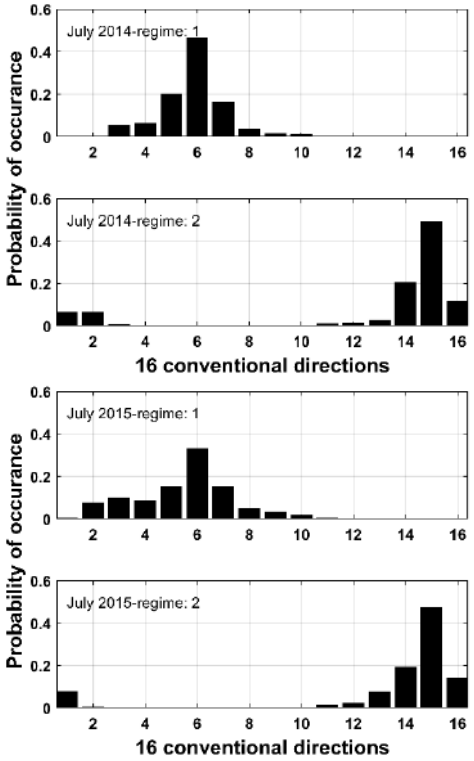

Figure 5. 16 probabilities associated with each state in regime 1 and regime 2 in July 2014 and July 2015

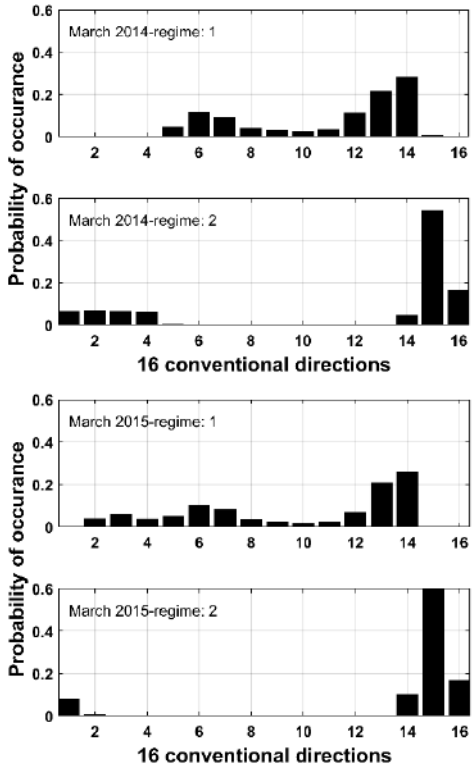

Figure 6. 16 probabilities associated with each state in regime 1 and regime 2 in March 2014 and March 2015

Since sets R_1 and R_2 are known in Equation (14), it is easy to find the current dominant regime as long as the wind direction can be measured online. For example, the wind direction of 93° is coded as 4 (as yields in the 4th zone of 16 conventional directions). So R_2 will be the dominant regime. In this case, for the next sample, R_2 will remain dominant with probability γ_{22} =0.97 and dominant regime will be changed from R_2 to R_1 with probability γ_{21} =0.03 according to Table 1.

As described in the previous section, Γ_1 is the transition probability matrix of the first-order MC of wind speed in regime 1. Regarding Equation (15), if R_1 is dominant regime in current and next steps, $V_t \times \Gamma_1$ is vector of probabilistic wind forecasting in the next step, when V_t representing the vector of current wind speed. Considering the possibility of transitions between regimes, the forecasting of wind speed in the next step would be as Equation (15),

$$\begin{cases} if\ d_t \in R_1 & \boldsymbol{V_{t+1}} = \gamma_{11}\,.\boldsymbol{V_t} \times \boldsymbol{\Gamma_1} + \gamma_{12}\,.\boldsymbol{V_t} \times \boldsymbol{\Gamma_2} \\ if\ d_t \in R_2 & \boldsymbol{V_{t+1}} = \gamma_{21}\,.\boldsymbol{V_t} \times \boldsymbol{\Gamma_1} + \gamma_{22}\,.\boldsymbol{V_t} \times \boldsymbol{\Gamma_2} \end{cases} \quad (15)$$

where γ_{ij} , $i,j = 1,2$ are the elements of regime transition probability matrix and d_t is the measured current wind direction. V_t is the current vector of wind speed; for example, it is [0 1 0 0 0 0] if there are six quantized levels for wind, and if the wind speed yields currently in the second level. V_{t+1} denotes the forecasting vector of the wind speed distribution in the next time step. Finally, Γ_i , $i = 1,2$ are wind speed transition probability matrices in regimes 1 and 2.

showing V_{t+1} as V_{t+1}^1 when $d_t \in R_1$ and as V_{t+1}^2 when $d_t \in R_2$, then Equation (16) will be obtained.

$$\begin{bmatrix} \boldsymbol{V_{t+1}^1} \\ \hline \boldsymbol{V_{t+1}^2} \end{bmatrix} = \begin{bmatrix} \gamma_{11} & \gamma_{12} \\ \gamma_{21} & \gamma_{22} \end{bmatrix} . \begin{bmatrix} \boldsymbol{V_t}\,.\boldsymbol{\Gamma_1} \\ \hline \boldsymbol{V_t}\,.\boldsymbol{\Gamma_2} \end{bmatrix} = \boldsymbol{\gamma}\,.\begin{bmatrix} \boldsymbol{V_t} & \boldsymbol{0} \\ \boldsymbol{0} & \boldsymbol{V_t} \end{bmatrix} . \begin{bmatrix} \boldsymbol{\Gamma_1} \\ \boldsymbol{\Gamma_2} \end{bmatrix} \quad (16)$$

where $\boldsymbol{\gamma}$ is a 2×2 matrix whose elements are γ_{11} to γ_{22}.

Equation (16) can be expanded for more number of regimes as Equation 17).

$$\begin{bmatrix} \boldsymbol{V_{t+1}^1} \\ \boldsymbol{V_{t+1}^2} \\ \vdots \\ \boldsymbol{V_{t+1}^m} \end{bmatrix} = \boldsymbol{\gamma}\,.\boldsymbol{diag}(\boldsymbol{V_t}).\begin{bmatrix} \boldsymbol{\Gamma_1} \\ \boldsymbol{\Gamma_2} \\ \vdots \\ \boldsymbol{\Gamma_m} \end{bmatrix} \quad (17)$$

where $\boldsymbol{\gamma}$ is an $m \times m$ transition probability matrix of HMM states, $\boldsymbol{diag}(\boldsymbol{V_t})$ is a diagonal matrix whose elements of its main diagonal are $\boldsymbol{V_t}$, and $\boldsymbol{\Gamma_i}$, $i = 1,..,m$ is the transition probability matrix of the first-order MC of wind speed for each separated group. Figure 7 shows the overall process, which is a two-layer Markov model.

3. RESULTS

The proposed method has the following two advantages compared with the first-order MC.

- Temporal stationary improvement.
- Regimes identification

3. 1. Temporal Stationary Improvement The First-order MC is the base of several extended methods that have been introduced by researchers for wind forecasting [9]. Extensions generally have been presented in the form of adding inner layers in the form of MC, ARMA, or semi-Markov process to the main MC [6, 10, 14]. In all of these works, a first-order MC in conjunction with some auxiliary process was utilized to

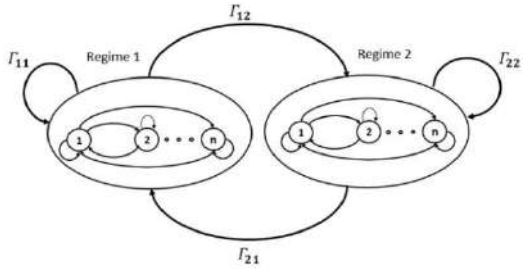

Figure 7. Schematic of the proposed model. The upper layer is a two-state HMM. The lower layer is an n-state MC

develop a more accurate method for modelling wind speed time-series. The proposed method in this article presents a new method for using wind direction time-series as extra information to enrich the MCs for modelling the wind speed time-series. In other words, the proposed method can be used as the base method instead of first-order MC in all of the presented complex methods as listed above.

To evaluate the efficiency of the proposed method, the results of the proposed method are compared with the results of the first-order MC, which introduced by Shamshad et al. [9] using real data.

The wind data of four consecutive years at IKIA wind station are processed using the first-order MC, and the temporal stationary index of two similar months is obtained in two consecutive and non-consecutive years. The results are presented in Table 3. Same processing was carried out using the proposed method with two, three and four regimes. The results are presented in Tables A1, A2 and A3 of the appendix as well as Figure 8. Obtaining temporal stationary index, for two similar months of two years as mentioned before, means using the one month as the training data and the other one as the testing data.

Comparing the results shows that the proposed method improves the temporal stationary index in most cases. For example, the first number on the top left of Table 3 (i.e., 144), shows that the temporal stationary value is 144 for January 2013 and January 2014 when the first-order MC is used. Meanwhile, it is 97.1 when the proposed method is used with two states (*m=2*), according to Table A1 of the appendix. According to Tables A2 and A3 of the appendix, the temporal stationary value is 81.97 when *m=3* and 74.81 when *m=4*.

TABLE 3. Temporal stationary values of the first-order MC for two identical months of two different years.

Month/Year	13-14	13-15	13-16	14-15	14-16	15-16
1	144	187	215	199	363	78
2	152	61	95	209	149	75
3	83	87	147	57	170	115
4	48	91	99	99	147	126
5	243	259	99	126	165	194
6	107	143	187	80	61	90
7	107	381	65	323	223	278
8	245	231	883	196	728	467
9	40	245	157	212	131	241
10	168	143	88	34	203	125
11	126	184	215	65	246	177
12	5	124	155	135	171	42

Inspecting the results show the proposed method improves temporal stationary value in about 70% of cases when *m=2*, 80% of cases when *m=3* and 85% of cases when *m=4* against the first-order MC.

Figure 8 shows the summarized results of the comparison of Table 3 and Tables A1 to A3 of the appendix. Percentage of improvement of the proposed method with the different number of regimes is shown in Figure 8. It is seen that the proposed method gives better temporal stationary index at least in 50% of cases in some months, while 100% improvement is not entirely rare. Improvement is better for larger values of m. However, increasing the number of states increases the computational cost. The computational cost of implementation of HMM has a proportional relation to the computational cost of the calculation of likelihood, as presented in Equation (7). The calculation of likelihood needs Tm^2 operations, where T is the number of elements of time-series of observation, and m is the number of regimes. As the T is constant, the computational cost ratio of m regime separation to first-order MC (m=1) is m^2. Figure 9 shows the percentage of improvement vs computational cost when the number of regimes increases to 4. It shows that increasing the number of regimes improves the results and increase the

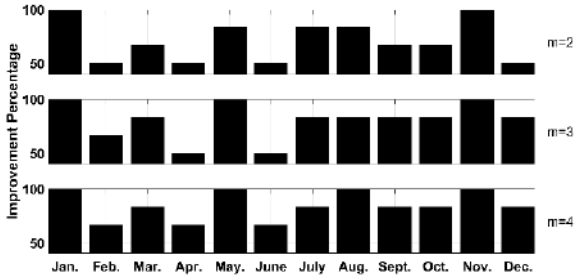

Figure 8. Percentage of improvement by the proposed method with 2, 3 and 4 regimes against first-order MC in different months.

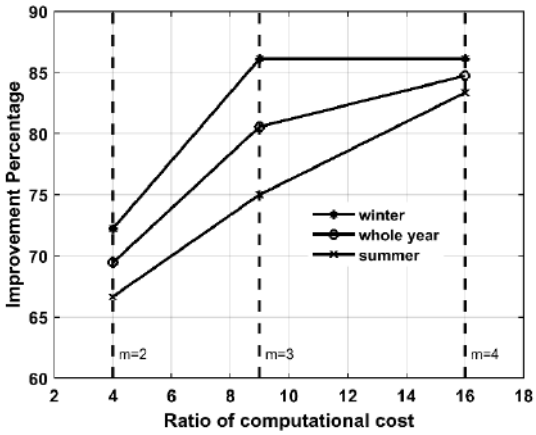

Figure 9. Improvement percentage vs ratio of the computational cost when the number of regimes increases

computational cost. Figure 9 shows that investing computational power four times more, with respect to the first-order MC results in the improvement percentage of 70% for 6×12=72 times of model rum. Improvement percentage for investing nine times (when m=3) and sixteen times(when m=4) more computational power with respect to the first-order MC are also shown in Figure 9. It is clear that increasing computational power doesn't offer the main changes in improvement percentage for a higher value of m. Figure 9 also shows that the effect of increasing the value of m from 2 to 3 in winter is much more than the summer

3. 2. Regimes Identification To see how this approach works for regime identification, the wind speed in March 2014 is forecasted a) with the first-order MC (results showed in Figure 10) and b) with the proposed method with m=2 (results showed in Figure 11 and Figure 12).

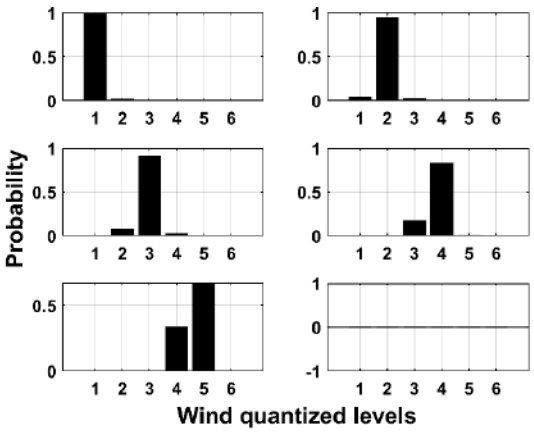

Figure 10. Results of wind speed forecasting based on the first-order MC. From left to right and then top to bottom, respectively, the graphs correspond to the current wind speed level of 1 to 6.

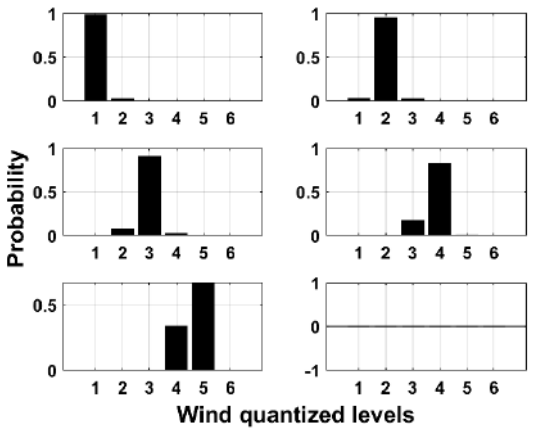

Figure 11. Results of wind speed forecasting based on the proposed method, when regime 1 is dominant. From left to right and then top to bottom, respectively, the graphs correspond to the current wind speed level of 1 to 6.

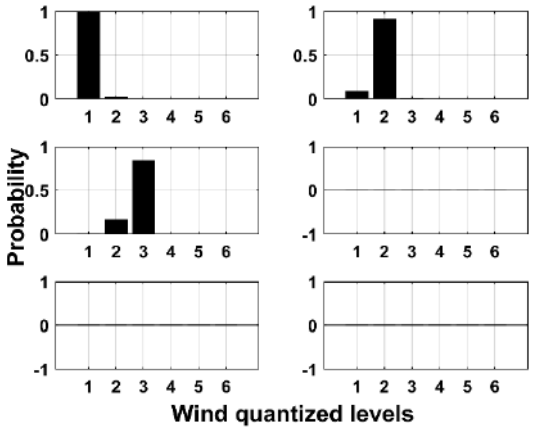

Figure 12. Results of wind speed forecasting based on the proposed method, when regime 2 is dominant. From left to right and then top to bottom, respectively, the graphs correspond to the current wind speed level of 1 to 6.

To define states of the first-order MC (Equation (3)), the wind speed is quantized into six levels, each taken as a Markov state. Each of the six graphs in Figure 10 shows the probability of wind level in the next step. The top-left graph in this figure shows this probability when the current level of wind is 1; the middle top graph shows that value when the current level of wind is 2, and so on. The same order (from left to right and then from top to bottom) was considered for Figures 11 and 12. In Figures 11 and 12, it is assumed that the dominant regime is currently 1 and 2, respectively .

This example shows that by applying the proposed model, the single probability distribution of Figure 10 is separated into two probability distributions, as shown in Figures 11 and 12. Now, the dominant regime can be determined by online measuring of wind direction from which the relevant probability distribution is selected (Figures 11 or 12). This separation increases the concentration of the predictive distributions. For example, Figure 12 shows that levels 4 and 5 of wind speed have zero occurrence probability in regime 2, while the occurrence probability for these two levels of wind speed is not zero in regime 1 (Figure 11). Also, it is seen that level 3 of wind speed in regime one will remain unchanged or goes to level 4 of wind speed (Figure 11), while in regime two it will remain unchanged or goes to level 2 (Figure 11). This kind of distinction is one of the advantages of the proposed method .

According to long-term observations, there are two dominant wind directions at the IKIA weather station. One direction is from mountain-to-plain at night, which flows from the northern elevations of Tehran to the desert in the direction from 270 to 360°. The other is desert wind toward the mountain, in the opposite direction from about 90 to 180°.

This phenomena matches with the output of the proposed method and is well visible in the results of the

separation of dual regimes performed for all months over the four years. In winter, when large-scale phenomena are mainly active, in addition to the two aforementioned wind directions due to local conditions, there is one more dominant wind direction from the south-west. This causes to have better results in three regimes separation in winter times against summer times.

4. CONCLUSIONS

This article presented a model for wind speed forecasting based on the classification of a wind data set into some groups (regimes). Each regime has specific statistical behaviour. Actually, the model has two cascade layers, so it is called "Hierarchical Markov Model". The first layer of the model detects and separates wind regimes as heterogenic groups of wind data by using wind direction data, based on HMM, and the second layer forecasts the wind speed under this regime using MC.

The model was implemented and tested with four years historical data belong to IKIA, and its results compared with those of a first-order MC-based method. For this comparison, two indices: temporal stationary and Probability Distribution Function (PDF) shape of the wind speed forecast, were used. The comparison results showed that the proposed method improves temporal stationary index (improves prediction accuracy) against the first-order MC in at least 70% of cases. Moreover, wind regimes identified by the proposed method match the long-term observations of local experts. Indeed, our method gives a PDF which is sharper than the one obtained with the first order MC for forecasted wind speeds; means that more precise prediction.

The proposed method can be used as a suitable tool for very short-term wind forecasting in aircraft landing and takeoff process, planning of wind power plants, and so on. The main restriction of the proposed method is its incapability to forecast rare events such as strong wind which doesn't have enough frequency to affect the element of MCs. It would be an area of future research to deploy the remote sensing instruments to capture the rare extreme events before the entrance to the target zone and enrich the forecasts.

5. REFERENCES

1. Zhanxin, Y., Fang, Z., Lixiong, X., Hongjun, L., Dapeng, X., Junnan, L., Yu, D. and Yalei, L., "Investigation on equivalent trans-utilization mode and benefit of wind energy", ***International Journal of Engineering, Transactions A: Basics***, Vol. 31, No. 10, (2018), 1708-1714. doi:10.5829/ije.2018.31.10a.13.
2. Keyhani, A., Ghasemi-Varnamkhasti, M., Khanali, M. and Abbaszadeh, R., "An assessment of wind energy potential as a power generation source in the capital of iran, tehran", ***Energy***, Vol. 35, No. 1, (2010), 188-201. doi: 10.1016/j.energy.2009.09.009.
3. Lei, M., Shiyan, L., Chuanwen, J., Hongling, L. and Yan, Z., "A review on the forecasting of wind speed and generated power", ***Renewable and Sustainable Energy Reviews***, Vol. 13, No. 4, (2009), 915-920. doi: 10.1016/j.rser.2008.02.002.
4. Han, K., Choi, J. and Kim, C., "Comparison of statistical post-processing methods for probabilistic wind speed forecasting", ***Asia-Pacific Journal of Atmospheric Sciences***, Vol. 54, No. 1, (2018), 91-101. doi: 10.1007/s13143-017-0062-z.
5. Wang, X., Guo, P. and Huang, X., "A review of wind power forecasting models", ***Energy procedia***, Vol. 12, (2011), 770-778. doi: 10.1016/j.egypro.2011.10.103.
6. Tagliaferri, F., Hayes, B., Viola, I. and Djokić, S., "Wind modelling with nested markov chains", ***Journal of Wind Engineering and Industrial Aerodynamics***, Vol. 157, (2016), 118-124. doi: 10.1016/j.jweia.2016.08.009.
7. Liu, L. and Hu, F., "Long-term correlations and extreme wind speed estimations", ***Advances in Atmospheric Sciences***, Vol. 36, No. 10, (2019), 1121-1128. doi: 10.1007/s00376-019-9031-z.
8. Liu, C., Fu, L., Yang, D., Miller, D.R. and Wang, J., "Non-gaussian lagrangian stochastic model for wind field simulation in the surface layer", ***Advances in Atmospheric Sciences***, Vol. 37, No. 1, (2020), 90-104. doi: 10.1007/s00376-019-9052-7.
9. Shamshad, A., Bawadi, M., Hussin, W.W., Majid, T. and Sanusi, S., "First and second order markov chain models for synthetic generation of wind speed time series", ***Energy***, Vol. 30, No. 5, (2005), 693-708. doi: 10.1016/j.energy.2004.05.026.
10. D'Amico, G., Petroni, F. and Prattico, F., "Wind speed modeled as an indexed semi-markov process", ***Environmetrics***, Vol. 24, No. 6, (2013), 367-376. doi: 10.1002/env.2215.
11. Suomalainen, K., Silva, C., Ferrão, P. and Connors, S., "Synthetic wind speed scenarios including diurnal effects: Implications for wind power dimensioning", ***Energy***, Vol. 37, No. 1, (2012), 41-50. doi: 10.1016/j.energy.2011.08.001.
12. Scholz, T., Lopes, V.V. and Estanqueiro, A., "A cyclic time-dependent markov process to model daily patterns in wind turbine power production", ***Energy***, Vol. 67, (2014), 557-568. doi: 10.1016/j.energy.2013.12.071
13. Karatepe, S. and Corscadden, K.W., "Wind speed estimation: Incorporating seasonal data using markov chain models", ***International Scholarly Research Notices***, Vol. 2013, (2013). doi: 10.1155/2013/657437.
14. Xie, K., Liao, Q., Tai, H.-M. and Hu, B., "Non-homogeneous markov wind speed time series model considering daily and seasonal variation characteristics", ***IEEE Transactions on Sustainable Energy***, Vol. 8, No. 3, (2017), 1281-1290. doi: 10.1109/TSTE.2017.2675445.
15. Ailliot, P. and Monbet, V., "Markov-switching autoregressive models for wind time series", ***Environmental Modelling & Software***, Vol. 30, (2012), 92-101. doi: 10.1016/j.envsoft.2011.10.011.
16. Ailliot, P., Bessac, J., Monbet, V. and Pene, F., "Non-homogeneous hidden markov-switching models for wind time series", ***Journal of Statistical Planning and Inference***, Vol. 160, (2015), 75-88. doi: 10.1016/j.jspi.2014.12.005.
17. Seyedarabi, H. and Feizi, A., "Application of combined local object based features and cluster fusion for the behaviors recognition and detection of abnormal behaviors", ***International Journal of Engineering, Transactions B: Applications***, Vol. 28, No. 11, (2015), 1597-1604. doi: 10.5829/idosi.ije.2015.28.11b.07.
18. Zucchini, W., MacDonald, I.L. and Langrock, R., "Hidden markov models for time series: An introduction using r, CRC press, (2017). doi: 10.1201/9781420010893.

19. Jiang, Y., Song, Z. and Kusiak, A., "Very short-term wind speed forecasting with bayesian structural break model", ***Renewable energy***, Vol. 50, (2013), 637-647. doi: 10.1016/j.renene.2012.07.041.
20. Schlipf, D., Schlipf, D.J. and Kühn, M., "Nonlinear model predictive control of wind turbines using lidar", ***Wind energy***, Vol. 16, No. 7, (2013), 1107-1129. doi: 10.1002/we.1533.
21. Khosravi, S., Zamanifar, M. and Derakhshan-Barjoei, P., "Analysis of bifurcations in a wind turbine system based on dfig", ***Emerging Science Journal***, Vol. 2, No. 1, (2018), 39-52. doi: 10.28991/esj-2018-01126.
22. Chiniforosh, N. and Latif Shabgahi, G., "Wind measuring devices: Challenges, methods and technology trend", ***Journal of Climate Research***, Vol. 1397, No. 33, (2018), 43-62. http://clima.irimo.ir/article_77185_f6f291e750d365d4005ec5a3010d214c.pdf
23. Abdulrazzaq, Z.T., Hasan, R.H. and Aziz, N.A., "Integrated trmm data and standardized precipitation index to monitor the meteorological drought", ***Civil Engineering Journal***, Vol. 5, No. 7, (2019), 1590-1598. doi: 10.28991/cej-2019-03091355
24. Thanh, N.T., "Evaluation of multi-precipitation products for multi-time scales and spatial distribution during 2007-2015", ***Civil Engineering Journal***, Vol. 5, No. 1, (2019), 255-267. doi: 10.28991/cej-2019-03091242.

6. APPENDIX

The wind data of four consecutive years at IKIA wind station are processed using the proposed method and the temporal stationary index of two similar months is obtained in two consecutive and non-consecutive years. The results are presented in Tables A1, A2 and A3.

TABLE A1. Temporal stationary values of the proposed method for two identical months of two different years. m=2

Month/Year	13-14	13-15	13-16	14-15	14-16	15-16
1	97.17	124.8	129.6	113.4	179.4	76.96
2	129.5	71.22	91.37	159.4	156.1	78.91
3	77.7	111.9	117.9	84.2	146.1	81.99
4	64.37	93.85	114.6	79.54	97.44	110.6
5	175.1	207.1	102.1	99.8	115.3	147.1
6	124.4	145.5	173.8	84.6	79.97	87.26
7	59.01	232.5	109	244.3	133.5	163.3
8	201.1	166	430.9	242.9	412.7	208.4
9	55.25	189.6	132.1	176.5	142.6	115.1
10	163.9	120.2	75.27	95.96	205	119.4
11	111.5	134.6	125.4	62.05	187.6	145.5
12	2.5	134	126.4	145.1	138.9	79

In Tables A1-A3, white cells show the cases for which, the proposed method improves the temporal stationary against first-order Markov chain (Table 3). Gray cells indicate the cases with no change, and dashed cells show the cases for which the proposed method worsens the temporal stationary compared to the first-order MC.

TABLE A2. Temporal stationary values of the proposed method for two identical months of two different years. *m=3*

Month/Year	13-14	13-15	13-16	14-15	14-16	15-16
1	81.77	128.1	122.1	107.7	175.5	75.08
2	109.1	62.73	93.84	132.1	129.4	98.67
3	63.83	78.59	108.5	82.07	117.9	82.58
4	69.87	94.3	103.5	70.71	99.06	91.28
5	132.1	166.8	93.57	89.65	80.78	134.6
6	120.5	133.9	153.9	91.22	83.38	82.49
7	62.79	207.8	102.1	218.4	129.8	153.7
8	185.5	150.5	378.7	196.4	344.9	181.5
9	51.82	216.7	111.1	166.5	113.8	143.7
10	116.3	102.9	59.96	71.76	131.8	88.49
11	75.91	82.19	101.4	51.27	135	102.8
12	1.898	114.1	90.36	121.6	99.11	68.33

TABLE A3. Temporal stationary values of the proposed method for two identical months of two different years. m=4

Month/Year	13-14	13-15	13-16	14-15	14-16	15-16
1	74.81	117.4	111.2	104.8	162.4	64.98
2	105.1	63.59	88.04	146.9	93.13	91.34
3	58.62	73.22	108	88.61	120.5	79.89
4	57.73	91.25	98.27	69.53	95.82	84.92
5	130.6	168.1	83.21	86.35	71.63	122.3
6	97.03	96.97	109.7	82.47	74.77	69.94
7	61.7	214.3	108	205.1	122.1	146.9
8	178	136.9	342.5	178.2	286.7	173.1
9	60.38	124.1	94.48	134.6	104.8	129.5
10	116.5	99.36	60.72	77.21	140	88.74
11	70.52	78.95	99.69	49.77	127.3	97.08
12	1.839	111.6	82.42	118.9	90.87	68.06

Persian Abstract

چکیده

این مقاله روشی جدید را با استفاده از مدل پنهان مارکوف (HMM) که به خوبی شناخته شده است، برای آشکارسازی ناهمگونی‌های موجود در داده‌های سری زمانی باد ارائه می‌دهد. در روش ارائه شده، HMM، سری زمانی باد را به گروه‌هایی که هر کدام معرف یک رژیم باد هستند طبقه‌بندی می‌کند. در داخل هر گروه از داده‌ها، یک زنجیره مارکوف مرتبه اول برای پیش‌بینی باد استفاده می‌شود و ترکیب خروجی همه رژیم‌ها پیش‌بینی نهایی سرعت باد را تولید می‌کند. مدل معرفی شده در این مقاله مدل سلسله مراتبی مارکوف نامیده می‌شود. لایه اول با استفاده از HMM، رژیم‌های باد را به عنوان گروه‌های ناهمگون در داده جهت باد جداسازی می‌کند و لایه دوم سرعت باد را با استفاده از زنجیره مارکوف پیش‌بینی می‌کند. روش پیشنهادی با استفاده از داده واقعی پیاده‌سازی و آزموده می‌شود و موثر بودن آن با مقایسه مقدار ایستایی زمانی با زنجیره مارکوف مرتبه اول سنجیده می‌شود. نتایج نشان از دست‌یافتنی بودن بهبود پیش‌بینی سرعت باد توسط مدل پیشنهادی در بیش از ۷۰ درصد موارد دارند. علاوه بر آن، مدل پیشنهادی پیش‌بینی تابع توزیع احتمال سرعت باد را تیزتر و متمرکزتر ارائه می‌دهد که به معنای پیش‌بینی دقیق‌تر است.

International Journal of Engineering

Journal Homepage: www.ije.ir

Human Action Recognition using Prominent Camera

P. S. Kavimandan*[a], R. Kapoor[b], K. Yadav[a]

[a] *Indira Gandhi Delhi Technical University for Women, Delhi, India*
[b] *Delhi Technological University, Delhi, India*

PAPER INFO

Paper history:
Received 19 August 2020
Received in revised form 03 November 2020
Accepted 05 November 2020

Keywords:
Action Recognitio
Modified Bag-of-Words
Prominent camer
Support Vector Machine

ABSTRACT

Human action recognition has undoubtedly been under research for a long time. The reason being its vast applications such as visual surveillance, security, video retrieval, human interaction with machine/robot in the entertainment sector, content-based video compression, and many more. Multiple cameras are used to overcome human action recognition challenges such as occlusion and variation in viewpoint. The use of multiple cameras overloads the system with a large amount of data, thus a good recognition rate is achieved with cost (in terms of both computation and data) as the overhead. In this research, we propose a methodology to improve the action recognition rate by using a single camera from multiple camera environments. We applied a modified bag-of-visual-words based action recognition method with the Radial Basis Function-Support Vector Machine (RBF-SVM) as a classifier. Our experiment on a standard and publicly available dataset with multiple cameras shows an improved recognition rate compared to other state-of-the-art methods.

***doi**: 10. 5829/ije.2021.34.02b.14*

1. INTRODUCTION

The development of technology has made the camera a very easily available gadget, to the point that almost everybody these days uses a digital camera for capturing pictures or recording videos on a daily basis. In profession video recording for film production many cameras are in use simultaneously. The director of the film decides which camera has captured the best scene for a particular moment. But it is not always possible for a human administrator to be present for making such decisions. Thus, an automated machine that can decide which camera has produced the best scene can be valuable. The best information depends on the best view which in turn depends on several points. A view from one angle for a particular action may not be a good view from another angle for that same action. Thus the analysis of the video is required to select the best camera for the particular action. With the advent of technology and the rising number of videos, analyzing a video for the purpose of action recognition has gained tremendous importance in the field of computer vision. Action recognition is quite helpful especially in fields such as surveillance, security, robotics, etc. It also plays a vital role in intelligent systems. The aim here is to identify the category of actions performed in the video from the viewpoint of a selected camera.

In this work, we propose a methodology to recognize human actions performed by an actor by selecting a prominent camera in the multi-camera scenario. This technique helps to avoid the data processing captured by all the cameras. We rely here on the principle that different cameras capture different views, all of which are not good enough to recognize the action. Thus, we develop a score for each of the cameras based on two factors: limb visibility and limb movement. Depending on the score, one of the cameras is chosen as the 'prominent camera and selected for further processing. To testify the methodology, standard databases such as IXMAS [23] are used. The structure of the remaining paper is as follows: literature survey is discussed in Section 2; Section 3 explains the methodology in detail; in Section 4 results are discussed; followed by a conclusion and future work in Section 5.

*Corresponding Author Email: *pranoti.sk@gmail.com* (P. S. Kavimandan)

Please cite this article as: P. S. Kavimandan, R. Kapoor, K. Yadav, Human Action Recognition using Prominent Camera, International Journal of Engineering, B: Applications Vol. 34, No. 02, (2021) 427-432

2. RELATED WORKS

Action recognition from multiple views has been broadly studied in two approaches, the 2D approach and the 3D approach. 2D approaches deal with methods that use data from multiple cameras captured independently; whereas 3D approaches deal with multiple cameras that have been set up at a fixed location [1]. 2D approaches can be divided into two categories. First, the view independent category where data from all cameras is captured independently. And then either action is represented with view-invariant features [2-5] or several classifiers are fused for classification [6]. In Yilmaz and Shah [2], a moving camera is used for capturing data. Thus along with humans, the camera trajectory is also moving. Authors proposed the geometry of dynamic scenes to recognize human action in a number of challenging sequences. Ashraf et al. [3] have used the notion of projective depth to implement the view-invariant action recognition method. Projective depth is unaffected by the camera's orientation and thus has been used to recognize similar actions. In Junejo et al. [4], self similarity descriptors are used since, according to the authors, they are very stable and do not require a correlation between multiple views. A novel action descriptor is constructed using a temporal Laplacian Eigen map that converts view-dependent videos to a stylistic invariant embedded manifold for every single view in Lewandowski et al. [5]. Ahmad and Lee [6] proposed a novel method to recognize human action from a random view by combining features from silhouettes and optical flow.

Other approaches used universal classifiers to recognize actions from the data received from each camera [7-10]. A novel algorithm based kernelized structural SVM is used as a classifier to recognize human action from a random view in Wu and Jia [7]. Zhu et al. [8] proposed a novel multi-sensor fusion method and the universal classifier random forest is used for action recognition. Action videos are represented as prototypes of human body postures using self-organizing maps that are spatially related in Iosifidis et al. [9]. Subsequently, action classification is done using multi-layer perceptrons in a Neural Network. Wang et al. [10] used cross-view action recognition with a K-NN-like classifier. Local features extracted from the input video form a bag of word using k-means clustering. The action is recognised bases on the transfer probability between visual words.

3D approaches usually combine all the visual information (2D human poses) gathered from each camera to represent it in the form of features that are eventually used for action recognition. Thus actions are represented as consecutive 2D human poses. Volumetric data helps to generate a system that is robust as proposed by Pierobon et al. [11]. It also helps to overcome the problem of self-occlusion that is obvious in the multi-camera environment. They have used only posture dependent characteristics as descriptors. Weinland et al. [12] have introduced Motion History Volumes (MHV) as a descriptor that is viewpoint independent. They used Fourier transforms in cylindrical co-ordinates around a vertical axis to align and compare their results. Another representation such as spherical harmonics has been used as a descriptor by Kazhdan et al. [13] with the purpose of avoiding calculations for the optimal alignment which are unfeasible. Their descriptor is rotation invariant. Gkalelis et al. [14] have used fuzzy vector quantization (FVQ) and linear discriminant analysis (LDA) to model and recognize different human movements. They have exploited rich data in multi-view videos and have used Discrete Fourier Transform (DFT), since it is circular and shift-invariant, to solve correspondence issues between training and testing samples. Holte et al. [15] took advantage of intensity and depth maps both captured by SwissRanger SR4000 camera. According to them this combination and the use of Motion Context (HMC) as an action descriptor improved the detection quality. Holte et al. [16] again used HMC along with 3D Motion Context (3D-MC) as the motion descriptor. Few authors, Feizi [17] and Sezavar et al. [18] have implemented Convolution Neural Network (CNN) for their methodologies, but Support Vector Machine (SVM) seems to be the better choice since the main focus is to reduce the computation time and cost [19]. Approaches based on 3D methods are found to be superior to approach based on 2D methods concerning recognition accuracy [20]. To deal with the important challenges in human action recognition such as variation in viewpoint and occlusion, the basic solution is to use multiple cameras, and thus literature concerning multiple cameras has been studied. But multiple camera usage hampers the complexity and running time of the system. To deal with it, in this research paper, we propose a human recognition technique to chose a prominent camera from the multi camera environment. We propose to gather initial data from multiple cameras but to process the data only from a prominent camera.

3. METHODOLOGY

Figure 1 shows the block diagram of the proposed methodology. The video along with the action expected

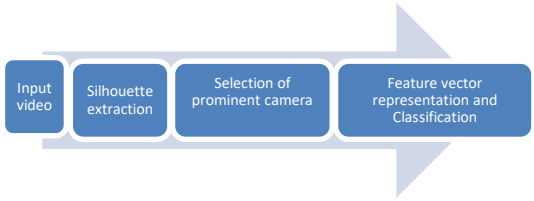

Figure 1. Flowchart of the proposed methodology

to be recognized is given as input. From the action, video silhouettes are extracted from all of the available cameras. Based on extracted silhouettes, information regarding limb visibility and movements can be discovered. We later calculate two scores namely, temporal score and spatial score for each camera. Based on the combination of these scores, a total score for each camera is calculated. The camera with the highest score is chosen as the most prominent camera, and the feature vector is represented for that prominent camera. These feature vectors act as input to the RBF-SVM classifier to recognize human action.

3. 1. Silhouettes Extraction The initial step in the methodology is silhouette extraction. This step requires background subtraction. Background subtraction has its own set of challenges such as variations in lighting, noise, etc. In the proposed methodology, the background has been modeled using a very popular technique known as the Gaussian Mixture Model (GMM) [21] since it is considered to be the most trustworthy background estimation method. This GMM technique is an adaptive mixture model that helps to deal with the problem of lighting variations, motion repetition, etc.

3. 2. Selection of a Prominent Camera To select a prominent camera, first of all, a score for each camera is developed for every camera on two factors. One is the limb movement and the other is limb visibility. We rely on the fact that when limb movement is significant, we can say that the silhouettes in the video will also move significantly. Thus a good motion of limbs indicates that the camera capturing it has a good chance of recognizing the action successfully and in lesser time. Lesser time here implies that the data from the camera other than the prominent camera need not be processed. A camera will develop a good score if it captures significant limb movement. This is called a score for temporal measure (C_t). Since we are interested in the limb movements, we picked out cameras which views show significant variations in movement, be it anywhere in the camera view. To calculate the limb movement, we need to develop the Motion Energy Image (MEI) [22]. MEI is found out using the following Equation (1):

$$MEI(x,y) = \bigcup_{t=0}^{\tau-1} B(x,y,t) \quad (1)$$

where, *B(x, y, t)* is a sequence of a binary images that highlights the area where motion has occurred. Let the most prevalent frame concerning the number of pixels be denoted by $B_{max}(x,y)$, thus we define the confidence score of the camera for temporal measure C_t by the following Equation (2):

$$C_t = 1 - \frac{\sum_{x,y} B_{max}(x,y)}{\sum_{x,y} MEI(x,y)} \quad (2)$$

The other fact that we rely on is that when limb visibility is good, the silhouettes tend to generate a concave profile. To find out the concavity of the shape, we define a spatial measure called a confidence score for the spatial measure $C_s$as given in Equation (3):

$$C_s = 1 - \frac{Vol_{st}}{Vol_{ch}} \quad (3)$$

where Vol_{st} is the Spatio-temporal volume and Vol_{ch} is the convex hull. Both C_t and $C_s$scores are delimited by 1, to always keep them positive. Both of these confidence scores for each camera are multiplied to calculate Confidence Score for a camera (C_c). Thus Confidence Score for a camera (C_c) is a combination of the Confidence score for temporal measure (C_t) and the Confidence score for spatial measure (C_s) as shown in Equation (4):

$$C_c = C_t . C_s \quad (4)$$

Thus we get the final score of each camera. Based on this score, the camera with the highest score will be chosen as the 'prominent camera' and feature vectors from that particular camera are processed further rather than processing data from all cameras. To recognize an action, we are using the modified bag-of-visual-words method described in literature [23].

3. 3. Feature Vector Representation and Classification Bag-of-visual-words methods are popular but these methods fail to preserve the information related to the geometry of the structure. Thus the method described in literature [23] is used to overcome this drawback. According to this method, a Harris 3D detector has been used to extract spatiotemporal points of interest.

The Histogram of Oriented Gradients (HOG) and Histogram of Optical Flow (HOF) descriptors are used to express interest points. Thus a bag-of-visual-word is created using these spatiotemporal interest points for representing an action and the contribution of cluster points is calculated. Depending on the difference among them the contextual distance among the points of a cluster is determined. Directed graphs are then created which are described by Laplacian. A Radial Basis Function Support Vector Machine (RBF-SVM) is fed with the feature vector corresponding to those Laplacians for action recognition.

4. RESULT DISCUSSION

The dataset used for validation is IXMAS [24]. It consists data of 11 actions performed by 5 male and 5 female actors from five static cameras. Figure 2(a-e) shows frames from the IXMAS dataset, and the actor here, namely ‘Daniel’, is acting a 'kick'. In Figure 3(a-e) the same actor is acting a 'punch'. Frames of all five cameras

have been shown for both of the actions, kick and punch in the figures. Figure 4(a-d) shows the result of the computation of temporal and spatial confidence scores C_t and C_s for different cameras. Table 1 shows temporal and spatial scores C_t and C_s calculated for all the five cameras, Camera 0-Camera 4 of the IXMAS dataset for

(a) Camera 0 (b) Camera 1 (c) Camera 2 (d) Camera 3 (e) Camera 4

Figure 2. (a-e) Frames from IXMAS dataset with actor Daniel acting 'kick' in all 5 cameras

(a) Camera 0 (b) Camera 1 (c) Camera 2 (d) Camera 3 (e) Camera 4

Figure 3. (a-e) Frames from IXMAS dataset with actor Daniel acting 'punch' in all 5 cameras, (a) C_t = 0.62, (b) C_t = 0.48, (c) C_s = 0.58, (d) C_s = 0.50

(a) (b) (c) (d)

Figure 4. Figure showing scores for different cameras; (a) C_t score for Daniel's kick action in Camera 0 (Figure 2 a); (b) C_t score for Daniel's kick action in Camera 2 (Figure 2 c); (c) C_s score for Daniel's punch action in Camera 0 (Figure 3 a); (d) C_s score for Daniel's punch action in Camera 3 (Figure 3 d)

TABLE 1. Temporal and spatial scores C_t and C_s and the final confidence score C_c calculated for all 5 cameras Camera 0-Camera 4 of IXMAS dataset. Prominent camera's Confidence score C_c is highlighted.

Action	Camera 0			Camera 1			Camera 2			Camera 3			Camera 4		
	Ct	Cs	Cc	Ct	Cs	Cc	Ct	Cs	Cc	Ct	Cs	Cc	Ct	Cs	Cc
Check watch	0.38	0.22	0.083	0.55	0.42	0.231	0.49	0.50	0.245	0.60	0.45	0.270	0.29	0.45	0.130
Cross arms	0.30	0.27	0.081	0.50	0.53	0.265	0.54	0.55	0.297	0.59	0.50	0.295	0.42	0.66	0.277
Scratch head	0.33	0.40	0.132	0.52	0.32	0.166	0.56	0.51	0.285	0.55	0.61	0.335	0.45	0.45	0.202
Sit down	0.54	0.52	0.280	0.53	0.56	0.296	0.52	0.58	0.301	0.56	0.60	0.336	0.32	0.28	0.089
Get up	0.28	0.35	0.098	0.52	0.55	0.286	0.50	0.52	0.260	0.51	0.49	0.249	0.49	0.52	0.254
Turn Around	0.34	0.47	0.159	0.36	0.45	0.162	0.45	0.57	0.256	0.52	0.59	0.306	0.27	0.31	0.083
Walk	0.53	0.50	0.265	0.55	0.49	0.269	0.53	0.49	0.259	0.56	0.50	0.280	0.30	0.42	0.126
Wave	0.50	0.58	0.290	0.45	0.59	0.265	0.42	0.54	0.226	0.60	0.58	0.348	0.49	0.60	0.294
Punch	0.55	0.58	0.319	0.58	0.61	0.353	0.45	0.48	0.216	0.49	0.50	0.245	0.52	0.60	0.312
Kick	0.62	0.58	0.359	0.60	0.58	0.348	0.48	0.50	0.240	0.52	0.45	0.234	0.49	0.54	0.264

10 actions such as checking the watch, crossing arms, scratching head, sitting down, getting up, turning around, walking, waving, punching and kicking. Prominent camera's confidence score C_c is highlighted. Figure 5 shows the graphical results for C_t, C_s, and C_c of all the five cameras for 10 actions in the IXMAS dataset. It can be noted from the graph that no single camera can be labeled as a prominent camera. It depends on the action to be recognized as in which camera would be the prominent camera. Table 2 shows the comparison of the proposed method with the other methods. As can be seen from the table, Camera 0 gives a good accuracy of 90.8% while recognizing the action 'Kick'. Camera 1 is good for actions 'Get up' and 'Punch' whereas Camera 2 for 'Cross arms' with an accuracy of 90.6% and 92.4% respectively. For all other actions, Camera 3 gives a worthy accuracy of 91.2%. Thus, we can also observe that if the prominent camera is chosen for action recognition, significant computation can be avoided by not processing the data from cameras other than the prominent camera.

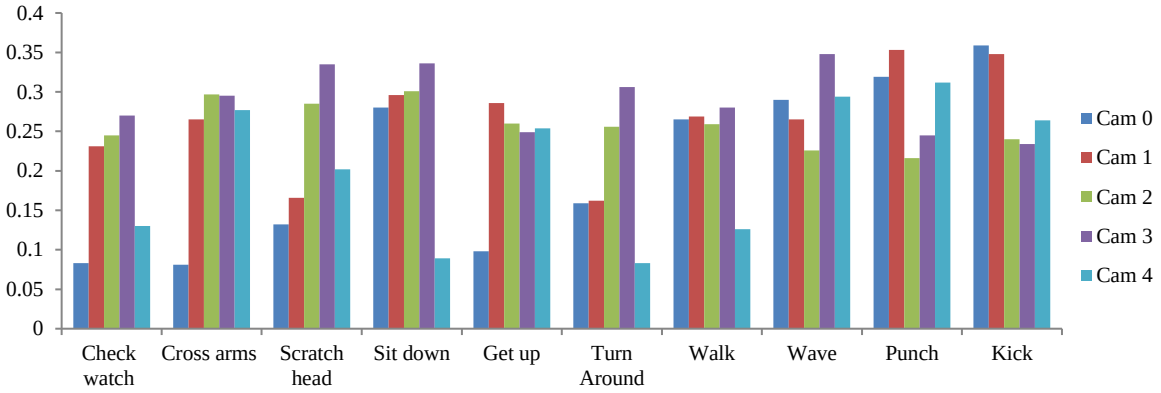

Figure 5. Shows the graphical results for confidence score C_c of all the five cameras for 10 actions in the IXMAS dataset

TABLE 2. Comparison of Proposed Method with other methods

Method	Accuracy (in Percentage)				
	Camera 0	**Camera 1**	**Camera 2**	**Camera 3**	**Camera 4**
Junejo I. et al. [4]	74.8	74.5	74.8	70.6	61.2
Wu, X. et al. [7]	86.5	83.8	86.1	84.5	87.4
Wang J. et al. [10]	88.4	85.3	88.3	86.5	87.2
Proposed Method	90.8 (Kick)	90.6 (Get Up, Punch)	92.4 (Cross Arms)	91.2 (All other actions)	90.6

5. CONCLUSION AND FUTURE WORK

In this paper, we have worked on the methodology of recognizing an action in an environment with multiple cameras. When multiple cameras are considered, along with their advantages comes the major disadvantage of computing time and cost because of the large amount of data. In our proposed methodology we have used the single camera with the most significant information for action recognition. We have given a score to each camera and based on this score the camera with the most significant information is chosen. As shown in Table 1, the prominent camera has been highlighted in yellow. The prominent camera may differ depending on the action, for example, the prominent camera in case of the action 'Checking watch' is Camera number 3 whereas, for the action 'Kich' it is Camera number 0. Thus, we processed the data from only a prominent camera among all the cameras to reduce the processing time and cost. In the future, we can fuse information from more than one prominent camera to further improve the recognition rate.

6. REFERENCES

1. Iosifidis, A., Anastasios T. and Ioannis P., "Multi-view Human Action Recognition: A Survey." 2013 Ninth International Conference on Intelligent Information Hiding and Multimedia Signal Processing (2013), 522-525, doi: 10.1109/IIH-MSP.2013.135.

2. Yilmaz A. and Shah M., "Recognizing human actions in videos acquired by uncalibrated moving cameras" Tenth IEEE International Conference on Computer Vision (ICCV'05) Volume 1, Beijing, (2005), 150-157, doi: 10.1109/ICCV.2005.201.
3. Ashraf, N., Sun, C. and Hassan, F., "View Invariant Action Recognition Using Projective Depth" ***Computer Vision and Image Understanding***, Vol. 123, (2014) doi.:10.1016/j.cviu.2014.03.005.
4. Junejo, I., Dexter, E., Laptev, Ivan and Pérez, P., "View-Independent Action Recognition from Temporal Self-Similarities," In IEEE Transactions on Pattern Analysis and Machine Intelligence, Vol. 33, No. 1, (2011), 172-185, doi.: 10.1109/TPAMI.2010.68.
5. Lewandowski, M., Dimitrios, M. and Jean-Christophe, N., "View and Style-Independent Action Manifolds for Human Activity Recognition." ECCV (2010). doi.org/10.1007/978-3-642-15567-3_40
6. Ahmad, M. and Lee, S. W., "HMM-based human action recognition using multiview image sequences", In Proceedings - 18th International Conference on Pattern Recognition, ICPR 2006, (2006), 263-266. doi.:10.1109/ICPR.2006.630
7. Wu, X. and Jia, Y., "View-Invariant Action Recognition Using Latent Kernelized Structural SVM", Fitzgibbon A., Lazebnik S., Perona P., Sato Y., Schmid C. (eds) Computer Vision – ECCV 2012, Lecture Notes in Computer Science, Vol. 7576. (2012) Springer, Berlin, Heidelberg. doi.: 10.1007/978-3-642-33715-4_30
8. Zhu, F., Shao, L. and Lin, M. "Multi-view action recognition Using local similarity random forests and sensor fusion", ***Pattern Recognition Letters***. Vol. 34, (2013) 20-24. doi.: 10.1016/j.patrec.2012.04.016.
9. Iosifidis, A., Tefas, A. and Pitas, I., "View-Invariant Action Recognition Based on Artificial Neural Networks," ***IEEE Transactions on Neural Networks and Learning System***s, Vol. 23, No. 3, (2012). 412-424, doi.: 10.1109/TNNLS.2011.2181865.
10. Wang, J., Zheng, H., Gao, J. and Cen, J., "Cross-View Recognition based ona Statistical Translation Framework", ***IEEE Transactions on Circuits and Systems for Video Technology***, Vol 26, (2014) doi. : 10.1109/TCSVT.2014.2382984
11. Pierobon, M. Marcon, M., Sarti, A. and Tubaro, S., "3-D Body Posture Tracking For Human Action Template Matching," 2006 IEEE International Conference on Acoustics Speech and Signal Processing Proceedings, Toulouse, (2006) doi.: 10.1109/ICASSP.2006.1660389.
12. Weinland, D., Ronfard, R. and Boyer, E., "Free viewpoint action recognition using motion history volumes", ***Computer Vision and Image Understanding***, Vol. 104, No. 2-3, (2006), 249-257, doi :https://doi.org/10.1016/j.cviu.2006.07.013
13. Kazhdan, M.M., Funkhouser, T.A., and Rusinkiewicz, S., "Rotation Invariant Spherical Harmonic Representation of 3D Shape Descriptors", Symposium on Geometry Processing, (2003) doi.:10.2312/SGP/SGP03/156-165
14. Gkalelis, N. Nokilaidis, N. and Pitas, I., "View independent human movement recognition from multi-view video exploiting a circular invariant posture representation", IEEE International Conference on Multimedia and Expo, (2009), 394-397. doi.: 10.1109/ICME.2009.5202517.
15. Holte M.B., Moeslund, T.B. and Fihl, P., "View-invariant gesture recognition using 3D optical flow and harmonic motion context", ***Computer Vision and Image Understanding***, Vol. 114, No. 12, (2010), 1353-136, https://doi.org/10.1016/j.cviu.2010.07.012
16. Holte, M.B., Moeslund, T., Nikolaidis, N. and Pitas, I., "3D Human Action Recognition for Multi-view Camera Systems", International Conference on 3D Imaging, Modeling, Processing, Visualization and Transmission, (2011), 342-349. doi.: 10.1109/3DIMPVT.2011.50.
17. Feizi, A., "Convolutional Gating Network for Object Tracking", ***International Journal of Engineering, Transactions A: Basics***, Vol. 32, No. 7, (2019), 931-939, https://dx.doi.org/10.5829/ije.2019.32.07a.05
18. Sezavar, A., Farsi, H. and Mohamadzadeh, S., "A Modified Grasshopper Optimization Algorithm Combined with CNN for Content Based Image Retrieval," ***International Journal of Engineering, Transactions A: Basics***, Vol. 32, No. 7, (2019), 924-930, https://dx.doi.org/10.5829/ije.2019.32.07a.04
19. Anding, K., Kuritcyn, P. and Garten, D., "Using artificial intelligence strategies for process-related automated inspection in the production environment", ***Journal of Physics: Conference Series***, Vol. 772, (2016). doi.:10.1088/1742-6596/772/1/012026.
20. Holte, M.B., Moeslund, T., Tran, C. and Trivedi M.M., "Human Action Recognition using Multiple Views: A Comparative Perspective on Recent Developments", MM'11-Proceedings of the 2011 ACM Multimedia Conference and Co-Located Workshops, (2011), doi.: 10.1145/2072572.2072588
21. Chen, Z. and Ellis, T.J., "A self-adaptive Gaussian mixture model", ***Computer Vision and Image Understanding***., (2014), Vol. 122, 35-46. https://doi.org/10.1016/j.cviu.2014.01.004
22. Bobick, A.F. and Davis, J.W., "The recognition of human movement using temporal templates," ***IEEE Transactions on Pattern Analysis and Machine Intelligence***, Vol. 23, No. 3, (2001), 257-267. doi.: 10.1109/34.910878.
23. Mishra, O., Kapoor, R. and Tripathi, M.M., "Human Action Recognition Using Modified Bag of Visual Word based on Spectral Perception", ***International Journal of Image, Graphics and Signal Processing***, Vol 11, (2019), 34-43. doi.: 10.5815/ijigsp.2019.09.04.
24. Weinland, D., Ronfard, R. and Boyer, E., "Free viewpoint action recognition using motion history volumes", ***Computer Vision and Image Understanding***, Vol. 104, No. 2-3, (2006), 249-257. doi: https://doi.org/10.1016/j.cviu.2006.07.013

Persian Abstract

چکیده

تشخیص عمل انسان بدون شک مدتهاست که تحت تحقیق بوده است. دلیل آن، کاربردهای گسترده آن مانند نظارت بصری، امنیت، بازیابی ویدئو، تعامل انسان با ماشین / ربات در بخش سرگرمی، فشرده‌سازی فیلم مبتنی بر محتوا و موارد دیگر است. از چندین دوربین برای غلبه بر چالش‌های تشخیص عملکرد انسان مانند انسداد و تغییر در دیدگاه استفاده می‌شود. استفاده از چندین دوربین سیستم را با مقدار زیادی داده بیش از حد بار می‌کند، بنابراین میزان شناخت خوبی با هزینه (از نظر محاسبه و داده) به عنوان سربار حاصل می‌شود. در این تحقیق، ما یک روش برای بهبود میزان تشخیص عملکرد با استفاده از یک دوربین منفرد از چندین محیط دوربین پیشنهاد می‌کنیم. ما یک روش اصلاح شده عمل مبتنی بر کلمات تصویری اصلاح شده با ماشین بردار عملکرد پشتیبانی-شعاعی (RBF-SVM) را به عنوان طبقه‌بندی اعمال کردیم. آزمایش ما بر روی یک مجموعه داده استاندارد و در دسترس عموم با چندین دوربین، میزان تشخیص بهتر در مقایسه با سایر روش‌های پیشرفته را نشان می‌دهد.

IJE TRANSACTIONS B: Applications Vol. 34, No. 02, (February 2021) 433-442

International Journal of Engineering

Journal Homepage: www.ije.ir

An Enhanced Self-checking Carry Select Adder Utilizing the Concept of Self-checking Full Adder

M. Valinataj

School of Electrical and Computer Engineering, Babol Noshirvani University of Technology, Babol, Iran

P A P E R I N F O

Paper history:
Received 23 May 2019
Received in revised form 10 November 2020
Accepted 14 December 2020

Keywords:
Carry Select Adder
Self-checking Adder
Fault/Error Detection

A B S T R A C T

In this paper, an enhanced self-checking carry select adder (CSeA) architecture is introduced. However, we first show that the carry select adder design presented by akbar and lee does not have the self-checking property in all of its parts in spite of the stated claim. Then, we present a corrected design with the self-checking property that requires more overheads. In addition, we reveal some mistakes in reporting the transistor count of the proposed design in the literature in different sizes, and correct them which again leads to more transistor count and overhead. At the end, due to the fact that the performance of a CSeA depends on its grouping structure, the area overheads of different CSeAs including the corrected designs and the best of previous self-checking designs will be evaluated with respect to the same-size and different-size grouping structures. These evaluations show the comparison of different CSeAs, more appropriate compared to the previous evaluations.

***doi**: 10.5829/ije. 2021.34.02b.15*

1. INTRODUCTION

Current technologies used for manufacturing digital processing units are highly susceptible to environmental effects which may lead to improper operation of a processing unit because of a fault or error. Therefore, handling the erroneous situations in the form of fault/error detection or correction is highly required.

Among the processing units, the adders are very important due to their usage as one of the main functions. Thus, there exist various reported designs to address error detection in the adders such as those reported in literature [1-5] in addition to the multipliers [6,7] even in the reversible logic domain. The carry select adder (CSeA) is one of the fast adders utilized in the processing systems. Many researches have been conducted in recent years to reduce the cost and enhance the performance and reliability of the CSeAs [1, 5, 8-10]. The self-checking CSeA design is discussed in the researches of Akbar and Lee [1, 8]. However, Valinataj et al. proposed a method to achieve multiple fault/error detection is proposed for the CSeAs [5]. Moreover, some improvements in delay, energy or power and the silicon area were reported in literature [9,10].

The CSeA proposed by Akbar and Lee [1] is the best design with respect to the area overhead among its previous CSeA designs that attempt to achieve the self-checking property. However, this design is not entirely self-checking because a fault on some parts can result in an erroneous output without any detection. The concept of self-checking is related to the fault detection, and includes fault-secure and self-testing characteristics. A design with these characteristics is called totally self-checking [11]. A circuit is said fault-secure if it remains unaffected by a fault or it indicates a fault once as soon as it occurs [11]. However, a circuit is said self-testing if it is guaranteed that for each modelled fault there is at least one input vector, occurring during the normal operation of the circuit that detects it [12]. In summary, a single fault will be detected in a self-checking design if it shows a wrong result. The CSeA operation of Akbar and Lee [1] is correct at the absence of faults. However, if a fault occurs and produces a wrong result, the error detection probability is not 100%. Thus, in this paper, the self-checking property of the CSeA presented by Akbar

*Corresponding Author Email: *m.valinataj@nit.ac.ir* (M. Valinataj)

Please cite this article as: M. Valinataj, An Enhanced Self-Checking Carry Select Adder Utilizing the Concept of Self-Checking Full Adder, International Journal of Engineering, Transactions B: Applications Vol. 34, No. 02, (2021) 433-442

and Lee [1] is attained by adding some gates. In addition, the mistakes regarding transistor count will be removed that were caused by the incorrect assumptions of the required transistors for some gates and modules.

The speed of the CSeA is because of the parallel additions and also its grouping structure. Many of the existing CSeAs in literature [13-15] incorporate the square-root (SQRT) architecture to have a lower delay. This architecture utilizes a different-size grouping. However, the same-size groups can be utilized as well, to consume lower area or transistor count. The basic CSeA with either the SQRT grouping or the same-size grouping includes two ripple carry adders (RCA) in parallel in each group. However, the binary to excess-1 convertor (BEC) was used by Ramkumar and Kittur [13] instead of the second RCA in each group, which leads to lower area and power consumption but more delay. In this paper, the corrected self-checking CSeA based on the design in literature [1] is also investigated with respect to different grouping structures as the existing design lacks this evaluation.

2. INVESTIGATION OF the CSeA proposed by Akbar and Lee

Akbar and Lee [1] designed a single-group or single-stage of CSeA with different sizes with the aim of being low-cost and self-checking. This design can be used in real CSeAs with a specific grouping structure. The foundation of this CSeA is the BEC-based CSeA design proposed in literature [13] in which the RCA with the input carry equal to '1' is replaced by the BEC circuit for lowering the required area and power consumption. Therefore, this design is naturally more cost effective than the predecessor self-checking CSeA in literature [8,16] which are based on the basic CSeA design. In the design of Akbar and Lee [1], the self-checking property of the CSeA is obtained utilizing the self-checking modules. This CSeA is stated below.

2. 1. Self-checking Full Adder There exist various full adder (FA) designs in the literature such as [17, 18]. However, the concept of self-checking FA was initially introduced by Akbar and Lee [1], and later was used in other researches [3, 5]. This concept is based on the fact that when all three inputs of a FA, i.e. two input operands A and B and input carry Cin, are equal, then, the output sum (Sum) and output carry (Cout) will be equal, as well. On the other hand, these outputs will not be equal if all of the three inputs are not equal. This property can be used for designing a self-checking FA if a tester circuit called the equivalence tester (Eqt) and the error detection logic are appended to the FA, as shown in Figure 1. In the following, Equations (1) and (2) describe the operation of FA according to Figure 2a, and Equations (3) and (4) show the Boolean operation of equivalence tester and error detection logic shown in Figure 1, respectively.

$$Sum = A \oplus B \oplus C_{in} \quad (1)$$

$$C_{out} = A.B + C_{in}.(A + B) \quad (2)$$

$$Eqt = \overline{A.B.C_{in} + \bar{A}.\bar{B}.\overline{C_{in}}} \quad (3)$$

$$Ef = Sum \odot C_{out} \odot Eqt \quad (4)$$

In the equations above, the symbols $\oplus$ and $\odot$ depict XOR and XNOR operations, respectively. Based on Equation (3), the equivalence tester checks the inputs, and Eqt will become '0' if the equivalence of the inputs is verified; otherwise, it will become '1'. Then, the error function (Ef) is computed in Equation (4) using two XNOR operations. This equation sets Ef to '1' if a single fault has been detected based on the values of two outputs and Eqt. Otherwise, the FA is fault-free or more than a

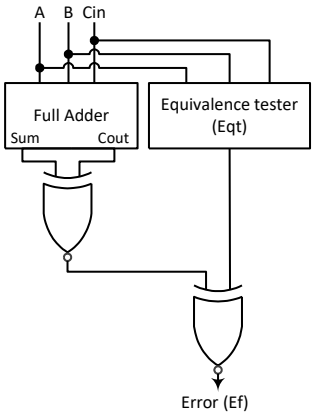

Figure 1. Proposed self-checking full adder in [1]

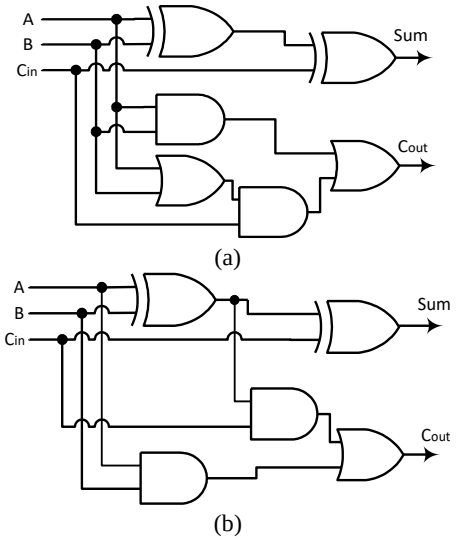

Figure 2. The full adder (a) without logic sharing used in [1], and (b) with logic sharing

single fault exist (which is not important because a self-checking design only guarantees single fault detection). It is worth mentioning that Equations (1) and (2) describe a FA without logic sharing between the outputs Sum and Cout as shown in Figure 2a. The usage of a FA without logic sharing is required to attain the self-checking property. In fact, a common logic between the outputs prevents to detect a single fault occurring in the common logic since it affects both outputs Sum and Cout, and destroys the self-checking property. The FA shown in Figure 2b uses a shared logic between the outputs and can be used for the low-cost adders.

2. 2. Entirely Self-checking Problem The two-bit single-group CSeA proposed by Akbar and Lee [1] is depicted in Figure 3. This design can be extended to larger groups by replicating the middle part (the logic for Sum bit 1) as many as required. In this CSeA, a NOT gate, some AND and XOR gates are used based on the BEC circuit which is utilized instead of the RCA with the input carry equal to '1'. The existing FAs constitute the RCA with the input carry equal to '0', and 2-to-1 multiplexers (MUX) operate in parallel to produce sum bits and the final C_{out} of the group based on the value of the input carry (C_{in}).

The CSeA shown in Figure 3 uses the self-checking FAs and thus any single fault in each self-checking FA will be detected by an *Ef* signal if it produces a wrong result. In [1] for making the entire CSeA a self-checking design, the pass-transistor-based XOR-XNOR gate from the literature [19] with the self-checking property is utilized instead of the XOR gates shown in Figure 3. This self-checking XOR-XNOR gate is shown in Figure 4. As shown in this figure, two inputs *a* and *b* with their complements enter the gate and the results of XOR and XNOR operations are produced. If a fault occurs inside this gate, the outputs will be the same instead of being the complement of each other and thus the fault can be detected. In addition, in [1] instead of the ordinary 2-to-1 MUX, the self-checking 2-to-1 MUX proposed in literature [16] is utilized. As shown by Vasudevan at al. [16], this 2-to-1 MUX produces two one-bit outputs that are complement of each other. Similar to the self-checking XOR-XNOR gate, if a fault occurs inside this MUX, the outputs will not be the complement of each other and the fault can be detected. It should be noted that the second outputs of self-checking XOR gates and multiplexers are not shown in Figure 3.

The main problem of the design shown in Figure 3 is that the NOT and AND gates are not self-checking and thus destroy the overall self-checking property. The output of these gates enters a self-checking MUX or XOR gate. However, due to the fact that these self-checking modules can help to detect only the internal faults, their outputs cannot assist to show an erroneous input. In fact, there is not any control on the inputs of these modules. For example, if a fault on the AND gate shown in Figure 3 causes its output to toggle, the output of the XOR gate in the MOFC part will definitely change, and this error can propagate to the output carry of the group. A similar case exists for the NOT gate in the first bit position of the adder that can make Sum bit 0 erroneously.

2. 3. Transistor Count Problem There exist some mistakes in the work of Akbar and Lee [1] regarding transistor count of some gates and modules based on the CMOS implementation as follows:

The first mistake is that the authors used the transistor count of FA presented by Vasudevan et al. [16] as the number of required transistors for their FA. However, the transistor implementation of the FA by Vasudevan et al. shows that it is a type of FA with logic sharing, and thus cannot be used inside a self-checking FA. Therefore, according to Figure 2a that shows the FA without logic sharing requires an extra OR gate compared to Figure 2b, the real transistor count for the FA part of the self-checking FA presented Akbar and Lee [1] will be more.

To obtain the transistor count of a FA shown in Figure 2a, different approaches can be used. The gate level implementation of carry generation logic requires 18 transistors, after adding 20 transistors for the two CMOS XNOR gates based on [16], the summation of 38 transistors is achieved. It should be noted that this is

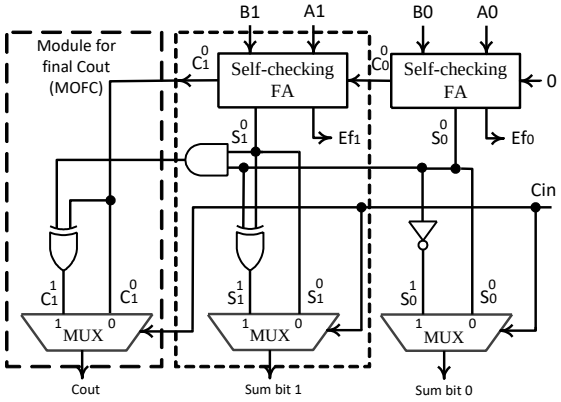

Figure 3. The 2-bit CSeA proposed in [1] as the self-checking design

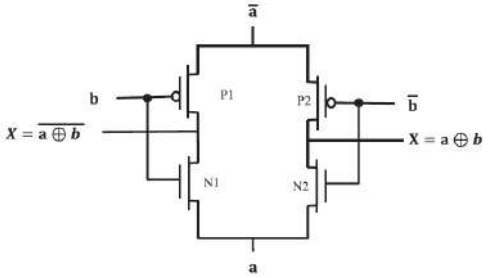

Figure 4. Self-checking XOR-XNOR gate proposed in [19]

based on the fact that the two XOR gates of Figure 2a can be replaced by two XNOR gates without altering the Sum. In another calculation, the FA without logic sharing has an extra OR gate compared to the FA with logic sharing. Thus, it requires 28 transistors based on [16] plus 6 transistors for the OR gate which leads to 34 transistors. Besides, if we use the 6-transistor CMOS XOR gate (such as the one discussed by Fathi et al. [20]) that does not lead to any voltage loss in the output, the minimum number of transistors require for the FA without logic sharing will be 18+2×6=30 in which 18 is for the carry generation logic and the other term is for two XOR gates. Therefore, the FA without logic sharing will have at least two more transistors than those stated Akbar and Lee [1].

The second mistake is that the mentioned number of transistors for the equivalence tester module is 12. However, according to Equation (3), this module cannot be implemented with less than 18 transistors because it includes six PMOS transistors, six NMOS transistors and three NOT gates according to the basic CMOS implementation depicted in Figure 5.

The third mistake is that the authors assumed four transistors for each self-checking XOR which is based on the self-checking XOR-XNOR gate proposed in literature [19]. However, Figure 4 shows that this gate requires eight transistors due to the fact that the inverted inputs should also be produced before entering the gate and these inverted inputs do not exist beforehand in the circuit.

The fourth mistake, as a minor mistake, is that the authors did not account the transistors of the NOT gate in the first bit position. It is obtained based on the transistor count calculation presented in Table 4 from the literature [1].

Table 1 shows the reported number of transistors in [1] and the corrected transistor counts for the related gates and modules. In this table, transistor count of the self-checking FA is computed based on its components

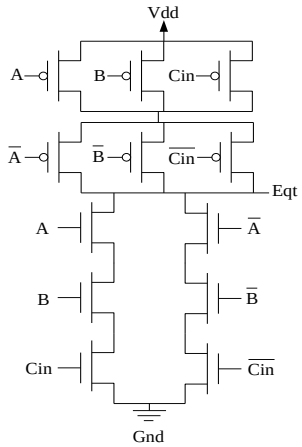

Figure 5. Transistor-level CMOS implementation of Equation (3) as *Eqt* signal

TABLE 1. Transistor count correction of different modules in CSeA

Module	No. of transistors reported in [1]	Corrected No. of transistors
FA	28	30
Equivalence tester (Eqt)	12	18
Self-checking FA	48	56
Self-checking XOR from [19]	4	8
Module for final C_{out} (MOFC)	16	20

including a FA, the equivalence tester and two XNOR gates for the error detection logic in which a four-transistor implementation is assumed for the XNOR gate. In addition, MOFC includes an XOR and a 2-to-1 MUX based on Figure 3, and will have 20 transistors since the self-checking MUX presented by Vasudevan et al. [16] includes 12 transistors and the self-checking XOR requires eight transistors.

2. 4. The Need for Two-pair Two-rail Checkers

As stated by Akbar and Lee [1], the proposed CSeA could remove a tree of two-pair two-rail checkers needed to compare the outputs of each two FAs of the *i*th location in the two RCAs of the self-checking CSeA proposed by Vasudevan et al. [16]. However, two complement outputs of each self-checking MUX in [1] were left intact similar to that of the design in [16]. In addition, the complement outputs of the self-checking XOR-XNOR gates used by Akbar and Lee [1] were left intact, as well. Despite the fact that each of these self-checking components produces two identical outputs when a fault internally occurs, there should be another circuit that produces a general error signal by investigating all existing output pairs. The best way for this integration is the use of two-pair two-rail checkers similar to the ones used Vasudevan et al. [16]. Therefore, for two output pairs of two multiplexers a two-pair two-rail checker is required that is implemented by eight transistors according to the literature [21]. Similarly, two output pairs of two self-checking XOR-XNOR gates require a two-pair two-rail checker. Two-pair two-rail checkers can be arranged in the tree structure, a tree for self-checking multiplexers and a tree for self-checking XOR-XNOR gates. An *m*-bit self-checking CSeA requires (*m*–1) two-pair two-rail checkers for each tree. Thus, the CSeA proposed by Akbar and Lee [1] requires around 15% to 20% more transistors for handling all of the complement outputs.

3. THE PROPOSED SELF-CHECKING CSeA

Based on the entirely self-checking problem described earlier, the corrected self-checking CSeA with the

general size of *n* bits is proposed according to Figure 6. Based on this figure, a small redundant logic is utilized for each non-self-checking gate (NOT or AND) in each bit position. It should be noted that the proposed corrected self-checking CSeA is an *n*-bit single-stage or single-group CSeA which can be used to construct larger CSeAs with the same-size or different-size groups.

In a self-checking design, a single fault is detected if it can change the output. Thus, to make entirely self-checking the first bit position of the CSeA depicted in Figure 6, a fault on the NOT gate must be detected as well as a fault inside the self-checking FA or MUX. This can simply be performed using an ordinary XNOR gate comparing S_0^0 and S_0^1 since these signals should be the complement of each other. To make entirely self-checking the bit positions from the second to the last, the same logic is used in these bit positions to cover the probable faultiness of the AND gates. In fact, in each bit position the complemented output of the AND gate is generated by a NAND gate, and then an ordinary XNOR gate compares these outputs. If these two outputs are the same, the output of the XNOR gate will be set to '1' indicating a fault inside the AND or NAND gate behind it. It is worth mentioning that the XNOR gates used for the comparisons to have the self-checking property is not required; because a fault on an XNOR gate will set its output to '1' remembering that a single fault is guaranteed in a self-checking design. The new error signals E_0 to $E_{(n-1)}$ shown in Figure 6 can enter an OR gate together with the *Ef* signals to produce the overall error detection signal.

The following theorem can be used to prove the self-checking property of the corrected CSeA shown in Figure 6:

Theorem 1. A logic fault occurred inside the CSeA shown in Figure 6 will be detected if it makes an internal or external error. Thus, this CSeA has the self-checking property.

Proof. The internal components of the CSeA shown in Figure 6 can be divided in three parts, the self-checking FAs, multiplexers, and the simple gates. As shown in Section 2.1, a single fault inside a self-checking FA will be detected if it affects one of its components including the internal FA, the equivalence tester logic or one of the XNOR gates producing the error signal *Ef*. In addition, all the multiplexers and XOR gates shown in Figure 6 are the self-checking designs according to Section 2.2, and each of them generates two complement outputs. Therefore, these complement outputs can be checked to detect probable internal errors. The remaining gates are a NOT and an XNOR in the first bit position, and three gates including AND, NAND and XNOR in the other bit positions. In the first bit position, an internal error in the NOT or XNOR will set E_0 to '1'. In the other bit positions (*i* from 1 to *n*–1), an internal error in the AND, NAND or XNOR will definitely set E_i to '1' since the outputs of AND and NAND gates must be the complement of each other. It is worth mentioning that most of internal errors lead to a wrong result (erroneous Sum or C_{out}). However, some internal errors such as the output of a faulty NAND gate do not lead to a wrong result although they activate an error signal.

Based on Theorem 1, the detection of a single logic fault is guaranteed. However, many multiple-fault situations can be detected in this CSeA because of the existence of many internal error indicators.

It should be noted that the delay of the proposed single-stage self-checking CSeA shown in Figure 6 is the same as that of the CSeA based on Figure 3 with the same size. In fact, the new gates and also all the error indicating signals are outside of the critical path.

4. EXPERIMENTAL RESULTS AND EVALUATIONS

In this section, at first, the effect of corrected transistor count on the CSeA design of Akbar and Lee [1] is evaluated along with the area overhead of the proposed corrected self-checking CSeA. Then, the effect of different grouping structures is evaluated when multi-group CSeAs with different sizes are constructed based on the corrected self-checking CSeA, the CSeA design of

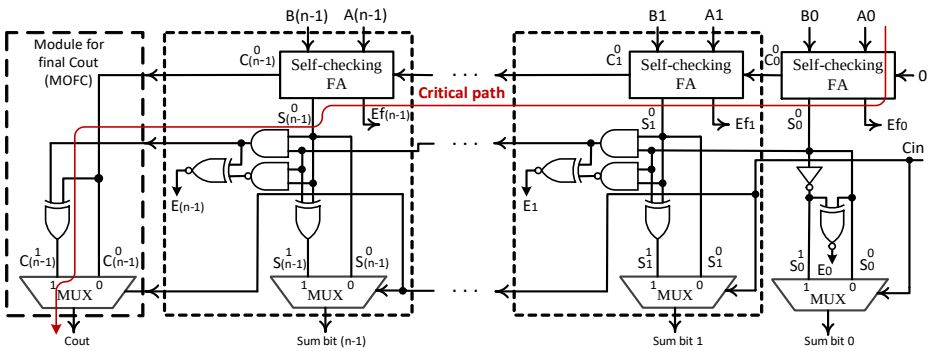

Figure 6. The proposed *n*-bit self-checking CSeA

Akbar and Lee [1] after transistor count correction, and the best of previous self-checking designs. As mentioned before, this investigation has not been performed by Akbar and Lee [1] and only single-group CSeAs have been evaluated.

4. 1. Area Estimation Transistor count has been used for the area estimation of the similar designs in literature [1,8,16]. Thus, in this paper this parameter is used for the comparisons. In addition to the corrected number of transistors presented in Table 1, we should know the transistor count of the remaining gates or components according to Table 2. In this table, similar to the work of Akbar and Lee [1], we assume four transistors for XNOR based on one of its CMOS implementations.

Based on Figure 3 and Tables 1 and 2, the first bit position of the CSeA in the literature [1] with corrected transistor count requires 70 transistors as it includes a self-checking FA, a self-checking MUX, and a NOT gate. But the other bit positions require 82 transistors. Moreover, based on Figure 6, the proposed corrected self-checking CSeA requires four and eight more transistors compared to that of the CSeA in [1], for the first and the remaining bit positions, respectively, because of the extra gates. Thus, the following equations can be used to compute the transistor count of each *n*-bit group in the CSeAs:

$$\text{T.C. of n-bit group after transistor count correction} = \text{T.C. of 1st bit position} + (n-1) \times \text{T.C. of other bit positions} + \text{T.C. of MOFC} = 70+82(n-1)+20 = 82n+8 \quad (5)$$

$$\text{T.C. of n-bit group in the corrected self-checking CSeA} = 74+90(n-1)+20 = 90n+4 \quad (6)$$

where T.C. stands for transistor count.

Table 3 depicts the number of transistors required for the implementation of CSeAs in addition to their overheads. The transistor overheads are obtained compared to the basic non-self-checking CSeA. It should be noted that all CSeAs in this table are single-stage or single-group which can be used to construct larger adders. In addition, for simplicity, extra two-pair two-rail checkers have not been accounted in the corrected results. As stated in Section 2.4, these checkers lead to more transistor count. For more illustration, Figure 7 shows the area overheads in percent based on transistor count for the initial CSeA in [1] and its corrected versions compared to the basic non-self-checking CSeA. As perceived from this figure, the real overheads are much more than the ones reported by Akbar and Lee [1].

4. 2. Effect of Grouping Structures If a CSeA is utilized as the adder part of a processing core, it is used in a multi-group structure. Thus, as none of the grouping structures has been investigated by Akbar and Lee [1], in this section, the area overheads are evaluated with respect to different grouping structures.

4. 2. 1. SQRT Grouping This structure utilizes a different-size grouping in such a way that it leads to the minimum delay. In fact, in a SQRT grouping, the group sizes are determined in such a way that the delay required for the preparation of two sum bits in a group to be almost the same as the delay for the input carry arrived from the previous group. A basic 16-bit CSeA with the SQRT grouping is shown in Figure 8. Based on this figure, the

TABLE 2. Transistor count of the other utilized gates or modules in the self-checking CSeA

Module	No. of transistors
NOT	2
2- input NAND	4
2- input AND	6
XNOR	4
Self-checking MUX from [16]	12

TABLE 3. Comparison of single-group CSeAs based on transistor count

Adder size (bit)	Non-self-checking CSeA	CSeA in [1] with mistakes		CSeA in [1] after transistor count correction		Proposed corrected self-checking CSeA (Figure 6)	
	Transistor count [16]	Transistor count [1]	Transistor overhead [1]	Transistor count	Transistor overhead	Transistor count	Transistor overhead
4	284	286	2	336	52	364	80
6	420	426	6	500	80	544	124
8	556	566	10	664	108	724	168
16	1100	1126	26	1320	220	1444	344
32	2188	2246	58	2632	444	2884	696
64	4364	4486	122	5256	892	5764	1400

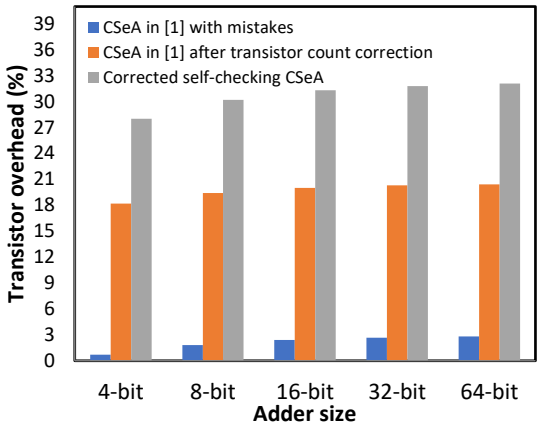

Figure 7. Transistor count overheads of the initial and corrected single-group CSeAs

16-bit SQRT CSeA consists of a single 2-bit RCA in the least significant bits and the groups with the sizes of 2, 3, 4 and 5 bits, respectively. The best SQRT grouping for the 8-bit CSeA includes a single 2-bit RCA in the least significant bits, and two groups with the sizes of 2 and 4 bits, respectively. For the 32-bit SQRT CSeA after the first 2-bit RCA, the groups with the sizes of 2, 3, 4, 6, 7 and 8 bits lead to the minimum delay, and for the 64-bit SQRT CSeA after the first 2-bit RCA, the groups with the sizes of 2, 3, 4, 6, 7, 8, 9, 11 and 12 bits are the best sizes [15,22].

Here, to achieve more real results compared to Section 4.1, a comparison is performed for the SQRT CSeAs between the basic or non-self-checking CSeA, the CSeA in [1] after transistor count correction, the corrected self-checking CSeA in this paper based on [1], and the self-checking CSeA in [8] as the best of predecessor self-checking designs. It should be noted that the design described in [8] is the corrected version of the CSeA design proposed Vasudevan et al. [16]. Thus, the design in [8] has been used for comparisons.

Figure 8 also shows the critical path for delay. The SQRT grouping reduces the delay compared to the same-size grouping by trying to make identical the delay of the multiplexers chain on the shown critical path and the delay of the RCAs in the last group. However, after synthesising, because of the increasing fan-out on the output carries of the groups, the multiplexers chain will have a higher delay. As a result, the corrected self-checking CSeA in this paper has the same delay compared to the self-checking CSeA in [1]. However, both have lower delay compared to the CSeA in [8] since it uses a tree of two-pair two-rail checkers in each group that finally increases the total delay. The exact delay improvement over [8] can be estimated using the method introduced by Fathi et al. [20].

As stated before, Equations (5) and (6) show the transistor count of the *n*-bit groups for the CSeA in [1] after transistor count correction and the corrected self-checking CSeA, respectively. However, these equations can be used to compute the transistor count of multi-group CSeAs with either different-size or same-size grouping because the total transistor count can be obtained by adding the transistor count of all the groups. To compute the transistor count of an *n*-bit group in the non-self-checking CSeA and the self-checking design in [8], some equations similar to Equations (5) and (6) can be derived which lead to $70n+14$ and $78n-4$, respectively. However, it should be noted that the self-checking CSeA in [8] requires some extra transistors equal to $8\times(m-1)$ that should be added to the total transistor count since an *m*-bit multi-group CSeA based on [8] requires $(m-1)$ number of two-pair two-rail checkers, as well. However, for a fair comparison, transistors of extra two-pair two-rail checkers have not been accounted.

Based on the literature [16], each two-pair two-rail checker can be implemented by eight transistors. In addition, each FA of the non-self-checking CSeA and the self-checking design in [8] is implemented by 28 transistors according to Vasudevan et al. [16].

Using the equations obtained for *n*-bit groups of four different CSeAs, the number of required transistors for each adder size is computed. The obtained results are shown in Table 4. For example, in the 8-bit corrected self-checking CSeA, a 2-bit RCA, a 2-bit group and a 4-bit group require 112, 184, and 364 transistors, respectively, which lead to the total transistor count of

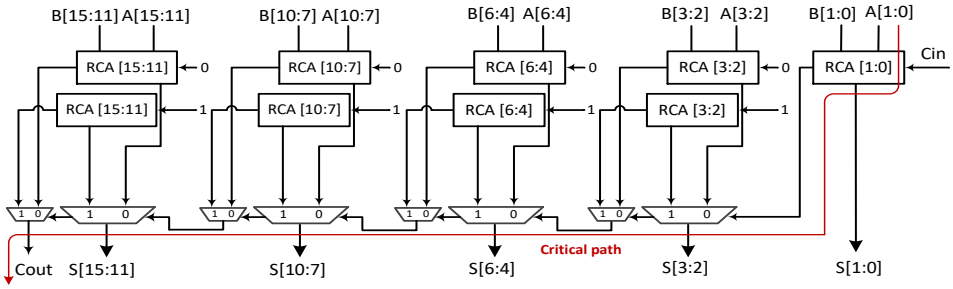

Figure 8. Basic non-self-checking 16-bit CSeA with the SQRT grouping

TABLE 4. Transistor count of different CSeAs utilizing the SQRT grouping

Adder size (bit)	Non-self-checking CSeA	Self-checking design [8]	CSeA in [1] after transistor count correction	Corrected self-checking CSeA
8	504	668	620	660
16	1092	1348	1292	1388
32	2240	2716	2620	2836
64	4522	5456	5268	5728

660. It is worth mentioning, in contrary to the other adders, the first 2-bit RCA in the self-checking design of [8] should be a 2-bit group in all adder sizes shown in Table 4 because of its own architecture to achieve the self-checking property.

For more illustration, Figure 9 depicts transistor overheads of three different SQRT CSeAs compared to the non-self-checking design based on Table 4. According to Figure 9, different from Figure 7, in all adder types the overhead decreases when the adder size increases. In addition, the corrected self-checking CSeA with the SQRT grouping requires lower overheads compared to its single-group counterpart based on Figure 7.

4. 2. 2. Same-size Grouping Another grouping structure utilized in the CSeAs is the same-size grouping in which all the groups and the single RCA in the least significant bits of the adder have the same size. Generally, this structure leads to lower transistor count compared to the SQRT grouping. However, it requires more delay, as well. The best size for the same-size groups is $\sqrt{m}$ for each m-bit CSeA.

Here to achieve the results for the same-size grouping, only the 4-bit and 8-bit sizes are investigated for simplicity, which are the best sizes for 16-bit and 64-bit CSeAs, respectively. Using the equations stated before for different CSeAs, the transistor counts of the CSeAs with the same-size grouping are obtained and shown in Tables 5 and 6 for 4-bit and 8-bit group sizes, respectively. In addition, Figures 10 and 11 depict transistor overheads of three different CSeAs compared to the non-self-checking design based on Tables 5 and 6, respectively. Similar to Figure 9, Figures 10 and 11 show that in all adder types the transistor overhead decreases when the adder size increases. Moreover, an important result is that the corrected self-checking CSeA which is based on the design in [1] is not always better than that

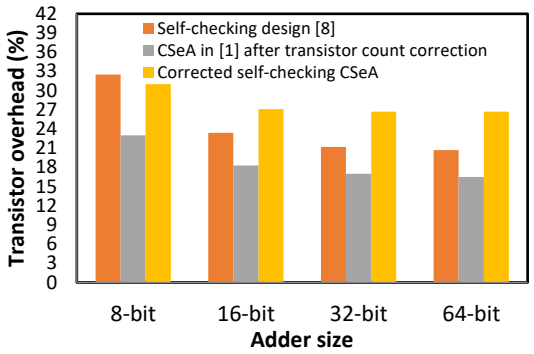

Figure 9. Transistor count overheads of the SQRT CSeAs

TABLE 5. Transistor count of different CSeAs utilizing 4-bit groups.

Adder size (bit)	Non-self-checking CSeA	Self-checking design [8]	CSeA in [1] after transistor count correction	Corrected self-checking CSeA
8	406	672	560	588
16	994	1352	1232	1316
32	2170	2712	2576	2772
64	4522	5432	5264	5684

TABLE 6. Transistor count of different CSeAs utilizing 8-bit groups

Adder size (bit)	Non-self-checking CSeA	Self-checking design [8]	CSeA in [1] after transistor count correction	Corrected self-checking CSeA
16	798	1360	1112	1172
32	1946	2728	2440	2620
64	4242	5464	5096	5516

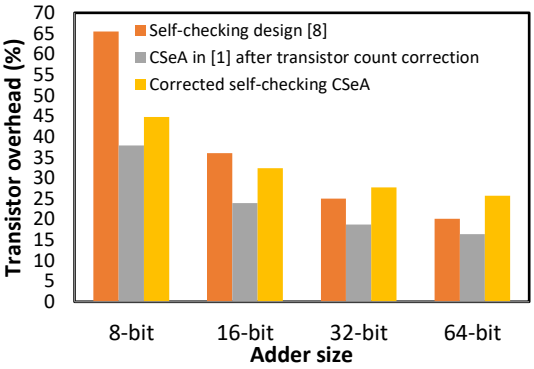

Figure 10. Transistor count overheads of the CSeAs with 4-bit groups

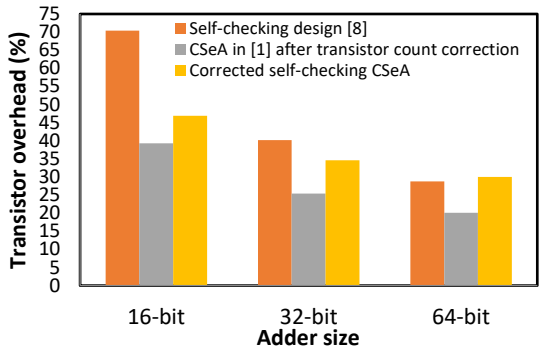

Figure 11. Transistor count overheads of the CSeAs with 8-bit groups

of in [8] with respect to transistor count. In fact, according to Figures 9 to 11 the corrected design is better in smaller sizes, and in larger CSeAs the self-checking design in [8] will require fewer transistors.

7. CONCLUSIONS

In this paper, we showed that the CSeA proposed by Akbar and Lee [1] is not a complete self-checking design and also has some mistakes in counting the number of required transistors. Thus, the transistor counts were re-evaluated, and a new design was proposed to achieve a self-checking CSeA. Both transistor count re-evaluation and design modification show that this CSeA incurs more overheads. Moreover, to obtain more realistic results and overheads, different grouping structures including the same-size and different-size groups were applied on the corrected CSeAs and the best of previous self-checking designs proposed in [8]. The evaluations revealed that the CSeA proposed in [1] after applying all needed corrections requires lower transistor count only in some adder sizes compared to the best of previous self-checking CSeAs.

8. REFERENCES

1. Akbar, M. A. and Lee, J., "Self-repairing adder using fault localization", ***Microelectronics Reliability***, Vol. 54, No. 6-7, (2014), 1443-1451. DOI: 10.1016/j.microrel.2014.02.033.
2. Mukherjee, A. and Dhar, A. S., "Real-time fault-tolerance with hot-standby topology for conditional sum adder", ***Microelectronics Reliability***, Vol. 55, No. 3-4, (2015), 704-712. DOI: 10.1016/j.microrel.2014.12.011.
3. Moradian, H., Lee, J.-A. and Hashmi, A., "Self-repairing radix-2 signed-digit adder with multiple error detection, correction, and fault localization", ***Microelectronics Reliability***, Vol. 63, (2016), 256–266. DOI: 10.1016/j.microrel.2016.06.010.
4. Moradian, H., Lee, J.-A. and Yu, J., "Efficient low-cost fault-localization and self-repairing radix-2 signed-digit adders applying the self-dual concept", ***Journal of Signal Processing Systems***, Vol. 88, No. 3, (2017), 297-309. DOI: 10.1007/s11265-016-1162-1.
5. Valinataj, M., Mohammadnezhad, A. and Nurmi, J., "A low-cost high-speed self-checking carry select adder with multiple-fault detection", ***Microelectronics Journal***, Vol. 81, (2018), 16-27. DOI: 10.1016/j.mejo.2018.08.014.
6. Valinataj, M., "Novel parity-preserving reversible logic array multipliers", ***The Journal of Supercomputing***, Vol. 73, No. 11, (2017), 4843-4867. DOI: 10.1007/s11227-017-2057-z.
7. Eslami-Chalandar, F., Valinataj, M. and Jazayeri, H., "Reversible logic multipliers: novel low-cost parity-preserving designs", ***International Journal of Engineering, Transactions C: Aspects***, Vol. 32, No. 3, (2019), 381-392. DOI: 10.5829/ije.2019.32.03c.05.
8. Akbar, M. A. and Lee, J., "Comments on "Self-Checking Carry-Select Adder Design Based on Two-Rail Encoding"", ***IEEE Transactions on Circuits and Systems-I: Regular Papers***, Vol. 61, No. 7, (2014), 2212-2214. DOI: 10.1109/TCSI.2013.2295930.
9. Nam, M., Choi, Y. and Cho, K., "High-speed and energy efficient carry select adder (CSLA) dominated by carry generation logic", ***Microelectronics Journal***, Vol. 79, (2018), 70-78. DOI: 10.1016/j.mejo.2018.07.001.
10. Mohammadnezhad, A. and Valinataj, M., "Enhancing speed, area and power consumption of carry select adders using a new grouping structure", ***Iranian Journal of Electrical and Computer Engineering***, Vol. 16, No. 4-B, (2019), 310-318.
11. Smith, J. E. and Lam, P. "A theory of totally self-checking system design", ***IEEE Trans. on Computers***, Vol. 32, No. 9, (1983), 831–844. DOI: 10.1109/TC.1983.1676332.
12. Carter, W. C. and Schneider, P. R., "Design of dynamically checked computers", 4th Congress IFIP, Vol. 2, (1968), 878-883.
13. Ramkumar, B. and Kittur, H. M., "Low-power and area-efficient carry-select adder", ***IEEE Transactions on Very Large Scale Integration Systems***, Vol. 20, No. 2, (2012), 371-375. DOI: 10.1109/TVLSI.2010.2101621.
14. Manju, S. and Sornagopal, V., "An efficient SQRT architecture of carry select adder design by common Boolean logic", Int. Conf. Emerging Trends in VLSI, Embedded System, Nano Electronics and Telecommunication System (ICEVENT), (2013), 1-5. DOI: 10.1109/ICEVENT.2013.6496590.
15. Mohanty, B. K. and Patel, S. K., "Area–delay–power efficient carry-select adder", ***IEEE Trans. on Circuits and Systems-II: Express Briefs***, Vol. 61, No. 6, (2014), 418-422. DOI: 10.1109/TCSII.2014.2319695.
16. Vasudevan, D. P., Lala, P. K. and Parkerson, J. P., "Self-checking carry-select adder design based on two-rail encoding", ***IEEE Trans. on Circuits and Systems-I: Regular Papers***, Vol. 54, No. 12, (2007), 2696-2705. DOI: 10.1109/TCSI.2007.910537.
17. Mehrabani, Y. S. and Shafiabadi, M. H., "Symmetrical, low-power, and high-speed 1-bit full adder cells using 32nm carbon nanotube field-effect transistors technology", ***International Journal of Engineering, Transactions A: Basics***, Vol. 28, No. 10, (2015), 1447-1454. DOI: 10.5829/idosi.ije.2015.28.10a.07.
18. Ghorbani, S., Ghorbani, S. and Kashyzadeh, K. R., "Taguchi approach and response surface analysis for design of a high-performance single-walled carbon nanotube bundle interconnects in a full adder", ***International Journal of Engineering, Transactions B: Applications***, Vol. 33, No. 8, (2020), 1598-1607. DOI: 10.5829/ije.2020.33.08b.18.
19. Belgacem, H., Chiraz, K., and Rached, T., "Pass transistor based self-checking full adder", ***International Journal of Computer Theory and Engineering***, Vol. 3, No. 5, (2011), 608-616. DOI: 10.7763/IJCTE.2011.V3.379.
20. Fathi, A, Mashoufi, B., and Azizian, S., "Very fast, high-performance 5-2 and 7-2 compressors in CMOS process for rapid parallel accumulations", ***IEEE Transactions on Very Large***

Scale Integration Systems, Vol. 28, No. 6, (2020), 1403-1412. DOI: 10.1109/TVLSI.2020.2983458.

21. Lo, J. C., "Novel area-time efficient static cmos totally self-checking comparator", ***IEEE Journal of Solid-State Circuits***, Vol. 28, No. 2, (1993), 165-168. DOI: 10.1109/4.192049.

22. Kim, Y. and Kim, L.-S., "64-bit carry-select adder with reduced area", ***Electronics Letters***, Vol. 37, No. 10, (2001), 614-615. DOI: 10.1049/el:20010430.

Persian Abstract

چکیده

در این مقاله، یک جمع‌کننده انتخاب رقم نقلی بهبودیافته با ویژگی خودتست معرفی می‌گردد. با این حال، در ابتدا نشان می‌دهیم که جمع‌کننده انتخاب رقم نقلی ارائه شده در [۱] برخلاف ادعای مطرح شده در آن دارای ویژگی خودتست در همه بخش‌های طرح نیست. سپس، طرح اصلاح شده با ویژگی خودتست که نیازمند سربارهای بیشتری است ارائه می‌گردد. علاوه براین، چندین اشتباه در محاسبه تعداد ترانزیستور طرح پیشنهادی [۱] برای اندازه‌های مختلف جمع‌کننده را بیان می‌نماییم که اصلاح آن‌ها منجر به تعداد ترانزیستور و سربار بیشتر می‌گردد. در پایان، با توجه به این که کارایی یک جمع‌کننده انتخاب رقم نقلی وابسته به ساختار گروه‌بندی استفاده شده در آن است، سربارهای مساحت جمع‌کننده‌های مختلف شامل طرح‌های اصلاح شده و بهترین طرح خودتست قبلی با توجه به گروه‌بندی‌های با اندازه یکسان و اندازه متفاوت مورد ارزیابی قرار خواهد گرفت. این ارزیابی‌ها در مقایسه با ارزیابی‌های گذشته، مقایسه میان جمع‌کننده‌های انتخاب رقم نقلی متفاوت را مناسب‌تر نشان می‌دهند.

International Journal of Engineering

Journal Homepage: www.ije.ir

Splicing Image Forgery Detection and Localization Based on Color Edge Inconsistency using Statistical Dispersion Measures

M. Habibi*[a], H. Hassanpour[b]

[a] *Faculty of Computer Engineering, Payame Noor University of South khorasan, Birjand, Iran*
[b] *Faculty of Computer Engineering and IT, Shahrood University of Technology, Shahrood, Iran*

PAPER INFO

Paper history:
Received 22 September 2020
Received in revised form 9 October 2020
Accepted 30 October 2020

Keywords:
Splicing Forgery Detection
Interquartile Range (IQR) Criterion
Contourlet Transform
Image Chroma
Image Segmentation

ABSTRACT

Nowadays, due to the availability of low-cost and high-resolution digital cameras, and the rapid growth of user-friendly and advanced digital image processing tools, challenges for ensuring authenticity of digital images have been raised. Therefore, development of reliable image authenticity verification techniques has high importance in digital life. In this paper, we proposed a blind image splicing detection method based on color distribution in the neighborhood of edge pixels. First, we extracted edge pixels using contourlet transform. Then, to accurately distinguish the authentic edges from tampered ones, Interquartile Range (IQR) criteria are utilized to illustrate the distribution of Cr and Cr histograms of the spliced boundaries in YCbCr color space. Finally, a segmentation method is used to improve the localization performance and to reduce especially the computational time. The effectiveness of the method has been demonstrated by our experimental results obtained using the Columbia Image Splicing Detection Evaluation (CISED) dataset in terms of specificity and accuracy. It is observed that the proposed method outperforms some state-of-the-art methods. The detection accuracy is approximately 97 with 100% specificity.

***doi**: 10.5829/ije.2021.34.02b.16*

1. INTRODUCTION

In recent years, the rapid development of digital technology has emerged a great demand for forgery detection algorithms. Forgery detection methods can be mainly divided into two categories: active and passive methods [1]. Active methods are based on the procedure of embedding a kind of information in authentic image. Passive methods detect tampering in a given image without any prior knowledge of the authentic image. Passive methods, popularly known as blind methods, can be classified into copy-move (copy–paste or cloning) and splicing forgery detection categories [2, 3]. In copy-move methods, one or more parts of the authentic image are copied and pasted onto other parts of the same image. Therefore, the copied/pasted parts belong to the same image. Image splicing forgery detection method involves composition or merging of more than one image to produce a forged image.

Most of the existing copy-move and splicing forgery detection approaches use a three-major-steps procedure. First, they extract representative features from a given image; then, a suitable classifier is chosen and trained using the features. Finally, the trained model is used to classify given image into authentic and forged image category [1, 3-11].

Some prior works have suggested image splicing detection based on the Camera Response Function (CRF) abnormality [12], and CRF inconsistency [13] in different image regions of the tampered images. Image splicing detection based on run length is proposed in literture [14, 15]. According to He et al. [14], the edge gradient matrix of an image is computed, and followed by approximate run length calculation. High detection accuracy and low computational complexity with fewer features is claimed in this method. Attempts to model the tampered boundary can be frequently found in the splicing detection approaches [16]. Some image splicing

*Corresponding Author's Email: maliheh_habibi@pnu.ac.ir (M. Habibi)

Please cite this article as: M. Habibi, H. Hassanpour, Splicing Image Forgery Detection and Localization Based on Color Edge Inconsistency using Statistical Dispersion Measures, International Journal of Engineering, Transactions B: Applications Vol. 34, No. 02, (2021) 443-451

detection methods based on Hilbert-Huang transform (HHT) and moments of characteristic functions (CF) with wavelet decomposition (IQMs) are introduced. The presence of sharp changes between different regions and surrounding is valuable point in splicing image detection techniques [17].

Inconsistency at splicing boundaries is an important feature in splicing detection technique. Splicing detection based on color edge inconsistency were considered [18, 19]. A color image splicing detection technique based on a grey level co-occurrence matrix (GLCM) of edge image was outlined by Wang et al. [18]. They showed that the Chroma channel (Cb or Cr component)performs better thanYluminance component for detecting tampered edge pixels. So, the splicing edges would be detectable in Chroma channel [18]. Fang et al. [19] proposed a color image splicing detection method based on luminance. This method shows, in HSV color space, Hue histograms of tampered boundaries contain separated double peaks than histograms of Saturation or Value channel. Hue histogram entropy is used to label tampering boundaries.

The reminder of this paper is organized as follows. In section 2, a brief review on contourlet transform is presented. The contourlet transform is used to detect edge pixels carefully. Section 3 describes our proposed splicing detection method by considering inconsistency at tampering boundaries in YCbCr color space. The experimental results and our analysis are reported in section 4. The conclusion of this paper is presented in section 5.

2. The COBTOURLET TRANSFORM

Detection of edge with low error rate has dominant influence on splicing detection algorithms based on tampering boundaries. For this reason, in this paper we use the contourlet transform for splicing detection. The contourlet transform as an improvement for curvelet transform was introduced by Do and Vetterli [20]. The contourlet transform is a directional multi-resolution image representation that is used to show curves and fine details in the image. It also can describe lines and textures of images [21]. The directional multi-resolution representation contourlet takes advantages of the intrinsic geometrical structure of images, and is appropriate for the analysis of the image edges [22]. Figure 1 illustrates a comparison between the basic elements of wavelet and contourlet transforms near a smooth contour. In contourlet transform, the basic elements are oriented at a variety of directions with different aspect ratios [20, 23]. Therefore, it can successfully detect curves in images.

The authentic contourlet transform is a double filter bank structure. It is constructed as a combination of Laplacian pyramid (LP) and directional filter bank (DFB). The LP decomposes image into low pass and high pass sub-bands, iteratively [24]. Each high pass sub-band is then further decomposed by DFB to show directional information [25]. Therefore, the point discontinuities are identified by the LP. Then, a directional filter bank is used to connect these points into linear structure., The contourlet filter bank is shown in Figure 2 [26]. In contourlet transform, there are various directions at each scale, and the number of sub-bands can be determined by the user (see Figure 2).

3. PROPOSED METHOD

As mentioned earlier, we use contourlet transform to extract edges efficiently. First, we extract edges of test image as edge image. Then, further process is performed on the edge image to demonstrate tampered edge pixels. A simplified diagram of the proposed method is illustrated in Figure 3.

3. 1. Abnormality of Tampered Boundary in Color Space

In this section, for appropriately distinguishing authentic edges from tampered ones, we extract features from image edges in color space, especially in chroma channel. Since human eye is more sensitive to luminance than to chrominance [21], most of splicing detection technique only use luminance component of the color space [8]. Mahalakshmi et al. [8] incorporated the inconsistency of color distribution at splicing boundaries which was used to detect forgery in HSV color space, especially from H channel. One may convert RGB to YCbCr color space and apply the forgery method on YCbCr images [18, 27-29]. In this paper, we use YCbCr color space by extracting features from Cb and Cr components (chrominance) rather than Y (luminance). In Figure 4, the Y, Cb and Cr histograms of authentic and tampered edge pixels of an image are shown respectively.

(a) (b)

Figure 1. The basic elements located along smooth curves: (a) wavelet versus (b) contourlet transform [23]

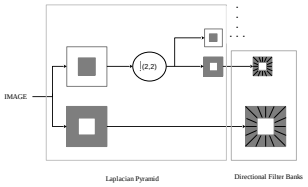

Figure 2. Contourlet filter bank (Pyramidal DFB). The point discontinuities are computed by the Laplacian Pyramid, and then linked into linear structure by Directional Filter Banks [26]

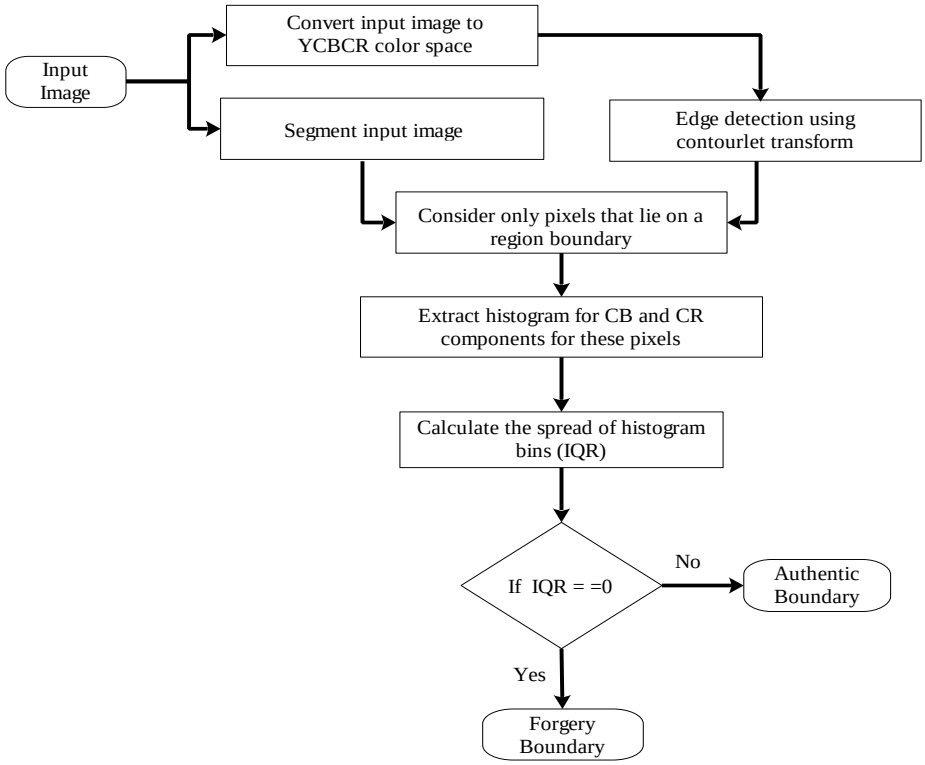

Figure 3. Flow chart of the proposed splicing image detection algorithm

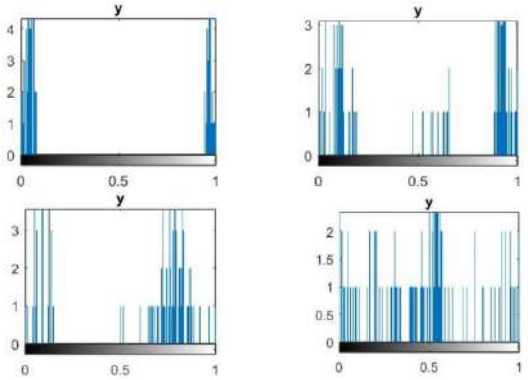

(a)

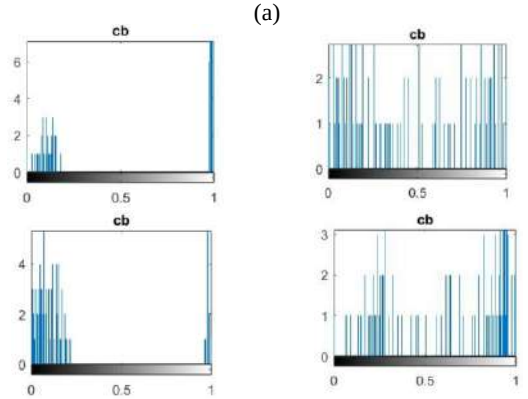

(b)

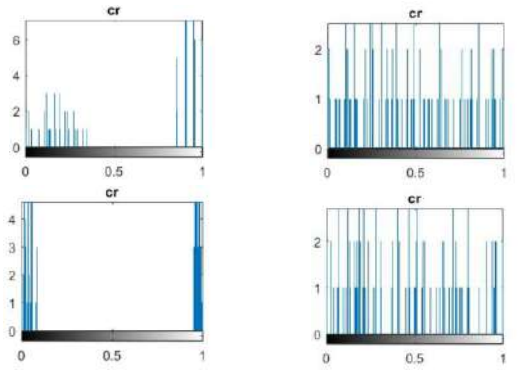

(c)

Figure 4. (a) Y component histograms, (b) Cb component histograms, and (c) Cr component histograms from two tampered (left) and authentic (right) edge pixels of an image

There is a little difference between the Y component histograms of tampered and authentic edge pixels, as shown in Figure 4(a). However, there are considerable differences between histograms of tampered and authentic edge pixel associated with the Cb and Cr components, as shown in Figures 4(b) and 4(c). In tampered edge pixels, the histogram values are left justified or right justified. In other words, the bins are empty in the middle for the Cb and Cr channels. For this end, the dispersion of histogram bins can be used to

discriminate between the forgery and authentic edge pixels. After further investigation on the statistical dispersion criteria, we consider interquartile range (IQR) for splicing edge pixels detection. IQR divides the data set into four equal parts from Q1 to Q3 (Figure 5). Hence, in this paper, we used the distance between Q1 and Q3 to distinguish splicing edge pixel from authentic one (subsections 3.2). For tampered pixels, IQR of Cb and Cr histogram bins is zero.

3. 2. Interquartile Range Criterion As shown above, the histograms associated with the Cb and Cr of the tampered edge pixels have no value for the bins around the middle. The interquartile range, also called the mid-spread or H-spread,is a measure of statistical dispersion, based on dividing a data set into quartiles [30, 31]. Quartiles tell us about the spread of a data set by dividing the data set into four equal parts (quarters). The values that separate parts are denoted by Q1, Q2, and Q3, respectively, which are obtained using the following equation:

$$Q_i = \frac{i*N}{4} + \frac{1}{2} \quad (1)$$

where Q_i is the i^{th} quartile (for $i = 1,3$) and N is the number of histogram bins.

The box shows the interquartile range (the distance between Q1 and Q3), as shown in Figure 5.

The IQR of a set of values is calculated by subtracting the first quartile (Q1) from the third quartile (Q3). The interquartile range is computed using the following equation:

$$IQR = Q_3 - Q_1 \quad (2)$$

For all edge pixels in edge image, IQR of Cb and Cr histogram bins are calculated. Then, each edge pixel with IQR equal to zero is labeled as tampered pixel.

3. 3. Improving the Splicing Detection Method by Segmentation Algorithm The proposed method in this paper considers splicing edge pixels from the image for forgery detection. Hence, edge pixels are extracted in a pre-processing step. Indeed, the input image is initially segmented, then, the border pixels of the segmented regions will be further processed. The pre-processing step slightly improves accuracy of the forgery detection and significantly reduces the execution time for forgery detection. After testing image segmentation methods [32-34], it is observed that the segmentation method does not significantly influence the proposed method's performance. We choose segmentation algorithm for pre-processing stage that is described by Nock et al. [33].

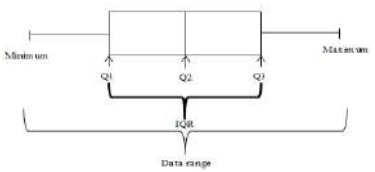

Figure 5. The interquartile range ($IQR = Q_3 - Q_1$)

4. EXPERIMENTAL RESULTS

To demonstrate effectiveness of the proposed approach, experimental results are presented in this section. We have evaluated our proposed approach with a series of experiments. We used the Columbia Image Splicing Detection Evaluation Dataset (CISED) for the experiments [35], which is a benchmark for image splicing detection algorithms. The database contains 183 authentic and 180 tampered color images of sizes range from 757×568 to 1002×66.

The tampered images were constructed from the authentic images. In this dataset, for each tampered image, there is one image that identified as 'edgemask' image. Hence, we use the edgemask image to evaluate our proposed method. The experiments were performed using the MATLAB (R2018b) tools on PC environment (the 64-bit version of Windows 10, Intel® core™ i7-4710HQ CPU, 2.50GHz and 8GB RAM). Figure 6 shows the results of the proposed method for two metrics: variance and the interquartile range. In Figures 6(b) and 6(c), the white pixels indicate the splicing boundary.

The second experiment is performed to test the effect of the segmentation algorithm on our method. By using the segmentation algorithm for preprocessing, the number of pixels are decreased for processing.

Therefore, our method reduces the computational complexity. Time consuming of our proposed approach with segmentation algorithm as preprocessing method for the images shown in Figure 7 is summarized in Table 1.

As seen above, by applying segmentation algorithm, not only the spliced boundaries are detected accurately, but also the time of our approach is decreased obviously, as can be seen in Figure 6 and Table 1. For further comparison, the average run-time of the proposed approach and some methods on CISED dataset are listed in Table 2.

In Table 2, it can be seen that our proposed method is better than the others.

The average time of the proposed approach by using segmentation algorithm is reduced by approximately one third, as shown in Table 2. Since we claim that our method with pre-processing step dramatically reduces the computation time, the time of our method with and without pre-processing step for each image in CISED dataset are shown in Figure 8.

For evaluation of the performance of the proposed method, we demonstrate a detailed analysis of the proposed approach based on evaluation metrics such

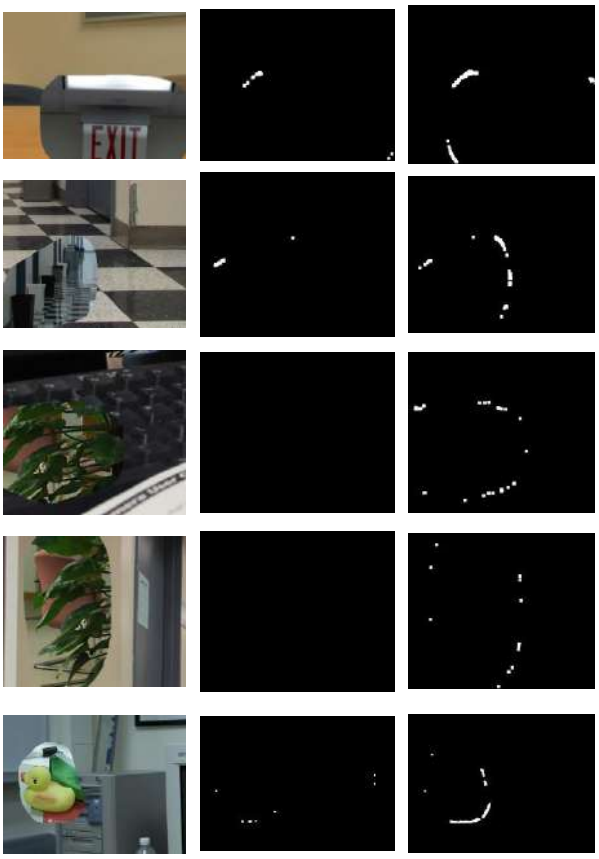

(a) (b) (c)

Figure 6. The sample results of the proposed method. (a) spliced image (b) variance metric (c) IQR metric

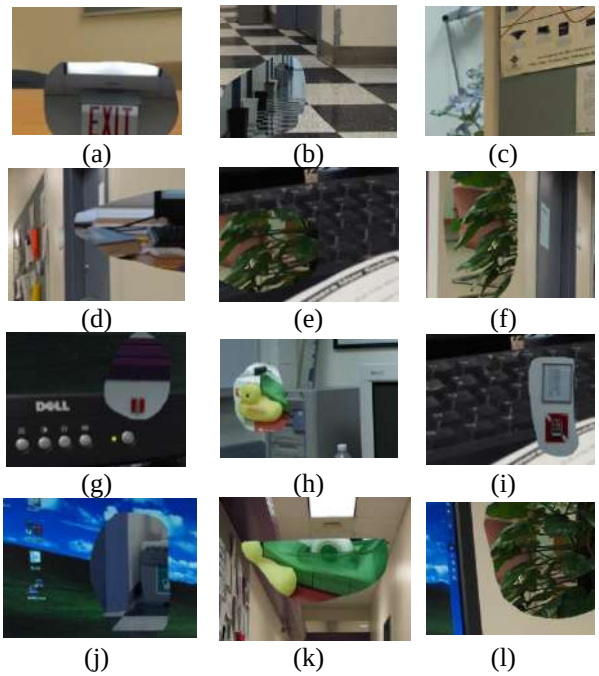

(a) (b) (c)

(d) (e) (f)

(g) (h) (i)

(j) (k) (l)

Figure 7. Some example splicing images of the CISED dataset (used in Table 1)

TABLE 1. Time cost of our proposed method by considering segmentation time (s)

Method Image	Our method (without segmentation)	Our method (with segmentation)
Figure 7.a	551	154
Figure 7.b	699	223
Figure 7.c	118	91
Figure 7.d	369	159
Figure 7.e	1424	244
Figure 7.f	515	180
Figure 7.g	931	89
Figure 7.h	277	176
Figure 7.i	1018	217
Figure 7.j	128	27
Figure 7.k	248	136
Figure 7.l	615	174

as specificity and accuracy by Equations (3) and (4).

$$Specificity\ (TNR) = \frac{TN}{TN+FP} \quad (3)$$

$$\text{Accuracy} = \frac{\text{TP+TN}}{\text{TP+TN+FP+FN}} \quad (4)$$

where TP (True Positive) is the number of spliced pixels which are detected correctly as spliced, FP (False Positive) is the number of authentic pixels which are detected wrongly as spliced, TN (True Negative) is the number of authentic pixels which are correctly detected as authentic and FN (False Negative) is the number of spliced pixels which are wrongly detected as authentic. In Figures 9(a) and 9(b), the specificity and accuracy rate of the proposed method with and without pre-processing step for each image in CISED dataset are shown, respectively.

In CISED dataset, the size of images changes from 757×568 to 1002×66. Hence, this is reason for increasing computation time at the right-hand side of the graph (Figure 8).

TABLE 2. Comparison of run time of various methods on CISED dataset

Methods	Running time (s)
Le-Tien[36] (input-450)	308.76
Le-Tien[36] (input-300)	243.75
Huh et. al.[37]	212.64
Xiao et. al.[38](patch-level CNN)	375.76
Our method (without segmentation)	573.72
Our method (with segmentation)	211.93

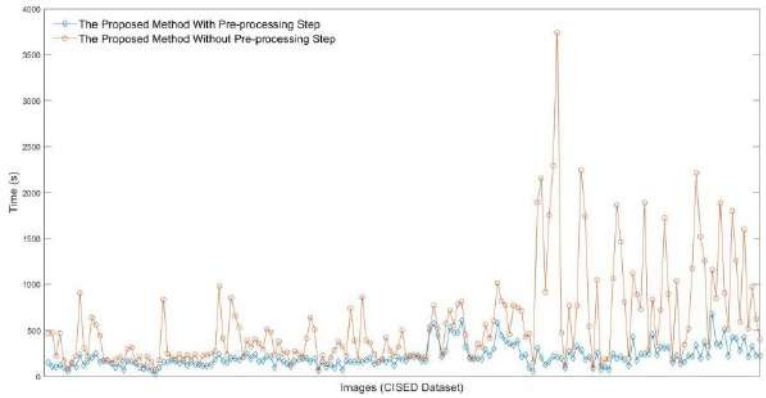

Figure 8. Comparisons time of the proposed approach with (blue solid line with diamond markers) and without (red solid line with circle markers) pre-processing step for each image in CISED dataset

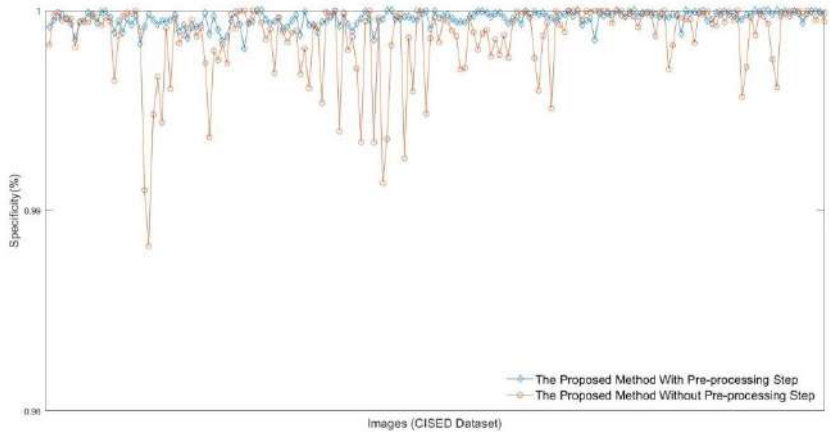

(a)

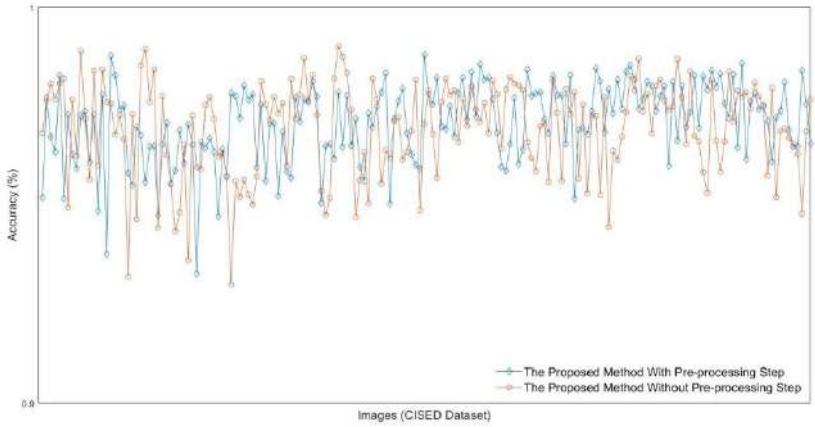

(b)

Figure 9. Comparisons (a) the specificity rate and (b) the accuracy rate of the proposed approach with (blue solid line with diamond markers) and without (red solid line with circle markers) pre-processing step for each image in CISED dataset

To evaluate the performance of our proposed method, the specificity and accuracy rate of our approach and other methods on CISED dataset is illustrated in Table 3. It is clearly seen that the proposed method performs better than some state-of-the-art methods.

According to the results summarized in Table 3, the specificity and accuracy rate of the proposed method are 99.96 and 97.08, on the CISED dataset, respectively. The proposed method has better accuracy rate compared to other methods except the methods proposed by Abrahim

et al. [39], and Jaiswal and Srivastava [40]; but the proposed method has the highest specificity rate.

In Figure 10, the bar graph represents the comparative result of our method with other state-of-the-art methods.

TABLE 3. The comparison of the proposed method with other detection methods in terms of detection accuracy and specificity rate on CISED dataset.

Methods	Specificity	Accuracy
Muhammad et al. [6]	95.53	96.39
Zhang and Zhao [41]	-	91.38
He and Lu [42]	94.32	93.55
Agarwal et. al. [43]	88.63	91.14
Saleh et. al. [44]	-	94.17
Zhao et al. [45]	-	93.14
Jaiswal and Srivastava [40]	98.58	98.80
Park et. al. [46]	-	94.80
Han et. al. [47]	94.58	92.89
Rao et. al.[48]	-	96.38
Zhao et. al [49]	93.75	93.36
Abrahim et. al.[39]	96.07	**99.43**
Huh et. al.[37]	-	87.00
Zhang et. al.[50]	95.33	94.10
Pomari et. al [51]	-	96.00
Our method (without segmentation)	99.86	96.94
Our method (with segmentation)	**99.96**	97.08

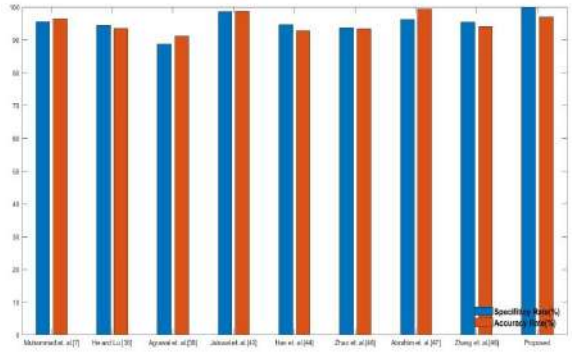

Figure 10. Specificity (blue) and Accuracy (orange) rate of our method and comparative methods

5. CONCLUSIONS

In this paper, we have proposed a splicing image detection approach based on color distribution of edge pixels in chroma space. At the initial stage, the input image is converted to YCbCr space. Next, edge image is extracted using contourlet transform. Finally, for each edge pixel, we use IQR metric of the Cb and Cr histogram bins to distinguish between the tampered and authentic edge pixels. In order to dramatically decrease the computational time and also improve the localization performance, the segmentation algorithm is used for pre-processing stage. Experimental results demonstrate that our proposed method outperforms all comparative the state-of-the-art methods on computational time and specificity rate. We can see the specificity and accuracy of our method are approximately to 100 and 97% on the CISED dataset, respectively.

6. REFERENCES

1. Huynh, T.K., Huynh, K.V., Le-Tien, T. and Nguyen, S.C., "A survey on image forgery detection techniques", in The 2015 IEEE RIVF International Conference on Computing & Communication Technologies-Research, Innovation, and Vision for Future (RIVF), IEEE. 71-76. DOI: 10.1109/RIVF.2015.7049877
2. Gill, N.K., Garg, R. and Doegar, E.A., "A review paper on digital image forgery detection techniques", in 2017 8th International Conference on Computing, Communication and Networking Technologies (ICCCNT), IEEE. 1-7. DOI: 10.1109/ICCCNT.2017.8203904
3. Li, X., Jing, T. and Li, X., "Image splicing detection based on moment features and hilbert-huang transform", in 2010 IEEE International Conference on Information Theory and Information Security, IEEE. 1127-1130. DOI: 10.1109/ICITIS.2010.5689754
4. De Carvalho, T.J., Riess, C., Angelopoulou, E., Pedrini, H. and de Rezende Rocha, A., "Exposing digital image forgeries by illumination color classification", ***IEEE Transactions on Information Forensics and Security***, Vol. 8, No. 7, (2013), 1182-1194. DOI: 10.1109/TIFS.2013.2265677
5. Mushtaq, S. and Mir, A.H., "Novel method for image splicing detection", in 2014 International Conference on Advances in Computing, Communications and Informatics (ICACCI), IEEE. 2398-2403. DOI: 10.1109/ICACCI.2014.6968386
6. Muhammad, G., Al-Hammadi, M.H., Hussain, M. and Bebis, G., "Image forgery detection using steerable pyramid transform and local binary pattern", ***Machine Vision and Applications***, Vol. 25, No. 4, (2014), 985-995. DOI: https://doi.org/10.1007/s00138-013-0547-4
7. Farid, H., "A survey of image forgery detection", ***IEEE Signal Processing Magazine***, Vol. 2, No. 26, (2009), 16-25.
8. Mahalakshmi, S.D., Vijayalakshmi, K. and Priyadharsini, S., "Digital image forgery detection and estimation by exploring basic image manipulations", ***Digital Investigation***, Vol. 8, No. 3-4, (2012), 215-225. DOI: https://doi.org/10.1016/j.diin.2011.06.004
9. Cao, G., Zhao, Y. and Ni, R., "Edge-based blur metric for tamper detection", ***Journal of Information Hiding and Multimedia Signal Processing***, Vol. 1, No. 1, (2010), 20-27.
10. Kirchner, M. and Fridrich, J., "On detection of median filtering in digital images", in Media forensics and security II, International Society for Optics and Photonics. Vol. 7541, 754110. DOI: https://doi.org/10.1117/12.839100
11. Birajdar, G.K. and Mankar, V.H., "Digital image forgery detection using passive techniques: A survey", ***Digital Investigation***, Vol. 10, No. 3, (2013), 226-245. DOI: https://doi.org/10.1016/j.diin.2013.04.007

12. Lin, Z., Wang, R., Tang, X. and Shum, H.-Y., "Detecting doctored images using camera response normality and consistency", in 2005 IEEE Computer Society Conference on Computer Vision and Pattern Recognition (CVPR'05), IEEE. Vol. 1, 1087-1092. DOI: 10.1109/CVPR.2005.125
13. Hsu, Y.-F. and Chang, S.-F., "Detecting image splicing using geometry invariants and camera characteristics consistency", in 2006 IEEE International Conference on Multimedia and Expo, IEEE. 549-552. DOI: 10.1109/ICME.2006.262447
14. He, Z., Sun, W., Lu, W. and Lu, H., "Digital image splicing detection based on approximate run length", ***Pattern Recognition Letters***, Vol. 32, No. 12, (2011), 1591-1597. DOI: https://doi.org/10.1016/j.patrec.2011.05.013
15. Dong, J., Wang, W., Tan, T. and Shi, Y.Q., "Run-length and edge statistics based approach for image splicing detection", in International workshop on digital watermarking, Springer. 76-87. DOI: https://doi.org/10.1007/978-3-642-04438-0_7
16. Zhou, Z.-p. and Zhang, X.-x., "Image splicing detection based on image quality and analysis of variance", in 2010 2nd International Conference on Education Technology and Computer, IEEE. Vol. 4, 4-242-V244-246. DOI: 10.1109/ICETC.2010.5529692
17. Qazi, T., Hayat, K., Khan, S.U., Madani, S.A., Khan, I.A., Kołodziej, J., Li, H., Lin, W., Yow, K.C. and Xu, C.-Z., "Survey on blind image forgery detection", ***IET Image Processing***, Vol. 7, No. 7, (2013), 660-670. DOI: 10.1049/iet-ipr.2012.0388
18. Wang, W., Dong, J. and Tan, T., "Effective image splicing detection based on image chroma", in 2009 16th IEEE International Conference on Image Processing (ICIP), IEEE. 1257-1260. DOI: 10.1109/ICIP.2009.5413549
19. Fang, Z., Wang, S. and Zhang, X., "Image splicing detection using color edge inconsistency", in 2010 International Conference on Multimedia Information Networking and Security, IEEE. 923-926. DOI: 10.1109/MINES.2010.196
20. Do, M.N. and Vetterli, M., "Contourlets: A directional multiresolution image representation", in Proceedings. International Conference on Image Processing, IEEE. Vol. 1, I-I. DOI: 10.1109/ICIP.2002.1038034
21. Barani, M.J., Ayubi, P., Jalili, F., Valandar, M.Y. and Azariyun, E., "Image forgery detection in contourlet transform domain based on new chaotic cellular automata", ***Security and Communication Networks***, Vol. 8, No. 18, (2015), 4343-4361. DOI: https://doi.org/10.1002/sec.1365
22. Ma, S.-f., Zheng, G.-f., Jin, L.-x., Han, S.-l. and Zhang, R.-f., "Directional multiscale edge detection using the contourlet transform", in 2010 2nd International Conference on Advanced Computer Control, IEEE. Vol. 2, 58-62. DOI: 10.1109/ICACC.2010.5487180
23. Do, M.N. and Vetterli, M., "The contourlet transform: An efficient directional multiresolution image representation", ***IEEE Transactions on Image Processing***, Vol. 14, No. 12, (2005), 2091-2106. DOI: 10.1109/TIP.2005.859376
24. Lee, J., "Advanced electrical and electronics engineering, Springer, (2011).
25. Sencar, H.T., Velastin, S., Nikolaidis, N. and Lian, S., "Intelligent multimedia analysis for security applications, Springer, Vol. 282, (2010).
26. Do, M.N. and Vetterli, M., "Framing pyramids", ***IEEE Transactions on Signal Processing***, Vol. 51, No. 9, (2003), 2329-2342. DOI: 10.1109/TSP.2003.815389
27. Luo, W., Huang, J. and Qiu, G., "Robust detection of region-duplication forgery in digital image", in 18th International Conference on Pattern Recognition (ICPR'06), IEEE. Vol. 4, 746-749. DOI: 10.1109/ICPR.2006.1003
28. Hussain, M., Muhammad, G., Saleh, S.Q., Mirza, A.M. and Bebis, G., "Image forgery detection using multi-resolution weber local descriptors", in Eurocon 2013, IEEE. 1570-1577. DOI: 10.1109/EUROCON.2013.6625186
29. Zhao, J. and Guo, J., "Passive forensics for copy-move image forgery using a method based on dct and svd", ***Forensic Science International***, Vol. 233, No. 1-3, (2013), 158-166. DOI: https://doi.org/10.1016/j.forsciint.2013.09.013
30. Upton, G. and Cook, I., "Understanding statistics, Oxford University Press, (1996).
31. Zwillinger, D. and Kokoska, S., "Crc standard probability and statistics tables and formulae, Crc Press, (1999).
32. Yang, A.Y., Wright, J., Ma, Y. and Sastry, S.S., "Unsupervised segmentation of natural images via lossy data compression", ***Computer Vision and Image Understanding***, Vol. 110, No. 2, (2008), 212-225. DOI: https://doi.org/10.1016/j.cviu.2007.07.005
33. Nock, R. and Nielsen, F., "Statistical region merging", ***IEEE Transactions on Pattern Analysis and Machine Intelligence***, Vol. 26, No. 11, (2004), 1452-1458. DOI: 10.1109/TPAMI.2004.110
34. Arbelaez, P., Maire, M., Fowlkes, C. and Malik, J., "Contour detection and hierarchical image segmentation", ***IEEE Transactions on Pattern Analysis and Machine Intelligence***, Vol. 33, No. 5, (2010), 898-916. DOI: 10.1109/TPAMI.2010.161
35. Columbia, D., *Research lab: Columbia image splicing detection evaluation dataset*. 2004.
36. Le-Tien, T., Phan-Xuan, H., Nguyen-Chinh, T. and Do-Tieu, T., "Image forgery detection: A low computational-cost and effective data-driven model", ***International Journal of Machine Learning and Computing***, Vol. 9, No. 2, (2019). DOI: 10.18178/ijmlc.2019.9.2.784
37. Huh, M., Liu, A., Owens, A. and Efros, A.A., "Fighting fake news: Image splice detection via learned self-consistency", in Proceedings of the European Conference on Computer Vision (ECCV). 101-117.
38. Xiao, B., Wei, Y., Bi, X., Li, W. and Ma, J., "Image splicing forgery detection combining coarse to refined convolutional neural network and adaptive clustering", ***Information Sciences***, Vol. 511, (2020), 172-191. DOI: https://doi.org/10.1016/j.ins.2019.09.038
39. Abrahim, A.R., Rahim, M.S.M. and Sulong, G.B., "Splicing image forgery identification based on artificial neural network approach and texture features", ***Cluster Computing***, Vol. 22, No. 1, (2019), 647-660.
40. Jaiswal, A.K. and Srivastava, R., "A technique for image splicing detection using hybrid feature set", ***Multimedia Tools and Applications***, (2020), 1-24.
41. Zhang, Y., Zhao, C., Pi, Y. and Li, S., Revealing image splicing forgery using local binary patterns of dct coefficients, in Communications, signal processing, and systems. 2012, Springer.181-189. DOI: https://doi.org/10.1007/978-1-4614-5803-6_19
42. He, Z., Lu, W., Sun, W. and Huang, J., "Digital image splicing detection based on markov features in dct and dwt domain", ***Pattern Recognition***, Vol. 45, No. 12, (2012), 4292-4299. DOI: https://doi.org/10.1016/j.patcog.2012.05.014
43. Agarwal, S. and Chand, S., "Image forgery detection using multi scale entropy filter and local phase quantization", ***International Journal of Image, Graphics & Signal Processing***, Vol. 7, No. 10, (2015). DOI: 10.5815/ijigsp.2015.10.08
44. Saleh, S.Q., Hussain, M., Muhammad, G. and Bebis, G., "Evaluation of image forgery detection using multi-scale weber local descriptors", in International Symposium on Visual Computing, Springer. 416-424. DOI: https://doi.org/10.1007/978-3-642-41939-3_40

45. Zhao, X., Li, S., Wang, S., Li, J. and Yang, K., "Optimal chroma-like channel design for passive color image splicing detection", ***EURASIP Journal on Advances in Signal Processing***, Vol. 2012, No. 1, (2012), 240. DOI: https://doi.org/10.1186/1687-6180-2012-240

46. Park, T.H., Han, J.G., Moon, Y.H. and Eom, I.K., "Image splicing detection based on inter-scale 2d joint characteristic function moments in wavelet domain", ***EURASIP Journal on Image and Video Processing***, Vol. 2016, No. 1, (2016), 30.

47. Han, J.G., Park, T.H., Moon, Y.H. and Eom, I.K., "Efficient markov feature extraction method for image splicing detection using maximization and threshold expansion", ***Journal of Electronic Imaging***, Vol. 25, No. 2, (2016), 023031. DOI: https://doi.org/10.1117/1.JEI.25.2.023031

48. Rao, Y. and Ni, J., "A deep learning approach to detection of splicing and copy-move forgeries in images", in 2016 IEEE International Workshop on Information Forensics and Security (WIFS), IEEE. 1-6. DOI: 10.1109/WIFS.2016.7823911

49. Zhao, X., Wang, S., Li, S. and Li, J., "Passive image-splicing detection by a 2-d noncausal markov model", ***IEEE Transactions on Circuits and Systems for Video Technology***, Vol. 25, No. 2, (2014), 185-199. DOI: 10.1109/TCSVT.2014.2347513

50. Zhang, Q., Lu, W. and Weng, J., "Joint image splicing detection in dct and contourlet transform domain", ***Journal of Visual Communication and Image Representation***, Vol. 40, (2016), 449-458. DOI: https://doi.org/10.1016/j.jvcir.2016.07.013

51. Pomari, T., Ruppert, G., Rezende, E., Rocha, A. and Carvalho, T., "Image splicing detection through illumination inconsistencies and deep learning", in 2018 25th IEEE International Conference on Image Processing (ICIP), IEEE. 3788-3792. DOI: 10.1109/ICIP.2018.8451227

Persian Abstract

چکیده

در سال‌های اخیر، دوربین‌های دیجیتال با تفکیک‌پذیری بالا و قیمت پائین می‌توانند در دسترس همگی قرار گیرند. از طرف دیگر، در زمینه پردازش تصاویر دیجیتالی، ابزارهای قدرتمند و کاربرپسند به سرعت توسعه می‌یابند. این عوامل باعث شده است که چالش‌هایی برای اطمینان از صحت تصاویر بدست آمده، به وجود آید. لذا، توسعه روش هایی برای تایید اعتبار یک تصویر، نقش به سزایی در زندگی دیجیتالی امروزی دارد. در این مقاله، یک روش تشخیص جعل بر اساس توزیع رنگ در همسایگی پیکسل های لبه پیشنهاد می‌شود. ابتدا، پیکسل‌های لبه با استفاده از تبدیل کونتورلت استخراج می‌شوند. سپس، به ازای هر پیکسل لبه، پیکسل‌های همسایگی آن نیز در نظر گرفته شده و هیستوگرام مولفه‌های Cb و Cr از فضای رنگ YCbCr ترسیم می‌شود. در این مقاله، برای شناسایی پیکسل جعلی از پیکسل واقعی، از معیار دامنه چارکی (IQR) برای تعیین نحوه توزیع میله‌های هیستوگرام‌های Cb و Cr استفاده می‌شود. در نهایت، برای کاهش زمان محاسباتی و افزایش دقت روش پیشنهادی در تشخیص مکان جعل، از الگوریتم قطعه‌بندی به‌عنوان یک گام پیش پردازش استفاده می‌شود. دو معیار accuracy و specificity، برای ارزیابی میزان کارایی روش پیشنهادی مورد استفاده قرار می‌گیرد. نتایج اعمال روش پیشنهادی بر پایگاه تصاویر CISED نشان می‌دهد که روش پیشنهادی بهتر از روش‌های مطرح در این زمینه عمل کرده است و accuracy وspecificity روش پیشنهادی به ترتیب ۹۷ درصد و نزدیک ۱۰۰ درصد است.

International Journal of Engineering

Journal Homepage: www.ije.ir

A Clustering-based Approach for Features Extraction in Spectro-temporal Domain using Artificial Neural Network

N. Esfandian*[a], K. Hosseinpour[b]

[a] *Department of Electrical Engineering, Qaemshahr Branch, Islamic Azad University, Qaemshahr, Iran*
[b] *Department of Artificial Intelligence and Robotics, Aryan Institute of Higher Education and Technology, Babol, Iran*

PAPER INFO

Paper history:
Received 07 October 2020
Received in revised form 03 November 2020
Accepted 05 November 2020

Keywords:
Artificial Neural Network
Auditory Model
Clustering
Feature Extraction
Spectro-temporal Features

ABSTRACT

In this paper, a new feature extraction method is presented based on spectro-temporal representation of speech signal for phoneme classification. In the proposed method, an artificial neural network approach is used to cluster spectro-temporal domain. Self-organizing map artificial neural network (SOM) was applied to clustering of features space. Scale, rate and frequency were used as spatial information of each point and the magnitude component was used as similarity attribute in clustering algorithm. Three mechanisms were considered to select attributes in spectro-temporal features space. Spatial information of clusters, the magnitude component of samples in spectro-temporal domain and the average of the amplitude components of each cluster points were considered as secondary features. The proposed features vectors were used for phonemes classification. The results demonstrate that a significant improvement is obtained in classification rate of different sets of phonemes in comparison to previous clustering-based methods. The obtained results of new features indicate the system error is compensated in all vowels and consonants subsets in compare to weighted K-means clustering.

doi: *.5829/ije.2021.34.02b.17*

1. INTRODUCTION

Spectro-temporal representation of the speech signal is considered as one of the important approaches to increase efficiency of speech recognition [1, 2]. One of the limitations of this model is its high dimensional output [3–5]. The output of auditory model is four-dimensional array including the scale, rate, frequency, and time. In recent years, auditory model was used to extract the spectro-temporal features in many applications of speech processing [6–13]. Because of large dimensions of spectro-temporal features space, selection of discriminative features is a crucial task for phoneme classification. Therefore, in recent researches, clustering methods were used to reduce dimension of spectro-temporal features space and extract valuable discriminative information of speech signal. In these methods, output of this model was considered as the primary features vectors and clustered using Gaussian Mixture Model and weighted K-Means [14–17]. Then, the mean vectors and covariance matrices elements of the clusters are considered as secondary features in each speech frame. However, the high computational cost of these methods limited their usability in practical applications. In this article a new method is proposed to extract the discriminative features in spectro-temporal domain. The specific contributions of the manuscript can be described as follows:

In the proposed method, the artificial neural network was used for clustering of spectro-temporal domain according to the capability of artificial neural networks to cluster high-dimensional data [18–21]. The scale, the rate, the frequency and magnitude of each point were assumed as primary features in input vector to cluster using the artificial neural network. The mean vectors, covariance matrices of clusters and the average of the amplitude components of each cluster points were considered as attributes in the secondary feature vectors. The proposed secondary feature vectors were used to classify different categories of phonemes.

*Corresponding Author Institutional Email: *na_esfandian@Qaemiau.ac.ir* (N. Esfandian)

Please cite this article as: N. Esfandian, K. Hosseinpour, A Clustering-based Approach for Features Extraction in Spectro-temporal Domain using Artificial Neural Network, International Journal of Engineering, B: Applications Vol. 34, No. 02, (2021) 452-457

Clustering-based spectro-temporal feature extraction method is briefly discussed in section 2. The proposed secondary feature extraction using the artificial neural network in spectro-temporal domain is presented in section 3. In section 4, the proposed features are experimentally evaluated for phoneme classification of English languages and compared to existing clustering-based approaches. Finally, the paper is concluded in section 5.

2. SECONDARY FEATURES EXTRACTION METHOD IN SPECTRO-TEMPORAL DOMAIN USING CLUSTERING METHOD

The auditory model has two main stages. In the primary stage of this model, an auditory spectrogram was extracted for the input acoustic signal. In the cortical stage, the spectro-temporal features of speech were extracted by applying a set of two dimensional spectro-temporal receptive field (STRF) filters on the spectrogram. The output of cortical stage of auditory model is 4-dimensional vector (scale, frequency, and time). In the clustering-based feature extraction method, the multi-dimensional cortical output was clustered using Gaussian Mixture Model (GMM) and Weighted K-Means (WKM) clustering algorithm. Then, attributes of the clusters such as components of mean and variance vectors were considered as secondary features. Finally, the extracted secondary features were sorted using their estimated weight in the clustering algorithm.

3. SPECTRO-TEMPORAL FEATURES EXTRACTION USING ARTIFICIAL NEURAL NETWORK

In recent researches, the artificial neural network was used to extract the secondary features in various application of speech processing [22–24]. In the proposed feature extraction method, the artificial neural network was used for clustering of spectro-temporal space. The overall architecture of the proposed method illustrated in Figure 1. As it is shown, in the first stage, the auditory spectrogram of the speech signal was computed. Then, in the cortical stage, spectro-temporal modulations were estimated. The auditory spectrogram was obtained using an infinite impulse response (IIR) filter bank with 128 frequency channels between 180 and 7246 Hz at the resolution of 24 channels per octave. In addition, a time constant of 8ms was used for the leaky time integration and filter-bank outputs were sampled every 4 ms to compute the auditory spectrogram. Temporal parameter of the filters (rate) ranging from 2 to 32 Hz and spectral parameter of the filters (scale) ranging from 0.25 to 8 cycle/octave are considered to represent the spectro-temporal modulations of the speech signal. In the next stage, the primary feature vector was extracted using thresholding techniques. The spatial information (scale, rate and frequency) and the magnitude of each point were considered in primary feature vectors. Therefore, primary feature vectors, $v_i = (r_i, s_i, f_i, |A_i|)$, were four-dimensional vector. In this vector, r_i denotes the rate, s_i is the scale, f_i is the frequency and $|A_i|$ is magnitude component of each point in spectro-temporal space. These vectors were clustered by the artificial neural network. Eventually, the secondary feature vectors were extracted using the output data of artificial neural network, and used for phoneme classification. In the primary feature extraction algorithm, the amplitude of each sample in spectro-temporal feature space ($|A_i|$) was compared with the maximum amplitude value ($|A_{max}|$) in a speech frame. If the amplitude of each point was higher than an empirically determined threshold value, this point was considered in input vector for clustering. Therefore, valuable discriminative information was only considered in the clustering process. In the proposed secondary feature extraction method, self-organizing map artificial neural network (SOM) was used for clustering of spectro-temporal feature space. SOM is the unsupervised networks. Primary feature vectors, v_i was 4-dimensional vector. Therefore, the input vector of SOM network was a $N \times 4$ matrix which contains N four-dimensional samples. As a result, N four-dimensional input was applied to the SOM network to cluster spectro-temporal domain. In the previous research, three clusters were used for clustering of spectro-temporal feature space in each frame. In this study, assuming three clusters in each frame, three neurons were considered for the artificial neural networks. Block diagram of SOM network is shown in Figure 2. Three-dimensional representation of extracted clusters using SOM network for /g/ phoneme is shown in Figure 3.

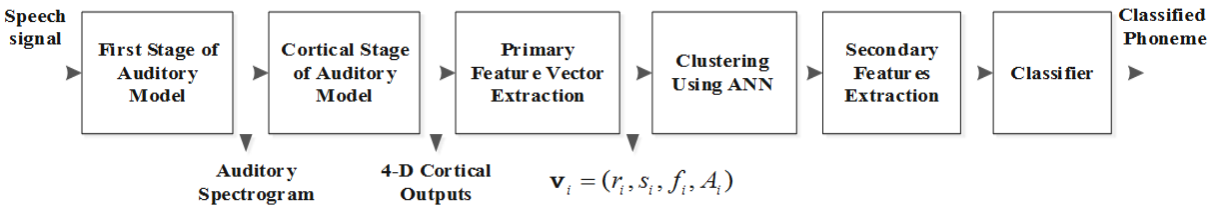

Figure 1. The overall architecture of proposed feature extraction method

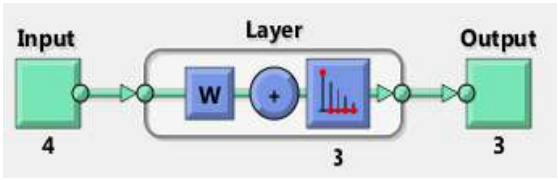

Figure 2. Block diagram of SOM network

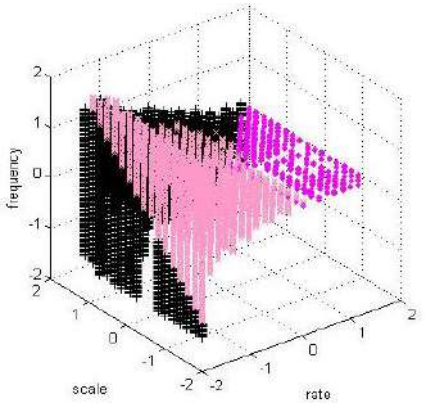

Figure 3. Representation of extracted clusters for /g/ phoneme using SOM network

3. 1. Clustering-based Features Extraction using SOM Network in Spectro-temporal Domain In proposed secondary feature extraction method, three mechanisms were considered for feature selection in spectro-temporal domain. In the first mechanism, 18 components consist of mean vector $\left(\mu_i = \left(\mu_{r_i}, \mu_{s_i}, \mu_{f_i}\right)\right)$ and variance vector of clusters $\left(\sigma_i = \left(\sigma_{r_i}, \sigma_{s_i}, \sigma_{f_i}\right)\right)$ were considered ($V_{SOM,18} = (\mu_i, \sigma_i)$). Spatial information of clusters was considered in this mechanism. The attributes of clusters were sorted with respect to their energy in spectro-temporal space. In the second mechanism, 24 attributes were considered in secondary features vectors ($V_{SOM,24}$). In this feature vector, mean and variance vectors of clusters were also sorted based on energy measure. Each mean or variance vector consists of four components as $\mu_i = \left(\mu_{r_i}, \mu_{s_i}, \mu_{f_i}, \mu_{A_i}\right)$ and $\sigma_i = \left(\sigma_{r_i}, \sigma_{s_i}, \sigma_{f_i}, \sigma_{A_i}\right)$. In this mechanism, spatial information and the magnitude component of each point were considered in the secondary features vectors. In the third feature selection mechanism, secondary features vectors consist of 27 attributes ($V_{SOM,27}$). In this mechanism, in addition to 4-dimensional information of clusters, the average of the amplitude components of each cluster points were considered as attribute. The average of the amplitude components of each cluster, $\bar{w}$, was calculated as follows:

$$\overline{W} = \frac{\sum_{i=1}^{n} w_i}{N} \quad (1)$$

where, w_i denotes the weight of each point (magnitude component) in spectro-temporal domain. n and N are the number of clusters and the number of points in each cluster.

4. EXPERIMENTAL RESULTS

To evaluate the performance of the proposed method, all types of secondary features vectors (secondary features vectors include 18, 24 and 27 attributes), were used for phonemes classification. The proposed features were evaluated on clean speech from TIMIT database [25]. In this study, SVM classifier was used for phoneme classification [26]. In addition, the optimum values of RBF-SVM parameters (kernel parameter γ and miss-classification cost *C*) were empirically determined using a grid search strategy to optimize the classification rate.

4. 1. Classification Test The classification error rate of phonemes (/ b /, / d /, / g /) was tabulated for some dialects of TIMIT database using the proposed features in compare to Mel-frequency cepstral coefficients (MFCC) [27] and WKM-based feature vectors (see Table 1).

It is obvious that, the classification results were improved using the proposed features in compare to MFCC and WKM-based features. Also, it is observed that the proposed feature vector consisting of mean and variance vectors of clusters and the average of the amplitude components, $V_{SOM,27}$, gave considerable better results for phoneme classification. Therefore, using the average of the amplitude components of each cluster in the secondary feature vectors improves the phoneme classification rate. Therefore, most of experiments were performed using proposed feature vector including 27 attributes ($V_{SOM,27}$). Confusion matrix for classification of (/b/, /d/, /g/) phonemes using WKM-based features and proposed features in were shown in Tables 2 and 3. It was found that the phoneme /d/ was recognized better than in compare to other phonemes and the greatest error rate was observed for the phoneme /b/ which was recognized incorrectly as /d/.

Simulation was down using MATLAB. Processing time evaluation of proposed features in comparison of MFCC and WKM-based features was shown in Table 4.

TABLE 1. /b/,/d/,/g/ phonemes classification error rate

Dialect	MFCC	WKM	$V_{SOM,18}$	$V_{SOM,24}$	$V_{SOM,27}$
Dialect1	32.1	25.9	24.9	23.3	22.8
Dialect2	35.6	29.2	31.6	29.0	28.1
Dialect3	35.7	28.4	28.1	26.2	26.7
Dialect7	35.1	29.3	27.4	28.4	28.6
Average	35.4	28.2	28.0	26.7	26.6

TABLE 2. Confusion matrix for phoneme classification using WKM-based features

		Recognized		
		b	**d**	**g**
Corrected	**b**	66.9	27.7	5.4
	d	10.1	82.3	7.6
	g	14.9	16.8	68.4

TABLE 3. Confusion matrix for phoneme classification using proposed features

		Recognized		
		b	**d**	**g**
Corrected	**b**	66.5	32.2	1.3
	d	8.9	83.3	7.8
	g	9.1	13.6	77.3

TABLE 4. Processing time evaluation of proposed features in comparison of WKM-based features

	MFCC	**WKM**	$V_{SOM,18}$	$V_{SOM,24}$	$V_{SOM,27}$
Processing Time (s)	49.1	45.7	32.1	34.5	36.8

As it can be observed, processing time of proposed feature extraction method is less than other features. Phoneme classification results in using the proposed features on different categories of phonemes were compared to multidimensional features (MDF) [28], MFCC and WKM clustering-based features as shown in Table 5. In consonant and vowel subsets, the classification error rate was improved using the proposed secondary features in comparison to MDF, MFCC and WKM-based features. In addition, the relative error improvement in phoneme classification in compare to WKM based features is shown in this table. In vowels, the greatest improvement was obtained for front vowel 50.2 and back vowel 50.4.

TABLE 5. Phonemes classification error rate using MDF, MFCC and WKM-based and proposed features

Phonemes	**MDF**	**MFCC**	**WKM**	**Proposed features**	**Relative improvement (%)**
Voiced Plosives (/b/,/d/,/g/)	32.1	38.4	25.9	22.8	11.9
Unvoiced Plosives (/p/,/t/,/k/)	32.3	37.1	31.9	30.3	5.0
Voiced Fricatives (/v/,/dh/,/z/)	16.6	25.9	18.9	16.1	14.8
unvoiced Fricatives (/t/,/s/,/sh/)	12.9	20.3	11.1	8.4	24.3
Nasals (/m/,/n/,/ng/)	49.9	50.3	49.7	42.6	14.2
Front Vowels (/ih/,/ey/,/eh/,/ae/)	43.0	41.5	35.6	17.7	50.2
Back Vowels (/uw/,/uh/,/ow/,/aa/)	29.4	38.1	36.5	18.1	50.4
Diphthongs (/ay/, /aw/, /oy/)	32.7	33.9	28.1	21.6	23.1

5. CONCLUSION

In this paper, clustering-based method was presented for secondary features extraction in spectro-temporal domain. In the proposed method, the spectro-temporal domain was clustered using SOM artificial neural networks to extract valuable discriminative information of speech signal. Three types of secondary feature vectors were applied for phonemes classification. Spatial information, the magnitude component of each sample in spectro-temporal domain and the average of the amplitude components of each cluster points were considered as attributes in proposed features vectors. The proposed features were evaluated in compare to MDF, MFCC and WKM clustering-based features for phonemes classification. The experimental results indicate that the proposed features performed better for phoneme classification in comparison to MFCC, MDF and WKM-based features. The greatest improvement was obtained for back vowel 50.4. In consonants, the greatest improvement was achieved for unvoiced fricatives 24.3.

6. REFERENCES

1. Mesgarani, N., David, S. V., Fritz, J. B., and Shamma, S. A., "Mechanisms of noise robust representation of speech in primary auditory cortex", ***Proceedings of the National Academy of Sciences of the United States of America***, Vol. 111, No. 18, (2014), 6792–6797. doi:10.1073/pnas.1318017111
2. Patil, K., and Elhilali, M., "Biomimetic spectro-temporal features for music instrument recognition in isolated notes and solo phrases", ***Eurasip Journal on Audio, Speech, and Music Processing***, Vol. 2015, No. 1, (2015), 27. doi:10.1186/s13636-015-0070-9
3. Mesgarani, N., Slaney, M., and Shamma, S. A., "Discrimination of speech from nonspeech based on multiscale spectro-temporal modulations", ***IEEE Transactions on Audio, Speech and Language Processing***, Vol. 14, No. 3, (2006), 920–930. doi:10.1109/TSA.2005.858055
4. Mesgarani, N., David, S. V., Fritz, J. B., and Shamma, S. A., "Phoneme representation and classification in primary auditory cortex", ***The Journal of the Acoustical Society of America***, Vol. 123, No. 2, (2008), 899–909. doi:10.1121/1.2816572
5. Mesgarani, N., Fritz, J., and Shamma, S., "A computational model of rapid task-related plasticity of auditory cortical receptive fields", ***Journal of Computational Neuroscience***, Vol. 28, No. 1, (2010), 19–27. doi:10.1007/s10827-009-0181-3
6. Zulfiqar, I., Moerel, M., and Formisano, E., "Spectro-Temporal Processing in a Two-Stream Computational Model of Auditory Cortex", ***Frontiers in Computational Neuroscience***, Vol. 13, (2020), 1–18. doi:10.3389/fncom.2019.00095

7. Huang, C., and Rinzel, J., "A Neuronal Network Model for Pitch Selectivity and Representation", ***Frontiers in Computational Neuroscience***, Vol. 10, (2016), 1–17. doi:10.3389/fncom.2016.00057
8. De Martino, F., Moerel, M., Ugurbil, K., Goebel, R., Yacoub, E., and Formisano, E., "Frequency preference and attention effects across cortical depths in the human primary auditory cortex", ***Proceedings of the National Academy of Sciences of the United States of America***, Vol. 112, No. 52, (2015), 16036–16041. doi:10.1073/pnas.1507552112
9. Ruggles, D. R., Tausend, A. N., Shamma, S. A., and Oxenham, A. J., "Cortical markers of auditory stream segregation revealed for streaming based on tonotopy but not pitch", ***The Journal of the Acoustical Society of America***, Vol. 144, No. 4, (2018), 2424–2433. doi:10.1121/1.5065392
10. Valipour, S., Razzazi, F., Fard, A., and Esfandian, N., "A Gaussian clustering based voice activity detector for noisy environments using spectro-temporal domain", ***Signal Processing-An International Journal (SPIJ)***, Vol. 4, No. 4, (2010), 228–238
11. Yen, F. Z., Huang, M. C., and Chi, T.-S., "A two-stage singing voice separation algorithm using spectro-temporal modulation features", Proceedings of the Annual Conference of the International Speech Communication Association, INTERSPEECH, Vols 2015-January, (2015), 3321–3324.
12. Yin, P., Fritz, J. B., and Shamma, S. A., "Rapid spectrotemporal plasticity in primary auditory cortex during behavior", ***Journal of Neuroscience***, Vol. 34, No. 12, (2014), 4396–4408. doi:10.1523/JNEUROSCI.2799-13.2014
13. Lu, K., Liu, W., Zan, P., David, S. V., Fritz, J. B., and Shamma, S. A., "Implicit memory for complex sounds in higher auditory cortex of the ferret", ***Journal of Neuroscience***, Vol. 38, No. 46, (2018), 9955–9966. doi:10.1523/JNEUROSCI.2118-18.2018
14. Esfandian, N., Razzazi, F., and Behrad, A., "A clustering based feature selection method in spectro-temporal domain for speech recognition", ***Engineering Applications of Artificial Intelligence***, Vol. 25, No. 6, (2012), 1194–1202. doi:10.1016/j.engappai.2012.04.004
15. Esfandian, N., Razzazi, F., and Behrad, A., "A feature extraction method for speech recognition based on temporal tracking of clusters in spectro-temporal domain", AISP 2012 - 16th CSI International Symposium on Artificial Intelligence and Signal Processing, (2012), 12–17. doi:10.1109/AISP.2012.6313709
16. Esfandian, N., Razzazi, F., Behrad, A., and Valipour, S., "A feature selection method in spectro-temporal domain based on Gaussian Mixture Models", ***International Conference on Signal Processing Proceedings, ICSP***, (2010), 522–525. doi:10.1109/ICOSP.2010.5656082
17. Esfandian, N., "Phoneme classification using temporal tracking of speech clusters in spectro-temporal domain", ***International Journal of Engineering, Transactions A: Basics***, Vol. 33, No. 1, (2020), 105–111. doi:10.5829/ije.2020.33.01a.12
18. Nithya, A., Appathurai, A., Venkatadri, N., Ramji, D. R., and Anna Palagan, C., "Kidney disease detection and segmentation using artificial neural network and multi-kernel k-means clustering for ultrasound images", ***Measurement: Journal of the International Measurement Confederation***, Vol. 149, (2020), 106952. doi:10.1016/j.measurement.2019.106952
19. Peng, J., Wang, X., and Shang, X., "Combining gene ontology with deep neural networks to enhance the clustering of single cell RNA-Seq data", ***BMC Bioinformatics***, Vol. 20, No. 8, (2019), 1–12. doi:10.1186/s12859-019-2769-6
20. Nida, N., Irtaza, A., Javed, A., Yousaf, M. H., and Mahmood, M. T., "Melanoma lesion detection and segmentation using deep region based convolutional neural network and fuzzy C-means clustering", ***International Journal of Medical Informatics***, Vol. 124, (2019), 37–48. doi:10.1016/j.ijmedinf.2019.01.005
21. Hu, G., Wang, K., Peng, Y., Qiu, M., Shi, J., and Liu, L., "Deep Learning Methods for Underwater Target Feature Extraction and Recognition", ***Computational Intelligence and Neuroscience***, Vol. 2018, (2018). doi:10.1155/2018/1214301
22. Xia, Y., Braun, S., Reddy, C. K. A., Dubey, H., Cutler, R., and Tashev, I., "Weighted Speech Distortion Losses for Neural-Network-Based Real-Time Speech Enhancement", ICASSP, IEEE International Conference on Acoustics, Speech and Signal Processing - Proceedings, Vols 2020-May, (2020), 871–875. doi:10.1109/ICASSP40776.2020.9054254
23. Li, A., Yuan, M., Zheng, C., and Li, X., "Speech enhancement using progressive learning-based convolutional recurrent neural network", ***Applied Acoustics***, Vol. 166, (2020), 107347. doi:10.1016/j.apacoust.2020.107347
24. Magnuson, J. S., You, H., Luthra, S., Li, M., Nam, H., Escabí, M., Brown, K., Allopenna, P. D., Theodore, R. M., Monto, N., and Rueckl, J. G., "EARSHOT: A Minimal Neural Network Model of Incremental Human Speech Recognition", ***Cognitive Science***, Vol. 44, No. 4, (2020). doi:10.1111/cogs.12823
25. Garofolo, J., Lamel, L., Fiscus, J., and Pallett, D., DARPA TIMIT Acoustic-Phonetic Continuous Speech Corpus Documentatio, National Institute of Standards and Technology, Gaithersburg, MD, (1993).
26. Burges, C. J. C., "A tutorial on support vector machines for pattern recognition", ***Data Mining and Knowledge Discovery***, Vol. 2, No. 2, (1998), 121–167. doi:10.1023/A:1009715923555
27. Davis, S. B., and Mermelstein, P., "Comparison of Parametric Representations for Monosyllabic Word Recognition in Continuously Spoken Sentences", ***IEEE Transactions on Acoustics, Speech, and Signal Processing***, Vol. 28, No. 4, (1980), 357–366. doi:10.1109/TASSP.1980.1163420
28. Fartash, M., Setayeshi, S., and Razzazi, F., "A noise robust speech features extraction approach in multidimensional cortical representation using multilinear principal component analysis", ***International Journal of Speech Technology***, Vol. 18, No. 3, (2015), 351–365. doi:10.1007/s10772-015-9274-8

Persian Abstract

چکیده

در این مقاله، یک روش جدید استخراج ویژگی بر مبنای بازنمایی طیفی- زمانی سیگنال گفتار برای طبقه‌بندی واج ارائه شده است. در روش پیشنهادی، از شبکه عصبی برای خوشه‌بندی فضای طیفی- زمانی استفاده می‌شود. شبکه عصبی نگاشت ویژگی خود سامان (SOM) برای خوشه‌بندی فضای ویژگی‌ها اعمال شد. مقیاس، نرخ و فرکانس به عنوان اطلاعات مکانی هر نقطه و مولفه دامنه به عنوان ویژگی شباهت در الگوریتم خوشه‌بندی استفاده شد. سه مکانیزم برای انتخاب ویژگی‌ها در فضای طیفی- زمانی در نظر گرفته شد. اطلاعات مکانی خوشه‌ها، مولفه دامنه نقاط در فضای طیفی- زمانی و میانگین مولفه‌های دامنه نقاط هر خوشه به عنوان ویژگی‌های ثانویه در نظر گرفته شد. بردارهای ویژگی پیشنهادی برای طبقه‌بندی واج‌ها استفاده شد. نتایج نشان می‌دهد، بهبود قابل ملاحظه‌ای در نرخ طبقه‌بندی در دسته‌های مختلف واج‌ها در مقایسه با ویژگی‌های مبتنی بر خوشه‌بندی موجود به دست آمده است. نتایج به دست آمده با استفاده از ویژگی‌های جدید، آشکار می‌کند که خطای سیستم در کلیه زیرگروه‌های واج‌های صدادار و بی‌صدا در مقایسه با خوشه‌بندی K میانگین وزن‌دار بهبود یافته است.

IJE TRANSACTIONS B: Applications Vol. 34, No. 02, (February 2021) 458-469

International Journal of Engineering

Journal Homepage: www.ije.ir

Semantic Segmentation of Lesions from Dermoscopic Images using Yolo-DeepLab Networks

F. Bagheri[a], M. J. Tarokh*[a], M. Ziaratban[b]

[1] *Department of Information Technology Engineering, Faculty of Industrial Engineering, K. N. Toosi University of Technology, Tehran, Iran*
[2] *Department of Electrical Engineering, Faculty of Engineering, Golestan University, Gorgan, Iran*

PAPER INFO

Paper history:
Received 23 July 2020
Received in revised form 07 November 2020
Accepted 08 December 2020

Keywords:
Deep Learning
Deeplab3+
Semantic Segmentation
Skin Lesion
Yolov3

ABSTRACT

Accurate segmentation of lesions from dermoscopic images is very important for timely diagnosis and treatment of skin cancers. Due to the variety of shape, size, color, and location of lesions in dermoscopic images, automatic segmentation of skin lesions remains a challenge. In this study, a two-stage method is presented for the segmentation of skin lesions using Deep Learning. In the first stage, convolutional neural networks (CNNs) estimate the approximate size and location of the lesion. A sub-image around the estimated bounding box is cropped from the original image. The sub-image is resized to an image of a predefined size. In order to segment the exact area of the lesion from the normal image, other CNNs are used in the DeepLab structure. The accuracy of the normalization stage has a significant impact on the final performance. In order to increase the normalization accuracy, a combination of four networks in the structure of Yolov3 is used. Two approaches are proposed to combine the Yolov3 structures. The segmentation results of the two networks in the DeepLab v3+ structure are also combined to improve the performance of the second stage. Another challenge is the small number of training images. To overcome this problem, the data augmentation is used along with different modes of an image in each stage. In order to evaluate the proposed method, experiments are performed on the well-known ISBI 2017 dataset. Experimental results show that the proposed lesion segmentation method outperforms the state-of-the-art methods.

***doi**: 10.5829/ije.2021.34.02b.18*

1. INTRODUCTION

Nowadays, cancer is one of the most common reasons of mortality in humans worldwide. One of the most prevalent cancers is melanoma skin cancer. This disease is initiated when a specific type of skin cell named melanocyte starts to over-grow out of control [1]. Therefore, attempts to diagnose this disease in early stages are very important for more rapid treatment and increasing the chance of survival [2]. Visual inspection during laboratory assessments and medical examination of skin lesions might cause misdiagnosis due to similarities of skin lesions and normal skin tissues [3]. In the recent decade, dermatologists have begun to use an invasive imaging tool called dermoscopy which provides an enlarged image of skin lesion through polarized light [4]. It shows more details of the skin structure and improves the correctness of the diagnosis in comparison to visual observation. However, observation and verification of dermoscopy images by dermatologists is subjective, difficult, and time-consuming [4]. Thus, an automatic accurate skin lesion recognition system is very critical to support dermatologists in decision-making. One essential primary stage in any computer-based diagnostic system for detecting melanoma is automated segmentation of skin lesions [5–7]. The lesion segmentation remains a challenge due to the large variety of skin lesions in color, shape, texture, location, and size in dermoscopy images. In addition, low contrast borders between lesions and surrounding tissues, existence of ruler sign, blood vessels, hair, air bubbles, and changes of brightness are amongst the barriers to accurate segmentation [8].

Generally, there are various methods for image segmentation, such as methods based on edge detection, thresholding, region detection, feature clustering [9-10],

*Corresponding Author Email: *mjtarokh@email.kntu.ac.ir* (M. J. Tarokh)

Please cite this article as: F. Bagheri, M. J. Tarokh, M. Ziaratban, Semantic Segmentation of Lesions from Dermoscopic Images using Yolo-DeepLab Networks, International Journal of Engineering, B: Applications Vol. 34, No. 02, (2021) 458-469

as well as supervised methods such as those based on deep neural networks [11]. Various supervised methods have been used for segmentation of skin lesions such as decision tree, support vector machine, and neural networks. Indeed, these methods use low-level features [8]. Recently, image segmentation based on deep learning has become one of the main image segmentation methods. Deep learning based on Convolutional Neural Networks (CNNs) is a powerful method. CNN is capable to exclude more appropriate features in comparison to the features extracted by conventional methods [12–14]. The first application of CNN-based method in semantic segmentation was presented by Ciregan et al. [15, 16].

In 2017, Burdick et al. investigated the effect of segmentation boundary expansion involving pixels around the target lesion. They used ISBI 2016 Challenge dataset [17] to evaluate the experiments. They found the preprocessing techniques that create bounds larger than the actual lesion can potentially improve the performance of the classifier [18]. You et al., in 2017 prersented a two-stage method to segment and classify skin lesions using fully convolutional residual network (FCRN). They examined their method on the ISBI 2016 dataset, and achieved the accuracy of 94.9% [19]. Yuan et al. in 2017 presented a method for segmentation of skin lesions using deep fully convolutional networks (FCN). They employed the Jaccard distance as a loss function of the FCN. They evaluated their method on ISBI 2016 and PH2 datasets, and reached the accuracy of 95.5%, and 93.8%, respectively [20].

In 2017, Lin et al. comprised two skin lesion segmentation approaches, C-means clustering and U-Net-based histogram equalization. Their work was evaluated on the ISBI 2017 dataset. The clustering technique achieved a dice index of 61% and the U-Net method results in the accuracy of 77% [21]. Li et al., proposed another approach based on a lesion index calculation unit (LICU) and multi-scale fully-convolutional residual networks. They evaluated their approach on the ISBI 2017 dataset and achieved 71.8% in Jaccard index [22]. Bi et al. followed the FCN architecture to add convolutional and deconvolutional layers, which upsample the feature maps derived from Resnet to output the score mask. They achieved Jaccard index of 76.1% on ISBI 2017 dataset [23]. Yuan and Lo proposed a method for segmentation of skin lesions based on convolutional-deconvolutional neural networks (CDNN). They trained their model through various color spaces. Their method was ranked first in the ISBI 2017 lesion segmentation challenge with a Jaccard index of 76.5% [24]. Al-Masni et al. (2018) conducted a study on segmentation of skin lesions and designed a full resolution convolutional network. They performed the examinations on ISBI 2017 and PH2 datasets, and achieved 77.11% and 84.79% by Jaccard criteria, respectively [8].

Baghersalimi et al. presented a full convolutional neural network, DermoNet, to segment skin lesions. In DermoNet, subsequent layers could reuse the information extracted from previous layers. The Jaccard values of DermoNet on ISBI 2017 dataset was 78.3% [25].

Hasan et al., proposed a Dermoscopic Skin Network (DSNet) to segment skin lesions. To reduce the number of network parameters, depth-wise separable convolution layers were used in their network. They achieved the Jaccard value of 77.5% on the ISBI 2017 dataset [26].

Tang et al. developed a skin lesion segmentation method based on separable U-Net and took advantage of the separable convolutional block and the U-Net architectures, simultaneously. The Jaccard index of their method on ISBI 2017 dataset was 79.26% [27].

For many applications, both local and global information on lesions and normal tissues are required to increase the segmentation accuracy. Many researchers have used multi-flow architectures to combine local and global information [28]. Chen et al. used three CNNs which receive information on lesion from different aspects as input. The features extracted from each CNN were concatenated as output, constituting the final feature vector [29]. Similarly, Kawaraha and Hamarneh introduced a method for classifying skin lesions using multi-flow CNN. In this method, the flows worked on various versions of resolution of the image [30].

These studies indicated that the combination of several CNNs with various details can improve the final performance. In this study, combinations of CNNs have been used to improve the accuracy of each stage of the proposed method.

Our contributions in this work are as follows: Using normalization stage before the segmentation stage.

- Using state-of-the-art CNNs in both normalization and segmentation stages.
- Combination of Yolo networks to improve the accuracy of the normalization stage.
- Proposing a novel combined structure for Yolov3 to combine the results of Yolo networks.
- Combination of DeepLab v3+ networks to improve the segmentation accuracy.
- Using various modes of images to overcome large variety of lesions and low number of training images.

2. MATERIALS AND METHODS

2. 1. Dataset The proposed segmentation method was evaluated on a well-known and open ISBI 2017 challenge dataset. This dataset was prepared by the International Skin Imaging Collaboration (ISIC) archive [31], and was presented online [32]. This dataset consists of 8-bit RGB dermoscopy images of sizes from 540×722 to 4499×6748 pixels. Out of 2750 images, 2000, 150, and

600 images have been categorized for training, validation, and test, respectively.

2. 2. Proposed Method The purpose of lesion segmentation is extraction of skin lesions from dermoscopy images in order to help disease diagnosis. In recent years, various methods such as U-Net and FCN have been used for medical image segmentation. FCN and U-Net, as well as other single-stage methods are sensitive to the lesion size. Very large and very small lesions decrease the accuracy of single-stage segmentation methods. In addition, various locations of lesions in images increase the complexity of networks and reduce the performance. In our experiments by using single-stage methods, we observed that a significant number of inaccurate segmentation occurred in two categories of skin images: the images in which the lesion was very big or very small, and the images in which the lesion was not in the center. Therefore, it is better to add a stage before the segmentation stage to normalize the size and location of lesions in images. This will reduce complexity of the network training in the segmentation stage. The proposed method consists of two stages of normalization and segmentation. The normalization stage estimates the approximate size and location of lesions. This stage yields normal images in which the lesions have similar sizes and are placed in the center. In the following stage, lesions will be more accurately segmented from the normalized images compared to the original input images. The overall framework of the proposed lesion segmentation method is illustrated in Figure 1.

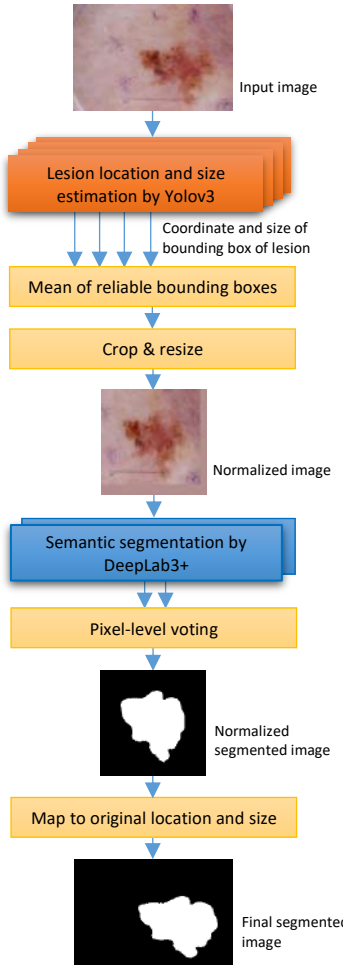

Figure 1. The overall framework of the proposed method

2. 3. Size and Location Normalization of Lesions Any error in the normalization stage leads to high costs in performance of the segmentation stage. Hence, the accuracy of the normalization stage is very important. One of the possible errors in the normalization stage occurs when the cropped image does not include any part of the lesion. It means that some pixels of the skin lesion do not exist in the output image of the normalization stage. For these images, before entering the segmentation stage, a part of the lesion is missed. Therefore, the high accuracy in the normalization stage is very important. If the accuracy of the normalization is not large enough, it might cause reduction in the final accuracy compared to single-stage segmentation methods (without normalization stage). In the proposed method, convolutional neural networks with definite structures presented for object detection will be used as the normalization stage. CNNs are very competent and practical in applications of object detection and classification. Various common deep networks based on CNN were being proposed and used for the above applications [33].

Object detection networks such as R-CNN [34], Fast R-CNN [35], and Faster R-CNN [36] combine convolutional networks with region proposal networks. Methods of Single Shot multi-box Detector (SSD) [37] and You Only Look Once (Yolo) [38] detect objects only in one convolutional process without region proposals [33]. Amongst various methods for object detection, Faster R-CNN usually shows appropriate accuracy, but its computational cost is very high as compared to Yolo [39]. The accuracy of Faster R-CNN might be higher than that of Yolo in many applications of detection, but the speed of Yolo is far greater than that of Faster R-CNN [40]. On the other hand, in implementations, the score value for Faster R-CNN is usually very close to 1, even in cases of misdetection. However, the score value in Yolo is usually proportional to the correctness of detection. In other words, Yolo presents lower scores for the samples which cannot be detectted definitely. As pointed above, one of the approaches that can be implemented to enhance the accuracy of the detection is the combination of the results of several detectors. This ability of Yolo that presents the scores proportional to the detection accuracy is very important and applicable in combining detectors. In this paper, due to the ability of

Yolo for combination as well as its reasonable accuracy and speed appropriateness, a combination of several Yolo detectors is used in the normalization stage.

Yolo is a CNN-based object detection algorithm which divides the image into several sub-regions. Then, it predicts bounding boxes and class probabilities for each of the sub-regions. Yolo algorithm predicts two values for any anchor box: one of them is the class probabilities, and the other one is the bounding box characteristics [38].

To improve the performance of Yolov1, a second version, Yolov2, was developed. Yolov2 uses an identity mapping and concatenating feature maps from a previous layer to capture low-level features [41].

In Yolov3, the feature map are taken from one of the last layers of a pre-trained network. The feature map is upsampled by 2. Another feature map from earlier in the network is concatenated with the upsampled features. This allows Yolov3 to get both meaningful semantic and finer-grained information from the feature maps. Some convolutional layers process these combined feature maps [42]. Yolov3 has two outputs in scales of 1 and 2 that are used in the training phase. We use the latest version of Yolo, Yolov3, in our experiments.

2. 4. Combining Networks in The First Stage

In order to improve the performance of the normalization stage, a combination of several networks is used with the overall structure of Yolov3 containing different pre-trained networks. Several pre-trained networks exist with each possessing specific characteristics. Indeed, if an inappropriate pre-trained network is used for an application, a suitable efficiency will not be achieved. The difference of each pre-trained network is due to the number of layers, the number of convolutional filters, and their complexities [43]. Using transfer learning concept, the weights of a network trained based on a specific dataset such as ImageNet, can be used and trained again by a different dataset to be used in another application. Utilizing learned weights in pre-trained networks, the model can be trained at a higher speed based on the new dataset. The first layers of pre-trained networks were trained to detect primary and main features of an image such as borders, corners, round formats, basic geometric shapes, and colors [33]. In this study, various pre-trained networks such as VGG [44], AlexNet [13], Resnet [45], GoogleNet [46], and Inception [47] are used as the basis networks of the Yolov3 structures. The constructed Yolo networks are further investigated, and those with a higher performance in the validation set are selected for combining the results in the normalization stage. As shown in Figure 1, the outputs of Yolo networks include the coordinates and size of the estimated bounding boxes of detected lesions. In the proposed method, two approaches to combine the Yolo networks are introduced.

In the first approach, the outputs of Yolo networks are combined by averaging the coordinates and size of the bounding boxes obtained by each Yolo network. Meanwhile, the outputs of some Yolo detectors might have a low score. Therefore, for an input image, amongst all N outputs of detectors, the M ($M \leq N$) outputs with the largest score are used to combine and determine the final bounding box.

To improve the performance of each Yolo network in the normalization stage, for an input image, totally four modes are considered and applied to the input of each Yolo network, as follows:

1. Input image
2. Horizontal flip of input image
3. Vertical flip of input image
4. Input image with 180 degrees rotation

Four corresponding outputs will be calculated by applying their inverse transforms. Thus, for each input image, each detector makes four bounding boxes with corresponding scores in the output. By combining N detectors, totally $4N$ bounding boxes will be achieved. $3N$ out of $4N$ bounding boxes with the largest score will be considered for averaging and determining the final bounding box as follows:

$$x = \frac{\sum_{i=1}^{N}\sum_{j=1}^{4}\alpha_{ij}x_{ij}}{\sum_{i=1}^{N}\sum_{j=1}^{4}\alpha_{ij}} \quad (1)$$

$$\alpha_{ij} = \begin{cases} 1 & Score_{ij} \text{ is in the set of } 3N \text{ largest scores} \\ 0 & \text{elsewhere} \end{cases} \quad (2)$$

where $Score_{ij}$ and x_{ij} are the estimation score and the x coordinate of upper left corner of the bounding box of the j-th mode of the input image estimated by the i-th network, respectively. y, w, and h of the final bounding box are calculated in a similar way.

In the second approach, the trained Yolo networks and an additional convolutional network are combined to construct a novel combined Yolo structure as shown in Figure 2. In this figure, the yellow boxes are the Yolov3 networks which are trained separately. The weights of layers of these networks are freezed during the training of the combined Yolo structure. To have better results, the outputs of trained Yolo networks should be combined with respect to the content of the input image. Hence, an additional convolutional network (green boxes) are employed to extract useful features from the input image to be used in the combination procedure. Briefly, in the second approach, the combined Yolov3 structure learns how to combine the outputs of frozen Yolo networks according to features of input images. Four parameters of convolution layers in Figure 2 are respectively the filter size, number of filters, stride, and the zero padding size.

To avoid missing any parts of lesion in the normal image, it is better to consider a margin around the estimated bounding box before the image cropping. To do this, the estimated bounding box is extended on both

sides in both vertical and horizontal directions. The extended box is cropped from the input image and is sent to the segmentation stage. The extent of margin around the estimated bounding box is considered as 30% of the size of bounding box in each direction. The bounding boxes estimated by Yolov3 structures based on four pre-trained networks, final estimated bounding box, extended box, and the normalized image for an instance image are displayed in Figure 3.

The bounding boxes estimated by Yolov3 structures based on four pre-trained networks, final estimated bounding box, extended box, and the normalized image for an instance image are displayed in Figure 3. The red, green, blue, and yellow colours in Figure 3(a-d) are related to the first, second, third, and forth modes of the input image. Green rectangle in Figure 3(e) is the correct bounding box of the lesion. The red and blue rectangles are the bounding boxes estimated by the first and the second Yolo results combination approaches, respectively. The red rectangles with dashed lines are the extended box around the lesion estimated by the first combination approach. The extended box is cropped and resized to construct the normal image (Figure 3(f)).

2. 5. Segmentation Stage Various methods and networks are used for semantic segmentation of images in different applications. One of the novel structures is the DeepLab structure [48].

DeepLab is a model of deep learning for segmentation of images. In general, the DeepLab architecture is based on a combination of two common Spatial Pyramid Pooling and Encoder-decoder networks architectures [49].

Different DeepLab structures have been proposed over time. DeepLab v1 [48], DeepLab v2 [50], DeepLab v3 [51], and DeepLab v3+ [49] are the various structures of DeepLab. DeepLab v1 uses atrous convolution to control the resolution at which feature maps are

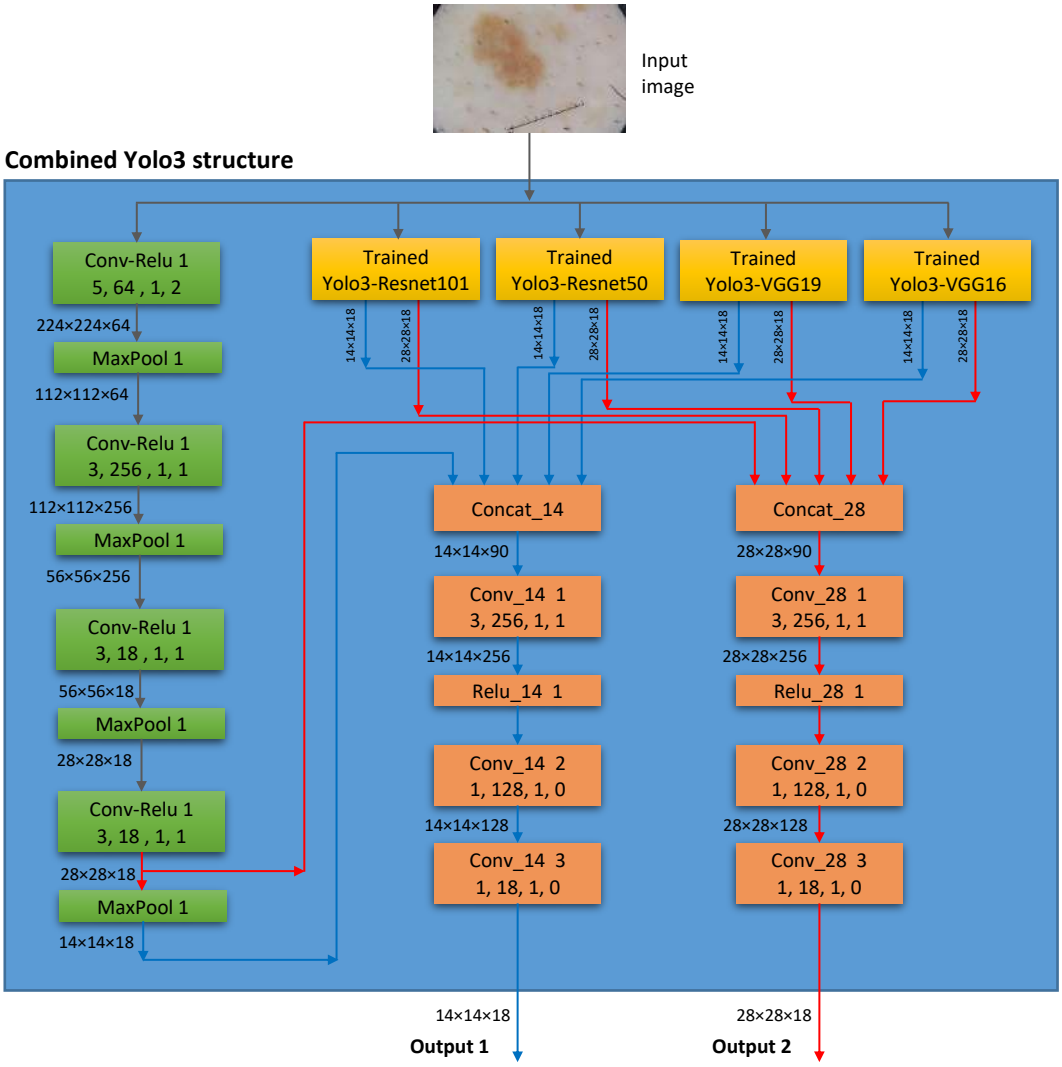

Figure 2. The proposed combined Yolov3 structure

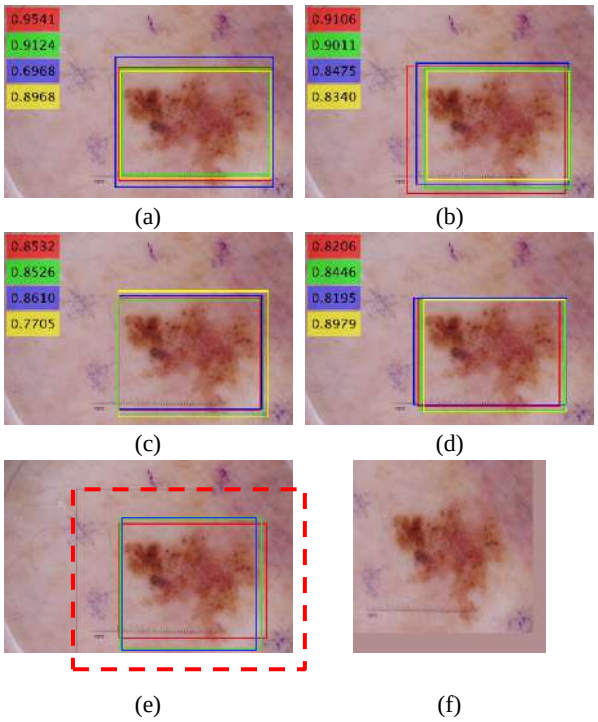

Figure 3. Result of normalization stage for a sample image. (a), (b), (c), and (d) are the bounding boxes estimated by Yolov3 structures based on Resnet50, Resnet101, VGG16, and VGG19, respectively. (e) The correct bounding box is shown with a green box. The red and blue rectangles are the bounding boxes estimated by the first and the second Yolo results combination approaches, respectively. The red dashed rectangle is the extended box around the lesion estimated by the first combination approach. (f) Normalized image.

computed [48]. In DeepLab v2, by using atrous spatial pyramid pooling (ASPP), objects are segmented on multiple scales with effective fields-of-view and filters at multiple sampling rates [50]. To capture more information, DeepLab v3 augments the ASPP module via image-level feature.

It also includes batch normalization parameters. DeepLab v3+ includes an effective decoder module to improve the segmentation results [49].

We use DeepLab3+ structure [49] in the segmentation stage of our proposed method. To improve the performance of our segmentation stage, totally eight different modes of input image are considered as follows:

- Input image, Horizontal and Vertical flips of the image, the image rotated by -45, 45, 90, 180, and 270 degrees.

The output of each input mode is rotated or is flipped back to the original mode. The final result is obtained by combining the outputs. The final output of the combination is a binary image in which, a pixel is considered as lesion if the corresponding pixel in at least n out of m output images are recognized as lesion.

2. 6. Combining Networks in the Second Stage Similar to the normalization stage, in order to increase the accuracy, combinational results of some networks can be used in the segmentation stage. In our experiments, combination of segmentation results of VGG19 and Resnet50 networks in DeepLab3+ structure has been used to improve the overall lesion segmentation performance.

2. 7. Evaluation Metrics A commonly used metric to evaluate object detection methods is the mean average precision (mAP). In our experiments, to evaluate performance of the normalization stage in more details, a metric named $BoxIOU$ is defined as the intersection over union (IOU) of the estimated bounding box with the correct bounding box of lesions in the ground truth:

$$BoxIOU = \frac{TP_{Box}}{TP_{Box}+FN_{Box}+FP_{Box}} \quad (3)$$

For evaluating semantic segmentation methods, the following metrics have been used in the literature. Sensitivity (SEN) represents the rate of pixels of skin lesion correctly detected. On the other hand, specificity (SPE) is the rate of pixels of non-skin lesions classified correctly [52]. The Jaccard index (JAC) is an intersection over union (IOU) of the result mask with the ground truth mask [53]. Index of Dice (DIC) measures the similarity of classified skin lesions through ground truth [54]. Accuracy (ACC) shows the overall performance of segmentation [53]. The Matthew correlation coefficient (MCC) measures the correlation between the segmented and annotated pixels. MCC returns values in a range of $[-1\ +1]$ [53]. All these criteria are computed from the confusion matrix elements as follows [53]:

$$SEN = \frac{TP}{TP+FN} \quad (4)$$

$$SPE = \frac{TN}{TN+FP} \quad (5)$$

$$JAC = \frac{TP}{TP+FN+FP} \quad (6)$$

$$SEN = \frac{2.TP}{(2.TP)+FP+FN} \quad (7)$$

$$ACC = \frac{TP+TN}{TP+FP+TN+FN} \quad (8)$$

$$MCC = \frac{TP.TN-FP.FN}{\sqrt{(TP+FP).(TP+FN).(TN+FP).(TN+FN)}} \quad (9)$$

2. 8. Results In our experiments, cropped images in the normalization stage were resized to 448×448 pixels. Due to the hardware limitation, the mini-batch size was set to 8 samples. Experiments were performed by using 6GB NVIDIA GeForce RTX2060 GPU.

Table 1 reports the values of the mean average precision (mAP) and $BoxIOU$ for each of the pre-trained networks using the Yolov3 structure in the normalization stage. The Jaccard index of final semantic segmentation is the main factor for comparison of different networks [32]. The values of this metric are reported in the last column of Table 1. The DeepLab3+ structure based on Resnet50 was used for segmentation in this table.

In the segmentation stage, two pre-trained networks, VGG19 and Resent50 were used in the DeepLab3+ structure. For an input image, by considering eight input modes and two segmentation structures, totally 16 output images were achieved. In the final output binary image, I_{BW}, a pixel was considered as lesion if at least it was recognized as lesion in 6 out of 16 output images as follows:

$$p_r\,(x\,,y) = \frac{1}{16}\left[\sum_{i=1}^{2}\sum_{j=1}^{7} o_{ij}\,(x,y)\right] \quad (10)$$

$$I_{BW}\,(x\,,y) = \begin{cases} 1 & p_r(x,y) \geq P_0 \\ 0 & else \end{cases} \quad (11)$$

where o_{ij} is the binary output image of i-th network corresponding to the j-th mode of the input image and $P_0 = \frac{6}{16}$. Table 2 provides the results of various combinations of networks in the normalization and segmentation stages. A comparison among various methods based on 7 evaluation metrics are given in Table 3. In the proposed method I, Yolov3 structure based on VGG19, and DeepLab3+ structure based on Resnet50 were used in the normalization and segmentation stages, respectively. The first and second combination approaches were employed in the normalization stages of the proposed method II and the proposed method III, respectively. The segmentation stages of the proposed method II and proposed method III consisted of the combination of two DeepLab3+ structures based on VGG19, and Resnet50.

TABLE 1. Performance of different Yolov3 structures based on various pre-trained networks

Backbone network of the Yolov3	*mAP* (%)	Mean BoxIOU (%)	Overall segmentation Jaccard (%)
Vgg 19	91.36	79.62	**79.12**
Resnet 101	90.55	77.97	78.92
Vgg 16	91.85	79.03	78.79
Resnet 50	90.68	78.93	78.77
Resnet 18	90.87	78.04	78.43
Densenet 201	90.68	78.86	78.40
Mobilenet v2	88.99	78.00	78.04
Shufflenet	89.49	77.52	78.04
Alexnet	88.87	75.81	77.75
Googlenet	84.69	74.06	76.31
Squeezenet	59.48	54.98	59.26
Xception	51.57	48.46	54.21
Inception v3	45.29	44.46	50.15

TABLE 2. Performance of different combinations of Yolov3 structures in normalization stage and different combinations of DeepLab3+ structures in segmentation stage

Normalization stage										Segmentation stage		
Vgg 19	Vgg 16	Resnet 50	Resnet 101	Resnet 18	Densenet 201	1st combination approach	2nd combination approach	*mAP* (%)	Mean BoxIOU (%)	Resnet 50	Vgg 19	Overall Jaccard (%)
*	*					*		92.25	79.84	*		79.38
*		*				*		91.68	79.61	*		79.39
*	*	*				*		91.67	79.74	*		79.48
*	*	*	*			*		92.20	80.09	*		79.53
*	*	*	*	*		*		93.09	80.24	*		79.52
*	*	*	*	*	*	*		92.92	80.40	*		79.48
*	*	*	*			*		92.20	80.09		*	79.49
*	*	*	*			*		92.20	80.09	*	*	79.77
*	*	*	*				*	92.29	80.31	*	*	**79.96**

3. DISCUSSION

In this paper, a method based on deep learning was proposed to segment lesions from dermoscopic images. Deep neural networks require many training images due to a large number of trainable parameters.

In applications for which enough training images are not available, two general techniques are used to compensate the lack of enough training data: data augmentation and transform learning. In this paper, for the data augmentation, rotation, horizontal, and vertical flips, image resizing with the ratio between 0.8 and 1.2, and brightness alteration were randomly applied to the training images and the augmented training set consisted of 8000 images.

In the proposed method, by adding the normalization stage prior to the segmentation stage, the inputs of the segmentation stage contained normalized lesions with far fewer varieties in size and location. This caused reduction in complexity of the training procedure in the segmentation stage and improved the segmentation performance. As can be observed in Table 1, the use of

TABLE 3. Comparison among various methods based on different metrics

	SEN	*SPE*	*ACC*	*MCC*	*AUC*	*DIC*	*JAC*
Yuan et al. [24]	82.50	97.50	93.40	-	-	84.90	76.50
Li et al. [22]	82.00	97.80	93.20	-	-	84.70	76.20
Bi et al. [23]	82.20	**98.50**	93.40	-	-	84.40	76.00
Lin et al. [21]	-	-	-	-	-	77.00	62.00
Al-masni et al. [8]	85.40	96.69	94.03	83.22	91.04	87.08	77.11
Baghersalimi et al. [25]	-	-	-	-	-	-	78.30
Tang et al. [27]	**89.53**	96.32	**94.31**	-	-	86.93	79.26
Hasan et al. [26]	87.5	95.5	-	-	-	-	77.5
Proposed method I	88.90	95.47	93.94	83.53	92.17	87.01	79.12
Proposed method II	89.07	96.01	94.26	84.19	92.54	87.46	79.77
Proposed method III	89.21	96.08	94.29	**84.35**	**92.61**	**87.57**	**79.96**

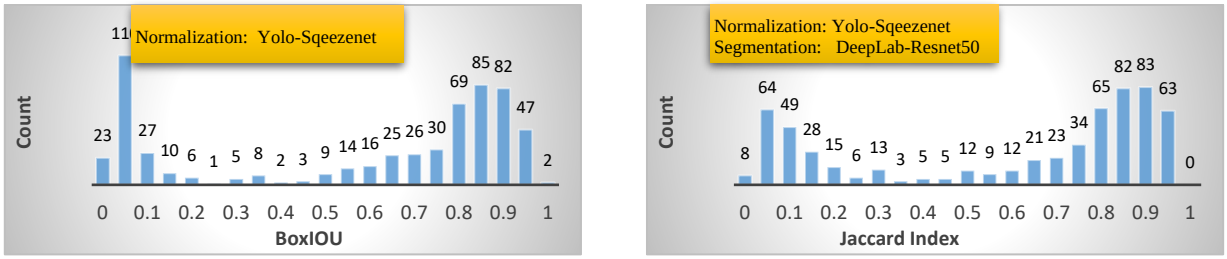

Figure 4. Distributions of BoxIOU (Detection Jaccard index) and overall Jaccard index obtained by Yolo-Squeeznet and DeepLab-Resnet50 respectively in the normalization and segmentation stages

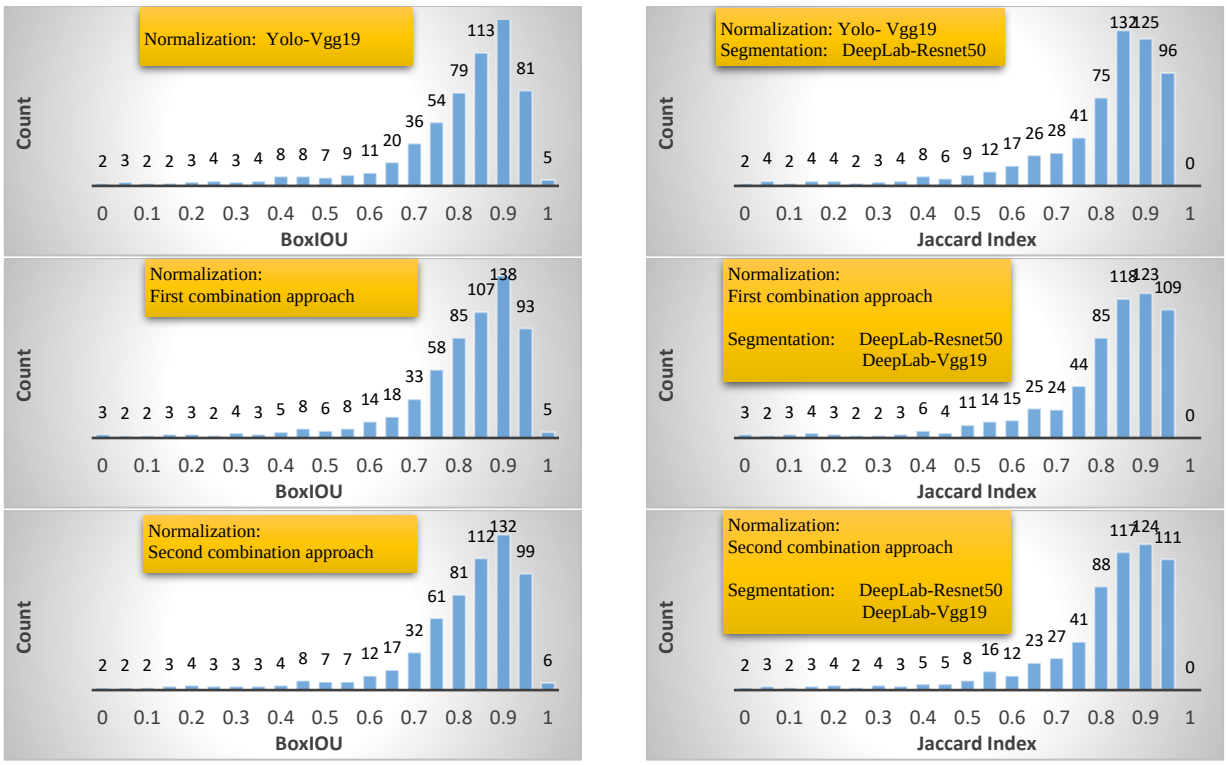

Figure 5. Distributions of *BoxIOU* (Detection Jaccard index) and overall Jaccard index obtained by different combinations of networks in the normalization and segmentation stages

inappropriate pre-trained networks in the normalization stage considerably reduced the overall performance.

The mAP values of the detection stage associated with some pre-trained networks such as Sqeezenet, Xception, and Inception v3 were obtained lower than 60%. The reason is that these networks had been particularly trained and optimized for mobile applications [39].

Further, Table 1 indicates that the final segmentation performance is proportional to the performance of the normalization stage. In other words, in cases where the value of mAP was achieved considerably larger than other cases, the value of final Jaccard was definitely greater.

To illustrate the effect of the normalization stage on the performance of our overall lesion segmentation method, distributions of $BoxIOU$ and overall Jaccard index method have been shown in Figures 4 and 5. In each row of these figures, similarity between distributions of $BoxIOU$ and overall Jaccard index demonstrates that the performance of the overall segmentation is highly affected by the performance of the detection in the normalization stage.

The use of the Yolo structure in the normalization stage made it possible to apply valid score values of the detection for combining the outputs of several networks. The results in Table 2 indicate that by combining four networks of Yolov3 based on the Resent and VGG networks, the value of mAP in the normalization stage as well as the final Jaccard index is increased.

The left and the right images in Figure 6 are respectively the results of the normalization stage and the final segmentation results of four difficult sample images. The proposed method could not correctly segment the lesions in these images and their Jaccard values have been obtained lower than 20%. As can be observed in the left column of Figure 6, the main reason of low segmentation accuracy of these images is that the proposed method could not accurately detect the lesion area in the normalization stage.

In Figures 6 and 7, rectangles with solid red and green lines are the estimated and the correct bounding boxes, respectively. The red rectangles with dashed lines are the extended estimated bounding boxes, which have been cropped and resized to enter the segmentation stage.

From the images in the right side, the green, red, yellow, and black areas respectively represent TP, FP, FN, and TN of the confusion matrix. In the first and second rows of Figure 6, the detected lesions were much wider than the correct lesions. In the third and fourth rows, the lesions have been detected smaller than the correct ones. As can be observed, segmentation of lesions in these images are very difficult even for experts.

On the other hand, four difficult images for which the Jaccard values have been obtained greater than 85% are illustrated in Figure 7.

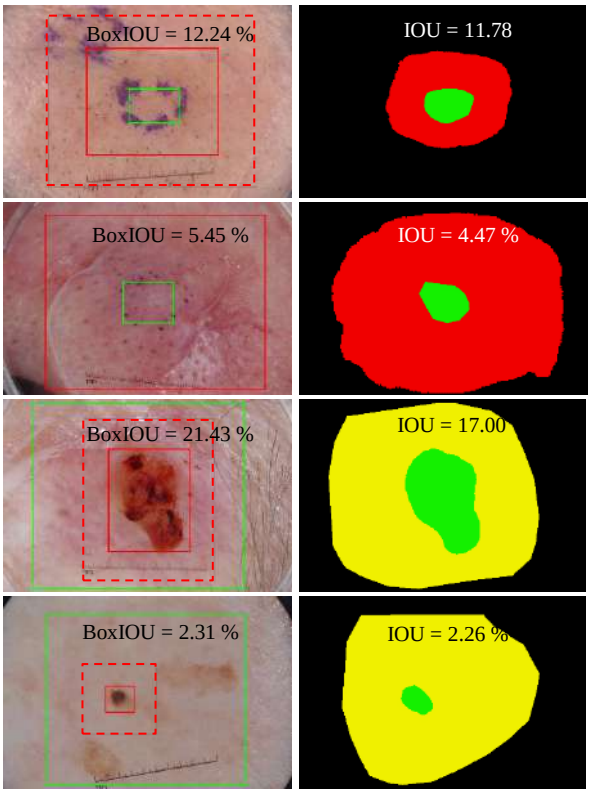

Figure 6. Four difficult sample images that have not been accurately normalized and segmented

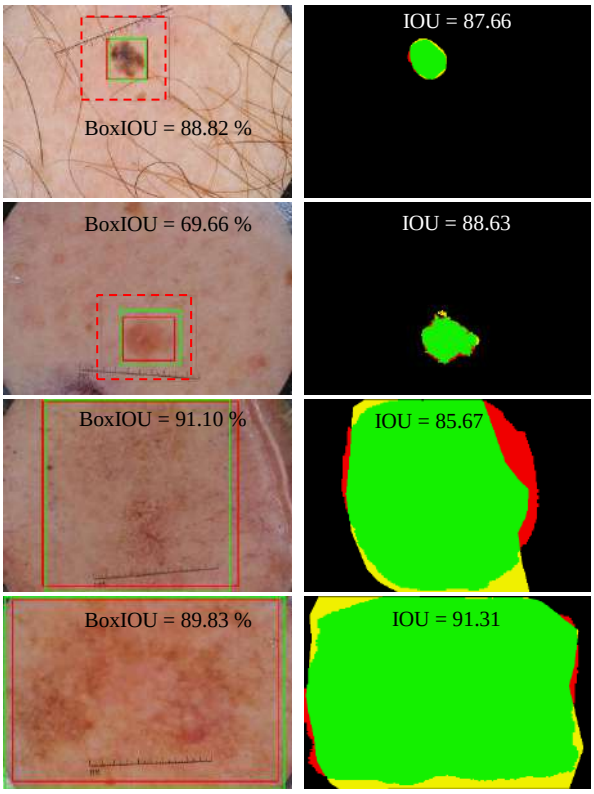

Figure 7. Four difficult sample images that have been accurately normalized and segmented

In these sample images, very small and very big lesions, lesions with low-contrast boundaries, various lesion locations, and existence of hairs and regions similar to lesions are the main challenges. However, the proposed method accurately detected and segmented the lesions.

The best results were obtained by using our combined Yolov3 structure in the normalization stage. The second combination approach in the normalization stage performed better compared to the first approach. The reason is that in the second approach, the combined structure was trained to combine the results of the Yolo networks. While in the first approach, the combination was performed without any learnable parameters.

4. CONCLUSION

Developing a highly accurate lesion segmentation system considerably helps dermatologists to diagnose skin cancer in a timely and correct manner. In this paper, a two-stage model was presented to improve the performance of skin lesion segmentation. In the proposed method, the images entered the normalization stage, in which the variety of sizes and locations of the lesions in the input images were reduced. A novel combined Yolov3 structure was proposed to combine results of four Yolov3 networks. The output of the normalization stage was an image, in which the lesion was approximately located in the centre and had a predefined size. The normalized images in the first stage were imported into the second stage. The segmentation stage consisted of a combination of two CNNs in the DeepLab3+ structure.

The main reason of applying the normalization stage before the segmentation part was that the segmentation methods are generally sensitive to the size and location of objects. The varieties of sizes and locations of objects in images complicate the training of the model. Normalization of the images greatly improved the performance of the proposed lesion segmentation method.

5. REFERENCES

1. National Cancer Institute, "SEER Cancer Stat Facts: Melanoma of the Skin", (2017). Retrieved from Bethesda, MD: https://seer. cancer. gov/statfacts/html/melan. html.
2. Balch, C. M., Gershenwald, J. E., Soong, S.-J., Thompson, J. F., Atkins, M. B., Byrd, D. R., Buzaid, A. C., and Al., E., "Final version of 2009 AJCC melanoma staging and classification", ***Journal of Clinical Oncology***, Vol. 27, No. 36, (2009), 6199–6206. doi:10.1200/JCO.2009.23.4799
3. Vestergaard, M. E., Macaskill, P. H. P. M., Holt, P. E., and Menzies, S. W., "Dermoscopy compared with naked eye examination for the diagnosis of primary melanoma: a meta-analysis of studies performed in a clinical setting", ***British Journal of Dermatology***, Vol. 159 No. (3), (2008), 669–676. doi 10.1111/j.1365-2133.2008.08713.x
4. Binder, M., Schwarz, M., Winkler, A., Steiner, A., Kaider, A., and Wolff, K. H., "a useful tool for the diagnosis of pigmented skin lesions for formally trained dermatologists", ***Arch Dermatol***, Vol. 131, No. 3, (1995), 286–291. doi: 10.1001/archderm.1995.01690150050011
5. Celebi, M. E., Iyatomi, H., Schaefer, G., and Stoecker, W. V., "Lesion border detection in dermoscopy images", ***Computerized Medical Imaging and Graphics***, Vol. 33, No. 2, (2009), 148–153. doi:10.1016/j.compmedimag.2008.11.002
6. Ganster, H., Pinz, P., Rohrer, R., Wildling, E., Binder, M., and Kittler, H., "Automated melanoma recognition", ***IEEE Transactions on Medical Imaging***, Vol. 20, No. 3, (2001), 233–239. doi:10.1109/42.918473
7. Celebi, M. E., Wen, Q., Iyatomi, H., Shimizu, K., Zhou, H., and Schaefer, G., "A state-of-the-art survey on lesion border detection in dermoscopy images", ***Dermoscopy Image Analysis***, Vol. 10, (2015), 97–129. doi:10.1201/B19107-5
8. Al-masni, M. A., Al-antari, M. A., Choi, M., Han, S., and Kim, T., "Skin lesion segmentation in dermoscopy images via deep full resolution convolutional networks", ***Computer Methods and Programs in Biomedicine***, Vol. 162, (2018), 221–231. doi:10.1016/j.cmpb.2018.05.027
9. Hassanpour, H., and Yousefian, H., "An improved pixon-based approach for image segmentation", ***International Journal of Engineering, Transactions A: Basics***, Vol. 24, No. 1, (2011), 25–35. Retrieved from http://www.ije.ir/article_71880_c9bb4bcef741659a548a0979992905c5.pdf
10. Nikbakhsh, N., Baleghi Damavandi, Y., and Agahi, H., "Plant classification in images of natural scenes using segmentations fusion", ***International Journal of Engineering Transactions C: Aspects***, Vol. 33, No. 9, (2020), 1743–1750. doi:10.5829/ije.2020.33.09c.07
11. Liu, X., Deng, Z., and Yang, Y., "Recent progress in semantic image segmentation", ***Artificial Intelligence Review***, Vol. 52, No. 2, (2019), 1089–1106. doi:10.1007/s10462-018-9641-3
12. LeCun, Y., Bengio, Y., and Hinton, G., "Deep learning", ***Nature***, Vol. 521, (2015), 436–444. doi: 10.1038/nature14539
13. Krizhevsky, A., Sutskever, I., and Hinton, G. E., "Imagenet classification with deep convolutional neural networks", ***Advances in Neural Information Processing Systems***, Vol. 25, No. 2, (2012), 1097–1105. doi:10.1145/3065386
14. Al-Masni, M. A., Al-Antari, M. A., Park, J. M., Gi, G., Kim, T. Y., Rivera, P., Valarezo, E., Han, S.-M., and Kim, T.-S., "Detection and classification of the breast abnormalities in digital mammograms via regional Convolutional Neural Network", Proceedings of 39th Annual International Conference of the IEEE Engineering in Medicine and Biology Society (EMBC), (2017), 1230–1233. doi:10.1109/EMBC.2017.8037053
15. Ciregan, D., Meier, U., and Schmidhuber, J., "Multi-column deep neural networks for image classification", 2012 IEEE Conference on Computer Vision and Pattern Recognition, (2012), 3642–3649. doi:10.1109/CVPR.2012.6248110
16. Cernazanu-Glavan, C., and Holban, S., "Segmentation of bone structure in X-ray images using convolutional neural network", ***Advances in Electrical and Computer Engineering***, Vol. 13, No. 1, (2013), 87–94. doi:10.4316/AECE.2013.01015
17. ISIC: ISBI, Skin lesion analysis towards melanoma detec- tion. Vol. 3, (2016). [Online]. Retrieved from Https://Goo.Gl/2A1913, Accessed 2016.
18. Burdick, J., Marques, O., Weinthal, J., and Furht, B., "Rethinking Skin Lesion Segmentation in a Convolutional Classifier", ***Journal of Digital Imaging***, Vol. 31, No. 4, (2017), 435–440. doi:10.1007/s10278-017-0026-y
19. Yu, L., Chen, H., Dou, Q., Qin, J., and Heng, P.-A., "Automated melanoma recognition in dermoscopy images via very deep

residual networks", ***IEEE Transactions on Medical Imaging***, Vol. 36, No. 4, (2017), 994–1004. doi:10.1109/TMI.2016.2642839

20. Yuan, Y., Chao, M., and Lo, Y.-C., "Automatic skin lesion segmentation using deep fully convolutional networks with Jaccard distance", ***IEEE Transactions on Medical Imaging***, Vol. 36, No. 9, (2017), 1876–1886. doi:10.1109/tmi.2017.2695227
21. Lin, B. S., Michael, K., Kalra, S., and Tizhoosh, H. R., "Skin lesion segmentation: UNets versus clustering", 2017 IEEE Symposium Series on Computational Intelligence (SSCI), (2017). doi:10.1109/SSCI.2017.8280804
22. Li, Y., and Shen, L., "Skin lesion analysis towards melanoma detection using deep learning network", ***Sensors***, Vol. 18, No. 2 (556), (2018), 1–16. doi:10.3390/s18020556
23. Bi, L., Kim, J., Ahn, E., and Feng, D., "Automatic Skin Lesion Analysis using Large-scale Dermoscopy Images and Deep Residual Networks", (2017), 6–9. Http://Arxiv.Org/Abs/1703.04197
24. Yuan, Y., and Lo, Y.-C., "Improving Dermoscopic Image Segmentation With Enhanced Convolutional-Deconvolutional Networks", ***IEEE Journal of Biomedical and Health Informatics***, Vol. 23, No. 2, (2019), 519–526. doi:10.1109/JBHI.2017.2787487
25. Baghersalimi, S., Bozorgtabar, B., Schmid-saugeon, P., Ekenel, H. K., and Thiran, J., "DermoNet : densely linked convolutional neural network for efficient skin lesion segmentation", ***EURASIP Journal on Image and Video Processing***, Vol. 71, (2019), 1–10. doi:https://doi.org/10.1186/s13640-019-0467-y
26. Hasan, M. K., Dahal, L., Samarakoon, P. N., Tushar, F. I., and Martí, R., "DSNet: Automatic dermoscopic skin lesion segmentation", ***Computers in Biology and Medicine***, Vol. 120, No. April, (2020), 103738. doi:10.1016/j.compbiomed.2020.103738
27. Tang, P., Liang, Q., Yan, X., Xiang, S., Sun, W., Zhang, D., and Coppola, G., "Efficient skin lesion segmentation using separable-Unet with stochastic weight averaging", ***Computer Methods and Programs in Biomedicine***, Vol. 178, (2019), 289–301. doi:10.1016/j.cmpb.2019.07.005
28. Litjens, G., Kooi, T., Bejnordi, B. E., Arindra, A., Setio, A., Ciompi, F., Ghafoorian, M., Laak, J. A. W. M. Van Der, Ginneken, B. Van, and Sánchez, C. I., "A survey on deep learning in medical image analysis", ***Medical Image Analysis***, Vol. 42, No. December 2012, (2017), 60–88. doi:10.1016/j.media.2017.07.005
29. Shen, W., Yang, F., Mu, W., Yang, C., Yang, X., and Tian, J., "Automatic localization of vertebrae based on convolutional neural networks", ***Proceedings of the SPIE on Medical Imaging***, Vol. 9413, (2015), 94132E. doi:10.1117/12.2081941
30. Kawahara, J., and Hamarneh, G., "Multi-resolution-tract CNN with hybrid pretrained and skin-lesion trained layers", Machine Learning in Medical Imaging. Cham: Springer International Publishing, Vol. 10019, (2016), 164–171. doi: 10.1007/978-3-319-47157-0_20
31. Codella, N. C. F., Gutman, D., Celebi, M. E., Helba, B., Marchetti, M. A., Dusza, S. W., Kalloo, A., Liopyris, K., Mishra, N., Kittler, H., and Halpern, A., "Skin Lesion Analysis Toward Melanoma Detection: a Challenge at The 2017 International Symposium on Biomedical Imaging (ISBI), Hosted By The International Skin Imaging Collaboration (ISIC)", Retrieved from ArXiv:1710.05006v3, (2017).
32. ISIC, Skin lesion analysis towards melanoma detection. (2017). Available: [Accessed 08 02 2020], Retrieved from Https://Challenge.Isic-Archive.Com/Landing/2017
33. Vaidya, B., and Paunwala, C., "Deep Learning Architectures for Object Detection and Classification (Chapter 4)", Springer International Publishing, (2019), 53–79. doi:10.1007/978-3-030-03131-2
34. Girshick, R., Donahue, J., Darrell, T., and Malik, J., "Rich feature hierarchies for accurate object detection and semantic segmentation", Proceedings of the IEEE Conference on Computer Vision and Pattern Recognition (CVPR), (2014), 580–587.
35. Girshick, R., "Fast R-CNN", 2015 IEEE International Conference on Computer Vision (ICCV), (2015). doi:10.1109/ICCV.2015.169
36. Ren, S., He, K., Girshick, R., and Sun, J., "Faster R-CNN : Towards Real-Time Object Detection with Region Proposal Networks", NIPS'15: Proceedings of the 28th International Conference on Neural Information Processing Systems, Vol. 1, (2015), 91–99.
37. Liu, W., Anguelov, D., Erhan, D., Szegedy, C., Reed, S., Fu, C., and Berg, A. C., "SSD : Single Shot MultiBox Detector", Computer Vision – ECCV 2016. Lecture Notes in Computer Science, Vol 9905. Springer, Cham, (2016). doi:10.1007/978-3-319-46448-0_2
38. Redmon, J., Divvala, S., Girshick, R., and Farhadi, A., "You Only Look Once: Unified, Real-Time Object Detection", 2016 IEEE Conference on Computer Vision and Pattern Recognition (CVPR), (2016). doi:10.1109/CVPR.2016.91
39. Zou, Z., Shi, Z., Guo, Y., and Ye, J., "Object Detection in 20 Years: A Survey", (2019), 1–39. Retrieved from Http://Arxiv.Org/Abs/1905.05055
40. He, Y., Zeng, H., Fan, Y., Ji, S., and Wu, J., "Application of Deep Learning in Integrated Pest Management: A Real-Time System for Detection and Diagnosis of Oilseed Rape Pests", ***Mobile Information Systems***, Vol. 2019, (2019), 1–14. doi:10.1155/2019/4570808
41. Redmon, J., and Farhadi, A., "YOLO9000: Better, faster, stronger", 2017 IEEE Conference on Computer Vision and Pattern Recognition (CVPR), (2017). doi:10.1109/CVPR.2017.690
42. Redmon, J., and Farhadi, A., "YOLOv3: An Incremental Improvement", (2018). Retrieved from ArXiv:1804.02767v1
43. Haridas, R., and R L, J., "Convolutional neural networks: A comprehensive survey", ***International Journal of Applied Engineering Research***, Vol. 14, No. 3, (2019), 780–789. doi:10.37622/IJAER/14.3.2019.780-789.
44. Simonyan, K., and Zisserman, A., "Very Deep Convolutional Networks For Large-Scale Image Recognition", International Conference on Learning Representations, (2015), 1–14.
45. He, K., Zhang, X., Ren, S., and Sun, J., "Deep Residual Learning for Image Recognition", 2016 IEEE Conference on Computer Vision and Pattern Recognition (CVPR), (2016). doi:10.1109/CVPR.2016.90
46. Szegedy, C., Liu, W., Jia, Y., Sermanet, P., Reed, S., Anguelov, D., Erhan, D., Vanhoucke, V., and Rabinovich, A., "Going Deeper with Convolutions", 2015 IEEE Conference on Computer Vision and Pattern Recognition (CVPR), (2015). doi:10.1109/CVPR.2015.7298594
47. Szegedy, C., Ioffe, S., Vanhoucke, V., and Alemi, A., "Inception-v4, Inception-ResNet and the Impact of Residual Connections on Learning", AAAI'17: Proceedings of the Thirty-First AAAI Conference on Artificial Intelligence, (2017), 4278–4284.
48. Chen, L.-C., Papandreou, G., Kokkinos, I., Murphy, K., and Yuille, A. L., "Semantic Image Segmentation with Deep Convolutional Nets and Fully Connected CRFs", International Conference on Learning Representations, (2015). Retrieved from https://arxiv.org/abs/1412.7062
49. Chen, L., Zhu, Y., Papandreou, G., Schroff, F., and Adam, H., "Encoder-Decoder with Atrous Separable Convolution for Semantic Image Segmentation", Proceedings of the European Conference on Computer Vision (ECCV), (2018), 801–818.

50. Chen, L. C., Papandreou, G., Kokkinos, I., Murphy, K., and Yuille, A. L., "DeepLab: Semantic Image Segmentation with Deep Convolutional Nets, Atrous Convolution, and Fully Connected CRFs", ***IEEE Transactions on Pattern Analysis and Machine Intelligence***, Vol. 40, No. 4, (2017), 834–848. doi:10.1109/TPAMI.2017.2699184

51. Chen, L.-C., Papandreou, G., Schroff, F., and Adam, H., "Rethinking Atrous Convolution for Semantic Image Segmentation", (2017). ArXiv Preprint Http://Arxiv.Org/Abs/1706.05587

52. Al-antari, M. A., Al-masni, M. A., Park, S. U., Park, J. H., Metwally, M. K., Kadah, Y. M., Han, S. M., and Kim, T.-S., "An automatic computer-aided diagnosis system for breast cancer in digital mammograms via deep belief network", ***Journal of Medical and Biological Engineering***, Vol. 38, (2018), 443–456. doi:10.1007/S40846-017-0321-6

53. Powers, D. M., "Evaluation: from precision, recall and F-measure to ROC, informedness, markedness and correlation", ***Journal of Machine Learning Technologies***, Vol. 2, No. 1, (2011), 37–63. Retrieved from https://arxiv.org/abs/2010.16061

54. Pereira, S., Pinto, A., Alves, V., and Silva, C. A., "Brain tumor segmentation using convolutional neural networks in MRI images", ***IEEE Transactions on Medical Imaging***, Vol. 35, No. 5, (2016), 1240–1251. doi:10.1109/TMI.2016.2538465

Persian Abstract

چکیده

جداسازی دقیق ضایعات از تصاویر پوستی در تشخیص و درمان به موقع سرطان پوست و جلوگیری از مرگ بیماران بسیار مهم است. به دلیل تنوع شکل، اندازه، رنگ و محل ضایعات در تصاویر درموسکوپی، جداسازی خودکار ضایعات پوستی همچنان یک چالش محسوب می‌شود. در این مطالعه، یک روش دو مرحله ای برای جداسازی ضایعات پوستی مبتنی بر یادگیری عمیق ارائه می‌شود. در مرحله اول، اندازه و موقعیت مکانی تقریبی ضایعه توسط شبکه های عصبی پیچشی تخمین زده می‌شود. یک زیرتصویر پیرامون مستطیلِ تخمین زده شده‌ی محیط بر ضایعه، از تصویر اصلی جدا شده و به یک تصویر با ابعادِ از پیش تعیین شده، نرمال می‌شود. به منظور جداسازی ناحیه دقیق ضایعه از تصویر نرمال شده، شبکه های عصبی پیچشی در ساختار DeepLab مورد استفاده می‌گیرند. دقت مرحله نرمال سازی بر عملکرد نهایی تاثیر بسزایی دارد. به منظور افزایش دقت مرحله نرمال سازی، از ترکیب چهار شبکه در ساختار Yolov3 استفاده می‌شود. دو روش به منظور ترکیب ساختارهای Yolov3 پیشنهاد می شود. نتایج جداسازی توسط دو شبکه در ساختار +DeepLab3 نیز با هم ترکیب می‌شوند تا دقت مرحله دوم نیز بهبود یابد. یکی دیگر از چالشها در این زمینه وجود تعداد کم تصاویر آموزشی است. برای غلبه بر این مساله، از راهکارهای اضافه کردن تعداد تصاویر آموزشی با ایجاد تغییراتی در تصاویر موجود و همچنین به کارگیری مودهای مختلفِ یک تصویر در هر مرحله از روش پیشنهادی استفاده می‌شود. به منظور ارزیابی روش پیشنهادی، آزمایشها بر روی مجموعه داده شناخته شده ISBI 2017 انجام می‌شوند. نتایج آزمایشها نشان می‌دهد که روش پیشنهادی عملکرد بهتری نسبت به تمامی روشهای موجود ارائه می‌کند.

International Journal of Engineering

Journal Homepage: www.ije.ir

A Blood Supply Chain Network with Backup Facilities Considering Blood Groups and Expiration Date: A Real-world Application

M. Asadpour[a,b,c], O. Boyer[b], R. Tavakkoli-Moghaddam[*d]

[a] *Department of Information Systems and Operations Management, Business School, The University of Auckland, Auckland, New Zealand*
[b] *Department of Industrial Engineering, Najafabad Branch, Islamic Azad University, Najafabad, Iran*
[c] *Young Researchers and Elite Club, Najafabad Branch, Islamic Azad University, Najafabad, Iran*
[d] *School of Industrial Engineering, College of Engineering, University of Tehran, Tehran, Iran*

PAPER INFO

Paper history:
Received 21 September 2020
Received in revised form 08 October 2020
Accepted 30 October 2020

Keywords:
Blood Supply Chain
Goal Programming
Blood Groups
Expiration Date
Backup Facilities

ABSTRACT

The purpose of this paper is to design a green Blood Supply Chain (BSC) network regarding expiration date and backup facilities. The proposed model is a bi-objective Mixed Integer Programming (MIP) one. The two objective functions are to minimize the total cost and the detrimental environmental impacts of shipping between facilities and generated wastes in the network. A Goal Programming (GP) approach is used to convert the multi-objective model into a single one. Moreover, to meet the demand, blood groups and plasma expiration date are also investigated. Since it has been proven that plasma of the people who have fully recovered from COVID-19, can help other patients to recover from this insidious disease; therefore, the proposed BSC network can supply the needs of this particular category of patients as well. To examine the feasibility of the proposed model, some random examples with different dimensions are generated and solved using the CPLEX solver of GAMS software. Furthermore, a real-case problem in Esfahan (Iran) was investigated to illustrate the applicability of the proposed model, and the sensitivity analysis was performed as well. Results approved the applicability of the proposed model in a real situation.

doi: *10.5829/ije.2021.34.02b.19*

1. INTRODUCTION

Blood Supply Chains (BSCs) have been one of the most interesting areas in the literature of the healthcare systems in recent years. What distinguishes the BSC from the other supply chains is that blood is not an ordinary commodity. Also, unlike the business supply chains, which are profit-oriented, the BSC is service-oriented. Besides, lack of blood products can increase the mortality rate. Meanwhile, blood products are very perishable. These criteria make BSC more complicated [1, 2].

The first step in the BSC is collecting blood from donors. After that, testing and production of blood products in the labs and sending them to hospitals are other steps which form a BSC. One of the most critical challenges for managers of the BSC is a continuous increase in demand for blood products while the rate of donors decreases so that American Red Cross reported in 2014, just 10% of US residents are blood donors. In addition, costs of testing, production of blood products, shipping, storage, and distribution are significant for officials of the healthcare systems. It means that managers expect to have a BSC that concurrently meets the demands, reduces wastages, and minimizes costs. Nonetheless, the perishability of most of the blood products leads to constraints and considerable costs for this sophisticated supply chain. Obviously, without a particular decision support framework, managers of the BSC will not be able to meet the demands for most of these products in a timely manner [3].

In the literature of the BSC, there are a wide variety of papers designed a BSC network regarding their own features. However, in Table 1, we only summarized some of them due to the page limitation.

* Corresponding Author Email: *tavakoli@ut.ac.ir* (R. Tavakkoli-Moghadam)

Please cite this article as: M. Asadpour, O. Boyer, R. Tavakkoli-Moghaddam, A Blood Supply Chain Network with Backup Facilities Considering Blood Groups and Expiration Date: A Real-world Application, International Journal of Engineering, Transactions B: Applications Vol. 34, No. 02, (2021) 470-479

TABLE 1. Selected papers of the BSC

Reference No.	Type of problem	Simulation	Mathematical modelling	Single objective	Multi-objective	Back up facilities	Blood groups	Expiration date	Solution method	Case study
[1]	Network design	*							Taguchi method	Tehran/ Iran
[4]	Network design		*	Cost minimization					Branch & Bound	Tehran/ Iran
[5]	Network design		*		Cost minimization; Transportation time minimization; Maximization of tests' reliability				ε-constraint	Tehran/ Iran
[6]	Network design		*		Cost minimization; Transportation time minimization				Max–Min; Utility function; Goal attainment; LP-metric; Goal Programming	Tehran/ Iran
[7]	Network design		*		Cost minimization; The average blood delivery time minimization				ε-constraint; Lagrangian relaxation	
[8]	Location-Allocation		*	Cost minimization		*			Tabu search; Bayesian belief network	Jamshedpur/ India
[9]	Network design	*	*	Cost minimization			*		Branch & Cut	Tehran/ Iran
[10]	Network design		*	Cost minimization		*			GAMS/CPLEX solver	Tehran/ Iran
[11]	Network design		*		Cost minimization; Shortage minimization	*			Goal Programming	Qaemshahr/ Iran
[12]	Network design		*		Cost minimization; Shortage minimization	*	*		Fuzzy VIKOR; GAMS/CPLEX solver	Tehran/ Iran
[13]	Network design		*	Cost minimization		*			Lagrangian relaxation	
[14]	Allocation		*	Shortage minimization			*		Greedy heuristic	Wenchuan/ China
[15]	Location-Inventory	*	*	Cost minimization			*		IBM ILOG CPLEX software	Sichuan/ China
[16]	Network design		*		Cost minimization; Shortage minimization		*		ε-constraint	
[17]	Network design		*	Cost minimization					GAMS/MIP solver	Not clear
[18]	Network design		*	Cost minimization		*			Self-Adaptive Imperialist Competitive; Invasive Weed Optimization	Mazandaran/ Iran
[19]	Network design		*		Cost minimization; Detrimental environmental impacts minimization; Total social impacts maximization	*			ε-constraint; Simulated Annealing; Harmony Search	
Present study	Network design		*		Cost minimization; Detrimental environmental impacts minimization	*	*	*	Goal Programming	Esfahan/ Iran

With respect to the above-mentioned studies, we have not observed any research on the BSC investigating backup facilities, wastes, blood groups, and expiration date in satisfying demands simultaneously. Also, it seems that there has been no research on the BSC in Esfahan up to this time. Hence, regarding the importance and necessity of the subject and lack of any research on this area, the purpose of this paper is to design a green BSC network considering backup facilities, wastes, blood groups, and expiration date for Esfahan.

Similar to the classic supply chains, costs of establishing a BSC are important. Furthermore, there is the possibility of generating wastes because of blood contamination during the processes (because of pollution of test tubes or other devices), blood corruption due to inappropriate temperature conditions, leaking blood bags, etc. Therefore, minimizing the costs of establishing a BSC, along with minimizing the costs of waste and other detrimental environmental impacts, are significant for managers of Esfahan Blood Transfusion Organization (EBTO).

Consequently, the proposed model is a bi-objective MIP model, in which the first objective function is to minimize the total costs, whereas the second objective function is a green function, which investigates the environmental aspects of the problem. Also, regarding the experts' opinions of the EBTO, this study focuses on plasma product. While the proposed network is able to supply the patients' needs the plasma in Esfahan, with minimum costs and the minimum amount of waste, it can also involve recovered patients of COVID-19. In other words, since it has been proven that plasma of people who have fully recovered from COVID-19 can help other patients recover from COVID-19; therefore, the current network can supply the needs of this particular category of patients as well.

To summarize, the most contributions of the present research can be highlighted and listed below:

- ✓ To the best of our knowledge, it is the first BSC study considering backup facilities, blood groups, and expiration date simultaneously.
- ✓ With respect to the type of variables and objective functions, the proposed model is a green one, which actually is novel compared with the previous studies in the BSC literature.
- ✓ It is the first BSC network for EBTO so far that can efficiently supply required demands.
- ✓ Because of considering different scenarios in satisfying demands, the proposed model is flexible enough to cope with fluctuations in demands.
- ✓ With respect to the significance of plasma in treating COVID-19 patients, the proposed model can be invaluable from the perspective of the COVID-19 pandemic as well.

The rest of this paper is organized as follows:

In section 2, the problem and assumptions are defined and the proposed model is formulated. Also, the solution approach is explained. Section 3 examines the feasibility of the proposed model and results of solving the model for a real-case study along with a sensitivity analysis and practical recommendations to managers are presented. Finally, in section 4, the most important results and directions for future research are provided.

2. MODEL AND METHODS

In this paper, a BSC network considering blood groups and expiration date has been designed. Figure 1 shows the network of this problem. As illustrated in this figure, the network of this paper has three echelons, including blood collecting centers, laboratories for quality assurance and producing blood products, and demand centers (hospitals).

Donors refer to blood collecting centers. These centers receive blood from donors and transfer to labs. Blood labs send blood products to demand points (hospitals) after completing the required tests. Also, there are two types of facilities at all echelons of the network, i.e. permanent facilities and backup facilities.

The proposed model is a bi-objective MIP model. The first objective function minimizes total costs, including the establishment cost of facilities, cost of transportation, and cost of holding inventory by designing appropriate constraints and taking into account the level of demand at the hospitals regarding blood groups. The second objective function minimizes the detrimental environmental impacts of shipping between facilities and the amount of generated wastes in the network.

In the proposed model of this study, according to the experts' opinions of the EBTO, a blood product; namely, plasma has been considered.

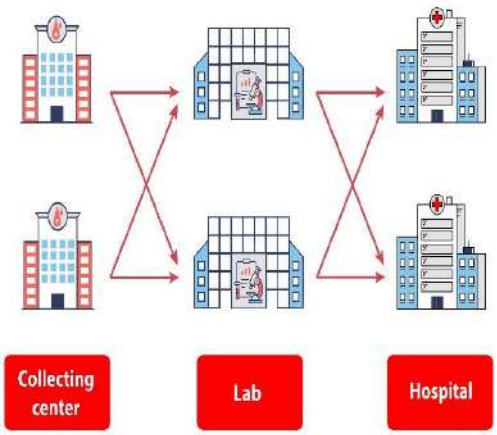

Figure 1. Proposed Blood Supply Chain Network

Moreover, in order to meet the demand, blood groups and plasma expiration date have also been investigated. The assumptions of the proposed model are as follows:

- The establishment cost of all facilities is deterministic and fixed.
- Operation and shipping costs are deterministic and fixed.
- The shipping and operation times are deterministic and fixed and are based on the "day" unit.
- All collected blood at collecting centers will transfer to labs.
- There is blood inventory neither in laboratories nor collecting centers. Inventory is kept just in hospitals.
- A blood product (plasma) is considered.
- There is a percentage of waste at the lab and hospital.

2. 1. Indices Let $I = (i, ib)$ be set of blood collecting centers, where i is permanent blood collecting center while ib indicates a backup blood collecting center. Also, $J = (j, jb)$ and $K = (k, kb)$ are set of labs and hospitals which similare to blood collceting centers, there are two types of labs and hospitals as well, i.e. permanent lab/hospital, and backup lab/hospital. Further, $G = \{g | g = 1, \dots, 8\}$ denotes blood groups. Additionally, V and T are vehicle set and period set respectively. Besides, S exhibit the set of scenarios as well.

The parameters and variables used in this model are presented as follows:

M	A very large number
a_i	Operation time at the blood collecting center for each unit of blood
a_j	Operation time at the lab for each unit of blood
a_k	Operation time at the hospital for each unit of blood
toi	Total operation time at the blood collecting center
toj	Total operation time at the lab
tok	Total operation time at the hospital
d_{kgst}	Blood demand of hospital *k* in period *t* for blood group *g* under scenario *s*
cap_{igt}	Capacity of blood collecting center *i* in period *t* for blood group *g*
h_{kgt}	Holding cost in hospital *k* in period *t* for blood group *g*
scj_{jgt}	Capacity of lab *j* in period t for blood group g
sck_{kgt}	Capacity of hospital *k* in period *t* for blood group *g*
c_{igt}	Operation cost of blood collecting center *i* in period *t* for blood group *g*
c'_{jgt}	Operation cost of lab *j* in period *t* for blood group *g*
c''_{kgt}	Operation cost of hospital *k* in period *t* for blood group *g*
cq_{ij}	Fixed cost of using arc between *i* and *j*
cq'_{jk}	Fixed cost of using arc between *j* and *k*
fi_i	Fixed cost of collecting center establishment
fib_{ib}	Fixed cost of backup collecting center establishment
fj_j	Fixed cost of lab establishment
fjb_{jb}	Fixed cost of backup lab establishment
fk_k	Fixed cost of hospital establishment
fkb_{kb}	Fixed cost of backup hospital establishment
tti_{ij}	Transportation time from the blood collecting center *i* to the lab *j*
tti_{jk}	Transportation time from the lab *j* to the hospital *k*
scv_v	Capacity of vehicle
cv_v	Setup cost of vehicle
T_{gmax}	Expiration date
$EIij_{ij}$	Environmental impacts of shipping between nodes *i* and *j*
$EIjk_{jk}$	Environmental impacts of shipping between nodes *j* and *k*
DC	Cost caused by generating each unit of waste
l_j	Waste percentage of lab
l_k	Waste percentage of hospital
x_{ijgst}	Amount of blood transported of group *g* from the blood collecting center *i* to the lab *j* in period *t* under scenario *s*
y_{jkgst}	Amount of plasma transported of group *g* from the lab *j* to the hospital *k* in period *t* under scenario *s*
inv_{kgst}	Amount of plasma inventory of group *g* in hospital *k* in period *t* under scenario *s*
wi_i	A binary variable which will be 1 if a collecting center is established at node *i*; 0, otherwise
wib_{ib}	A binary variable that will be 1 if a backup collecting center is established at node *i*; 0, otherwise
wj_j	A binary variable that will be 1 if a lab is established at node *j*; 0, otherwise
wk_k	A binary variable that will be 1 if a hospital is established at node *k*; 0, otherwise
wkb_{kb}	A binary variable that will be 1 if a backup hospital is established at node *k*; 0, otherwise
vh_v	A binary variable that will be 1 if a vehicle *v* is used; 0, otherwise
q_{ij}	A binary variable that will be 1 if arc between *i* and *j* is used; 0, otherwise
q'_{jk}	A binary variable that will be 1 if arc between *j* and *k* is used; 0, otherwise
HP_t	Amount of waste at period *t*

2. 2. Model Formulation

$$\begin{aligned}\text{Min } Z_1 = {} & \sum_i \sum_j \sum_g \sum_s \sum_t c_{igt} . x_{ijgst} + \\ & \sum_i \sum_j \sum_g \sum_s \sum_t c'_{jgt} . x_{ijgst} + \\ & \sum_j \sum_k \sum_g \sum_s \sum_t c''_{kgt} . y_{jkgst} + \\ & \sum_k \sum_g \sum_s \sum_t h_{kgt} . inv_{kgst} + \sum_i fi_i . wi_i + \\ & \sum_j fj_j . wj_j + \sum_k fk_k . wk_k + \sum_{ib} fib_{ib} . wib_{ib} + \\ & \sum_{jb} fjb_{jb} . wjb_{jb} + \sum_{kb} fkb_{kb} . wkb_{kb} + \\ & \sum_i \sum_j cq_{ij} . q_{ij} + \sum_j \sum_k cq'_{jk} . q'_{jk} + \sum_v cv_v . vh_v\end{aligned} \quad (1)$$

$$\text{Min } Z_2 = \sum_i \sum_j EIij_{ij} . q_{ij} + \sum_j \sum_k EIjk_{jk} . q'_{jk} + \sum_t DC . HP_t \quad (2)$$

s.t.

$$\sum_j y_{jkgst} - HP_t = d_{kgst} + inv_{kgst} - inv_{kgst-1} \quad \forall k, g, s, \quad (3)$$

$$\sum_j x_{ijgst} \le cap_{igt}.wi_i \quad \forall i, g, s, t \quad (4)$$

$$\sum_i x_{ijgst} \ge \sum_k y_{jkgst} \quad \forall j, g, s, t \quad (5)$$

$$\sum_i x_{ijgst} \le scj_{jgt}.wj_j \quad \forall j, g, s, t \quad (6)$$

$$\sum_j y_{jkgst} \le sck_{kgt}.wk_k \quad \forall k, g, s, t \quad (7)$$

$$\sum_{ib} wib_{ib} \ge 1 \quad (8)$$

$$\sum_{jb} wjb_{jb} \ge 1 \quad (9)$$

$$\sum_{kb} wkb_{kb} \ge 1 \quad (10)$$

$$\sum_i \sum_g x_{ijgst} \le \sum_v scv_v.vh_v \quad \forall j, s, t \quad (11)$$

$$\sum_j \sum_g y_{jkgst} \le \sum_v scv_v.vh_v \quad \forall k, s, t \quad (12)$$

$$(tti_{ij}.q_{ij}) + (tti_{jk}.q'_{jk}) + (toi.wi_i) + (toj.wj_j) + (tok.wk_k) \le T_{gmax} \quad \forall i, j, k \quad (13)$$

$$a_i.\sum_j \sum_g \sum_s \sum_t x_{ijgst} \le toi \quad \forall i \quad (14)$$

$$a_j.\sum_k \sum_g \sum_s \sum_t y_{jkgst} \le toj \quad \forall j \quad (15)$$

$$a_k.\sum_k \sum_g \sum_s \sum_t d_{kgst} \le tok \quad \forall k \quad (16)$$

$$\sum_g \sum_s \sum_t x_{ijgst} \le M.q_{ij} \quad \forall i, j \quad (17)$$

$$\sum_g \sum_s \sum_t y_{jkgst} \le M.q'_{jk} \quad \forall j, k \quad (18)$$

$$\sum_g \sum_s \sum_t x_{ijgst} \ge M.(1 - q_{ij}) \quad \forall i, j \quad (19)$$

$$\sum_g \sum_s \sum_t y_{jkgst} \ge M.(1 - q'_{jk}) \quad \forall j, k \quad (20)$$

$$HP_t = \sum_j \sum_g \sum_s l_j.y_{jkgst} + \sum_g \sum_s l_k.inv_{kgst} \quad \forall k, t \quad (21)$$

$$x_{ijgst}, y_{jkgst}, inv_{kgst}, HP_t \ge 0 \quad (22)$$

$$wi_i, wj_j, wk_k, wib_{ib}, wjb_{jb}, wkb_{kb}, vh_v, q_{ij}, q'_{jk} \in \{0,1\} \quad (23)$$

The objective function (1) minimizes the total cost of the network, including transportation costs, holding inventory cost, and the establishment cost of centers. The objective function (2) minimizes the amount of generated wastes and the detrimental environmental impacts of shipping between facilities.

Constraint (3) ensures that each hospital's demand is met. Constraint (4) states that the amount of the sent blood from each collecting center should not be greater than the capacity of that center. Constraint (5) states that the amount of plasma that is transferred from the lab to the hospital cannot exceed the amount of blood that is sent from the collecting center to the lab. Constraint (6) states that the amount of the sent blood to the lab should not exceed the capacity of the lab. Constraint (7) states that the amount of the sent plasma to each hospital should not exceed the hospital's capacity. Constraints (8) to (10) assure the establishment of backup facilities in each echelon of the network. Constraints (11) and (12) state that the transferred blood from the collecting center to the lab, and the transferred plasma from the lab to the hospital should not exceed the vehicle capacity.

Constraint (13) provides the maximum allowed time for consuming the plasma. Constraint (14) relates to the operation time at the collecting center and indicates that the operation time at the collecting center should not exceed a certain limit. Constraint (15) relates to the operation time in the lab and indicates that the operation time of the lab should not exceed a certain limit. Constraint (16) relates to the operation time at the hospital and indicates that the operation time at the hospital should not exceed a certain limit. Constraints (17) to (20) relate to using arcs between collecting centers and labs, and arcs between labs and hospitals. Constraint (21) specifies the amount of the generated wastes in each period in the laboratory and hospital. Eventually, constraints (22) and (23) define the domains of the decision variables.

2. 3. Solution Approach Multi-objective problems are problems that have more than a single objective function. These objectives usually are not compatible. In fact, optimizing one of the objectives can lead to a non-optimal solution for others. In such a situation, some methods make a trade-off among all objectives' solutions [11, 20, 21].

Goal Programming (GP) is one of these methods, which have been deployed in this research. In this paper, we use the GP approach for solving the bi-objective problem. The method is based on determining goals for all objectives and then minimizing the deviations from these goals. In this procedure, we should use deviation variables. There are two types of deviation variables. The d_i^+ means the amount of objective is more than the goal while d_i^- means the amount of objective is less than the goal. The GP model minimizes the sum of these deviations [11].

The following GP approach is employed in the current research for solving the bi-objective problem:

$$\mathbf{Min} \sum_{i=1}^{n} \boldsymbol{W_i}(\boldsymbol{d_i^+} + \boldsymbol{d_i^-}) \quad (24)$$

s.t.

$$\boldsymbol{h_k(X) = or \le or \ge 0} \qquad \boldsymbol{k = 1, 2, \dots, q} \quad (25)$$

$$\boldsymbol{f_i(X) - d_i^+ + d_i^- = g_i} \qquad \boldsymbol{i = 1, 2, \dots, n} \tag{26}$$

$$\boldsymbol{d_i^+, d_i^- \geq 0} \qquad \boldsymbol{i = 1, 2, \dots, n} \tag{27}$$

where d_i^+ and d_i^- will be calculated using Equations (28) and (29):

$$\boldsymbol{d_i^+ = \begin{cases} f_i(X) - g_i & \text{if } f_i(X) > g_i \\ 0 & \text{otherwise} \end{cases}} \tag{28}$$

$$\boldsymbol{d_i^- = \begin{cases} g_i - f_i(X) & \text{if } f_i(X) < g_i \\ 0 & \text{otherwise} \end{cases}} \tag{29}$$

It should be noted that the sum of weights should be 1.

$$\sum_{i=1}^{n} W_i = 1 \tag{30}$$

The solution steps of the problem are as follows:

I. The problem is solved for each objective function separately to determine the value of goals.
II. The value of its goal is used as the right-hand side for each objective function and by adding deviation variables, the equation is considered as a new constraint in the initial model.
III. Pareto solutions are calculated by using different weights of objective functions.
IV. Based on experts' opinions, the best answer is selected among the dominant solutions.

3. RESULTS AND FINDINGS

To approve the accuracy and feasibility of the proposed model, the model is implemented for sample problems with different dimensions that are generated randomly. All computations are done using CPLEX solver of GAMS software on a laptop with Intel Core i5, 2.5 GHz and 4 GB of RAM. Tables 2 and 3 depict dimensions of the sample problems and values of input parameters respectively. Also, results of solving sample problems are presented in Table 4.

After solving the sample problems and validating the proposed model, to verify the applicability of the proposed model, a real problem is investigated in Esfahan, a metropolitan city in Iran with about 2,000,000 residents according to the last census in 2016. Tables 5 and 6 show the parameters of the case study. Moreover, demands with respect to different blood groups in each scenario have been presented in Tables 7 to 9.

After solving the problem for Esfahan, Pareto solutions are obtained and Table 10 includes these values. It should be noted that for more convenience, all values in this table are divided into 10,000,000.

TABLE 2. Dimensions of sample problems

Problem No.	Collecting center No.	Lab No.	Hospital No.	Blood group No.	Period No.	Vehicle No.	Scenario No.
1	2	2	3	2	1	1	2
2	4	4	6	4	2	4	2
3	10	8	12	8	4	4	2
4	20	12	25	8	4	8	4
5	25	15	30	8	7	12	4

TABLE 3. Distribution of input parameters

Parameter	Values	Parameter	Values
fi_i	uniform(150,250)	fib_{ib}	uniform(30, 50)
fj_j	uniform(250,350)	fjb_{jb}	uniform(50, 75)
fk_k	uniform(300,500)	fkb_{kb}	uniform(80, 100)
d_{kgs1t}	uniform(1,3)	d_{kgs2t}	uniform(3,6)
$EIjk_{jk}$	uniform(1,10)	$EIij_{ij}$	uniform(1,10)
tti_{ij}	uniform(0.3,0.5)	tti_{jk}	uniform(0.3,0.5)
c_{igt}	uniform(2,9)	c'_{jgt}	uniform(4,18)
c''_{kgt}	uniform(2,9)	cq_{ij}	uniform(1,5)
cq'_{jk}	uniform(1,5)	h_{kgt}	uniform(3,8)

TABLE 4. Objective values of sample problems

Problem No.	Objective functions	Objective values
1	f1	6477
	f2	75
2	f1	11728
	f2	527
3	f1	28780
	f2	923
4	f1	63976
	f2	2290
5	f1	89518
	f2	3173

TABLE 5. Establishment costs of facilities

Parameter	Values(IRR)	Parameter	Values(IRR)
fi_i	8500	fib_{ib}	180
fj_j	20500	fjb_{jb}	630
fk_k	76000	fkb_{kb}	3000

TABLE 6. Capacities of facilities

Parameter	Values	Parameter	Values
cap_{igt}	1000	scj_{jgt}	1000
scv_v	600	sck_{kgt}	5000

TABLE 7. Demands in the first Scenario

Blood Group	Period 1	Period 2	Period 3	Period 4
A^+	194	227	274	299
B^+	214	233	248	276
AB^+	221	242	245	290
O^+	235	284	341	360
A^-	28	31	34	41
B^-	31	49	57	63
AB^-	39	45	50	53
O^-	15	17	26	29

TABLE 8. Demands in the second Scenario

Blood Group	Period 1	Period 2	Period 3	Period 4
A^+	386	418	475	519
B^+	331	339	364	387
AB^+	315	328	336	394
O^+	451	490	549	588
A^-	48	55	59	67
B^-	65	69	71	77
AB^-	58	61	64	69
O^-	34	41	48	51

TABLE 9. Demands in the third Scenario

Blood Group	Period 1	Period 2	Period 3	Period 4
A^+	523	560	616	639
B^+	418	441	499	521
AB^+	429	456	484	510
O^+	751	805	838	895
A^-	75	81	86	93
B^-	89	93	94	102
AB^-	76	88	96	97
O^-	55	55	63	71

Furhtermore, Figure 2 presents a Pareto frontier of the case study problem and clearly reveales conflicting between objcetive functions. Since the cost of the first objective function is sharply higher than the second one, experts of EBTO selected the 11th Pareto solution as the best possible solution for the network. Therefore, the objective values are 25,182,674,000,000 IRR for the first objective function, and 20,160,000,000 IRR for the second objective function. Accordingly, the network

TABLE 10. Pareto solutions

Weight of Z_1 (W1)	Weight of Z_2 (W2)	Pareto solution No.	Z_1 value (IRR)	Z_2 value (IRR)
1	0	1	6,378,300.000	240.862
0.9	0.1	2	5,974,800.000	275.600
0.8	0.2	3	5,690,600.000	326.900
0.7	0.3	4	5,149,100.000	443.300
0.6	0.4	5	4,486,700.000	663.100
0.5	0.5	6	4,087,200.000	822.000
0.4	0.6	7	3,716,300.000	1,016.600
0.3	0.7	8	3,427,800.000	1,201.400
0.2	0.8	9	3,138,500.000	1,372.900
0.1	0.9	10	2,657,700.000	1,813.700
0	1	11	2,518,267.400	2,016.000

includes 10 blood collecting centers, eight labs, 10 hospitals, and four vehicles. Figure 3 shows the established BSC network for Esfahan. Also, as a sample, in Tables 11 and 12, the flow between two collecting center and lab, and lab and hospital are presented according to the first scenario.

3. 1. Sensitivity Analysis In this section, a sensitivity analysis is performed for the a_j; namely, operation time at the lab for each unit of blood based on experts' opinions. The range of parameter variations is examined from a 50% decrease to a 200% increase.

Table 13 depicts the results of these changes. Also, Figure 4 illustrates the changes in the first objective function as well. It should be noted that for more convenience, all values in Table 13 and Figure 4 have been divided into 10,000,000.

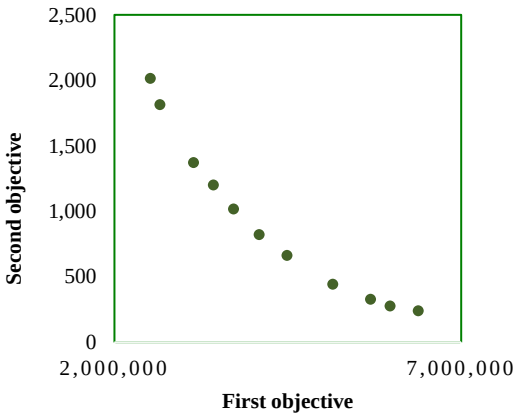

Figure 2. Pareto frontier of case study

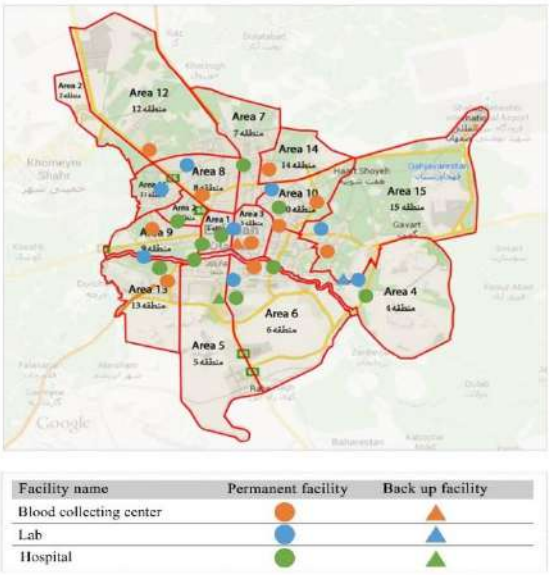

Figure 3. BSC Network for Esfahan

TABLE 11. Blood flow between Collecting center 1 & Lab 1

Blood Group	Period 1	Period 2	Period 3	Period 4
A^+	15		34	28
B^+		27	32	
AB^+	32	25		29
O^+	37	24	35	15
A^-			7	11
B^-	6	13		5
AB^-	8	7	11	
O^-	3		2	5

TABLE 12. Product flow between Lab 1 & Hospital 1

Blood Group	Period 1	Period 2	Period 3	Period 4
A^+	32	45		57
B^+	66		46	
AB^+	40	59	27	35
O^+	52	55	38	73
A^-		6	7	11
B^-	8			8
AB^-	3	5	5	
O^-	4	2	5	6

As shown in Figure 4, the value of the first objective function goes down with any drop in a_j. Whereas the difference between values of the first objective function regarding 10 and 25% decrease in a_j is not very significant, by 50% reduction in a_j, the value of first objective function declines noticeably. Also, the first objective function is infeasible for either 10% or higher growth in a_j. Further, the second objective function is not sensitive to changes in a_j. Additionally, similar to the first objective function, the second objective function is infeasible for a 10% or higher rise in a_j. Hence, EBTO managers should be aware of the critical time of operation in the lab, and it may be advisable that by increasing the capacity (in the form of either expanding existing labs or establishing new labs) provides an amount of float for a_j.

3. 2. Managerial Insight In this research, a BSC for Esfahan is designed, whose results are helpful for the managers of EBTO in some certain aspects. In particular, we have formulated a BSC regarding specific features and constraints of EBTO that can satisfy the demands in a timely manner. While in real situations, demand can be affected by unexpected occurrences (e.g. disaster), we deployed different scenarios to better capture demand fluctuations. However, the managers of EBTO are advised to monitor the status of demands periodically and once they see a trend (usually ascending trend) immediately take required decisions to be ready for

TABLE 13. Results of the sensitivity analysis in a_j

a_j (%)	-50	-25	-10	0	10	25	50	100	200
First objective function	2509481.4	2516524.4	2516535.4	2518267.4	Infeasible	Infeasible	Infeasible	Infeasible	Infeasible
Second objective function	2016	2016	2016	2016	Infeasible	Infeasible	Infeasible	Infeasible	Infeasible

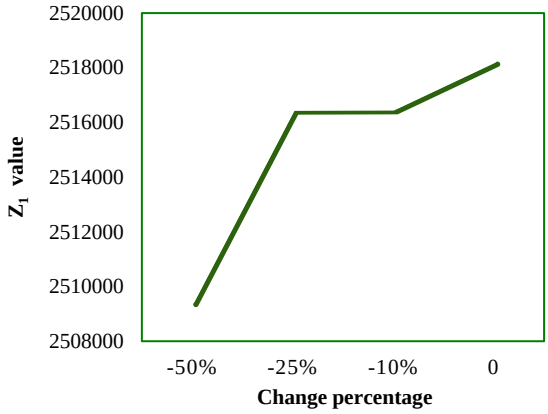

Figure 4. First objective function values based on changes in operation time in the lab

satisfying the possible increasing demand. Furthermore, results of the sensitivity analysis revealed that the situation in the lab (from the operation time perspective) is somehow fragile. Thus, the EBTO managers should consider possible alternatives to prevent network disruption due to forming a bottleneck in the lab (test and production echelon).

4. CONCLUSION AND FUTURE RESEARCH

In this paper, a BSC network considering backup facilities, blood groups, and expiration date has been designed. The proposed model is a bi-objective location-allocation-inventory model that, by designing appropriate constraints and considering inventory at the demand points, not only minimizes total costs but also satisfies hospitals' demand. Furthermore, demands have been met with regard to blood groups. Also, the proposed network can involve recovered patients of COVID-19. More specifically, since it has been proven that plasma of people who have fully recovered from COVID-19, can help other patients recover from COVID-19. Therefore, the proposed BSC network can supply the needs of this particular category of patients as well. A Goal Programming approach has been applied to solve the bi-objective problem and has been examined in a real case in Esfahan, Iran. Besides, a sensitivity analysis has been performed to provide additional managerial suggestions for the decision-makers in EBTO.

In future research, researchers can investigate the possibility of storing inventory at all echelons of the BSC network. Additionally, designing and modeling a multi-product BSC network under assumptions of this paper, applying a robust approach for facing uncertain parameters, considering wastes for collecting centers, and developing heuristic and meta-heuristic techniques for solving problems in large scales would be interesting for future studies.

5. REFERENCES

1. Zahraee, S. M., Rohani, J. M., Firouzi, A., and Shahpanah, A., "Efficiency improvement of blood supply chain system using Taguchi method and dynamic simulation", ***Procedia Manufacturing***, Vol. 2, (2015), 1-5. doi: 10.1016/j.promfg.2015.07.001.
2. Samani, M. R. G., Torabi, S. A., and Hosseini-Motlagh, S. M., "Integrated blood supply chain planning for disaster relief", ***International Journal of Disaster Risk Reduction***, Vol. 27, (2018), 168-188. doi:10.1016/j.ijdrr.2017.10.005.
3. Osorio, A. F., Brailsford, S. C., and Smith, H. K., "A structured review of quantitative models in the blood supply chain: a taxonomic framework for decision-making", ***International Journal of Production Research***, Vol. 53, No. 24, (2015), 7191-7212. doi:10.1080/00207543.2015.1005766.
4. Jabbarzadeh, A., Fahimnia, B., and Seuring, S., "Dynamic supply chain network design for the supply of blood in disasters: A robust model with real world application", ***Transportation Research Part E: Logistics and Transportation Review***, Vol. 70, (2014), 225-244. doi:10.1016/j.tre.2014.06.003.
5. Fazli-Khalaf, M., Khalilpourazari, S., and Mohammadi, M., "Mixed robust possibilistic flexible chance constraint optimization model for emergency blood supply chain network design", ***Annals of Operations Research***, Vol. 283, No. 1, (2019), 1079-1109. doi:10.1007/s10479-017-2729-3.
6. Khalilpourazari, S., and Khamseh, A. A., "Bi-objective emergency blood supply chain network design in earthquake considering earthquake magnitude: a comprehensive study with real world application", ***Annals of Operations Research***, Vol. 283, No. 1, (2019), 355-393. doi:10.1007/s10479-017-2588-y.
7. Fahimnia, B., Jabbarzadeh, A., Ghavamifar, A., and Bell, M. "Supply chain design for efficient and effective blood supply in disasters", ***International Journal of Production Economics***, Vol. 183, (2017), 700-709. doi:10.1016/j.ijpe.2015.11.007.
8. Sharma, B., Ramkumar, M., Subramanian, N., and Malhotra, B., "Dynamic temporary blood facility location-allocation during and post-disaster periods", ***Annals of Operations Research***, Vol. 283, No. 1, (2019), 705-736. doi:10.1007/s10479-017-2680-3.
9. Salehi, F., Mahootchi, M., and Husseini, S. M. M., "Developing a robust stochastic model for designing a blood supply chain network in a crisis: A possible earthquake in Tehran", ***Annals of Operations Research***, Vol. 283, No. 1-2, (2019), 679-703. doi:10.1007/s10479-017-2533-0.
10. Cheraghi, S., and Hosseini-Motlagh, S. M., "Optimal blood transportation in disaster relief considering facility disruption and route reliability under uncertainty", ***International Journal of Transportation Engineering***, Vol. 4, No. 3, (2017), 225-254. doi:10.22119/IJTE.2017.43838.
11. Habibi-Kouchaksaraei, M., Paydar, M. M., and Asadi-Gangraj, E., "Designing a bi-objective multi-echelon robust blood supply chain in a disaster", ***Applied Mathematical Modelling***, Vol. 55, (2018), 583-599. doi:10.1016/j.apm.2017.11.004.
12. Cheraghi, S., and Hosseini-Motlagh, S. M., "Responsive and reliable injured-oriented blood supply chain for disaster relief: a real case study", ***Annals of Operations Research***, (2018), 1-39. doi:10.1007/s10479-018-3050-5.
13. Rahmani, D., "Designing a robust and dynamic network for the emergency blood supply chain with the risk of disruptions", ***Annals of Operations Research***, Vol. 283, No. 1, (2019), 613-641. doi:10.1007/s10479-018-2960-6.
14. Ma, Z. J., Wang, K. M., and Dai, Y., "An emergency blood allocation approach considering blood group compatibility in disaster relief operations", ***International Journal of Disaster Risk Science***, Vol. 10, No. 1, (2019), 74-88. doi:10.1007/s13753-018-0212-7.
15. Chen, S., and Wang, C., "Incorporating a Bayesian Network into Two-Stage Stochastic Programming for Blood Bank Location-Inventory Problem in Case of Disasters", ***Discrete Dynamics in Nature and Society***, (2019). doi:10.1155/2019/7214907.
16. Naghipour, M., and Bashiri, M., "Designing a Bi-Objective Stochastic Blood Supply Chain Network in a Disaster", In 15th Iran International Industrial Engineering Conference (IIIEC), (2019), 171-177. doi: 10.1109/IIIEC.2019.8720727.
17. Ghasemi, S., "The Location Allocation Problem of After Disaster Blood Supply Chain", In 15th Iran International Industrial

Engineering Conference (IIIEC), (2019), 127-131. doi:10.1109/IIIEC.2019.8720635.

18. Haghjoo, N., Tavakkoli-Moghaddam, R., Shahmoradi-Moghadam, H., and Rahimi, Y., "Reliable blood supply chain network design with facility disruption: A real-world application", ***Engineering Applications of Artificial Intelligence***, Vol. 90, (2020), 103493. doi: 10.1016/j.engappai.2020.103493.
19. Eskandari-Khanghahi, M., Tavakkoli-Moghaddam, R., Taleizadeh, A. A., and Amin, S. H., "Designing and optimizing a sustainable supply chain network for a blood platelet bank under uncertainty", ***Engineering Applications of Artificial Intelligence***, Vol. 71, (2018), 236-250. doi: 10.1016/j.engappai.2018.03.004.
20. Saeidi-Mobarakeh, Z., Tavakkoli-Moghaddam, R., Navabakhsh, M., and Amoozad-Khalili, H., "A Bi-level Meta-heuristic Approach for a Hazardous Waste Management Problem", ***International Journal of Engineering, Transactions A: Basics***, Vol. 33, No. 7, (2020), 1304-1310. doi:10.5829/IJE.2020.33.07A.17.
21. Akbarpour, N., Hajiaghaei-Keshteli, M., and Tavakkoli-Moghaddam, R., "New Approaches in Meta-heuristics to Schedule Purposeful Inspections of Workshops in Manufacturing Supply Chains", ***International Journal of Engineering, Transactions B: Applications***, Vol. 33, No. 5, (2020), 833-840. doi:10.5829/IJE.2020.33.05A.15.

Persian Abstract

چکیده

هدف مقاله حاضر طراحی شبکه سبز زنجیره تامین خون با توجه به تاریخ انقضا و تسهیلات پشتیبان است. مدل پیشنهادی یک مدل سبز چند هدفه برنامه ریزی مختلط عدد صحیح است. تابع هدف اول، حداقل سازی هزینه کل است و تابع هدف دوم، اثرات مخرب زیست محیطی ناشی از حمل و نقل و پسماندهای تولید شده در شبکه را به حداقل می رساند. برای حل مدل چندهدفه پیشنهادی از یک رویکرد برنامه ریزی آرمانی استفاده شده است. علاوه بر این ، تامین تقاضا با توجه به گروههای خونی و تاریخ انقضا پلاسما صورت می گیرد. از آنجا که ثابت شده است که پلاسمای افرادی که به طور کامل از بیماری COVID-19 بهبود یافته اند می تواند به بهبودی بیماران دیگر کمک نماید، بنابراین، شبکه پیشنهادی می تواند نیاز این دسته از بیماران را نیز تأمین کند. به منظور اعتبارسنجی مدل پیشنهادی مسائل تصادفی در ابعاد مختلف ایجاد و با استفاده از نرم افزار GAMS حل شده اند. همچنین مدل پیشنهادی برای یک مساله واقعی در اصفهان حل و بر روی نتایج به دست آمده تحلیل حساسیت انجام گرفته است. نتایج، کارایی مدل پیشنهادی در شرایط واقعی را تأیید می کند.

International Journal of Engineering

Journal Homepage: www.ije.ir

Laser Cladding of PAC 718, Tribaloy T-700 and METCO 41 C Hard Facing Powders on AISI SS 304L Substrate

S. R. More[a], D. V. Bhatt[b], J. V. Menghani[b], C. P. Paul[c], G. R. Desale[d]

[a] *V R Siddhartha Engineering College, Vijayawada, A.P, India*
[b] *S V N I T, Surat, Gujarat, India*
[c] *RRCAT, Indore, M.P. India*
[d] *CSIR-NCL Pune, Maharashtra, India*

PAPER INFO

Paper history:
Received 25 June 2020
Received in revised form 12 September 2020
Accepted 29 October 2020

Keywords:
Fiber Laser
Laser Cladding
Clad Properties
Micro-hardness
Hard Powder
SS304L

ABSTRACT

The present investigation aims to deposit the three different hard facing powder (Triboloy T-700 and PAC 718, and TETCO 41 C) on SS 304L using laser cladding technique. The single and overlapped clad track was deposited using 2 kW laser power system. The optimized laser process parameters and 50% overlap clad track was used to deposit a large surface area. The optimum laser process parameters were finalised using single clad structure study. The cross-sections of the clad layers were used to obtain the microstructure and micro-hardness from different regions namely, clad layer, diffusion layer, and substrate. Throughout the study, the laser power was kept constant i.e. 1.2 kW. For single clad deposition, the scanning speed and powder feed rate varied from 0.3 to 0.5 m/min and 4 to 9 g/min, respectively. T-700 and PAC 718 shows uniform developing micro-structure while METCO 41 C shows the development of mixed dendritic and cellular type microstructure. The Triboloy shows the maximum surface hardness of 534 Hv, 321 Hv for PAC 718, and 294 Hv for METCO 41 C.

***doi**: 10.5829/ije.2021.34.02b.20*

1. INTRODUCTION

Laser cladding technique is an effective way to develop hard powder coating on different engineering components. The powder coating applied for a reduction in the failure of the mechanical component due to erosion-corrosion wear. The laser cladding process having two methods i.e. pre-placed (two-stage) and direct method (one stage). In the two-stage method, the re-melting of pre-placed coating powder was done with a laser beam. In one-stage method coating material in the form of powder or wire was supplied and melted simultaneously using a laser beam. Laser cladding techniques have some great advantages like good metallurgical bonding between coating and substrate, minimum dilution, less porosity and thermal distortion over the other coating methods. The quality of laser clad depends on clad geometrical properties and good geometrical properties depend on laser process parameters. Table 1 shows the effect of an increase in laser process parameters on clad geometrical properties [1-4].

Many studies on laser cladding were carried out using different coating powders like Aluminium alloys, Stellite, Titanium alloys, Inconel, Stainless Steels, mild steel, etc. Co, Cr, and Ni-base alloy have been widely used for engineering applications because of good erosion-corrosion resistance properties. Khorram et al. [4] used the RSM technique to investigate the response of scanning speed, pulse width and laser frequency on clad geometry, hardness and dilution ratio. They found that pulse width and laser frequency have a positive effect on clad angle, width and dilution ration and negative effect on hardness and clad height. Moradi et al. [5, 6] Investigated the effect of laser power, focal plane position in powder stream and scanning pattern on mechanical characterization, dimensional properties and Micro-structural changes on satellite 6 powder. They found lower Distortion, higher micro-hardness, lower

*Corresponding Author Institutional Email: moresatish11@yahoo.co.in (S. R More)

Please cite this article as: S. R. More, D. V. Bhatt, J. V. Menghani, C. P. Paul, G. R. Desale, Laser Cladding of PAC 718, Tribaloy T-700 and METCO 41 C Hard Facing Powders on AISI SS 304L Substrate, International Journal of Engineering, Transactions B: Applications Vol. 34, No. 02, (2021) 480-486

TABLE 1. Function clad properties (Increase= +; Reduction= -) [1]

Parameters	Clad Properties				
	Clad Height	Clad Depth	Dilution	Hardness	Clad Thickness
Laser Power	-	+	+	-	+
Coating Material Quantity	+	-	-	+	+
Powder Feed Rate	+	-	-	+	-
Laser Beam Spot	+	-	-	+	-

grain size, and higher stability obtained by applying a unidirectional scanning pattern. In addition, they observed that laser power leads to change in the width and height of clad. Vyas et al. [7] investigated mechanical and metallurgical properties of high entropy alloy (AlFeCuCrCoNi-WC10) laser cladding coating on SS 316. They found a 4.5 fold improvement in micro-hardness as compared to the base metal and fine-grained non-directional microstructure away and columnar grains near the base material.

However, it is necessary to study the setting of laser process parameters for achieving good quality clad surface. Limited work is available on selection of laser process parameters especially for Nickel, cobalt and Fe base alloy cladding on SS 304L using one stage cladding process. There is scope to found the best possible laser process parameters for Nickel, cobalt and Fe base alloys coating on SS 304L. In the present work, all three powders are used to develop hard facing coating on SS 304L material and find out how the single clad is useful to investigate the best possible laser coating parameters for developing large surface coatings. In addition, the effect of laser cladding process parameters on microstructure and micro-hardness were briefly investigated.

2. EXPERIMENTAL SET UP

The laser cladding work was carried out at Department of Atomic Energy Raja Ramanna Centre for Advanced Technology (RRCAT), Indore (MP) India, using a 2 kW C-W fibre laser system as shown in Figure 1. The system consists of 2 kW fibre laser, 5 axis manipulator in a glove box, coaxial nozzle, computer numerical controller, twin powder feeder, a camera with image processing hardware and gas analyzers [8].

(a) Photographic view of LRM lab arrangement (b) Arrangement of Co-axial nozzle

Figure 1. Photographic view of 2 kW C-W fiber laser system

3. EXPERIMENTAL PROCEDURE AND MATERIAL USED

3. 1. Laser Cladding Process The SS304L plates of size 75 mm diameter and 10 mm thickness were used for laser cladding of three different hard facing powders. Before starting the laser cladding process, the substrates are cleaned with water and acetone to remove any contaminant present on the surface of the substrate. The coaxial nozzle and powder feeder are calibrated for various powder flow rates by collecting and measuring the weight of powder for a known period. The pressurized Argon gas is used to regulate the flow rate of cladding powder. The hard face laser cladding powders are preheated using a co-axial nozzle and 1.2 kW higher power laser beam. The substrate surface is scanned using a laser beam and cladding powder; and accordingly, the thin layer of substrate and cladding powder is melted to develop the melt pool. The melted thin layer from the substrate is known as wetting of the substrate. The clad track on the substrate surface is formed due to rapidly solidified melt pool by self-quenching when the laser beam left the melted pool. The effect of laser processing parameters on clad geometry, i.e. clad width and height, dilution and porosity are examined by depositing single clad track of length 50 mm on the substrate material. From the single clad track analysis, the optimum laser processing parameters are selected for cladding the larger surface area of the substrate. The 50% overlapped cladding process is used to clad the large surface area. These laser cladding samples are used for characterizations and microscopic analysis. The location of laser spot point is 2 mm above the powder concentration plane [5].

3. 2. Properties of Material Used The present investigation is based on SS304 L as target (substrate) material. This material is commonly used in various industries and power plants because it has no effect of radiation; its chemical composition is shown in Table 3.

Three different powders namely, Tribaloy T-700, PAC 718 and METCO 41 C are used for cladding on steel by using 2 kW C-W fiber lasers.

Tables 2 and 3 show the physical properties and chemical composition of cladding powders. The size of powder maintained range of 45-106 μm, because it is easy to feed through feeder during the cladding process. The SEM micrographs of three powders are shown in Figure 2, which reveals the particle shape and size.

3. 3. Range of Parameters Table 4 shows the range of parameters used for single clad track for laser process parameters optimization and 50% overlapped clad for complete cladding process for all three powders on the substrate. For the process of single and 50% clad the laser power kept constant i.e. 1.2 kW. For single clad track, process the scanning speed and powder feed rate varied from 0.3 to 0.5 m/min and 4 to 9 g/min, respectively. From the result of process parameters optimization and single clad structure study, it was decided to carry out overlap cladding on stainless steel according to the parameters shown in the last column of Table 4 for all three powders. During laser cladding process the substrate was kept open in at atmospheric temperature.

3. 4. Microscopic Analysis with Sample Preparation The transverse section of single and 50% overlap clad track was obtained by cutting the clad track with a diamond cutter. The cut sample was mounted using resins with hot mounting process. After hot mounting, initially, the sample was ground using abrasive belt (180 grit) grinder. Then, fine polishing was done on sandpapers of different size up to # 1200. The mirror finishes of the sample obtained by polishing on wheel machine with the size of 1 μm diamond paste. The microstructure of claded samples with three types of powders was observed by using samples etched with an etchant of composition: 10% Oxalic acid in water kept for 60 sec. at 12 Volts and 2 Amp current. The Vickers hardness tester is used to measure the micro-hardness of laser clad samples. The micro-hardness is measured by applying 0.981 N loads on polished laser clad surface for the 30-sec.

4. RESULTS AND DİSCUSSİON

4. 1. Single Clad Structure Study The laser cladding process parameters are responsible for the quality and quantity of clad track. Figure 3 (a-c) shows the photographic view of a single clad structure for all three powders. Figure 4 (a and b) shows the effect of powder feed rate and scanning speed on the width of

TABLE 2. Physical properties of cladding powders

Powder	Density (g/cm^3)	Melting Temp (°C)	Micro Hardness (0.981 N)	Grain Size (μm)
Tribaloy T-700	7.92	1200 -1300	543 Hv	
PAC 718	8.19	1260 – 1336	353 Hv	106 /45
MEC 41-C	8.35	1000 – 1150	344 Hv	

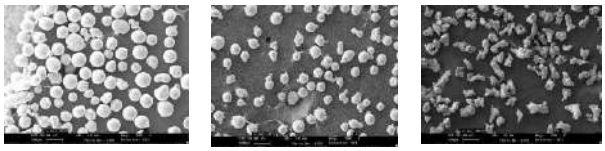

(a) Tribaloy T-700 (b) PAC 718 (c) METCO 41C

Figure 2. SEM of Three Hard Facing Powders

TABLE 3. Major chemical composition of substrate material and three different cladding powders

Substrate and Powder	Major elemental composition (wt. %)									
	C	Mn	Si	Cr	Ni	Mo	Fe	Ti	Co	Al
AISI SS304L	0.03	2.0	0.75	17.50-19.50	8-12	---	---	---	----	----
Tribaloy T-700	0.08	--	3.4	16	Balance	32	1.5	---	1.5	----
PAC 718	0.08	0.35	0.35	17-21	50-55	2.80-3.30	1.5	0.65-1.15	1	0.20-0.80
MEC 41-C	0-1	--	1	17	12	2-5	Balance	--	--	--

TABLE 4. Range of parameters for laser cladding

Substrate (base) material	Cladding Powder	Laser beam power, kW	Laser Beam Diameter, mm	Laser scanning speed, m/min	Powder feed rate, g/min	Overlapping, 50 %	
						Scan Speed	Powder Feed Rate
AISI SS 304 L	Tribaloy T-700	1.2	2.5	0.3, 0.4, 0.5	5, 7, 9	0.4 m/min	7 g/min
	PAC 718	1.2	2.3	0.3, 0.4, 0.5	4, 6, 8	0.4 m/min	6 g/min
	METCO 41 C	1.2	2.5	0.3, 0.4, 0.5	5	0.4 m/min	5 g/min

(a) Tribaloy T–700 (b) PAC 718 (c) METCO 41 C

Figure 3. Photographic view of single pass clad track of different materials

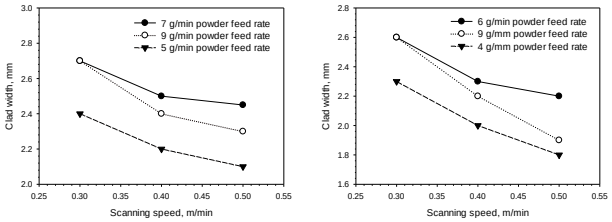

(a) Tribaloy T-700 (b) PAC 718

Figure 4. Clad width as a function of powder feed rate for single track clad layer on AISI SS304 L

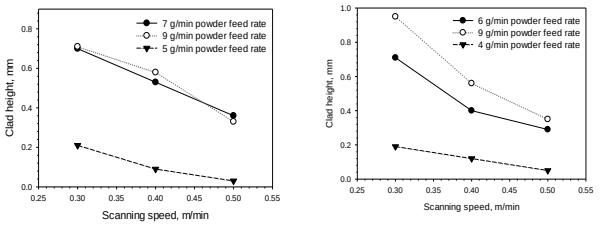

(a) Tribaloy T-700 (b) PAC 718

Figure 5. Clad height as a function of powder feed rate for single track clad layer on AISI SS304 L

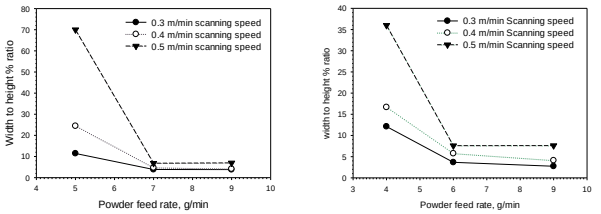

(a) Tribaloy T-70 (b) PAC 718

Figure 6. Dilution as function of powder feed rate for single track clad layer on AISI SS304 L

clad track for Tribaloy T-700 and PAC 718, respectively. Width of the clad layer is approximately equal to the laser beam diameter and inversely proportional to laser scanning speed with constant feed rate [9, 11]. This happens due to shorter contact time and heat (laser beam) on the surface of the substrate, as available laser beam power (J/mm) decreases with a reduction in scanning speed. Most of the time clad track width is small as compared to laser beam diameters. This happens due to higher laser scanning speed with the laser power decreases [10].

Similarly, Figures 5(a) and 5-b) show the effect of feed rate and laser scanning speed on clad height. The clad height increases with reducing scanning speed at constant feed rate. In addition, clad height increases by increasing powder feed rate at constant scanning speed as shown in Figure 5 (b) [10, 12]. The powder feed rate is a significant parameter for clad track height as it has stronger effect on variation in dilution. The lower scanning speed is more significant as compared to higher speed for different powder feed rate on different clad heights as shown in Figure 5 (a and b) [15]. The width to height ratio of clad layer was calculated for both Tribaloy T-700 and PAC 718 powders. Figures 6(a) and 6(b) show the effect of change in scanning speed and powder feed rate on clad geometry. The results show that the percentage width to height ratio of the clad layer decreases with increasing the scanning speed and powder flow rate, a trend generally reported in the literature [10-16]. The ratio of clad width to height is directly proportional to laser scanning when flow rate of clad powder remains constant. This is happened due to availability of cladding per unit length is less, so higher amount of availability of laser energy on substrate surface causes the increasing the surface melting and depth of penetration of substrate surface [10, 15]. The highest percentage width to height ratio of 70% was observed for Tribaloy T-700 clad layer at the 5 g/min, 0.5 m/min powder flow rate and scanning speed, respectively. For PAC 718 it 37% at 4 g/min, 0.5 m/min powder flow rate and scanning speed, respectively. For both coating powders the lowest percentage of width to height ratio 5 to 7% is obtained at 9 g/min, 0.3 m/min powder flow rate and scanning speed, respectively as shown in Figure 6.

4. 2. Overlapped Clad Structure Study The 50% overlapped clad tracks for three powders were performed based on single pass clad experimental study at 1.2 kW laser power with a scanning speed of 0.4 m/min for three powders. Powder feed rate was kept at 7g/min for Tribaloy T-700, 6 g/min for PAC 718 and 5 g/min for METCO 41 C. Figure 7 (a-c) shows the surface morphologies of Tribaloy T-700, PAC 718 and METCO 41 C hard face clad layer on the substrate (SS 304L). These figures did not show any porosity, distortion and cracks on overlap clad surface of all three powders. The microstructures of clad layers of three powders at the junction and clad surface along the cross-section were examined under optical microscope (Figure 7 (a-c)). PAC 718 and Tribaloy T-700

microstructures show the development of a uniform type of dendritic growths along the direction of clad height at the junction and clad surface (Figure 7 (a,b)). Whereas, mixed dendritic and cellular type microstructure was observed for the clad layer of METCO 41C (Figure 7(c)).

The Vickers hardness tester was used to measure the micro-hardness of all three laser clad layer (Tribaloy T-700, PAC 718 and METCO 41 C). Micro-hardness was measured in three regions along the cross-section on the base metal (SS 304L), the junction (fusion line) and clad layers to investigate variations developed in hardness due to laser cladding as shown in Figure 7. The distance between two indentations was kept at 0.05 mm of all three regions for micro-hardness testing. Figure 7 (a-c) shows the size difference in micro-hardness indentation marks for all three regions. It shows that the size of the indentation mark decreases from the substrate to the top layer of the clad surface. This shows that micro-hardness increases from the substrate to the top layer of the clad surface. In addition, porosity and the crack was not observed on the fusion line (interfacial region), which indicates good bonding between the coating material and base metal (substrate) [3, 18]. Figure 8 is the graphical representation of micro-hardness distribution on the clad cross-section for three different clad powders. The two different zones appear in the graphical representation of micro-hardness curve corresponding to clad layer and base metal. On base metal 212 Hv (0.981), micro-hardness was observed which is representative and nearer to SS 304L (substrate). The Tribaloy T-700 shows the noticeable improvement in micro-hardness 246 Hv (0.981) on fusion line as compared to the other two powders cladding. The significant improvement in micro-hardness value i.e. 246 to 510 Hv (0.981 N) is observed from fusion line to top layer of Tribaloy T-700 clad surface. This sudden change in micro-hardness may be credited due to change in microstructure along the interface in the clad layer [3, 17]. Similarly, micro-hardness of clad layer PAC 718 and METCO 41C was investigated on 0.981 N load and graphically represented in Figure 10. The PAC 718 shows 206 Hv, 202 Hv at base metal and fusion line (interaction region), respectively as shown in Figure 8. Approximate micro-hardness values of 260 and 290 for PAC 718 and METCO 41C, respectively were observed by further increasing distance of indentation from interaction (fusion line) towards the top surface of the clad layer. Then, the value of micro-hardness suddenly drops to 211 Hv and 202 Hv for PAC 718 and METCO 41C, respectively at the top surface of the clad layer. This may be due to presence of some porosity, or inappropriate sample preparation (not up to the mark). Thus, it can be concluded that desirable micro-hardness on the substrate material could not be achieved by cladding with either of PAC 718 and METCO 41 C powders; this can be attributed to the higher dilution and growth of grains.

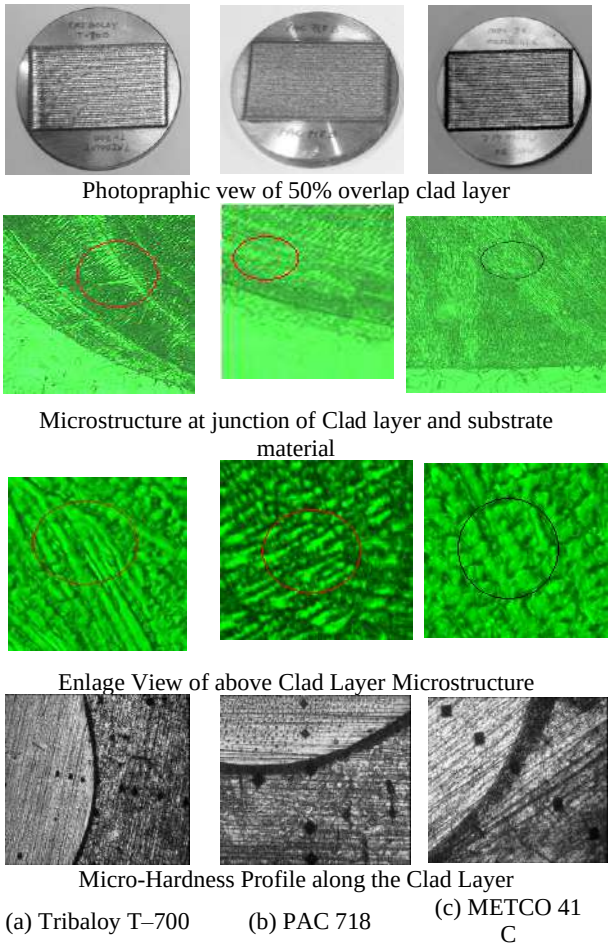

Figure 7. Photographic view of 50 % overlapped cladding structure

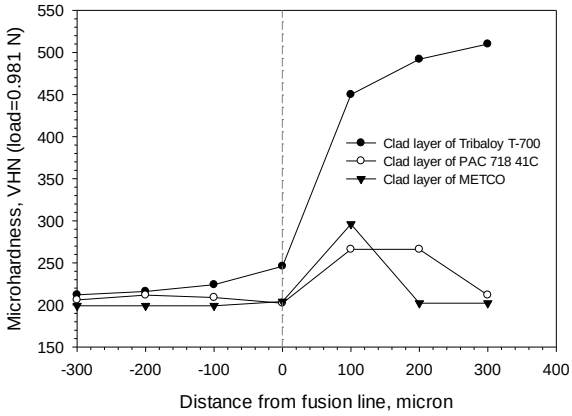

Figure 8. Micro-hardness profile of clad layer on substrate at 1.2 kW laser power

5. CONCLUDING REMARKS

The single-pass clad tracks were observed free from cracks, porosity and any distortion. The size, shape and quality of clad track is based on variation in cladding process parameters. The higher percentage of width to height ratio of 27% is obtained for Tribaloy T-700 cladding,while 17% for PAC 718 cladding. The maximum micro-hardness (0.981 N) at the clad surface was observed to have remarkable improvement around 246-534 Hv for Tribaloy T-700 clad, 202-321 Hv for entire PAC 718 clad and 196-294 Hv for METCO 41 C which is nearer to that of substrate (204 Hv). The microhardness of Tribaloy T-700, PAC 718 and METCO 41C are approximately 2.61, 1.5 and 1.4 times higher than the substrate, respectively. The cladding zone microstructure shows uniform type of dendritic growth along the direction of clad height at the junction for Triboloy T-700 and PAC 718, while mixed dendritic and cellular type microstructure was observed for the clad layer of METCO 41C.

6. ACKNOWLEDGEMENT

The present work was supported by CSIR-National Chemical Lab Pune and RRCAT Indore. Thanks to Director NCL Pune and Director RRCAT Indore.

7. REFERENCES

1. Schneider M. F, "laser cladding with powder effect of some machining parameters on clad properties", Ph.D. Thesis University of Twente. Enschede. The Netherlands, (1998).
2. Khajesarvi, A., Akbari, G., "Effect of Mo addition on Nanostructure Ni50Al50 intermetallic component synthesized by mechanical alloying", ***International Journal of Engineering Transaction C: Aspects***, Vol. 28, (2015), 1328-1353, doi: 10.5829/idosi.ije.2015.28.09c.10.
3. Chiu, K. Y., Cheng, F. T., Man, H. C., "A preliminary study of cladding steel with NiTi by microwave-assisted brazing", ***Materials Science and Engineering: A***. Vol. 407, No. 1-2, (2005), 273-281, https://doi.org/10.1016/j.msea.2005.07.013.
4. Khorram, A., Jamaloei, A. D., Paidar, M., Cao, X., "Laser cladding of Inconel 718 with 75Cr3C2 + 25(80Ni20Cr) powder: Statistical modeling and optimization", ***Surface & Coatings Technology,*** Vol. 378, (2019), https://doi.org/10.1016/j.surfcoat.2019.124933 .
5. Moradi, M., Ashoori, A., Hasani, A., "Additive manufacturing of stellite 6 superalloy by direct laser metal deposition – Part 1: Effects of laser power and focal plane position", ***Optics and Laser Technology***, https://doi.org/10.1016/j.optlastec.2020.106328.
6. Moradi, M., Hasani, A., Beiranvand, Z. M., Ashoori, A., "Additive manufacturing of stellite 6 superalloy by direct laser metal deposition – Part 2: Effects of scanning pattern and laser power reduction in different layers", ***Optics and Laser Technology***, https://doi.org/10.1016/j.optlastec.2020.106455.
7. Vyas, A., Menghani, J., Natu, H., "Metallurgical and Mechanical Properties of Laser Cladded AlFeCuCrCoNi-WC10 High Entropy Alloy Coating", ***International Journal of Engineering Transactions A: Basics***, Vol. 33, No. 7 (2020), 1397-1402. https://dx.doi.org/10.5829/ije.2020.33.07a.27.
8. Paul, C. P., Bhargava, P., Mishra, S. K., Premsingh, C. H., Verma, A., Pathak, A. K., Atul Kumar, Kukreja, L. M., "Development of a 2 kW fiber laser based Rapid Manufacturing System", ***Proc. DAE-BRNS National Laser Symposium (NLS-20)***. Anna University, Chennai (2012).
9. Kuldeep, B., Ravikumar, K. P., Pradeep, S., "Effect of hexagoanal boron nitrate on Micro-structure and Mechanical Behaviour of Al7075 Metal Matrix Composite Producing by stir casting Technique", ***International Journal of Engineering Transactions A: Basics***, Vol. 32, No. 7 (2019), 1017-1022, https://dx.doi.org/10.5829/ije.2019.32.07a.15.
10. Qian, M., Lim, L. C., Chen, Z. D., Chen, W. L., "Parametric studies of laser cladding processes", ***Journal of Materials Processing Technology***, Vol. 63, (1997), 590-593, https://doi.org/10.1016/S0924-0136(96)02689-1.
11. Sun, S., Durandet, Y., Brandt, M., "Parametric investigation of pulsed Nd: YAG laser cladding of stellite 6 on stainless steel", ***Surface and Coatings Technology,*** Vol. 194, (2005), 225-231, https://doi.org/10.1016/j.surfcoat.2004.03.058.
12. Pinkerton, A. J., Li, L., "Multiple-layer cladding of stainless steel using high-powered diode laser: an experimental investigation of the process characteristics and material properties", ***Thin Solid Films***. Vol. 453-454, (2004), 471-476, https://doi.org/10.1016/j.tsf.2003.11.140.
13. Jabbar Hassan, A., Boukharouba, T., Miroud, D., and Ramtani, S., "Metallurgical and Mechanical Behaviour of AISI 316-304 During friction welding process", ***International Journal of Engineering, Transactions B: Applications***, Vol. 32, No. 2 (2019), 306-312, doi: 10.5829/ije.2019.32.02b.16.
14. Liu, Z., Sun, J. L., Steen, W. M., Watkins, K. G., Lee, C., Brown, W. P., "Laser cladding of Al-Sn alloy on a mild steel", ***Journal of Laser Applications***, Vol. 9, (1997), 35-41, https://doi.org/10.2351/1.4745443.
15. Yadav, A., Arora, N., Gandhi, B. K., Paul, C. P., Nath, A. K., "SS316L powder cladding on structural steel using continuous wave CO_2 laser", ***8th National Conference of Indian Society of Mechanical Engineers. IIT Roorkee.*** Paper No. PE-063, (2003).
16. Gupta, D., Gandhi, B. K., Gupta, S. R., Paul, C. P., Nath, A. K., "Hardfacing of AISI 304L Stainless Steel Using High Power CO_2 Laser", ***Proceedings of International Welding Conference***, 18-20 February 2005. Mumbai. India. Paper No. IWA-105, (2005)..
17. Zhong, M., Yao, K., Liu, W., "High-power laser cladding stellite 6 + WC with various volume rates", ***Journal of Laser Application,*** Vol. 13, No. 6, (2001), 247-251, https://doi.org/10.2351/1.1418706.

Persian Abstract

چکیده

پژوهش حاضر با هدف رسوب‌دهی سه پودر مختلف سخت‌کاری (Triboloy T-700)، (PAC 718) و (TETCO 41 C) روی فولاد زنگ‌نزن 304L با استفاده از روش روکش‌کاری لیزری انجام شده است. مسیر پوشیده شده یک‌پارچه و هم‌پوشان با استفاده از سیستم لیزر ۲ کیلووات رسوب کرده است. پارامترهای فرایند لیزری بهینه شده و مسیر ۵۰٪ پوشانده شده برای برهم‌نشینی یک سطح وسیع استفاده شد. پارامترهای بهینه‌ی فرایند لیزری با استفاده از مطالعه‌ی ساختار تک‌پوش نهایی شد. از سطح مقطع لایه‌های پوشیده‌شده برای به دست آوردن ریزساختار و ریزسختی مناطق مختلف، یعنی لایه‌ی روکش‌شده، لایه‌ی انتشار و بستر استفاده شد. در طول مطالعه، قدرت لیزر در سطح ۱.۲ کیلووات ثابت بود. برای رسوب تک‌پوش، سرعت اسکن و میزان تغذیه‌ی پودر به‌ترتیب از ۰.۳ تا ۰.۵ میلی متر در دقیقه و ۴ تا ۹ گرم در دقیقه متفاوت بود. ریزساختار در حال توسعه‌ی T-700 و PAC 718 یک‌نواخت است، درحالی که METCO 41 C توسعه‌ی ریزساختار مخلوط دندریتیک و نوع سلولی را نشان می‌دهد. بر اساس آزمون Triboloy سختی سطح بیشینه‌ی 534 Hv؛ 321 Hv برای PAC 718 و 294 Hv برای METCO 41 C است.

IJE TRANSACTIONS B: Applications Vol. 34, No. 02, (February 2021) 487-492

International Journal of Engineering

Journal Homepage: www.ije.ir

Simulation of Photovoltaic System as a Tool of a State's Energy Security

V. Martynyuk*[a], M. Voynarenko[b], J. Boiko[c], O. Svistunov[d]

[a] *Department of Automation, Computer-Integrated Technologies and Telecommunications, Khmelnytskyi National University, Ukraine*
[b] *Department of Accounting, Auditing and Taxation, Khmelnytskyi National University, Ukraine*
[c] *Department of Telecommunications and Radio Engineering, Khmelnytskyi National University, Ukraine*
[d] *State Enterprise "Novator" Khmelnytskyi, Ukraine*

PAPER INFO

Paper history:
Received 10 November 2019
Received in revised form 23 December 2019
Accepted 04 January 2020

Keywords:
Simulation
Photovoltaic System
Solar Energy
Electric Grid
Energy Security

ABSTRACT

This article is devoted to the photovoltaic system simulation. Photovoltaic systems operate in different conditions such as changing solar irradiance and environmental temperature. Analysis of the existing methods for photovoltaic system simulation was carried out in this paper. The formal model of the electricity consumption system was developed, which included the photovoltaic system and the electrical storage system. The expediency of using simulation modeling tools in the design of solar panel optimization tools was shown by application of maximum power point tracking methods. The developed software provides the ability to build current-voltage and high-voltage characteristics of solar cells at different values of the intensity of solar radiation and temperature.. The voltage and load current differ up to 50% from the voltage and current of the operating point of the solar panel, which is set to the optimal value using maximum power point tracker. The architecture of the software extends the capabilities of simulation modeling of systems based on solar panels. The optimizer model block along with the implementation of the maximum power point tracking algorithm can be further refined by using more sophisticated algorithms. The developments are innovative and their practical implementation will have a significant impact on the energy security of countries.

***doi**: 10.5829/ije.2021.34.02b.21*

NOMENCLATURE

P_{load}	Is the power consumption (W)	I_s	Is the reverse saturation current (A)
$P_{\max}$	Is the maximum power of the photovoltaic system (W)	T	Is the absolute temperature of the p-n junction (K)
$P_{\lim}$	Is the maximum power that can be taken from the external grid (W)	V_{oc0}	Is the open short circuit voltage under test conditions
P_1, P_2, P_3	Energy flows (W)	K_V	Is the temperature coefficient of the open circuit voltage
$P_{3\max}$	Is the maximum energy due to capacity of the electrical storage system (W)	m	Is the diode ideality coefficient
N	Is the number of time intervals with constant load	I_{ph}	Is the photocurrent (A)
I_d	Is the current flowing through the diode (A)	**Greek Symbols**	
R_s	Is the serial resistance (Ω)	α_1, α_2, α_3	Are coefficients of the objective function
R_{sh}	Is the parallel resistance or shunt resistance (Ω)		

1. INTRODUCTION[1]

Solar energy is by far one of the most promising emerging sectors of renewable energy which become key factors of a state's energy security. Photovoltaic systems require an energy storage buffer to supply the loads when there is not enough solar energy. Lead acid batteries and super-high capacitors are typically used for this purpose [1-4]. High and fast energy (current) demands from the load can degrade the performances and lifetime of such batteries. Because of the output

*Corresponding Author Email: *martynyuk.valeriy@gmail.com* (V. Martynyuk)

Please cite this article as: V. Martynyuk, M. Voynarenko, J. Boiko, O. Svistunov, Simulation of Photovoltaic System as a Tool of a State's Energy Security, International Journal of Engineering, Transactions B: Applications Vol. 34, No. 02, (2021) 487-492

dependence on weather conditions, photovoltaic systems produce incomplete charge/discharge cycles, resulting in a low State of Charge (SOC). In these conditions, batteries cannot cope with fast and sudden energy demands from the load, as necessary for the applications such as motors and water pumps characterized by transients or start-ups with current requirements for a few seconds up to 6-8 times higher than the rated current. For this reason, the photovoltaic systems are not the best energy source to charge batteries [5-8].

The National Renewable Energy Laboratory (NREL, USA) is the main developer of free software for modeling solar power plants, offering two open source software packages online: PVWatts and System Advisor Model (SAM). Currently these software packages are widely used to simulate solar panels.

Helioscope is one of the most modern computing platforms allowed to model solar power plants with a capacity of up to 5 MW.

The software proposed in this article, in contrast to the existing one, will allow to simulate the operation of the solar panel and string in real time when changing the basic parameters of the panel. This software can optimize the process of studying the effective operation of the solar panel by selecting the maximum power point.

2. LITERATURE REVIEW

Smart grids are the next generation of electricity distribution networks. The development of smart grids is due to the emergence of new equipments for monitoring, automation and communication of generators and consumers of electricity. The use of smart grids can improve the quality of electricity, managing electricity prices, monitoring sources and demand for electricity [9-13].

The energy management system (EMS) of the electrical system for a luxury ship (yacht) is discribed in [14-17]. From the architectural side, a DC electrical distribution on-board has been adopted in place of the existing AC. Moreover, the DC micro-grid has been integrated with renewable energy sources (RES) based generators, as well as an energy storage system (ESS). The ESS compensates the power missing for the entire duration of the cold start up of the auxiliary generator. In case of big overload, the ESS provides the exceeding power with respect to the rated one, thus avoiding potential micro-grid instability problems.

In recent years, the management and operation of micro-grids are considered by many advanced societies with regard to the development of scattered energy resources [18-22]. The main goals that are paid attention in micro-grid management are the operation cost and pollution rate, which the aggregation of such contradictory goals in an optimization problem can provide an appropriate response to the management of the micro-grid.

Grid integration of photovoltaic (PV) system with a hybrid energy storage can help not only in increasing penetration of PV system into the network but also in improving the power system dynamics and control in addition to helping the demand side management [23-25]. The PV system with a hybrid energy storage including a battery array and a super capacitor bank is going to work as an active generator with innovative load management and power flow control strategies for managing the active power demand locally considering the grid constraints.

3. MATERIALS AND METHODS

3. 1. The Mathematical Model of Power Supply System Let's consider the generalized power supply system, which consists of the electricity consumers, the external grid, the photovoltaic system and the electrical storage system [26-30].

The mathematical model of this power supply system is based on the condition of the electricity balance between the nodes of the system. The generalized power supply system block diagram is shown in Figure 1.

The electrical system balance is provided by the following equations:

$$\begin{cases} P_1 + P_2 = P_{load} \\ P_1 + P_3 \le P_{\max} \\ P_2 \le P_{\lim} \end{cases} \quad (1)$$

where, P_{load} is the power consumption; $P_{\max}$ is the maximum power of the photovoltaic system; $P_{\lim}$ is the maximum power that can be taken from the external grid.

The system from Equation (1) is a balance of electric energy over a period of time Δt during which P_{load} and $P_{\lim}$ can be considered as constant:

$$\begin{cases} P_{load}(t) = const \\ P_{\max}(t) = const \end{cases} \quad (2)$$

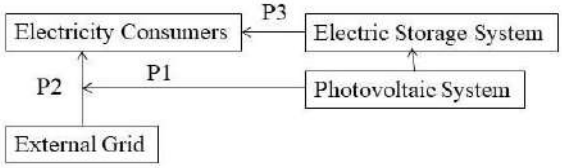

Figure 1. The generalized power supply system block diagram

The energy flows P_1 and P_2 are assumed to be positive.

$$\begin{cases} P_1 \geq 0 \\ P_2 \geq 0 \end{cases} \quad (3)$$

The energy flow P_3 is the energy that consumes the charge and discharge of the electrical storage system and it can be both positive and negative.

$$-P_{3\max} \leq P_3 \leq P_{3\max} \quad (4)$$

where, $P_{3\max}$ is the maximum energy due to capacity of the electrical storage system.

For each time interval Δt_i, if the conditions in Equation (2) are satisfied, we can write the system of Equations (1) and supplement it with the charge of the electrical storage system:

$$\sum_i^N \Delta t_i P_3 = 0 \quad (5)$$

where, N is the number of time intervals with constant load.

Let's introduce the objective function:

$$F = \sum_i^N \Delta t_i \left(\alpha_1 P_1^i + \alpha_2 P_2^i + \alpha_3 P_3^i \right) \quad (6)$$

where, α_1, α_2 and α_3 are coefficients of the objective function.

In the case of the objective function optimization by the criterion of minimum cost of energy resources, the coefficients of the objective function in Equation (6) are the corresponding tariffs for electricity and the cost of operating the photovoltaic system and the electrical storage system [31-36].

3. 2. The Linear Optimization Method The linear optimization methods are quite effective for solving this type of optimization problem. Under the condition in Equation (4) the variable P_3 can take negative values. Since a sign is not defined at the beginning of the problem-solving procedure, let's present it as a difference:

$$P_3 = x_1 - x_2 \quad (7)$$

where, $x_1 \geq 0$ and $x_2 \geq 0$ are the positive numbers.

We finally have the following system of linear constraints:

$$\begin{cases} P_1^i + P_2^i = P_{load}^i \\ P_1^i + x_1^i - x_2^i \leq P_{\max}^i \\ P_2^i \leq P_{\lim} \\ \sum_i^N \Delta t_i \left(x_1^i - x_2^i \right) \leq 0 \end{cases} \quad (8)$$

where, i takes values from 1 to N.

The last equality in system from Equation (8) was replaced by inequality in order for the system to be compatible and to have solutions.

The final expression for the objective function is:

$$G = \sum_i^N \Delta t_i \left(\alpha_1 P_1^i + \alpha_2 P_2^i + \alpha_3 \left(x_1^i - x_2^i \right) \right) \quad (9)$$

In Equation (9), the choice of the coefficients α_1, α_2 and α_3 depends on the optimization criteria. Thus, the formal problem is to find the optimal objective function using Equation (9) under the constraints in Equation (8).

4. EXPERIMENTAL RESULTS

Figure 2 shows a Simulink model for simulating the operation of a solar panel when changing the intensity of solar radiation using the maximum power point tracker (MPPT). This scheme involves measuring the values of current, voltage and power directly at the output of the solar panel and the external load.

The MPPT represented by the element "MPPT" takes the original values of current and voltage of the solar panel and returns the optimal value of the duty cycle D used to generate pulse width modulated (PWM) signal, which in turn controls the DC-DC converter. The latter thus adjusts the output voltage of the solar panel by setting it equal to the voltage at the MPPT.

Figure 3 shows the change in time of the solar radiation intensity during the simulation.

Figure 4 shows the current, voltage and power obtained from the simulation.

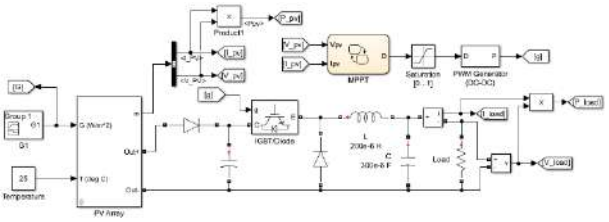

Figure 2. Scheme for modeling the process of MPPT when changing the intensity of solar radiation

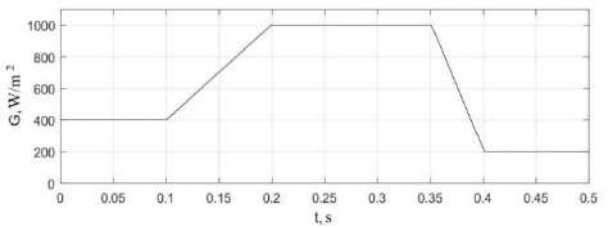

Figure 3. The changes of the solar radiation intensity

As can be seen from Figure 6, for a time period from 0 to 0.1 s, the solar radiation intensity is 400 W/m²; during the next 0.1 s, it increases linearly to a maximum value of 1000 W/m², and then falls again to a value of 200 W/m².

Figure 4 shows the dotted line current, voltage and power on the load; the corresponding values obtained directly at the load and the solid line corresponds to the solar panel. As can be seen from these diagrams, the voltage and load current differ from the voltage and current of the operating point of the solar panel, which is set to the optimal value using MPPT.

The Stateflow element was used to implement the incremental conductivity algorithm in the Matlab/Simulink environment. Stateflow is a graphical development tool that can be used to model simple logic problems and complex control system problems. It is easy to create and explore different behavioral scenarios of complex systems. The Stateflow element has been widely used in the modeling of embedded systems, human-machine interfaces, and hybrid systems [26].

Stateflow are based on finite automata. The transition from one state to another is determined by the condition of transition to this state.

The Stateflow diagram consists of the block sets that determine the possible states of the system and the conditional transition sets that specify the conditions for the transition of the system from one state to another.

Figure 5 shows the implementation of the incremental proficiency algorithm in the form of the Stateflow diagram.

As can be seen from Figure 5 the diagram consists of four main states, the transitions between which occur according to the algorithm.

The developed model is presented in the form of the subsystem PV Array, which takes as input the solar radiation G and temperature T. It has two electrical outputs ("Out+" and "Out-"), compatible with SimPowerSystems components and the output vector *m* of the measured values.

The PV Array subsystem requires the following parameters I_{sc0}, V_{oc0}, K_I, K_V, m, N_s, R_s and R_{sh} to be specified using the subsystem mask. A controlled current source was used to simulate the load, which simulates a linear increase in the load current.

The structure of the PV Array subsystem is shown in Figure 6. It includes internal subsystems for current simulation I_{ph}, I_s and I_d. The output current for the electrical output terminals is set by the controlled current source. The output vector *m* consists of the values of current and voltage at the output of the solar panel, the current value I_d, temperature value T and insolation G.

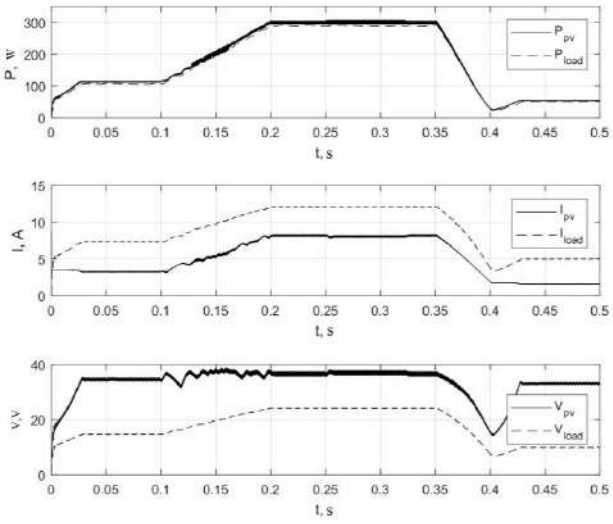

Figure 4. Power, current and voltage obtained from the simulation

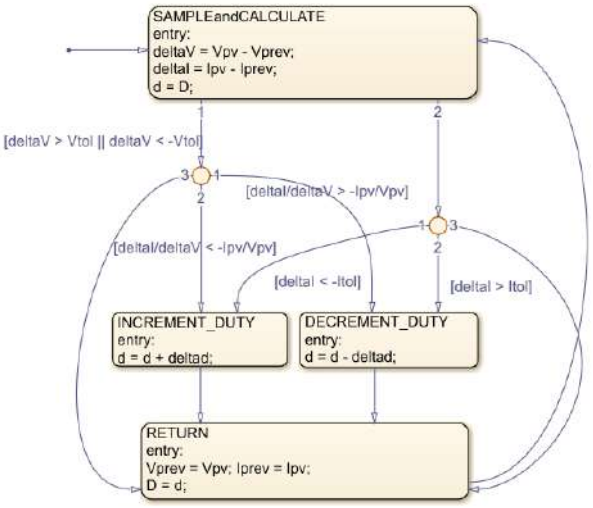

Figure 5. Implementation of the incremental conductivity algorithm as the Stateflow diagram

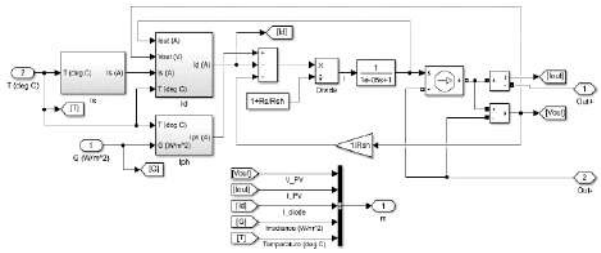

Figure 6. Internal structure of the PV Array subsystem

5. CONCLUSION

Considering the obtained results of the photovoltaic system simulation by means of the developed application, it can be concluded that this software shows adequate results and meets its requirements. The values of the maximum power point are obtained as a result of simulation under nominal conditions corresponding to the declared data sheet of the considered solar panels.

The architecture of the software application extends the capabilities of the photovoltaic system simulation. The block model of the optimizer with the implementation of the algorithm tracking the maximum power point can be further improved by using more sophisticated algorithms, and the interface of its interaction with other modules of the system will remain unchanged.

The simulation software supports the function of explicitly setting the operating point of the photovoltaic system simulation by changing the value of current or voltage. This module can be expanded by implementing the complex load model.

6. REFERENCES

1. Vdovin, O., Martynyuk, V. and Surdu, M., "A combined method for measuring super-high capacitors absorption characteristics", in Proc. Of the 11th IMEKO TC4 Symposium on “Trends in Electrical Measurements and Instrumentation” and 6th IMEKO TC4 Workshop on ADC Modelling and Testing, Lisbon, Portugal, 372-374, (2001). ISBN 972-98115-4-7
2. De Wildt, T. E., Chappin, E. J.L., van de Kaa, G., Herder, P. M. and van de Poel, I. R., "Conflicting values in the smart electricity grid a comprehensive overview", ***Renewable and Sustainable Energy Reviews***, Vol. 111, (2019), 184-196. https://doi.org/10.1016/j.rser.2019.05.005
3. Hosseini Rad, A., Ghadamian, H., Haghgou, H. R. and Sarhaddi, F., "Energy and Exergy Evaluation of Multi-channel Photovoltaic/Thermal Hybrid System; Simulation and Experiment", ***International Journal of Engineering, Transactions B: Applications***, Vol. 32, No. 11, (2019), 1665-1680. DOI: 10.5829/IJE.2019.32.11A.18
4. Accetta, A. and Pucci, M., "Energy Management System in DC Micro-Grids of Smart Ships: Main Gen-Set Fuel Consumption Minimization and Fault Compensation," ***IEEE Transactions on Industry Applications***, Vol. 55, No. 3, (2019), 3097-3113. DOI: 10.1109/TIA.2019.2896532
5. Aghajani, G. and Ghadimi, N., “Multi-objective energy management in a micro-grid”, ***Energy Reports***, Vol. 4, (2018), 218-225. https://doi.org/10.1016/j.egyr.2017.10.002
6. Konara, K. M.S.Y., Kolhe, M. and Sharma, A. “Power flow management controller within a grid connected photovoltaic based active generator as a finite state machine using hierarchical approach with droop characteristics”, ***Renewable Energy***, Vol. 155, (2020), 1021-1031. https://doi.org/10.1016/j.renene.2020.03.138
7. Boutabba, T., Drid, S., Chrifi-Alaoui, L. and Benbouzid, M. E., “A New Implementation of Maximum Power Point Tracking based on Fuzzy Logic Algorithm for Solar Photovoltaic System”, ***International Journal of Engineering, Transactions A: Basics***, Vol. 31, No. 4, (2018), 580-587. doi: 10.5829/ije.2018.31.04a.09
8. Sureshkumara, K. and Ponnusamyb V., “Power flow management in micro grid through renewable energy sources using a hybrid modified dragonfly algorithm with bat search algorithm”, ***Energy***, Vol 181, (2019), 1166-1178. https://doi.org/10.1016/j.energy.2019.06.029
9. Martynyuk, V., Vdovin, O., Boyko, J., and Vlasenko, N., “Super-high capacitor analyzer with compensation of common-mode error”, in Proc. of the 11th IMEKO TC-4 Symposium “Trends in electrical measurement and instrumentation”, Lisbon, Portugal, 340-343, (2001).
10. Martynyuk, V., Fedula, M., Ortigueira, M. and Savenko, O., “Methodology of Electrochemical Capacitor Quality Control with Fractional Order Model”, ***AEU - International Journal of Electronics and Communications***, Vol. 91, (2018), 118-124. https://doi.org/10.1016/j.aeue.2018.05.005
11. Hadi, A. A., Silva, C. A. S., Hossain, E. and Challoo, R., "Algorithm for Demand Response to Maximize the Penetration of Renewable Energy," ***IEEE Access***, vol. 8, (2020), 55279-55288. DOI: 10.1109/ACCESS.2020.2981877
12. Kalair, A. R., Abas, N., Hasan, Q. Ul, Seyedmahmoudian, M. and Khan, N. "Demand side management in hybrid rooftop photovoltaic integrated smart nano grid," ***Journal of Cleaner Production***, Volume 258, (2020), 120747. https://doi.org/10.1016/j.jclepro.2020.120747
13. Sagar, G. V. R. and Debela, T., “Implementation of Optimal Load Balancing Strategy for Hybrid Energy Management System in DC/AC Microgrid with PV and Battery Storage”, ***International Journal of Engineering, Transactions A: Basics***, Vol. 32, No. 10, (2019), 1437-1445. doi: 10.5829/ije.2019.32.10a.13
14. Nizami, M. S.H., Hossain, M. J., Haque, A. N.M.M. and Nguyen, P. H., “On the application of Home Energy Management Systems for power grid support”, ***Energy***, Vol. 188, (2019), 116104. https://doi.org/10.1016/j.energy.2019.116104
15. Rajeev K. C. and Kalpana C., “Building automation system for grid-connected home to optimize energy consumption and electricity bill”, ***Journal of Building Engineering***, Vol. 21, (2019), 409-420. https://doi.org/10.1016/j.jobe.2018.10.032
16. Garrab, A., Bouallegue, A. and Bouallegue, R., “An Agent Based Fuzzy Control for Smart Home Energy Management in Smart Grid Environment”, ***International Journal of Renewable Energy Research***, Vol. 7 No. 2, (2017), 599-612.
17. Dhass, A.D., Natarajan, E. and Lakshmi, P., “An Investigation of Temperature Effects on Solar Photovoltaic Cells and Modules”, ***International Journal of Engineering, Transactions B: Applications***, Vol. 27, No. 11, (2014), 1713-1722.
18. Ciupageanu, D., Barellia, L. and Lazaroiub G., “Real-time stochastic power management strategies in hybrid renewable energy systems: A review of key applications and perspectives”, ***Electric Power Systems Research***, Vol. 187, (2020), 106497. https://doi.org/10.1016/j.epsr.2020.106497
19. Kiran, A. and Arun, K. “Network selection criterion for ubiquitous communication provisioning in smart cities for smart energy system”, ***Journal of Network and Computer Applications***, Vol. 127, (2019), 82-91. https://doi.org/10.1016/j.jnca.2018.11.011
20. López-Ramosa, F., Nasini, S., H.Sayedd, M., “An integrated planning model in centralized power systems”, ***European Journal of Operational Research***, Vol. 287, Iss. 1, (2020), 361-377. https://doi.org/10.1016/j.ejor.2020.05.006
21. Simões D., Lau N., Reis L. P., “Multi-agent actor centralized-critic with communication”, ***Neurocomputing***, Vol. 390, (2020), 40-56. https://doi.org/10.1016/j.neucom.2020.01.079

22. Wang, Y., Nguyen T. L., Xu Y. and Shi, D. "Distributed control of heterogeneous energy storage systems in islanded microgrids: Finite-time approach and cyber-physical implementation", ***International Journal of Electrical Power & Energy Systems***, Vol. 119, (2020), 105898. https://doi.org/10.1016/j.ijepes.2020.105898
23. Khan, M. W., Wang, J., Ma, M., Xiong, L., Li, P, and Wu, F., "Optimal energy management and control aspects of distributed microgrid using multi-agent systems", ***Sustainable Cities and Society***, Vol.44, (2019), 855-870. https://doi.org/10.1016/j.scs.2018.11.009
24. Rahman, M.S. and Oo, A.M.T., "Distributed multi-agent based coordinated power management and control strategy for microgrids with distributed energy resources", ***Energy Conversion and Management***, Vol. 139, (2017), 20-32. https://doi.org/10.1016/j.enconman.2017.02.021
25. Sampaio F. C., Leão R. P.S., Sampaio R. F., Melo L S., and Barroso G. C., "A multi-agent-based integrated self-healing and adaptive protection system for power distribution systems with distributed generation", ***Electric Power Systems Research***, Vol. 188, (2020), 106525. https://doi.org/10.1016/j.epsr.2020.106525
26. Sovacool B. K. and Furszyfer Del Rio D. D. "Smart home technologies in Europe: A critical review of concepts, benefits, risks and policies", ***Renewable and Sustainable Energy Reviews***, Vol. 120, (2020), 109663. https://doi.org/10.1016/j.rser.2019.109663
27. Kolen, S., Molitor, C., Wagner, L. and Monti, A., "Two-level agent-based scheduling for a cluster of heating systems", ***Sustainable Cities and Society***, Vol. 30, (2017), 273-281. https://doi.org/10.1016/j.scs.2017.01.014
28. Davarzani, S., Granell, R., Taylor, G. A., Pisica, I. "Implementation of a novel multi-agent system for demand response management in low-voltage distribution networks", ***Applied Energy***, Vol. 253, (2019), 113516. https://doi.org/10.1016/j.apenergy.2019.113516
29. Santos A. Q., Monaro R. M., Coury D. V. and Oleskovicz M., "A new real-time multi-agent system for under frequency load shedding in a smart grid context", ***Electric Power Systems Research,*** Vol. 174, (2019), 105851. https://doi.org/10.1016/j.epsr.2019.04.029
30. Mokhtaraa, C., Negroua, B., Bouferrouk, A., Yao, Y., Settoua, N. and Ramadan, M., "Integrated supply–demand energy management for optimal design of off-grid hybrid renewable energy systems for residential electrification in arid climates", ***Energy Conversion and Management***, Vol. 221, (2020), 113192. https://doi.org/10.1016/j.enconman.2020.113192
31. Martynyuk, V., "Supercapacitor Data Acquisition Systems", in 4th IEEE Workshop on Intelligent Data Acquisition and Computing System: Technology and Applications IDAACS'2007, Dortmund, Germany,. 24-28, (2007). DOI: 10.1109/IDAACS.2007.4488365
32. Ogunjuyigbe, A. S., Ayodele, T. R. and Akinola, O. A., "User satisfaction-induced demand side load management in residential buildings with user budget constraint", ***Applied Energy***, Vol. 187, (2017), 352-366. https://doi.org/10.1016/j.apenergy.2016.11.071
33. Voynarenko, M., Dykha, M., Mykoliuk, O., Yemchuk, L. and Danilkova, A., "Assessment of an enterprise's energy security based on multi-criteria tasks modeling". ***Problems and Perspectives in Management***, Vol. 16, No. 4, (2018), 102-116.
34. Liu J., Chen X., Cao S., and Yang H. "Overview on hybrid solar photovoltaic-electrical energy storage technologies for power upply to buildings", ***Energy Conversion and Management***, Vol. 187, (2019), 103-121. https://doi.org/10.1016/j.enconman.2019.02.080
35. Confrey, J., Etemadi, A. H., Stuban, S. M. F. and Eveleigh, T. J., "Energy Storage Systems Architecture Optimization for Grid Resilience With High Penetration of Distributed Photovoltaic Generation," ***IEEE Systems Journal***, Vol. 14, No. 1, (2020), 1135-1146. DOI: 10.1109/JSYST.2019.2918273
36. Lingguo K., Jiamin Y. and Guowei C., "Modeling, control and simulation of a photovoltaic /hydrogen/ supercapacitor hybrid power generation system for grid-connected applications", ***International Journal of Hydrogen Energy***, Vol. 44, Iss. 46, (2019), 25129-25144. https://doi.org/10.1016/j.ijhydene.2019.05.097

Persian Abstract

این مقاله به شبیه سازی سیستم فتوولتائیک اختصاص دارد. سیستم های فتوولتائیک در شرایط مختلف مانند تغییر تابش خورشید و دمای محیط کار می کنند. تجزیه و تحلیل روش های موجود برای شبیه سازی سیستم فتوولتائیک در این مقاله انجام شده است. مدل رسمی سیستم مصرف برق ساخته شد که شامل سیستم فتوولتائیک و سیستم ذخیره برق بود. مصلحت استفاده از ابزار مدل سازی شبیه سازی در طراحی ابزارهای بهینه سازی صفحه خورشیدی با استفاده از روش های ردیابی حداکثر توان نشان داده شد. این نرم افزار توسعه یافته توانایی ایجاد خصوصیات ولتاژ جریان و ولتاژ بالا سلولهای خورشیدی را در مقادیر مختلف شدت تابش خورشید و دما فراهم می کند. ولتاژ و بار بار تا ۵۰٪ با ولتاژ و جریان کار متفاوت است نقطه پانل خورشیدی ، که با استفاده از ردیاب نقطه حداکثر قدرت روی مقدار مطلوب تنظیم می شود. معماری این نرم افزار قابلیت های شبیه سازی سیستم های مبتنی بر صفحات خورشیدی را گسترش می دهد. بلوک مدل بهینه ساز همراه با اجرای الگوریتم ردیابی نقطه حداکثر توان با استفاده از الگوریتم های پیچیده تر می تواند بیشتر اصلاح شود. این تحولات نوآورانه است و اجرای عملی آنها تأثیر بسزایی در امنیت انرژی کشورها خواهد داشت.

International Journal of Engineering

Journal Homepage: www.ije.ir

Hydroxyapatite Coating on Stainless Steel 316L using Flame Spray Technique

F. Gapsari[a], N. A. Hidayati[a], P. H. Setyarini[a], M. Alan P. N.[a], R. Subagyo[b], A. Andoko[c]

[a] *The Mechanical Engineering Department of Brawijaya University, Malang, Indonesia*
[b] *Mechanical EngineeringDepartment, University of Lambung Mangkurat, Banjarmasin, Indonesia*
[c] *Mechanical EngineeringDepartment, State University of Malang, Malang, Indonesia*

PAPER INFO

Paper history:
Received : 07 September 2020
Received in revised form: 17 Nopember 2020
Accepted: 05 Desemeber 2020

Keywords:
Coating
Corrosion
Hydroxyapatite
Oxygen Flowrate
Air Pressure

ABSTRACT

This study was a preliminary study on flame spray coating with hydroxyapatite (HAp). Coating is one of the technique to improve metal resistance to corrosion. In this study, flame spray coating using HAp was performed on stainless steel 316 L as a material for medical devices. This synthetic compound contains elements which are biocompatible and bioactive in human body where they can stick to body tissues or muscles.HAp has been extensively used as a bone substitute because of its crystal structure, biocompatibility and osteoconductive nature. In this study, 316L SSwas coated by HAp using flame spray method with varied oxygen flowrate and air pressure. The result of this study showed that the air pressure of 1 bar and oxygen flowrate of 25 l/min had the thickest coating which was 123.5µm and the lowest corrosion rate which was 0.0261 mm/year. The air pressureof 3 bar and oxygen flowrate of 35 l/min produced the lowest thickness which was 32.5µm and the highest corrosion rate which was 0.0761 mm/year. The use of high air pressure and oxygen flowrate decreased the coating thickness and the corrosion rate. The result revealed that flame spray method was effective to be used to coat HAp on 316L SS.

doi: *10.5829/ije.2021.34.02b.22*

1. INTRODUCTION

Biomaterial is used to create surgical implants and devices to replace parts or the function of body organs safely and economically. Metal types that are commonly used are Ti alloys, Co-Cr alloys and stainless steel. The type of stainless steel which is generally used for implants is 316L SS. The 316L SS needs to be protected to restrain corrosion rate because even though it is a biomaterial implant; it still corrodes in the human body. ASTM has standardized stainless steel for implants in standard ASTM F13 [1], F899 [2] and F2181 [3]. The metal has been selected because of its structural function and inertness (having no ability to react with environment). However, in the newest development, implants are expected to possess bioactivity and bio functionality such as being compatible with blood (hemocompatible) and surface modifiable. Therefore, the metal is coated with HAp to make it conducive with human bones [4]. HAp is mostly applied in medical field especially for bone implants; because, it has very similar characteristics with components of human bones and teeth. Besides being applied as material for bone implants, HAp is also used as coating material for metal which is implanted into human body. HAp is biocompatible and bioactive with human body where it can stick to body tissues or muscles. The coating process is performed by depositing HAp on the substrate surface. Previous studies revealed that HAp is effective in increasing corrosion rate of 316L SS using some methods applying functionalized multiwalled carbon nanotubes (f-MWCNT)[5], nano particles [6], tissue engineering [7], and low velocity oxyfuel (LVOF) spray [8]. One of the coating methods which can be done is flame spray coating. Flame spray coating is one of the coating techniques which can use the most varied materials and geometries to coat [9]. Flame spray coating can also be defined as sticking coating material using a special

*Corresponding Author Institutional Email: memi_kencrut@ub.ac.id (F.Gapsari)

Please cite this article as: F. Gapsari, N. A. Hidayati, P.H. Setyarini, M. Alan P.N, R. Subagyo, Andoko, Hydroxyapatite Coating on Stainless Steel 316L using Flame Spray Technique, International Journal of Engineering,, Transactions B: Applications, Vol. 34, No. 02, (2021) 493-499

instrument that is able to melt and push the material onto the substrate surface which has been prepared previously. One of the types of flame spray coating is powder flame spray where the heat is produced from fuel combustion with oxygen. In this case, the fuel being used is acetylene. The feedstock being used is in the form of powder [10]. Some previous studies were conducted to improve the quality of metal surface and one of the approaches is to perform coating. On CrCr/NiCr coating with the method of HVOF spraying, the setting of powder feed rate, stand-off distance and gun barrel length can affect the temperature of the particles. Stand off distance and oxygen flow rate are the main factors which affect the molten particle speed [11]. Determining the level of pressure in coating process with high velocity air fuel method (HVAF) can affect particle speed of the particle, flame temperature and coating thickness (deposition efficiency [12]. The factor of coating thickness can effect on corrosion resistance where thicker coating makes better protection from corrosion [13]. The purpose of the study is to know the effect of pressure and oxygen flow rate in conventional flame spray coating on coating thickness and corrosion rate. The findings of this study is the right parameter in the use of flame spray in HAp coating. We expect that this study can be reference in the continuation of the use of flame spray in biomaterial coating.

2. MATERIALS AND METHODS

2. 1. Materials The specimen in the study was 316L SS. Furthermore, its compositions is written in Table 1.

The roughness of the specimen surface without treatment had Ra value of 5.482µm. The specimen dimension is displayed in Figure 1.

TABLE 1. Compositions of 316L SS (% weight)

Composition	Weight Percentage
C	0.023
Mn	1.31
Si	0.34
P	0.032
S	0.001
Cr	16.7
Mo	2.02
Ni	10.1
N	0.04
Fe	69.434

Figure 1. The specimen dimension

The formula of HAp that was used in the study was $HCa_5O_{13}P_3$. It had melting point of 1100˚C, density of 3.140 g/cm^3 and the particle size of 30 µm.

2. 2. Flame Spray Coating Flame spray coating was performed by using Metco 5P-II combustion powder spray gun with varied oxygen flow rate: 25, 30 and 35 l/min and varied air pressure: 1, 2 and 3 bars. Substrate surface s peed during the coating process was made constant with the fuel flow rate staying at 25 l/min. The flame spray tool was equipped with Matco 5P-II combustion powder spray gun. The process of gas consumption used acetylene ranging from 13.5 – 31.5 NLPM, hydrogen ranging from 90 – 144 NLPM, oxygen ranging from 20 – 45 NLPM and compressed air of 0.85 m^3/min at 4.5 bars. Air requirements used was the standard of air cap which was 10 to 15 psi, with pinch air cap of 5 psi in maximum, cooling air of10 – 20 psi, and air jet assembly of 50 – 90 psi. Flame temperature of the gun produced 2500- 3750ºC.The spray distance was 120 mm at an angle of 90˚. The coating was performed to make two coats. The result of experiment can be seen in Figure 2.

2. 3. The Coating Thickness Measurement The coating thickness was measured using NOVOTEST TP-1M. Novotest TP-1M is able to measure the thickness of the coating on ferrous and non ferrous metal. Probe used to measure the coating thickness on Ferous metal was F 0.5 max 500 ɥm).Probe used to measure the coating thickness on non Ferous metal was max 2000 µm. After the coating process, coating thickness was measured. The

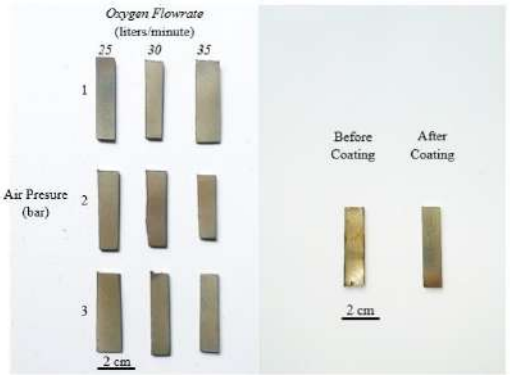

Figure 2. Specimen after coating

measurement was performed in these sequences. First, it was done by pressing the on button on the coating thickness gauge. Then, the probe stylus was directed to the surface of the work piece. Next, the stylus was pressed gently on the surface of the specimen until the display showed the measurement result. The last step was to make note about the measurement result of each coated specimen.

2. 4. The Potentiodynamic Polarization Test The measurement of corrosion rate used Hank's balanced salt solution (HBSS) with pH specification 7.4 ± 0.2, osmolality 290 ± 20 mOsm and Endotoxin < 0.1 EU/ml. This is an artificial blood condition.

The potentiodynamic polarization measurement was performed at room temperature (298K).The Autolab PGSTAT 204N functioning as a potential source was set at ± 0.1 mV and the scan rate was 0.001V/s. Three-cell electrode was set with the workpiece as the working electrode, platinum as the counter electrode and Ag/AgCl (KCl 3 M) as the reference electrode. The coated specimen was exposed into HBSS solution for 1 cm^2. Autolab PGSTAT 204 N was connected with software NOVA 11.0. In the measurement, workpiece density, molecular weight and surface width were added. In order to calculate the parameters of the corrosion such as Icorr, βa and βC, the polarization curves were extrapolated.

Corrosion rate or a rate at which a material is taken as a consequence of a chemical action, which is an important parameter stated as corrosion penetration rate (corrosion penetration rate/CPR) or the thickness of a material which is lost per unit time for the given equation:

$$\text{CPR} = \frac{KW}{\rho At} \quad (1)$$

where,W is the lost weight after contact over time (t), ρ is density of material, A is the width of a specimen which is exposed and K is a constant which the amount depends on the unit system used.

Based on Faraday's law, the corrosion rate was obtained in Equation 2.

$$CR(mpy) = \frac{0.129 \times I_{corr} \times EW}{\rho} \quad (2)$$

where, I_{corr} is current density, EW is equivalent weight. I_{corr} was calculated by using Equation 3.

$$I_{corr} = \frac{b_a \times b_c}{2.3(b_a + b_c)} \times \frac{1}{R_p} \quad (3)$$

2. 5. The Surface Roughness Measurement Surface roughness measurement was performed using Mitutoyo Surface Roughness Tester SJ-210.

2. 6. The Morphology of the Surface Micrograph of the specimens with coating was measured using Scanning Electron Microscope (SEM). The type of SEM used was Phenom G2 Pro. The SEM measurement was performed in cross section.

3. RESULTS AND DISCUSSIONS

The data of HAp coating thickness measurement of 316L SS with variations in pressure and oxygen flowrates are displayed in Figure 3.

Figure 3 displays the data of coating thickness measurement with variations in pressure. It is shown that increasing the pressure can decrease the coating thickness.

This happens because high pressure will increase the particle speed of HAp particles which reduces time to heat the particles [12]. This leads to a condition where HAp particles are not heated well and cannot melt perfectly. The result is that the particles do not stick to the substrate surface maximally [14].

3. 1. The Effect of Oxygen Flowrate on Coating Thickness The measurement of coating thickness produced from varied oxygen flowrate shows that increasing the oxygen flowrate can decrease the coating thickness, as shown in Figure 4.

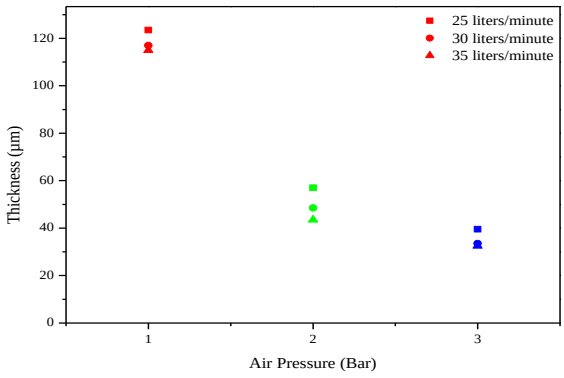

Figure 3. The effect of pressure on coating thickness

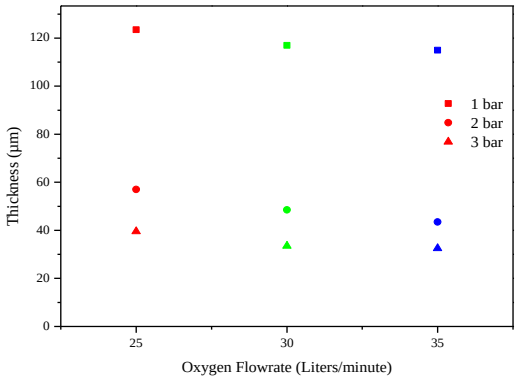

Figure 4. The effect of oxygen flow rate on coating thickness

The thickest coating was obtained at 25 l/min of fuel flow rate. The imbalanced amount of fuel flow rate and oxygen flow rate decreases the flame temperature of the torch. This causes the heating of HAp particle not maximum and thus the particles do not melt and stick to the substrate surface [15]. An increase in oxygen flow rate causes a decrease in flame temperature and it produces higher porosity level and the abundant particles melting which causes lower bound strength. The use of too high oxygen flowrate decreases the coating thickness.

The increase of oxygen flowrate will increase the flame temperature which can melt the HAp particles. However, the abundant use of oxygen flowrate can decrease the flame temperature. Consequently, the HAp particles do not melt perfectly and cannot stick to the substrate surface [11, 15].

3. 2. The Effect of Pressure on Surface Roughness

Figure 5 presents the result of the surface roughness measurement with respect to pressure variation. It is seen that surface roughness values are mostly similar at all variations of pressure. The values are not different significantly even though they were produced at different variations of the pressure.

The increase in flame temperature and molten particle speed causes the particles dispersion on the substrate surface and thus produces low roughness value [8]. However, the surface roughness values produced in this study are not significantly different. This is because the composition of the fuel and the oxygen at pressure of 3 bars produces flame with higher temperature. Thus, much HAp melts. The best pressure is not the higher one, but the most optimum. However, higher pressure does not always produce a lower coating roughness. At low pressure, HAp will produce fine particles. High pressure enables much HAp melts which leads to high roughness [16].

Coating roughness which was produced from varied pressure of 1, 2 and 3 bars with 25 l/min of oxygen flowrate has Ra values of 4.553, 4.376 and 4.532 µm, respectively. The use of oxygen flowrate of 30 l/min has surface roughness values of 4.020, 4.688 and 4.629 µm. Then, the use of oxygen flowrate of 35 l/min has values of 4.603, 4.580 and 4.686 µm .The results show that the flame spray coating is not able to produce even coating, especially when it is performed manually by human.

The surface roughness especially on the coating result provides stabilization during the implant placement until the bone can grow and adhere to the implant surface to increase the implant bonding.

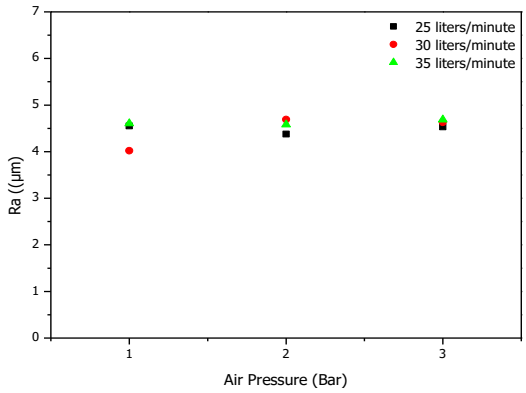

Figure 5. The effect of pressure on surface roughness

3. 3. The Effect of Pressure and Oxygen Flowrate on Corrosion Rate

The tafel plot of different pressures and oxygen flowrates effect on corrosion rate are illustrated in Figures 6-8.

In Figure 6, it can be seen that the lower the pressure is, the more the tafel curve slides down. Tafel curve which slides down indicates the decrease of Icorr value and thus the corrosion rate gets lower [17]. Figures 7 and 8 display the results of potentiodynamic polarization test

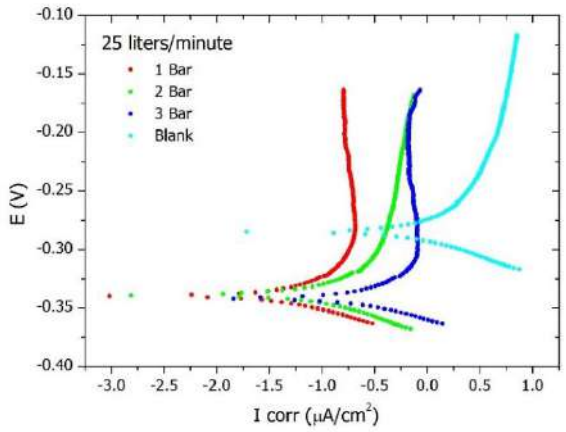

Figure 6. The tafel curve of pressure and oxygen flowrate with variation of 25 l/min

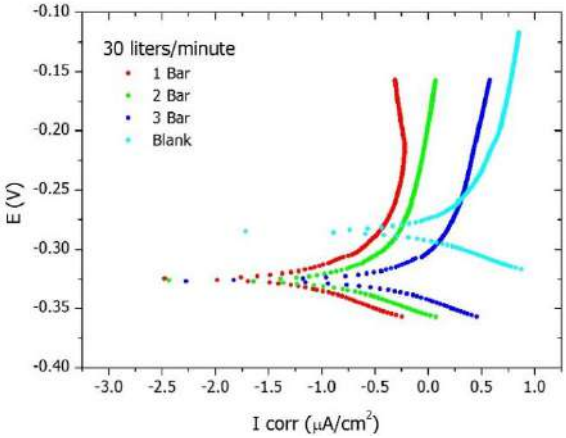

Figure 7. The tafel curve of pressure and oxygen flowrate with variation of 30 l/min

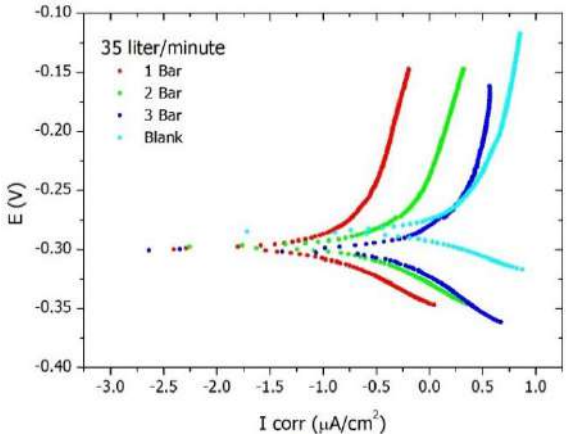

Figure 8. The tafel curve of pressure and oxygen flowrate with variation of 35 l/min

of the specimens which had been treated with flame spray. From curves in Figures 6- 8, it can be compared that the current density is low at overall potential range on all coated materials.This indicates that the corrosion rate on the substrate decreases. Low current density will produce low corrosion rate as well [18, 19]. In the oxygen flow rate variation of 0.25 l/min, the coating results have better passivation ability than other variations. This shift to the right or in the passive direction indicates that there is an increase in electron retention activity which attacks (cuases corrosion) where corrosion activity becomes passive on the coating result compared to that without coating [20]. Corrosion rate depends on the current density which appears. The corrosion rate will be higher if the current density is higher. The parameter values of potentiodynamic polarization of the Tafel curve in Figures 6-8, also can be seen in Table 2.

TABLE 2. The Data of Potentiodynamic Polarization Parametermodel

Pressure (bar)	Oxygen flowrate (liters/minute)	βa (V/dec)	Bc (V/dec)	Ecorr (V)	Icorr (μA/cm²)	CR (mmpy)
Blank		0.0935	-1.19	-0.3249	7.7050	0.08154
1	25	0.0390	0.071	-0.3394	2.4674	0.02611
2	25	0.0416	0.095	-0.3745	2.4888	0.02634
3	25	0.0440	0.149	-0.3412	3.4224	0.03622
1	30	0,0593	0.079	-0.3240	2.6994	0.02857
2	30	0.0620	0.135	-0.3253	3.5456	0.03752
3	30	0.0548	0.194	-0.3781	3.6430	0.03855
1	35	0.0816	-1.13	-0.2991	4.7869	0.05066
2	35	0.1021	0.326	-0.3613	5.0841	0.05380
3	35	0.5916	0.171	-0.3008	7.1888	0.07608

The decrease in corrosion rate is caused by the use of low pressure. If the pressure is getting lower, the particle speed of the HAp part will be slower and thus gives longer time toget to the substrate surface [12]. The effect is that HAp particles can be heated and can stick better to the substrate surface. This will increase the coating thickness which protects the substrate from the environment and decrease the corrosion rate. The measurements of coating thickness and corrosion rate support each other. At low pressure, the particles produced are finer and it leads to smoother surface. The increase in spray distance leads to fine size of the particles on the surface. Bigger particles tend to form big droplets with the volume which partly melts [21]. Closer distance of the gun will produce less smooth or rough surface. This is because the particles have not melted perfectly. Thus, when reaching the substrate surface, the particle size is still round. The roundness can produce hollows on the surface of the coating result which causes higher roughness value and porosity [22]. The variation of oxygen flowrate and air pressure are able to prevent the electrolite ion of HBSS or electrons to get in to the surface of 316L SS.

The decrease in corrosion rate happens because of more balanced use of oxygen flowrate and fuel flowrate. In this study, the fuel flowrate used was 25 l/min. The decrease in the use of oxygen flowrate will increase the flame temperature because the oxygen flowrate and fuel flowrate are more balanced, and thus the heating of HAp particles is better. The effect is that the particles can stick better to the substrate surface [14, 23, 24]. This results in the increase in coating thickness which protects the substrate from the environment and decreases the corrosion rate. This can be seen from the result of micro photograph in Figures 9-10.

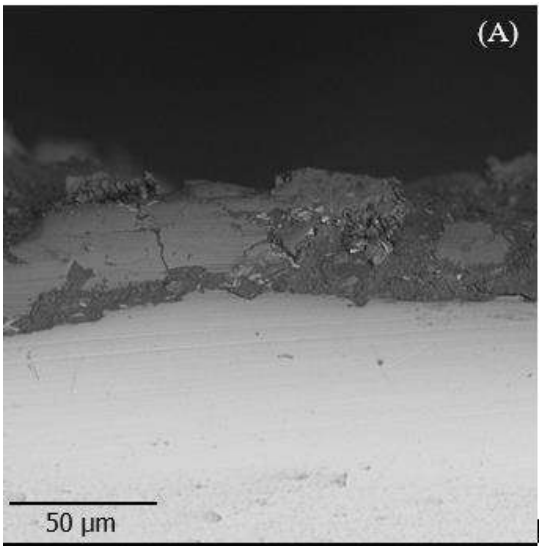

Figure 9. The micro photograph with pressure of 1 bar and oxygen flowrate of 25 l/min

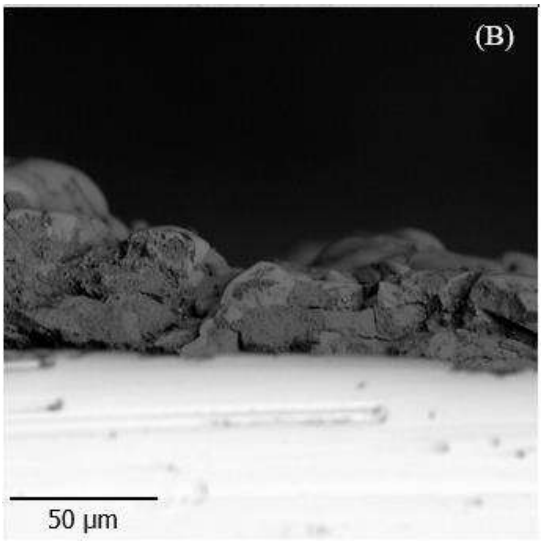

Figure 10. The micro photograph with pressure of 3 bar and oxygen flowrate of 35 l/min

Figure 10 presents the specimen which has been treated with pressure of 1 bar and oxygen flowrate of 25 l/min of oxygen flowrate. In Figure 11, the specimen is given pressure of 3 bars and oxygen flowrate of 35 l/min. From the coating result, it can be known that the specimen in Figure 9 has solid coating while the specimen in Figure 10 has more porous coating which is not as solid as the specimen in Figure 9. In another words, specimen in Figure 10 has better coating quality compared with the specimen in Figure 10 [25]. It is also found that the specimen in Figure 9 has the lowest corrosion rate while the specimen in Figure 10 has the highest corrosion rate. The coating result influences the corrosion rate.

4. CONCLUSION

The result of this study showed that variation of pressure of 1 bar and oxygen flowrate of 25 l/min produced the thickest coating which is 123.5µmand the lowest corrosion rate which is 0.0261mm/year. The variation of pressure of 3 bars and oxygen flowrate of 35 l/min produces the lowest thickness which is 32.5µm and the highest corrosion rate which is 0.0761 mm/year.

The use of high pressure and oxygen flowrate will decrease the coating thickness and the corrosion rate. This is because high pressure increases the particle speed of HAp particles. This makes much HAp metal meltand agglomerate on the surface. The result is that the nonhomogeneous and porous coating. The porosity triggers higher corrosion rate on the coating. This condition will reduce time to heat HAp particles and thus the particles are not heated well and cannot stick to the substrate. This results in the porous coating and the specimen is not protected well from the environment.The specimens which are coated with HAp produces lower corrosion rate compared to those were not reported. This study can initiate future research on flame spray coating on biomaterial.

5. REFERENCES

1. ASTM and F138, A., "Standard specification for wrought 18chromium-14nickel-2.5 molybdenum stainless steel bar and wire for surgical implants (uns s31673)", ***West Conshohocken: ASTM International***, (2003).DOI: 10.1520/F0138-03
2. ASTM and F899, A., "Standard specification for wrought stainless steels for surgical instruments", ***West Conshohocken: ASTM International***, (2011).DOI: 10.1520/F0899-11.
3. ASTM and F899, A., "Standard specification for wrought seamless stainless steel tubing for surgical implants", ***WestConshohocken: ASTM International***, (2009). DOI: 10.1520/F2181-09.
4. Habibovic, P., Barrere, F., Van Blitterswijk, C.A., de Groot, K. and Layrolle, P., "Biomimetic hydroxyapatite coating on metal implants", ***Journal of the American Ceramic Society***, Vol. 85, No. 3, (2002), 517-522. DOI: https://doi.org/10.1111/j.1151-2916.2002.tb00126.x.
5. Sivaraj, D., Vijayalakshmi, K., Ganeshkumar, A. and Rajaram, R., "Tailoring cu substituted hydroxyapatite/functionalized multiwalled carbon nanotube composite coating on 316l ss implant for enhanced corrosion resistance, antibacterial and bioactive properties", ***International Journal of Pharmaceutics***, Vol. 590, (2020), 119946. DOI: https://doi.org/10.1016/j.ijpharm.2020.119946.
6. Erdem, U., Dogan, M., Metin, A.U., Baglar, S., Turkoz, M.B., Turk, M. and Nezir, S., "Hydroxyapatite-based nanoparticles as a coating material for the dentine surface: An antibacterial and toxicological effect", ***Ceramics International***, Vol. 46, No. 1, (2020), 270-280. DOI: https://doi.org/10.1016/j.ceramint.2019.08.260.
7. Zhou, H. and Lee, J., "Nanoscale hydroxyapatite particles for bone tissue engineering", ***Acta biomaterialia***, Vol. 7, No. 7, (2011), 2769-2781.DOI: https://doi.org/10.1016/j.actbio.2011.0.
8. Tiwari, S. and Mishra, S., "Post annealing effect on corrosion behavior, bacterial adhesion, and bioactivity of lvof sprayed hydroxyapatite coating", ***Surface and Coatings Technology***, (2020), 126500. DOI: https://doi.org/10.1016/j.surfcoat.2020.126500.
9. Wielage, B., Lampke, T. and Grund, T., "Thermal spraying of wear and corrosion resistant surfaces", in Key Engineering Materials, Trans Tech Publ. Vol. 384, (2008), 75-98. DOI: https://doi.org/10.4028/www.sciencetific.net/KEM.384.75.
10. Cizek, J., Khor, K.A. and Prochazka, Z., "Influence of spraying conditions on thermal and velocity properties of plasma sprayed hydroxyapatite", ***Materials Science and Engineering: C***, Vol. 27, No. 2, (2007), 340-344. DOI: https://doi.org/10.1016/j.msec.2006.05.002.
11. Lih, W.-C., Yang, S., Su, C., Huang, S., Hsu, I. and Leu, M., "Effects of process parameters on molten particle speed and surface temperature and the properties of hvof crc/nicr coatings", ***Surface and Coatings Technology***, Vol. 133, (2000), 54-60. DOI: https://doi.org/10.1016/S0257-8972(00)00873-2.
12. Milanti, A., Matikainen, V., Koivuluoto, H., Bolelli, G., Lusvarghi, L. and Vuoristo, P., "Effect of spraying parameters on

the microstructural and corrosion properties of hvaf-sprayed fe–cr–ni–b–c coatings", ***Surface and Coatings Technology***, Vol. 277, (2015), 81-90.DOI: https://doi.org/10.1016/j.surfcoat.2015.07.018.

13. Idora, M., Rahman, M., Ismail, M. and Nik, W., "Effect of zinc coating thickness on corrosion performance of mild steel in atmospheric and seawater environment", in Applied Mechanics and Materials, Trans Tech Publ. Vol. 554, (2014), 213-217.DOI: https://doi.org/10.4028/www.sciencetific.net/AMM.554.213.
14. Min-Su, H., Yong-Bin, W., Seok-Cheol, K., Jeong, Y.-J., Seok-Ki, J. and Seong-Jong, K., "Effects of thickness of al thermal spray coating for sts 304", ***Transactions of Nonferrous Metals Society of China***, Vol. 19, No. 4, (2009), 925-929.DOI: https://doi.org/10.1016/S1003-6326(08)60379-9.
15. Murugan, K., Ragupathy, A., Balasubramanian, V. and Sridhar, K., "Optimizing hvof spray process parameters to attain minimum porosity and maximum hardness in wc–10co–4cr coatings", ***Surface and Coatings Technology***, Vol. 247, (2014), 90-102.DOI: https://doi.org/10.1016/j.surfcoat.2014.03.022.
16. Saito, M., Tobe, S., Iwao, T. and Inaba, T., "Effect of pressure on surface roughness treated by cathode spots of low pressure arc", in 2006 International Symposium on Discharges and Electrical Insulation in Vacuum, IEEE. Vol. 2, (2006), 550-553.
17. Gapsari, F., Wijaya, H., Andoko, A. and Suprapto, A., "The performance of bee wax propolis inhibitor on the ductile cast iron (dci) in saline and acidic environment", ***International Review on Modelling and Simulations (IREMOS)***, Vol. 12, No. 3, (2019), 163.DOI: https://doi.org/10.15866/iremos.v12i3.17085.
18. Gapsari, F., Setyarini, P.H. and Fajrin, E.F., "The effect of electrophoretic deposition current to tinplate coating with chitosan", ***International Journal of Integrated Engineering***, Vol. 11, No. 5, (2019), 23-28.DOI: https://doi.irg/10.30880/ijie.2019.11.05.003
19. Gapsari, F., Madurani, K.A., Simanjuntak, F.M., Andoko, A., Wijaya, H. and Kurniawan, F., "Corrosion inhibition of honeycomb waste extracts for 304 stainless steel in sulfuric acid solution", ***Materials***, Vol. 12, No. 13, (2019), 2120.DOI: https://doi.org/10.3390/ma12132120.
20. Kumari, R. and Majumdar, J.D., "Studies on corrosion resistance and bio-activity of plasma spray deposited hydroxylapatite (ha) based tio2 and zro2 dispersed composite coatings on titanium alloy (ti-6al-4v) and the same after post spray heat treatment", ***Applied Surface Science***, Vol. 420, (2017), 935-943.DOI: https://doi.org/10.1016/j.apsusc.2017.05.208.
21. Sobolev, V., Guilemany, J. and Martin, A., "Flattening of composite powder particles during thermal spraying", ***Journal of thermal Spray Technology***, Vol. 6, No. 3, (1997), 353-360.DOI: https://doi.org/10.1007/s11666-997-0070-0.
22. Sarikaya, O., "Effect of some parameters on microstructure and hardness of alumina coatings prepared by the air plasma spraying process", ***Surface and Coatings Technology***, Vol. 190, No. 2-3, (2005), 388-393.
23. Hou, G., An, Y., Zhao, X., Zhou, H. and Chen, J., "Effect of alumina dispersion on oxidation behavior as well as friction and wear behavior of hvof-sprayed cocralytacsi coating at elevated temperature up to 1000 c", ***Acta Materialia***, Vol. 95, (2015), 164-175. DOI: https://doi.org/10.1016/j.actamat.2015.05.025.
24. Killinger, A. and Gadow, R., "High velocity thermal spraying of powders and suspensions containing micron, submicron and nanoparticles for functional coatings", in Key Engineering Materials, Trans Tech Publ. Vol. 533, (2013), 99-114.DOI: https://doi.org/10.4028/www.sciencetific.net/KEM.533.99.
25. Gadow, R., Killinger, A. and Stiegler, N., "Hydroxyapatite coatings for biomedical applications deposited by different thermal spray techniques", ***Surface and Coatings Technology***, Vol. 205, No. 4, (2010), 1157-1164.DOI: https://doi.org/10.1016/j.surfcoat.2010.03.059.

Persian Abstract

چکیده

این مطالعه یک مطالعه مقدماتی روی پوشش اسپری شعله با هیدروکسی آپاتیت (HAp)بود. پوشش یکی از تکنیک های بهبود مقاومت فلز در برابر خوردگی است. در این مطالعه ، پوشش اسپری شعله با استفاده از HAp بر روی فولاد ضد زنگ ۳۱۶ L به عنوان ماده ای برای دستگاه های پزشکی انجام شد. این ترکیب مصنوعی حاوی عناصری است که در بدن انسان سازگار و زیست فعال هستند و در آنجا می توانند به بافت های بدن یا عضلات بچسبند. از HAp به دلیل ساختار بلوری ، سازگاری زیستی و ماهیت استخوان سازی به عنوان جانشین استخوان استفاده گسترده ای شده است. در این مطالعه استیل ، ۳۱۶ L با استفاده از روش اسپری شعله با جریان متنوع اکسیژن و فشار هوا توسط HAp پوشانده شد. نتیجه این مطالعه نشان داد که فشار هوا ۱ بار و جریان اکسیژن ۲۵ لیتر در دقیقه دارای ضخیم ترین پوشش که ۱۲۳/۵ میکرومتر بود و کمترین میزان خوردگی آن ۰.۲۶۱ میلی متر در سال بود. فشار هوا از ۳ بار و جریان اکسیژن ۳۵ لیتر در دقیقه کمترین ضخامت را نشان داد که ۳۲/۵ میکرومتر بود و بیشترین میزان خوردگی را ۰/۰۷۷ میلی متر در سال نشان داد. استفاده از فشار هوای بالا و جریان اکسیژن باعث کاهش ضخامت پوشش و میزان خوردگی می شود. نتیجه نشان داد که روش اسپری شعله برای استفاده برای پوشاندن HAp روی استیل 316L موثر بود.

International Journal of Engineering

Journal Homepage: www.ije.ir

Experimental Study on Mechanical, Thermal and Antibacterial Properties of Hybrid Nanocomposites of PLA/CNF/Ag

K. Sheikh, H. Shahrajabian*

Department of Mechanical Engineering, Najafabad branch, Islamic Azad University, Najafabad, Iran

P A P E R I N F O

Paper history:
Received 23 September 2020
Received in revised form 15 October 2020
Accepted 30 October 2020

Keywords:
Antibacterial Properties
Cellulose Nano-fiber
Poly Lactic Acid
Silver Nanoparticles
Thermal Properties

A B S T R A C T

The main purpose of this study is preparation of the nanocomposite samples with synergistic properties containing the mechanical, thermal and antibacterial properties. For this purpose, the combination of cellulose nanofiber (CNF) and Ag (silver) nanoparticles were incorporated into polylactic acid (PLA) matrix by solution casting method. The CNF in constant content of 1 wt.% and Ag nanoparticles in the content of 1, 3, and 5 wt.% were incorporated into the PLA matrix. The structure and morphology of the nanocomposite samples was characterized by FE-SEM, and mechanical, antibacterial, and thermal properties of the nanocomposites were evaluated by tensile, agar disk-diffusion, and DSC tests, respectively. FE-SEM images showed the uniform dispersion of the nanoparticles within the polymer matrix. The simultaneous addition of two nanoparticles significantly raised the mechanical properties such as tensile strength and tensile modulus by 40 and 9%, respectively. However, CNF had no considerable effect on the thermal and antibacterial properties of the PLA matrix. Unlike CNF, Ag nanoparticles significantly improved the antibacterial properties of the nanocomposites against *staphylococcus aureus* and *Escherichia coli* bacteria, and enhanced the thermal stability of the PLA matrix. Ag nanoparticles improved the degree of crystallinity of PLA from 10.5% to 17.9%, and T_m from 147.8 to 153.6 °C. By incorporating 5wt.% Ag nanoparticles, the inhibition duameter increased from 20 mm to 39 mm for *staphylococcus aureus*.

***doi**: 10.5829/ije.2021.34.02b.23*

NOMENCLATURE

X_c	degree of crystallinity	ΔH_m^c	The heat of diffusion
ΔH_m	The melting enthalpy		

1. INTRODUCTION

Consuming the syntactic polymers manufactured by petrochemical industries cusses environmental damage seriously [1,2]. A considerable amount of plastic material (approx. 45%) is used for disposable packaging [3]. The use of compatible and biodegradable polymers (natural polymers) for consuming in various industries, especially for food packing, could reduce these environmental problems significantly [4]. Poly (lactic acid) (PLA) as a biodegradable polyester is a favorite environmental-friendly polymer that is used widely in the packing industry [5]. PLA has some advantages such as abundant sources of PLA, good resistance to ultraviolet, ease of processability, low toxicity, and acceptable hydrophobicity [6-8]. Notwithstanding these advantages, some defects such as poor heat resistance, high brittleness, poor disinfection properties, and low barrier properties limit the application of PLA [9,10].

The nanotechnology is a new technology which could improve the properties of various materials. Hamedi et al. [11] improved the mechanical properties of asphalt by adding nano silica. Saeid et al. [12] improved the performance of warm mix asphalt by incorporating nano

*Corresponding Author Institutional Email: *h.shahrajabian@pmc.iaun.ac.ir* (H. Shahrajabian)

Please cite this article as: K. Sheikh, H. Shahrajabian, Experimental Study on Mechanical, Thermal and Antibacterial Properties of Hybrid Nanocomposites of PLA/CNF/Ag, International Journal of Engineering, Transactions B: Applications Vol. 34, No. 02, (2021) 500-507

bentonite and fatty Arbocel. A useful method that is proposed by researchers to improve overcome these defects is incorporating the nano-particles into the PLA matrix to improve the properties such as mechanical properties (tensile strength, tensile modulus, etc.), barrier properties, antibacterial properties, and thermal properties [13]. Among the various nanofillers introduced into the PLA matrix, nano-cellulose has received much attention from researchers due to high availability, low price, high mechanical properties, and biodegradability [14,15]. Trifol et al. [16] compared the effect of cellulose nanofibers (CNF) and clay nanoparticles on the mechanical properties of the PLA matrix film. They observed a slight improvement in the mechanical properties of PLA/CNF film compared to PLA/clay film. Rezaei et al. [17] improved tensile strength and tensile modulus of PLA matrix film up to 32 and 19% by incorporating CNFs, respectively. Jonoobi et al. [18] increased tensile strength and tensile modulus of PLA matrix from 58 to 71 MPa, and 2.9 to 3.6 GPa, respectively, by incorporated CNF content of 1 to 5 wt.%. Arrieta et al. [19] showed that introduce the CNFs into PLA matrix composite increased the transition glass temperature (Tg), and concluded that CNFs restrict the mobility of the polymer chains. Frone et al. [20] increased the degree of crystallinity of the PLA matrix from 39% to 47% by adding the CNFs in the content of 2.5 wt.%.

As mentioned above, one of the major applications of PLA is the food packing industry for meat products, fruits, vegetables, and beverage bottles [21,22]; therefore, the antibacterial property is an essential characteristic for PLA. Among the nano-particles, silver (Ag), with its strong antibacterial properties, can kill the various microorganisms such as *E. coli*, *Staphylococcus aureus*, and *Neisseria gonorrhoeae* [23,24]. Other important properties of Ag include acceptable antiviral effects [25], antiparasitic activities [26], and antifungal properties [27]. Manikandan et al. [28] coated nanoporous Sodium Alginate (SA)/ Poly Vinyl Alcohol (PVA) composite scaffold with Ag nanoparticles for antibacterial activity. Maroti et al. [29] investigated the effect of Ag nanoparticles on thermal and antibacterial properties of PLA for use in 3D print of biomedical devices. Their results showed that PLA/Ag nanocomposites are suitable for biomedical devices. Gan et al. [30] showed that the combined effect of Ag and carbon nanotube (CNT) could improve the antibacterial properties, thermal stability and, tensile strength of the PLA matrix. Fan et al. [31] concluded that the migration of Ag nanoparticles in PLA/Ag nanocomposites increased by Ag content. Growing the migration time made the film rougher, and increased the crystallization temperature of the nanocomposite films.

It is also found that the combination of two nanofillers into the polymer matrix could merge the properties of the both of nanofillers to matrix [27]. Therefore, the co-incorporation of CNFs and Ag nanoparticles into PLA matrix is potential to manufacture the nanocomposite samples with synergistic properties containing mechanical, thermal and antibacterial properties. Since no research has been done to investigate the co-incorporation of CNF and Ag nanoparticles into PLA matrix, in this study, PLA matrix nanocomposites reinforced by CNFs and Ag nanoparticles were prepared by the solution casting method. CNFs in the content of 1 wt.% were added into PLA matrix to improve mechanical properties, and Ag nanoparticles in the content of 1, 3, and 5 wt.% were added to improve anti-bacterial properties of the PLA matrix. The dispersion of nano-fillers in the PLA matrix was investigated by field emission scanning electron microscopy (FE-SEM). Tensile, antibacterial, and differential scanning calorimetry (DSC) tests were done to evaluate mechanical, antibacterial, and thermal properties of the nanocomposite samples.

2. MATERIALS AND METHODS

2. 1. Materials Bio-flex®F 6510 commercial grade of poly(lactic acid) (PLA) with molecular weight (Mw) of 197000 g/mol, the density of 1.25 g/cm^3, and melting temperature point of 160 °C was supplied from Fkur GmbH company. Cellulose nanofiber (CNF) gel (3 wt.%) was prepared from Nano-Novin-Polymer Co. (Iran). Ag nanoparticles with the density of 10.5 g/cm^3, an average diameter of 20 nm, and purity of 99.9% were purchased from Nanosany Co. (Iran). The analytical grade of chloroform (as a solvent), methanol, acetone, and ethanol were purchased from Arman Sina Co. (Iran).

2. 2. Preparation The PLA films and nanocomposite films are prepared by the solution casting method. For the preparation of PLA film, 5 g of PLA was added into 100 ml chloroform, and was stirred by a mechanical a stirrer at rotary speed of 2000 rpm for 6 h, at ambient temperature. The prepared solution was poured in the mold, and was dried at ambient temperature for 24 h to remove the solvent. To remove the solvent completely, the samples were dried in a vacuum oven for 7 days at a temperature of 45 °C. In order to add CNF into PLA solution, the CNF gel in a certain amount was suspended in solvents of methanol, ethanol, acetone, and chloroform respectively and finally centrifuged at a rotary speed of 8000 rpm for 10 min. It should be noted that for each of the mentioned solvents, this procedure was repeated five times. Finally, the CNF content for all the nanocomposite samples was the same in the content of 1 wt.% (because in some literature this content was optimum content [32]). The CNF in the content of 1 wt.% and Ag nanoparticles in content of 1, 3, and 5 wt.% were

added into PLA solution, followed by stirring by mechanical stirrer at 2000 rpm for 2 h. For better dispersion of nano-fillers into PLA, the solution was homogenized by the ultrasonic homogenizer model of UP400St (manufactured in Hielscher Co., Germany) for 45 min (Three 15 min intervals). Drying the nanocomposite films was exactly like drying the PLA films. The composition of the samples has been shown in Table 1.

2. 3. Characterization Field emission-scanning electron microscopy (FE-SEM) was used to investigate the morphology of the samples by the MIRA3 TESCAN (manufactured by Tescan company in the Czech Republic). Fourier transform infrared spectra (FTIR) was conducted using the Tensor 27 Bruker instrument with a resolution of 4 cm^{-1}. The mechanical properties of the nanocomposite films such as tensile strength, tensile modulus, and elongation were measured by tensile machine test of H25KS manufactured by Hounsfield Co. at ambient temperature with the speed of 20 mm/min. For each sample, 5 tests was done on the film samples in a dimension of 160 mm×20mm×0.1 mm. The thermal analysis of the samples was evaluated by differential scanning calorimetry (DSC) test using a SANAF DSC analyzer. The samples heated under a nitrogen atmosphere from 20 °C to 200 °C, and cooled to 40 °C with a melting and cooling rate of 10 °C/min. The antibacterial test was investigated by the agar disk-diffusion method. The standard strains of *staphylococcus aureus* (ATCC: 25923) and *E. coli* (ATCC: 25922) as the target bacteria were selected to evaluate the antibacterial properties of the film samples. The disk samples in diameter of 20 mm were cut from nanocomposite films. Both target bacteria were cultivated in the culture media of the blood agar (BA) and tryptic soy broth (TSB). The bacteria suspension of 0.5 MakFarland (1.5×108 CFU/ml) was sprayed over the surface of culture dishes. Then the disk samples were located on the bacterial agar plate, and the dishes were incubated at 37 °C for 24 h. The antibacterial properties of the composite samples were determined by measuring the diameter of the inhibition growth zone by the caliper.

TABLE 1. The composition of the samples

Sample	CNF (wt.%)	Ag (wt.%)	PLA (wt.%)
PLA	-	-	100
PCNF	1	-	99
PCNAg1	1	1	98
PCNAg3	1	3	96
PCNAg5	1	5	94

3. RESULTS

3. 1. Morphology The morphology of the samples was investigated by FE-SEM. Figure 1 shows FE-SEM images of the fracture surface of PCNF, PCNAg1and PCNAg3 nanocomposites. The distribution of the nanoparticles (cellulose and Ag) in PCNAg1 and PCNAg3 has been shown in Figures 1(a), and 1(b), respectively. One of the most important factors affecting the properties of the polymer matrix nanocomposites is the distribution of the nanofillers in the polymer matrix. Uniform dispersion of nanoparticles within the polymer matrix can improve the mechanical and physical properties of the matrix, but on the contrary, the agglomeration of the nanoparticles reduces the properties. Figure 1(a) shows the uniform dispersion of Ag nanoparticles within the PLA matrix in the PCNAg1 sample (the bright points are the Ag nanoparticles). The dispersion of nanoparticles (Ag and cellulose) within the polymer matrix in the PCNAg3 sample has been shown in Figure 1(b). As shown in Figure 1(b), the nanoparticles were almost uniformly dispersed within the matrix. In PCNAg3, several agglomerates with a dimension lower than 5 μm can be seen. By increasing the Ag nanoparticle content in PCNAg5, the agglomeration sites increased, and the surface is more rough compared to PCNAg3, as shown in Figure 1(c). Figures 1(d), and 1(e) illustrate the distribution of nanoparticles in nanoscale. As shown in Figure 1, the nanoparticles the particles are well distributed on a nanoscale.

3. 2. ATR-FTIR The interaction between nanofillers (Ag and cellulose nanoparticles) can be observed by ATR-FTIR measurement. FTIR spectra of neat PLA and PLA/CNF/Ag nanocomposite samples are shown in Figure 2. It can be seen that the neat PLA and nanocomposite samples have the sharp peaks at 1000-1200 cm^{-1} and 1750 cm^{-1}, belonging to the stretching vibration of C-O-C and C=O of PLA. A sharp peak at 1749 cm^{-1} (crystalline sensitive band) is observed, which is due to the C=O ester group. The other peaks were positioned at 1452 cm^{-1} and 1363 cm^{-1} due to the bending vibration of CH_3 (alkyl group). It is also observed from the FTIR spectrum that nanocomposite samples have a small peak at 1253 cm^{-1} (C-O-C), a stretching vibration in the crystalline phase, while in pure PLA, this peak is negligible. This indicates that the nanofillers have an effect on the characteristic band intensities.

3. 3. Mechanical Properties The impact of nanoparticles (cellulose and Ag) on the mechanical properties of the pure PLA and nanocomposite samples has been investigated using a tensile test. Figure 3 shows the stress-strain curve of PLA, PLA/CNF, and

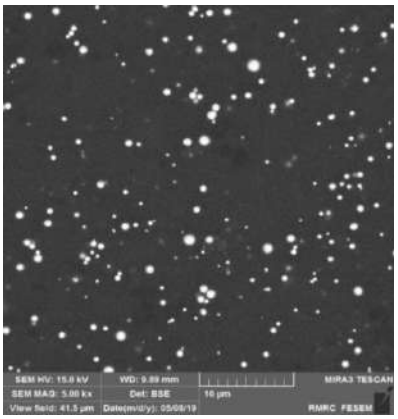

(a) Ag distribution in PCNAg1

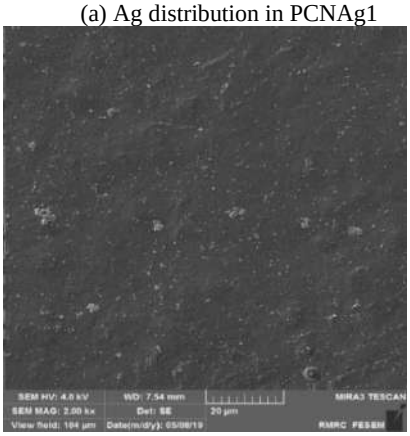

(b) Nano particles distribution in PCNAg3

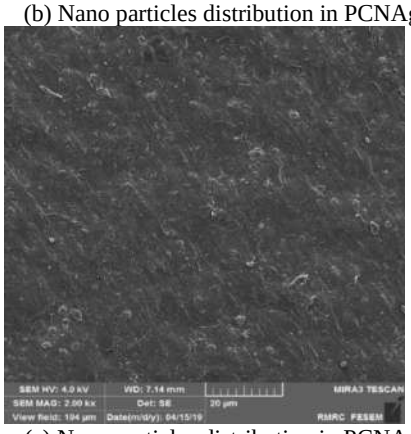

(c) Nano particles distribution in PCNAg5

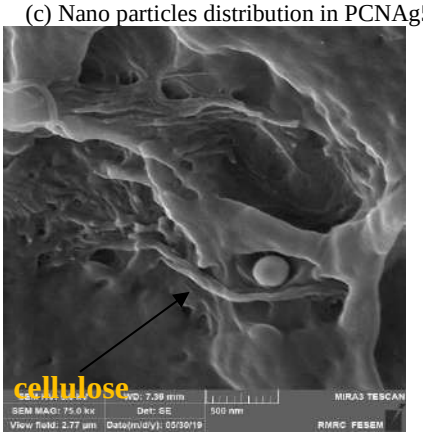

(d) High magnification image of PCNF

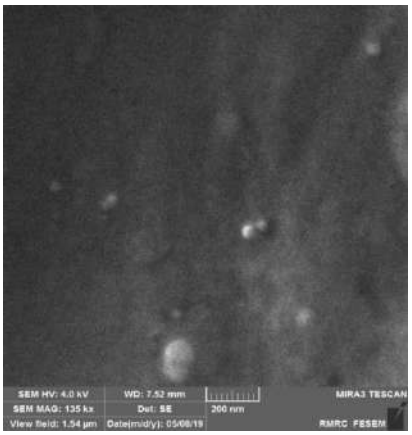

(e) High magnification image of PCNAg1

Figure 1. FE-SEM images of the samples

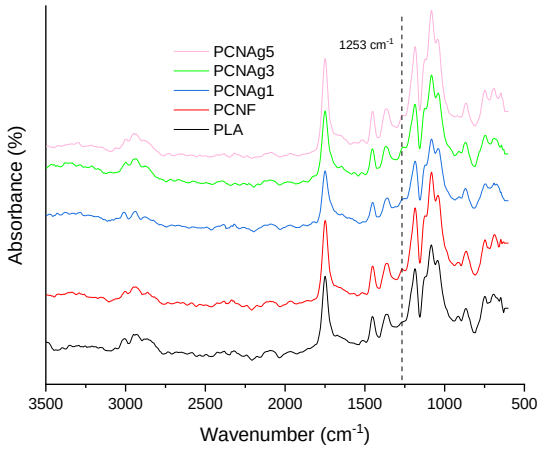

Figure 2. ATR- FTIR spectra of PLA/CNF/Ag nanocomposites

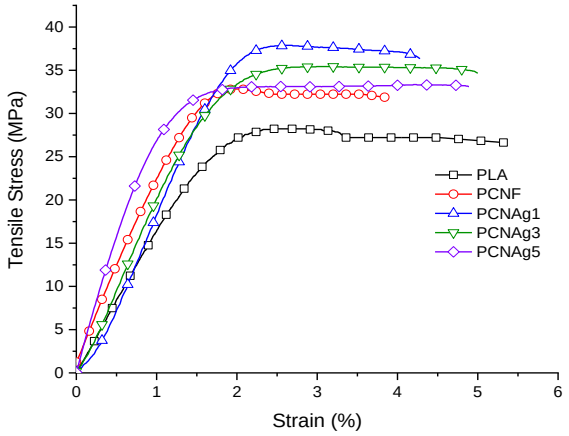

Figure 3. Stress-strain curve for PLA, PLA/CNF, PLA/CNF/Ag nanocomposite films.

PLA/CNF/Ag nanocomposites. Based on the results presented in Table 2, the neat PLA has a tensile strength

of 27.1 MPa with elongation (strain at break point) of ~ 6%, and tensile modulus (Young modulus) of 1856 MPa. The results show that adding the CNF and Ag nanoparticles improve the tensile properties of the PLA matrix, indicating a strong interaction between nano-fillers and PLA matrix. The film containing 1 wt% of CNF (PCNF), the tensile strength, Young's modulus increased by 20 and 21%, respectively, and elongation decreased by 34%. The Ag nanoparticles in the content of 1, 3, and 5 wt.% was incorporated into PLA/CNF nanocomposites to investigate the effect of Ag nanoparticles on the tensile properties of nanocomposite films. The results indicate that the adding Ag nanoparticles decreased Young's modulus of PLA/CNF films from 2259 to 2010 MPa, but increased the tensile strength from 32.5 to 38 MPa. The simultaneous increase of tensile strength and elongation after adding the Ag nanoparticles can be due to very small size of nanoparticles that is close to polymer chains and these nanoparticles act as a cross between chains. By increasing the nanoparticle content from 1 to 5 wt.% the Young's modulus increased from 2010 to 2593 MPa, and tensile strength decreased from 38 to 33.2 MPa. A decrease in tensile strength by Ag nanoparticles content can be due to nanoparticles aggregation in higher-level loading of nanoparticles. The agglomeration sites of the Ag nanoparticles can acts as a holes in the polymer matrix and therefore, has negative effect on mechanical and thermal properties of PLA. On the other hand, agglomeration decrease the adhesion between nanoparticles and the polymer matrix.

3. 4. Thermal Properties The thermal behavior of pure PLA and PLA/CNF/Ag nanocomposite films was investigated by DSC analysis. The melting and cooling curves of the samples has been shown in Figures 4 and 5, respectively, with the results such as glass transition temperature (T_g), melting point temperature (T_m), crystallization temperature (T_c), and degree of crystallinity (χ) shown in Table 3. The degree of crystallinity was calculated through Equation (1):

$$X_c(\%) = \frac{\Delta H_m}{\Delta H_m^c} \times 100 \quad (1)$$

TABLE 2. Tensile properties of PLA, PLA/CNF, PLA/CNF/Ag nanocomposite films

Sample	Young's modulus (MPa)	Tensile strength (MPa)	Elongation (%)
PLA	1856±210	27.1±2.3	5.81±0.31
PCNF	2259±340	32.5±4.4	3.84±0.22
PCNAg1	2010±150	38.0±3.7	4.28±0.33
PCNAg3	2119±240	35.5±5.2	5.01±0.43
PCNAg5	2593±310	33.2±3.7	4.75±0.55

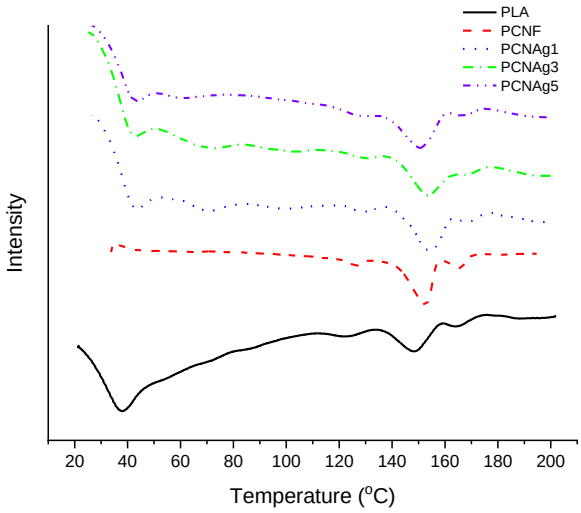

Figure 4. DSC melting scans for the samples

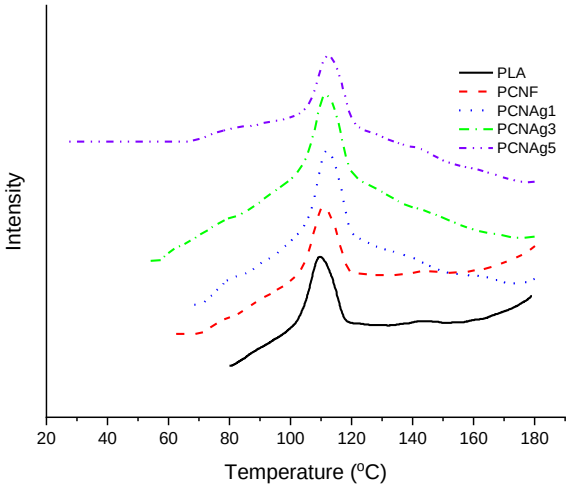

Figure 5. DSC cooling scans for the samples.

TABLE 3. The DSC data for the film samples

Sample	T_g (°C)	T_m (°C)	T_c (°C)	ΔH_m (Jg^{-1})	χ (%)
PLA	48.2	147.8	111	8	10.5
PCNF	47.9	149.7	112.1	7.61	9.98
PCNFAg1	52.5	153.6	112.8	11.1	15
PCNFAg3	51.1	153.2	112.9	12.6	16.5
PCNFAg5	51	150.9	112.7	13.7	17.9

where ΔH_m^c with value of 93 J/g is the heat of diffusion for 100% crystallite PLA.

The data of the DSC test were presented in Table 3 shows that incorporating the CNF into the PLA matrix does not aeffect on T_g, T_m, T_c, and χ of the PLA matrix. The addition of Ag nanoparticles in the content of 1 wt.% increased Tg of PLA matrix from 48.2 to 52.5 °C. The T_g

has related to the mobility of the polymer chains of the amorphous phase in the PLA matrix. The increase of T_g with the introducing the Ag nanoparticles shows that Ag nanoparticles have been able to hinder effectively mobility of the molecular chains. Enhancement of T_g by incorporating the Ag nanoparticles could be due to the strong interactions between nanoparticles and PLA matrix [33]. The increase in T_g by using the nanoparticles in the PLA matrix was reported in the other literature. Adding the hydroxyapatite and GO nanoparticles increases the T_g of PLA [34, 35]. The further increase of Ag content has no considerable effect on T_g. The melting point temperature of the PCNAg1 containing 1 wt.% of Ag is 153.6 °C, which is 5.8 °C higher than pure PLA. The amount of T_m depends on the thickness of lamellae, so that the T_m increases by the lamellae thickness. Therefore, it can be concluded that introducing the Ag nanoparticles has increased the lamellae thickness in the crystalline phase. This increase in the melting point temperature of PLA has been observed in other researches [35]. By increasing the Ag content up to 3 wt.%, the considerable change in T_m was not observed, however by further increase of Ag nanoparticles to 5 wt.%, T_m decreased to 150.9 °C, probably due to nanoparticles agglomeration. The results presented in Tabl 3 show that the degree of crystallinity (χ) for pure PLA and PCNF is 10.5 and 9.98%, respectively, indicating that CNF is almost ineffective on χ. Unlike the PCNF sample, the χ for the PCNAg1, PCNAg3, and PCNAg5 increased up to 15, 16.5, and 17.9%, respectively. This increase in χ of the PLA matrix indicates that the Ag nanoparticles are useful to provide more nucleation sites. Frone et al. [20] observed that 2.5 wt.% of nano-cellulose increase the degree of crystallinity of PLA from 39 to 47%. Mukherjee et al. [36] improved the degree of crystallinity of PLA by 4% by adding 2.5 wt.% of microcrystal cellulose.

3. 5. Anti-bacterial Properties The antibacterial properties of PLA and PLA/CNF/Ag nanocomposite films against the positive strain of staphylococcus aureus and negative strain of *E. coli* were investigated by agar disk diffusion method. For this purpose, the round samples with 20 mm in diameter were separated from the films, and then placed on the Mueller Hinton Agar (MHA) plate on which negative and positive strains have been cultivated. Figure 6 shows the agar plates of *E. coli* and *staphylococcus aureus* treated with the prepared nanocomposites for 24 h. The samples of pure PLA, PCNF, and PCNAg1 are not shown in Figure 6, because, as anticipated, they did not have any antibacterial activity within the tested time (in the PCNAg1 sample, Ag nanoparticles content was insufficient). When Ag nanoparticles in the content of 3 and 5 wt.% were added into PLA, the PLA/CNF/Ag nanocomposite samples showed significant antibacterial performances. The diameter of the inhibition growth zone around the samples is a suitable criterion to estimate antibacterial properties of the nanocomposite samples. Table 4 presents the diameter of inhibition growth zone of nanocomposites. It could be clearly seen in Figure 6 and Table 4 that by increasing the Ag nanoparticles content from 3 to 5 wt.% the inhibition growth diameter increased from 23 to 34 mm for *E. coli*, and from 27 to 39 mm for *Staphylococcus aureus*, indicating a promising antibacterial activity of the nanocomposite samples. By comparing the results presented in Table 4 for two different strains, it can be concluded that Ag nanoparticles have better prevented the growth of staphylococcus aureus strains. The Ag nanoparticles may accumulate in the membrance of bacteria cytoplasmic to increase the permeability of the bacteria considerably, and as a result the cells were killed [37].

4. CONCLUSION

In this study, PLA/CNF/Ag nanocomposite films with constant content of CNF (1 wt.%), and different content of Ag nanoparticles were prepared by solution casting method. The mechanical test showed that the simultaneous addition of CNF and Ag nanoparticles

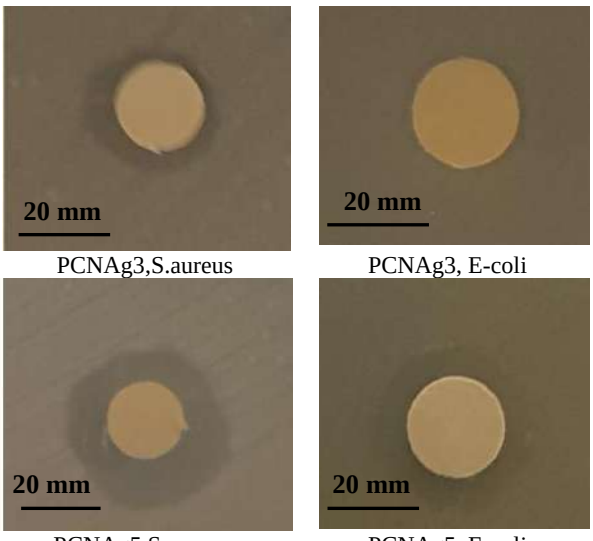

PCNAg3,S.aureus PCNAg3, E-coli

PCNAg5,S. aureus PCNAg5, E-coli

Figure 6. Antibacterial properties of PLA/CNF/Ag composites

TABLE 2. The diameter of inhibition growth zone of the samples

Bacteria \ Sample	PCNAg3	PCNAg5
E-coli	23 mm	34 mm
Staphylococcus aureus	27 mm	39mm

could improve the mechanical properties of nanocomposite samples compared with neat PLA samples. The tensile strength and tensile modulus increased by 40 and 39% for PCNAg1 and PCNAg5, respectively. CNF had no considerable effect on the thermal properties of the PLA matrix, but incorporating Ag nanoparticles increased T_g, T_m, and degree of crystallinity of the PLA matrix. T_m and T_g increased from 147.8 to 153.6 °C, and 48.2 to 52.5 °C, respectively. The degree of crystallinity of the PLA was increased from 10.5 to 17.9% by incorporating 5 wt.% Ag nanoparticles. Moreover, the addition of Ag nanoparticles in the content of 3 and 5 wt.% promoted the antibacterial properties of the nanocomposite samples against *staphylococcus aureus* and *E. coli*. When 5 wt.% Ag nanoparticles was added into PLA the inhibition diameter increased from 20 to 34 mm for *E. coli* and from 20 to 39 mm for *staphylococcus aureus*.

5. REFERENCES

1. Sari, M. G., Vahabi, H., Gabrion, X., Laheurte, P., Zarrintaj, P., Formela, K., Saeb, M. R. "An attempt to mechanistically explain the viscoelastic behavior of transparent epoxy/starch-modified ZnO nanocomposite coatings", ***Progress in Organic Coatings,*** Vol. 119, (2018), 171-182, DOI:10.1016/j.porgcoat.2018.02.016
2. Zarrintaj, P., Ahmadi, Z., Saeb, M. R., Mozafari, M. "Poloxamer-based stimuli-responsive biomaterials", ***Materials Today: Proceedings,*** Vol. 5, No. 7, (2018), 15516-15523, DOI:10.1016/j.matpr.2018.04.158
3. Gutiérrez, T. J., Alvarez, V. A. "Bionanocomposite films developed from corn starch and natural and modified nano-clays with or without added blueberry extract", ***Food Hydrocolloids,*** Vol. 77, (2018), 407-420, DOI:10.1016/j.foodhyd.2017.10.017
4. Gutiérrez, T. J. Polymers for Food Applications. Springer, 2018, doi:10.1007/978-3-319-94625-2_1.
5. Babu R. P., O'Connor, K., Seeram, R. "Current progress on bio-based polymers and their future trends", ***Progress in Biomaterials,*** No. 1, (2013), 8. DOI:10.1186/2194-0517-2-8
6. Ebnesajjad, S., Handbook of biopolymers and biodegradable plastics: properties, processing and applications. William Andrew, 2012.
7. Zhang, X., Liu, X., Yang, C., Li, N., Ji, T., Yan, K., Zhu, B., Yin, J., Zhao, J., Li, Y. "A V2O5-nanosheets-coated hard carbon fiber fabric as high-performance anode for sodium ion battery", ***Surface and Coatings Technology,*** Vol. 358, (2019), 661-666, DOI:10.1016/j.surfcoat.2018.11.096.
8. Zhou, Y., Lei, L., Yang, B., Li, J., Ren, J. "Preparation and characterization of polylactic acid (PLA) carbon nanotube nanocomposites", ***Polymer Testing,*** Vol. 68, (2018), 34-38, DOI:10.1016/j.polymertesting.2018.03.044.
9. Samsudin, H., Auras, R., Mishra, D., Dolan, K., Burgess, G., Rubino, M, Selke, S., Soto-Valdez, H. "Migration of antioxidants from polylactic acid films: A parameter estimation approach and an overview of the current mass transfer models", ***Food Research International,*** Vol. 103, (2018), 515-528, DOI:10.1016/j.foodres.2017.09.021.
10. Liu, Y., Yin, J., Liu, X., Zhao, X., Chen, M., Li, J., Zhao, H., Zhu, C., Su, B. "Fabrication of polymer composite films with carbon composite nanofibers doped MWNTs-OH for multilevel memory device application", ***Composites Part B: Engineering,*** Vol. 156, (2019), 252-258, DOI:10.1016/j.compositesb.2018.08.045.
11. Hamedi, G.H., Sohrabi, M., Sakanlou, F. "Comparing the Effect of Nanomaterial and Traditional Fillers on the Asphalt Mixture Properties", ***Civil Engineering Journal***, Vol. 5, No. 2, (2019), 320-331, DOI: 10.28991/cej-2019-03091247
12. Saedi, S., Oruc, S. "The Effects of Nano Bentonite and Fatty Arbocel on Improving the Behavior of Warm Mixture Asphalt against Moisture Damage and Rutting", ***Civil Engineering Journal***, Vol. 6, No. 5, (2020), 877-888, DOI: 10.28991/cej-2020-03091514.
13. Campardelli, R., Della, P. G., Gomez, V., Irusta, S., Reverchon, E., Santamaria, J. "Encapsulation of titanium dioxide nanoparticles in PLA microspheres using supercritical emulsion extraction to produce bactericidal nanocomposites", ***Journal of Nanoparticle Research,*** Vol. 15, No.10, (2013), 1987, DOI:10.1007/s11051-013-1987-5.
14. Bian, H., Wei, L., Lin, C., Ma, Q., Dai, H., Zhu, J. "Lignin-containing cellulose nanofibril-reinforced polyvinyl alcohol hydrogels", ***ACS Sustainable Chemistry & Engineering,*** Vol. 6, No. 4, (2018), 4821-4828, DOI: 10.1021/acssuschemeng.7b04172
15. Harahap, H., Nawansyah, R., Nasution, H., Iriany, T. "Isolationand Characterization of Nanocrystal from Corncob Waste Using H2SO4 Hydrolysis Method", ***International Journal of Engineering, Transactions A: Basics***, Vol. 31 No. 4, (2017), 533-537, DOI: 10.5829/ije.2018.31.04a.03.
16. Trifol, J., Plackett, D., Sillard, C., Hassager, O., Daugaard, A. E., Bras, J., Szabo, P. "A comparison of partially acetylated nanocellulose, nanocrystalline cellulose, and nanoclay as fillers for high-performance polylactide nanocomposites", ***Journal of Applied Polymer Science,*** Vol. 133, No. 14, (2016), 43257-43268, DOI:10.1002/app.43257.
17. Rezaeigolestani, M., Misaghi, A., Khanjari, A., Basti, A. A., Abdulkhani, A., Fayazfar, S. "Antimicrobial evaluation of novel poly-lactic acid based nanocomposites incorporated with bioactive compounds in-vitro and in refrigerated vacuum-packed cooked sausages", ***International Journal of Food Microbiology,*** Vol. 260, (2017), 1-10, DOI: 10.1016/j.ijfoodmicro.2017.08.006.
18. Jonoobi, M., Harun, J., Mathew, A. P., Oksman, K. "Mechanical properties of cellulose nanofiber (CNF) reinforced polylactic acid (PLA) prepared by twin screw extrusion", ***Composites Science and Technology,*** Vol. 70, No.12, (2010), 1742-1747, DOI: 10.1016/j.compscitech.2010.07.005.
19. Arrieta, M. P., Fortunati, E., Dominici, F., López, J., Kenny, J. M. "Bionanocomposite films based on plasticized PLA–PHB/cellulose nanocrystal blends", ***Carbohydrate Polymers,*** Vol. 121, (2015), 265-275, DOI:10.1016/j.carbpol.2014.12.056
20. Frone, A. N., Berlioz, S., Chailan, J. F., Panaitescu, D. M. "Morphology and thermal properties of PLA–cellulose nanofibers composites", ***Carbohydrate Polymers,*** Vol. 91, No. 1, (2013), 377-384, DOI:10.1016/j.carbpol.2012.08.054.
21. Polat, S., Fenercioglu, H., Unal Turhan, E., Guclu, M. "Effects of nanoparticle ratio on structural, migration properties of polypropylene films and preservation quality of lemon juice", ***Journal of Food Processing and Preservation,*** Vol. 42, No.4, (2018), 13541, DOI.org/10.1111/jfpp.13541.
22. Kechek'yan, P., Bazhenov, S., Kechek'yan, A. "The Influence of Biaxial Orientation on the Mechanical Properties of Polyethylene Filled with ZnO Nanoparticles", ***Polymer Science, Series A,*** Vol. 60, No. 3, (2018), 373-380, DOI: 10.1134/S0965545X18030057.
23. Kumari, G. V., Mathavan, T., Srinivasan, R., Jothirajan, M. "The influence of physical properties on the antibacterial activity of lysine conjugated chitosan functionalized silver nanoparticles", ***Journal of Inorganic and Organometallic Polymers and***

Materials, Vol. 28, No. 6, (2018), 2418-2426, DOI: 10.1007/s10904-018-0944-2.

24. Augustine, R., Augustine, A., Kalarikkal, N., Thomas, S. "Fabrication and characterization of biosilver nanoparticles loaded calcium pectinate nano-micro dual-porous antibacterial wound dressings", ***Progress in Biomaterials,*** Vol. 5, No. 3-4, (2016), 223-235, DOI: 10.1007/s40204-016-0060-8.
25. Elechiguerra, J. L., Burt, J. L., Morones, J. R., Camacho-Bragado, A., Gao, X., Lara, H. H., Yacaman, M. J. "Interaction of silver nanoparticles with HIV-1", ***Journal of Nanobiotechnology,*** Vol. 3, No. 1, (2005), 6-16, DOI:10.1186/1477-3155-3-6.
26. Marimuthu, S., Rahuman, A. A., Rajakumar, G., Santhoshkumar, T., Kirthi, A. V., Jayaseelan, C., Bagavan, A., Zahir, A. A., Elango, G., Kamaraj, C. "Evaluation of green synthesized silver nanoparticles against parasites", ***Parasitology Research***, Vol. 108 No. 6, (2011), 1541-1549, DOI: 10.1007/s00436-010-2212-4
27. Panáček, A., Kolář, M., Večeřová, R., Prucek, R., Soukupova, J., Kryštof, V., Hamal, P., Zbořil, R., Kvítek, L. "Antifungal activity of silver nanoparticles against Candida spp", ***Biomaterials***, Vol. 30, No.31, (2009), 6333-6340, DOI: 10.1016/j.biomaterials.2009.07.065.
28. Manikandan, G., Yuvashree, M., Sangeetha, A., Bhuvana, K.P., Sanjay, K. "Liver Tissue Regeneration using Nano Silver impregnated Sodium Alginate/PVA Composite Nanofibres", ***SciMedicine Journal***, Vol. 2, No. 1, (2020), 16-21, DOI: 10.28991/SciMedJ-2020-0201-3
29. Maróti, P., Kocsis, B., Ferencz, A., Nyitrai, M., Lőrinczy, D. "Differential thermal analysis of the antibacterial effect of PLA-based materials planned for 3D printing", ***Journal of Thermal Analysis and Calorimetry***, Vol. 139, No. 1, (2020), 367-374, DOI:10.1007/s10973-019-08377-4.
30. Gan, L., Geng, A., Jin, L., Zhong, Q., Wang, L., Xu, L., Mei, C. "Antibacterial nanocomposite based on carbon nanotubes–silver nanoparticles-co-doped polylactic acid", ***Polymer Bulletin,*** Vol. 77, No. 2, (2020), 793-804, DOI: 10.1007/s00289-019-02776-1.
31. Fan, C., Cui, R., Lu, W., Chen, H., Yuan, M., Qin, Y. "Effect of high pressure treatment on properties and nano–Ag migration of PLA-based food packaging film", ***Polymer Testing,*** Vol. 76, (2019), 73-81, DOI:10.1016/j.polymertesting.2019.03.005.
32. Abdulkhani, A., Hosseinzadeh, J., Ashori, A., Dadashi, S., Takzare, Z. "Preparation and characterization of modified cellulose nanofibers reinforced polylactic acid nanocomposite", ***Polymer Testing,*** Vol. 35, (2014), 73-79, DOI: 10.1016/j.polymertesting.2014.03.002
33. Jing, M., Che, J., Xu, S., Liu, Z., Fu, Q. "The effect of surface modification of glass fiber on the performance of poly (lactic acid) composites: Graphene oxide vs. silane coupling agents", ***Applied Surface Science,*** Vol. 435, (2018), 1046-1056, DOI:10.1016/j.apsusc.2017.11.134.
34. Buzarovska, A. "PLA nanocomposites with functionalized TiO2 nanoparticles", ***Polymer-Plastics Technology and Engineering,*** Vol. 52, No. 3, (2013), 280-286, DOI: 10.1080/03602559.2012.751411.
35. Liu, C., Wong, H. M., Yeung, K. W. K., Tjong, S. C. "Novel electrospun polylactic acid nanocomposite fiber mats with hybrid graphene oxide and nanohydroxyapatite reinforcements having enhanced biocompatibility", ***Polymers,*** Vol. 8, No. 8, (2016), 287, DOI:10.3390/polym8080287.
36. Mukherjee, T., Sani, M., Kao, N., Gupta, R. K., Quazi, N., Bhattacharya, S. "Improved dispersion of cellulose microcrystals in polylactic acid (PLA) based composites applying surface acetylation", ***Chemical Engineering Science,*** Vol. 101, (2013), 655-662, DOI:10.1016/j.ces.2013.07.032.
37. Tsou, C.H., Yao, W.H., Lu, Y.C., Tsou, C.Y., Wu, C.S., Chen, J., Wang, R.Y., Su, C., Hung, W.S., De Guzman, M. "Antibacterial Property and Cytotoxicity of a Poly (lactic acid)/Nanosilver-Doped Multiwall Carbon Nanotube Nanocomposite", ***Polymers***, Vol. 9, (2017), 100-111, DOI: 10.3390/polym9030100.

Persian Abstract

چکیده

در این پژوهش نانوکامپوزیت پلیمر با زمینه پلی لاکتیک اسید و تقویت کننده‌های نانوذرات نقره و نانوالیاف سلولوز به روش ریخته‌گری حلال تهیه شد. مقدار نانوسلولوز ثابت و به میزان ۱ درصد وزنی در نظر گرفته شد و مقدار نانوذرات نقره به میزان ۱، ۳ و ۵ درصد وزنی به زمینه پلیمری اضافه شدند. مورفولوژی سطح شکست نمونه‌ها توسط FE-SEM آنالیز شده و خواص مکانیکی، حرارتی و آنتی باکتریال نمونه‌ها به ترتیب توسط آزمون کشش، آزمون کالریمتری روبشی تفاضلی و نفوذ دیسک آگار ارزیابی شدند. تصاویرFE-SEM نشان داد که نانوذرات بصورت نسبتاً همگن و یکنواخت در زمینه پلیمری پراکنده شده‌اند. اضافه کردن همزمان دو نانوذره به زمینه پلیمری باعث افزایش خواص مکانیکی از قبیل استحکام کششی و مدول کششی به مقدار به ترتیب ۴۰٪ و ۹٪ شد، اما نانو الیاف سلولوز تاثیر قابل توجهی بر خواص حرارتی پلی لاکتیک اسید نداشت. برخلاف نانوالیاف سلولوز، نانوذرات نقره پایداری حرارتی زمینه پلیمری را بهبود داده و بطور قابل توجهی خواص آنتی باکتریال پلی لاکتیک اسید را در برابر سویه‌های ای کویل و استافیلوکوس افزایش داد.

IJE TRANSACTIONS B: Applications Vol. 34, No. 02, (February 2021) 508-516

International Journal of Engineering

Journal Homepage: www.ije.ir

Optimization of Green Technique Develop for Europium (III) Extraction by using Phosphonium Ionic Liquid and Central Composite Design Approach

M. Asadollahzadeh*, R. Torkaman, M. Torab-Mostaedi

Nuclear Fuel Cycle Research School, Nuclear Science and Technology Research Institute, Tehran, Iran

PAPER INFO

Paper history:
Received 03 October 2020
Received in revised form 11 November 2020
Accepted 07 December 2020

Keywords:
Ionic Liquid
Cyphos IL 104
Central Composite Design Approach
Optimized Condition
Europium

ABSTRACT

Rare earth compounds widely used in industrial applications and new processes with green solvents are appropriate for recovering these elements. In this study, the ionic liquid application development was investigated to extract europium ions in single and binary systems. A green procedure for europium (III) extraction from aqueous chloride solution was investigated using phosphonium ionic liquid Cyphos IL 104. Comparative conditions were investigated for analyzing better results with the presence of organic extractant such as Cyanex272, D2EHPA in the batch experiments. The experiment design was carried out based on the central composite design principles to analyze the relationships between the responses and the significant parameters. The obtained data revealed that the quadratic equation has good desirability to predict the extraction percentage. Investigation of the extraction process showed that the ionic liquid Cyphos IL104 has selective power in the extraction of europium and the efficiency is higher than the organophosphorus extractants. Accordingly, optimum conditions for maximum removal of europium ions were obtained equal to 5.5, 1, 16 min, and 0.008 M for feed acidity (pH), phase ratio, time, Cyphos IL 104 concentration. Examination of binary systems of rare earth elements showed that ionic liquid had positive and negative effects on the separation factor. The high efficiency of ionic liquid in the reuse condition indicated that the system is appropriate from an economic perspective.

***doi**: 10.5829/ije.2021.34.02b.24*

1. INTRODUCTION

The demand for rare earth elements due to their increasing critical applications has been increased in recent years [1]. New rules and regulations have been reported according to these elements' application types in various industries [2, 3]. Their increasing prices led to improvements in their extraction and separation from ore in their recovery from wastes in electric and electronic equipment or other industrial materials [4]. It is associated with the introduction of new routes for production [5]. For example, lanthanum nanoparticles with optical properties synthesized during the sol-gel procedure [6]. Nowadays, paths are more favorable with less environmental impact [7], and ecological processes such as electrodialysis have expanded to reduce COD of contaminated water [8]. Solvent extraction is one of the conventional techniques in the extraction of rare earth metals. This technique is coupled with the simplicity of the system, facilitating the separation process.

Still, the high-volume of organic solvent and environmental pollutants are the disadvantages of this approach [9]. Therefore, it led to other procedures such as adsorption or liquid membranes with different types such as emulsion liquid membrane [10], supported liquid membrane, bulk liquid membrane [11], etc. Many adsorbents from simple materials in nature to complex nanocomposite materials have been described in the literature to extract these elements [1]. The supported liquid membranes with the aim of separation of rare earth elements have been reported in various studies [12]. The research work by Asadollahzadeh and co-workers [13]

*Corresponding Author Institutional Email: masadollahzadeh@aeoi.org.ir (M. Asadollahzadeh)

Please cite this article as: M. Asadollahzadeh, R. Torkaman, M. Torab-Mostaedi, Optimization of Green Technique Develop for Europium (III) Extraction by using Phosphonium Ionic Liquid and Central Composite Design Approach, International Journal of Engineering, Transactions B: Applications, Vol. 34, No. 2, (2021) 508-516

showed that the combination of ionic liquid and organophosphorus solvents with stabilization in the supported liquid membrane was an appropriate procedure in the separation of yttrium ions. But the coefficients of separation factor in the solvent extraction technique are much higher than other methods [14]. Thus, this method by modifying the input organic matter has been investigated in many studies [15-17]. In addition to the type of organic solvent, the type of equipment is also useful in solvent extraction and the increment in the mass transfer coefficients [18-21]. It has been studied in various studies with rotating and pulsed columns for rare earth separation [22-24]. Different organic solvents of anionic, cationic, and soluble extractants have been utilized to recover rare earth elements [25, 26]. Alongside these solvents, ionic liquids as environmental green solvents have been found to have particular applications in the extraction and separation procedure of rare earth elements [27]. The separation factor of gadolinium from samarium equal to 8.47 obtained in the combination of TBP, Cyanex272, [C_6MIM][PF_6] in one contact of both phases [28]. In another work, cerium ion recovery investigated from glass polishing powder waste using the synergistic effects of imidazolium ionic liquids and TOPO and TBP [29].

Europium is one of the rare earth elements that has been received particular attention in recent years. The neutron absorbers, europium phosphors on television, fluorescent powders, and lamps are applications that are reported by the use of these ions in the industry [30]. Recently, the discussion of ionic liquids for the extraction of europium ions has been received special attention [31]. The results of the investigation with undiluted ionic liquids from the thiocyanate family [C101][SCN] showed that the four extraction steps achieved with the high efficiency for the recovery of europium on the organic/aqueous phase ratio equal to 1/10 [32]. In the study of Dai et al. [33], a homogeneous extraction technique with ionic liquids [DHbet][Tf_2N] and [THbet][Tf_2N] showed that the europium ions recovered from aqueous solution with the extraction efficiency higher than 90% during the four extraction stages. The utilization of Cyphos IL 104 was evaluated for the extraction abilities in the recovering of Eu(III) in the rotating disk column with an asymmetrical structure [34]. The percentage increase for overall mass-transfer coefficients obtained using this solvent and the higher mixing rate [34].

Examination of eight imidazolium ionic liquids as a diluent, and Octyl(phenyl)-N, N-diisobutyl carbamoyl-methylphosphine oxid (CMPO) as an extractant showed that the ligand/metal ratio in the extracted complex with ionic liquids was far higher than that of the use of n-dodecane as a diluent [35]. A combination of solvation and cation-exchange mechanisms proposed to extract europium with imidazolium ionic liquids. The temperature was reported as a critical factor in the exothermic reaction to remove europium ions with these ionic liquids [35]. In similar results conducted by Tan and co-workers [36], the combination of 2,6-bis(5,6-diethyl-1,2,4-triazin-3-yl) pyridine (C2-BTP) and [Cnmim][NTf_2] imidazolium ionic liquid, the temperature rise was favorable for the europium extraction, and cation-exchange proposed as an extraction mechanism.

Rao et al. [37] investigated the examination of the behavior of the two extractants such as T2EHDGA, and CMPO diluted in the bis(trifluoromethylsulfonyl)imide ([N1444] [NTf_2]) ionic liquid. The europium ions' extraction revealed that the contribution of three and two molecules of two extractants under ion-exchange reactions led to the desired removal [37]. In the research conducted by Atanassova and Kurteva [38], similar results were reported from a chloride solution with a mixture of CMPO, HTTA, and [Cnmim][NTf_2]. The investigation of the separation factor of europium from gadolinium with ionic liquid [A336][P204] compared with the P204 extractant. The results showed that the higher separation factor under the same conditions provided by ionic liquid [39].

The species of $Eu(OHA)_4(H_2O)_4(PF_6)_3$ is the result of complex formation between the ionic liquid 1-alkyl-3-methylimidazolium hexafluorophosphate and 4-oxaheptanediamides extractant for the europium recovery during the ion exchange mechanism as the studies by Niu and co-workers [40].

Research conducted by Larsen and Benjamin [41] showed that with ionic liquids and a chelating agent (EDTA), the light rare earth elements separated from heavy elements with the higher separation factor. In this research, ionic liquid tricaprylmethylammonium nitrate [A336][NO_3] was used as an organic solvent, which was highly desirable in the extraction. With all the benefits of ionic liquids, the limitations such as the loss of cations in imidazolium ionic liquids, the low thermal stability of ammonium-based ionic liquids lead to an increase in the tendency towards phosphonium ionic liquids.

Limited studies have carried out on the separation of rare earth elements with phosphonium types of ionic liquids. Therefore, in this study, the phosphonium ionic liquid was investigated to extract europium from chloride solution. Extraction conditions were investigated by examining various factors such as temperature, pH, ionic liquid concentration, and acidity in the recovery rate. The results using of organic solvents such as D2EHPA and Cyanex272 were reported for comparison and conclusion.

The use of the central composite design approach for the separation of europium ions from chloride solution with phosphonium ionic liquid as a green solvent is the innovation of this study that has not been observed in the literature.

2. EXPERIMENTAL

2. 1. Reagents In this study, the ionic liquid trihexyl (tetradecyl) phosphonium bis(2,4,4-trimethylpentyl) phosphinate with purity of higher than 90% was supplied by Sigma-Aldrich company. The organic solvents such as Cyanex272 (Solvay, 85%>) and D2EHPA (Sigma-Aldrich) were used for the preparation of the organic phase in comparison with ionic liquid. The commercial kerosene from the Iranian petroleum oil refinery was used as a diluent. The salt of europium(III) nitrate pentahydrate from Sigma-Aldrich company was used for the preparation of the aqueous phase containing Eu(III) ions for solvent extraction procedure (ion concentration equals 250 mg/L). The sulfuric, nitric, and hydrochloric acids (Merck company) were utilized to prepare acidic solutions.

2. 2. Experimental Procedure By selecting three solvents (D2EHPA, Cyanex272, and Cyphos IL 104) to extract europium ions, the design process of the extraction experiments was performed for each solvent with the selective parameters as summarized in Table 1.

Two aqueous and organic phases were prepared for the extraction process. The aqueous phase was prepared by only europium ions as a single element or by other ions (La(III), Ce(III), Nd(III), Gd(III), Dy(III)) to investigate the behavior of different elements.

The organic phase was prepared from ionic liquid dissolution in kerosene solvent. This ionic liquid was substituted for comparing with the D2EHPA or Cyanex272 extractant. Polyethylene containers were used for two-phase contact. The amount of 10 mL of phases added to the container. The bottles were incorporated into the shaker for the mixing process.

After a specific time, the separation of two phases was performed by the decanter. The measurement of the europium ions in the aqueous phase was performed with a UV instrument (UNICO model), and arsenazo material. The concentration of ions in the aqueous phase is the criterion for the objective parameter. It is defined based on the distribution coefficient (D) as follows:

TABLE 1. Definition of independent variables and their levels in the central composite design

Independent Variables	Symbols	-α	-1	0	+1	+α
Time, min	X_1	2	6	11	16	20
Concentration of ionic liquid or extractant, M	X_2	0.001	0.003	0.006	0.008	0.01
pH of aqueous solution	X_3	1	2	3.5	5	6

$$D = \frac{[Eu(III)]_{org}}{[Eu(III)]_{aq}} \quad (1)$$

$$\%E = \frac{D}{D + \frac{V_{aq}}{V_{org}}} \times 100 \quad (2)$$

In the above equation, E, V_{aq}, and V_{org} are the extraction efficiency, the volume of the aqueous phase, and the volume of the organic phase, respectively.

3. RESULTS AND DISCUSSION

3. 1. Results from the Experimental Design Approach In this study, the experiments were carried out based on Table 1, analyzed in three-dimensional graphs, as shown in Figures.1 to 3. The results in Figure 1 described that the ionic liquid Cyphos IL 104 at low concentrations (0.001 to 0.01 M) is highly desirable for the extraction of europium ions. This feature helps extract with the maximum extraction efficiency higher than 98% with 0.01 M Cyphos IL 104 diluted in kerosene. But, D2EHPA extractant at low concentrations showed the maximum extraction efficiency higher than 60% in 0.01 M concentration, and this parameter is below 10% by using Cyanex272 in 0.01 M value.

This figure illustrated that the enhancement in ionic or extractant liquid concentration led to the rise in the extraction rate. These results are due to more solvents for the complex formation, which is associated with an increment in the transfer of europium ions to the organic phase. But, no desirable extraction is obtained with the Cyanex272 at these concentrations. Therefore, an increase in the extraction efficiency higher than 99%, it would be necessary to increase the extraction concentration of Cyanex272 higher than 0.5 M.

The time variation showed that the D2EHPA extractant behavior is faster than the ionic liquid for the complex formation. The maximum extraction efficiency reached with the final desirability equal to 2 minutes. But, the ionic liquid contributed more slowly to the formation of the complex, and it required about ten minutes to reach the maximum ion transport to the organic phase.

The variation in pH in Figures 2 and 3 showed that the extraction behavior depends on the acidity of the aqueous solution. The D2EHPA extractant from a pH value higher than two faces fewer hydrogen ions in the aqueous solution, so the extraction reaction led to the release of more hydrogen ions. This process is associated with an increase of complex formation and, consequently, greater extraction efficiency. The oxygen in the ionic liquid tends to form a reaction with more hydrogen ions than the europium ions. This effect causes the tendency for the europium ions to be negligible when

the amount of hydrogen in the aqueous solution is high. Still, with increasing pH and the decrease in the soluble acidity, the hydrogen ions' reduction tends towards the europium ions and increases the extraction efficiency.

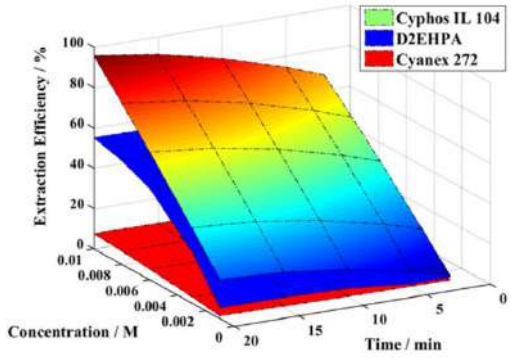

Figure 1. Response surface graphs for the extraction efficiency of Eu(III) with the effect of time, and concentration of ionic liquid or extractant (O/A ratio=1, temperature=25 ◦C, pH of aqueous phase=3.5)

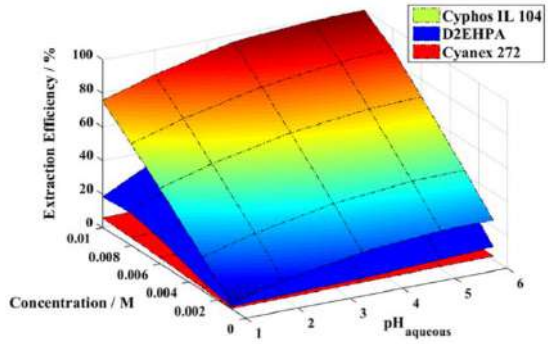

Figure 2. Response surface graphs for the extraction efficiency of Eu(III) with the effect of aqueous pH, and concentration of ionic liquid or extractant (O/A ratio=1, temperature=25 ◦C, time=20 min)

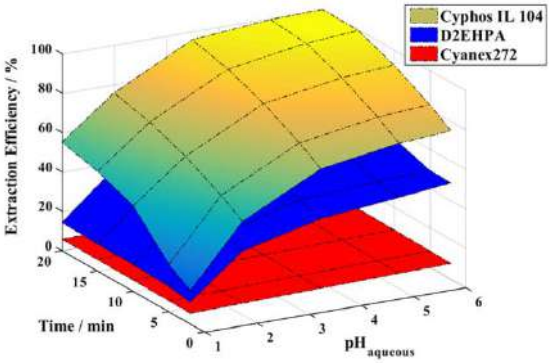

Figure 3. Response surface graphs for the extraction efficiency of Eu(III) with the effect of aqueous pH, and time (concentration of ionic liquid or extractant=0.01 M, O/A ratio=1, temperature=25 ◦C, time=20 min)

In the next step, the obtained data were evaluated using the statistical AVOVA results, as shown in Table 2. The data for F-value and p-value illustrate that the model is essential or not. This table shows that F-values equals 21.36, 14.67 for Cyphos IL 104, and D2EHPA extractant and p-value equal to 0.0001, which led the model important for the response.

The F and P values are essential for the selected model, and their significance is determined in the Design-Expert® Software for the proposed model. These values may not be meaningful in some parameters due to the interaction of the parameters. But the significance value is essential for the selected model and should be evaluated explicitly by examining other parameters (R^2 coefficient, adjusted R^2 coefficient, average absolute relative errors).

The values of R^2 for the selected model were examined by linear, quadratic, and cubic models. The high values equal to 0.9505 and 0.9260 from the quadratic model for extraction with Cyphos IL 104, and D2EHPA extractant, respectively, indicated that the model is highly accurate for predicting extraction efficiency (see Figure 4). As a result, quadratic model equations representing the extraction efficiency (Y) in the reactive condition acquired as Equations (3), and (4):

$$\text{Cyphos IL104}: \quad Y = -34.016 + 1.953X_1 + 7268.762X_2 + 10.303X_3 + 70.536X_1X_2 + 0.008X_1X_3 + 186.048X_2X_3 - 0.050X_1^2 - 74613.069X_2^2 - 0.943X_3^2 \quad (3)$$

TABLE 2. ANOVA data for europium extraction in the reactive condition with Cyphos IL 104

Source	Sum of Squares	degree freedom	F-Value	P-Value
model	7485.83	9	21.36	<0.0001
X_1	624.12	1	16.03	0.0025
X_2	6063.74	1	155.70	<0.0001
X_3	699.92	1	17.97	<0.0017
X_1X_2	8.16	1	0.21	0.6559
X_1X_3	0.036	1	9.36×10^{-4}	0.9762
X_2X_3	4.38	1	0.11	0.7443
X_1^2	29.93	1	0.77	0.4013
X_2^2	4.11	1	0.11	0.7519
X_3^2	62.62	1	1.61	0.2335
Residual	389.44	10	-	-
Lack of Fit	383.46	5	64.18	0.0002
Pure Error	5.98	5	-	-
Cor Total	7875.27	19	-	-

$$\text{D2EHPA} \quad \begin{aligned} Y = & -36.788 + 0.449X_1 + 11005.221X_2 + \\ & 12.801X_3 + 17.896X_1X_2 + 0.241X_1X_3 + \\ & 384.352X_2X_3 - 0.046X_1^2 - 684645.028X_2^2 - 1.936X_3^2 \end{aligned} \quad (4)$$

The average absolute relative errors equal to 7.83 and 11.29% with Equations (3) and (4) indicate that the selected model is very appropriate for the prediction of extraction efficiency.

As shown in Figure 4, this model is also applicable to the Cyanex272 extractant, but since the extraction rate is low, no proposed model reported for the extraction of Eu(III) ions with Cyanex272.

The maximum extraction efficiency was selected as the criterion in the experiments in the optimization condition. All independent variables were kept within range. The results were obtained by using Design-Expert® Software, as shown in Table 3. Besides, under optimal points, the experiments were conducted in the optimal points, and the results of extraction efficiency for Cyphos IL 104 and D2EHPA extractant were added in this Table. As can be observed in Table 3, the predicted values from models were compatible with the experimental data. The research results were reviewed at the optimal point with studies conducted by Mishra and Devi [42]. The results showed that the obtained data correspond to the conditions examined in reference [42]. The accuracy of the results compared with the data in the literature is also revealed in this study.

3. 2. Results from the Investigation of other Parameters

3. 2. 1. Synergistic Factor This study showed that at low concentrations, Cyanex272 is not suitable for the extraction of europium ions. The synergistic effect can help to the incremental trend for the extraction of these ions. For this purpose, the combination of the extractants and the ionic liquid was investigated in this study. The critical parameter is the synergistic factor as defined by the following equation:

$$SF = \frac{D_{mix(1,2)}}{D_1 + D_2} \quad (5)$$

The results of the study of the effect of the synergistic factor are shown in Figure 5. The results described that adding ionic liquid to the Cyanex272 extractant helps to increase the extraction rate. The SF coefficients more significant than one showed synergistic effects between the Cyanex272 and Cyphos IL 104. Also, the addition of an ionic liquid to the D2EHPA extractant showed the formation of synergistic effects. Therefore, the extraction efficiency of europium ions improves by ionic liquid at low concentrations of the extractants. Extraction with a smaller amount of organic solvent indicated that more favorable conditions would be provided with less environmental impact in the extraction of rare earth elements.

3. 2. 2. Organic/ Aqueous Phase Ratio The ratio of aqueous to organic phases is a parameter that affects the rate of ions extraction. The increase or decrease of the A/O ratio on the extraction of europium ions is shown in Figure 6. The results in this diagram described that large amounts of the organic phase over the aqueous phase increase the value of complexing agents caused by ionic liquids or extractant. This increase is an upward trend in the extraction of ions and their transfer to the organic phase.

3. 2. 3. Temperature Factor The temperature behavior of the europium extraction was investigated under optimum conditions. The results of extraction with Cyphos IL 104 showed that the increase in temperature from 298.15 K with the distribution coefficient equals 778.43 led to the increment in the extraction of europium ions with a D value equal to 1386.8 at 328.15 K. This increase indicates that the extraction process is endothermic. The examination of the logarithmic graph

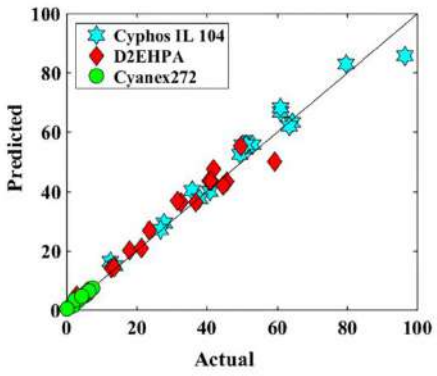

Figure 4. Diagnostic plots of the central composite design model for europium extraction (predicted value versus actual value)

TABLE 3. The optimal point for the reactive extraction of europium ions with Cyphos IL 104, and D2EHPA extractant

Organic Phase	Time/ min	Concentration of Solvent/ M	pH of aqueous solution	Predicted Extraction Efficiency (%)	Experimental Extraction Efficiency (%)	Deserability
Cyphos IL 104	16	0.008	5.5	87.95	86.23	1
D2EHPA	5	0.01	4.3	63.74	61.84	1

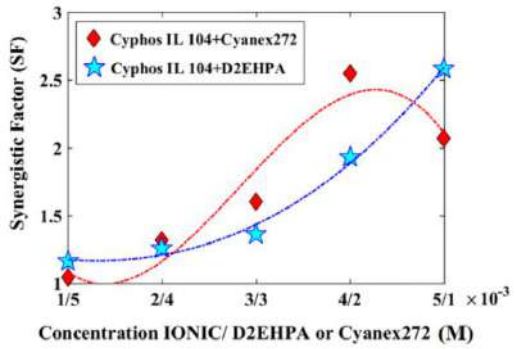

Figure 5. Synergistic effect on the extraction of Eu(III) ions by using Cyphos IL 104, Cyanex272, and D2EHPA (pH of aqueous solution=3.5, O/A ratio=1, temperature=25 ◦C, time=20 min)

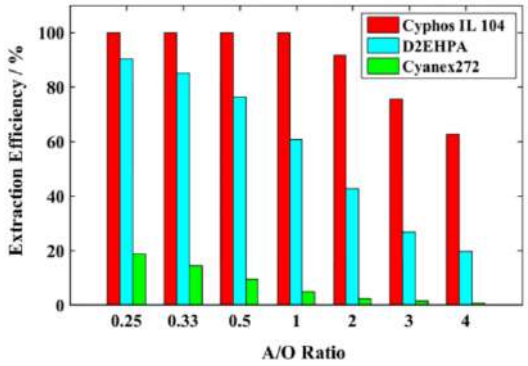

Figure 6. Effect of A/O ratio on the extraction efficiency of Eu(III) with ionic liquid Cyphos IL 104, D2EHPA, and Cyanex272 (concentration of ionic liquid or extractant=0.01 M, pH of aqueous solution=3.5, temperature=25 ◦C, time=20 min)

of the distribution coefficient in terms of temperature described that the reaction enthalpy was 15.35 KJ/mol. The variation of temperature by using D2EHPA extractant from 298.15 to 328.15 K showed the changing in D values in the range 1.51-1.55 that temperature factor has little effect on the extraction of europium that ambient temperature is more favorable for the reaction. A small enthalpy value of calculations was derived equally to 0.145 KJ/mol for Eu(III) extraction with D2EHPA extractant.

3. 2. 4. Stripping Aqueous Solution The stripping of the organic solution containing D2EHPA or Cyphos IL 104 with water is impossible due to the strong ionic bonds between the ionic liquid or D2EHPA, and Eu(III) ions. Three different acidic solutions, including sulfuric, chloride, and nitric acid, were investigated for stripping study, as shown in Table 4. The present results

TABLE 4. Effect of stripping agents on the recovery of Eu(III) ions from the organic phase

Stripping Agent	Concentration / M	Ionic	DE	CYA
H_2SO_4	0.5	61.23	58.98	40.78
H_2SO_4	1	67.45	87.43	91.44
H_2SO_4	2	70.77	98.45	99.88
HCl	0.5	50.37	65.11	70.33
HCl	1	59.87	89.67	87.77
HCl	2	66.19	83.76	80.14
HNO_3	0.5	74.56	66.33	72.45
HNO_3	1	98.91	99.56	99.12
HNO_3	2	90.23	98.45	93.45

described that the stripping percent is enhanced by the acid concentration from 0.5 to 2 molar. The nitric acid in the reaction medium dramatically affects the stripping efficiency from the organic phase containing ionic liquid, D2EHPA, or Cyanex272.

3. 2. 5. Diluent Effect The effect of diluent in the extraction of europium ions is shown in Figure 7. The extraction rate with Cyphos IL 104 is not dependent on the diluent impact. Approximately the same values for extraction efficiencies were obtained by using different diluents. In the extraction of metals with the organophosphorus extractant, a diluent with a lower dielectric constant is more appropriate. The results in Figure 7 showed that the solubility of D2EHPA in non-polar diluents is better than polar solvents. Therefore, the higher transfer for Eu(III) ions occurs in the reactive extraction with kerosene as a diluent.

3. 2. 6. Impact of other Rare-earth Ions in Aqueous Solution Binary systems containing europium ions and other rare earth elements were investigated with the organic system containing ionic liquid under optimum conditions. The results showed that the variation in separation factor ($\beta = \frac{D_1}{D_2}$), were desirable in the separation of the europium from the light elements, and the separation factor equals to 9.51, 3.98, 2.24 was obtained for binary systems of $\beta_{Eu/La}$, $\beta_{Eu/Ce}$, and $\beta_{Eu/Nd}$, respectively. But in the separation of europium from heavy rare earth elements, the ionic liquid exhibits synchronous behavior in the extraction of both elements. Therefore, a high separation factor for binary compounds $\beta_{Gd/Eu}$, and $\beta_{Dy/Eu}$ equal to 1.12, 1.34, respectively, was observed in the experimental study.

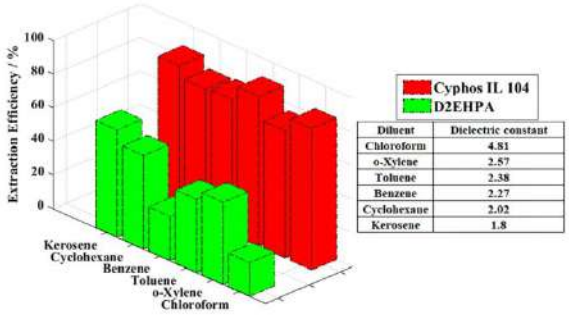

Diluent	Dielectric constant
Chloroform	4.81
o-Xylene	2.57
Toluene	2.38
Benzene	2.27
Cyclohexane	2.02
Kerosene	1.8

Figure 7. Role of diluents in the extraction of europium ions by using of Cyphos IL 104, and D2EHPA in the organic phase in the optimum condition

4. CONCLUSION

The development of a solvent extraction process is crucial for the extraction and separation of rare-earth metals, and attention has been shifted to the application of green solvents. In this research work, the phosphonium ionic liquid Cyphos IL 104 as a green solvent was investigated in the europium extraction from chloride solution by using the new predicted model. The extraction process was performed using the experimental design technique to minimize the number of experiments and identify the interaction effects of the critical parameters. The results showed that the ionic liquid had higher extraction efficiency compared to the D2EHPA and Cyanex272 extractant. But, the variation of E% with time and aqueous pH showed that the response rate of Cyphos IL 104 for attracting ions and transferring them to the organic phase is slower than applying the D2EHPA extractant.

The optimum conditions for maximum removal of europium ions were obtained equal to 5.5, 1, 16 min, and 0.008 M for feed acidity (pH), phase ratio, time, Cyphos IL 104 concentration. The values equal to 4.3, 1, 5 min, and 0.01 M for these parameters, respectively, were obtained by extraction procedure with D2EHPA extractant.

The Cyanex272 at low concentrations showed inferior performance, but its combination with ionic liquid due to the synergistic effect was identified as a desirable extraction system at low concentrations. The binary system of rare-earth ions with ionic liquid showed that this solvent is very suitable for the separation of light rare earth elements.

5. REFERENCES

1. Asadollahzadeh, M., Torkaman, R., and Torab-Mostaedi, M. "Extraction and Separation of Rare Earth Elements by Adsorption Approaches: Current Status and Future Trends", ***Separation and Purification Reviews***, Article in Press (2020) DOI: 10.1080/ 15422119. 2020.1792930.
2. Gallucci, R.H. "Risk-Reduction Credit for Very Early Warning Fire Detection at Nuclear Power Plants: From FAQ to Fiction", ***Civil Engineering Journal***, Vol. 5, No. 2, (2019), 309-319. DOI: 10.28991/cej-2019-03091246
3. Gallucci, R.H. "Risk-Deformed Regulation: What Went Wrong with NFPA 805", ***Civil Engineering Journal***, Vol. 4, No.12, (2018), 2894-2876. DOI: 10.28991/cej-03091205
4. Torkaman, R., Safdari, J., Torab-Mostaedi, M., Moosavian, M.A., Asadollahzadeh, M. "Extraction of samarium and gadolinium from aqueous nitrate solution with D2EHPA in a pulsed disc and doughnut column", ***Journal of the Taiwan Institute of Chemical Engineers***, Vol. 48, (2015), 18-25. DOI: 10.1016/ j.jtice. 2014. 10.016.
5. Balaram, V. "Rare earth elements: A review of applications, occurrence, exploration, analysis, recycling, and environmental impact", ***Geoscience Frontiers***, Vol. 10, No. 4, (2019), 1285-1303. DOI: 10.1016/j.gsf.2018.12.005
6. Theingi, M., Tun, K.T., and Aung, N.N. "Preparation, Characterization and Optical Property of LaFeO3 Nanoparticles via Sol-Gel Combustion Method", ***SciMedicine Journal***, Vol. 1, (2019), 151-157. DOI: 10.28991/SciMedJ-2019-0103-5
7. Ali, S.H. "Social and Environmental Impact of the Rare Earth Industries", ***Resources***, Vol. 3, No.1, (2014), 123-134. DOI: 10.3390/resources3010123
8. Parsa, N., Khajouei, G., Masigol, M., Hasheminejad, H., and Moheb, A. "Application of Electrodialysis Process for Reduction of Electrical Conductivity and COD of Water Contaminated By Composting Leachate", ***Civil Engineering Journal***, Vol. 4, No. 5, (2018), 1034-1045. DOI: 10.28991/cej-0309154
9. Jha, M.K., Kumari, A., Panda, R., Kumar, J.R., Yoo, K., and Lee, J.Y. "Review on hydrometallurgical recovery of rare earth metals", ***Hydrometallurgy***, Vol. 165, (2016), 2-26. DOI: 10.1016/ j.hydromet. 2016.01.035
10. Laguel, S., and Samar, M.H. "Removal of Europium(III) from water by emulsion liquid membrane using Cyanex 302 as a carrier", ***Desalination Water Treatment***, Vol. 165, (2019), 269-280. DOI:10.5004/ dwt.2019.24551
11. Belova, V.V. "Development of solvent extraction methods for recovering rare earth metals", ***Theoretical Foundation Chemical Engneering***, Vol. 51, (2017), 599-609. DOI: 10.1134/S004057951605002X
12. Asadollahzadeh, M., Torkaman, R., and Torab-Mostaedi, M. "Recovery of gadolinium ions based on supported ionic liquid membrane: parametric optimization via central composite design approach", ***International Journal of Environmental Science and Technology***, Vol. 17, (2020) 3983-3996. DOI: 10.1007/s13762-020-02743-8
13. Asadollahzadeh, M., Torkaman, R., and Torab-Mostaedi, M. "Recovery of yttrium ions from fluorescent lamp waste through supported ionic liquid membrane: process optimisation via response surface methodology", ***International Journal of Environmental Analytical Chemistry***, Article in Press, (2020), DOI: 10.1080/ 03067319. 2020.1763976.
14. Hidayah, N.N., and Abidin, S.Z. "The evolution of mineral processing in extraction of rare earth elements using liquid-liquid extraction: A review", ***Minerals Engineering***, Vol. 121, (2018), 146-157. DOI: 10.1016/j.mineng.2018.03.018
15. Tunsua, C., Lapp, J.B., Ekberg, C., and Retegan, T. "Selective separation of yttrium and europium using Cyanex 572 for applications in fluorescent lamp waste processing", ***Hydrometallurgy***, Vol. 166, (2016), 98-106. DOI: 10.1016/j.hydromet.2016.10.012.
16. Lu, X., Zhang, D., He, S., Feng, J., Reda, A.T., Liu, C., Yang, Z., Shi, L., and Li, J. "Reactive extraction of europium(III) and neodymium(III) by carboxylic acid modified calixarene derivatives: Equilibrium, thermodynamics and kineticsc",

Separation and Purification Technology, Vol. 188, (2017), 250-259. DOI: 10.1016/j.seppur.2017.07.040

17. Torkaman, R., Torab-Mostaedi, M., Asadollahzadeh, M., "Studies of Drop Behavior and Prediction of Sauter Mean Drop Diameter in Various Rotary Agitated Extraction Columns", ***International Journal of Engineering, Transactions B: Applications***, Vol. 29, No. 8, (2016) 1047-1055. DOI: 10.5829/ idosi.ije.2016.29.08b.03

[18. Asadollahzadeh, M., Shakib, B., Torab-Mostaedi, M., Outokesh, M. "Extraction of Molybdenum (VI) and Vanadium (V) from Nitrate Solutions Using Coupling of Acid and Solvating Extractants", ***International Journal of Engineering, Transactions A: Basics***, Vol. 32, No. 10 (2019) 1366-1371. DOI: 10.5829/ije.2019.32.10a.0

19. Asadollahzadeh, M., Torkaman, R., and Torab-Mostaedi, "Optimization of lanthanum extraction in asymmetric rotation pilot plant column by using central composite methodology", ***Geosystem Engineering***, Vol. 23, No. 2, (2020), 101-111. DOI: 10.1080/ 12269328. 2020. 1719905.

20. Torkaman, R., Asadollahzadeh, M., and Torab-Mostaedi, M. "Determination of slip and characteristic velocities in reactive extraction with experiments in the Oldshue-Rushton column and presence of samarium and gadolinium metals", ***Chemical Engineering and Processing***, Vol. 111, (2017) 7-13. DOI: 10.1016/j.cep.2016.10.018

21. Asadollahzadeh, M., Torkaman, R., and Torab-Mostaedi, M. "Coupling minimum cross-entropy model with experimental data to determine the drop size distribution for lanthanum extraction in ARDC column", ***Separation Science and Technology***, Article in Press, (2020), DOI:10.1080/01496395.2020.1754429.

[22. Asadollahzadeh, M., Torkaman, R., and Torab-Mostaedi, M. "Study on the feasibility of using a pilot plant Scheibel extraction column for the extraction and separation of lanthanum and cerium from aqueous solution", ***Korean Journal of Chemical Engineering***, Vol. 37 (2020) 322-331. DOI: 10.1007/s11814-019-0443-3.

23. Asadollahzadeh, M., Torkaman, R., Torab-Mostaedi, and M., Moazami, F. "Estimation of Performance with the Two Truncated Probability Density Functions, Case Study: Using Mixco Column to Extract Samarium and Gadolinium", ***Separation Science Technology***, Article in Press, (2020), DOI:10.1080/ 01496395. 2020.1757713.

24. Shakib, B., Torab-Mostaedi, M., Outokesh, M., and Asadollahzadeh, M. "Direct extraction of Mo(VI) from sulfate solution by synergistic extractants in the rotation column", ***Chinese Journal of Chemical Engineering***, Vol. 28, No. 2, (2019), 445-455. DOI: 10.1016/ j.cjche. 2019.11.011.

25. Zhang, J., Zhao, B., and Schreiner, B. "*Separation Hydrometallurgy of Rare Earth Elements*", Springer, New York (2018).

26. Pradhan, S., Swain, N., Prusty, S., Sahu, R.K., and Mishra, S. "Role of extractants and diluents in recovery of rare earths from waste materials", ***Materials Today***, Vol. 30, (2020), 239-245. DOI: 10.1016/ j.matpr. 2020.01.288

27. Wang, K., Adidharm, H., Radosz, M., Wan, P., Xu, X., Russell, C.K., Tian, H., Fan, M., and Yu, J. "Recovery of rare earth elements with ionic liquids", ***Green Chemistry***, Vol. 19, (2017), 4469-4493. DOI: 10.1039/C7GC02141K

28. Asadollahzadeh, M., Torkaman, R., Torab-Mostaedi, M., Hemmati, A., and Ghaemi, A. "High performance separation of gadolinium from samarium with the imidazolium ionic liquid through selective complexation of organophosphorus extractants", ***Environmental Technology & Innovation***, Vol. 19, (2020), 100979. DOI: 10.1016/j.eti.2020.100979.

29. Asadollahzadeh, M., Torkaman, R., Torab-Mostaedi, M., and Hemmati, A. "Enhancing Cerium Recovery from Leaching Solution of Glass Polishing Powder Waste Using Imidazolium Ionic Liquid", ***Waste and Biomass Valorization***, Article in Press, (2020). DOI:10.1007/s12649-020-01070-w.

30. Abhilash; Akcil, A. "*Critical and Rare Earth Elements: Recovery from Secondary Resources*", CRC Press, New York, (2019).

31. Chen, J. "*Application of Ionic Liquids on Rare Earth Green Separation and Utilization*", Springer, New York, (2016).

32. Banda, R., Forte, F., Onghena, B., and Binnemans, K. "Yttrium and europium separation by solvent extraction with undiluted thiocyanate ionic liquids", ***RSC Advances***, Vol. 9, (2019), 4876-4883. DOI: 10.1039/C8RA09797F

33. Dai, Y., Cao, B., Zhong, S., Xie, G., Wang, Y., Liu, Y., Zhang, Z., Liu, Y., and Cao, X. "Homogeneous liquid–liquid extraction of europium from aqueous solution with ionic liquids", ***Journal of Radioanalytical Nuclear Chemistry***, Vol. 319, No. 3, (2019), 1219-1225. DOI: 10.1007/s10967-019-06419-7

34. Asadollahzadeh, M., Torkaman, R., and Torab-Mostaedi, M. "Continuous Extraction of Europium(III) by Ionic Liquid in the Rotating Disk Column with an Asymmetrical Structure Aimed at the Evaluation of Reactive Mass Transfer", ***ACS Omega***, Vol.5, No.30, (2020), 18700-18709. DOI: 10.1021/acsomega.0c01636

35. Sun, T., Zhang, Y., Wu, Q., Chen, J., Xia, L., and Icon, C.X.O. (2017) "Comparative study on the extraction of trivalent americium and europium by CMPO in imidazolium-based ionic liquids and dodecane", ***Solvent Extraction Ion Exchange***, Vol. 35, No. 6, (2017), 408-422. DOI: 10.1080/ 07366299. 2017.1379142

36. Tan, C., Zhang, X., Cao, S., Li, S., Guo, H., Tian, Y., Chena, D., Tian, W., Wang, L., and Qin, Z. "Solvent extraction of americium(III) and europium(III) with 2,6-bis(5,6-diethyl-1,2,4-triazin-3-yl) pyridine in ionic liquids: Experimental study and molecular dynamics simulation", ***Separation Purification and Technology***, Vol. 192, (2018), 302-308. DOI: 10.1016/j.seppur.2017.09.033

37. Rao, C.V., Rout, A., and Venkatesan, K.A. "Europium(III) complexation behaviour in an alkyl ammonium ionic liquid medium containing neutral extractants", ***Separation Purification and Technology***, Vol. 213, (2019), 545-552. DOI: 10.1016/ j.seppur. 2018.12.076

38. Atanassova, M., and Kurteva, V. "Synergism in the Solvent Extraction of Europium(III) with Thenoyltrifluoroacetone and CMPO in Methylimidazolium Ionic Liquids", ***Journal of Solution Chemistry***, Vol. 48, No. 1, (2019), 15-30. DOI: 10.1007/s10953-019-00844-8

39. Ismail, N.A., Yunus, M.Y.M., Aziz, M.A.A., Abidin, M.A., "Comparison of optimal solvent extraction stages between P204 and [A336][P204] for the separation of europium and gadolinium", *IOP Conference Series: Materials Science and Engineering*, Kuantan, Pahang, Malaysia, 2019.

40. Niu, Y.N., Ren, P., Zhang, F., Yan, Z.Y. "Solvent extraction of Eu3+ with 4-oxaheptanediamide into ionic liquid system", ***Separation Science and Technology***, Vol. 53, No. 17, (2018), 2750-2755. DOI: 10.1080/ 01496395. 2018.1471507

41. Larsson, K., Binnemans, K. "Separation of Rare Earths by Solvent Extraction with an Undiluted Nitrate Ionic Liquid", ***Journal of Sustainable Metallurgy***, Vol. 3, (2016), 73-78. DOI: 10.1007/s10953-019-00844-8

42. Mishra, B.B., and Devi, N. "Solvent extraction and separation of europium (III) using a phosphonium ionic liquid and an organophosphorus extractant-A comparative study", ***Journal of Molecular Liquids***, Vol. 271, (2018), 389-396. DOI: 10.1016/ j.molliq. 2018.08.160

Persian Abstract

چکیده

ترکیبات عناصر نادر خاکی به طور گسترده در کاربردهای صنعتی استفاده می‌شوند و فرآیندهای جدید با حلال‌های سبز برای بازیابی این عنصر مطلوب می‌باشند. در این مطالعه، توسعه کاربرد مایعات یونی برای استخراج یون‌های یوروپیوم از سیستم‌های تک جزئی و دوتایی مورد تحقیق قرار گرفت. فرآیند سبز برای استخراج یوروپیوم (III) از محلول کلرید آبی با مایع یونی فسفونیوم Cyphos IL 104 بررسی شد. شرایط مقایسه‌ای برای آنالیز بهتر نتایج با حضور Cyanex272 و D2EHPA در آزمایش‌های ناپیوسته بررسی شد. طراحی آزمایش‌ها بر مبنای مفاهیم طراحی مرکب مرکزی با بررسی پارامتر بین پاسخ‌ها و پارامترهای موثر انجام شد. نتایج بدست آمده از فرآیند استخراج نشان می‌دهد که معادله درجه دوم از مطلوبیت خوبی در پیش بینی درصد استخراج برخوردار است. تحقیقات فرآیند استخراج با مایع یونی Cyphos IL 104 از قدرت انتخابی بالایی در استخراج یوروپیوم برخوردار است و درصد استخراج بسیار بالاتر با حضور استخراج‌کننده‌های اورگانوفسفر است. شرایط بهینه برای ماکزیمم استخراج یوروپیوم برابر با ۵/۵، ۱ min، ۱۶ و ۰/۰۰۸ M برای اسیدیته خوراک (pH)، نسبت فازی، زمان، غلظت Cyphos IL 104 بدست آمد. ارزیابی سیستم‌های دوتایی عناصر نادر خاکی نشان داد که مایع یونی اثرات مثبت و منفی روی فاکتور جداسازی دارد. بازده بالای مایعات یونی در شرایط استفاده مجدد نشان می‌دهد که سیستم از نقطه نظر اقتصادی مناسب است.

IJE TRANSACTIONS B: Applications Vol. 34, No. 02, (February 2021) 517-527

International Journal of Engineering

Journal Homepage: www.ije.ir

Analytical Approach of Fe_3O_4-Ethylene Glycol Radiative Magnetohydrodynamic Nanofluid on Entropy Generation in a Shrinking Wall with Porous Medium

U. Humphries[a], M. Govindaraju[b], P. Kaewmesri[a], P. Hammachukiattikul[c], B. Unyong[c], G. Rajchakit*[d], R. Vadivel[c], N. Gunasekaran[e]

[a] *Department of Mathematics, Faculty of Science, King Mongkut's University of Technology Thonburi (KMUTT), ThungKhru, Thailand*
[b] *Department of Mathematics, Padmavani Arts and Science College for Women, Salem, Periyar University, Tamil Nadu, India*
[c] *Department of Mathematics, Faculty of Science and Technology, Phuket Rajabhat University, Phuket, Thailand*
[d] *Department of Mathematics, Faculty of Science, Maejo University, Chiang Mai, Thailand*
[e] *Department of Mathematical Sciences, Shibaura Institute of Technology, Saitama, Japan*

P A P E R I N F O

Paper history:
Received 29 September 2020
Received in revised form 04 November 2020
Accepted 10 November 2020

Keywords:
Entropy
Fe_3O_4-Ethylene Glycol Nanofluid
Heat Absorption
Heat Generation
Shrinking Wall

A B S T R A C T

This research mainly focuses on the effects of heat absorption/generation and radiation on the hydromagnetic flow of Fe_3O_4-ethylene glycol nanofluid through a shrinking wall with porous medium and the computation of the entropy generation. We considered basic governing ordinary differential equations into partial differential equations by using appropriate similarity solutions. Moreover, hyper geometric function is employing to determine the formulated problem. We analyze the effects of appropriate physical parameters on the Bejan number, Entropy generation, Nussult number, skin friction, fluid temperature and velocity profiles. In addition, the derived result of the present study is compared with those in the existing literature. We noted that the presence of heat absorption and suction parameters reduces the Bejan number and increases the entropy generation, and the heat source, porous medium, radiation parameters minimize the entropy production. The presence of porosity parameter reduced the fluid velocity, improved fluid temperature and minimized the entopy production. Nanosolid volume fraction parameter reduced both Nussult number and skin friction coefficient.

***doi**: 10.5829/ije.2021.34.02b.25*

NOMENCLATURE

.	magnetic field strength	T_w	wall temperature
Br	Brinkman number	T_∞	temperature far away from the sheet
C_p	specific heat at constant temperature	k_{nf}	thermal conductivity of the nanofluid
M_3	Hartmann number	k_f	thermal conductivity of the base fluid
M	Kummer's function	k_s	thermal conductivity of the nanoparticles
Nr	radiation parameter	k^*	The absorption coefficient of the fluid
Ns	entropy generation number	σ	electric conductivity
Pr	Prandtl number	σ^*	Stephan-Boltzman constant
T	local temperature of the fluid	S_{G0}	characteristic entropy generation rate
Q	Temperature dependent volumetric rate of heat source	ΔT	temperature difference
Qr	radiative heat flux	Ω	dimensionless temperature difference
Re_x	Reynolds number	θ	dimensionless temperature
S	Suction parameter	ϕ	the solid volume fraction
S_G	local volumetric Entropy generation rate	β	uniform heat generation/absorption

*Corresponding Author Institutional Email: *kreangkri@mju.ac.th* (G. Rajchakit)

Please cite this article as: U. Humphries, M. Govindaraju, P. Kaewmesri, P. Hammachukiattikul, B. Unyong, G. Rajchakit, R. Vadivel, N. Gunasekaran, Analytical Approach of Fe_3O_4-Ethylene Glycol Radiative Magnetohydrodynamic Nanofluid on Entropy Generation in a Shrinking Wall with Porous Medium, International Journal of Engineering, B: Applications Vol. 34, No. 02, (2021) 517-527

1. INTRODUCTION

There are several systematic challenges pertaining to efficient heat transfer of heat in different processes, example, in batteries, drug formulation, chemical reactions, fuel cells, solar cells, and others. This phenomenon has been studied through the field of nanotechnology. The most important performance of nanotechnology is nanofluids. Many scientific and technological fields utilize nanofluid models. Choi [1] introduced the notion of increase in the thermal conductivity of nanofluid. Ibrahim et al. [2] analyzed the nanofluid heat transfer effects with hydromagnetic and stagnation point flow numerically. Various types of nanoparticle, including Cu, Ag, Al_2O_3 and TiO_2, used in the base fluid towards a porous stretching surface has been examined by Hayat et al. [3]. Al_2O_3-water with hydromagnetic flow towards a vertical microtubefor enhancement of the heat transfer rate has been researched by Malvandi and Ganji [4]. The effects of flow towards a shrinking sheet using nanofluid with slip conditions have been developed by Rahman et al. [5]. The phenomenon of flow through a shrinking porous sheet, along with analytical result of Fe_3O_4-water hydrodynamic nanofluid flow was researched by shaha et al. [6].

Over the most recent few decades, incredible interest has been shown by scientists on the subject of stretching surfaces with magnetic field because of its colossal applications in various mechanical and engineering procedures. Some of these fascinating and amazing applications are glass plastic expulsion, fiber drawing, crystal developing, petroleum industries, paper creation, plasma studies, etc. Heat transfer effects in CuO–water nanofluid flow with magnetic field were analyzed by Sheikholeslami et al. [7]. Jamaludin et al. [8] researched the effects of shrinking surface flow of heat generation or absorption and hydromagnetic Cu and Al_2O_3 based hybrid nanofluid flow numerically. Heat conduction effects on shrinking porous surface with Cu and Ag - $C_6H_9NaO_7$ Corrosion based nanofluids flow has been studied by Dero et al. [9]. It is clear that copper and silverbased volume fraction nanoparticle improves the thermal conduction and reduces the fluid velocity. Heat conduction effects of shrinking porous surface with thermal radiation and copper based nanofluid flow were studied by Haq et al. [10]. Heat conduction of various types of nanofluid flow towards shrinking surface was reported in literature [11-14].

On the other hand, entropy represents an irreversibility process and it is utilized to enhance the capacity of machine. The entropy models can be related to manufacturing and engineering processes pertaining to nanofluids. This has been an active research area recently. Hayat et al. [15] investigated thermal irreversibility analysis for energy activation and non-linear thermal radiation of Jeffrey nanofluid flow towards stretchable sheet. Hosseinzadeh et al. [16] studied thermal irreversibility analysis for Fe_3O_4-Ethylene glycol nanofluid with nonlinear thermal radiation and Lorentz force effects. Shahsavar at al. [17] presented an analysis of heat and irreversibility study of Fe_3O_4nanofluid flow through a concentric annulus. Mehrali at al. [18] researched the impacts of Fe_3O_4 nanofluid flow and conducted an analysis of entropy on magnetic. Very recently, López et al. [19] investigated the effects of Al_2O_3nanofluid flow and analyzed the entropy on hydromagnetic, nonlinear radiation and slip conditions. Shukla et al. [20] have studied a homotopy method for irreversibility analysis of vertical cylinder flow of viscous dissipation and magnetohydrodynamic (MHD) nanofluid flow. Hayat et al. [21], investigated on MHD nonlinear thermal radiation and joule heating effects with respect to nanofluid flow with entropy analysis has been conducted. Rana and Shukla [22] provided an analytical solution for an irreversibility study of aligned MHD nanofluid flow towards a plate with Ohmic dissipation and viscous dissipation effects.

The study of boundary layer MHD nanofluid flow and heat transfer due shrinking wall with porous medium is very significant because of its several applications in engineering and industrial processes, such as extrusion of polymer sheets from a die, drawing of plastic films, polyester thin wall heat shrink tubing, shrink film, wire drawing, glass fiber, and paper production. Govindaraju et al. [23] researched the irreversibility mechanism of Ag-water MHD nanofluid fluid flow with heat source or sink and radiation effects. Abdul Hakeem et al. [24] presented the non-uniform heat source or sink and radiation effects on Ag-water MHD nanofluid flow, along with the analysis of entropy. Ganga et al. [25] researched the effects of the irreversibility and Ag-water inclined MHD nanofluid flow towards a stretching sheet. Recently, the irreversibility phenomenon of various types of nanofluid flow was investigated by many researchers [26-32]. Some researchers reported data by demonstration of experimental work [33-38]. To the best of author's knowledge, upto now, no theoretical results are given for the effects of heat transfer and irreversibility of hydromagnetic Fe_3O_4-ethylene glycol nanofluid flow in a shrinking wall with porous medium, heat sink or source and thermal radiation. This is the main motivation of our present study.

Motivated by the above discussions, we designed analytically the heat sink or source, MHD and thermal radiation effects on Fe_3O_4-ethylene glycol nanofluid flow in a shrinking wall with porous medium. The fluid velocity, heat transfer process, Bejan number and the irreversibility phenomenon, skin friction co-efficient and temperature transfer rate are examined with the graphs, in which our solutions are in good agreement with earlier published results.

The contents of this paper are divided up as follows:

The description of physical model is clearly prescribed in section 2. In this section, the mathematical model for the 2-Dimentional incompressible flow of Fe_3O_4-ethylene glycol based nanofluid has been presented. Section 3 is devoted to the solution of these models equations by hyper geometric function method. The Entropy generation and Bejan number has been computed in section 4. The results and discussion has been presented in section 5. Finally, the main findings of the current study have been given in section 6.

2. MATHEMATICAL ANALYSIS

In this investigation, consider the incompressible 2-dimentional flow of Fe_3O_4-Ethylene glycol based nanofluid towards a shrinking wall with porous medium. The fluid flow is along the *x*-axis (horizontal) and the *y*-axis is the vertical dimension, then *y>0* is the occupied volume of the fluid. Suppose normal to the flow of an applied magnetic field is *B(x)* with velocity *u=ax* (Figure 1). The two-dimensional thermal radiation with magnetohydrodynamic flow of governing equations are given, as follows [26, 39-41] (Figure 2):

$$\frac{\partial u}{\partial x}+\frac{\partial v}{\partial y}=0 \tag{1}$$

$$u\frac{\partial u}{\partial x}+v\frac{\partial u}{\partial y}=\frac{\mu_{nf}}{\rho_{nf}}\frac{\partial^2 u}{\partial y^2}-\frac{\upsilon_{nf}}{K_p}u-\frac{\sigma_{nf}B(x)^2}{\rho_{nf}}u \tag{2}$$

$$u\frac{\partial T}{\partial x}+v\frac{\partial T}{\partial y}=\alpha_{nf}\frac{\partial^2 T}{\partial y^2}-\frac{1}{(\rho C_p)_{nf}}\frac{\partial q_r}{\partial y}+\frac{Q(T-T_\infty)}{(\rho C_p)_{nf}} \tag{3}$$

Here *u* and *v* denote the velocity components along the *x*-axis and the *y*-axis, respectively; *B(x)* represents the magnetic parameter; υ_{nf}, μ_{nf}, ρ_{nf}, α_{nf} denote the kinematic viscosity, dynamic viscosity, density, thermal diffusivity, respectively. The subscript *nf* indicates the nanofluid; *T* denoted as fluid temperature, while *Q* represents the volumetric heat sink or source rate.The heat flux q_r [26, 41] through the Rosseland approximation is defined as:

$$q_r=-\frac{\sigma^*}{3k^*}\frac{\partial T^4}{\partial y}. \tag{4}$$

Here k* is the absorption coefficient of the fluid, from Equations (3) and (4), we have

$$u\frac{\partial T}{\partial x}+v\frac{\partial T}{\partial y}=\alpha_{nf}\frac{\partial^2 T}{\partial y^2}-\frac{16\sigma^* T_\infty^3}{3k^*(\rho C_p)_{nf}}\frac{\partial^2 T}{\partial y^2}+\frac{Q(T-T_\infty)}{(\rho C_p)_{nf}} \tag{5}$$

The heat conductivity can be expressed as follows:

$$\mu_{nf}=\frac{\mu_f}{(1-\varphi)^{2.5}},\qquad \rho_{nf}=(1-\varphi)\rho_f+\varphi\rho_s$$
$$(\rho C_p)_{nf}=(1-\varphi)(\rho C_p)_f+\varphi(\rho C_p)_s,$$
$$k_{nf}=\frac{k_s+2k_f-2\varphi(k_f-k_s)}{k_s+2k_f-\varphi(k_f-k_s)},\qquad \alpha_{nf}=\frac{k_{nf}}{(\rho C_p)_{nf}}, \tag{6}$$
$$\frac{\sigma_{nf}}{\sigma_f}=1+\frac{3\left(\frac{\sigma_{nf}}{\sigma_f}-1\right)\phi}{\left(\frac{\sigma_{nf}}{\sigma_f}+2\right)-\left(\frac{\sigma_{nf}}{\sigma_f}-1\right)\phi}$$

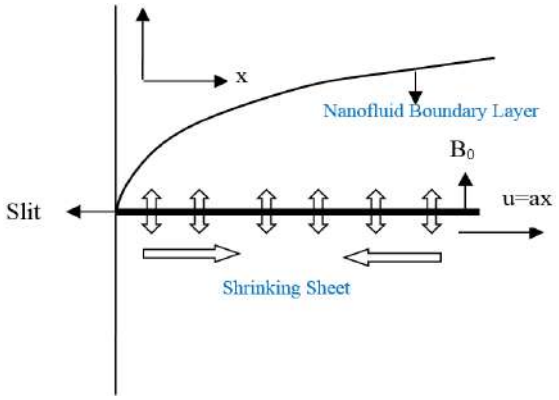

Figure 1. Schematic representation of the flow diagram

where the physical problem of the surface conditions is

$$u=-U_x, v=-v_x, T=T_w=T_\infty+T_0(x)^n, \text{at } y=0,$$
$$u\to u=0,\qquad T\to T_\infty, \text{as } y\to\infty. \tag{7}$$

Here, v_x noted as wall mass transfer velocity; in which $v_x<0$and $v_x>0$ are the injection and suction parameters. The non-dimensional and similarity variables are [26, 42, 43].

$$u=axf'(\eta), v=-(\nu a)^{\frac{1}{2}}f(\eta), \theta(\eta)=\frac{T-T_\infty}{T_w-T_\infty}$$
$$\eta=y\left(\frac{a}{\nu}\right)^{1/2} \tag{8}$$

After applying the similarity transformation of Equations (2) and (3), we have

$$f'''+B_1B_2ff''-B_1B_2f'^2-B_2(M_3-B_1k)f'=0 \tag{9}$$

$$\omega\theta''+Pr\,f\,\theta'-nPrf'\theta+\beta\,Pr\,\theta=0. \tag{10}$$

With

$$f(\eta)=S, f'(\eta)=-1, \theta(\eta)=1 \text{ at } \eta=0\ \ f'(0)\to 0, \theta(\eta)\to 0 \text{ as } \eta\to\infty \tag{11}$$

Based on Equations (9), (10) and (11), Prandtl number $Pr=\frac{\upsilon_f}{\alpha_f}$, porosity parameter $k=\frac{\upsilon_f}{aK_p}$, $\beta=\frac{Q}{a(\rho C_p)_f}$ noted heat sink or source parameter, $M_3=\frac{2L\sigma B_0^2}{\rho}$ noted as Hartmann number. In addition,

$B_1=\left(1-\varphi\left(1-\frac{\rho_s}{\rho_f}\right)\right)$, $B_2=(1-\varphi)^{5/2}$, $B_3=\frac{k_{nf}}{k_f}$,
$B_4=1-\varphi+\varphi\frac{(\rho Cp)_s}{(\rho Cp)_f}$, $\omega=\frac{B_3}{B_4}\frac{3NrB_3+4}{3NrB_3}$, $Nr=\frac{k^*k_f}{4\sigma^*T_\infty^3}$.

3. ANALYTICAL SOLUTION OF FLOW FIELD AND THERMAL ANALYSIS

The shrinking sheet fluid flow solution of (9) with (11) is obtained as follows [26, 41]:

$$f(\eta) = S - \frac{1-e^{-\alpha\eta}}{\alpha}, \quad \text{with } \alpha = \frac{SB_1B_2+\sqrt{(SB_1B_2)^2-4B_1B_2+4B_2M_3-4kB_1B_2}}{2} \tag{12}$$

Substituting Equation (12) into Equation (10), we have

$$\omega\theta'' + Pr\left(S - \left(\frac{1-e^{-\alpha\eta}}{\alpha}\right)\right)\theta' - nPre^{-\alpha\eta}\theta + \beta\, Pr\,\theta = 0. \tag{13}$$

Here, we introduce a new variable

$$\xi = \frac{Pre^{-\alpha\eta}}{\omega\alpha^2} \tag{14}$$

Substituting Equation (14) into Equation (13) , we have

$$\xi\theta_{\xi\xi} + (1 - a_0 + \xi)\theta_\xi + \left(n + \frac{\beta Pr}{\omega\alpha^2\xi}\right)\theta = 0. \tag{15}$$

From Equation (11), it becomes

$$\theta(\xi) = 1, \theta(0) = 0\,. \tag{16}$$

Using Kummer's function [26,43], we obtain the solution of Equations (14), (15), and (16), in terms of η

$$\theta(\eta) = e^{-\alpha\left(\frac{a_0+b_0}{2}\right)\eta}\frac{M\left[\frac{a_0+b_0}{2}-n;1+b_0;\frac{\Pr e^{-\alpha\eta}}{\omega\alpha^2}\right]}{M\left[\frac{a_0+b_0}{2}-n;1+b_0;\frac{\Pr}{\omega\alpha^2}\right]} \tag{17}$$

where $a_0 = \frac{Pr}{\omega\alpha}\left(S - \frac{1}{\alpha}\right)$, $b_0 = \sqrt{{a_0}^2 - 4\frac{\beta Pr}{\omega\alpha^2}}$.

The dimensionless wall temperature gradient is

$$\theta'(0) = -\alpha\left(\frac{a_0+b_0}{2}\right) + \alpha\frac{\frac{a_0+b_0}{2}-n}{1+b_0}\frac{M\left[\frac{a_0+b_0+2}{2}-n;\ 2+b_0;\ \frac{Pr}{\omega\alpha^2}\right]}{M\left[\frac{a_0+b_0}{2}-n;\ 1+b_0;\ \frac{Pr}{\omega\alpha^2}\right]}. \tag{18}$$

We denote the skin friction and Nusselt number as

$$C_f = \frac{\tau_w}{\rho u_w^2} = \frac{\mathrm{Re}_x^{-1/2}}{B_1} f''(0), B_1C_f\,\mathrm{Re}_x^{-1/2} = -f''(0)$$

$$Nu = \frac{-k_{nf}x\left(\frac{\partial T}{\partial y}\right)_{y=0}}{k_f\left(T_w - T_\infty\right)} = -\frac{k_{nf}}{k_f}\mathrm{Re}_x^{1/2}\,\theta'(0), \tag{19}$$

$$\frac{k_f}{k_{nf}}Nu_xRe_x^{-\frac{1}{2}} = -\theta'(0)$$

4. ANALYSIS OF ENTROPY AND BEJAN NUMBER

Now, using the second law of thermodynamics, the analysis of entropy generation expression of magnetohydrodynamic nanofluid flow with thermal radiation is given by

$$S_G = \frac{k_{nf}}{T_\infty^2}\left[\left(\frac{\partial T}{\partial x}\right)^2 + \left(1+\frac{16\sigma^*T_\infty^3}{3k_{nf}^*k_{nf}}\right)\left(\frac{\partial T}{\partial y}\right)\right] + \frac{\mu_{nf}}{T_\infty}\left(\frac{\partial u}{\partial y}\right)^2 + \frac{\sigma B_0^2}{T_\infty}u^2 + \frac{\nu_{nf}}{k_{nf}}u^2 \tag{20}$$

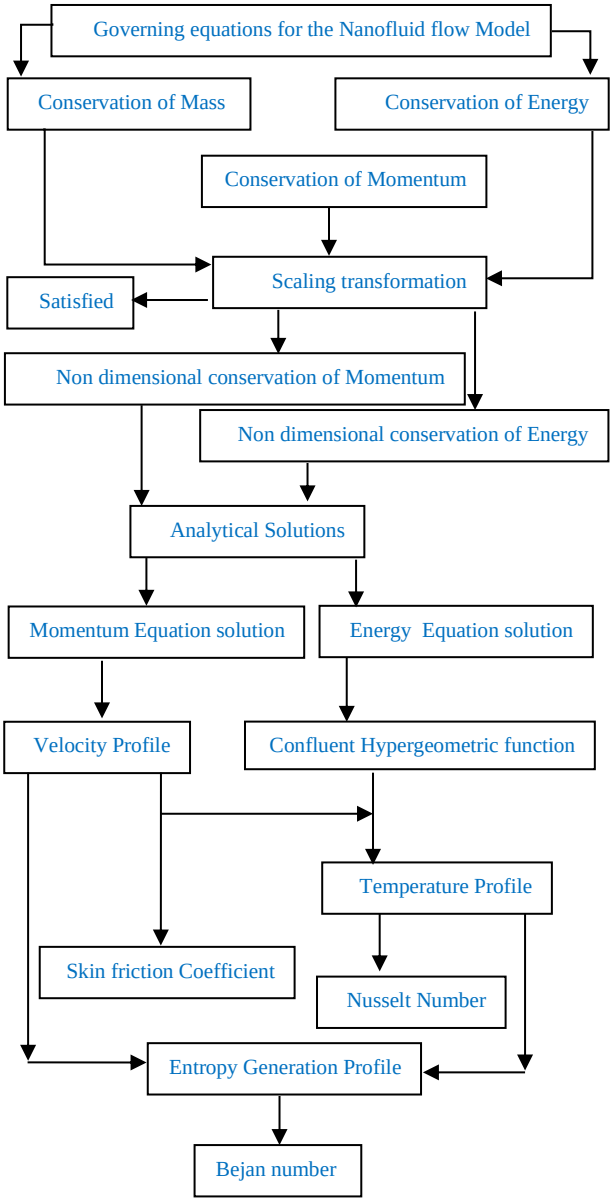

Figure 2. Flowchart of the study

The rate of entropy generation characteristic is given by

$$(S_G)_0 = \frac{k_{nf}(\Delta T)^2}{x^2T_\infty^2}. \tag{21}$$

Using Equations (20) and (21), we obtain the entropy generation number

$$N_s = \frac{S_G}{(S_G)_0}. \tag{22}$$

From Equations (17), (20), (21) and (22), we can specify the entropy generation number as

$$N_s = \left(\frac{3+4Nr}{3}\right)\theta'^2(\eta)\mathrm{Re}_x + \frac{\mathrm{Br}}{\Omega}f''^2(\eta)\mathrm{Re}_x + \frac{\mathrm{Br}}{\Omega}(M_3 + k)f'^2(\eta), \tag{23}$$

where *Br* is the Brinkman number and Hartmann number denoted as M_3.

$$Br = \frac{\mu_{nf} u_w^2}{k_{nf}\Delta T}, \quad \Omega = \frac{\Delta T}{T_\infty}, \tag{24}$$

The Bejan number (Be) was proposed by Bejan with respect to the energy optimization problem utilized by the solution of thermal irreversibility. Thermal irreversibility pertaining to the sum of all entropy in the model is given as:

$$Be = \frac{Eh}{Eh+Em} \tag{25}$$

5. RESULTS AND DISCUSSION

In this study, the analytical solutions are established for Fe_3O_4-ethylene glycol nanofluid through a shrinking wall with porous medium and the computation of entropy generation is analyzed. Figures 3 to 21 depict the effects of various important physical parameters, including the Bejan number, velocity of the fluid, Nusselt number, heat profile, entropy generation and skin friction co-efficient. The important physical parameters, nanosolid volume fraction (ϕ), heat sink or source (β), porosity parameter (*k*), radiation parameter (Nr), Hartmann number (M_3), suction parameter (S) effects are analyzed based on the trends in the respective figures. The current results have been discussed to the solutions achieved by Muhaimin et al. [39] and Bhattacharyya [40] (see Table 2). The presented results showed a good agreement with data reported in literature [39, 40].

5. 1. Fluid Flow and Heat Transfer The profiles of fluid velocity along with various settings of the nanosolid volume fraction, suction and porosity parameters are presented in Figures 3-5, respectively. From these figures, increasing the porosity and nanosolid volume fraction parameters result in a reduction of the fluid flow, while increasing the suction parameters causes enhancing the fluid flow. The presence of both porosity and nanosolid volume fraction slows down the fluid velocity. The impact of ϕ variation on $f'(\eta)$ is presented in Figure 3, while the variation of porosity parameter on$f'(\eta)$ is represented in Figure 4. Figure 5 demonstrates the evolution of suction parameter on $f'(\eta)$. It is noted that the enhancing of ϕ and k reducesf′(η), while increasing S leads to a reduction in $f'(\eta)$.

The thermal profile for various settings of the nanosolid volume fraction, porosity, suction, radiation, heat sink or source parameters are presented in Figures 6-10, respectively. Increasing the value of Fe_3O_4

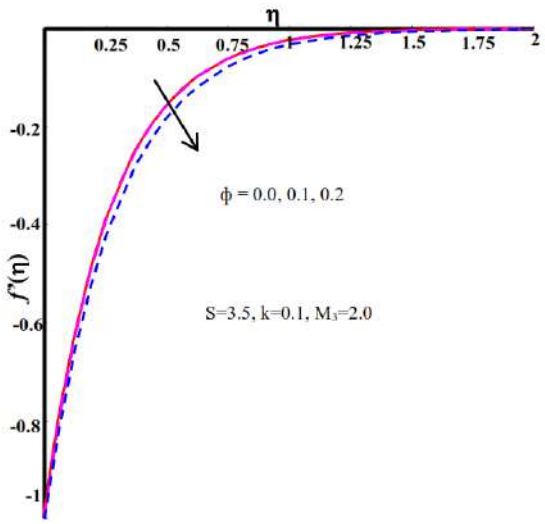

Figure 3. Impact of nanoparticles volume fraction parameter on f'(η)

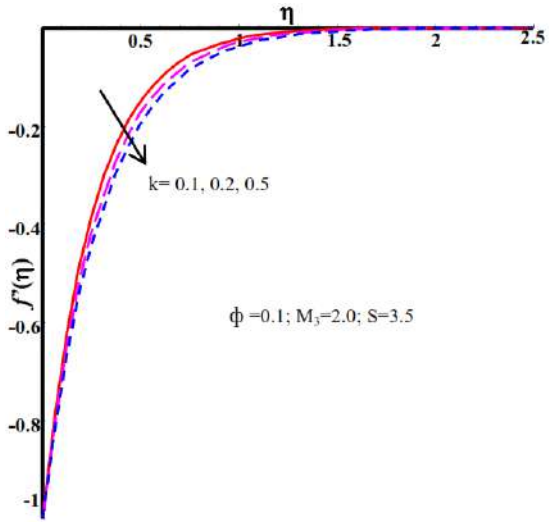

Figure 4. Impact of porosity parameter on f'(η)

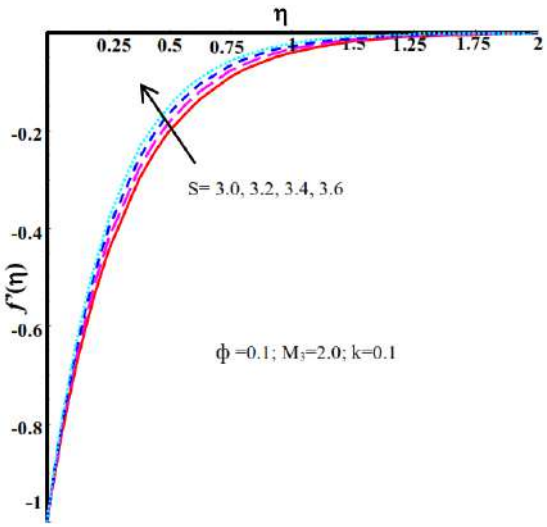

Figure 5. Impact of suction parameter on f'(η)

nanoparticle leads to a development of heat conduction in Ethylene glycol based nanofluid. The porosity parameter also increases heat conduction in Ethylene glycol based nanofluid. But, the presence of radiation and suction parameters reduces heat conduction in Ethylene glycol based nanofluid. The effect of ϕ on θ(η)is exhibited in Figure 6, while that of the porosity parameter on θ(η) is shown in Figure 7. Both parameters enhance the thermal transfer in nanofluid flow, but the opposite result is given by the radiation and suction parameters, as shown in Figures 8 and 9, respectively. Further, the presence of Fe_3O_4 nanoparticle enhances with the temperature profile. This is because Fe_3O_4 particles have high thermal conductivity, so the thermal boundary layerthickness increases. The porosity parameter also develops the thermal boundary layer thickness. However, the presence of thermal radiation and suction parameters are reduces the thermal boundary layer thickness.

The impacts of the heat sink or source parameter with respect to the heat profile are presented in Figure 10. It generates energy in the boundary layer, which is caused by the heat source (β>0) on the heat profile. Energy is absorbed in the boundary layer, which arises from the heat sink (β<0) on the heat profile.

5. 2. Nusselt Number and Skin Friction Figure 11 represent the effect of skin friction coefficient $-f''(0)$ for various values of Hartmann number and nanosolid volume fraction parameters against suction parameter. The skin friction coefficient $-f''(0)$ diminish for higher values ofϕ while the overturn trend is checked for large value of Hartmann number. Against Hartmann number, the different values of radiation, suction, nanosolid volume fraction parameters on Nusselt number has been depicted in Figure 12. The heat transfer rate improved with large value of radiation and suction parameters and reduced value of nanosolid volume fraction.

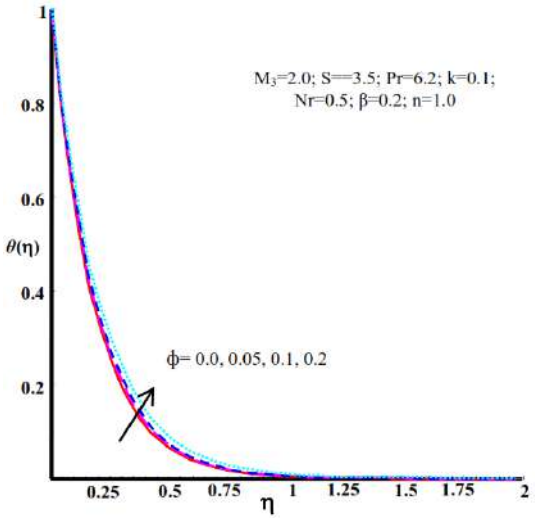

Figure 6. Impact of nanoparticles volume fraction parameter on θ(η)

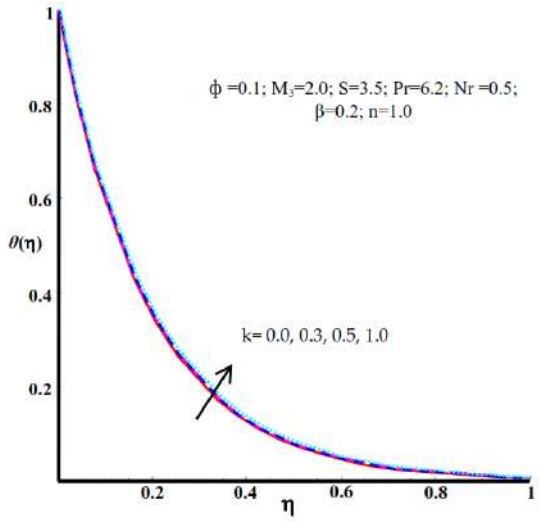

Figure 7. Impact of porosity parameter on θ(η)

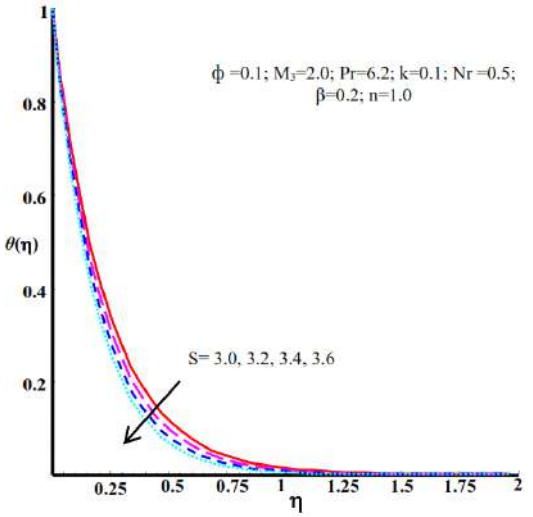

Figure 8. Impact ofsuction parameter on θ(η)

5. 3. Bejan Number and Entropy Generation The effects of the porosity, heat sink or source, nanosolid volume fraction, radiation, suction parameters pertaining to the entropy generation profile are presented in Figures 13-17. In Fe_3O_4-ethylene glycol nanofluid, the entropy generation increases with the increase in the suction and heat sink (β<0) parameters. Furthermore, the presence of heat source (β>0), radiation, porosity, nanosolid volume fraction parameters diminishes the production of entropy. The characteristics of entropy generation with respect to φ are shown in Figure 13. Figure 14 indicates the results ofentropy generation for different porosity parameters. The effects of the suction parameter on Ns are shown in

Figure 15. Figures 16 and 17 depict the characteristics of radiation and heat sink or source parameters, respectively. It is clear that the presence of Fe_3O_4 nanofluid volume fraction, porosity parameter, thermal radiation, uniform heat source parameters are control the more entropy production. But the suction parameter develop the entropy production.

The influence of Bejan number with respect to various physical parameters like Brinkman number, nanosolid volume fraction, heat sink or source, suction parameters have been depicted in Figures 18-21. From the figures, the Bejan number is improved with the heat source ($\beta>0$) and nanosolid volume fraction parameters, but is reduced with the heat sink ($\beta<0$), suction and Brinkman number. Figure 18 shows the variation of φ on Be. Figure 19. depicts the impact of *S* onBe. Figures 20 and 21 indicate the results of Be with respect to different values of Brinkman number and heat sink or source parameters, respectively.

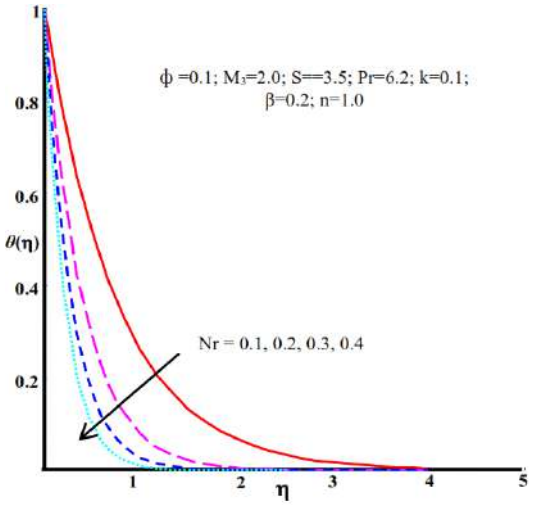

Figure 9. Impact of radiation parameter on θ(η)

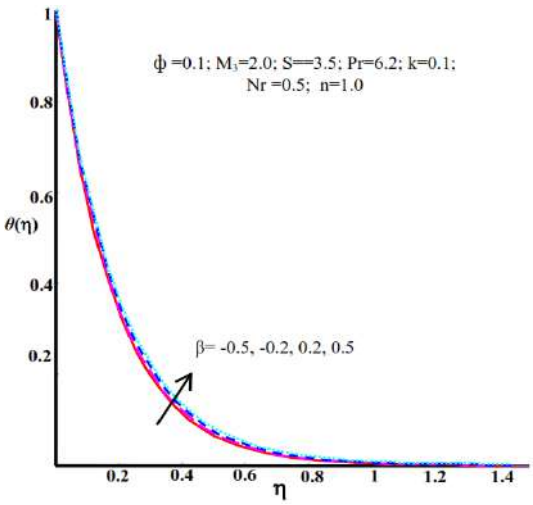

Figure 10. Impact of β on θ(η)

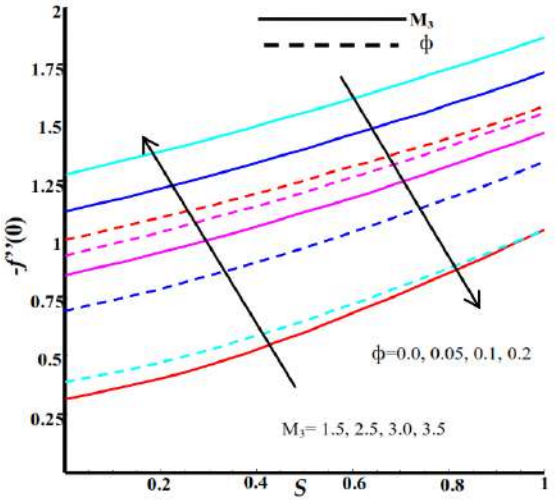

Figure 11. Impact of ϕ and M_3on -f''(0)

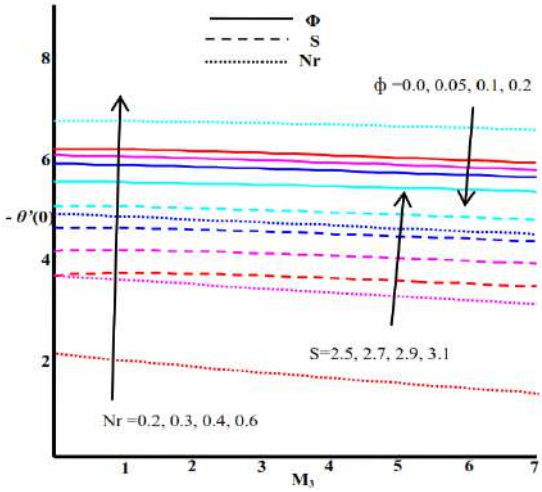

Figure 12. Impactof ϕ, S and Nr on –θ'(0)

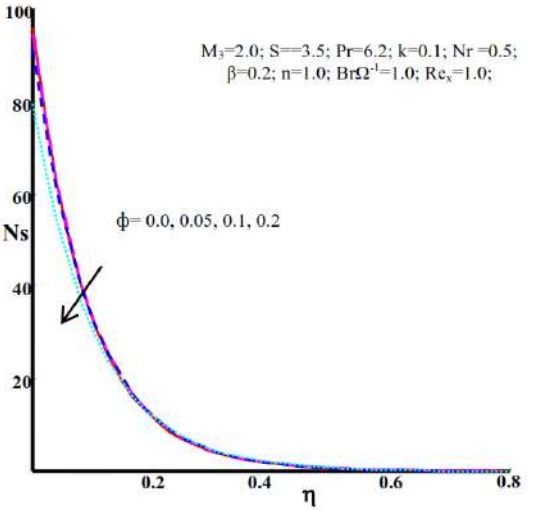

Figure 13. Impact of nanoparticles volume fraction parameter on Ns

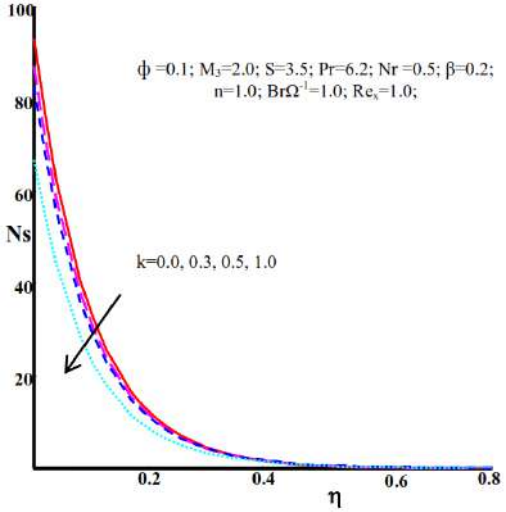

Figure 14. Impact of porosity parameter on Ns

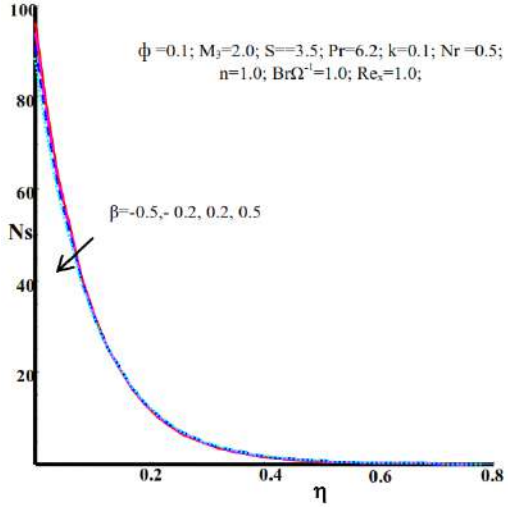

Figure 17. Impact of heat source/sink parameter on Ns

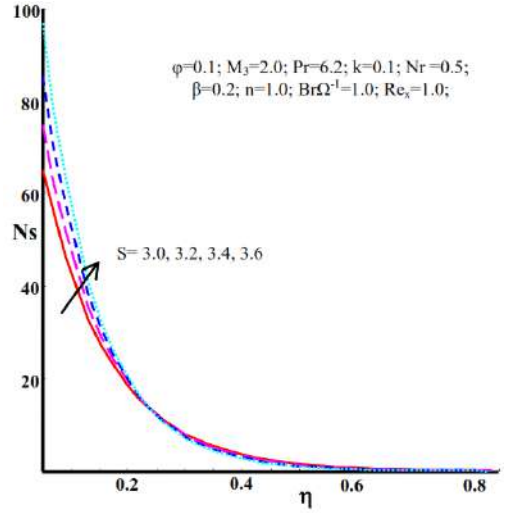

Figure 15. Impact of suction parameter on Ns

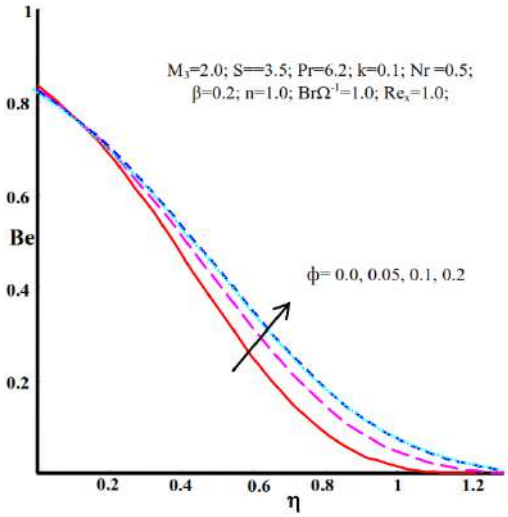

Figure 18. Impact of nanoparticles volume fraction parameter on Be

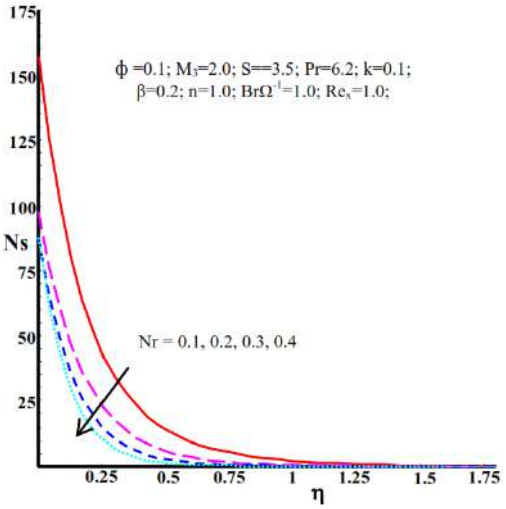

Figure 16. Impact of radiation parameter on Ns

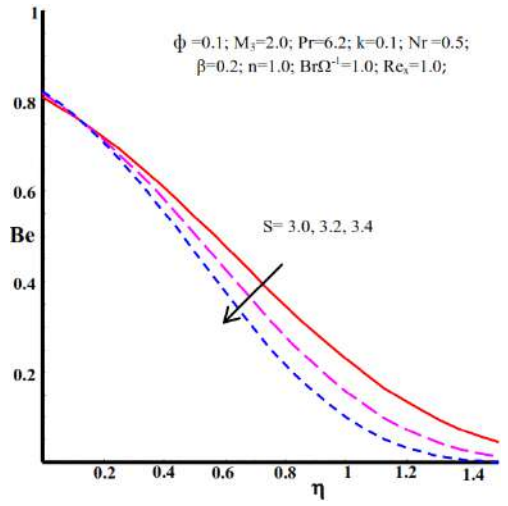

Figure 19. Impact of suction parameter onBe

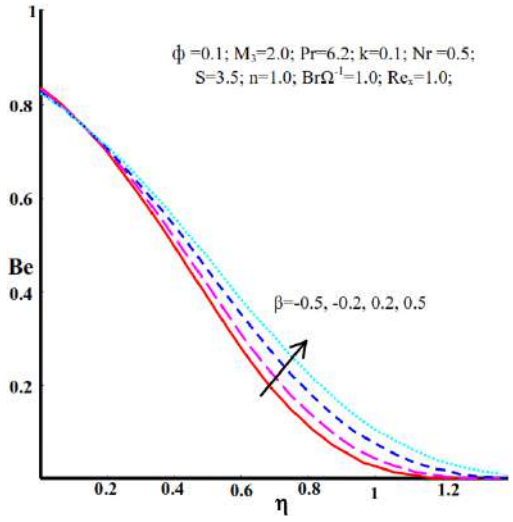

Figure 20. Effect of heat source/sink parameteron Be

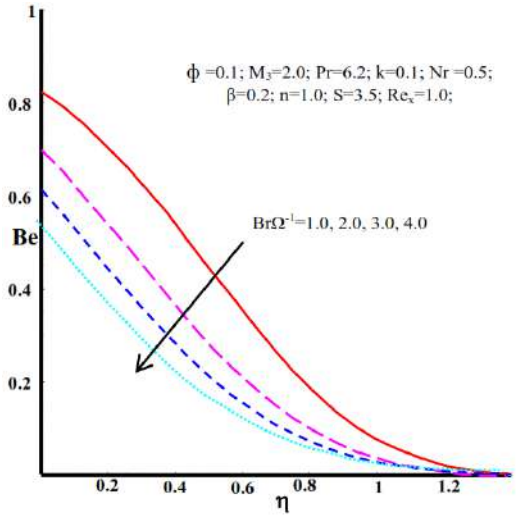

Figure 21. Impact of $Br\Omega^{-1}$on Be

TABLE 1. Thermo-physical properties of ethylene glycol and nanoparticles [42]

	ρ(kg/m³)	C_p(j/kgk)	k (W/m.k)
Ethylene glycol	1110	2400	0.26
Fe_3O_4	*5200*	*670*	*6*

TABLE 2. Evaluate solution of Skin friction for different values of S with M_3 = 2 When ϕ=k=0

S	[39]	[40]	Present results
2	2.414214	2.414217	2.41421
3	3.302776	3.302772	3.30278
4	4.236068	4.236073	4.23607

6. CONCLUSIONS

We have presented an analytical approach pertaining to entropy generation on Fe_3O_4-Ethylene glycol MHD nanofluid through a shrinking wall with porous medium in the presents of heat sink or source and thermal radiation. We have obtainedthe important results, as follows:

- The velocity of Fe_3O_4-ethylene glycol nanofluidis enhanced with the increase in the suction parameters, but it slows down with respect to the nanosolid volume fraction and porosity parameters. The heat of Fe3O4-Ethylene glycol nanofluidis enhanced with the increase in the heat source,nanosolid volume fraction and porosity and its decreases with the heat sink, suction and radiation parameters.The presence of Fe3O4 nanoparticle enhances with the temperature profile. This is because Fe3O4 particles have high thermal conductivity, so the thermal boundary layer thickness increases. The porosity parameter also develops the thermal boundary layer thickness. But the presence of thermal radiation and suction parameters are reduces the thermal boundary layer thickness.
- The skin friction increases with the Hartmann number, but decreases with nanosolid volume fraction. The Nusselt number is enhanced with radiation and suction parameters, but it is reduced with nanosolid volume fraction.
- The entropy generation profile is maximized with suction and heat sink, but it is minimized with nanosolid volume fraction, porosityand heat source. It is clear that the presence of Fe_3O_4 nanofluid volume fraction, porosity parameter, thermal radiation, uniform heat source parameters are control the more entropy production. But the suction parameter develop the entropy production.

The Bejan number increases with nanosolid volume fraction and heat source, but decreases with suction, Brinkman number and heat sink. In the future, this paper can be extended for different nanofluids considering the effect of magnetic field with nonlinear thermal radiation in different types of boundary conditions.

7. REFERENCES

1. Choi, S.U.S.,"Enhancing thermal conductivity of fluids with nanoparticles", In: Proceedings of the 1995 ASME International Mechanical Engineering Congress and Exposition, San Francisco, Calif, USA, Vol. 66, (1995), 99-105
2. Ibrahim, W., Shankar, B.,Nandeppanavar, M. M.,"MHD stagnation point flow and heat transfer due to nanofluid towards a stretching sheet", ***International Journal of Heat and Mass Transfer***, Vol. 56, (2013) 1-9. DOI: 10.1016/j.ijheatmasstransfer.2012.08.034

3. Hayat, T.,Imtiaz, M.,Alsaedi, A.,Mansoor, R., "MHD flow of nanofluids over an exponentially stretching sheet in a porous medium with convective boundary conditions", ***Chinese Physics B***, Vol. 23, No. 5, (2014), 054701. DOI:10.1088/1674-1056/23/5/054701
4. Malvandi A.,Ganji D. D.,"Magnetohydrodynamic mixed convective flow of Al_2O_3-water nanofluid inside a vertical micro tube", ***Journal of Magnetism and Magnetic Materials***, Vol. 369, (2014), 132-141. DOI: 10.1016/j.jmmm.2014.06.037
5. Rahman, M. M.,Rosca, A.V., Pop, I.,"Boundary layer flow of a nanofluid past a permeable exponentially shrinking/stretching surface with second order slip using Buongiorno's model", ***International Journal of Heat and Mass Transfer***, Vol. 77, (2014), 1133-1143. DOI: 10.1016/j.ijheatmasstransfer.2014.06.013
6. Shaha, Z.,Ebraheem, O.,Alzahranib, Abdullah, D.,Asad, U.,IkramullahK.,"Influence of Cattaneo-Christov model on Darcy-Forchheimer flow of MicropolarFerrofluid over a stretching/shrinking sheet", ***International Communications in Heat and Mass Transfer***, Vol. 110, (2020), 104385. DOI: 10.1016/j.icheatmasstransfer.2019.104385
7. Sheikholeslami, M., Bandpy, M. G.,Ellahi, R.,ZeeshanA.,"Simulation of MHD CuO-water nanofluid flow andconvective heat transfer considering Lorentz forces", ***Journal of Magnetism and Magnetic Materials***, Vol. 369, (2014) 69–80. DOI: 10.1016/j.jmmm.2014.06.017
8. Jamaludin, A.,Naganthran, K.,Nazar, R., Pop, I.,"MHD mixed convection stagnation-point flow of Cu-Al_2O_3/water hybrid nanofluid over a permeable stretching/shrinking surface with heat source/sink*", **European Journal of Mechanics / B Fluids***, Vol. 84, (2020), 71-80. DOI: 10.1016/j.euromechflu.2020.05.017
9. Dero, S.,Rohni, A. M.,Saaban, A.,"Stability analysis of Cu-$C_6H_9NaO_7$ and Ag-$C_6H_9NaO_7$nanofluids with effect of viscous dissipation over stretching and shrinking surfaces using a single phase model", ***Heliyon***, Vol. 6, (2020), 03510. DOI: 10.1016/j.heliyon.2020.e03510
10. Haq, R. U.,Raza, A.,Ebrahem A.,Algehynec, Tlili, I.,"Dual nature study of convective heat transfer of nanofluid flow over a shrinking surface in a porous medium", ***International Communications in Heat and Mass Transfer***, Vol. 114, (2020), 104583. DOI: 0.1016/j.icheatmasstransfer.2020.104583
11. Shah Naqvi, S.M.R., Muhammad, T.,Saleem, S., Kim, H.M.,"Significance of non-uniform heat generation/absorption in hydromagnetic flow of nanofluid due to stretching/shrinking disk", ***Physica A,*** Vol. 553, (2020), 123970. DOI: 10.1016/j.physa.2019.123970
12. Khan, U.,Zaib, A.,Zahir S.,Dumitru B., El-Sayed M. Sherif.,"Impact of magnetic field on boundary-layer flow of Sisko liquid comprising nanomaterials migration through radially shrinking/stretching surface with zero mass flux", ***Journal of Material Research and Technology***,Vol. 9, No.3, (2020), 3699-3709. DOI: 10.1016/j.jmrt.2020.01.107
13. Khashi'ie, N. S.,Arifina, N. M., Pop, I.,Nazar, R.; Hafidzuddin, E.H.,Wahi, N.,"Three-Dimensional Hybrid Nanofluid Flow and Heat Transfer past a Permeable Stretching/Shrinking Sheet with Velocity Slip and Convective Condition", ***Chinese Journal of Physics***, Vol. 66, (2020), 157-171. DOI: 10.1016/j.cjph.2020.03.032
14. Gireesha, B. J.,Umeshaiah, M.,Prasannakumara, B. C.,Shashikumar N. S.,Archana, M.,"Magnetohydrodynamic three dimensional boundary layer flow of Jeffrey nanofluid over a nonlinearly permeable stretching sheet", ***Physica A***, Vol. 549, (2020), 124051. DOI: 10.1016/j.physa.2019.124051
15. Hayat,T.,Kanwal, M., Qayyum, S.,Alsaedi, A.,"Entropy generation optimization of MHD Jeffrey nanofluid past a stretchable sheet with activation energy and non-linear thermal radiation", ***Physica A: Statistical Mechanics and its Applications,*** Vol. 544, (2020), 123437. DOI: 10.1016/j.physa.2019.123437
16. Hosseinzadeh, K H.,Mogharrebi, A. R.,Asadi, A.,Sheikhshahrokhdehkordi, M.,Seyedmohammad M.,Ganji, D.D.,"Entropy generation analysis of mixture nanofluid ($H_2O/C_2H_6O_2$)–Fe_3O_4 flow between two stretching rotating disks under the effect of MHD and nonlinear thermal radiation", ***International Journal of Ambient Energy***, (2019), 1-13. DOI: 10.1080/01430750.2019.1681294
17. Shahsavar, A.,Moradi, M.,Bahiraei, M.,"Heat transfer and entropy generation optimization for flow of a non-Newtonian hybrid nanofluid containing coated CNT/Fe_3O_4 nanoparticles in a concentric annulus", ***Journal of the Taiwan Institute of Chemical Engineers***, (2018), 1-13. DOI: 10.1016/j.jtice.2017.12.029
18. Mehrali, M.,Sadeghinezhad, E.,Akhiani, A.R.,Latibari, S.T.,Metselaar, H.S.C.,Kherbeet, A.Sh.,Mehrali, M.,"Heat transfer and entropy generation analysis of hybrid graphene/Fe3O4 ferro-nanofluid flow under the influence of a magnetic field", ***Powder Technology***, Vol. 308, (2017), 149-157. DOI: 10.1016/j.powtec.2016.12.024
19. López, A., Ibáñez, G.,Pantoja, J., Moreira, J.,Lastres, O.,"Entropy generation analysis of MHD nanofluid flow in a porous vertical microchannel with nonlinear thermal radiation, slip flow and convective-radiative boundary conditions", ***International Journal of Heat and Mass Transfer***, Vol. 107, (2017), 982-994. DOI: 10.1016/j.ijheatmasstransfer.2016.10.126
20. Shukla, N., Rana, P., Anwar Bégb, O.,Bani S.,Kadir, A.,"Homotopy study of magnetohydrodynamic mixed convection nanofluid multiple slip flow and heat transfer from a vertical cylinder with entropy generation", ***Propulsion and Power Research,*** Vol. 8, (2019), 147-162. DOI: 10.1016/j.jppr.2019.01.005
21. Hayat, T.,Rabiya Y.,SumairaQ.,Alsaedi,A.,"Entropy generation optimization in nanofluid flow by variable thicked sheet", ***Physica A: Statistical Mechanics and its Applications***, Vol.551, (2020). DOI: https://doi.org/10.1016/j.physa.2019.124022
22. Rana, P.,Shukla, N.,"Entropy generation analysis for non-similar analytical study of nanofluid flow and heat transfer under the influence of aligned magnetic field", ***Alexandria Engineering Journal,*** Vol. 57, (2018), 3299-3310. DOI: https://doi.org/10.1016/j.aej.2017.12.007
23. Govindaraju, M., Ganga, B., Abdul Hakeem, A.K.,"Second law analysis on radiative slip flow of nanofluid over a stretching sheet in the presence of lorentz force and heat generation/absorption", ***Frontiers in Heat and Mass Transfer (FHMT)***, Vol. 8, No. 10, (2017), 1-10. DOI: http://dx.doi.org/10.5098/hmt.8.10
24. Abdul Hakeem, A. K.,Govindaraju, M., Ganga, B., Kayalvizhi, M., "Second law analysis for radiative MHD slip flow of a nanofluid over a stretching sheet with non-uniform heat source effect", ***ScientiaIranica F***,Vol. 23, No. 3, (2016), 1524-1538. DOI: 10.24200/SCI.2016.3916
25. Ganga, B., Govindaraju, M., Abdul Hakeem, A.K.,"Effects of Inclined Magnetic Field on Entropy Generation in Nanofluid Over a Stretching Sheet with Partial Slip and Nonlinear Thermal Radiation", ***Iranian Journal of Science and Technology, Transactions of Mechanical Engineering***, (2018), 1-12. DOI: https://doi.org/10.1007/s40997-018-0227-0
26. Rashid.,Sagheer, M.,Hussain, S.,"Entropy formation analysis of MHD boundary layer flow of nanofluid over a porous shrinking wall", ***Physica A***, Vol. 536, (2019), 122608. https://doi.org/10.1016/j.physa.2019.122608

27. Seth, G. S., Bhattacharyya, A., Kumar, R.,Chamkha, A. J.,"Entropy generation in hydromagneticnanofluid flow over a non-linear stretching sheet with Navier's velocity slip and convective heat transfer", ***Physics of Fluids***, Vol. 30, (2018), 122003. DOI: https://doi.org/10.1063/1.5054099

28. Acharya, N., Das, K., Kumar Kundu, P.,"On the heat transport mechanism and entropy generation in a nozzle of liquid rocket engine using ferrofluid: A computational framework", ***Journal of Computational Design and Engineering***, Vol. 6, (2019), 739-750. DOI: https://doi.org/10.1016/j.jcde.2019.02.003

29. Daniel, Y. S., Abdul Aziz, Z., Ismail, Z., Salah, F.,"Entropy analysis in electrical magnetohydrodynamic (MHD) flow of nanofluid with effects of thermal radiation, viscous dissipation, and Chemical reaction", ***Theoretical & Applied Mechanics Letters***, Vol. 7, (2017), 235-242. DOI: https://doi.org/10.1016/j.taml.2017.06.003

30. Ellahi, R., Sultan Z A., Abdul B.,Majeed, A.,"Effects of MHD and slip on heat transfer boundary layer flow over a moving plate based on specific entropy generation", ***Journal of Taibah University for Science,*** Vol. 12, No. 4, (2018), 476-482. DOI: https://doi.org/10.1080/16583655.2018.1483795

31. SheikholeslamiM.,"New computational approach for exergy and entropy analysis of nanofluid under the impact of Lorentz force through a porous media",***Computer Methods in Applied Mechanics and Engineering,*** Vol. 344, (2019), 319-33. DOI: https://doi.org/10.1016/j.cma.2018.09.044

32. Riaz, A.,Bhatti, M.M.,Ellahi, R.,Zeeshan, A.,Sait, S.M.,"Mathematical analysis on an asymmetrical wavy motion of blood under the influence entropy generation with convective boundary conditions", ***Symmetry,*** Vol.2, No.1,(2020), 102. DOI: https://doi.org/10.3390/sym12010102

33. Döner**,** A.**,** Comparison of corrosion behaviors of bare Ti and TiO_2, ***Emerging Science Journal,*** Vol. 3, No. 4, (2019), 235-240. DOI: http://dx.doi.org/10.28991/esj-2019-01185

34. Slavova, M, MihaylovaDimitrova, E, Mladenova, E,Abrashev, B,Burdin, B,Vladikova, D., "Zeolite based air electrodes for secondary batteries", ***Emerging Science Journal,*** Vol. 4, No. 1, (2020), 18-24. DOI: http://dx.doi.org/10.28991/esj-2020-01206

35. Kostikov, Y. A, Romanenkov, A. M., "Approximation of the multidimensional optimal control problem for the heat equation (Applicable to computational fluid dynamics (CFD))",***Civil Engineering Journal,*** Vol. 6, No. 4, (2020), 743-768. DOI: 10.28991/cej-2020-03091506

36. Kostikov, Y. A, Romanenkov, A. M., "The technology of calculating the optimal modes of the disk heating (Ball)", ***Civil Engineering Journal,*** Vol. 5, No. 6, (2019), 1395-1406. DOI: 10.28991/cej-2019-03091340

37. Theingi, M, ThiTun, K,Aung, N. N., "Preparation, characterization and optical property of LaFeO3 nanoparticles via Sol-Gel combustion method", ***SciMedicine Journal,*** Vol. 1, No. 3, (2019), 151-157.

38. Zhang, W., Yang, X., Wang, T., Peng, X., Wang, X, "Experimental study of a gas enginedrivenheat pump system for space heating and cooling",***Civil Engineering Journal,*** Vol. 5, No. 10, (2019), 2282-2295. DOI: 10.28991/cej-2019-03091411

39. Muhaimin., Kandasamy, R., Azme B. Khamis., "Effects of heat and mass transfer on nonlinear MHD boundary layer flow over a shrinking sheet in the presence of suction", ***Applied Mathematics and Mechanics,*** Vol. 29, No. 10, (2008),1309-1317. DOI: 10.1007/s10483-008-1006-z

40. Bhattacharyya, K.,"Effects of radiation and heat source/sink on unsteady MHD boundary layer flow and heat transfer over a shrinking sheet with suction/injection", ***Frontiers of Chemical Science and Engineering,*** Vol. 5, No. 3, (2011), 376-384. DOI: 10.1007/s11705-011-1121-0

41. Rashid, I.,RizwanUlHaq., Khan, Z. H.,Qasem M. Al-Mdallal.,"Flow of water based Alumina and Copper nanoparticles along a moving surface with variable temperature", ***Journal of Molecular Liquids,*** Vol.246, (2017), 354-362. DOI: 10.1016/j.molliq.2017.09.089

42. Sheikholeslami, M.,Shamlooei, M.,Moradi, R.,"Fe_3O_4-Ethylene glycol nanofluid forced convection inside a porous enclosure in existence of Coulomb force", ***Journal of Molecular Liquids,*** Vol. 249, (2018), 427-439. DOI: 10.1016/j.molliq.2017.11.048

Persian Abstract

چکیده

این تحقیق عمدتاً بر تأثیرات جذب / تولید گرما و تابش بر جریان هیدرو مغناطیسی نانوسیال Fe_3O_4–اتیلن گلیکول از طریق دیواره کوچک شده با محیط متخلخل و محاسبه تولید آنتروپی متمرکز است. ما معادلات دیفرانسیل معمولی حاکم را با استفاده از راه‌حل‌های مشابهت مناسب به معادلات دیفرانسیل جزئی در نظر می‌گیریم. علاوه بر این، عملکرد هندسی بیش از حد برای تعیین مسئله فرموله شده استفاده می‌شود. ما اثرات پارامترهای فیزیکی مناسب را بر روی تعداد Bejan، تولید آنتروپی، تعداد Nussult، اصطکاک پوست، دمای مایع و پروفیل سرعت تجزیه و تحلیل می‌کنیم. علاوه بر این، نتیجه حاصل از مطالعه حاضر با نتایج موجود در ادبیات موجود مقایسه می‌شود. ما متذکر شدیم که وجود پارامترهای جذب حرارت و مکش، تعداد Bejan را کاهش می‌دهد و باعث افزایش تولید آنتروپی می‌شود و پارامترهای تابش منبع حرارت، محیط متخلخل، تولید آنتروپی را به حداقل می‌رسانند. وجود پارامتر تخلخل سرعت سیال را کاهش می‌دهد، دمای سیال را بهبود می‌بخشد و تولید آنتروپی را به حداقل می‌رساند. پارامتر کسری حجمی نانوسولید هم تعداد Nussult و هم ضریب اصطکاک پوست را کاهش داد.

IJE TRANSACTIONS B: Applications Vol. 34, No. 02, (February 2021) 528-535

International Journal of Engineering

Journal Homepage: www.ije.ir

Statistical Modeling Optimization and Sensitivity Analysis of Tool's Geometrical Parameters on Process Force in Automatic Cortical Bone Drilling Process

M. Safari*, V. Tahmasbi, P. Hassanpour

Department of Mechanical Engineering, Arak University of Technology, Arak, Iran

PAPER INFO

Paper history:
Received 03 July 2020
Received in revised form 08 November 2020
Accepted 04 December 2020

Keywords:
Bone Drilling Process
Crack
Statistical Sensitivity Analysis
Drilling Force

ABSTRACT

One of the most prevalent machining processes in medical treatments is bone drilling process. During bone drilling, excessive process force can cause breakage, crack initiation and severe damage to bone tissue. In this paper, a systematic study with simultaneous use of response surface method, sensitivity analysis based on Sobol method and regression analysis is performed for investigation the effect of helix angle and point angle of the tool as the most important geometrical parameters on imposed force to the bone during drilling process. Initially, using design of experiments and response surface method, imposed force to the bone is modeled and the governing second order linear regression equation is derived and verified. Then, using Sobol sensitivity analysis, with ability to quantify the sensitivity, it is attempted to investigate the effect of input parameters on drilling force. Finally, optimization of the process inputs is followed to find the best combination which yields the desired drilling force. The minimum drilling force, within the range of input parameters, coincides with point angle of 90 and helix angle of 18. This minimal force is lower than the force in surgery and standard tools. The results showed that an increasing in point angle leads to an increase in drilling force. Also, it is concluded that there is an optimum value for using the helix angle in bone drilling process with minimum imposed force.

doi: *10.5829/ije.2021.34.02b.26*

1. INTRODUCTION

Bone is an important limb in different species including humans. The goal of bone surgery is to keep damaged segments of the bone close to each other in the way that self-recovery of the bone is guaranteed. Drilling is quite often a must in order to keep bone segments fixed. As ubiquitously known, when bone tissue undergoes excessive force, the tissue would be severely damaged and can eventuate in crack initiation or breakage. During bone drilling, the axial force is imposed on bone. Many parameters such as process and tool geometry parameters affect the axial force of bone drilling process. In case of tool geometry, the tool diameter, point angle and also helix angles are prominent ones. There are some reports addressing the minimization of the axial force in the literature. Singh et al. [1] compared the effects of rotational speed, feed rate and tool diameter on cutting force and temperature in conventional and rotary ultrasonic bone drilling. They concluded that the cutting force up to 40% and temperature up to 55% were lesser in rotary ultrasonic technique. Ying et al. [2] compared the conventional cutting (CC) and ultrasonic vibration assisted cutting (UVAC) bone drilling processes. Their results showed that UVAC can decreases the cutting force but increases the temperature. Shu et al. [3] proposed a novel drill bit with the ability of self-centering for drilling of low-trauma bones. They reported that the proposed drill bit could significantly reduce the cutting force. They also developed an experimental setup for comprehensive analysis of bone drilling process. Zhang et al. [4] compared the cutting force between continuous and step-by-step bone drilling process. They concluded that step-by-step drilling technique can reduce the cutting force in drilling process of cortical bones. Gupta et al. [5] studied the effects of various drilling techniques such as conventional surgical drilling, rotary ultrasonic bone

*Corresponding Author Institutional Email: m.safari@arakut.ac.ir
(Mehdi Safari)

Please cite this article as: M. Safari, V. Tahmasbi, P. Hassanpour, Statistical Modeling Optimization and Sensitivity Analysis of Tool's Geometrical Parameters on Process Force in Automatic Cortical Bone Drilling Process, International Journal of Engineering,, Transactions B: Applications, Vol. 34, No. 02, (2021) 528-535

drilling and rotary bone drilling of cutting force in bone drilling process. Their results showed that rotary ultrasonic technique using hollow tool can significantly reduce the cutting force. Sui and Sugita [6] studied the effects of process parameters and bone material on drilling force. They concluded that increasing the feed rate and drill diameter lead to increasing the drilling force. Also, they proved that drilling force is the highest in bovine cortical bone while it is the lowest for Sawbones 3401. Sarparast et al. [7] investigated the force and temperature in high-speed bone drilling process. Their results showed that the high-speed drilling process leads to decrease in drilling force and temperature. Also, they concluded that rotational speed, feed rate and tool diameter are as the most important affecting parameters in high-speed drilling process. Alam et al. [8] studied the effect of drill wear on bone temperature and cutting force in drillibg process. They concluded that the sharp drill has a significant effect on decreasing the cutting force and temperature. Zolfaghari et al. [9] developed a model based on response surface methodology to investigate the effects of tool rotational speed, feed rate and tool diameter on temperature in bone drilling process. They showed that the process temperature will be increased with increasing the rotational speed and tool diameter. Singh et al. [10] reported that the point angle between 130- 140 can minimized the process force. Augustin et al. [11] reported that with increasing the bore diameter, contact surface of the bone-tool increases leading to higher frictional forces and process force. Considering saw bone they also mentioned that with an increase in bore diameter, bone strength decreases and that lengthen the recovery period. Up to now, there is no standard code to dictate standard geometry for the bone drilling tool. Currently there are some studies working to present the standard tool geometry for bone drilling process. Some find the conventional drilling tool for metals very promising for bone drilling process. Pandey et al. [12] reported that the dimensional accuracy of the bore and drilling force are preferable when standard tool with point angle of 118 and helix angle of 30 are used in bone drilling. Tuijthof et al. [13] considering different tools, including the diameter of 3.5 mm, studied the effect of tool geometry and feed rate on drilling axial force on both cortical and trabecular bones. They found conflicting effects in combination of parameters. However, they reported with a constant tool diameter, the most influential parameters are point angle and helix angle and there should be an optimum combination of them both. Singh et al. [14] considering three different tool geometries with the same diameter of 4 mm studied the dimensional accuracy and bore surface roughness and found the standard geometry the best among all three. Green et al. [15] studied different point and helix angles found that point angle of 118 and helix angle of 28 would eventuate into the lowest drilling force. Höller [16] reviewing surgery and machining standards and handbooks and reviewing the literature found conflicting reports. He eventually, for the diameter of 3.5 mm for drilling tool, introduces point angle of 105 and helix angle of 27 as the optimized minimum force state. While surgery standards, confirm a tool with point angle of 78 and helix angle of 14. Metal machining standard, also, proves a different combination of point angle of 118 and helix angle of 22-30. Tahmasbi et al. [17] using design of experiment found that lowering tool diameter causes the lower bone drilling force while increasing feed rate raises the force. Having a general look over the reported studies one can notice different inferences and presented data which is attributed to the incorrect and incomplete relation between studied input and output parameters. To address this issue and achieving the optimum tool geometry for bone drilling requires an accurate design of experiment to quantify the effect of point angle, helix angle and rake angle on drilling force and temperature [18]. It should be born in mind that the material and coating of the tool should meet the medical requirement of a surgery. Moreover, up to now, no statistical sensitivity analysis has been applied to quantify the effect of different tool parameters on bone drilling force.

In this paper considering the main tool geometry parameters like point and helix angles, for the first time a linear second order regression equation was derived using response surface method in order to predict bone drilling force. The interactional effects and individual effects were analyzed and optimization was performed. Furthermore, Sobol sensitivity analysis was used to quantitatively obtained the effect of different parameters on bone drilling force.

1. 1. Application of Mathematical and Statistical Methods in Process Analysis In engineering problems involving experimentation and simulation, where output is complicatedly dependent on many input factors, using experiment designed by statistical methods can markedly assist design, modeling and analysis of the process. One of the greatest methodologies in this field is response surface method [19]. Design of experiments not only helps to save time and effort, but also reveals defects of experimentation along with trouble nshooting [20]. The accuracy of experimentation as well as fitted model, the interactional effect of parameters, optimization of the process is revealed by response surface methodology (RSM) and are considered as advantages of this method [21]. This method is capable to find a relation between input and output parameters in the form of a second order linear regression equation. General form of the equation considering parameters and their interactions can be written in the form of equation (1).

$$y = \beta_0 + \sum_{i=1}^{k} \beta_i x_i + \sum_{i=1}^{k} \beta_{ii} x_i^2 + \sum_i \sum_j \beta_{ij} x_i x_j + \varepsilon \quad (1)$$

1. 2. Sensitivity Analysis Methods Sensitivity analysis is robust for the case of system analysis and it illustrates the effect of input parameters on outputs of a system. Sensitivity analysis studies the uncertainties of the output and relates that to the uncertainties of the input parameters [22]. One of the main methods is Sobol sensitivity analysis. In this method, for the defined model Y=f(X), where Y is the output and $X(x_1, x_2, \dots, x_n)$ is the vector of input parameters, output variance (V) can be defined as the summation of each separated term as defined in Equation (2):

$$V(Y) = \sum_{i=1}^{n} V_i + \sum_{i \le j \le n} V_{ij} + \cdots + V_{1,\dots,n} \quad (2)$$

where V_i is the first order effect for each input factor $x_i (V_i = V[E(Y|x_i)])$ and $V_{ij} = V[E(Y|x_i, x_j)] - V_i - V_j$ to $V_{1, \dots, n}$ shows the interaction among n factors. Sensitivity index can be defined as the ratio of variance of every order to the total variance e.g. $S_i = \frac{V_i}{V}$ is the first order sensitivity index and $S_{ij} = \frac{V_{ij}}{V}$ is the second order sensitivity index and so on. The overall index which defines the effectiveness of each parameter is defined as the summation of its ordered sensitivity indices as presented in Equation (3) [23].

$$S_{Ti} = S_i + \sum_{i \ne j} S_{ij} + \cdots \quad (3)$$

2. MATERIALS AND METHODS

As previously mentioned, in this paper, a systematic study with simultaneous use of response surface method, sensitivity analysis based on Sobol method and regression analysis is performed for investigation the effect of helix angle and point angle of the tool as the most important geometrical parameters on imposed force to the bone during drilling process. For this purpose, point angle and helix angle are considered as input variables and maximum drilling force during the process was considered as the output of the process. Fresh bovine bone (cow having age of 3 to 4 years) was used for making experimental samples (Figure 1) [24]. To ease experimentation both ends of bovine ankle bone was cut with a saw. The depth of the drilling was limited to 4 mm. As bone properties changes dramatically with time, it was attempted to be sure that the carcass which was to give the bone, is fresh [25]. Figure 2 depicts geometry of a standard tool with different specifications. Tools are HSS standard steels with diameter of 3.5 mm and in order to guarantee sharp edges they were un-used (Figure 3). The reason behind tool selection is the general inclination of the researchers and surgeons and also marketing availability. These tools possess three different helix angle of 14, 20.5 and 27 and point angle was formed with a too sharpener tool with angles of 90, 112.5 and 135 and angles were checked with angular gauges (Table 1). Tabriz automatic drilling machine was used to perform experimentation. To measure drilling force a laboratory load cell was used (Figure 4). Snapshot of an experimentation is depicted in (Figure 5). Rotational speed and feed rate were tuned to 2000 rpm and 30 mm/min, respectively.

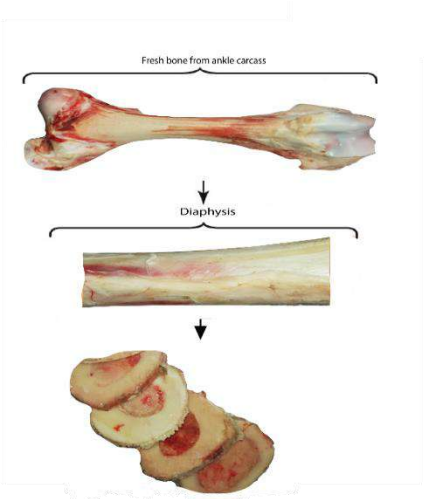

Figure 1. Fresh bovine bone from fresh ankle carcass

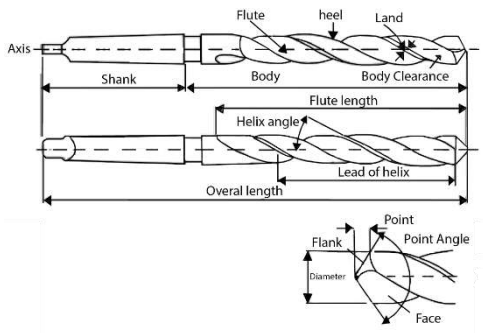

Figure 2. Standard drilling tool with geometrical specifications

Figure 3. Standard drilling tool (Diameter: 3.5 mm) with different point and helix angles

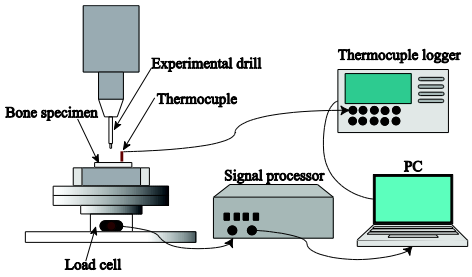

Figure 4. CNC automatic drilling machine

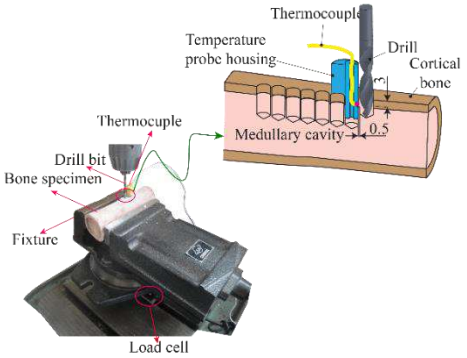

Figure 5. Experimentation in bone drilling process

TABLE 1. Machining input parameters in three different stages

	Minimum	Mean	Maximum
Helix angle	14	20.5	27
Point angle	90	112.5	135

According to design matrix (Table 1), 11 sets were examined. Table 2 shows the results. Using response surface method and data analysis a governing second order linear regression equation was derived considering the best fit to the data points and analysis of the output data was performed.

2. ANALYSIS AND MODELING OVER DATA

Considering the results from force analysis using analysis of variance (ANOVA) listed in Table 3. ANOVA shows the effect of different parameters mentioned in regression equation and therefore, it is crucial in analysis and modeling of data. ANOVA table in design of experiments reveals the input factors and their interactional effects over the response of the system [20].

Considering a preferable reliability of experimentation equal to 95% in this study, the p-value of 0.05 was considered to obtain the effect of different parameters [20]. PRESS of the fitted model to data point can show the accuracy of the governing equation which

TABLE 2. Layout of experiments based of RSM

	Helix angle (Degree)	Point angle (Degree)	Force (N)
1	14	90	25.6
2	14	135	102.4
3	27	90	65.2
4	27	135	153.4
5	20.5	90	37.4
6	20.5	135	59.3
7	14	112.5	54.4
8	27	112.5	103.7
9	20.5	112.5	52.17
10	20.5	112.5	55.5
11	20.5	112.5	58.9

TABLE 3. Analysis of variance for cortical bone drilling force

Source	DF	Seq SS	Adj SS	Adj MS	F-Value	P-Value
Model	4	11784.6	11784.6	2946.15	12.43	0.005
Linear	2	9083.9	9083.9	4541.97	19.16	0.002
helix angle	1	3262	3262	3262	13.76	0.01
point angle	1	5821.9	5821.9	5821.93	24.56	0.003
Square	2	2700.6	2700.6	1350.32	5.7	0.041
(H.A)* (H.A)	1	2699.7	2482.2	2482.22	10.47	0.018
(P.A)* (P.A)	1	0.9	0.9	0.92	0	0.952
Error	6	1422.4	1422.4	237.07		
Total	10	13207				

is critical in the field of design of experiments. Lower value of this factor means the more accuracy of the prediction. In this paper the minimum value was achieved for second order full quadratic regression model [20]. Considering the values R-sq= 89.23 %, R-sq (pred)= 53.94% and R-sq (adj)= 82.23% as well as favorable distribution of the analysis of residuals, according to Figure 5, it can be implied that the presented model possesses a great precision. In case of RSM, a great factor showing the accuracy of the fitted model is R-sq which can be computed using Equation (2). As R-sq approaches 1 (100%) the correlation of the fitted model increases and therefore more precise prediction of the model is expected. Another prominent parameter is the analysis of the distribution of the residuals based on

Equation (4). A fitted model should pass close to the data points and the difference between the model and data points should be random in nature. The distance between model and data points can be discovered by R-sq and its random distribution can be seen in figure 6. Both proves that fit was perfect and random in terms of distribution of residuals.

$$\text{FORCE} = 150 - 26.79(\text{HA}) + 1.12(\text{PA}) + 0.741(\text{HA})^2 + 0.0012(\text{PA})^2 \quad (4)$$

Figure 7 shows a 3D surface plot that describes the variations of drilling force with point and helix angles as input variables.

3. 1. Effect of Input Variables on Bone Drilling Force In this section, considering the established model and effective parameters, it is attempted to clarify the effect of point angle and helix angle on drilling axial force. Diagrams in Figures 7 to 10 show the force evolution based on variation in input parameters using developed model by RSM [23].

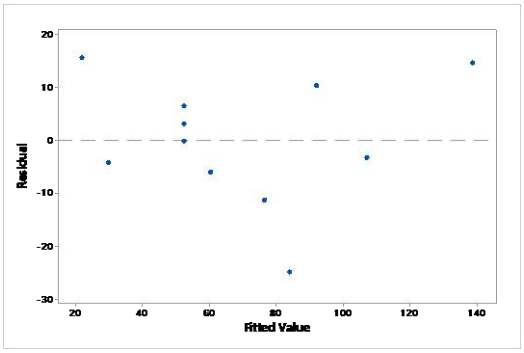

Figure 6. Distribution of residuals when fitted model is compared with data point (point graph produced by Minitab software package)

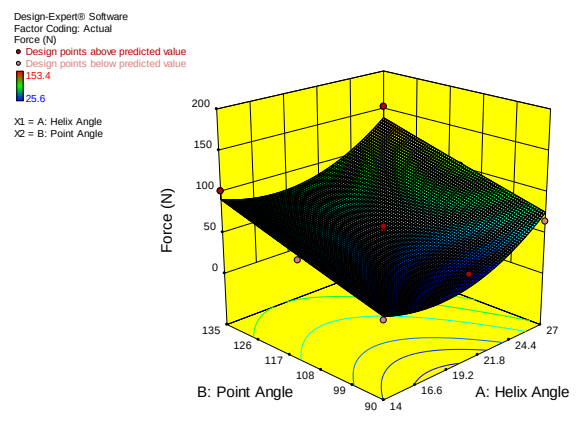

Figure 6. Distribution of residuals when fitted model is compared with data point (point graph produced by Minitab software package)

3. 1. 1. Effect of Helix Angle on Drilling Force Considerong Figures 8, 10 and 11, it can be inferred that with increase in helix angle, firstly axial force experiences a reduction and then it increases. Increasing the helix angle up to 18° eases the chip removal and causes lower frictional and preventive forces between chips and bore wall and therefore causes a reduction in axial force. However, increasing helix angle more than 18°, due to the boosting surface, normal force and frictional forces causes the accumulation of chips in tools slot and therefore, an increase in axial force. In the former part of the diagram, the effect of chip's weight overweighs that of friction but in the latter part the frictional forces are dominant. It can be implied therefore, that for keeping the drilling force minimized, the helix angle should be opted around 18°.

3. 1. 2. Effect of Point Angle on Drilling Force As depicted in Figures 9, 10 and 12, the lower point angle leads to decreasing the axial force. As point angle reduces, the surface of the tool in contact with the bone decreases and therefore penetrating force reduces and material removal is facilitated with lower required force. On the contrary, if the point angle increases, the required force for penetrating in the bone will be increased [26, 27]. When process force is higher, there is higher possibility for bone damage or breakage. Contour of Figure 10 reveals that in order to have the minimized force, helix angle and point angle should be selected as 18 and 90, respectively.

3. 1. 3. Sobol Sensitivity Analysis of Point and Helix Angles on Axial Drilling Force As Before considering the Sobol sensitivity analysis, some points should be presented based of managerial insight. In using the Sobol method, the regression equation must be sufficiently accurate. Changes should be made between test intervals and the experimental data should be accurate enough.

Also, as the dimension of input parameters has no effect on the accuracy of the analysis, there is no sensitivity on the units of input parameters. Considering

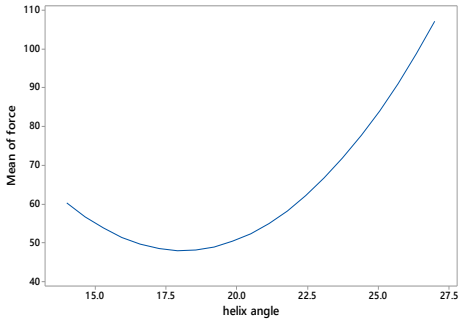

Figure 8. Effect of helix angle on drilling force

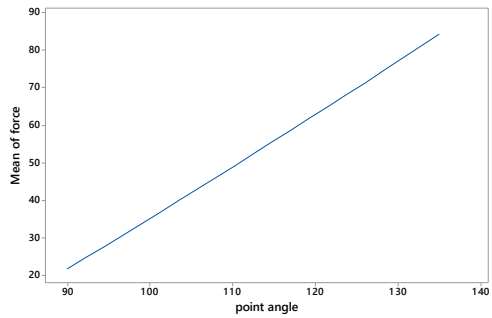

Figure 9. Effect of point angle on drilling force

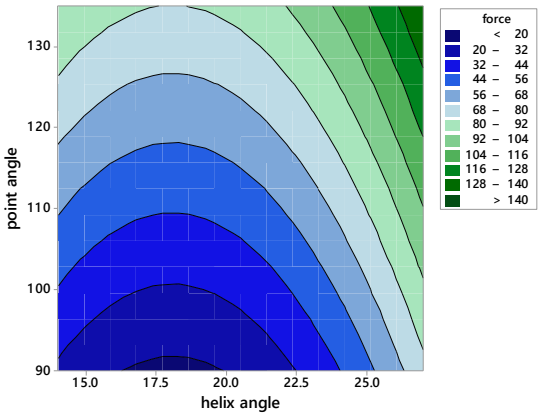

Figure 10. 2D contour plot of drilling force with point and helix angles as input variables

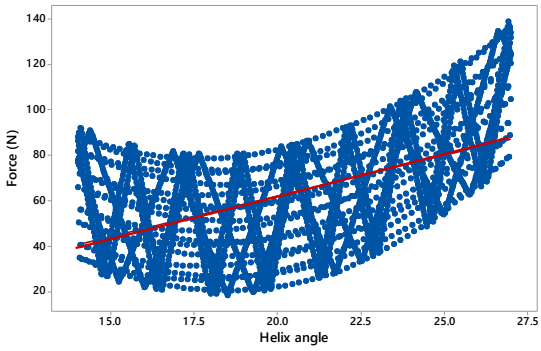

Figure 11. Sensitivity analysis of drilling force with variation in helix angle

Figures 11 and 12, along with ANOVA in RSM, it is inferred that within defined ranges of the point and helix angles, and considering the variation of all parameters at the same time, point and helix angle are similarly effective on drilling force, since, the slope of the diagrams which defines the influence of each parameter is similar for both parameters. Figure 13 shows the results of sensitivity analysis using Sobol method which confirms the produced results. Figure 13 illustrates the effectiveness of input parameters using Sobol method in which all input parameters can vary at the same time, by using SIMLAB software [23].

3. 1. 4. Optimization of Axial Force in Bone Drilling Process and Comparison with Surgery Tool and Standard Tools Considering the analysis over the drilling force, optimization of input variables to achieve the minimum drilling force was followed. Computing the minimum drilling force from the model and taking into account the desirability limit, the optimization result is shown in Figure 14. Optimum results and validation

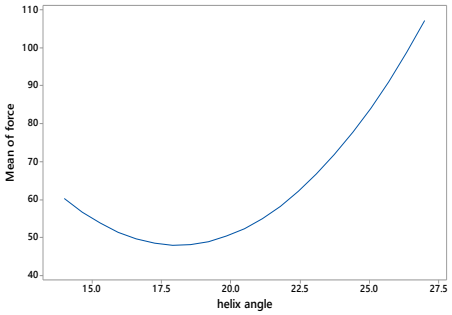

Figure 12. Sensitivity analysis of drilling force with variation in point angle

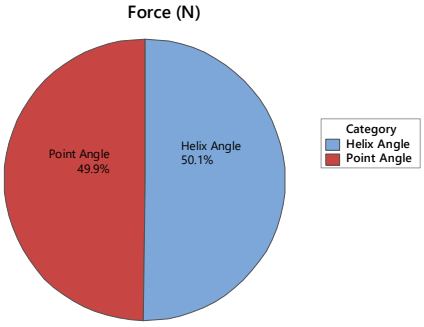

Figure 13. Effect of helix and point angles of drilling force obtained by Sobol sensitivity analysis

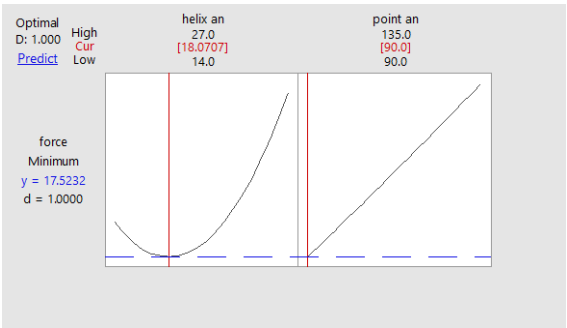

Figure 14. Parameter optimization to achieve minimum drilling force (produced by Minitab software package)

results are listed in Table 4. Moreover, optimum drilling force reported by Farnworth [14], Fuchsberger [12], Green [15] and Natali [13] is presented in Table 5 with the results of current study. Table 5 shows that considering point angle of 90 and helix angle of 18 the minimum force happened.

TABLE 4. Comparison of the optimum combination between experimental and established model

Force (N)	P.A	H.A	Optimization
17.52	90	18	Regression equation
18.40	90	18	Experiment
4.7%	-	-	Error %

TABLE 5. Comparison of optimum states in bone drilling process among different studies

	H.A	P.A	FORCE
Natali et al. [28]	24.0	118.0	82.7
Farnworth et al. [29]	27.0	130.0	132.7
Green et al. [15]	28.0	118.0	129.7
Pandey et al. [12]	30	118	162.4
Standard Surgery drill bit [16]	14	90	30.7
Standard drill bit [16]	26	118	103.2
Holler [16]	27	105	97.5
This research	18.0	90.0	18.4

4. CONCLUSION

In this study using RSM, modeling and optimization of the bone drilling process was followed. Point and helix angles are considered as input parameters and maximum drilling force during the process was taken as the output. The governing second order regression equation was derived and its accuracy was examined. Considering analysis performed, following findings can be highlighted:

1. Regression model can accurately predict drilling tool within the range of input parameters.
2. The results showed that with an increase in the point angle, the contact surface between tool and bore wall expands which boosts frictional forces leading to increase in axial force in bone drilling process.
3. In case of the effect of helix angle on axial force in bone drilling, there is an optimum value. Increasing helix angle up to 18 facilitates chip removal and decreases friction and consequently causes a lower drilling force. However, more raise (upper than 18) in helix angle, leads to a higher drilling force due to higher surface normal and frictional force.
4. Sobol sensitivity analysis quantitatively revealed the effect of each input parameters on drilling force. Accordingly, helix angle has the effectiveness of 50.1% and point angle has the effectiveness of 49.9%.
5. Considering the optimization performed, point angle of 90 and helix angle of 18 results in the lowest axial drilling force in cortical bone drilling process.
6. Drilling force by presented optimum combination (point angle of 90, helix angle of 18 and tool diameter of 3.5 mm) is lower than that by either standard metal drilling tool or surgery tool. This finding can assist tool design at its initial stages.

5. REFERENCES

1. Singh, R. P., Pandey, P. M., Behera, Ch., Mridha, A. R. "Effects of rotary ultrasonic bone drilling on cutting force and temperature in the human bones.", ***Proceedings of the IMechE, Part H: Journal of Engineering in Medicine,*** (2020). DOI: 10.1177/0954411920925254
2. Ying, Zh., Shu, L., Sugita, N. "Experimental and Finite Element Analysis of Force and Temperature in Ultrasonic Vibration Assisted Bone Cutting.", ***Annals of Biomedical Engineering,*** Vol. 48, (2020), 1281–1290. DOI: 10.1007/s10439-020-02452-w
3. Shu, L., Li, Sh., Terashima, M., Bai, W., Hanami, T., Hasegawa, R., Sugita, N. "A novel self-centring drill bit design for low-trauma bone drilling.", ***International Journal of Machine Tools and Manufacture,*** Vol. 154, (2020), 103568, DOI: 10.1016/j.ijmachtools.2020.103568
4. Zhang, A., Bian, C., Zhang, X., Zhang, J., Liu, Z., Zhang, S. "Effect of feed condition on thrust force and torque during continuous and step-by-step drilling of cortical bone.", ***Procedia CIRP,*** Vol. 89, (2020), 201-206. DOI: 10.1016/j.procir.2020.05.143
5. Gupta, V., Singh, R. P., Pandey, P. M., Gupta, R. "In vitro comparison of conventional surgical and rotary ultrasonic bone drilling techniques.", ***Proceedings of the IMechE, Part H: Journal of Engineering in Medicine,*** (2020). DOI: 10.1177/0954411919898301
6. Sui, J., Sugita, N. "Experimental Study of Thrust Force and Torque for Drilling Cortical Bone.", ***Annals of Biomedical Engineering,*** Vol. 47, (2019), 802-812. DOI: 10.1007/s10439-018-02196-8
7. Sarparast, M., Ghoreishi, M., Jahangirpoor, T., Tahmasbi, V. "Modelling and optimisation of temperature and force behaviour in high-speed bone drilling.", ***Biotechnology & Biotechnological Equipment,*** Vol. 33, No. 1, (2019), 1616-1625. DOI: 10.1080/13102818.2019.1684841
8. Alam, K., Piya, S., Al-Ghaithi, A., Silberschmidth, V. "Experimental investigation on the effect of drill quality on the performance of bone drilling.", ***Biomedical Engineering,*** Vol. 65, No. 1, (2019), 113-120. DOI: 10.1515/bmt-2018-0184
9. Zolfaghari, M., Ghoreishi, M., Tahmasbi, V. "Temperature in bone drilling process: Mathematical modeling and Optimization of effective parameters.", ***International Journal of Engineering, Transactions A: Basics,*** Vol. 29, No. 7, (2016), 946-953. DOI: 10.5829/idosi.ije.2016.29.07a.09
10. Singh, G., Jain, V., Gupta, D., Sharma, A. "Parametric effect of vibrational drilling on osteonecrosis and comparative histopathology study with conventional drilling of cortical bone.", ***Proceedings of the IMechE, Part H: Journal of Engineering in***

Medicine, Vol. 232, No. 10, (2018), 975-986. DOI: 10.1177/0954411918794983

11. Augustin, G., Zigman, T., Davila, S., Udilljak, T., Staroveski, T., Brezak, D., Babic, S. "Cortical bone drilling and thermal osteonecrosis.", ***Clinical Biomechanics (Bristol, Avon),*** Vol. 27, No. 4, (2011), 313-325. DOI: 10.1016/j.clinbiomech.2011.10.010
12. Pandey, R. K., Panda, S. S. "Evaluation of delamination in drilling of bone.", ***Medical Engineering and Physics,*** Vol. 37, No. 7, (2015), 657-664. DOI: 10.1016/j.medengphy.2015.04.008
13. Tuijthof, G., Frühwirt, C., Kment, C. "Influence of tool geometry on drilling performance of cortical and trabecular bone.", ***Medical Engineering and Physics,*** Vol. 35, No. 8, (2013), 1165-1172.
14. Singh, G., Jain, V., Gupta, D., Ghai, A. "Optimization of process parameters for drilled hole quality characteristics during cortical bone drilling using Taguchi method.", ***Journal of the Mechanical Behavior of Biomedical Materials,*** Vol. 62, (2016), 355-365. DOI: 10.1016/j.jmbbm.2016.05.015
15. Green, S. A., Dahl, M. T., Intramedullary Limb Lengthening. Gewerbestrasse: Springer International Publishing, 2017.
16. Höller, C., Technical and Economic Analysis of the Process of Surgical Bone Drilling and Improvement Potentials. Master's Theses, Graz University of Technology, 2015.
17. Tahmasbi, V., Ghoreshi, M., Zolfaghari, M. "Temperature in bone drilling process: Mathematical modeling and Optimization of effective parameters.", ***International Journal of Engineering, Transactions A: Basics,*** Vol. 29, No. 7, (2016), 946-953. DOI: 10.5829/idosi.ije.2016.29.07a.09
18. Sui, J., Sugita, N. "Experimental Study of Thrust Force and Torque for Drilling Cortical Bone.", ***Annals of Biomedical Engineering,*** Vol. 47, No. 3, (2019), 802-812. DOI: 10.1007/s10439-018-02196-8
19. Ghoreishi, M., Tahmasbi, V. "Optimization of material removal rate in dry electro-discharge machining process.", ***Modares Mechanical Engineering,*** Vol. 14, No. 12, (2015), 113-121.
20. Montgomery, D. C., Design and Analysis of Experiments: Second Edittion. New York: John Wiley & Sons, 2008.
21. Hou, T. H., Su, C. H., Liu, W. L. "Parameters optimization of a nano-particle wet milling process using the Taguchi method, response surface method and genetic algorithm.", ***Powder Technology,*** Vol. 173, No. 3, (2007), 153-162. DOI: 10.1016/j.powtec.2006.11.019
22. Sobol, I. M. "Global sensitivity indices for nonlinear mathematical models and their Monte Carlo estimates.", ***Mathematics and Computers in Simulation,*** Vol. 55, No. 1-3, (2001), 271-280. DOI: 10.1016/S0378-4754(00)00270-6
23. Korayem, M. H., Rastegar, Z., Taheri, M. "Sensitivity analysis of nano-contact mechanics models in manipulation of biological cell.", ***Nanoscience and Nanotechnology,*** Vol. 2, No. 3, (2012), 49-56. DOI: 10.5923/j.nn.20120203.02
24. Wang, W., Shi, Y., Yang, N., Yuan, X. "Experimental analysis of drilling process in cortical bone.", ***Medical Engineering and Physics,*** Vol. 36, No. 2, (2014), 261-266. DOI: 10.1016/j.medengphy.2013.08.006
25. Alam, K., Ghodsi, M., Al-Shabibi, A., Silberschmidt, V. "Experimental Study on the Effect of Point Angle on Force and Temperature in Ultrasonically Assisted Bone Drilling.", ***Journal of Medical and Biological Engineering,*** Vol. 38, No. 2, (2018), 236-243. DOI: 10.1007/s40846-017-0291-8
26. Knight, W. A., Boothroyd, G., Fundamentals of metal machining and machine tools. Florida: CRC Press, 2005.
27. Altintas, Y., Manufacturing automation: metal cutting mechanics, machine tool vibrations, and CNC design. Cambridge: Cambridge university press, 2012.
28. Natali, C., Ingle, P., Dowell, J. "Orthopaedic bone drills–can they be improved? Temperature changes near the drilling face.", The Journal of Bone and Joint Surgery. British volume, Vol. 78-B, No. 3, (1996) 357-362. DOI: 10.1302/0301-620X.78B3.0780357
29. Farnworth, G., Burton, J., "Optimization of drill geometry for orthopaedic surgery.", in Proceedings of the Fifteenth International Machine Tool Design and Research Conference 1975. Springer, 10.1007/978-1-349-01986-1_27

Persian Abstract

چکیده

یکی از رایج ترین فرآیندهای ماشینکاری در درمان های پزشکی، فرآیند سوراخکاری استخوان است. طی سوراخکاری استخوان، نیروی فرآیند بیش از حد می تواند سبب شکستگی، شروع ترک و آسیب شدید به بافت استخوانی شود. در این مقاله، یک مطالعه سیستماتیک با استفاده همزمان از روش پاسخ سطح، آنالیز حساسیت بر مبنای روش سوبل و آنالیز رگرسیون به منظور بررسی اثر زوایای مارپیچ و رأس مته به عنوان مهمترین پارامترهای هندسی بر نیروی وارد شده بر استخوان حین فرآیند سوراخکاری انجام می شود. ابتدا، با استفاده از طراحی آزمایش ها و روش پاسخ سطح، نیروی وارد شده بر استخوان مدلسازی شده و معادله رگرسیون خطی مرتبه دوم حاکم بر آن استخراج و تایید می گردد. سپس با استفاده از آنالیز حساسیت سوبل، با توانایی تعیین مقدار حساسیت، تلاش می شود که اثر پارامترهای ورودی بر نیروی سوراخکاری بررسی شود. نهایتاً، بهینه سازی پارامترهای ورودی فرآیند به منظور یافتن بهترین ترکیب که منجر به دستیابی به نیروی سوراخکاری مورد نظر شده دنبال می گردد. حداقل نیروی سوراخکاری، در محدوده پارامترهای ورودی، با زاویه رأس ۹۰ درجه و زاویه مارپیچ ۱۸ درجه به طور همزمان اتفاق می افتد. حداقل نیرو کمتر از نیرو در جراحی و ابزارهای استاندارد می باشد. نتایج نشان می دهند که افزایش در زاویه رأس منجر به افزایش نیروی سوراخکاری می شود. همچنین، نتیجه گرفته می شود که یک مقدار بهینه برای استفاده از زاویه مارپیچ در فرآیند سوراخکاری استخوان با حداقل نیروی وارد شده وجود دارد.

IJE TRANSACTIONS B: Applications Vol. 34, No. 02, (February 2021) 536-546

International Journal of Engineering

Journal Homepage: www.ije.ir

Effects of Road Roughness, Aerodynamics, and Weather Conditions on Automotive Wheel Force

S. M. Saleh Mousavi-Bafrouyi[a], K. Reza Kashyzadeh*[b], S. M. Khorsandijou[a]

[a] *Department of Mechanical Engineering, South Tehran Branch, Islamic Azad University, Tehran, Iran*
[b] *Department of Mechanical and Instrumental Engineering, Academy of Engineering, Peoples' Friendship University of Russia (RUDN University), 6 Miklukho-Maklaya Street, Moscow, 117198, Russian Federation*

PAPER INFO

Paper history:
Received 09 October 2020
Received in revised form 31 October 2020
Accepted 06 November 2020

Keywords:
Aerodynamical Force
Air Temperature
Half-vehicle Model
Humidity
Road Roughness
Weather Conditions
Wheel Force

ABSTRACT

Taking road roughness, aerodynamics, and weather conditions, viz temperature and humidity, into consideration, the force applied to the wheel of a half-vehicle model traveling at constant speed has been calculated. A D-type rough horizontal road according to ISO 8606 evaluations was chosen for the experiment and the surface profile of which was measured by means of a topographic camera of Leica series to acquire discrete data to model the road roughness. The data have been converted from discrete points into smooth continuous linear functions with quadratic blends, because of the fact that the governing differential equations of motion of the vehicle model require the road roughness and the time rate of change of them. The line of action of wind or aero-dynamical force applied to vehicle model has been assumed to pass through the vehicle mass center. The vibrations of the half-vehicle model have been found via the Runge-Kutta method. Design of Experiments (DoE) has been used to investigate the effects of air temperature and humidity on the front and rear wheels. It was found that the value of force applied to the front wheel is far greater than that applied to the rear wheel (about 16.5%). Also, the role of the air temperature is much more effective on the wheel force than the air humidity. Moreover, the force of the front wheel is directly related to the values of weather parameters and the force of the rear wheel is inversely related to it.

***doi**: 10. 5829/ije.2021.34.02b.27*

Nomenclature

Ω	Spatial frequency	X_s	Vertical displacement of mass body
$Sg(\Omega)$	Power spectral density	X_{uf}	Vertical displacement of front tire
W	Total weight	X_{ur}	Vertical displacement of rear tire
W_f	Front wheel force	y_f	Applied external excitation to front wheel
W_r	Rear wheel force	y_r	Applied external excitation to rear wheel
α	Slope of road	K_{sf}	Front suspension stiffness
L	Distance between rear and front axles	K_{uf}	Front tire stiffness
b	Distance between front axle and gravity center	K_{sr}	Rear suspension stiffness
c	Distance between rear axle and gravity center	K_{ur}	Rear tire stiffness
h	Height of gravity center	C_{sf}	Front suspension damping
D_A	Aerodynamic force	C_{uf}	Front tire damping
h_a	Height position of aerodynamic loading	C_{sr}	Rear suspension damping
R_{hz}	Vertical load of tow	C_{ur}	Rear tire damping
R_{hx}	Longitudinal load of tow	L_f	Distance between front axle and center gravity
h_h	Height position of tow loading	L_r	Distance between rear axle and center gravity
d_h	Distance between location of tow loading and rear axle	V	Vehicle velocity

*Corresponding Author Institutional Email: *reza-kashi-zade-ka@rudn.ru* (K. Reza Kashyzadeh)

Please cite this article as: S. M. Saleh Mousavi-Bafrouyi, K. Reza Kashyzadeh, S. M. Khorsandijou, Effects of Road Roughness, Aerodynamics, and Weather Conditions on Automotive Wheel Force, International Journal of Engineering, B: Applications Vol. 34, No. 02, (2021) 536-546

F_{xf}	Thrust force of front wheel	C_d	Drag coefficient
F_{xr}	Thrust force of rear wheel	A	Reference area
R_{xf}	Rolling friction force between the front wheel and the ground	ρ	Air density
R_{xr}	Rolling friction force between the rear wheel and the ground	v	Flow velocity related to the vehicle
M_s	Body mass	P	Absolute pressure
I_s	Inertia moment of body	R	Specific gas constant
M_{uf}	Front tire mass	T	Temperature
M_{ur}	Rear tire mass	B	Barometric pressure
C	Center gravity of vehicle	P_v	Partial vapor pressure
θ	Rotation angle in the pitch motion	$\rho_{\%}$	Density of moist air

1. INTRODUCTION

Tire is a major connecting link between vehicle chassis and road surface, and transfers reaction force from road to the wheel of vehicle. It plays an important role in vehicle stability. The magnitude of the force applied to wheel of vehicle is dependent on vehicle velocity, road roughness, air flow or wind relative to vehicle surface, and weather conditions such as air temperature and humidity.

The road-tire contact force and the reaction force transmitted to vehicle wheel from road under snowy, rainy, and dry weather conditions has been investigated, and the effects of road roughness and weather parameters, namely air temperature, humidity and pressure, have been taken into consideration [1–3]. Influences of vehicle unbalanced-tires and air pressure, temperature and humidity over the dynamical behavior of vehicle have been investigated [4]. Stability and resonance of a one degree of freedom (DoF) quarter-car suspension model with hysteretic nonlinear dampers were studied by Naik and Singru [5]. Vibration of a nonlinear full-vehicle model was analyzed by Fakhraee et al. [6] for investigating the effect of passengers on the vibration. Kashyzadeh et al. [7] revealed the roles of road roughness type and vehicle speed in fatigue life of the steering knuckle, as a highly critical mechanical component of a vehicle. Ahmadi et al. [8] numerically estimated the fatigue life of the spot welds in the body of a vehicle vibrated due to passing over rough roads with various speeds.

Road roughness is referred to as the change of the height of road surface along and/or across the road (Figure 1). Several types of profilers such as topographic cameras are devices that are commonly used for measuring the profile of road roughness. For measuring road roughness, a few empirical procedures have been proposed by Sayers et al [9, 10]. Data collection of roughness of roads was accomplished by Sayers and Karamihas [11] for the Federal Highway Organization (FHO). González et al. [12] utilized accelerometers for estimating road roughness. Johannesson and Rychlik [13] applied time-invariant Laplace transform in order to model the features of road roughness in accordance with ISO and IRI standards.

Vehicle dynamics has been simulated by Imine et al. [14] who took road roughness profile and road-tires contact force into consideration. Vehicle passive and semi-active suspension systems have been analyzed under the influence of road roughness by Reza Kashyzadeh et al. [15]. Samandari and Rezaee [16] have investigated the influence of road roughness over the dynamical behavior of quarter and half-vehicle models with nonlinear springs and dampers.

Performance of suspension system was optimized by Shojaeefard et al. [17] via multi-objective theory and the optimum stiffness for spring and the optimum coefficient for damper were found for driver seat of a five DoF vehicle model passing over a rough road with random profile. Recently, various data mining techniques and DOE algorithms have been highly regarded by automotive engineers in order to optimize and improve product quality. Naga Raju et al. [18] have used Taguchi design algorithm-based on the finite element simulation to assess the static behavior of leaf spring with the aim of choosing the most suitable material for its manufacture. Also, the grey-fuzzy-Taguchi method has been used to optimize the beam-like structure of a vehicle body [19]. Zhang and Wang [20] have investigated and optimized the suspension system of the half-vehicle model integrated with an arm-teeth regenerative shock absorber by utilizing Taguchi approach.

Based on the literature review, many researchers have studied the effects of road conditions on the dynamic behavior of auto parts. However, other influential parameters such as weather conditions (i.e., air temperature, humidity, wind speed and wind direction)

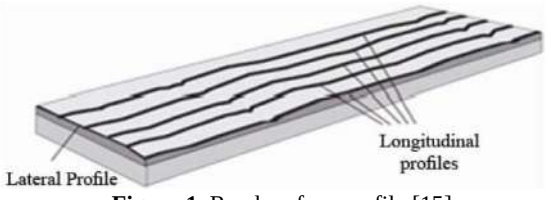

Figure 1. Road surface profile [15]

have been rarely considered (there is only qualitative expression for them). Therefore, one of the novelty of the present research is to investigate the effects of different parameters simultaneously on the vehicle wheel forces. In this regard, the rear- and front-wheel force were calculated based on the parameters variations including road roughness (laboratory data using topographic camera), aerodynamics, and weather factors. Also, it was done by assuming constant vehicle velocity and neglecting slope of road, dive acceleration, and load of tow. Next, the Runge-Kutta (RK) method was used to solve the vibration equations of half-car model. Eventually, for the first time, Taguchi approach (TA) as one of the well-known DOE techniques was applied to analyze the sensitivity of the wheel forces to parameter changes. The most important and ineffective parameters on the front and rear wheel forces were reported.

2. ROAD ROUGHNESS MEASUREMENT

Different methods have been presented to evaluate road roughness. Among all of them, there are two common and practical methods. The First method uses a topographic camera that directly records ups and downs of the road (geometrical measurement). In other words, road roughness are measured using static devices such as topographic camera. Figure 2 presents a schematic of the implementation of this process [9]. Another method is response type approaches which work on the basis of data collected from different types of sensors installed in different parts of the car [21–23]. Therefore, these methods are called dynamic data collection. It means that the equipment is installed on the car body or axle and data is taken while the car is moving. These equipments include laser profilometer, mobile measuring devices, accelerometers, h-sensor, and vibrometer. After data collection, a calibrated relationship can be extracted using a programming code (MATLAB) and road classification standards based on the Power Spectral Density (PSD) function.

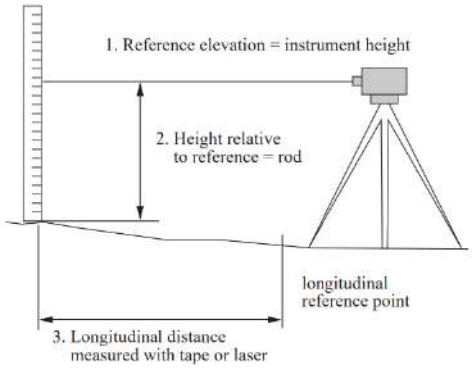

Figure 2. Schematic of topographic camera performace for measuring road profile [9]

In the present research, road data collection was performed using topographic camera of Leica series of total Station TS02 model (Figure 3). In this camera model, angular and longitudinal accuracy are 7 second and 2 picometer, respectively.

The mapping was conducted on an asphalt suburban road by recording 500 points. Next, numerical integration method, i.e., Simpson's rule was used to calculate Power Spectral Density (PSD) function. Figure 4 depicts the PSD of asphalt suburban road based on the mapping data.

The mentioned road was considered as D-class compared to the road classification of ISO-8606 [24]. According to this standard, as illustrated in Figure 5, the road roughness approximates by two straight lines and different slopes in the log-log scale.

The PSD in terms of spatial frequency (1/wavelength) is calculated from the following formula [24]:

$$if \quad \Omega \le \frac{1}{2\pi} \quad then \quad S_g(\Omega) = S_g(\Omega_0) \times \left(\frac{\Omega}{\Omega_0} \right)^{-N_1} \tag{1}$$

$$if \quad \Omega > \frac{1}{2\pi} \quad then \quad S_g(\Omega) = S_g(\Omega_0) \times \left(\frac{\Omega}{\Omega_0} \right)^{-N_2} \tag{2}$$

Figure 3. Topographic camera of leica series of total station TS02 model

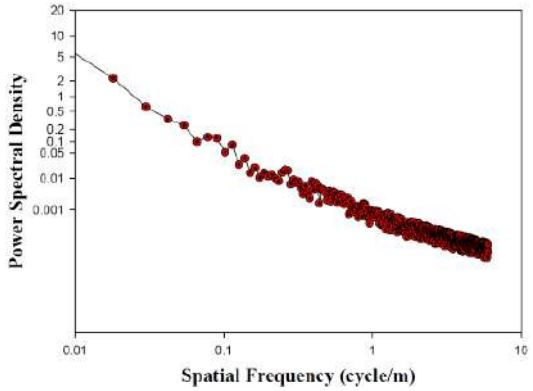

Figure 4. PSD of asphalt suburban road based on the mapping data in the present research

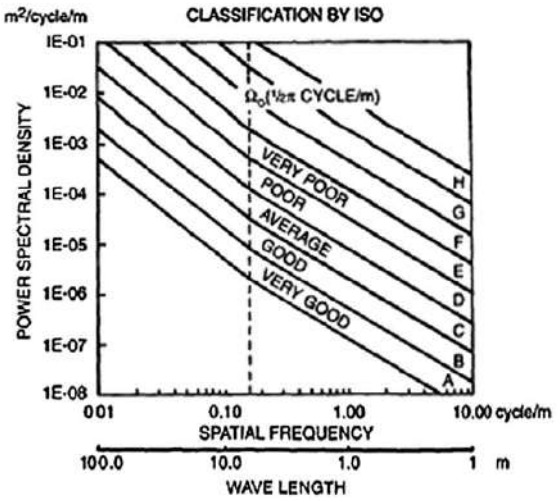

Figure 5. Proposed road roughness classification by ISO (International Standard Organization) [24]

Table 1 presents the value of $S_g(\Omega_0)$ considering the spatial frequency of $\Omega_0 = \frac{1}{2\pi}\ Cycle/m$ for different roads [25]. Also, constant coefficients of N_1 and N_2 are 2.0 and 1.5, respectively.

Obviously, the road profile is constant, nevertheless, the tires cannot touch all the roughness. In other words, there is a difference between real road roughness and its simulation as the external excitation. Moreover, the jump phenomenon occurs at high vehicle speeds. Therefore, the vehicle, especially wheels and tires, does not experience some parts of road roughness. However, in some cases, these jumps can be considered as new elevation with larger amplitude. In the previous researches, the second author of the current paper has studied the effect of vehicle velocity on the simulation of road roughness [26]. The results showed that low and high speeds had a negligible effect on high quality road (e.g., road class A). Furthermore, these effects will be visible on the bad quality road like road class E.

In the present research, the vehicle velocity of 80 km/h was considered to evaluate excitation. Selection of this speed may be justified; as it is allowable driving speed on suburban roads of different Asian countries. Figure 6 illustrates the time history of this excitation.

TABLE 1. Parametrical classification of road roughness suggested by ISO [24, 25]

Road Class	Degree of Roughness Range	$S_g(\Omega_0)\cdot 10^{-6}\ m^2/cycles/m$ Geometric Mean
A (Very Good)	< 8	4
B (Good)	8 – 32	16
C (Average)	32 – 128	64
D (Poor)	128 – 512	256
E (Very Poor)	512 – 2048	1024
F	2048 – 8192	2048
G	8192 – 32768	4096
H	More than 32768	16384

3. VERTICAL VIBRATION OF THE HALF-CAR MODEL

Figure 7 illustrates a half-car model with four Degrees of Freedom (DoF). The Lagrange's method was used to derive vibration equations (Equation (3)).

$$[M][\ddot{S}]+[C][\dot{S}]+[K][S]=[F] \tag{3}$$

where

$$[K]=\begin{bmatrix} K_{sr}+K_{sf} & -K_{sf} & -K_{sr} & K_{sf}L_f-K_{sr}L_r \\ -K_{sf} & K_{sf}+K_{uf} & 0 & -K_{sf}L_f \\ -K_{sr} & 0 & K_{sr}+K_{ur} & K_{sr}L_r \\ K_{sf}L_f-K_{sr}L_r & -K_{sf}L_f & K_{sr}L_r & K_{sr}L_r^{\,2}+K_{sf}L_f^{\,2} \end{bmatrix} \tag{4}$$

$$[C]=\begin{bmatrix} C_{sr}+C_{sf} & -C_{sf} & -C_{sr} & C_{sf}L_f-C_{sr}L_r \\ -C_{sf} & C_{sf}+C_{uf} & 0 & -C_{sf}L_f \\ -C_{sr} & 0 & C_{sr}+C_{ur} & C_{sr}L_r \\ C_{sf}L_f-C_{sr}L_r & -C_{sf}L_f & C_{sr}L_r & C_{sr}L_r^{\,2}+C_{sf}L_f^{\,2} \end{bmatrix} \tag{5}$$

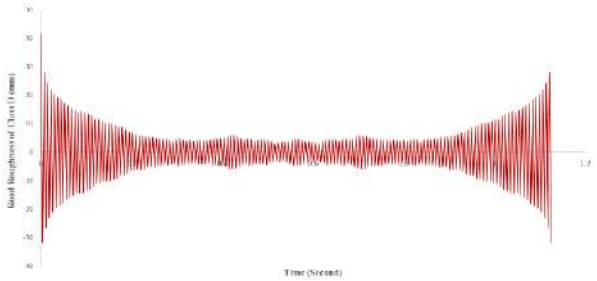

Figure 6. Time-history of excitation for an asphalt suburban road (Class D)-vehicle velocity of 80 km/h

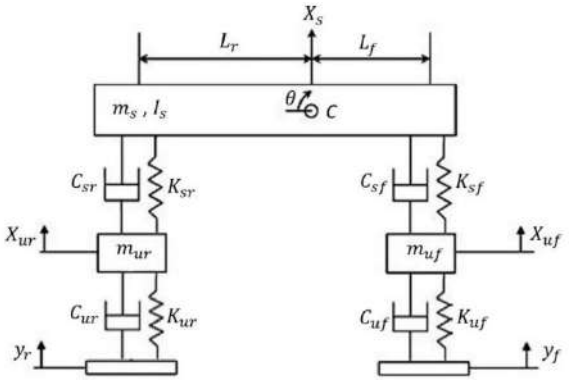

Figure 7. The 4-DoF half-car model (bicycle model) considering two separated external excitations [27]

$$[M]=diag(M_s, M_f, M_r, I_s)=\begin{bmatrix} M_s & 0 & 0 & 0 \\ 0 & M_f & 0 & 0 \\ 0 & 0 & M_r & 0 \\ 0 & 0 & 0 & I_s \end{bmatrix} \quad (6)$$

$$[F]=\begin{bmatrix} 0 & 0 \\ 0 & C_{uf} \\ C_{ur} & 0 \\ 0 & 0 \end{bmatrix}\begin{bmatrix} \dot{Y}_r \\ \dot{Y}_f \end{bmatrix}+\begin{bmatrix} 0 & 0 \\ 0 & K_{uf} \\ K_{ur} & 0 \\ 0 & 0 \end{bmatrix}\begin{bmatrix} Y_r \\ Y_f \end{bmatrix} \quad (7)$$

The elements of the above matrices, viz $[M],[C],[K],[S],[F],[\dot{S}],[\ddot{S}],Y_r,Y_f,M_s,M_f,M_r,I_s,L_f,L_r,K_{sr},K_{sf},K_{uf},K_{ur},C_{sr},C_{sf},C_{uf}$ and C_{ur} are introduced in Nomenclature.

The body and suspension system containing tire were considered as sprung and un-sprung masses, respectively. The Runge-Kutta (RK) method was used to solve coupled equations of vibration.

The motion Equation (3) and the excitation forces (7) show that a travelling half-car model is excited by the roughness and the time rate of change of them. The speed of the travelling half-car model is assumed 80 km/h in this article. Time rate of change of the road roughness can appropriately be achieved neither from discretely-acquired road roughness nor from non-smooth reconstruction of the road roughness. As a result, a smooth reconstruction of the road roughness is required, because, contrary to non-smooth curves and discrete data, smooth curves are differentiable. In this regard, a smooth curve including linear functions with quadratic blends has been proposed in Appendix A for smooth reconstruction of the road roughness from discretely-acquired data [28].

The governing differential equations of motion of the vehicle model requires road roughness and the time rate of change of the roughness as excitation. The excitations to the rear and front wheels have been considered the same, but with a delay time. The delay time depends on the vehicle velocity and the distance between the two axles, and is calculated using the following equation.

$$time\ delay:\quad t=\frac{L}{speed}=\frac{2415\ mm}{80\ km/hr}=0.108675\ s \quad (8)$$

The road roughness are available in discrete form from experiment, but the smooth continuous form of them are required by the vehicle governing equations as well as the continuous time-rate of change of them. As a smooth continuous form of the road roughness, the linear functions with quadratic blends according to Appendix A and Figure 8 has been taken into consideration. The reconstruction by linear functions smoothly connected by quadratic functions are plotted in black color in Figure 8 where a non-smooth continuous reconstruction of road roughness by linear functions is plotted in red.

Expressions (A1)-(A7) of Appendix A show how one might construct a smooth countinuous function for road roughness, namely a smooth function composed of adequate linear functions being smoothly connected to each other. Obviously, the rate of change of the smooth function is a non-smooth continuous function.

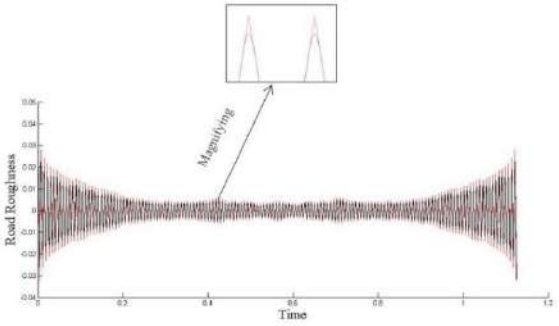

Figure 8. Smooth reconstruction of road roughness by linear functions with quadratic blends (plotted in black) according to Apendix A, and non-smooth reconstruction of road roughness by linear functions (plotted in red) from discretely-acquired road roughness (time axis in seconds represents the axis of distance divided by the vehicle velocity of 80 km/h).

Eventually, the height fluctuation of gravity center was extracted. The values of parameters used in this research based on an Iranian passenger car are reported in Table 2 [29].

4. WHEEL FORCE CALCULATION IN TERMS OF WEATHER PARAMETERS

Dynamic equations were derived for a full vehicle on steep road. A schematic of these forces and their location is shown in Figure 9.

TABLE 2. Vehicle parameters [29]

Symbol	Value	Unit
m_s	1347	kg
I_s	2160	Kg. m
m_{uf}	42.218	kg
m_{ur}	42.218	kg
K_{sf}	35900	N/m
K_{uf}	173000	N/m
K_{sr}	33100	N/m
K_{ur}	173000	N/m
C_{sf}	1368	Ns/m
C_{uf}	3105	Ns/m
C_{sr}	1368	Ns/m
C_{ur}	3105	Ns/m
L_f	1.090624	m
L_r	1.324376	m

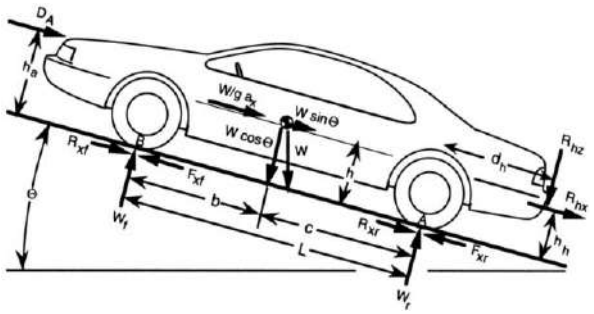

Figure 9. Vehicle dynamics analysis on the steep road [27]

The wheel forces were achieved by using torque calculation at point A and B locating under the rear- and front-tires, respectively (Equation (9) and Equation (10)). Clearly, the sum of torques at point A is zero by neglecting dive acceleration [27].

$$W_f = \frac{-1}{L}\left[D_A\, h_A + \frac{W}{g} a_x\, h + R_{hx}\, h_h + R_{hz}\, d_h + W h \sin(\alpha) + W c \cos(\alpha)\right] \quad (9)$$

$$W_r = \frac{1}{L}\left[D_A\, h_A + \frac{W}{g} a_x\, h + R_{hx}\, h_h + R_{hz}\,(d_h + L) + W h \sin(\alpha) + W b \cos(\alpha)\right] \quad (10)$$

In the present research, the wheel forces were calculated by assuming constant vehicle velocity of 80 km/h and neglecting slope of road, dive acceleration, and load of tow. The drag, in the vehicle aerodynamic is calculated using Equation (11):

$$D_A = \frac{C_d A \rho v^2}{2} \quad (11)$$

Air density is a function of temperature, pressure, and humidity. The air density is about 1.225 kg/m^3 at the sea level and temperature of 15 °C [30]. Figure 10 shows air density vs temperature.

In addition to the above-mentioned conditions, the density of air will vary as humidity content. The water vapor is a relatively light gas compared to diatomic oxygen and nitrogen. Therefore, when water vapor increases, the amount of oxygen and nitrogen decrease per unit volume, and then the density decreases because the mass is decreasing [31]. Figure 11 shows the air density vs humidity. Also, the empirical relation between density and humidity is defined by Equation (12) [31]:

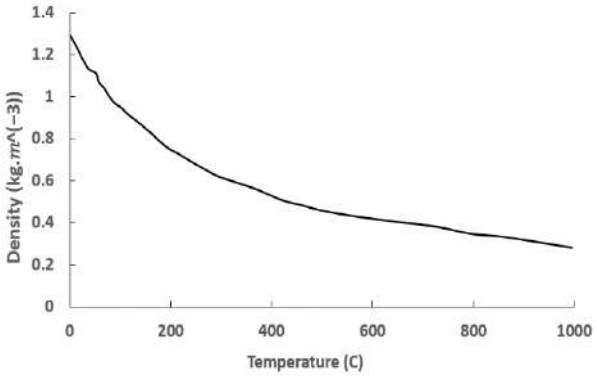

Figure 10. Air density versus temperature [30]

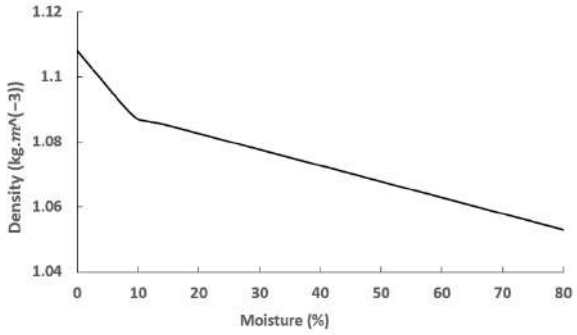

Figure 11. Air density versus humidity [31]

$$\rho_{\%} = 1.2929 \times \frac{273.15}{T} \times \frac{B - 0.3783\, P_v}{1.013 \times 10^5} \quad (12)$$

where T is temperature in Kelvin, B and P_v are barometric pressure and partial vapor pressure in Pascal, respectively.

To study the effect of wind on the wheel forces, time history of wind speed was used based on meteorological data [32]. The wind loading versus time for stormy weather is demonstrated in Figure 12. Moreover, three different wind directions ($\theta = 0°. 90°.\ and\ 180°$) were considered to evaluate wind effect on the wheel forces. Therefore, zero value of θ means the direction of the wind and the movement of the car are the same.

5. DESIGN OF EXPERIMENT

To study the effects of weather parameters on the wheel forces of passenger car, Taguchi Approach (TA) as one of the well-known Design of Experiment (DOE) techniques was used [33–35]. To this end, four parameters, including wind speed, wind direction, air temperature, and air humidity were considered as input variables. Also, the maximum values of rear- and front-wheel forces were considered as output parameters. Different levels of input parameters used in this research are presented in Table 3.

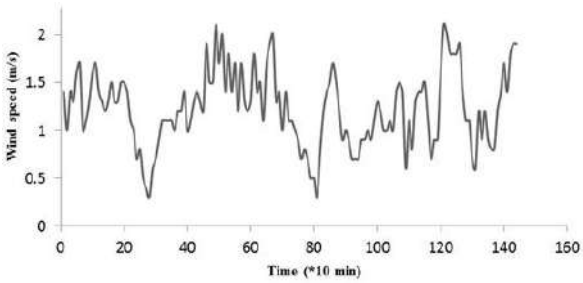

Figure 12. Wind loading versus time for stormy weather [32]

TABLE 3. Variables and their levels used as input data in the present research

Parameters	Symbol	Levels		
		L1	L2	L3
Wind speed (m/s)	V	1	1.2	1.4
Wind direction ($degree$)	θ	0	90	180
Air temperature (℃)	T	0	20	40
Air humidity (%)	M	0	40	80

To perform Taguchi sensitivity analysis, the formulation of smaller is better was considered for both rear- and front-wheel forces. The L9 orthogonal matrix was used as reported in Table 4.

6. RESULTS AND DISCUSSION

The wheel forces variation depends on temperature and humidity are demonstrated in Figures 13 and 14, respectively. As Figure 13-a clearly shows, the front-wheel force increases by increasing air temperature. However, this change is not significant (e.g., raising the temperature from zero to 60 degrees will only lead to a change in front-wheel force about 0.1 %). But, the rear-wheel force decreases by increasing air temperature (Figure 13-b). Also, the effect of temperature changes on the rear-wheel force is greater than its effect on the front-wheel force (the reduction in the rear-wheel force is approximately 0.15 % by increasing the air temperature from zero to 60 degrees). Moreover, it is clear that the value of force on the front wheel is far greater than the force on the rear wheel. In the case of T=20 ℃, the force difference between the rear and front wheels is about 16.5 %.

From Figure 14, as the air humidity increases, the value of force on the front and rear wheels increases and decreases, respectively, but these changes are negligible.

TABLE 4. The Orthogonal Matrix of Taguchi for L9

Run No.	V	θ	T	M
1	L1	L1	L1	L1
2	L1	L2	L2	L2
3	L1	L3	L3	L3
4	L2	L1	L2	L3
5	L2	L2	L3	L1
6	L2	L3	L1	L2
7	L3	L1	L3	L2
8	L3	L2	L1	L3
9	L3	L3	L2	L1

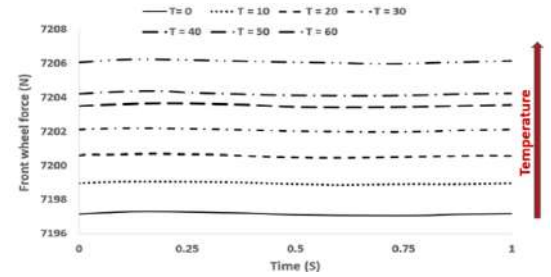

(a) Front wheel

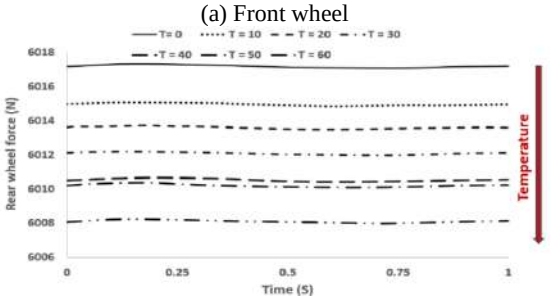

(b) Rear wheel

Figure 13. Effect of air temperature (in celsius) on wheels force

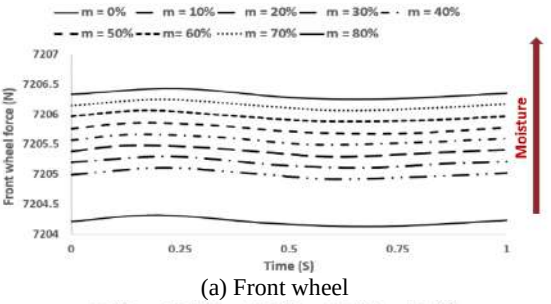

(a) Front wheel

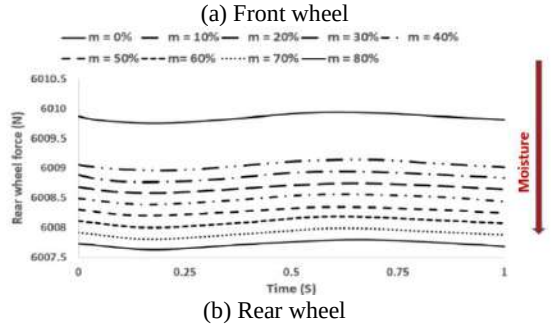

(b) Rear wheel

Figure 14. Effect of air humidity (in percentage) on wheels force

The force changes for both wheels are the same (maximum of 0.03 %).

Next, Figure 15 shows the effect of wind direction on the wheel forces. The value of front-wheel force is maximum when the direction of the wind and the movement of the vehicle are opposite. And in this case, the value of the rear-wheel force is minimal. The results show that the maximum change in force due to the wind direction in the front and rear wheels is approximately 0.14 and 0.17 %, respectively.

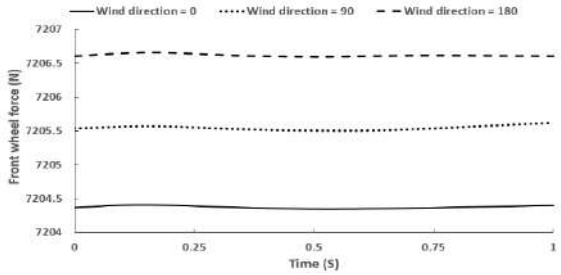

(a) Front wheel

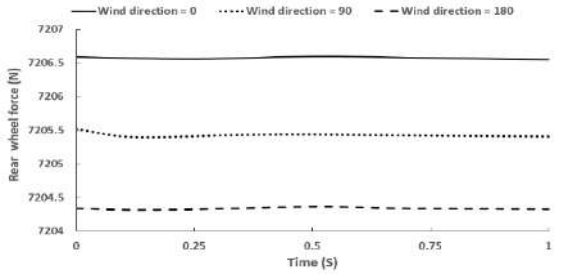

(b) Rear wheel

Figure 15. Effect of wind direction (in degrees) on wheels force

In Taguchi approach, the main effect plots for means and signal to noise ratios were used to compare the wheel force effects against other factors. Figures 16 and 17 show these diagrams for front- and rear-wheel, respectively.

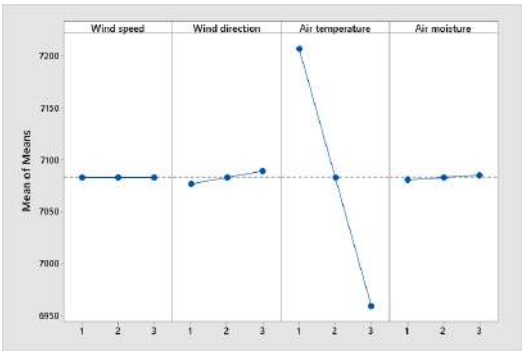

(a) Mean of means

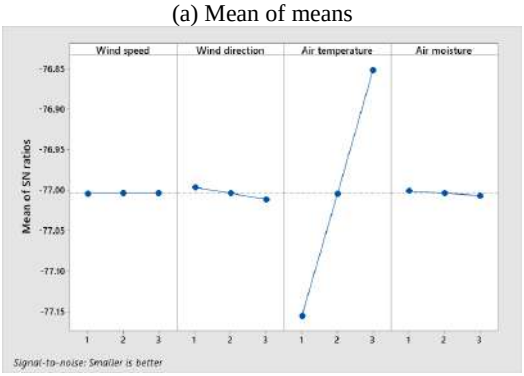

(b) Mean of SN ratios

Figure 16. Means of front wheel force under the influence of wind, temperature, and humidity

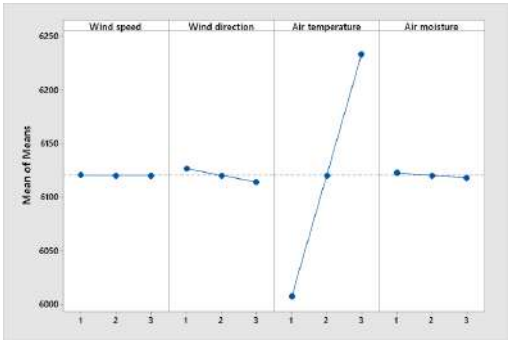

(a) Mean of means

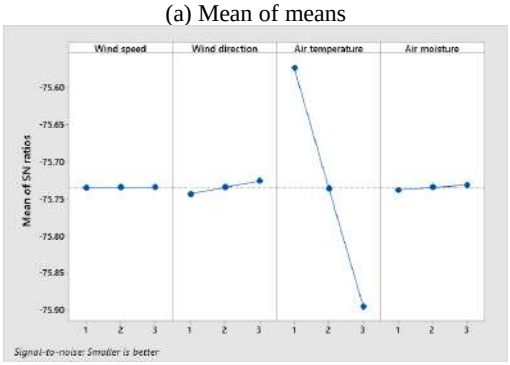

(b) Mean of SN ratios

Figure 17. Means of rear wheel force under the influence of wind, temperature, and humidity

The above-diagrams show that the number of data for parameters wind direction, air temperature, and air humidity is acceptable. But, the results show that the wind speed parameter cannot be discussed. Because, the number of data for this parameter is insufficient or the value range considered for this parameter has no effect on the wheel force. In other words, changes in wind speed on a stormy day are ineffective. Therefore, it is recommended, in future research, to study the effects of wind speed in a stormy day relative to a calm day. Based on the results obtained by Taguchi approach, the wheel force is mainly affected by air temperature (Figure 18). Moreover, the results indicate that air humidity is the most ineffective parameter on the value of force in both front and rear wheels.

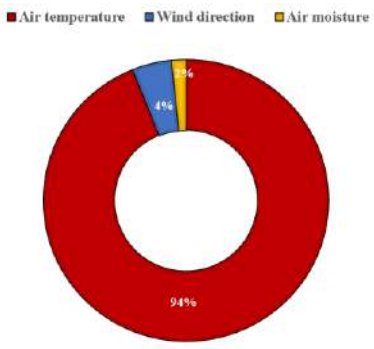

(a) Front wheel force

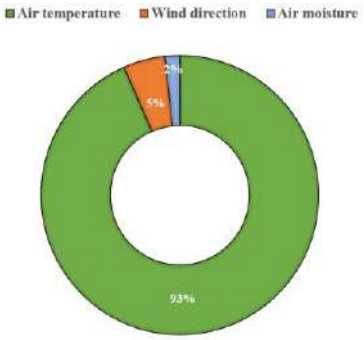

(b) Rear wheel force

Figure 18. Roles of air humidity and wind direction vis-à-vis that of air temperature in wheels forces found based on taguchi sensitivity analysis

7. CONCLUSION

In this study, the wheel forces of a passenger car were calculated in terms of weather parameters. Firstly, road roughness was measured using a topographic camera, then the classification of desired road was determined by utilizing Fast Fourier Transform (FFT) function and comparison with the ISO standard. Road class-D and vehicle velocity of 80 Km/h were considered as external excitation for both front and rear wheels with a delay time. The RK method was used to solve the coupled vibration equations of half-car model, and the height fluctuation of gravity center was extracted. Eventually, dynamic equations were introduced to calculate wheel force in terms of weather parameters. Next, the effects of various parameters (wind speed, wind direction, air temperature, and air humidity) were investigated on the wheel forces using numerical analysis and Taguchi sensitivity analysis. The most important achievements of this research are:

- The value of force applied to the front wheel is far greater than that applied to the rear wheel. The difference between the forces is about 16.5 % at T = 20 ℃.
- By increasing the air temperature, the front wheel force increases and the rear wheel force decreases. The amount of decrease in the rear wheel force is greater than the amount of increase in the front wheel force.
- By increasing the air humidity, the front wheel force very slightly increases and the rear wheel force very slightly decreases.
- The results found through Taguchi approach reveal that the air temperature is the most effective parameter and the air humidity is the least effective parameter with respect to the parameters investigated in this research.
- The results of this research indicate that variations of wind speed on a stormy day have no effect on the wheel forces.

8. ACKNOWLEDGMENTS

This paper has been supported by the RUDN University Strategic Academic Leadership Program.

9. REFERENCES

1. Waluś, K. J., and Olszewski, Z., "Analysis of Tire-road Contact Under Winter Conditions", Proceedings of the World Congress on Engineering 2011 Vol III, London, U.K., (2011), 1–4.
2. Ghandour, R., Victorino, A., Doumiati, M., and Charara, A., "Tire/road friction coefficient estimation applied to road safety", 18th Mediterranean Conference on Control and Automation, MED'10, (2010), 1485–1490. doi:10.1109/MED.2010.5547840
3. Ahn, C. S., Robust Estimation of Road Friction Coefficient for Vehicle Active Safety Systems, PhD dissertation, University of Michigan.
4. Sayers, M. W., Gillespie, T. D., Paterson, W. D. 0, World, T., and Washington, B., Guidelines for Conducting and Calibrating Road Roughness Measurements,University of Michigan, Ann Arbor, Transportation Research Institute, (1986).
5. Naik, R. D., and Singru, P. M., "Resonance, stability and chaotic vibration of a quarter-car vehicle model with time-delay feedback", ***Communications in Nonlinear Science and Numerical Simulation***, Vol. 16, No. 8, (2011), 3397–3410. doi:10.1016/j.cnsns.2010.11.006
6. Fakhraee, J., Mohammad Khanlo, H., Ghayour, M., & Faramarzi, K. (2016). The influence of road bumps characteristics on the chaotic vibration of a nonlinear full-vehicle model with driver. **International Journal of Bifurcation and Chaos**, 26(9), 1650151. DOI: 10.1142/S0218127416501510
7. Reza Kashyzadeh, K., Farrahi, G. H., Shariyat, M., and Ahmadian, M. T., "Experimental accuracy assessment of various high-cycle fatigue criteria for a critical component with a complicated geometry and multi-input random non-proportional 3D stress components", ***Engineering Failure Analysis***, Vol. 90, (2018), 534–553. doi:10.1016/j.engfailanal.2018.03.033
8. Ahmadi, A., Farrahi, G. H., Kashyzadeh, K. R., Azadi, S., and Jahani, K., "A comparative study on the fatigue life of the vehicle body spot welds using different numerical techniques: Inertia relief and modal dynamic analyses", ***Frattura Ed Integrita Strutturale***, Vol. 14, No. 52, (2020), 67–81. doi:10.3221/IGF-ESIS.52.06
9. Sayers, M. W., and Karamihas, S. M., The Little Book of Profiling Basic Information about Measuring and Interpreting Road Profiles, University of Michigan, Ann Arbor, Transportation Research Institute, (1998).
10. Sayers, M. W., Gillespie, T. D., and V Queiroz, C. A., The International Road Roughness Experiment Establishing Correlation and a Calibration Standard for Measurements, University of Michigan, Ann Arbor, Transportation Research Institute, (1986).
11. Sayers, M. W., and Karamihas, S. M., interpretation of road roughness profile data, University of Michigan Transportation Research Institute, (1996).
12. González, A., O'Brien, E. J., Li, Y. Y., and Cashell, K., "The use of vehicle acceleration measurements to estimate road roughness", ***Vehicle System Dynamics***, Vol. 46, No. 6, (2008), 483–499. doi:10.1080/00423110701485050
13. Johannesson, P., and Rychlik, I., "Modelling of road profiles using roughness indicators", ***International Journal of Vehicle Design***, Vol. 66, No. 4, (2014), 317–346. doi:10.1504/IJVD.2014.066068

14. Imine, H., Delanne, Y., and M'Sirdi, N. K., "Road profile input estimation in vehicle dynamics simulation", ***Vehicle System Dynamics***, Vol. 44, No. 4, (2006), 285–303. doi:10.1080/00423110500333840
15. Reza-Kashyzadeh, K., Ostad-Ahmad-Ghorabi, M. J., and Arghavan, A., "Investigating the effect of road roughness on automotive component", ***Engineering Failure Analysis***, Vol. 41, (2014), 96–107. doi:10.1016/j.engfailanal.2013.12.008
16. Samandari, H., and Rezaee, M., "The stability and chaos analysis of a nonlinear wheeled vehicle model under road excitation", ASME 2010 10th Biennial Conference on Engineering Systems Design and Analysis, ESDA2010, Vol. 3, (2010), 115–120. doi:10.1115/ESDA2010-24451
17. Shojaeefard, M. H., Khalkhali, A., and Erfani, P. S., "Multi-Objective Suspension Optimization of a 5-DOF Vehicle Vibration Model Excited by Random Road Profile", ***International Journal of Advanced Design and Manufacturing Technology***, Vol. 7, No. 1, (2014), 1–7.
18. Raju, B. N., Kranthi Kiran, G., Manojana, P., Sateesh, K., Yashaswini, K., and Babu, K., "Material Selection and STATIC Analysis of Leaf spring Using FEA and Taguchi Method", ***JAC : A Journal of Composition Theory***, Vol. 13, No. 3, (2020), 497–509
19. Yao, W., Cai, K., and Xu, Y., "Optimizing the beam-like structure of a vehicle body using the grey–fuzzy–Taguchi method", ***Engineering Optimization***, Vol. 53, No. 1, (2021), 49–70. doi:10.1080/0305215X.2019.1698033
20. Zhang, R., and Wang, X., "Parameter study and optimization of a half-vehicle suspension system model integrated with an arm-teeth regenerative shock absorber using Taguchi method", ***Mechanical Systems and Signal Processing***, Vol. 126, (2019), 65–81. doi:10.1016/j.ymssp.2019.02.020
21. Mahmoudzadeh, A., Golroo, A., Jahanshahi, M., and Firoozi Yeganeh, S., "Estimating Pavement Roughness by Fusing Color and Depth Data Obtained from an Inexpensive RGB-D Sensor", ***Sensors***, Vol. 19, No. 7, (2019), 1655. doi:10.3390/s19071655
22. Abulizi, N., Kawamura, A., Tomiyama, K., and Fujita, S., "Measuring and evaluating of road roughness conditions with a compact road profiler and ArcGIS", ***Journal of Traffic and Transportation Engineering (English Edition)***, Vol. 3, No. 5, (2016), 398–411. doi:10.1016/j.jtte.2016.09.004
23. Arbabpour Bidgoli, M., Golroo, A., Sheikhzadeh Nadjar, H., Ghelmani Rashidabad, A., and Ganji, M. R., "Road roughness measurement using a cost-effective sensor-based monitoring system", ***Automation in Construction***, Vol. 104, (2019), 140–152. doi:10.1016/j.autcon.2019.04.007
24. Wong, J., Theory of Ground Vehicles, (2008) John Wiley & Sons.
25. Nickmehr, N., Ride Quality and Drivability of a Typical Passenger Car subject to Engine/Driveline and Road Non-uniformities Excitations, Master thesis, Linkoping University of Sweden, (2011).
26. Reza-Kashyzadeh, K., Ostad-Ahmad-Ghorabi, M. J., and Arghavan, A., "Study effects of vehicle velocity on a road surface roughness simulation", ***Applied Mechanics and Materials***, Vol. 372, (2013), 650–656. [In Persian] doi:10.4028/www.scientific.net/AMM.372.650
27. Gillespie, T., Fundamentals of Vehicle Dynamics, (Vol. 400). Warrendale, PA: Society of Automotive Engineers, (1992).
28. Craig, J. J., Introduction to Robotics, Pearson Education International, (2005).
29. Reza Kashyzadeh, K., Farrahi, G. H., Shariyat. M., & Ahmadian. M. T. (2018). The role of wheel alignment over the fatigue damage accumulation in vehicle steering knuckle. **Journal of Stress Analysis,** 3(1), 21-33. DOI: 10.22084/jrstan.2018.15722.1042
30. ICAO, Manual of the ICAO Standard Atmosphere, Doc 7488-CD, Third Edition, (1993), ISBN 92-9194-004-6.
31. Monteith, J., and Unsworth, M., "Principles of environmental physics", (2008).
32. Reza Kashyzadeh, K. (2015). Fatigue life estimation under multi-axial random loading in light poles. **Ciência e Natura**, 37(6-1), 183-189. DOI: 10.5902/2179460X20845
33. Farrahi, G. H., Reza Kashyzadeh, K., Minaei, M., Sharifpour, A., and Riazi, S., "Analysis of resistance spot welding process parameters effect on the weld quality of three-steel sheets used in automotive industry: Experimental and finite element simulation", ***International Journal of Engineering, Transactions A: Basics***, Vol. 33, No. 1, (2020), 148–157. doi:10.5829/ije.2020.33.01a.17
34. Maleki, E., Unal, O., and Reza Kashyzadeh, K., "Efficiency Analysis of Shot Peening Parameters on Variations of Hardness, Grain Size and Residual Stress via Taguchi Approach", ***Metals and Materials International***, Vol. 25, No. 6, (2019), 1436–1447. doi:10.1007/s12540-019-00290-7
35. Omidi Bidgoli, M., Reza Kashyzadeh, K., Rahimian Koloor, S. S., and Petru, M., "Estimation of Critical Dimensions for the Crack and Pitting Corrosion Defects in the Oil Storage Tank Using Finite Element Method and Taguchi Approach", ***Metals***, Vol. 10, No. 10, (2020), 1372. doi:10.3390/met10101372

APPENDIX A

Smoothly-reconstructing Road Roughness from Discretely-acquired Road Roughness by Linear Functions with Quadratic Blends

The discretely-acquired data of the road roughness y_n at t_n are given by (A1).

$$\begin{aligned} & t_1 < t_2 < \cdots < t_{n-1} < t_n < t_{n+1} < \cdots < t_{N-1} < t_N \\ & y_n \equiv y(t_n) \qquad , \quad 1 \le n \le N \end{aligned} \tag{A1}$$

Considering the parameters in (A2), and in order to smoothly-reconstruct the road roughness, a smooth curve might be composed of the connection lines (A3) between each couple of adjacent points of the discretely-acquired data of the road roughness (A1) and the quadratic blends (A4) between them.

$$\begin{aligned} & t_1 = \beta_1 < \cdots < \beta_{n-2} < \alpha_{n-1} < t_{n-1} < \beta_{n-1} < \alpha_n < t_n < \beta_n < \alpha_{n+1} < t_{n+1} < \beta_{n+1} < \cdots < \beta_{N-1} < \alpha_N = t_N \\ & \beta_{n-1} < \alpha_n < t_n < \beta_n \qquad , \quad 2 \le n \le N-1 \end{aligned} \tag{A2}$$

$$\begin{cases} y(t)=m_n t+h_n \quad , \quad \beta_{n-1}\le t\le \alpha_n \quad , \quad 2\le n\le N \\ \dot{y}(t)=m_n \\ \ddot{y}(t)=0 \end{cases} \qquad \begin{cases} m_n \equiv \dfrac{y_n-y_{n-1}}{t_n-t_{n-1}} \\ h_n \equiv y_n - m_n t_n \end{cases} \tag{A3}$$

$$\begin{cases} y(t)=a_n t^2+b_n t+c_n \quad , \quad \alpha_n < t < \beta_n=\alpha_n+\tau_n \quad , \quad 2\le n\le N-1 \\ \dot{y}(t)=2a_n t+b_n \\ -g\le \ddot{y}(t)=2a_n \le ACC_{allowable}>0 \end{cases} \tag{A4}$$

Smoothness conditions (A5):

$$\begin{aligned} &a_n\alpha_n^{\,2}+b_n\alpha_n+c_n-m_n\alpha_n-h_n=0 \quad , \quad 2a_n\alpha_n+b_n-m_n=0 \quad , \\ &a_n\beta_n^{\,2}+b_n\beta_n+c_n-m_{n+1}\beta_n-h_{n+1}=0 \quad , \quad 2a_n\beta_n+b_n-m_{n+1}=0 \quad , \quad 2\le n\le N-1 \end{aligned} \tag{A5}$$

Either τ_n which is introduced in (A4) or the allowable acceleration that can be tolerated, ie $ACC_{allowable}^{Max}$ and that required for holding vehicle-road contact, ie $ACC_{allowable}^{Min}$, can be imposed to a problem. Consider for instance options of (A6).

$$either \quad \tau_n \equiv \frac{1}{10}\,Minimum\{t_{n+1}-t_n\,,\ t_n-t_{n-1}\}$$

$$or \quad \begin{cases} ACC_{allowable}^{Max}=g \\ ACC_{allowable}^{Min}=-g \end{cases} \Rightarrow \quad -g\le \ddot{y}(t)=2a_n=\frac{m_{n+1}-m_n}{\tau_n}\le g \Rightarrow -g\le \frac{m_{n+1}-m_n}{\tau_n}\le g$$
$$\Rightarrow \quad \tau_n \ge \frac{|m_{n+1}-m_n|}{g} \Rightarrow \tau_n=\frac{|m_{n+1}-m_n|}{g} \tag{A6}$$

Having τ_n from either options of (A6), the unknowns are found as given by (A7).

$$\begin{aligned} &a_n=\frac{m_{n+1}-m_n}{2\tau_n} \quad , \quad \alpha_n=\frac{-\tau_n}{2}-\frac{h_{n+1}-h_n}{m_{n+1}-m_n} \quad , \quad \beta_n=\alpha_n+\tau_n \quad , \quad b_n=m_n-2a_n\alpha_n \quad , \\ &c_n=h_n+(m_n-b_n)\alpha_n-a_n\alpha_n^{\,2} \quad , \quad 2\le n\le N-1 \end{aligned} \tag{A7}$$

Persian Abstract

چکیده

نیروی وارد بر چرخ خودرو در مدل ۱/۲ که با سرعت ثابت حرکت می¬کند با در نظر گرفتن ناهمواری جاده، آیرودینامیک و شرایط آب و هوایی مانند دما و رطوبت هوا محاسبه شده است. یک جاده با ناهمواری کلاس D مطابق با استاندارد ISO-8606 برای انجام آزمایش انتخاب شد و پروفیل سطح آن با استفاده از یک دوربین توپوگرافی از سری Leica اندازه¬گیری شد تا داده¬های گسسته به منظور مدل¬سازی زبری جاده بدست آید. داده¬ها از حالت گسسته به پیوسته هموار با استفاده از توابع خطی درجه دوم تبدیل شدند، با توجه به این واقعیت که معادلات دیفرانسیل حرکت خودرو وابسته به ناهمواری جاده و نرخ زمان تغییرات آن است. چنین فرض شده است که خط اثر باد یا نیروی آیرودینامیکی اعمال شده به مدل خودرو از مرکز جرم خودرو می¬گذرد. برای بدست آوردن ارتعاشات مدل ۱/۲ خودرو از روش رانگ-کوتا استفاده شده است. از طراحی آزمایش به منظور بررسی اثرات دما و رطوبت هوا بر چرخ¬های عقب و جلو استفاده شده است. مشخص شد که نیروی وارد به چرخ جلوی خودرو به مراتب بیشتر از نیرویی است که به چرخ عقب خودرو وارد می¬شود (حدود ۱۶/۵ درصد). همچنین، اثر دمای هوا بر نیروی چرخ بسیار بیشتر از اثر رطوبت هوا است. علاوه بر این، نیروی چرخ جلو با مقادیر پارامترهای آب و هوایی رابطه مستقیم دارد و رابطه نیروی چرخ عقب با آنها بصورت عکس است.

IJE TRANSACTIONS B: Applications Vol. 34, No. 02, (February 2021) 547-555

International Journal of Engineering

Journal Homepage: www.ije.ir

Numerical modeling and Optimization of Respirational Emergency Drug Delivery Device using Computational Fluid Dynamics and Response Surface Method

M. Yousefi[a], H. Safikhani*[a], E. Jabbari[a], M. Yousefi[b], V. Tahmasbi[c]

[a] *Department of Mechanical Engineering, Faculty of Engineering, Arak University, Arak, Iran*
[b] *School of Engineering, RMIT University, Melbourne, Australia*
[c] *Mechanical Engineering Faculty, Arak University of Technology, Arak, Iran*

PAPER INFO

Paper history:
Received 21 August 2020
Received in revised form 26 October 2020
Accepted 30 October 2020

Keywords:
Computational Fluid Dynamics
Drug Delivery Device
Endotracheal Tube
Optimization
Respirational Patients
Response Surface Method

ABSTRACT

Studies have shown that most of the particles sprayed on emergency respirational patients, accumulate inside the endotracheal tube and its connector. In this paper, applying Computational Fluid Dynamics (CFD) and Response Surface Method (RSM), an optimized geometry is introduced for higher efficiency of the drug delivery for patients with emergency respiratory diseases. In CFD modeling, finite volume method and for two-phase flow modeling, Lagrangian method is used. Reynolds averaged Navier–Stokes equations with Reynolds stress turbulence model are solved using SIMPLE pressure correction algorithm within the computational domain. The velocity fluctuations are simulated using the Discrete Random Walk (DRW). For optimization process, six different parameters including three dimensions of the connector of the tube: connector length, connector diameter and injection diameter, injection velocity of the drug particles, air flow velocity and particle size are investigated. Using Design of Experiments (DOE) and RSM, the output efficiency of the model and second-order regression equation model are derived and accuracy of the model is confirmed. Then the effect of each input parameter on the efficiency is investigated. Dringer algorithm is applied to optimize the process and the best combination of input parameters yielding the highest efficiency is introduced.

doi: *10.5829/ije.2021.34.02b.28*

1. INTRODUCTION

Today, human activity on the planet has caused the production of dangerous chemicals into the atmosphere which are inhaled by humans every day and cause different damages to the human digestive system. Chronic Obstructive Pulmonary Diseases (COPD) including emphysema, chronic bronchitis, asthma, when there is a blockage in the path of the air entering the lung. Bronchitis is when inflammation occurs in bronchi. In emphysema, very tiny air pockets at the end of the lung's air path are gradually dead. Diseases like severe asthma, COPD and recently emerged COVID-19 adversely affect the lung's tissue and obstacle the natural respiration. In such cases generally mechanical ventilators are implemented to assist breathing. It is vital, however, sometimes, in addition to help patients in breathing, there is a need to send some drugs to the respiration system of the patients. Such drugs, generally in the form of suspension, including salbutamol, hydrofluoroalkane (HFA) and/or chlorofluorocarbon (CFC) particles. It is evident that such drug delivery system, through respiration, is quite effective in healing respiratory conditions [1-3]. In this state, drug after being sprayed builds up a two-phase flow with the oxygen flow and can directly find access to the infected areas of the lung. Treating patient using such a direct method would require lower dosage of drug and eliminate possible side effects as it is directly headed to the area where it is needed [4-6]. Nowadays different respiratory sprays like Nebulizers, dry powder inhalers and Metered-Dose inhalers (MDIs) are commercially available. Such sprays

*Corresponding Author Institutional Email: h-safikhani@araku.ac.ir
(H. Safikhani)

Please cite this article as: M. Yousefi, H. Safikhani, E. Jabbari, M. Yousefi, V. Tahmasbi, Numerical modeling and Optimization of Respirational Emergency Drug Delivery Device using Computational Fluid Dynamics and Response Surface Method, International Journal of Engineering, Transactions B: Applications Vol. 34, No. 02, (2021) 547-555

are suitable for patients who are breathing naturally and are physically able to put the spray in their mouth [7, 8].

At emergency condition for sending oxygen and drug to the lungs by an artificial air path, Endotracheal tube (ETT), is used. ETT is a flexible plastic tube and through the mouth it is mounted on the windpipe and it can transfer the oxygen and anesthetizers to the lung when patients are in a coma. For drug injection such a tube is equipped with spray-producing mechanism for drug injection which is connected to the tube with a connector. Figure 1 illustrates the schematic of such a system. The application of such tube system improves the respiration of patients as it keeps the breathing path opened and delivers oxygen to the lungs [9]. Such tubes have length of 160 to 300mm and internal diameter of 3 to 9 mm based on the application and age of the patients. When drug is sprayed evidently enormous amount of its particles is blocked in the tube, connector and connections and this remarkably reduces the efficiency of drug delivery. The lower amount of particles occupying the tube system means that higher dosage of drug was delivered to the lung and desirable efficiency is achieved. Mazela et al. [10] reported that the efficiency of particle delivery through such a system is heavily dependent upon the size of the particle; it is 100% for small particles and almost 0% for particles bigger than 7 micrometers. Ahrens et al. [11] investigated the blockage of the drug particles in tube system with different tube diameters of 3, 6 and 9 mm. They used a tube system where drug was delivered to the lung through a T connector connected to the tube. They reported that when size of the particles was smaller, about 0.54 micrometer, the blockage in the system remarkably decreased. However, it was evident that the distribution of the particles in two-phase flow and also properties of the flow are more important in delivery of the particles than the tube diameter. The effect of tube diameter was also examined and it was found that no remarkable change in delivery would occur with altering tube diameter from 7 mm to 9 mm [12]. Generally, though tube diameter is effective in the performance of drug delivery system, this effectiveness is varied in different systems and there exist other more influential parameters. Fuller argued that type of the spray: Nebulizers or MDI is influential over drug delivery [13].

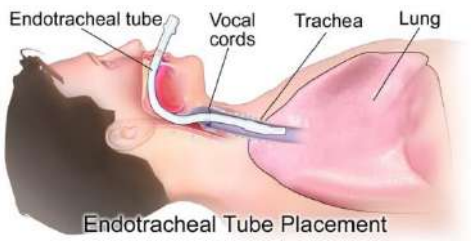

Figure 1. Schematic application of endotracheal tube in emergency respiratory patients

Many reports have been released on the influence of the type of the spray which confirms better performance of the MDIs and chambers than nebulizers. Although both nebulizers and MDIs similarly function in terms of delivering the drug, the dosage required by nebulizers is considerably higher than that for MDIs. Yousefi [14] improved drug delivery using a one-way chamber with MDI. Later in 2017 using an acoustic wave surface they altered the creation of the particles in the chamber and then suggested the optimum condition of the chamber [15]. In another study, Yousefi et al. [16], investigated the effect of different parameters like particle velocity, particle distribution, particle injection angle and air flow rate. They reported an effectiveness on drug delivery to the lung. Very few studies are available concerning the design of the ventilator especially the connector to minimize the blockage of the drug in the system. It is expected that maximum blockage occurs in the area where path of the flow suddenly alters (change in the diameter of the path or the direction) [17]. In ventilator circuit maximum blockage would occur in the ETT and collector. The size of ETT is limited to the anatomy of the patient though tubes with higher diameter are more successful in delivering particles [10, 18]. Ivri [19] proposed connector angles less than 16˚ to improve through-ventilator drug delivery. This, however, would require longer connections in ventilator circuit. Recently, Mazela et al. [20] re-designed a Y shape connector. But the blockage of particles increased in modified design. Longest suggested a linearized connector where no abrupt changes existed in the path of the flow using gradually smoothing sections and they successfully reduced the blockage of particles from 30% to 5% for a T connector [16]. They examined their linearized connector for a Y shape connector and found that output particles increased from 40% to 70% using flow of 30 l/min of air and particle size of 4 micrometers [20, 21]. Also, in recent years, many researchers have conducted effective and relevant research in this field [22-29].

In this paper using Computational Fluid Dynamics (CFD) and Response Surface Method (RSM) an optimized geometry for better drug delivery performance of ventilator considering six different parameters including three dimensions of collector, particle injection velocity, flow rate and particle size is derived. For numerical modeling, finite volume method and for modeling two-phase flow, Lagrangian method is used. To evaluate the effect of each parameter on drug delivery and in order to validate the numerical model, design of experiments and response surface method are applied and then governing second order regression equation is derived. Finally using Dringer algorithm an optimum combination of parameters yielding the highest drug delivery performance and lowest blockage of the particle is investigated.

TABLE 1. Design variables

Design Variable	Symbol	Unit	From	To
Connector length	L	mm	10	30
Connector diameter	d1	mm	10	20
Injection diameter	d2	mm	2	6
Particle diameter	dP	μm	1	9
Particle velocity	VP	m/s	100	150
Air velocity	Va	m/s	4	8

2. MATHEMATICAL MODELING

The data required for optimization is extracted from numerical modeling. The detail of numerical modeling is elaborated in this section.

2. 1. Geometry Figure 2 schematically illustrates the geometry of the system. This system includes an Endotracheal tube (ETT) entering the patient mouth, the connector with two opening: one through which drug is sprayed and the other is connected to the ventilator. For optimization purpose particle injection speed, particle size, air flow and three dimensions of the connector are taken into account. The variables range used in optimization is listed in Table 1.

2. 2. Governing Equation The air flow is assumed to be incompressible and Newtonian. Moreover, 3D continuity and momentum conservation equations and Reynolds-averaged Navier-Stokes equations are solved using *k-ω* turbulence method as follows:

$$\frac{\partial \overline{u_i}}{\partial x_i} = 0 \tag{1}$$

$$u_j \frac{\partial u_i}{\partial x_j} = -\frac{1}{\rho_f}\frac{\partial p}{\partial x_j} + \frac{\partial}{\partial x_j}\left[\left(\nu_f + \nu_T\right)\left(\frac{\partial u_i}{\partial x_j} + \frac{\partial u_j}{\partial x_i}\right)\right] \tag{2}$$

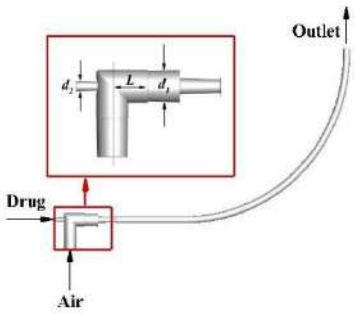

Figure 2. Details of endotracheal tube and definition of geometrical design variables

Discrete phase model and Lagrangian particle tracking approach are used for particle movement simulation. In this method to track each particle from equilibrium condition, integration is performed.

$$\vec{F} = m_p . \frac{d\vec{u_p}}{dt} \tag{3}$$

where u_p is particle velocity, t is time and F is the force, constitute of 12 different components presented in Equation (4):

$$\begin{aligned}\vec{F} &= \vec{F}_D + \vec{F}_b + \vec{F}_g + \vec{F}_{Saffman} \\ &+ \vec{F}_{virtualmass} + \vec{F}_{p.gradient} + \vec{F}_{Faxen} \\ &+ \vec{F}_{Basset} + \vec{F}_B + \vec{F}_T + \vec{F}_m + \vec{F}_M\end{aligned} \tag{4}$$

Where components are drag, Buoyancy, gravity, Saffman lift, virtual mass, pressure gradient, facen, basset, Brownian, thermoforsis, Magnus and magnetic forces respectively. Many of these components are negligible. For instance, since the density of the particles is much higher than that of the fluid, buoyancy and basset forces are negligible. Gravity forces, also, are prominent only for lower flow rates. Browny movement and saffman lift forces are applicable for sub-micron particles [30, 31]. Magnetic force can be discarded as no magnetic field exists over the path of the particle. Finally, Fax force can be ignored because its value is remarkable only when length scale of the particle and the system possess the same order. Thus the equilibrium equation of the particle can be rewritten as presented in Equation (5):

$$\vec{F} = m_p . \frac{d\vec{u_p}}{dt} = \vec{F}_D \tag{5}$$

Stocks drag force over a smooth spherical particle is presented in Equation (6) [32]:

$$\vec{F}_D = \frac{18\mu}{\rho_p d_p^2}\frac{m_p f\ \mathrm{Re}_p}{24}\left(u_f - u_p\right) \tag{6}$$

where drag coefficient is computed in Equation (7):

$$f = a_1 + \frac{a_2}{\mathrm{Re}_p} + \frac{a_3}{\mathrm{Re}_p^2} \tag{7}$$

where $\mathrm{Re}_P = \frac{\rho_f d_P \left|u_P - u_f\right|}{u_f}$ is Reynolds number for each particle and a_1, a_2 and a_3 are empirical constants which are applicable in the range of $0 \le \mathrm{Re}_P \le 5\times10^4$ [33]. Moreover, for the sake of simplification, the effect of particle evaporation or particle concentration and also electrostatic charge of the walls were neglected.

2. 3. Boundary Condition For numerical simulation, equations derived in the previous section should be solved with appropriate boundary conditions. Air with a certain flow rate enters the connector and exits the end of the ETT. On the walls of connector and ETT,

no-slip condition is considered and it is assumed that particles stick to the wall right away after coming into contact with the wall for the first time. At the end of the ETT it is assumed that air flow rate remains constant. All particles are assumed to enter the ETT particles with certain speed and size.

2. 4. Numerical Method Here, numerical method is based on finite volume method. Second order upwind was used to divide different variables. SIMPLE algorithm is used to solve the couple of the velocity and pressure fields. To ensure the accuracy of the results independent from the discretization, different mesh sizes are used and in each case the optimum grids with acceptable accuracy and low computational cost are selected. An essential assumption in DPM model is that the second phase of the two-phase flow, here is the particle size, possesses negligible volume fraction even for the high flow rates. Therefore, it seems necessary to check this volume fraction in each element to be less than 12% because the proposed model is only valid when this condition is satisfied. One-way coupling is defined so that the collision of each particle to the flow field and also to other particles is neglected.

On average, 500000 elements are used. A sample of generated mesh is shown in Figure 3. Mesh independence is examined for proposed model in Figure 4 are mesh networks with 170000, 270000, 490000 and 923000 elements made readily slight variation in flow rate values. Finally, total number of elements equal to 490000 is used for the further investigation.

2. 5. Modeling of Spray Particles The distribution of the particles in the input of the ETT should have no influence over the convergence of the results. For example, if a distribution with concentration towards the center of the tube's cross section exists, it would lead to a premature convergence which yields fallacious results. Therefore, a uniform distribution of the particles in the entrance of the ETT is necessary. Here a computer code

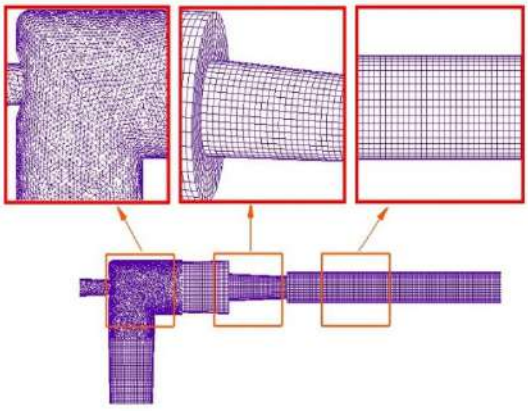

Figure 3. A sample of generated mesh using in CFD process

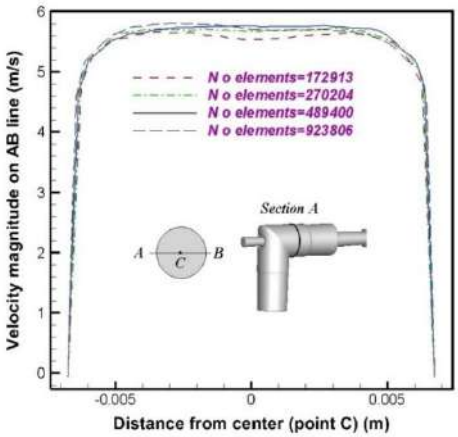

Figure 4. Results of grid independency test

to produce a uniform distribution has been used. Figure 5 compares the uniformity in the article distribution before and after using this computer code. Total 6000 particles are injected into the connector with 120 m/s velocity in the entrance cross section with diameter of 2.4 mm.

2. 6. Validation of Numerical Results To validate numerical results, comparisons should be made with reliable data. Since experimentation for drug blockage in the ventilator system is astronomically costly, there is no reported data available. Therefore, comparison of derived data here with results of the ETT with a 90-degree elbow reported elsewhere is followed [34]. Figure 6 shows the blockage value in a 90-degree-elbow ETT reported elsewhere [35] which affirm great correlation. The discrepancy in the results is attributed to the assumed condition of with-a-first-contact absorption of the particles to the wall and also one-way coupling condition which are different with what would happen in real experimentation setting.

3. RSM AND DATA ANALYSIS

Using DOE and RSM, six different parameters of air flow rate, particle injection velocity, particle size and three

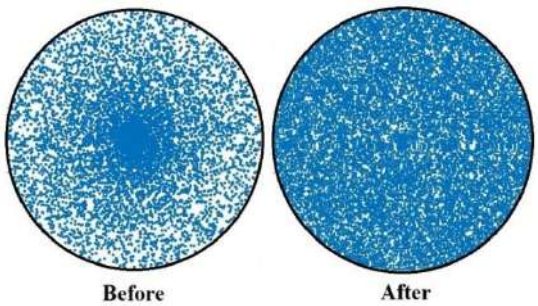

Figure 5. Details of endotracheal tube and definition of geometrical design variables

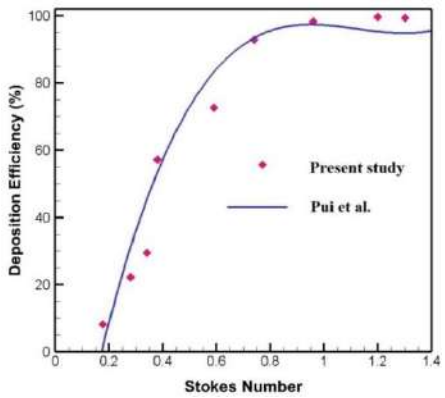

Figure 6. Details of endotracheal tube and definition of geometrical design variables.

dimensions of connector (Table 1) are considered as influential parameters. Governing equation of the fitted model are derived and then the model accuracy is confirmed. Then, in addition to studying the effect of each individual parameter, Dringer method is used to obtain optimum combination of input parameters to maximize drug delivery and minimize drug blockage within the ETT system.

In this method, the overall goal is to convert response (yi) to a dimensionless unique utility function (di) that changes over the entire interval as follows:

$$0 \le d_i \le 1 \tag{8}$$

If answer (y_i) is the goal of optimization then $d_i = 1$ and if the answer is acceptable outside an area then $d_i = 0$, as shown schematically in Figure 7. In the present study, the value of $d_i = 1$ is obtained for the utility limit function and is expressed in the Figure 7, which indicates convergence and access to the optimal value in this research [36].

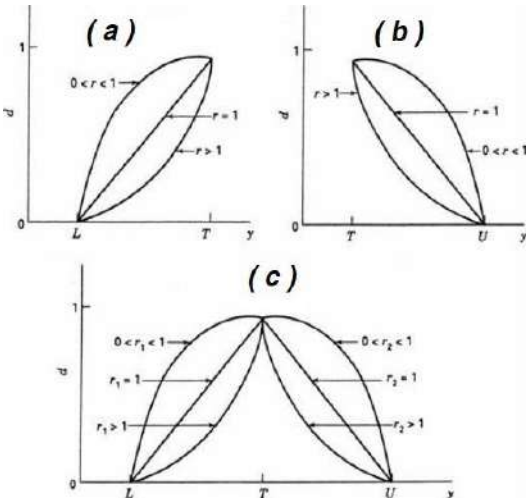

Figure 7. Details of endotracheal tube and definition of geometrical design variables [37]

3. 1. Response Surface Method (RSM) In analysis of engineering problems especially experimental and numerical approaches where the output relies on different input variables, carrying out statistical methods can remarkably improve design, modeling, analysis and optimization steps. Response surface method is very promising in saving time and cost of design and analysis of models. It specifies the precision of the fitted model and establishes a mathematical model to the problem. Its advantages include yielding the diagrams of interaction effect of parameters, optimization and ensuring the model accuracy [34]. RSM can relate input parameters to the output through a second order linear regression equation. General form of such equation is presented in Equation (9) [37]:

$$y = \beta_0 + \sum_{i=1}^{k} \beta_i x_i + \sum_{i=1}^{k} \beta_{ii} x_i^2 + \sum_i \sum_j \beta_{ij} x_i x_j + \varepsilon \tag{9}$$

where, y is the output, β is the regression equation coefficients, x_i is main input parameter, x_i^2 is the squared of main input parameters, $x_i x_j$ is the second order interaction effect of input parameters [38]. The proposed model, if established precisely, can successfully predict the output over the entire range of input variables [39].

3. 2. Input and Output Variables of the Drug Delivery Process In this research considering the variation of the six design variables according to Figure 2 and Table 1, in total 45 different sets of design variables are considered for modeling and optimization using composite central design (CCD). To avoid unpredicted errors, simulations are done randomly [40]. Minitab version 18 and Design Expert version 10 software packages are used for data analysis and extracting regression equation. Using RSM, a governing equation is derived with fitting the model to the data points. Then sensitivity analysis and optimization of the model are followed.

3. 3. Data analysis and Model Establishment ANOVA defines the effectiveness of each of regression

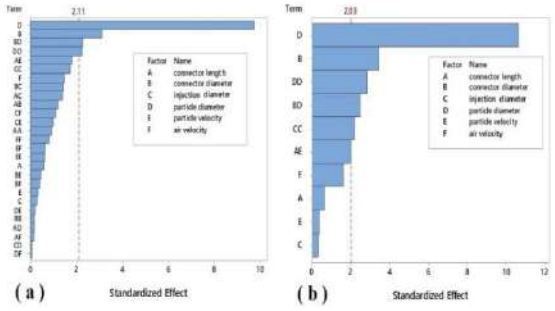

Figure 8. Details of endotracheal tube and definition of geometrical design variables

parameters which in turn defines the effectiveness of each input variables as well as their interactions [39]. Considering generally accepted reliability of 95% for engineering problems, Pvalue less than 0.5 is considered to ascertain the effectiveness of different parameters [36]. Figure 8 shows the term before and after modification. PRESS which defines the precision of the model fitted to the process is prominent in the field of design of experiment. The lower PRESS value is, more accurately model can predict the outputs. In this model the minimum PRESS coincided with full quadratic regression model. Considering minimal value of 35544.02 for PRESS the second order regression model of process can be defined using Equation (10):

$$\begin{aligned}\eta &= -48.3 + 5.42L + 5.17d_2 - 53.4d_1/2 \\ &-6.62d_p + 0.855V_p - 2.01V_a \\ &+13.16(d_1/2)^2 + 1.040(d_p)^2 \_ 0.0447LV_p \\ &-0.692d_2d_p\end{aligned} \quad (10)$$

Considering the value R-sq=88.85% and appropriate distribution of residuals it can be inferred that proposed model is desirably accurate. R-sq which shows the precision of the fitted model can be computed using Equation (11):

$$R^2 = \frac{SS_R}{SS_T} = 1 - \frac{SS_{Res}}{SS_T}, \quad (11)$$

The closer to unity (100%) is this value, the correspondence of the model to the data point is higher and more accurate prediction is expected [5]. another important factor playing a role in accuracy of the model is the distribution of residuals. The fitted model should pass close to the data points with random distances. This value is defined in R-sq and its distribution is shown in Figure 9. Generally, from both the value of fitted points and the random nature of this fit, presented model is desirable.

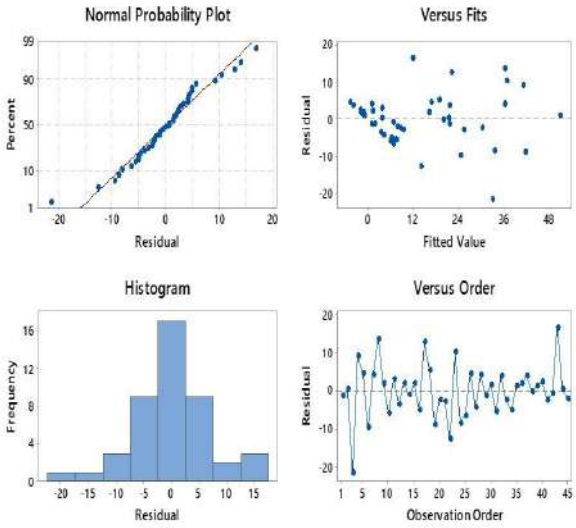

Figure 9. Details of endotracheal tube and definition of geometrical design variables

4. OPTIMIZATION RESULTS

In this section, considering developed model, it is attempted to specify the effectiveness of the input parameters over the efficiency of the drug delivery. Appropriate main effect, interaction and contour plots will be presented.

Surface plot of drug delivery process is illustrated in Figure 10. To analyze the effect of connector diameter, main effect plot in Figure 11(a), interaction plot in Figures 11(e) and 11(f) and contour plot presented in Figure 12. It can be implied that efficiency of the system increases with a raise in connector diameter. The interaction effect of connector diameter and particle size confirms that with simultaneous increase in connector diameter and decrease in particle size the efficiency considerably rises. This can be explained that the more spacious is the path; there is lower chance for particles to collide to each other or to the walls. Having that said, with increase in diameter of the connector the velocity of two-phase flow decreases because it is assumed that air flow rate is constant. With lower velocity it is less probable for particles to collide and therefore blockage would decrease. Additionally, it can be seen from plots in Figures 11 and 12 that reduction in particle size improves the efficiency while increasing particle size noticeably drops the efficiency. This is attributed to the fact that with bigger particles the probability of collision of a particle with other particles or wall increases and blockage would ascend. Considering connector length and particles velocity presented in Figure 13, it can be observed that maximum efficiency coincides with either shortest connector length and highest particle velocity or longest connector length and lowest particle velocity. This inference can be confirmed according to Figure 12. When connector is long, particles spends more time inside the connector and with turbulence in the connector the collision probability and blockage increases. In this condition, if particles are injected with lower velocity the chance of collision decreases and efficiency improves while higher injection velocities increase the collision and boosts blockage. On the other hand, if short connector is used, in an arbitrary time frame lower number of particles exists in the connector and the collision of particles no longer plays an important role in the efficiency of drug delivery. Whereas, with higher speed of particle injection, more particles pass the connector quickly without being blocked in it and therefore, efficiency increases.

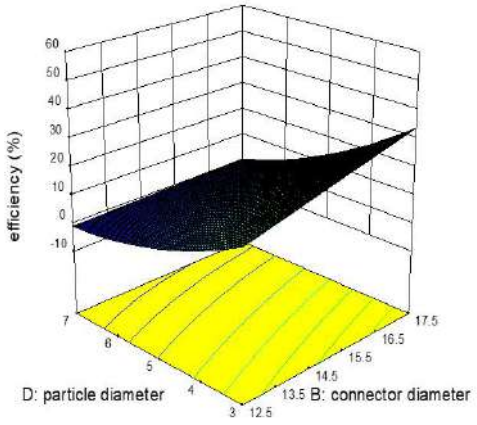

Figure 10. Details of endotracheal tube and definition of geometrical design variables

Considering injection diameter, Figure 11(c) reveals that the highest efficiency coincides with lowest injection diameters. With a low cross section-area of injection the concentration of particles towards center rises which decreases the scatter of the particles. However, concentration of particles toward center increases the chance of collision. Due to the short length of the entrance mouth, nonetheless, the collision is not the main reason of blockage. The injection diameter is not among main factors and in the regression model, only, its second order is presented. Nevertheless, according to Figure 11(c), after passing a threshold with a bigger diameter of injection efficiency again increases. According to ANOVA table the effect of air flow rate is negligible on efficiency of drug delivery though Figure 11(d) shows that with a decrease in air flow speed, the efficiency of the system slightly improves. This is attributed to the fact that when particles are taken by the flow their speed gradually matches the speed of the flow. With lower flow speeds the chance of collision and blockage would be lower though this parameter is almost ineffective for the considered system.

Based on the analysis of drug particles blockage within the Endotracheal tube system, optimization is performed for maximizing the efficiency. Considering the upper level of efficiency in the tests and considering Desirability limit the results of optimization are shown in Figure 13. According to the results maximum efficiency of 89% coincides with minimum connector length (10mm), maximum connector diameter (20 mm), the lowest injection diameter (2mm), the lowest particle diameter (1 mm), the highest particle velocity (150 m/s) and minimum air flow rate (4 m/s). The extracted optimal device can be used in all respiratory patients who need to breathe in unusual and emergency conditions such as anesthesia in corona virus. The extracted optimal geometry can be easily mass-produced by medical equipment manufacturers.

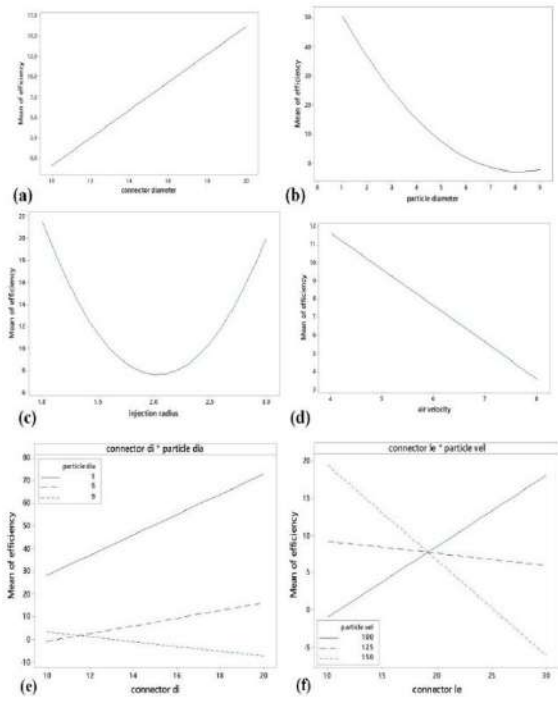

Figure 11. Details of endotracheal tube and definition of geometrical design variables

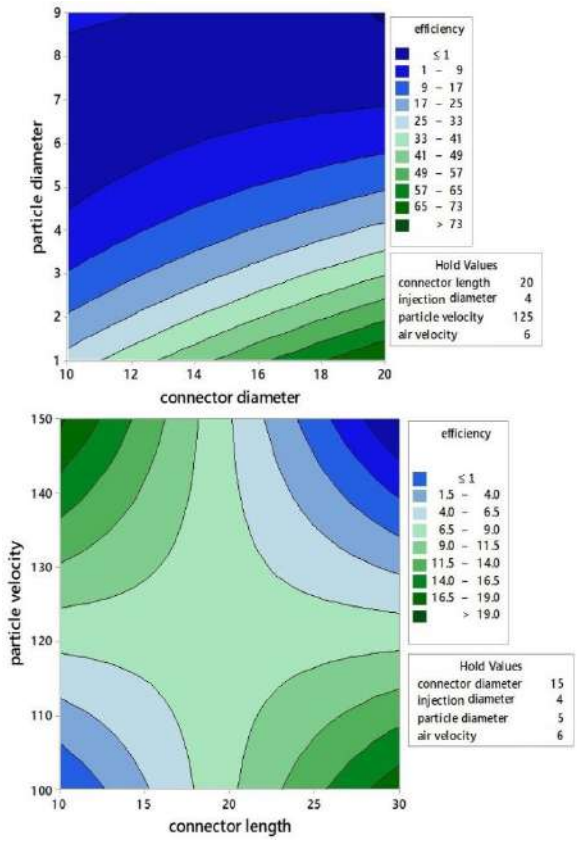

Figure 12. Details of endotracheal tube and definition of geometrical design variables

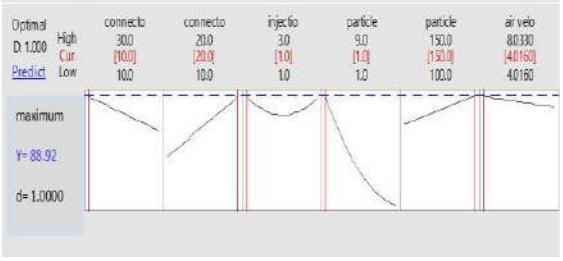

Figure 13. Details of endotracheal tube and definition of geometrical design variables

5. CONCLUSION

In this paper, applying CFD and RSM, an optimized geometry was introduced for higher efficiency of the drug delivery for patients with emergency respiratory diseases. In CFD modeling, finite volume method and for two-phase flow modeling, Lagrangian method was used. Reynolds averaged Navier–Stokes equations with Reynolds stress turbulence model were solved using SIMPLE pressure correction algorithm within the computational domain. The velocity fluctuations were simulated using the Discrete Random Walk (DRW).

For optimization process, six different parameters including three dimensions of the connector of the tube: connector length, connector diameter and injection diameter, injection velocity of the drug particles, air flow velocity and particle size were investigated. Using Design of Experiments (DOE) and RSM, the output efficiency of the model and second-order regression equation model were derived and accuracy of the model was confirmed. Then the effect of each input parameter on the efficiency is investigated. Dringer algorithm was applied to optimize the process and the best combination of input parameters yielding the highest efficiency is introduced. According to the results maximum efficiency of 89% coincides with minimum connector length (10mm), maximum connector diameter (20 mm), the lowest injection diameter (2mm), the lowest particle diameter (1 mm), the highest particle velocity (150 m/s) and minimum air flow rate (4 m/s). The extracted optimal device can be used in all respiratory patients who need to breathe in unusual and emergency conditions such as anesthesia in corona virus. The extracted optimal geometry can be easily mass-produced by medical equipment manufacturers.

6. REFERENCES

1. Broeders, M.E., Sanchis, J., Levy, M.L., Crompton, G.K. and Dekhuijzen, P.R., "The admit series—issues in inhalation therapy. 2) improving technique and clinical effectiveness", ***Primary Care Respiratory Journal***, Vol. 18, No. 2, (2009), 76-82. DOI: 10.4104/pcrj.2009.00025.
2. Smola, M., Vandamme, T. and Sokolowski, A., "Nanocarriers as pulmonary drug delivery systems to treat and to diagnose respiratory and non respiratory diseases", ***International Journal of Nanomedicine***, Vol. 3, No. 1, (2008), 1. doi.org/10.2147/IJN.S1045.
3. Virchow, J., Crompton, G., Dal Negro, R., Pedersen, S., Magnan, A., Seidenberg, J. and Barnes, P., "Importance of inhaler devices in the management of airway disease", ***Respiratory medicine***, Vol. 102, No. 1, (2008), 10-19. DOI: 10.1016/j.rmed.2007.07.031.
4. Chrystyn, H. and Price, D., "Not all asthma inhalers are the same: Factors to consider when prescribing an inhaler", ***Primary Care Respiratory Journal***, Vol. 18, No. 4, (2009), 243-249. doi: 10.4104/pcrj.2009.00029
5. Khilnani, G. and Banga, A., "Aerosol therapy", ***Journal, Indian Academy of Clinical Medicine***, Vol. 5, (2004), 114-123. doi: 10.1186/s13054-016-1448-5.
6. Vincken, W., Dekhuijzen, R. and Barnes, P., "The admit series—issues in inhalation therapy. 4) how to choose inhaler devices for the treatment of copd", ***Primary Care Respiratory Journal***, Vol. 19, No. 1, (2010), 10-20. doi: 10.4104/pcrj.2009.00062.
7. Haughney, J., Price, D., Barnes, N.C., Virchow, J.C., Roche, N. and Chrystyn, H., "Choosing inhaler devices for people with asthma: Current knowledge and outstanding research needs", ***Respiratory Medicine CME***, Vol. 3, No. 3, (2010), 125-131. doi:10.1016/j.rmedc.2010.10.004.
8. Price, D., Roche, N., Virchow, J.C., Burden, A., Ali, M., Chisholm, A., Lee, A.J., Hillyer, E.V. and von Ziegenweidt, J., "Device type and real-world effectiveness of asthma combination therapy: An observational study", ***Respiratory Medicine***, Vol. 105, No. 10, (2011), 1457-1466. doi:10.1016/j.rmed.2011.04.010.
9. Dhand, R., "Special problems in aerosol delivery: Artificial airways", ***Respiratory Care***, Vol. 45, No. 6, (2000), 636-645.
10. Mazela, J., Moskal, A., Sosonowski, T. and Gadzinowski, J., "Relation between neonatal endotracheal (et) tube size and aerosol penetration-computational fluid dynamic study (cfd)", ***Pediatric Research***, Vol. 70, No. 5, (2011), 531-531. DOI: 10.1038/pr.2011.756.
11. Ahrens, R.C., Ries, R.A., Popendorf, W. and Wiese, J.A., "The delivery of therapeutic aerosols through endotracheal tubes", ***Pediatric Pulmonology***, Vol. 2, No. 1, (1986), 19-26. doi.org/10.1002/ppul.1950020108.
12. O'riordan, T.G., Greco, M.J., Perry, R.J. and Smaldone, G.C., "Nebulizer function during mechanical ventilation1-3", ***Am Rev Respir Dis***, Vol. 145, (1992), 1117-1122. DOI: 10.1164/ajrccm/145.5.1117.
13. Fuller, H., Dolovich, M., Posmituck, G., Wong Pack, W. and Newhouse, M., "Pressurized aerosol versus jet aerosol delivery to mechanically ventilated patients", ***Am Rev Respir Dis***, Vol. 141, No. 2, (1990), 440-444. DOI: 10.1164/ajrccm/141.2.440.
14. Yousefi, M., "Cfd analysis of spacer and metered dose inhaler functionality and efficiency", (2017).
15. Yousefi, M., Pourmehran, O., Gorji-Bandpy, M., Inthavong, K., Yeo, L. and Tu, J., "Cfd simulation of aerosol delivery to a human lung via surface acoustic wave nebulization", ***Biomechanics and Modeling in Mechanobiology***, Vol. 16, No. 6, (2017), 2035-2050. DOI: 10.1007/s10237-017-0936-0.
16. Yousefi, M., Inthavong, K. and Tu, J., "Effect of pressurized metered dose inhaler spray characteristics and particle size distribution on drug delivery efficiency", ***Journal of Aerosol Medicine and Pulmonary Drug Delivery***, Vol. 30, No. 5, (2017), 359-372. doi.org/10.1089/jamp.2016.1299.
17. Longest, P.W., Golshahi, L. and Hindle, M., "Improving pharmaceutical aerosol delivery during noninvasive ventilation: Effects of streamlined components", ***Annals of Biomedical Engineering***, Vol. 41, No. 6, (2013), 1217-1232. DOI: 10.1007/s10439-013-0759-9

18. Everard, M.L., Stammers, J., Hardy, J. and Milner, A., "New aerosol delivery system for neonatal ventilator circuits", ***Archives of Disease in Childhood***, Vol. 67, No. 7 Spec No, (1992), 826-830. doi: 10.1136/adc.67.7_spec_no.826.
19. Ivri E, a.F.J., "Aerosol delivery apparatus and method for pressure-assisted breathing systems", ***United States Patent***, (2007).
20. Mazela, J., Chmura, K., Kulza, M., Henderson, C., Gregory, T.J., Moskal, A., Sosnowski, T.R., Florek, E., Kramer, L. and Keszler, M., "Aerosolized albuterol sulfate delivery under neonatal ventilatory conditions: In vitro evaluation of a novel ventilator circuit patient interface connector", ***Journal of Aerosol Medicine and Pulmonary Drug Delivery***, Vol. 27, No. 1, (2014), 58-65. DOI: 10.1089/jamp.2012.0992.
21. Longest, P.W., Azimi, M., Golshahi, L. and Hindle, M., "Improving aerosol drug delivery during invasive mechanical ventilation with redesigned components", ***Respiratory Care***, Vol. 59, No. 5, (2014), 686-698. DOI: 10.4187/respcare.02782
22. A. Abdi, A.M.F.-F., M. Hajiaghaei-Keshteli, "A set of calibrated metaheuristics to address a closed-loop supply chain network design problem under uncertainty", ***International Journal of Systems Science: Operations & Logistics***, No. 1-18. DOI: 10.1007/s00500-020-04812-z.
23. A. M. Fathollahi-Fard, K.G., M. Hajiaghaei-Keshteli, A. Ahmadi, "A green home health care supply chain: New modified simulated annealing algorithms", ***Journal of Cleaner Production***, (2019), 240, 118200. DOI: 10.1007/s11356-020-10175-7.
24. A. M. Nezhadroshan, A.M.F.-F., Mostafa Hajiaghaei-Keshteli, "A scenario-based possibilistic-stochastic programming approach to address the resilient humanitarian logistics considering travel time and resilience levels of facilities", ***International Journal of Systems Science: Operations & Logistics***, (2020). DOI: 10.3390/app9183770.
25. M. Eftekhari, M.A., M. Gheibi, H. Azizi-Toupkanloo, A. Mohammad Fathollahi-Fard, G, "Tian, cadmium and copper heavy metal treatment from water resources by high-performance folic acid-graphene oxide nanocomposite adsorbent and evaluation of adsorptive mechanism using computational intelligence, isotherm, kinetic, and thermodynamic analyses", ***Environ Sci Pollut Res Int***, (2020). DOI: 10.3233/JIFS-182843.
26. M. M. Fathollahi-Fard, M.H.-K.R.T.-M., "Red deer algorithm (rda): A new nature-inspired meta-heuristic", ***Soft Computing***, No. 24, (2020), 14637–14665. DOI: 10.1080/23302674.2019.1610197.
27. S. Bahadori-Chinibelagh, A.M.F.-F., M. Hajiaghaei-Keshteli, "Two constructive algorithms to address a multi-depot home healthcare routing problem", ***IETE Journal of Research***, (2019). DOI: 10.1080/03772063.2019.1642802.
28. S. Mojgana, A.M.F.-F., T. Guangdong, L. Zhiwue, "A multi-objective supplier selection and order allocation through incremental discount in a fuzzy environment", Vol. 37, No. 1,

(Journal of Intelligent & Fuzzy Systems), 1435-1455. DOI: 10.1016/j.jclepro.2019.118200.
29. Y. Feng, Z.Z., G. Tian, A. M. Fathollahi-Fard, N. Hao, Z. Li, W. Wang and J. Tan, " A novel hybrid fuzzy grey topsis method: Supplier evaluation of a collaborative manufacturing enterprise", ***Applied Sciences***, No. 9, (2018). doi.org/10.1080/23302674.2020.1769766.
30. Crowe, C.T., Schwarzkopf, J.D., Sommerfeld, M. and Tsuji, Y., "Multiphase flows with droplets and particles, CRC press, (2011).
31. Ounis, H., Ahmadi, G. and McLaughlin, J.B., "Brownian diffusion of submicrometer particles in the viscous sublayer", ***Journal of Colloid and Interface Science***, Vol. 143, No. 1, (1991), 266-277. https://doi.org/10.1016/0021-9797(91)90458-K.
32. Wen, D., Zhang, L. and He, Y., "Flow and migration of nanoparticle in a single channel", ***Heat and Mass Transfer***, Vol. 45, No. 8, (2009), 1061-1067. DOI: 10.1007/s00231-009-0479-8.
33. Morsi, S. and Alexander, A., "An investigation of particle trajectories in two-phase flow systems", ***Journal of Fluid Mechanics***, Vol. 55, No. 2, (1972), 193-208. https://doi.org/10.1017/S0022112072001806.
34. Pui, D.Y., Romay-Novas, F. and Liu, B.Y., "Experimental study of particle deposition in bends of circular cross section", ***Aerosol Science and Technology***, Vol. 7, No. 3,(1987),301-315. https://doi.org/10.1080/02786828708959166.
35. T. H. Hou, C.-H.S., W.-L. Liu, , Powder technology, "Parameters optimization of a nano-particle wet milling process using the taguchi method, response surface method and genetic algorithm", Vol. 173, (2007), 153-162. https://doi.org/10.1016/j.powtec.2006.11.019.
36. Montgomery, D.C., " Design and analysis of experiments", ***John Wiley & Sons***, (2008).
37. Nekahi, A. and Dehghani, K., "Modeling the thermomechanical effects on baking behavior of low carbon steels using response surface methodology", ***Materials & Design***, Vol. 31, No. 8, (2010), 3845-3851. https://doi.org/10.1016/j.matdes.2010.03.038.
38. Moradi, M., Ghoreishi, M., Frostevarg, J. and Kaplan, A.F., "An investigation on stability of laser hybrid arc welding", ***Optics and Lasers in Engineering***, Vol. 51, No. 4, (2013),481-487. https://doi.org/10.1016/j.optlaseng.2012.10.016.
39. Moradi, M., Ghoreishi, M. and Torkamany, M., "Modelling and optimization of nd: Yag laser and tungsten inert gas (TIG) hybrid welding of stainless steel", ***Lasers in Engineering (Old City Publishing)***, Vol. 27, (2014).

Persian Abstract

چکیده

مطالعات انجام شده نشان می دهد که بیشتر ذرات اسپری شده به بیماران ریوی در حالت اورژانسی، در داخل لوله تراشه و کانکتور متصل به آن انباشت می شوند. در این مقاله به وسیله دینامیک سیالات محاسباتی و سپس استفاده از روش بهینه سازی سطح پاسخ، به معرفی یک هندسه بهینه جهت بهبود عملکرد داروورسانی و افزایش بازده داروورسانی توسط این دستگاه پرداخته شده است. در این مطالعه ۶ پارامتر طراحی جهت تحویل بهینهٔ دارو به بیماران بررسی شده است. این پارامتر ها عبارتند از : ابعاد کانکتور متصل به لولهتراشه (۳ پارامتر)، سرعت تزریق ذرات، سرعت جریان هوا و اندازه ذرات. جهت مدلسازی عددی از روش حجم محدود و جهت مدلسازی جریان دوفازی از روش لاگرانژی استفاده شده است. در قسمت بهینه سازی با استفاده از روش طراحی آزمایشها و روش سطح پاسخ، بازده خروجی مدل سازی دستگاه و معادله رگرسیون خطی مرتبه دوم حاکم بر مدل استخراج گردیده و از دقت آن اطمینان حاصل شده است. اثر رفتار هریک از پارامترها بر روی بازده مورد بررسی قرار گرفته است. همچنین با استفاده از الگوریتم درینگر، بهینه سازی بر مدل حاکم بر فرآیند صورت گرفته است و مقادیر بهینه هریک از پارامترهای ورودی به منظور دستیابی به بیشترین مقدار تحویل دارو به ریه های بیمار ارائه گردیده است.

International Journal of Engineering

Journal Homepage: www.ije.ir

The Prediction of Stress and Strain Behaviors in Composite Gears using FEM

M. Bigdeli, V. Monfared*

Department of Mechanical Engineering, Zanjan Branch, Islamic Azad University, Zanjan, Iran

PAPER INFO

Paper history:
Received 03 October 2020
Received in revised form 31 October 2020
Accepted 05 November 2020

Keywords:
Alloys
Composites
Metal Matrix Composite Gears
Strain
Stress

ABSTRACT

Metal matrix composite (MMC) gears are used as a major component in the industry and are responsible for providing high-quality power transfer at high speeds. High quality, including high strength and impact-resistance, low brittleness, and long lifetime, is very important and needed in the industry. Gears are made of different materials, and, nowadays, researchers and industrialists have turned to designing, manufacturing, and using composite gears more than other gears due to their low weight, high hardness and strength, and better mechanical properties. In this research, the stress and strain behaviors are predicted in the composite gears made of aluminum silicon carbide with 3 different SiC volume fractions, namely 55 vol.%, 40 vol.%, and 30 vol.%, and with specifications of (Al45/SiC55, Al60/SiC40, and Al70/SiC30) and gears made of aluminum oxide with 3 different alumina weight fractions, namely 94 wt.%, 96 wt.%, and 99.5 wt.% to evaluate and compare the stress behavior due to different forces exerted on a single gear tooth in MMC gears. The Al45/SiC55 composite experienced the largest stress compared to other composites such as Al60/SiC40 and Al70/SiC30. The strain values (unlike the stress values) reduced with increasing in the volume fraction of the SiC reinforcement. Moreover, 94% aluminum oxide composite showed larger stress compared to 96% aluminum oxide and 99.5% aluminum oxide. The spur gear is designed and analyzed using SOLID WORKS and ANSYS Workbench softwares.

doi: *10.5829/ije.2021.34.02b.29*

1. INTRODUCTION

Gears are different in terms of type (spur, helical, bevel, worm, and rack and pinion) and material (gray cast iron, alloy cast iron, steel, brass, bronze, plastic, etc.). One of the simplest types of gears is spur gears, which have straight teeth that are parallel to the gear axis. For example, one of the important industrial applications of the composite "Al-SiC" is in internal combustion engine, like piston crown, cylinder liners where alumina and carbon fiber reinforced aluminum have shown a suitable substitute for cast iron. Also, the composite of "Al/SiC" has many applications in structural and industrial aims, where suitable weight and high strength-to-weight is required. In addition, the obtained results show and prove that the composite "Al/SiC" considerably increased the mechanical properties. So, it can be concluded that the mentioned composite can be the best-suited engineering material with characteristics in the application of the engine cylinder liner to get the modern demands of the automotive industries in the world. The teeth are tasked with transferring force between two parallel shafts. These gears are easy to design and manufacture and are used in a wide range of applications, such as trains, agricultural machinery, motorcycles, automobiles, aircraft, and similar applications [1, 2]. Nowadays, MMC gears have drawn the interest of researchers and industrialists due to their features such as improved hardness, low weight, and high tensile strength [3, 4]. Composites consist of a matrix and reinforcement. They can be divided into several categories in terms of the types of the matrix and reinforcement. Metal Matrix Composites (MMC's) are lightweight materials composed of a metal matrix and hard reinforcement particles that provide suitable strength and stiffness. Recently, researchers and manufacturers have shown interest in using MMCs in automotive, airplane, helicopter, and spacecraft industries due to their good physical and mechanical properties. MMCs have better characteristics such as resistance to high heat, high thermal conductivity, high

*Corresponding Author Institutional Email: vahid_monfared@alum.sharif.edu (V. Monfared)

Please cite this article as: M. Bigdeli, V. Monfared, The Prediction of Stress and Strain Behaviors in Composite Gears using FEM, International Journal of Engineering, B: Applications Vol. 34, No. 02, (2021) 556-563

strength and stiffness, resistance against erosion, and high strength to weight ratio, Composites with aluminum alloy matrices have attracted most research and development programs and commercial applications. Reinforcements used for aluminum composites include alumina, aluminosilicate, silicon carbide, and graphite. Reinforcements can be in the form of particles, continuous and discontinuous fibers, and whiskers and constitute 10% to 60% of the volume of the composite. Continuous fibers MMCs include carbon, silicon carbide, boron, alumina, and refractory metals [5–7]. In this research, the aim is to examine the stress and strain behaviors in an aluminum silicon carbide composite gear with different SiC volume fractions (55 vol.%, 40 vol.%, 30 vol.%) and an aluminum oxide composite gear with weight fractions of 94 wt.%, 96 wt.% and 99.5 wt.%. Among the available research works published in this field, one can name the paper by Singla et al. [8] in which the authors made a silicon aluminum part by casting and concluded from the test that hardness and impact-resistance increase with an increase in the SiC weight fraction [8]. MMCs have been used in power transmission gear applications, and the results show that aluminum oxide gears are also noteworthy for power transmission [9, 10]. In other cases, aluminum oxide has been used in dentistry to replace teeth and dental implants and in various fields such as artificial joints, artificial bones, and the electronic industry due to such features as high mechanical strength, high hardness and resistance, high thermal conductivity, and high erosion-resistance [11, 12], and other types of composites particularly Al/SiC's composites in many industries [13–21]. Also, recently applied and interesting research works have been done about composite materials analysis [22–29]. It should be mentioned that it has been used from MatWeb's searchable database of material properties includes data sheets of many material data for simulations. In this research, a spur gear has been modeled in 3D in the SOLIDWORKS software, and the mechanical data of the metal composite materials, including aluminum silicon carbide with the specifications (Al45/SiC55, Al60/SiC40, and Al70/SiC30) and aluminum oxide with the specifications (94% Aluminum Oxide, 96% Aluminum Oxide, and 99.5%Aluminum Oxide) have been defined in the ANSYS Workbench software. Then, we exerted various forces on a gear tooth and evaluated the stress corresponding to each force and gear material.

2. MATERIALS AND METHODS

2. 1. Composite Materials Composites consist of matrix and reinforcement. They can be divided into several categories in terms of the types of matrix and reinforcement. In terms of the matrix type, they are classified into metal, polymer, ceramic, and intermetallic matrix composites. Metal matrix composites have drawn the most attention among the various types. Methods of manufacturing metal matrix composites include powder metallurgy, spray deposition, mechanical alloying, and various casting techniques such as squeeze casting, slip casting, and compo casting. All of these techniques are based on the addition of reinforcement particles, in powder or molten form, to the matrix [7, 13].

2. 2. Aluminum Silicon Carbide Most metal matrix metals have commercial and industrial applications with an aluminum matrix, i.e., most of them are focused on an aluminum matrix. Aluminum matrix metals feature low weight, high strength, and very good mechanical properties, which have made the alloys of this metal popular. It is easy to fabricate this composite due to the low melting point of aluminum. Examples of reinforcements used in aluminum composites are alumina, aluminosilicate, silicon carbide, and graphite. Similar to silicon carbide (SiC) reinforcement particles, MMCs are a famous group of composites due to their characteristics such as stiffness, hardness, strength, erosion-resistance, and availability. Casting is a common method of producing these MMCs [14–16]. Here, three different SiC volume fractions, namely 55 vol.%, 40 vol.%, and 30 vol.%, are used to analyze three types of Al-SiC MMC. The mechanical properties of aluminum silicon carbide composites (Al45/SiC55, Al60/SiC40, Al70/SiC30) composites are shown in Table 1.

2. 3. Aluminum Oxide Aluminum oxide has the chemical formula Al_2O_3 and is commonly known as alumina. Alumina has strong ionic inter-atomic bonds. Moreover, it represents a family of engineering ceramics that feature availability and a low price. Among the different and prominent properties of alumina are such mechanical properties as high compressive strength, hardness, and refractoriness. Due to the high hardness and erosion-resistance of alumina, it is used in various applications such as erosion-resistant coatings for pipes and conduits, pumps, and valves. Also, due to its high hardness at high temperatures, it is utilized as a tooltip material in metal cutting [17–19]. Three different weight fractions of aluminum oxide, namely 94 wt.%, 96 wt.%, and 99.5 wt% have been used here for analysis. For high-temperature use, a purity of 94% to 99.5% is available. The mechanical properties corresponding to each purity level of alumina are provided in Tables 2-4.

2. 4. Gear Design Gears are among the most common power and motion transmission tools. A gear mechanism is a system composed of at least two gears working as a pair. Gears have various types, such as spur, helical, bevel, worm, and rack and pinion [1, 20]. Since the goal of this research is comparing and analyzing

TABLE 1. Mechanical Properties of Al70/SiC30, Al60/SiC40, Al45/SiC55*

Property	SI	Al70/SiC30	Al60/SiC40	Al45/SiC55
Composition (vol. %)	-	Al70/SiC30	Al60/SiC40	Al45/SiC55
Density, ρ	(g/cm^3)	2.78	2.87	2.96
Poisson's Ratio, ϑ	-	0.29	0.28	0.25
Young's Modulus, E	(GPa)	125	150	200
Thermal Conductivity, k	(W/m.K)	160	160	160
Specific Heat	(J/kg.K)	820	750	730
Ultimate Tensile Strength	(MPa)	370	370	340
Flexural Strength	(MPa)	NA	NA	NA
Fracture Toughness	($MPa.\sqrt{m}$)	15	14	13
Damping Factor	(%Zeta)	0.26	---	0.58
Specific Stiffness, (E/ρ)	GPa. g/cm^3	45	52	68
Thermal Stability, (k/α)	$J/K.m^3$	11	13	14

* Adapted from http://www.mmmt.com/resources/standard-materialproperties.html

TABLE 2. Mechanical Properties of 94% aluminum oxide*

Mechanical	Units of measure	SI/Metric	Imperial
Density	gm/cc (lb/ft^3)	3.69	230.4
Flexural Strength	MPa ($lb/in^2 \times 10^3$)	330	47
Elastic Modulus	GPa ($lb/in^2 \times 10^6$)	300	43.5
Shear Modulus	GPa ($lb/ in^2 \times 10^6$)	124	18
Bulk Modulus	GPa ($lb/ in^2 \times 10^6$)	165	24
Poisson's Ratio	---	0.21	0.21
Compressive Strength	MPa ($lb/ in^2 \times 10^3$)	2100	304.5
Hardness	Kg/mm^2	1175	---
Fracture Toughness $\mathbf{k_{Ic}}$	$MPa.m^{1/2}$	3.5	---
Maximum Use Temperature(no load)	℃ (°F)	1700	3090
Specific Heat	J/kg.°K (Btu/lb.°F)	880	0.21
Thermal Conductivity	W/m.°K (BTU.in/ft^2.h.°F)	18	125
Coefficient of Thermal Expansion	10^{-6}/°C (10^{-6}/°F)	8.1	4.5

* Adapted from http://www.matweb.com/

TABLE 3. Mechanical Properties of 96% aluminum oxide*

Mechanical	Units of measure	SI/Metric	Imperial
Density	gm/cm^3 (lb/ft^3)	3.72	232.2
Flexural Strength	MPa ($lb/in^2 \times 10^3$)	345	50
Elastic Modulus	GPa ($lb/in^2 \times 10^6$)	300	43.5
Shear Modulus	GPa ($lb/ in^2 \times 10^6$)	124	18
Bulk Modulus	GPa ($lb/ in^2 \times 10^6$)	172	25
Poisson's Ratio	---	0.21	0.21
Compressive Strength	MPa ($lb/ in^2 \times 10^3$)	2100	304.5
Hardness	kg/mm^2	1100	---
Fracture Toughness $\mathbf{k_{Ic}}$	$MPa.m^{1/2}$	3.5	---
Maximum Use Temperature(no load)	℃ (°F)	1700	3090
Specific Heat	J/kg.°K (Btu/lb.°F)	880	0.21
Thermal Conductivity	W/m.°K (BTU.in/ft^2.h.°F)	25	174
Coefficient of Thermal Expansion	10^{-6}/°C (10^{-6}/°F)	8.2	4.6

* Adapted from http://www.matweb.com/

TABLE 4. Mechanical Properties of 99.5% aluminum oxide*

Mechanical	Units of measure	SI/Metric	Imperial
Density	gm/cc (lb/ft^3)	3.89	242.8
Flexural Strength	MPa ($lb/in^2 \times 10^3$)	379	55
Elastic Modulus	GPa ($lb/in^2 \times 10^6$)	375	54.4
Shear Modulus	GPa ($lb/ in^2 \times 10^6$)	152	22
Bulk Modulus	GPa ($lb/ in^2 \times 10^6$)	228	33
Poisson's Ratio	---	0.22	0.22
Compressive Strength	MPa ($lb/ in^2 \times 10^3$)	2600	377
Hardness	Kg/mm^2	1440	---
Fracture Toughness $\mathbf{k_{Ic}}$	$MPa.m^{1/2}$	4	---
Maximum Use Temperature(no load)	℃ (°F)	1750	3180
Specific Heat	J/Kg.°K (Btu/lb.°F)	880	0.21
Thermal Conductivity	W/m.°K (BTU.in/ft^2.hr.°F)	35	243
Coefficient of Thermal Expansion	10^{-6}/°C (10^{-6}/°F)	8.4	4.7

* Adapted from http://www.matweb.com/

MMCs, the spur gear has been used for the analysis. Spur gears have a simple design and are widely used in the industry due to their ease of manufacture. The methods of manufacturing gears include machining, forging, casting, stamping, powder metallurgy, and plastic injection molding. The most common gear manufacturing method is machining, which is divided into gear hobbing and form milling [20, 21].

In this study, the spur gear along with its shaft was designed in the SOLIDWORKS 2016 software. The design procedure can be seen in the figures below. Figure 1 shows the design of a single gear tooth.

As shown in Figure 2, the number of teeth was increased to 20 using the Circular Pattern command.

Finally, the 3D model of the gear was completed by adding the shaft, as shown in Figure 3.

2. 5. Analysis using ANSYS Workbench After designing the gear, the mechanical properties of aluminum silicon carbide and aluminum oxide composites with the specifications [Al45/SiC55, Al60/SiC40, and Al70/SiC30] and [94% aluminum oxide, 96% aluminum oxide, and 99.5% aluminum oxide] were defined in the Engineering Data Sources of ANSYS Workbench software. Then, fine meshing was performed on the gear geometry for stress and strain analyses, as shown in Figure 4.

After the meshing, a gear tooth is selected, and [100 N, 200 N, 300 N, 400 N, 500 N] forces are applied to a (Al45/SiC55, Al60/SiC40, Al70/SiC30) aluminum silicon carbide tooth. Moreover, [100 N, 350 N, 600 N, 800 N, 1000 N] forces are exerted on a (94% Aluminum Oxide, 96% Aluminum Oxide, 99.5% Aluminum Oxide) aluminum oxide tooth. An example of a force (350 N) applied to a gear tooth is shown in Figure 5.

In the final part of modeling, the stress and strain results of the composite gears in terms of the exerted forces are derived so that they could be analyzed and compared. An example of this stress computation process for the Al45/SiC55 with Force=400 N is displayed in Figure 6.

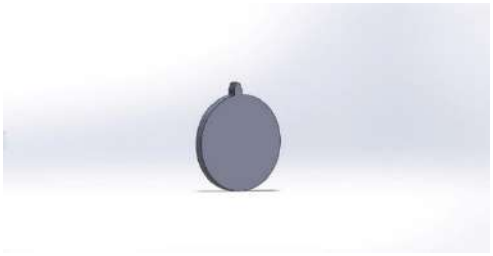

Figure 1. Design of a simple gear tooth in SOLIDWORKS 3D environment

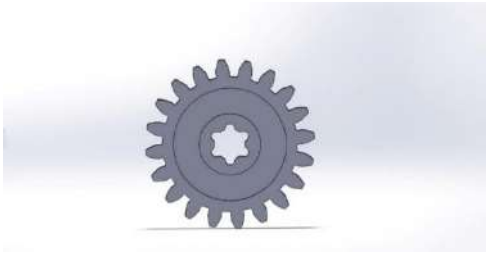

Figure 2. Modeling of 20 gears in SOLIDWORKS 3D environment

Figure 3. Spur gear model with the shaft in SOLIDWORKS 3D environment

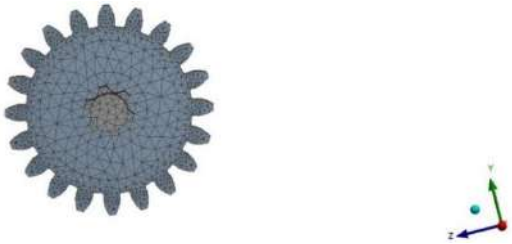

Figure 4. Meshing on the gear geometry

Figure 5. Application of 350 N force on a gear tooth

Figure 6. Al45/SiC55 gear analysis with Force = 400 N

Also, the stress analysis for the 94% aluminum oxide composite gear with Force = 350 N is presented in Figure 7.

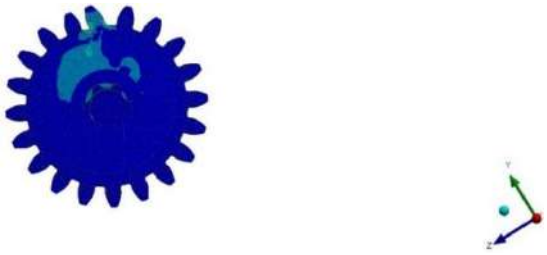

Figure 7. Stress analysis for the 94% aluminum oxide composite gear with Force = 350 N

3. RESULTS AND DISCUSSIONS

After applying force on a single gear tooth, the stress and strain results for aluminum silicon carbide gears with 3 different SiC volume fractions, i.e., 30 vol.%, 40 vol.%, and 55 vol.% and with the specifications (Al45/SiC55, Al60/SiC40, Al70/SiC30) and aluminum oxide gears with 3 different alumina weight fractions, i.e., 94 wt.%, 96 wt.%, and 99.5 wt.%, were analyzed and compared. The stress and strain results of each gear in terms of the exerted forces have been shown in Tables 5-12, and the stresses of the gears relative to each other are displayed in Figures 8 and 9. These tables and figures show good results for aluminum silicon carbide and aluminum oxide metal matrix composites. According to the results, the gears made of aluminum silicon carbide of the type Al45/SiC55 exhibited less stress compared to 2 other gears made of Al60/SiC40 and Al70/SiC30 under forces of [100 N, 200 N, 300 N, 400 N, 500 N]. Hence, the Al45/SiC55 gears can be used in sensitive applications in the industry where gears must bear larger pressures.

The stress (strength) and strain (elongation and deformation) values increase with an increase in the applied forces (Table 5). The combination of "SiC" (reinforcement) and Al (matrix) significantly increases the stress values, such as the yield strength, compressive strength, ultimate tensile strength, Young's modulus, yield and fracture stresses, hardness, and wear properties and decreases the elongation, strain (ductility and strain rate), and toughness of the composites in comparison with those of the matrix alloy. Moreover, the "SiC" reinforcement particles are the most effective strengthening particulates for higher strength, hardness, and grain size reduction. Also, Table 6 indicates the maximum stress and strain results for the Al60/SiC40 gear.

According to the obtained results for the "Al/SiC" composite, it is concluded that the strain values decrease with an increase in the volume fraction of the "SiC" reinforcement particles (unlike the stress values). Table 7 shows the maximum stress and strain results for the Al70/SiC30 gear.

The stress results for each of the aluminum silicon carbide composite gears with SiC volume fractions of (55 vol.%, 40 vol.%, 30 vol.%) are shown in Figure 8. The results of Figure 8 and the following table show that the stress has increased with an increase in the volume fraction of the SiC reinforcement. In other words, the strength of the gear increases with an increase in the volume fraction of SiC.

Given the obtained stress values, the results of Figure 8 indicate that the Al45/SiC55 composite gear has experienced higher stress compared to Al70/SiC30 and

TABLE 5. Stress and strain results for Al45/SiC55 gear

Number	Force (KN)	Stress maximum (MPa)	Strain maximum (m/m)
1	0.1	1.0701	5.66×10^{-6}
2	0.2	2.1402	1.13×10^{-5}
3	0.3	3.2103	1.70×10^{-5}
4	0.4	4.2804	2.27×10^{-5}
5	0.5	5.3506	2.83×10^{-5}

TABLE 6. Stress and strain results for Al60/SiC40 gear

Number	Force (KN)	Stress maximum (MPa)	Strain maximum (m/m)
1	0.1	1.0653	7.52×10^{-6}
2	0.2	2.1305	1.50×10^{-5}
3	0.3	3.1958	2.26×10^{-5}
4	0.4	4.2611	3.01×10^{-5}
5	0.5	5.3263	3.76×10^{-5}

TABLE 7. Stress and strain results for Al70/SiC30 gear

Number	Force (KN)	Stress maximum (MPa)	Strain maximum (m/m)
1	0.1	1.0637	9.01×10^{-6}
2	0.2	2.1274	1.80×10^{-5}
3	0.3	3.1911	2.70×10^{-5}
4	0.4	4.2548	3.61×10^{-5}
5	0.5	5.3185	4.51×10^{-5}

TABLE 8. Results for Al45/SiC55, Al60/SiC40, Al70/SiC30

		Stress maximum (MPa)		
Number	Force (KN)	Al45/SiC55	Al60/SiC40	Al70/SiC30
1	0.1	1.0701	1.0653	1.0637
2	0.2	2.1402	2.1305	2.1274
3	0.3	3.2103	3.1958	3.1911
4	0.4	4.2804	4.2611	4.2548
5	0.5	5.3506	5.3263	5.3185

Al60/SiC40 composite gears. Hence, Al45/SiC55 can be employed to manufacture gears with good mechanical properties and high impact-resistance.

The stress and strain results for the 94% aluminum oxide composite gear are shown in Figure 9. The strain results in Tables 9-11 indicate that the stress under different forces has decreased with a decrease in the weight fraction of alumina. For example, for Force = 1 KN, the stress in the composite gear with a weight fraction of 94 wt.% is 12.727, which is larger than those corresponding to composite gears with weight fractions of 99.5 wt.% and 96 wt.%.

The stress and strain results for the 96% aluminum oxide composite gear are shown in Table 10.

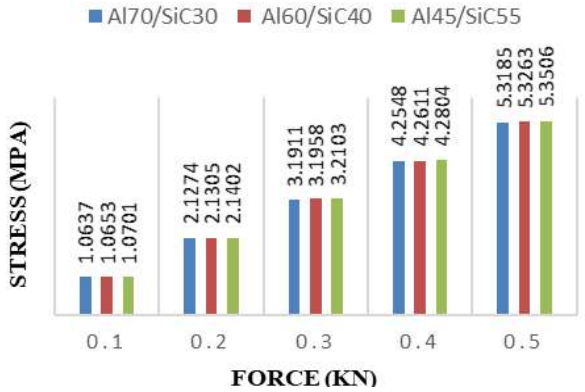

Figure 8. Stress results for Al45/SiC55, Al60/SiC40, Al70/SiC30 composite gears

TABLE 9. Stress and strain results for 94% Aluminum Oxide composite material

Number	Force (KN)	Stress maximum (MPa)	Strain maximum (m/m)
1	0.1	1.2727	4.51×10^{-6}
2	0.35	4.4543	1.58×10^{-5}
3	0.6	7.636	2.71×10^{-5}
4	0.8	10.181	3.61×10^{-5}
5	1	12.727	4.51×10^{-5}

TABLE 10. Stress and strain results for 96% Aluminum Oxide composite material

Number	Force (KN)	Stress maximum (MPa)	Strain maximum (m/m)
1	0.1	1.266	4.29×10^{-6}
2	0.35	4.431	1.50×10^{-5}
3	0.6	7.5959	2.57×10^{-5}
4	0.8	10.128	3.43×10^{-5}
5	1	12.66	4.29×10^{-5}

The stress and strain results for the 99.5% aluminum oxide composite gear are shown in Table 11 The results show smaller stress for the composite gear with a weight fraction of 99.5 wt.% compared to those for weight fractions of 94 wt.% and 96 wt.%.

The stress results for 94% Aluminum Oxide, 96% Aluminum Oxide, 99.5% Aluminum Oxide are shown in Table 12 and Figure 9. According to Figure 9 and the obtained results, the composite gear made of 99.5% aluminum oxide has the lowest stress and the composite gear made of 94% aluminum oxide has the highest stress under different forces. In other words, the 94% aluminum

TABLE 11. Stress and strain results for 99.5% Aluminum Oxide composite material

Number	Force (KN)	Stress maximum (MPa)	Strain maximum (m/m)
1	0.1	1.2592	3.33×10^{-6}
2	0.35	4.4072	1.17×10^{-5}
3	0.6	7.5552	2.00×10^{-5}
4	0.8	10.074	2.67×10^{-5}
5	1	12.592	3.33×10^{-5}

TABLE 12. Stress results (MPa) for 94% aluminum oxide, 96% aluminum oxide, and 99.5% aluminum oxide composite material gears

Number	Force (KN)	94% aluminum oxide	96% aluminum oxide	99.5% aluminum oxide
1	0.1	1.2727	1.266	1.2592
2	0.35	4.4543	4.431	4.4072
3	0.6	7.636	7.5959	7.5552
4	0.8	10.181	10.128	10.074
5	1	12.727	12.66	12.592

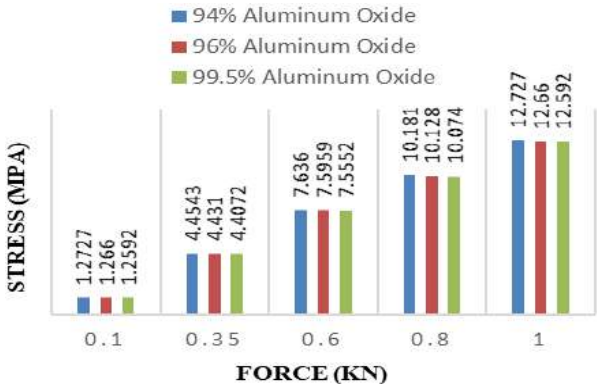

Figure 9. Stress results for 94% aluminum oxide, 96% aluminum oxide, and 99.5% aluminum oxide composite material gears

oxide composite gear can be employed where the teeth are required to carry larger loads.

According to Figure 10, the teeth can fracture or fail under forces greater than the load capacities of the gears. Therefore, reinforcing the regions of the teeth under the highest pressure can reduce the probability of failure or fracture.

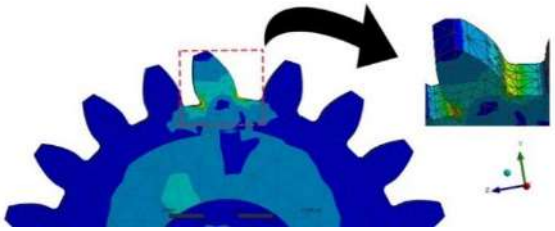

Figure 10. Strengthening specified areas to reduce the failure probability

4. CONCLUSION

The (Al45/SiC55, Al60/SiC40, Al70/SiC30) aluminum silicon carbide composite with (55 vol.%, 40 vol.%, 30 vol.%) SiC volume fractions and aluminum oxide composite with (94 wt.%, 96 wt.%, 99.5 wt.%) weight fractions were analyzed and compared, and the following results were obtained,

- The Al45/SiC55 composite material experiences higher and larger stresses compared to Al60/SiC40 and Al70/SiC30 composite materials.
- An increase in the volume fraction of SiC reinforcement particles in the aluminum silicon carbide composite gear, increases stress under different forces, thus improving the strength of the gear is resulted.
- The results of the investigation on the aluminum oxide composite gears showed that the 94% aluminum oxide experienced higher and larger stress values under different forces compared to the 95% aluminum oxide and 99.5% aluminum oxide composite materials. In other words, the stress has increased with a decrease in the weight fraction of alumina.
- The higher stresses in the Al45/SiC55 and 94% aluminum oxide gears under different forces compared to the composite gears studied in this research are remarkable and can satisfy the needs of industrialists in many industries for gears with high fracture-resistance.
- The strain values decrease with an increase in the volume fraction of SiC reinforcement particles.
- Reinforcing the tooth areas under can reduce the probability of fracture and failure. Finally the engineers and researchers can trust to the ANSYS results for predicting the composite gear behaviors in the practical and academic fields.

5. REFERENCES

1. Radzevich, S., Dudley's Handbook of Practical Gear Design and Manufacture, (2012) CRC press.
2. Mayuram, M., and Gopinath, K., Machine Design II, (2008) Indian Institute of Technology, Madras.
3. Karthik, J. P., Sai, T. R., and Praneeth, S. S., "Design and Optimization of Metal Matrix Composite (MMC'S) Spur Gear", ***International Journal of Advanced Design & Manufacturing Technology***, Vol. 9, No. 3, (2016), 49–56.
4. Pawar, P. B., and Utpat, A. A., "Analysis of Composite Material Spur Gear Under Static Loading Condition", ***Materials Today: Proceedings***, Vol. 2, Nos. 4–5, (2015), 2968–2974. doi:10.1016/j.matpr.2015.07.278
5. Karl, U., Metal Matrix Composites: Custom-Made Materials for Automotive and Aerospace Engineering, (2006) Basics of Metal Matrix Composites, Wiley.
6. Haghshenas, M., "Metal–Matrix Composites", Reference Module in Materials Science and Materials Engineering, (2016) Elsevier. doi:10.1016/b978-0-12-803581-8.03950-3
7. Chawla, K. K., "Metal Matrix Composites", ***Composite Materials***, (2012), 197–248. doi:10.1007/978-0-387-74365-3_6
8. Singla, M., Deepak Dwivedi, D., Singh, L., and Chawla, V., "Development of Aluminium Based Silicon Carbide Particulate Metal Matrix Composite", ***Journal of Minerals & Materials Characterization & Engineering***, Vol. 8, No. 6, (2009), 455-467.
9. Ganesan, N., and Vijayarangan, S., "A static analysis of metal matrix composite spur gear by three-dimensional finite element method", ***Computers and Structures***, Vol. 46, No. 6, (1993), 1021–1027. doi:10.1016/0045-7949(93)90088-U
10. Sharma, A., Aggarwal, M. L., and Singh, L., "Experimental investigation into the effect of noise and damping using composite spur gear", ***Materials Today: Proceedings***, Vol. 4, No. 2, (2017), 2777–2782. doi:10.1016/j.matpr.2017.02.156
11. Ratner, B., Hoffman, A., Schoen, F., and Lemons, J., Biomaterials Science: An Introduction to Materials in Medicine, (2004) Academic Press.
12. Ishikawa, K., Matsuya, S., Miyamoto, Y., and Kawate, K., "Bioceramics", ***Comprehensive Structural Integrity***, Vol. 9, (2007), 169–214. doi:10.1016/B0-08-043749-4/09146-1
13. Kar, K., Composite Materials: Processing, Applications, Characterizations, (2016) Springer.
14. Loos, M., "Composites", Carbon Nanotube Reinforced Composites: CNR Polymer Science and Technology, (2015), 37–72 Elsevier Inc. doi:10.1016/B978-1-4557-3195-4.00002-3
15. Agnihotri, R., and Dagar, S., "Mechanical Properties of Al-SiC Metal Matrix Composites Fabricated by Stir Casting Route", ***Research in Medical & Engineering Sciences***, Vol. 2, No. 5, (2017), 178–183. doi:10.31031/rmes.2017.02.000549
16. Poovazhagan, L., Kalaichelvan, K., Rajadurai, A., and Senthilvelan, V., "Characterization of hybrid silicon carbide and boron carbide nanoparticles-reinforced aluminum alloy composites", ***Procedia Engineering***, Vol. 64, (2013), 681–689. doi:10.1016/j.proeng.2013.09.143
17. McKeen, L. W., "Pigments, Fillers, and Extenders", Fluorinated Coatings and Finishes Handbook, (2006), 59–76. doi:10.1016/b978-081551522-7.50008-x
18. Park, S. J., and Seo, M. K., Element and Processing, Interface Science and Technology, Vol. 18, (2011) ,. doi:10.1016/B978-0-12-375049-5.00006-2
19. Ebnesajjad, S., "Surface Treatment and Bonding of Ceramics",

Surface Treatment of Materials for Adhesive Bonding, (2014), 283–299 Elsevier. doi:10.1016/b978-0-323-26435-8.00011-3

20. Goldfarb, V., Trubachev, E., and Barmina, N., New Approaches to Gear Design and Production, Vol. 81, (2020) Cham, Springer International Publishing. doi:10.1007/978-3-030-34945-5
21. Watson, H. J., "Methods of Manufacture", ***Modern Gear Production***, (1970), 117–129 Elsevier. doi:10.1016/b978-0-08-015835-8.50010-9
22. Monfared, V., Mondali, M., and Abedian, A., "Steady-state creep analysis of polymer matrix composites using complex variable method", ***Proceedings of the Institution of Mechanical Engineers, Part C: Journal of Mechanical Engineering Science***, Vol. 227, No. 10, (2013), 2182–2194. doi:10.1177/0954406212473391
23. Monfared, V., "A displacement based model to determine the steady state creep strain rate of short fiber composites", ***Composites Science and Technology***, Vol. 107, (2015), 18–28. doi:10.1016/j.compscitech.2014.11.019
24. Aswad, M. A., Awad, S. H., and Kaayem, A. H., "Study on Iraqi Bauxite ceramic reinforced aluminum metal matrix composite synthesized by stir casting", ***International Journal of Engineering, Transactions A: Basics***, Vol. 33, No. 7, (2020), 1331–1339. doi:10.5829/IJE.2020.33.07A.20
25. Mekonnen, B. Y., and Mamo, Y. J., "Tensile and flexural analysis of a hybrid bamboo/jute fiber-reinforced composite with polyester matrix as a sustainable green material for wind turbine blades", ***International Journal of Engineering, Transactions B: Applications***, Vol. 33, No. 2, (2020), 314–319. doi:10.5829/IJE.2020.33.02B.16
26. Vosough, M., Sharafi, S., and Khayati, G. R., "Co-tio2 nanoparticles as the reinforcement for fe soft magnetic composites with enhanced mechanical and magnetic properties via pulse electrodeposition", ***International Journal of Engineering, Transactions A: Basics***, Vol. 33, No. 10, (2020), 2030–2038. doi:10.5829/IJE.2020.33.10A.21
27. R., B., Al Madhani, M., and Al Madhani, R., "Study on Retrofitting of RC Column Using Ferrocement Full and Strip Wrapping", ***Civil Engineering Journal***, Vol. 5, No. 11, (2019), 2472–2485. doi:10.28991/cej-2019-03091425
28. Hanoon, A. N., Abdulhameed, A. A., Abdulhameed, H. A., and Mohaisen, S. K., "Energy Absorption Evaluation of CFRP-Strengthened Two-Spans Reinforced Concrete Beams under Pure Torsion", ***Civil Engineering Journal***, Vol. 5, No. 9, (2019), 2007–2018. doi:10.28991/cej-2019-03091389
29. Song, J.-H., Lee, E.-T., and Eun, H.-C., "Shear Strength of Reinforced Concrete Columns Retrofitted by Glass Fiber Reinforced Polyurea", ***Civil Engineering Journal***, Vol. 6, No. 10, (2020), 1852–1863. doi:10.28991/cej-2020-03091587

Persian Abstract

چکیده

چرخ دنده‌های کامپوزیتی MMC به عنوان یکی از قطعات اصلی در صنعت به کار می‌روند و وظیفه اصلی آنها کیفیت انتقال قدرت در سرعت‌های بالاست. نیاز به داشتن کیفیت بالا اعم از استحکام و مقاومت بالا در مقابل ضربه و شکنندگی کمتر و عمر طولانی بسیار حائز اهمیت و نیاز صنعتکاران است، چرخ دنده‌ها از جنس‌های مختلفی ساخته می‌شوند و امروزه محققان و صنعتکاران روی به سوی طراحی، ساخت و استفاده از چرخ دنده‌های کامپوزیتی نسبت به دیگر چرخ دنده‌ها آورده‌اند به دلیل وزن پایین، هزینه کمتر، سختی، استحکام بالا و خاصیت مکانیکی بهتر. در این پژوهش پیش‌بینی تنش را در چرخ دنده‌های کامپوزیتی از جنس Aluminum Silicon Carbide با سه درصد حجمی مختلف از SiC یعنی 30 vol.%, 40 vol.% , 55 vol.% با مشخصات (Al45/SiC55, Al60/SiC40, Al70/SiC30) و همچنین چرخ دنده‌هایی از جنس Aluminum Oxide با سه درصد وزنی مختلف از alumina یعنی 94 wt.% , 96 wt.%, 99.5 wt.% مورد ارزیابی قرار دادیم تا رفتار تنش در نیروهای مختلف وارده بر یک دنده چرخ دنده را درچرخ دنده‌های کامپوزیتی MMC مورد مقایسه و بررسی قرار دهیم. ماده کامپوزتی Al45/SiC55 بیشترین مقدار تنش را نسبت به دیگر ماده‌های کامپوزیتی نظیر Al60 SiC40 و Al70SiC30 داشت، نتایج مقدار کرنش (برخلاف نتایج مقدار تنش) با افزایش درصد حجمی تقویت‌کننده 'SiC' کاهش یافت، همچنین ماده کامپوزیتی 94% Aluminum Oxide بیشترین مقدار تنش را نسبت به ماده‌های کامپوزیتی 96% Aluminum Oxide و 99.5% Aluminum Oxide نشان داد. طراحی چرخ دنده از نوع ساده با استفاده از نرم‌افزار Solid Works 2016 و تعریف داده‌های مکانیکی مواد به چرخ دنده وتحلیل تنش و کرنش در نرم‌افزار ANSYS Workbench 16.1 انجام گردیده است.

International Journal of Engineering

Journal Homepage: www.ije.ir

Experimental Investigation of Tungsten Inert Gas Welding Input Parameters Effects on Mechanical Characteristics

F. Salehpour-Oskouei*[a], V. Nematifard[b], G. Marami[c], A. Afkar[d]

[a] *Mechanical Engineering Department, Islamic Azad University, Shabestar Branch, Shabestar, Iran*
[b] *Islamic Azad University, Ilkhchi Branch, Ilkhchi, Iran*
[c] *Mechanical Engineering Department, Tabriz University, Tabriz, Iran*
[d] *Research Center of Technology and Engineering, Standard Research Institute, Karaj, Iran*

PAPER INFO

Paper history:
Received 12 November 2020
Received in revised form 02 December 2020
Accepted 04 December 2020

Keywords:
Tungsten Inert Gas
Mechanical Arm
Tensile Strength
316 Stainless Steel

ABSTRACT

Tungsten inert gas (TIG) welding process is one of the complex production methods. The reason is the drastic changes in the metallurgical structure of welding parts due to the heating and cooling cycle during welding. These changes cause various metallurgical and mechanical defects of the parts and weaken the mechanical properties of the parts. Many parameters in welding have different effects on the quality of welding parts. To create a suitable weld, it is necessary to identify the effect of these parameters and to be able to estimate it and select the appropriate and optimal conditions. Accordingly, In this study, an experimental investigation were conducted on determining the mechanical characteristics of the pieces through variation of three main welding parameters including advance speed, welding amperage and preheating temperature. Due to the difficulty of changing the rate of advance speed in manual welding, a robotic welding arm was designed for welding 316 stainless steel in the current paper, in which a microcontroller tuned the speed and welding length. By collecting the practical data, the effect of the input data (advance speed, welding amperage and preheating temperature) investigated in durability and strength of the joints. In other words, the tension and durability of the joints for stainless steels are proposed for various welding parameters to enhance the optimal conditions based on the experimental results. In samples with low advance speed, in addition to increase the solidification time, the coarseness of the structure and the burning of the edges of the welded parts due to the low speed and high amps, reduce the tensile strength. Also, the results showed that by increasing the amperage, the strength of welding parts decreases due to the burn defect of the plate edges, which can be minimized by increasing the welding speed and reducing the effect of extreme heat on the edges. Finally, by analyzing the effect of the input parameter on the output, the best conditions of the adjustment parameters in butt-welding were acquired among existed samples for welding 316 stainless steel.

doi: *10.5829/ije.2021.34.02b.30*

1. INTRODUCTION

Newly, there has been a regular shift from merely theoretical to applied research, especially in the field of information processing, and for issues, which are complicated or have no clear-cut solutions. Hence, there has been an increasing interest in the theoretical development of intelligent dynamic systems of free models, which are based on experimental data. Now, the Unmanned Flexible Manufacturing System (UFMS) is growing without human presence [1]. For this reason, different sensors are required to control and gain information from process conditions. Nonetheless, the information on these sensors must be processed in some ways, and decisions must be made to control and supervise the process. Hence, the decision-making unit must be a sort of intelligent system [2]. In other study, the deposition ratio of welding bead for gas arc of SS316 optimized by the Taguchi method [3]. Their results showed the efficiency of the optimization method in

*Corresponding Author Institutional Email: Farzin.salehpour@gmail.com (F. Salehpour-Oskouei)

Please cite this article as: F. Salehpour-Oskouei, V. Nematifard, G. Marami, A. Afkar, Experimental Investigation of Tungsten Inert Gas Welding Input Parameters Effects on Mechanical Characteristics, International Journal of Engineering, Transactions B: Applications Vol. 34, No. 02, (2021) 564-571

welding process. The control factors of the tungsten inert gas welding and its penetration for the thin layers were presented in literature [4]. In addition, the activated tungsten inert gas (ATIG) welding procedure was optimized for ASTM/UNS S32205 DSS joints to enhance intended aspect ratio [5].

The welding process is considered one of the complex production methods [6]. In some researches, the effect of welding parameters on joint quality were investigated [7-9]. Halimi et al. [7] have investigated the effect of welding parameters such as speed and power on dissimilar pulsed laser joint between nickel-based alloy and austenitic stainless steel AISI 304l. Findings showed that the highest-quality none-similar joints could be achieved by optimizing the proposed welding parameters [7]. Saeheaw [8] represented that the length of joining of very dissimilar material increased, by using a ring weld path, assist the achievement of sufficient joint strength and findings in efficient application of the restricted area accessible for welding performance. In addition, welding speed on characteristics of the welding and joint of dissimilar parts discussed by Langari and Kolahan [9]. The parameter analysis including the speed and rotational rate, microstructure, defects, and mechanical properties of aluminum alloys joint in welding. Kurt and Samur, [10] have estimated the mechanical characteristics of the TIG welded joints for a determined set of input parameters. In proposed study, microstructure evolution and mechanical properties of 316 austenitic stainless steel (SS) jointed by tungsten inert gas (TIG) welding by using 308 stainless steel filler wire were examined. In the closest research to the present study, Kumar et al. [11] have focused on the optimization of the procedure parameters of TIG joining procedure. Applied material in the proposed research is AISI 304. It was concluded that the current is the most influential parameters in case of tensile strength as indicated by response value graph [12]. One of the substantial methods of welding is the TIG method and, as mentioned, one of the main disadvantages of this method is that in this method, welding is performed manually [13]. On the other hand, since the welding process is done manually, the initial speed parameter and distance between the tips of the electrode to the workpiece cannot be kept constant and measured accurately. Moreover, since the speed of the welding operator's hand is not stable, the welding is not carried out uniformly and the quality of the welding is reduced [14].

In this research, a smart mechanical arm will be designed and built for tungsten electric arc welding, in which a microcontroller controls the welding speed and distance advanced. Assessing the impact of the welding input parameters on tensile strength for 316 stainless steel, which is one of the most widely used metals in the food industry, and its welding requires high skills. Hence, initially, a 316 stainless steel sheet with a thickness of 3 mm will be prepared in the dimensions of 3*60*250 mm according to the Minitab design of experiment (Taguchi optimization). To carry out and determine tensile tests with different Amp parameters at three levels of 90,110,120 amperes and four levels of advance speed of 1, 2, 3, 4 mm per second and three preheat temperatures of 120,180 ˚C and ambient temperature, the welding process is performed by a smart mechanical arm. To build this mechanism, closed-loop control will be utilized by embedding the shaft encoder in the mechanism axis, in a way that its speed can be controlled online via computer at the beginning of practical tests as desired. Next, the welded joints are prepared and examined to carry out investigations and tensile tests, and the mechanical properties of the welded joints will be practically measured. The input variables are current intensity, torch advance speed, and preheat temperature. The output is also the tensile strength and distortion of the welding joints

2. RESEARCH METHODS

2. 1. Designing an Automatic Welding Arm The welding quality of the tungsten arc welding process is higher than other processes due to its high reliability, cleanliness, and high weld strength [15]. The quality of the weld depends to the initial input variables of the welding [16]. In this survey, to assess and control the impact of speed parameters on the mechanical properties of welded joints in the tungsten arc welding, a welding arm was designed and made on AISI 316 stainless steel with a thickness of 3 mm. After designing and manufacturing the mechanical parts according to Figure 1, the components of the electronic speed control by installing the Shaft Encoder EN50S8 in the DC motor shaft with 110v power supply and with the aid of an ATMEGA8 microcontroller, which is from AVR family, was manufactured to control the speed and distance. To calculate the speed and distance advanced in the automatic arm, it is assumed that with each rotation of the mechanism, the automatic arm will advance a distance equal to the circumference of the wheel according to

Figure 1. Mechanical components of the automatic arm of the gas tungsten arc welding

Figure 2. Therefore, by multiplying the wheel circumference by the number of turns per unit time, the distance that the mechanism advances per unit time can be achieved.

Shaft encoder generates 2500 pulses per each turn of DC motor. Given Equation (1) and the diameter of the wheel (d_i), which is 67.034 mm, the course length (L) at each turn is 210.478 mm. Using a 1.800 gearbox, and considering that each turn of the wheel requires 800 turns from the DC motor shaft, and also that the shaft encoder produces 2500 pulses per round; hence, for one turn of the wheel, the output of shaft encoder will be virtually 2,000,000 pulses. By dividing course length by number of shaft encoder pulses, the rate of motion (RoM) of the automatic mechanism at each pulse is obtained according to Equation (2):

$$L=d_i\times\pi \quad (1)$$

$$\text{RoM}= \text{L/number of pulses}$$
$$\text{RoM} =210.478\div2000000= 0.00010521 \text{ mm/pulse} \quad (2)$$

Therefore, in order to convert the rate of arm movement at each pulse to speed, it is enough to set time to 0.00001 through adjusting the microcontroller, according to Equation (3), in which V indicates the torch advance speed. That is to say, the microcontroller can evaluate and control all calculations, including distance and speed, according to the transmitted pulses and their number.

$$V=X/t \quad (3)$$

The speed control system of the automatic welding arm, by pulse width modulation method (PWM), implies changing the correlation coefficient of a signal in order to send information to a communication channel or adjust the amount of power sent to the load. Pulse width Modulation, or PWM, is a signal that can be generated from a digital IC such as a microcontroller or timer 555. The output signal is a pulse train, and these pulses form a square waveform. In other words, at any given time, the wave will be in the high or low position. In this way, according to Figure 3, it should be adjusted using the feedback obtained by sending the pulse by the shaft encoder and converting it to the speed unit and comparing the speed set in the software with the aid of computer and PID routine (proportional–integral–derivative) to achieve the desired speed. After attaining the actual speed of the automatic arm movement, which is performed 10,000 times per second (due to setting the time of micro-measurement on 0.1 ms), the results obtained are delivered to the PID routine, and after carrying out the necessary software calculations, PWM is instructed to reduce or increase the speed to the desired speed and limit with the pulse width modulation method. This value is based on a unit of 0.1 mm/s and can be defined from 0.1 mm/s to 25 mm/s. The connection between the controlled automatic welding arm and the computer is done through RS-232.

The circuit was then printed using the Protel electronic circuit design program.

2. 2. Welding and Preparing Samples After manufacturing an automatic arm, to begin practical tests, to optimize and reach the best possible results with the least number of tests, designing experiments was performed using statistical and optimization techniques by RSM method and of Box-Behnken type in Minitab 1.5 software [17]. The experimental factors and test levels were conducted according to the order and conditions mentioned by this software in four modes of torch speed, three current intensity modes, and three preheat temperatures according to Table 1. In this survey, AISI 316 stainless steel with a thickness of 3 mm was applied and the steel parts were examined for chemical analysis, which is presented in Table 2. The samples after welding by the automatic arm is shown in Figure 4. Welding of joints in the dimensions of 60 × 250 mm was performed, according to Figure 5, through utilizing argon shielding gas with the double-sided torch to further protect the molten pool of the welding area from atmospheric factors.

3. RESULTS

3. 1. Experimental Sample Preparation for Distortion Distortion and deformation are some

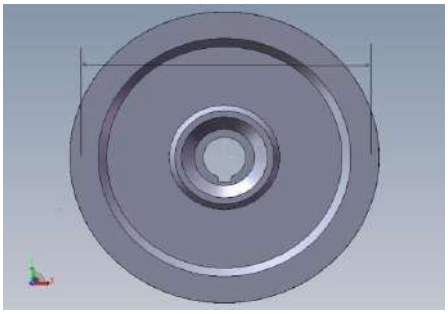

Figure 2. Wheel designed for automatic arm movement

Figure 3. Double-sided torch to further protect argon from subsamples

TABLE 1. Design of experiments in Minitab software

Experimental samples	Advance speed (mm/s)	current intensity (A)	Preheat temperature (^{0}C)
1	4	130	180
2	1	90	25
3	1	130	180
4	4	90	25
5	3	130	25
6	2	90	180
7	4	90	180
8	1	130	25
9	3	90	120
10	2	110	25
11	3	110	180
12	1	110	120
13	4	110	120
14	2	130	120
15	3	130	180
16	2	130	180
17	2	90	25
18	1	110	25

TABLE 2. Results of chemical analysis and its comparison with the standard

Element	Min	Max	Available
C	0	0.080	0.075
S	0	0.030	0.025
p	0	0.045	0.042
Mn	0	2.000	1.160
Si	0	0.750	0.479
Ni	10.00	14.00	10.110
Cr	16.00	18.00	17.771
Mo	2	3	2.133
N	0	0.10	0.043
Co	0	0	0.030
Cu	0	0	0.090

of the significant issues caused by the expansion factor, the amount of contraction in the solid state, the design error, and the welding operation technique. During welding operations, due to the application of local heat flux to the weld and the cooling rate of the welding site, the contraction, that was supposed to be distributed throughout the part, will inevitably be reduced to the same range. Moreover, if this contraction is in a place that

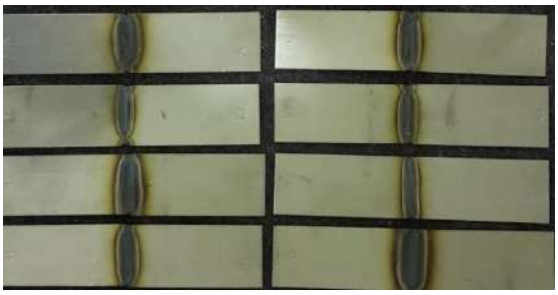

Figure 4. Samples after welding by the automatic arm

is geometrically angular, it will lead to angular distortion according to the schematic Figure 6. Angular distortion was measured using a profile projector (Figure 5). The obtained results are summarized in Table 3.

3. 2. Preparation of Tension Sample

316 stainless steel samples, after welding by an automatic arm to perform tensile tests in accordance with EN895 standard of the DIN standard series, were initially milled using milling machines according to the dimensions of Figure 6. Then, sandpapers to reduce the stress concentration sanded their edges and surfaces. Finally, they were prepared according to Figure 7.

The mechanical properties of metals, including elastic reactions, are due to the application of force or the

Figure 5. Profile projector device

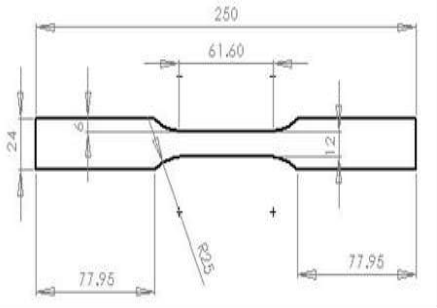

Figure 6. Dimensions of sample preparation according to EN895

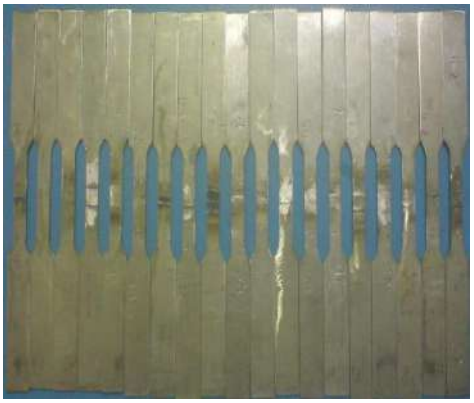

Figure 7. Samples prepared for practical tests

relationship between tension and their relative length change. Tensile strength is the maximum tensile force that the body will withstand before failure. To investigate the mechanical properties, ZWICK tensile tester according to Figure 8 tested the prepared samples. The results obtained are shown in Table 3. During the tensile test, it was observed that all test samples were broken from the weld site, which is a testament to the correctness of the samples based on the standards.

4. ANALYSIS AND DISCUSSION

Given the repeatability of the results of practical experiments is essential, the repetition of the experiment was conducted for some samples. After securing the repeatability of the test results, its values are listed in Table 3.

4. 1. The Effect of Advance Speed on the Distortion of Joints Figure 9 indicates the impact of speed on the distortion of welding joints (samples 1, 3, 15, 16 and 12, 13 according to Table 3) in the same conditions of temperature and initial amperage, in which by altering the advance speed of the torch, its effect on the output is investigated. The results of the samples' analysis demonstrate that as the advance speed of torch increases, the angular distortion rate of the welded joints decreases.

4. 2. The Impact of Welding Current Intensity on Components Distortion Figure 10, which assesses the impact of welding current intensity on component distortion, reinforces the fact that with the constant initial parameters, torch advance speed and preheat plate temperature, different amps do not have a considerable effect on the angular distortion of the welding joints.

4. 3. The Effect of Preheat Temperature of Joints on Tensile Strength In the experimental study of the samples mentioned in Figure 11, it was found that by increasing the preheat temperature in the same initial conditions, the angular distortion of the joints decreases after welding. Furthermore, the results of the samples' analysis indicate that as the advance speed of the welding torch and the preheat temperature increases, the angular distortion rate of the welded joints decreases, which is in accordance with the theory mentioned in the first chapter. Preheating, heat management during welding, and machining, if possible, after welding can also bring distortion reduction. The results illustrate that the most optimal setting values of the initial parameters, to reduce the distortion of the welded samples, were acquired by setting the speed value to 3 mm/s, the amperage to 90 amps, and the preheat temperature to 120 ˚C.

4. 4. The Effect of Advance Speed on Tensile Strength Figure 12 demonstrates the effect of speed on the tensile strength of welding joints in the same

Figure 8. ZWICK tester in welding test mode

TABLE 3. Results of tensile tests on experimental samples

Experimental samples	Speed (mm/s)	Current (A)	Preheat temp (^{0}C)	Tensile strength (MPa)	Distortion angle (degrees)
1	4	130	180	715.26	1.34
2	1	90	25	631.13	4.85
3	1	130	180	492.01	2.87
4	4	90	25	398.39	2.004
5	3	130	25	662.23	4.24
6	2	90	180	682.26	2.01
7	4	90	180	230.54	1.83
8	1	130	25	546.27	4.45
9	3	90	120	457.69	1.32
10	2	110	25	661.59	2.84
11	3	110	180	604.31	2.76
12	1	110	120	583.63	4.05
13	4	110	120	445.98	3.18
14	2	130	120	591.34	4.36
15	3	130	180	703.65	2.11
16	2	130	180	604.47	2.53
17	2	90	25	678.22	3.04
18	**1**	**110**	**25**	**585.37**	4.73

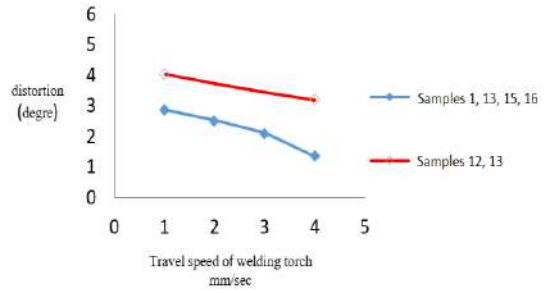

Figure 9. The effect of advance speed on distortion in welding joints with constant current and preheat temperature

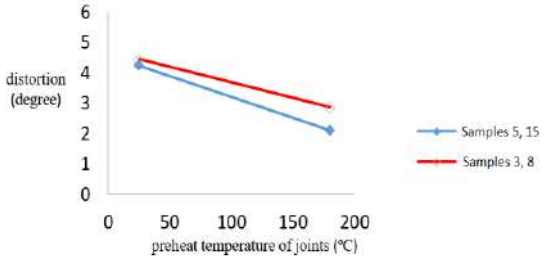

Figure 11. The effect of preheat temperature on distortion in welding joints with constant advance speed and current intensity

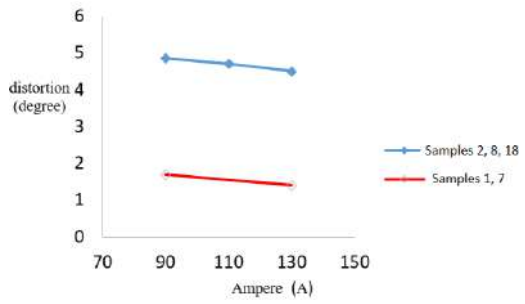

Figure 10. The impact of welding current intensity on distortion in weld procedure with constant advance speed and preheat temperature

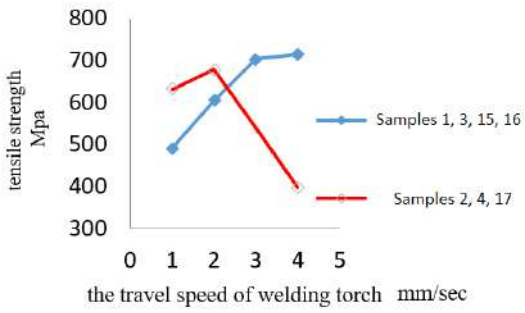

Figure 12. The effect of advance speed on tensile strength in welding joints with constant current intensity and preheat temperature

conditions of initial temperature and amperage, in which by changing the torch advance speed, its effect on the output is checked. In samples 1, 3, 15, 16, the first sample due to low speed, in addition to increasing the freezing time, causes coarse-grained structure. On the other hand, given the burning defect of the edges of the welding joints (Under Cut), due to the low speed and high amperage, it reduces the tensile strength. The increase in tensile strength is due to the increase in the advance speed, which is the result of the reduction of the two main defects mentioned. In samples 2, 4, 17, the increase in strength to the speed equal to 2 (mm/s) is valid. However, at the speed equal to 4 (mm/s), the tensile strength decreases due to the enormous reduction in melting time of the molten pool and the uncompleted melting of the edges, due to the reduction of amperage and the increase in speed.

4. 5. The Effect of Welding Current Intensity on Tensile Strength Examination of Figure 13 indicates that with the stability of the initial welding parameters except for the amperage, the strength of the welding joints decreases due to the burn defect of the plate edges. This defect can be minimized by increasing the welding speed and reducing the impact of extreme heat on the edges. Given the samples 11 and 15, an increase can be seen in durability because the increase in amperage is accompanied by an increase in the advance speed. This is mainly because of the reduction of the impact of extreme heat on the edges and therefore the reduction of the burn defects of the plate edges.

4. 6. The effect of Preheat Temperature of Joints on Tensile Strength Investigating Figure 14 shows that preheat temperature has little effect on tensile strength, and according to the results, its greatest effect is on the angular distortion of the welding joints.

The overall results demonstrated that the most optimal setting values of the initial parameters in order to increase the tensile strength, is through setting the speed to 4 mm per second, the amperage to 130 amps, and the preheat temperature to 180 ˚C.

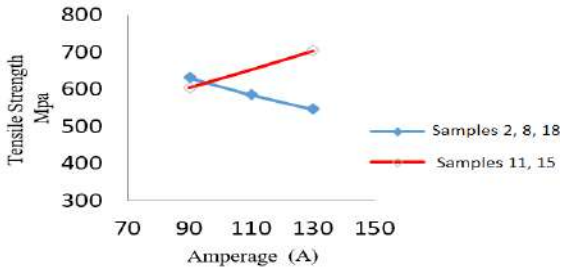

Figure 13. The effect of welding current intensity on tensile strength in welding joints with constant advance speed and preheat temperature

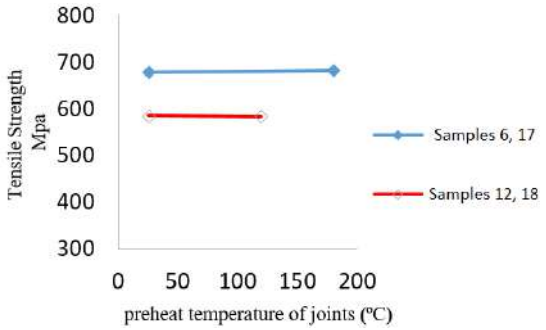

Figure 14. The effect of preheat temperature on tensile strength in welding joints with constant advance speed and current intensity

5. CONCLUSION

Tensile strength of welding joint and its deformity are the main indicators of welding quality. In this study, TIG welding processes was performed on 316 stainless steel in butt mode with different initial parameters including advance speed, amperage and preheats temperature. Then practical experiments were performed to obtain mechanical properties such as tensile strength and angular distortion of samples. Scientifically, the independent effect of each of the welding input parameters on the tensile strength and distortion were specified, and by examining the effect of the input parameter on the output, the best adjustment parameters of butt-welding were extracted for stainless steel welding 316.

The results show that by keeping the amperage and the preheating temperature constant, reducing the advance speed on the one hand increases the solidification time and coarseness of the structure and on the other hand leads to burns of the edges of welded parts which results in reduced tensile strength. In addition, by keeping the advance speed and preheating temperature constant and increasing the amperage, the tensile strength is reduced due to the burning defect of the edges of the parts. However, by performing various experiments, it was found that in conditions of high amperage, the mentioned defect could be eliminated by increasing the advance speed. Finally, by keeping the advance speed and amperage constant and changing the preheating temperature, no significant effect on tensile strength was observed.

According to the illustrated survey of the effect of all input values separately on output values, required measures should be taken in designing and adapting the initial welding parameters. According to the outcomes of this study, so as to obtain the desired mechanical properties, applying machines and robots are more advantageous and preferable than manual welding, due to the exact control of the initial parameters.

6. REFERENCES

1. Ethiraj N, Sivabalan T, Sivakumar B, Vignesh Amar S, Vengadeswaran N, Vetrivel K. "Effect of Tool Rotational Speed on the Tensile and Microstructural Properties of Friction Stir Welded Different Grades of Stainless Steel Joints", ***International Journal of Engineering*, *Transactions A: Basics,*** Vol. 33, No. 1, (2020), 141-147, DOI: 10.5829/ije.2020.33.01a.16

2. Subrammanian A., Pvsenthii L., Jabaraj DB. & Jayaprakash J. "Effect of process parameters on the mechanical performance of resistance spot welded joints of AISI409M ferritic stainless steel", ***Indian Journal of Engineering and Material Sciences***, Vol. 25, (2018), 11-18, http://nopr.niscair.res.in/handle/123456789/44450

3. Atul Raj, A.S., Phanden, R.K., & Gehlot, N. "Optimization of Deposition Rate of Weld Bead for Gas arc welding of Stainless Steel (SS316) using Taguchi Methods", ***International Journal for Technological Research in Engineering***, Vol. 2, No. 7, (2015), 3-13, http://www.ijtre.com/images/scripts/14289.pdf

4. Mbonde N. "Penetration Management in Tungsten inert Gas (TIIG) welding of thin plates by detecting oscillation of the molten pool", ***International Journal of Scientific Engineering And Applied Science***, Vol. 3, No. 5, (2017), 3-13, http://ijseas.com/volume3/v3i5/ijseas20170543.pdf

5. Ibrahim, M., Maqsood, SH., Khan, R., Amjad, M., & Jaan, SH. "Optimization of Gas Tungsten Arc welding parameters on penetration depth and bead width using the TAGUCHI method". ***Journal of Engineering Applied Science***, Vol. 35, No. 2, (2016), 78-89, https://doi.org/10.25211/JEAS.V35I2.2060

6. Teng, T. L., Lin, C. C., "Effect of welding condition on residual stresses due to butt welds, International Journal of Pressure Vessel and Piping", Vol. 75, (1998), 857-864, https://doi.org/10.1016/S0308-0161(98)00084-2

7. Halimi H., Vakili G., Safari E. "Effect of Welding Parameters on Dissimilar Pulsed Laser Joint between Nickel-Based Alloy Hastelloy X and Austenitic Stainless Steel AISI 304L", ***Scientia Iranica***, (2019), in press, https://doi.org/10.24200/sci.2019.52221.2602.

8. Saeheaw T. "Regression Modeling and Process Analysis of Plug and Spot Welds Used in Automotive Body Panel Assembly". ***International Journal of Engineering*, *Transactions B: Applications,*** Vol. 33, No. 11, (2020), 2384-2398. 10.5829/ije.2020.33.11b.29.

9. Langari J., Kolahan F., "The effect of friction stir welding parameters on the microstructure, defects, and mechanical properties of AA7075-T651 joints", ***Scientia Iranica***, (2019), in press, https://doi.org/10.24200/sci.2018.5700.1434.

10. Kurt, H.I., Samur, R. "Study on Microstructure, Tensile Test, and Hardness 316 Stainless Steel Jointed by TIG Welding", ***International Journal of Advances in Engineering*, *Science and Technology,*** Vol. 3, No. 1, (2013), 2249-2258, http://www.ijaest.com/docs/IJAEST13-03-01-006.pdf

11. Kumar S., Jena S., Lahoty V., Paswan M., Sharma B., Patel D., Prasad S.B., Kumar Sharma V., "Experimental investigation on the effect of welding parameters of TIG welded joints using ANOVA", ***Materials Today Proceedings***, Vol. 22, No. 4, (2020), 3181-3189, https://doi.org/10.1016/j.matpr.2020.03.455

12. Saleem M. "Microplane modeling of the elasto-viscoplastic constitution", ***Journal of Research in Science, Engineering and Technology,*** Vol. 8, No. 3, (2020), https://doi.org/10.24200/jrset.vol8iss3pp%25p

13. Basavaraju, Ch., "Simplified analysis of shrinkage in a pipe to pipe butt welds", ***Nuclear Engineering and Design***, Vol. 197, (2000), 239-247, https://doi.org/10.1016/S0029-5493(99)00302-7

14. Patchett, B. M. "The metals blue book: welding filler metals", Vol. 3, (1998), Asm International., https://www.casti.ca/books_ebooks/lite/BlueBookLite.pdf

15. Saha M., Dhami, S. "Effect of TIG Welding Parameter of Welded Joint of Stainless Steel SS304 by TIG Welding", ***Trends in Mechanical Engineering & Technology***, Vol. 5, No. 3, (2018), 18-27, https://doi.org/10.37591/tmet.v8i3.1433

16. Hu, X., Ma, C., Yang, Y. "Study on Residual Stress Releasing of 316L Stainless Steel Welded Joints by Ultrasonic Impact Treatment", ***International Journal Steel Structure***, Vol. 20, (2020), 1014-1025. https://doi.org/10.1007/s13296-020-00338-0.

17. Uematsu Y, Kakiuchi T, Ogawa D, Hashib K., "Fatigue crack propagation near the interface between Al and steel in dissimilar Al/steel friction stir welds", ***International Journal of Fatigue***, Vol. 138, (2020), 105706, https://doi.org/10.1016/j.ijfatigue.2020.105706.

Persian Abstract

چکیده

فرآیند جوشکاری گاز بی اثر تنگستن (TIG) یکی از روشهای پیچیده تولید است. دلیل آن تغییرات شدید در ساختار متالورژی قطعات جوشکاری ناشی از چرخه گرمایش و سرمایش در هنگام جوشکاری است. این تغییرات باعث نقص های مختلف متالورژیکی و مکانیکی قطعات شده و خصوصیات مکانیکی قطعات را تضعیف می کند. بسیاری از پارامترها در جوشکاری تأثیرات متفاوتی بر کیفیت قطعات جوشکاری دارند. برای ایجاد یک جوش مناسب ، لازم است اثر این پارامترها مشخص شود و بتوان آن را تخمین زده و شرایط مناسب و بهینه را انتخاب کرد. بر این اساس ، در این مطالعه ، یک تحقیق آزمایشی در مورد تعیین مشخصات مکانیکی قطعات از طریق تغییر سه پارامتر اصلی جوشکاری از جمله سرعت پیشروی ، آمپراژ جوش و دمای پیش گرم انجام شد. به دلیل دشواری تغییر سرعت پیشروی در جوشکاری دستی ، یک بازوی جوشکاری رباتیک برای جوشکاری فولاد ضد زنگ ۳۱۶ در مقاله فعلی طراحی شده است که در آن میکروکنترلر، سرعت و طول جوشکاری را تنظیم می کند. با جمع آوری داده های عملی ، تأثیر داده های ورودی (سرعت پیشروی ، آمپراژ جوشکاری و دمای پیش گرمایش) در دوام و مقاومت کششی اتصالات بررسی می شود. به عبارت دیگر ، کشش و دوام اتصالات برای فولادهای ضد زنگ برای پارامترهای مختلف جوشکاری پیشنهاد می شود تا شرایط بهینه بر اساس نتایج تجربی افزایش یابد. در نمونه هایی با سرعت پیشروی پایین ، علاوه بر افزایش زمان انجماد ، درشت دانه‌گی ساختار و سوختن لبه های قطعات جوشکاری شده به دلیل سرعت کم و آمپر زیاد ، مقاومت کششی را کاهش می دهد. همچنین نتایج نشان داد که با افزایش آمپراژ ، مقاومت قطعات جوشکاری به دلیل نقص سوختگی لبه های صفحه کاهش می یابد که می توان با افزایش سرعت جوشکاری و کاهش اثر گرمای شدید بر روی لبه ها ، آن را به حداقل رساند. سرانجام ، با تجزیه و تحلیل تأثیر پارامتر ورودی بر خروجی ، بهترین شرایط پارامترهای تنظیم در جوشکاری لب به لب در میان نمونه های موجود برای جوشکاری فولاد ضد زنگ ۳۱۶ بدست آمد.

IJE TRANSACTIONS B: Applications Vol. 34, No. 02, (February 2021) 572-580

International Journal of Engineering

Journal Homepage: www.ije.ir

The Effect of Stochastic Properties of Strength Reduction Function on the Time-Dependent Reliability of Reinforced Concrete Structures

S. A. Hosseini*[a], N. Shabakhty[b], S. S. Mahini[c]

[a] *Faculty of Technology and Mining, Yasouj University, Choram, Iran*
[b] *School of Civil Engineering, Iran University of Science and Technology,Tehran, Iran*
[c] *Center for Timber Durability and Design Life, University of Sunshine Coast, Australia*

P A P E R I N F O

Paper history:
Received 30 May 2020
Received in revised form 03 September 2020
Accepted 03 September 2020

Keywords:
Time-dependent Reliability
Reinforcement Corrosion
Stochastic Model
Strength Reduction Function
Probability of Failure

A B S T R A C T

Quantitative calculation of structural safety using its specific limit-states is of great importance. Due to the stochastic properties of strength, loading, and environmental reduction functions, these parameters cannot be considered as deterministic variables. In this paper, a probabilistic model including the stochastic properties of the strength reduction factor was proposed to calculate the time-dependent reliability of concrete structures. In this model, the statistical properties of applied loads were also considered. The strength reduction model was calculated quantitatively using the statistical properties of the reducing agent. In this research, the major factor contributing to the strength reduction is the reduction in the cross-section of the steel bars, reduction of bonding strength, and the spalling of the concrete cover due to reinforcement corrosion induced by chloride ingress. The results of this model were compared to the calculation of reliability using the direct implementation of strength values and another simplified method that only considers initial strength as a random variable. In the methods under investigation, the effect of the uncertainty of reducing factor on the mean and coefficient of variation of results was also studied. The results showed that the probability of failure increases between 25 to 50% when the uncertainty of the reducing factor is taken into account. The proposed model has more realistic results than the simplified model, and these results could be improved for achieving more exact outcomes with lower uncertainty.

***doi**: 10.5829/ije.2021.34.02b.31*

NOMENCLATURE

c	Concrete clear cover (cm)	P_{fD}	Deterministic failure probability
C_{cr}	Threshold chloride ions required to corrosion initiate (kg/m^3)	P_{fi}	Instantaneous failure probability
C_s	Chloride ion content at the surface of concrete (kg/m^3)	P_{fR}	Real failure probability
C_0	Initial chloride content in concrete (kg/m^3)	P_{fS}	Stochastic failure probability
Dc_0	diffusion coefficient of chloride ions in concrete (Cm^2/year)	q, Q	load
D_0	Reinforcement diameter (mm)	r, R	strength
f_Q, f_R	Probability density function of load and strength	R_0	Initial strength
f_θ	Probability density function of θ	s, S	load
F_Q, F_R	Cumulative distribution function of load and strength	t	time (year)
g, G	limit-stat function	t_L	life time
i_{cor}	corrosion current density (μA/cm^2)	T_i	corrosion initiation time (year)
L	Structural reliability	V_i	Coefficient of variation of i

Greek Symbols

θ	Strength random coefficient
λ_Q	mean occurrence rate of live load

*Corresponding Author Institutional Email: a.hosseini@yu.ac.ir (S. A. Hosseini)

Please cite this article as: S. A. Hosseini, N. Shabakhty, S. S. Mahini, The Effect of Stochastic Properties of Strength Reduction Function on The Time-Dependent Reliability of RC Structures, International Journal of Engineering, Transactions B: Applications Vol. 34, No. 02, (2021) 572-580

1. INTRODUCTION

Structures are affected by environmental agents and aging over time. These phenomena are associated with time-dependent changes in material properties and lead to a decline in the system performance in the operational lifetime [1]. Reinforcement corrosion due to carbonation and chloride ion penetration affects the efficiency of reinforced concrete (RC) structures. In aggressive environments, premature failure of RC systems due to reinforcement corrosion was considered one of the most critical durability issues [2,3]. The key causes of exposure to chloride ion are the deicing salts, seawater, and airborne salt [4]. The net cross-sectional area of the reinforcements is reduced during the corrosion process, and the resulting damaging effects emerge. Cover cracking, decrement of the concrete cross-sectional area and bond reduction between the concrete and the reinforcement are the most significant effects of reinforcement corrosion, which affect the strength and workability of the structures [5,6].

To evaluate the failure probability of a system, strength reduction mechanisms and their stochastic properties as well as the load history have to be taken into account [7]. A major factorin the structural reliability is the uncertainty of load and strength parameters [8,9]. Some uncertainties do not change over time, but others known as stochastic processes do [10].

The out-crossing rate approach is connventionally employed for calculating the reliability of structures under the effect of reducing factors [11,12]. It leads to a lower bound estimation for the probability of failure. Considering the random properties of strength parameters, Mori and Ellingwood introduced an approach to calculating time-dependent reliability [13]. Accordingly, loads are assumed as a stochastic process and modeled as a Poisson process. The method introduced by Mori and Ellingwood is based on the calculation of the probability of failure using the adaptive Monte Carlo sampling method. The method has been employed for the assessment of the lifetime of many concrete structures [14,15]. Vu and Stewart adopted this method to calculate the time-dependent reliability of concrete bridge deck [16]. The important issue associated with the calculation of time-dependent reliability in this method is how to employ the strength reduction model. The manner of strength reduction over time influences the calculation of reliability [17]. In this method, strength at each time, $R(t)$, is obtained based on multiplying the initial strength, $R_{0,}$ in the strength reduction function, $G(t)$. In this model, the effect of variations of strength parameters and reducing factors on $G(t)$ and also the effect of these variations on reliability are considered qualitatively, and the stochastic properties are considered only in the initial strength. However, only a few studies have been conducted on the effect of strength reducing factor and its stochastic properties on structural safety [18,19].

In this study, a strength reduction function was obtained by considering the stochastic properties of reducing factors and the statistical properties of materials. The stochastic properties of reducing agent and strength parameters were applied using a coefficient factor multiplied by the ratio of degraded strength at each time to the initial strength. In this paper, chloride ions ingress into the concrete is considered as the environmental aggressive factor that causes degradation of concrete strength over its lifetime. Bending strength at each time is calculated using the Monte Carlo random sampling method, and then the statistical parameters of strength are obtained for different scenarios. The reliability of the RC beam is calculated using the obtained stochastic coefficient. Time-dependent reliability was also calculated by two other methods: (1) considering degradation function as deterministic and applying stochastic properties of strength only in initial strength; and (2) direct implementation of degraded strength with its stochastic properties in reliability calculation. Results indicate that without considering the stochastic properties of environmental factors on the reduction function, the reliability value will be an upper limit of reliability which does not coincide with real conditions.

2. TIME-DEPENDENT STRENGTH AND STOCHASTIC LOAD PROCESS

To consider load and strength uncertainties, these variables are assumed as random variables [20]. The stochastic properties of load and strength and time variations of the strength of a structure exposed to the Q and S loads are schematically shown in Figure 1. These loads have the probability density function $f_{S,Q}$ and are exerted on the structure with varying intensities of (S_i) and (Q_i) over time. In this figure, strength value decreases over time, so the strength probability density function is shown as $f_R(r,t)$ at any time. As seen in this figure, if structural reliability at any time is calculated only on the basis of the instantaneous strength and load values, the resulting value will be the upper limit for the reliability at that time. The reason is that at that specific time, the collective effects of the previous times and the loading history are not taken into account.

In RC structures, material properties, environmental condition and some structural parameters change in the service lifetime. The probabilistic models of structural strength reduction are obtained using either mathematical models or the accelerated testing methods. Sometimes, a combination of both methods is employed [21-23]. The mathematic models used in the analysis of time dependent reliability are generally qualitative

models [18]. The need for quantitative models for the prediction of future structural performance has led to the development of stochastic strength reduction models based on the Gamma model [24,25] and analytical models based on the effect of the reducing factors on the structural performance [26]. The application of this model with statistical distributions covering uncertainties of parameters leads to a better assessment of the stochastic behavior of structures. Moreover, through the reliability methods, a model for structural failure probability is obtained which helps develop a probabilistic model for prediction life time of structure. Mori and Ellingwood (1993) defined strength at each time, *R(t)*, as follows for the assessment of time-dependent reliability of degraded structure:

$$R(t) = R_0 G(t) \tag{1}$$

where, R_0 is the initial resistance and $G(t)$ is the resistance reduction function, which is defined qualitatively based on the type of reducing factor as a linear, parabolic or square root function. In calculations of reliability, the $G(t)$ function is assumed to be deterministic and randomness of strength at each time is applied through the stochastic properties of initial strength.

To study the application of loads to structures various models have been proposed. These models consider the effect of concurrency of loads as well [15]. the occurrence and changes of the transient loads applied to the structure during time and place is assumed as a random process (Q_n in Figure 1). For these loads, in addition to the randomness of the intensity of the applied load, the duration of load is also random. The stochastic modeling of these loads is carried out based on the assumption that their occurrence is described by Poisson point process.

3. TIME-DEPENDENT RELIABILITY ANALYSIS

Assuming the strength model *R* and loading model *Q*, the structural component reliability at each time is expressed as follows:

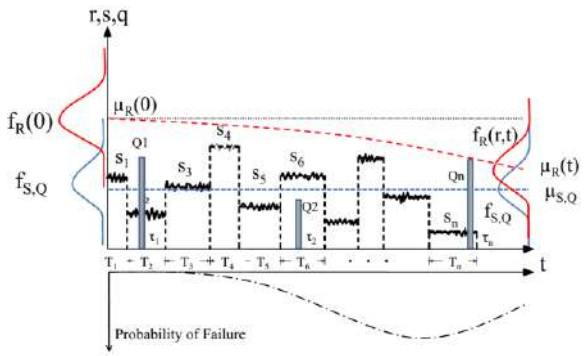

Figure 1. strength degradation and stochastic load process

$$L(0,t) = P\left[R(t) > Q(t)\right] = \int_0^\infty F_Q(r,t) f_R(r,t) dr \tag{2}$$

where, f_R is the strength probability density function and F_Q is the probability distribution function of the load. In order to calculate reliability at a specific time (e.g. t_L) all load events prior to this time shall not exceed the strength of the member.

In Equation (2), which is used to calculate reliability, the effect of the randomness of influencing parameters has to be taken into account. Hence, using the law of total probability, the number of occurrences of loads and initial strength are changed to the random variable, and reliability is obtained as follows:

$$L\left\{(0,t_L)\right\} = \int_0^\infty \int_0^\infty \exp[K_1] f_S(s) f_{R_0}(r) ds dr$$

where

$$K_1 = -\lambda_Q t_L \left[1 - \frac{1}{t_L}\int_0^{t_L} F_Q\left\{R_0 G(t) - s\right\} dt\right] \tag{3}$$

where, f_{R_0} is the probability density function of the resistance of the structure, f_s is the probability density function of the load *S* and F_Q is the probability distribution function of the load *Q*. Also, λ is the mean occurrence rate of this load. In addition, in this equation, it is assumed that among the *S* and *Q* forces applied to the structure, *S* is applied permanently and the stochastic properties of the strength are applied only through the initial strength R_0 , where the randomness of aggressive agent is omitted. If actual values of structural strength are used at any time, there is no need to estimate strength based on the initial strength and the strength reduction function. Hence, in Equation (3), actual values of calculated strength (obtained based on the stochastic properties of the effect of the reducing factor) are used instead of the initial strength probability distribution function, $f_{R_0}(r)$, and strength degradation function.

In this paper, stochastic properties of strength are defined through a coefficient factor that represents the randomness of the ratio of strength at each time to initial strength:

$$G(t) = \theta(t) g(t) \tag{4}$$

where, $g(t)$ is a deterministic function indicating the ratio of mean strength at each time to initial strength, and $\theta(t)$ is a random variable that applies the effect of the randomness of strength reducing factors to the strength reduction function. The mean value of $\theta(t)$ is equal to one and time-dependent coefficient of variation of this parameter is similar to the values of the strength

reduction function. In order to apply the stochastic properties of corrosion to the strength reduction function, Equation (4) is put into Equation (1) to obtain the strength model at each time for the calculation of time-dependent reliability:

$$G(t) = R_0\theta(t)g(t) \tag{5}$$

By changing the strength reduction function to a function with stochastic properties, Equation (3) changes as follows:

$$L\{(0,t_L)\} = \int_0^\infty\int_0^\infty\int_0^\infty \exp[K_2] f_\theta(\theta) f_S(s) f_{R_0}(r)\, d\theta ds dr$$

where

$$K_2 = -\lambda_Q t_L \left[1 - \frac{1}{t_L}\int_0^{t_L} F_Q\{\theta R_0 g(t) - s\}\right] dt \tag{6}$$

By calculating strength at each time, the strength reduction function and its statistical parameters are obtained. Moreover, the best probabilistic distribution that reflects the randomness of this function is fitted to it to calculate $\theta(t)$. There is some uncertainty in the calculation of statistical parameters of the coefficient $\theta(t)$; thus, the calculated time-dependent reliability from Equation (6) have uncertainty too. Therefore, for the evaluation of this coefficient, time-dependent reliability is calculated based on applying degraded strength directly in Equation (3). Using stochastic properties of real strength at each time changes Equation (3) as follows:

$$L\{(0,t_L)\} = \int_0^\infty\int_0^\infty \exp[K_3] f_{R(t)}(r(t)) f_S(s)\, dr(t)\, ds$$

where

$$K_3 = -\lambda_Q t_L \left[1 - \frac{1}{t_L}\int_0^{t_L} F_Q\{R(t) - s\}\right] dt \tag{7}$$

where $f_{R(t)}$ is probability density function of real strength at time "t". Equation (7) is the best tool for evaluating time-dependent reliability if stochastic properties of degraded strength are known at each time.

4. ANALYTICAL MODEL

4. 1. Strength Degradation In this paper, the time-dependent reliability of reinforced concrete beam under the effect of chloride induced corrosion is studied. For this, the bending strength of the RC beam is calculated based on the cross-sectional reduction of corroded reinforcement, bond strength reduction and the spalling of the concrete cover due to reinforcement corrosion induced by chloride ingress.

In the period of corrosion propagation, it is critical to use parameters that can be immediately measured to determine the extent and severity of corrosion. Measuring the weight difference between corroded rebar and reference rebar is the most reliable method in this respect. For the measurement of the corrosion rate of reinforcement in structural concrete, many electrochemical and non-destructive techniques are available that the corrosion rate estimated in terms of a corrosion current density, i_{cor} [27,28].

Different models for estimating the remaining the cross-section of the reinforcement have been proposed based on the type of corrosion [29]. The time-variant diameter of reinforcement at time t is calculated as follow:

$$D(t) = D_0 - 0.0278 i_{cor}(I) \times (t - T_i)^{0.71} \tag{8}$$

where, T_i (year) is the corrosion initiation time and $i_{cor}(I)$ ($\mu A/cm^2$) is the corrosion current density in the corrosion initiation year.

The reinforcement corrosion due to chloride ingress is started when the chloride ion concentration at the reinforcement reaches a threshold value (C_{cr}). Fick's second law of diffusion is the most acceptable method that describes the penetration of chlorides through concrete [30]. Accordingly, the corrosion initiation time is calculated as follows:

$$T_i = \frac{c^2}{4D_{c0}}\left(erf^{-1}\left(\frac{C_s - C_{cr}}{C_s - C_0}\right)\right)^{-2} \tag{9}$$

where, C_{cr} is the threshold concentration of chloride ions required to corrosion initiate (kg/m^3); C_s is the chloride ion content at the surface of concrete (kg/m^3); C_0 is the initial chloride content in concrete (kg/m^3); D_{c0} is the diffusion coefficient of chloride ions in concrete (Cm^2/year); c is the concrete clear cover of reinforcement (cm); and erf is the error function.

Bond reduction between corroded reinforcement and concrete is evaluated by a model proposed by Bhargava et al., and concrete cover spalling is estimated based on empirical crack propagation model by Rodriguez *et al.* [14, 31].

Figure 2 shows the cross-section of a 4-m long simply supported RC beam. This beam is subjected to the live and dead loads. Also, it is assumed that this beam is subjected to chloride induced corrosion with corrosion current density of 1 μA/cm^2 and 3 μA/cm^2. These values cause moderate to severe effects on the concrete beam, respectively [14,32]. In order to study the effect of the strength reducing factor on the resistance reduction function, coefficients of variation V_i, of 0.1 and 0.3 are assumed for corrosion current density [14]. When the concentration of chlorid ions around the reinforcement reaches a critical value, reinforcement corrosion is initiated [32]. In order to

calculate the corrosion initiation time for this model, the diffusion model was used based on Fick's second law [33].

For calculating corrosion initation time, the threshold chloride concentration is assumed as a uniform random variable within the range of 0.6- 1.2 kg/m3 [34]. Applying this assumption and using Equation (9) for a moderat environmental condition, Hosseini reported the random properties of the corrosion initiation time [35]. The mean corrosion initiation time for this beam is assumed to be T_i=10 years with the coefficient of variation (V_T) of 0.3.

The bending strength of RC beam reduces over time because of a reduction in the cross section of reinforcements, the bond reduction between the reinforcement and concrete, and reduction in concrete section due to cover spalling. The bending strength of the beam in the middle was calculated at each time considering the section dimensions and materials properties as random variable using the Monte Carlo Sampling method (MCS) [5]. In the MSC, a series of values of random variables with specified probability distribution is generated using invers transform method. If a_i is the generated uniformly distributed number within the rane of 0-1, the inverse transform method is adopted to equate a_i to the cumulative distribution function of random variable x_i as follows [36]:

$$F_X(x_i) = a_i \quad \text{or} \quad x_i = F_X^{-1}(a_i) \tag{10}$$

where F_X is the cumulative distributation function of random variable x.

Table 1 presents the mean values of the strength reduction function, $M_{G(t)}$, and the coefficient of variation of this function, $V_{G(t)}$, for i_{cor}=1.0 and V_i=0.3. Based on the results, the coefficient of θ(t) follows the lognormal distribution. Statistical properties of this parameter during the corrosion propagation period are shown in Table 1. These stochastic parameters are used in Equation (6) to calculate reliability at each time.

The mean value of $\theta(t)$ is equal to 1.0 and its standard deviation is determined proportionally to the strength reduction function $G(t)$. To calculate the

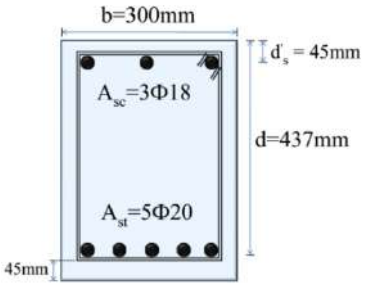

Figure 2. Cross-section of reinforced concrete beam at mid span

TABLE 1. Statistical parameters of strength degradation function and coefficient factor (i_{cor}= 1.0 µA/cm^2, Vi=0.3)

Time (Year)	$\sigma_{\ln(\theta)} \times 100$	$-\mu_{\ln(\theta)} \times 100$	$\mu_{G(t)}$	$V_{G(t)}$
1	0.59	10.91	1.0	0.11
10	0.44	9.26	0.95	0.11
20	0.17	5.88	0.81	0.11
25	0.17	5.84	0.77	0.12
30	0.18	5.98	0.74	0.15
35	0.18	6.03	0.71	0.16
40	0.19	6.19	0.68	0.15
45	0.19	6.22	0.65	0.14
50	0.21	6.41	0.63	0.13
55	0.20	6.38	0.61	0.13
60	0.22	6.58	0.59	0.13

stochastic properties of $\theta(t)$, samples generated from the MCS method are divided by the mean values at each time. Next, the statistical properties of the samples are calculated.

The coefficient of variation of $\theta(t)$ and mean values of degradation function over time are shown in Figures 3 and 4 for different corrosion scenarios. As shown in these figures, before starting the corrosion effects, the coefficient of variation of bending strength is approximately equal to 0.12. This parameter begins to increase after the onset of corrosion due to the effect of the uncertainty associated with the reducing agent. An abrupt increase was observed in the coefficient of variation related to the time of concrete spalling and reduction of the bond strength. It is clear from Figure 4 that V_θ is sensitive to the uncertainty in the corrosion current density, so that with larger coefficient of variation of the i_{cor} , the coefficient of variation of $\theta(t)$ increases. However, as shown in Figure 4, this increase does not affect the mean residual strength. It can also be

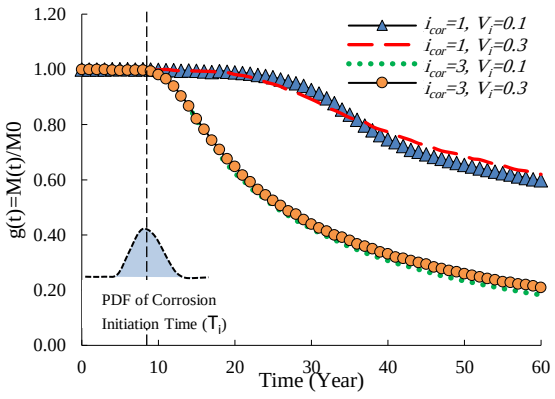

Figure 3. The mean values of degradation function

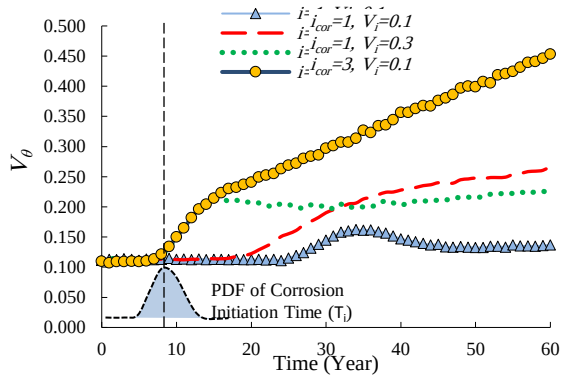

Figure 4. Coefficient of variation of $\theta(t)$

concluded from this figure that due to the significant changes in the coefficient of variation of resistance over time, using the stochastic properties of initial resistance is not a valid assumption in reliability calculations.

4. 2. Time-dependent Reliability In this part, the failure probability of RC beam is calculated in three ways. The first method consists of calculating reliability based on Equation (3). In this method, stochastic properties of resistance at each time is only applied to the strength reduction function through the initial strength. The failure probability obtained through this method is shown by P_{fD} which stands for a deterministic reduction function. In the second method, reliability is obtained through Equation (6) and stochastic properties of strength are also calculated both through initial strength and by coefficient $\theta(t)$ to the time-dependent reliability. Probability of failure calculated in this method is introduced as P_{fS}. In the third method, the resistance at each time is directly calculated through the MC random sampling method and the resulting values are also directly used in the calculation of reliability. The probability of failure based on this method is shown as P_{fR}. In all of the three methods, the Monte Carlo and numerical integration methods are employed simultaneously to calculate the reliability and probability of failure. Loads applied to the RC beam are live and dead loads. Live load is applied to the structure transiently with a mean occurrence rate of λ while the dead load is permanently applied. It is assumed that the loads are statistically independent. Occurrence of live load follows the Poisson distribution and has *extreme type I* probability density function [32]. Dead load is applied permanently with a normal probability distribution function.

The probability of failure calculated by all of the three methods are shown for V_i=0.1 and V_i=0.3 in Figures 5 and 6. It is clear from these figures that the probability of failure that is calculated on the basis of random properties of the initial resistance, P_{fD} , is less than P_{fS} which uses the random properties of the resistance reduction function. In fact, the effect of the stochastic properties of the reduction factors has elevated the probability of failure during the time. It is also evident from Figures 5 and 6 that raising the uncertainty in the reducing factor applied through V_i has led to higher probability of failure in all the three methods. The results indicate that the probability of failure is low in the first and second methods. This situation, especially when the uncertainty in the decreasing factor is low, shows a greater difference. As shown in Figures 5-8, for the bending strength up to the time of spalling and reduction of the bond strength, the probability of failure from all the three methods is equal. This means that the values of P_{fD} can be used to estimate the probability of failure during this time, but after that, other methods should be employed. Moreover, the results show that the proposed method has better results than the P_{fD} method. In Figures 5-8, P_{fi} represents the instantaneous probability of failure calculated regardless of the load history effect. This instantaneous failure probability is less than real values, which is sometimes used for the probability of failure of structures.

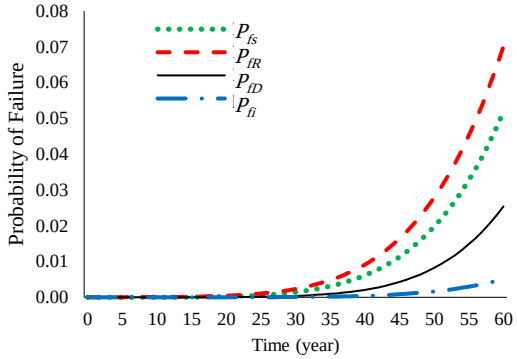

Figure 5. P_{fD} , P_{fS} and P_{fR} for corrosion current density of 1.0 μA/cm^2(V_i=0.1)

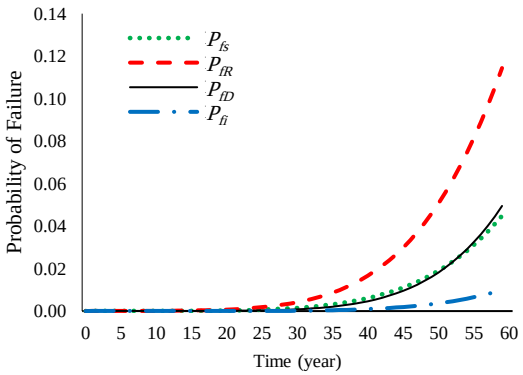

Figure 6. P_{fD} , P_{fS} and P_{fR} for corrosion current density of 1.0 μA/cm^2 (V_i=0.3)

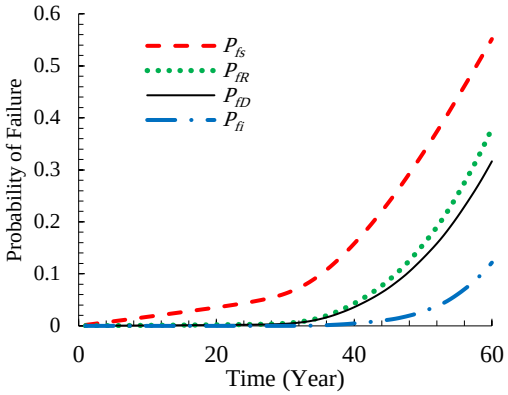

Figure 7. P_{fD} , P_{fS} and P_{fR} for corrosion current density of 3.0 µA/cm^2(V_i=0.1)

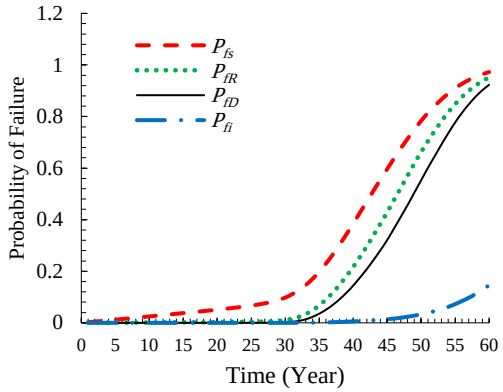

Figure 8. P_{fD} , P_{fS} and P_{fR} for corrosion current density of 3.0 µA/cm^2(V_i=0.3)

Figures 9 and 10 show the coefficient of variation of the proposed method (V_{PfS}). As shown in thess figures, because the number of samples is constant in the MC method, the amount of uncertainty has diminished due to higher probability of failure. It should be noted that the value presented in this figure represents the

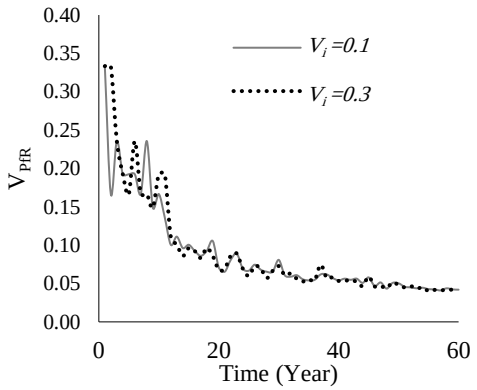

Figure 9. Coefficient of variation of P_{fS} i_{cor}= 1 µA/cm^2

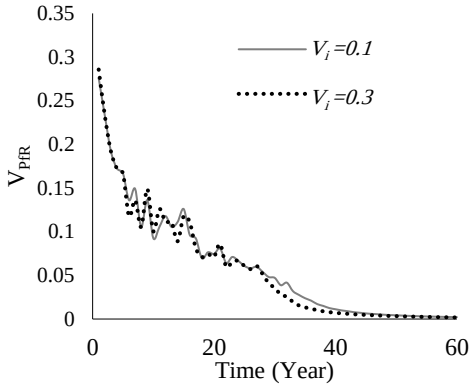

Figure 10. Coefficient of variation of P_{fS}, i_{cor} = 3 µA/cm^2

instantaneous uncertainty, and the calculation of the total uncertainty follows the cumulative effect of the preceding times.

5. CONCUSION

In this paper, the effect of stochastic properties of strength reducing factor on the estimation of time-dependent failure probability of concrete beam was studied. The reducing factor considered in this research was the effect of reinforcement corrosion on the bending strength of the RC beam. The stochastic properties of this effect on bending strength were simplified using a coefficient factor. The probability of failure at each time was calculated through the effect of the coefficient factor on the mean strength value. Also, a comparison was made between the results obtained based on the real values of strength and those with the use of the deterministic mean strength only. According to the results, the application of uncertainties of the reducing factor leads to more accurate results by the application of the coefficient factor for the calculation of the probability of failure. For chloride ingress as an aggressive agent, the simplified qualitative method (P_{fD}) can be used before the initiation of the occurrence of spalling and the reduction of the bond between reinforcement and concrete, for the ease of calculation. However, after the initiation,the stochastic properties of reducing agent should be taken into account.

6. REFERENCES

1. Kiahosseini, S. R., Borzouyi Kutenayi, S., Talebpour, M. H. "The Effect of Caspian Sea Water on Corrosion Resistance and Compressive Strength of Reinforced Concrete Containing Different SiO_2 Pozzolan." ***International Journal of Engineering, Transactions A: Basics***, Vol 30, No. 10, (2017), 1464-1470.

2. Hájková, K., Šmilauer, V., Jendele, L., Červenka, J. "Prediction of reinforcement corrosion due to chloride ingress and its effects on serviceability." ***Engineering Structures***, Vol. 174, (2018), 768-777. https://doi.org/10.1016/j.engstruct.2018.08.006
3. Islam, M., Arifuzzaman, A. "Deterioration of Concrete in Ambient Marine Environment (Research Note)." ***International Journal of Engineering, Transactions B: Applications***, Vol. 25, No. 4, (2012), 289-302.
4. Gao, Y., Zheng, Y., Zhang, J., Wang, J., Zhou, X., Zhang, Y. "Randomness of critical chloride concentration of reinforcement corrosion in reinforced concrete flexural members in a tidal environment." ***Ocean Engineering***, Vol. 172, (2019), 330-341. https://doi.org/10.1016/j.oceaneng.2018.11.038
5. Hosseini, S. A., Shabakhty, N., Mahini, S. S. "Correlation between chloride-induced corrosion initiation and time to cover cracking in RC Structures." ***Structural Engineering and Mechanics***, Vol. 56, No. 2, (2015), 257-273. https://doi.org/10.12989/sem.2019.72.4.479
6. Yu, S., Jin, H. "Modeling of the corrosion-induced crack in concrete contained transverse crack subject to chloride ion penetration." ***Construction and Building Materials***, Vol. 258, (2020), 119645. https://doi.org/10.1016/j.conbuildmat.2020.119645
7. Basiri, M. H., sharifi, M. R., Ostadi, B. "Reliability and Risk Assessment of Electric Cable Shovel at Chadormalu Iron Ore Mine in Iran." ***International Journal of Engineering, Transactions A: Basics***, Vol. 33, No. 1, (2020), 170-177. https://dx.doi.org/10.5829/ije.%202020.33.01a.20
8. Jeong, S., Seong, H. K., Kim, C. W., Yoo, J. "Structural design considering the uncertainty of load positions using the phase field design method." ***Finite Elements in Analysis and Design***, Vol. 161, (2019), 1-15. https://doi.org/10.1016/j.finel.2019.04.002
9. Bagheri, M., Chahkandi, A., Jahangir, H. "Seismic reliability analysis of RC frames rehabilitated by glass fiber-reinforced polymers." ***International Journal of Civil Engineering***, Vol. 17, No. 11, (2019), 1785-1797. https://doi.org/10.1007/s40999-019-00438-x
10. Bagheri, M., Hosseini, S. A., Keshtegar, B., Correia, J. F., Trung, N. T. "Uncertain time-dependent reliability analysis of corroded RC structures applying three-term conjugate method." ***Engineering Failure Analysis***, (2020): 104599. https://doi.org/10.1016/j.engfailanal.2020.104599
11. Mejri, M., Cazuguel, M., Cognard, J.-Y. "A time-variant reliability approach for ageing marine structures with non-linear behaviour." ***Computers & Structures***, Vol. 89, No. 20, (2011), 1743-1753. https://doi.org/10.1016/j.compstruc.2010.10.007
12. Gray, W. A., Melchers, R. E. "Modifications to the 'directional simulation in the load space'approach to structural reliability analysis." ***Probabilistic Engineering Mechanics***, Vol. 21, No. 2, (2006),148-158. https://doi.org/10.1016/j.probengmech.2005.08.002
13. Mori, Y., Ellingwood, B. R. "Reliability-based service-life assessment of aging concrete structures." ***Journal of Structural Engineering***, Vol. 119, No. 5, (1993), 1600-1621. https://doi.org/10.1061/(ASCE)0733-9445(1993)119:5(1600)
14. Bhargava, K., Mori, Y., Ghosh, A. "Time-dependent reliability of corrosion-affected RC beams—Part 1: Estimation of time-dependent strengths and associated variability." ***Nuclear Engineering and Design***, Vol. 241, No. 5, (2011), 1371-1384. https://doi.org/10.1016/j.nucengdes.2011.01.005
15. Mori, Y. Ellingwood, B. R. "Reliability assessment of reinforced concrete walls degraded by aggressive operating environments." ***Computer-Aided Civil and Infrastructure Engineering***, Vol. 21, No. 3, (2006), 157-170. https://doi.org/10.1111/j.1467-8667.2006.00424.x
16. Vu, K. A. T., Stewart, M. G. "Structural reliability of concrete bridges including improved chloride-induced corrosion models." ***Structural Safety***, Vol. 22, No. 4, (2000), 313-333. https://doi.org/10.1016/S0167-4730(00)00018-7
17. Ellingwood, B. R. Mori, Y. "Probabilistic methods for condition assessment and life prediction of concrete structures in nuclear power plants." ***Nuclear Engineering and Design***, Vol. 142, No. 2-3, 155-166. https://doi.org/10.1016/0029-5493(93)90199-J
18. Ciampoli, M. Ellingwood, B. "Probabilistic methods for assessing current and future performance of concrete structures in nuclear power plants." ***Materials and Structures***, Vol. 35 No. 1, (2002), 3-14. https://doi.org/10.1007/BF02482084
19. Dubourg, V., Sudret, B., Deheeger, F. "Metamodel-based importance sampling for structural reliability analysis." ***Probabilistic Engineering Mechanics***, Vol. 33, (2013), 47-57. https://doi.org/10.1016/j.probengmech.2013.02.002
20. Melchers, R. E. Beck, A. T. "Structural reliability analysis and prediction." John Wiley & Sons, 2018. https://doi.org/10.1002/9781119266105.ch7
21. Neves, R., Branco, F., De Brito, J. "Field assessment of the relationship between natural and accelerated concrete carbonation resistance." ***Cement and Concrete Composites***, Vol. 41, (2013), 9-15. https://doi.org/10.1016/j.cemconcomp.2013.04.006
22. Younsi, A., Turcry, P., Aït-Mokhtar, A., Staquet, S. "Accelerated carbonation of concrete with high content of mineral additions: effect of interactions between hydration and drying."***Cement and Concrete Research***, Vol. 43, (2013), 25-33. https://doi.org/10.1016/j.cemconres.2012.10.008
23. Finozzi, I. B. N., Berto, L., Saetta, A. "Structural response of corroded RC beams: a comprehensive damage approach." ***Computers and Concrete***, Vol. 15, No. 3, (2015), 411-436. https://doi.org/10.12989/cac.2015.15.3.411
24. Guida, M., Postiglione, F., Pulcini, G. "A time-discrete extended gamma process for time-dependent degradation phenomena." ***Reliability Engineering & System Safety***, Vol. 105, (2012), 73-79. https://doi.org/10.1016/j.ress.2011.12.016
25. Pan, Z., Balakrishnan, N. "Reliability modeling of degradation of products with multiple performance characteristics based on gamma processes." ***Reliability Engineering & System Safety***, Vol. 96, No. 8, (2011), 949-957. https://doi.org/10.1016/j.ress.2011.03.014
26. Lu, C., Jin, W., Liu, R. "Reinforcement corrosion-induced cover cracking and its time prediction for reinforced concrete structures." ***Corrosion Science***, Vol. 53, No. 4, (2011), 1337-1347. https://doi.org/10.1016/j.corsci.2010.12.026
27. Borzouyi Kutenayi, S., Kiahosseini, S., Talebpour, M. (2017). 'The Effect of Caspian Sea Water on Corrosion Resistance and Compressive Strength of Reinforced Concrete Containing Different SiO_2 Pozzolan', ***International Journal of Engineering, Transactions A: Basics***, 30(10), pp. 1464-1470.
28. Val, D. V., Stewart, M. G., Melchers, R. E. "Effect of reinforcement corrosion on reliability of highway bridges." ***Engineering Structures***, Vol. 20, No. 11, (1998), 1010-1019. https://doi.org/10.1016/S0141-0296(97)00197-1
29. Salarvand, A., Poursaiedi, E., Azizpour, A. "Probability Approach for Prediction of Pitting Corrosion Fatigue Life of Custom 450 Steel." ***International Journal of Engineering, Transactions A: Basics*** , Vol. 31, No. 10, (2018), 1773-1781.
30. Stewart, M. G., Rosowsky, D. V. "Time-dependent reliability of deteriorating reinforced concrete bridge decks."***Structural Safety***, Vol. 20, No. 1, (1998), 91-109. https://doi.org/10.1016/S0167-4730(97)00021-0
31. Rodriguez, J., Ortega, L., Casal, J. "Load carrying capacity of concrete structures with corroded reinforcement." ***Construction***

and Building Materials, Vol. 11, No. 4, (1997), 239-248. https://doi.org/10.1016/S0950-0618(97)00043-3

32. Hosseini, S. A., Shabakhty, N., Azhdary Khankahdani, F. "Sensitivity analysis of flexural strength of RC beams influenced by reinforcement corrosion." ***Structural Engineering and Mechanics***, Vol. 72, No. 4, (2019), 479-489. https://doi.org/10.12989/sem.2019.72.4.479
33. Bastidas-Arteaga, E., Chateauneuf, A., Sánchez-Silva, M., Bressolette, P., Schoefs, F. "A comprehensive probabilistic model of chloride ingress in unsaturated concrete." ***Engineering Structures***, Vol.33, No. 3, (2011), 720-730. https://doi.org/10.1016/j.engstruct.2010.11.008
34. Wang, Y., Liu, C., Wang, Y., Li, Q., Liu, Z. "Investigation on chloride threshold for reinforced concrete by a test method combining ANDT and ACMT." ***Construction and Building Materials***, Vol. 214, (2019), 158-168. https://doi.org/10.1016/j.conbuildmat.2019.04.108
35. Hosseini, S. "Probabilistic Calculation of the Corrosion Initiation of steel reinforcement Using Reliability Methods." ***Concrete Research***, Vol. 12, No. 3, (2019), 137-145. (in persian). https://dx.doi.org/10.22124/jcr.2019.11702.1318
36 Choi, S. K., Grandhi, R., & Canfield, R. A. "Reliability-based structural design". Springer Science & Business Media (2006).

Persian Abstract

چکیده

محاسبه ایمنی سازه به صورت کمی و بر اساس تابع شرایط حدی تعریف شده برای آن منجر به ارزیابی عمر سازه می‌شود. به دلیل خواص تصادفی مقاومت، بارهای اعمالی به سازه و همچنین اثر عوامل مخرب محیطی، نمی‌توان پارامترهای موثر را به صورت قطعی در نظر گرفت. در این پژوهش یک مدل احتمالاتی مقاومت که در برگیرنده خواص تصادفی عوامل کاهنده مقاومت می‌باشد برای محاسبه احتمال خرابی سازه بتنی پیشنهاد شده است. در این مدل خواص تصادفی نیرو نیز در نظر گرفته شده است. عامل اصلی کاهنده مقاومت که مورد بررسی قرار گرفته است شامل خوردگی میلگرد ناشی از نفوذ یون کلر به همراه اثرات آن بر مقاومت خمشی بوده است. نتایج حاصل از مدل پیشنهادی با دیگر مدل‌های موجود مقایسه شده است. نتایج نشان می‌دهد که در نظر گرفتن عدم قطعیت به صورت مدل پیشنهادی موجب محاسبه احتمال خرابی بزرگتری برای سازه مورد نظر می‌شود که بیانگر نزدیک بودن به شرایط واقعی سازه است. محاسبه احتمال خرابی وقتی که اثر عدم قطعیت صرفاً مقاومت اولیه در نظر گرفته می‌شود باعث محاسبه قابلیت اطمینان سازه به صورت دست بالا (بین ۲۵ تا ۵۰ درصد) و غیر محافظه کارانه خواهد شد. نتایج نشان می دهد تا زمان قبل از رخداد پوسته شدن و کاهش باند بین بتن و میلگرد می‌توان از مدل‌های ساده شده موجود استفاده کرد و بعد از این رویدادها، نتایج مدل‌های قبلی غیر محافظه کارانه خواهد بود.

IJE TRANSACTIONS B: Applications Vol. 34, No. 02, (February 2021) 581-586

International Journal of Engineering

Journal Homepage: www.ije.ir

Study of Bonding Strength at Salt-cement Interface During Cementation of Salt Layers

N. I. Nikolaev[a], S. S. Tabatabaee Moradi[b]

[a] *Well Drilling Department, Oil and Gas Faculty, Saint Petersburg Mining University, Saint Petersburg, Russia*
[b] *Faculty of Petroleum and Natural Gas Engineering, Sahand University of Technology, Tabriz, Iran*

PAPER INFO

Paper history:
Received 07 August 2020
Received in revised form 11 September 2020
Accepted 26 October 2020

Keywords:
Oil Well Cement
Halite
Portland Cement
Water to Cement Ratio

ABSTRACT

Cement has been used for decades in industry to serve various important functions inside oil and gas wells. Due to the complications and variations in the geological and technical conditions of a well, various cement compositions are designed and utilized in different world regions. Many hydrocarbon reservoirs are covered by thick salt formations, which are considered problematic and costly to be drilled and cemented. Cement slurry, as a water based solution, interacts with salt rock, as a result of which cement properties are changed that consequently may jeopardize well integrity across salt formations and successful exploitation of beneath hydrocarbon reservoirs. In this study, based on experimental and industrial experiences, a cement composition is developed that meet the requirements of cementation in salt layers. Experimental investigations are conducted on the bonding strength at the salt-cement interface, as the bonding strength is considered as one of the factors that significantly affect overall cement efficiency in providing well integrity. Results confirm the effectiveness of the developed composition for cementation of salt layers.

***doi**: 10.5829/ije.2021.34.02b.32*

NOMENCLATURE

C_3S	Tricalcium silicate	*PVP*	Polyvinylpyrrolidone
C_3A	Tricalcium aluminate	*CaO*	Calcium oxide
W/C	Water to cement mass ratio		

1. INTRODUCTION

In many locations worldwide, salt layers overlie hydrocarbon reservoirs and serve as high-quality cap rocks in the petroleum system. Thus, effective exploitation of such hydrocarbon reservoirs requires successful passing through these salt layers. However, based on industrial practices, drilling and cementing wells through theses layers are usually challenging and costly [1].

Salts are water soluble, with low porosity and permeability; behave plastically in high pressure and high temperature conditions, which may lead to their flow into the wellbore and subsequent problems in the adjacent cement and casing strings.

*Corresponding Author Institutional Email: stabatabaee@sut.ac.ir (S.S. Tabatabaee Moradi)

Challenges of cementing salt layers may be divided into two main categories:

- Creep load of salt on cement
- Interaction of cement slurry with salt layer

Creep is defined as the gradual material deformation under constant stresses over time and in the case of salt layers, may lead to its movement toward the subsequent cement and casing string. To avoid potential risks of cement failure and casing collapse under this load, a uniform cement composition with adequate strength properties should be utilized in the annular space between the casing and formation [2, 3].

Creep load and its effect on wellbore integrity have been subjects of several researches. Wang et al. [4] used a geomechanical model of casing, cement sheath and salt rock to describe the long-term rheological behavior of salt rock and cement sheath under in situ stresses.

Please cite this article as: N. I. Nikolaev, S. S. Tabatabaee Moradi, Study of Bonding Strength at Salt-cement Interface During Cementation of Salt Layers, International Journal of Engineering, Transactions B: Applications Vol. 34, No. 02, (2021) 581-586`

In the work of Jandhyala et al. [5], finite element analysis and structural mechanics are used to study the effect of salt creep load on the stresses inside the cement sheath at various stages of well service life, including drilling, cementing, shut-in, completion, and production. They concluded that addition of elastomers into cement composition could help in withstanding applied loads.

Beside creep load, interaction of cement and salt formation is another important consideration. Most of the formation salts are soluble in slurry as cements are generally water-based systems. This dissolution reaction has two main disadvantageous effects. First of all, salt dissolution in the slurry leads to hole enlargement, which jeopardize the annular space uniformity and overall wellbore integrity. Secondly, slurry and set cement properties are changed after salt dissolution, which may lead to a low-quality cementing operation.

Several authors investigated effects of salt on slurry and set cement properties. The salt may be added as an additive for preparation of cement or it may enter to the cement system from the formation.

Islam et al. [6] studied the effect of sea water with enhanced salt concentrations on the samples from two grades of concrete exposed to simulated sea environment over a year and showed that concrete exposed to sea water of different salt concentrations suffered a loss of compressive strength.

Teodoriu and Asamba [7] studied the effect of NaCl, as an additive, on API class G cement. They showed variations of some main cement properties, including slurry thickening time, set cement compressive strength, dynamic E-modulus and permeability with change in salt concentration. Based on experimental tests, authors concluded that NaCl, as an available and cost-effective additive, produce some attractive effects on well cement performance.

In the work of Lago et al. [8], effect of NaCl salt in the hydration process of class G Portland cement was studied on the first 24 hours of cement hydration. Authors came to the conclusions that presence of NaCl up to 10%, accelerates the hydration process and increases the hydration of C_3S (tricalcium silicate) and C_3A (tricalcium aluminate), while the 20% salt concentration leads to delayed hydration.

Simao et al. [9] evaluated the effect of different concentrations of halite (NaCl), carnalite ($KMgCl_3.6H_2O$) and taquidrite ($CaMgCl_3.12H_2O$) on the main characteristics of a semi-saturated cement, including free fluid content, thickening time, compressive strength and rheological properties. Based on experimental results, authors suggested that using a semi-saturated slurry for cementing salt layers in Brazil provide a good quality cementing operation.

Among the cement properties that are studied in the abovementioned works, almost no attention is paid to the bonding strength between cement and formation, which defines quality of the process at the formation-cement interface and is considered as one of the factors that significantly affect overall efficiency of the well cementing operation [10, 11].

As a result of ion exchange between excess slurry water and salt rock, most of the salts dissolves in cement even after it's hardening, which leads to formation of a saltwater gap at formation-cement interface and consequently a low-quality cementing operation.

In this work, a salt saturated slurry composition is developed and used for cementing a salt rock sample in a laboratory model to investigate the quality of cementing operation by analyzing the bonding strength at cement-salt rock interface.

2. MATERIAL AND METHODS

To select optimum cement composition, following techniques are considered to have a good bonding strength at salt-cement interface at all stages of their interaction:

- Reduction of excess water in the cement slurry.
- Providing volume expansion in set cement.
- Preparation of cement slurry with an aqueous solution of a similar salt.

Water to cement mass ratio (W/C) is a slurry parameter that can be adjusted in a specific range to control the water content of the cement slurry. To see the effect of water reduction on boning strength at salt-cement interface, cement slurry with W/C of 0.5 and 0.45 were prepared and result were compared.

Polyvinylpyrrolidone (PVP) was added as a plasticizing (fluidizing) agent, which provides the possibility of W/C reduction without any further problem in cement flow-ability and pumping.

To provide volume expansion in set cement, calcium oxide (CaO) was added to the system as an expanding agent. Finally, NaCl was used in the mixing water of cement slurry to minimize salt dissolution from rock sample in the cement.

Cement samples were prepared based on standard procedures, which involved dry premixing of ordinary Portland cement, PVP and CaO an then mixing the dry power with water at a rate of 2000 revolution per minutes for 2 minutes. All chemicals were provided by local producers in the Russian Federation. Prepared samples with different additive are presented in Table 1.

Cylindrical NaCl samples (diameter of 40 mm and, height of 50 mm) were prepared using a special coring machine (Figure 1) from bulky salt samples in laboratory and placed at the middle of a steel cylinder. Cement slurry of developed composition was poured then around the salt rock sample. The whole cement and salt system was left in the laboratory conditions

(temperature 24 ˚C, atmospheric pressure, exposure to air) for hardening as the time passes (Figure 2).

To determine bonding strength at salt-cement interface at different hardening stages, tangential stress, required to press-out cylindrical salt samples (Figure 2) from cement of different compositions was measured and reported.

Schematic of the device, which has been used for tangential stress measurement is shown in Figure 3.

The press machine applies force to move out the salt sample from the cement ring. This force is recorded to be used in the following tangential stress formula:

$$\sigma_t = \frac{F}{A_t} \quad (1)$$

where F is the force, applied by press machine to move out salt sample form cement ring, A_t is the lateral area of cement ring and σ_t is tangential stress. Calculated tangential stress is reported as the contact bonding strength.

TABLE 1. Different cement compositions

No.	Composition	W/C
1	**Base composition:** Portland cement, water	0.5, 0.45
2	Portland cement, water, CaO (5, 7, 10 % wt.)	0.5
3	Portland cement, water, NaCl (2, 5 % wt.)	0.5
4	**Final composition:** Portland cement, PVP (0.25% wt.), Cao (5% wt.), NaCl (2% wt.)	0.45

Figure 1. Preparation of NaCl samples using coring machine

Figure 2. Cylindrical salt sample inside cement

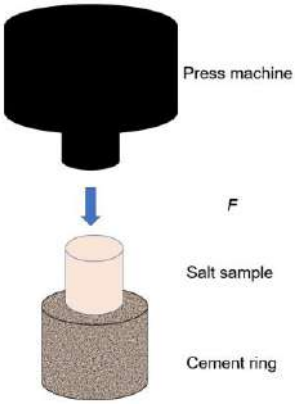

Figure 3. Schematic of the measuring device

3. RESULTS AND DISCUSSION

Figure 4 shows process of cement interaction with cylindrical salt (NaCl) sample during hardening process. Visual observations showed that at the stage of cement hydration there is an active interaction between excess water of cement slurry with the surface of the salt sample; while due to the hygroscopicity of the salt, its outer surface is actively dissolved and a salt-saturated water layer is created between the salt sample and the cement at the final stage of its hardening, which practically leads to a low bonding strength at the salt-cement interface.

Figure 5 shows the results of bonding strength evaluation at the interface of base cement composition (W/C = 0.5) and salt sample (all experimental data are presented in Appendix 1 in tabular form).

Presented data in Figure 5 indicate that there is almost no contact bonding strength of the cement with the salt sample (less than 0.02 MPa after a week of hardening). At the same time, spontaneous falling out of the salt sample from the cement rock was observed during the preparation for pressing-out on the press machine.

Figure 6 shows the variation of bonding strength at base cement-salt interface with a decrease in W/C.

As it can be seen, the tangential stresses at the salt-cement interface increase by more than 5 times with a decrease in W/C to 0.45. This is due to the fact that minimizing water content in the cement slurry leads to less solubility of the salt rock on the surface of the sample during its initial contact with the cement slurry.

Variation of bonding strength at salt-cement interface with the concentration of CaO in the composition of base cement is presented in Figure 7. It

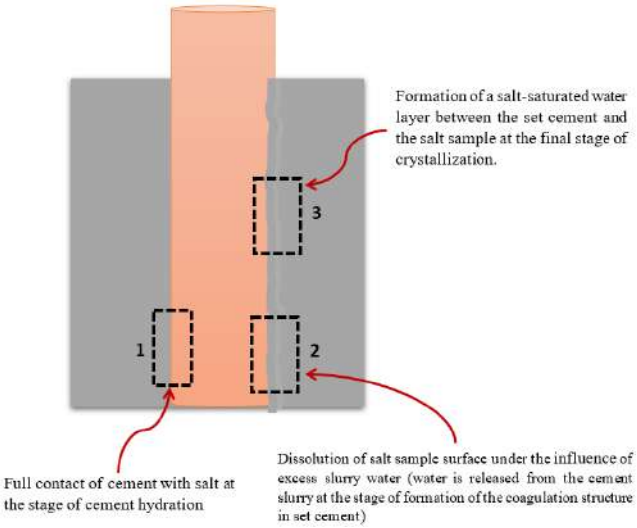

Figure 4. Schematics of the interaction between the cement and salt sample at different stages of cement hardening

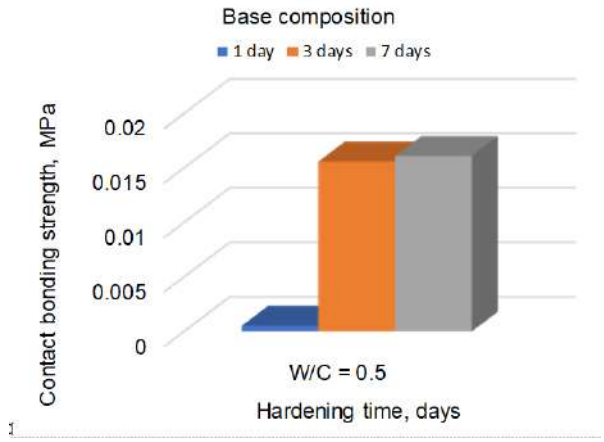

Figure 5. Contact bonding strength of the base cement composition (W/C=0.5) with NaCl

is evident that the volume expansion of the cement composition leads to an increase in the bonding strength of cement rock with salt from 7 to 20 times in compare to the base composition.

Since, as it was noted earlier, the processes of hydration and hardening of cement samples are significantly influenced by presence of sodium chloride in the cement mixing water, studies were conducted to investigate the effect of NaCl in the cement composition on the bonding strength of cement rock with salt rock. Results are presented in Figure 8.

As the data in Figure 8 show, when NaCl concentration of 5% is reached, the bonding strength of cement with salt is significantly reduced; therefore, the NaCl concentration in the cement slurry must be limited. Large concentrations of halite in the cement

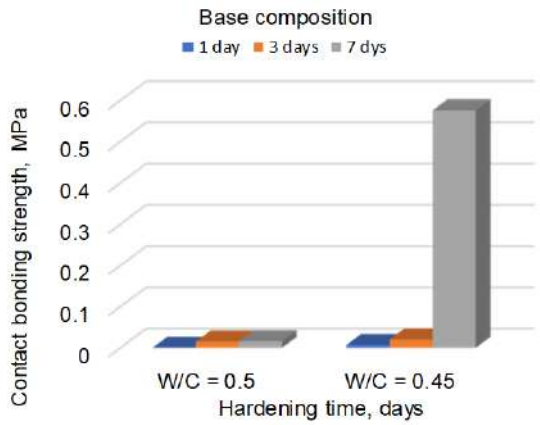

Figure 6. Contact bonding strength of the base cement composition (W/C=0.5 and W/C=0.45) with NaCl

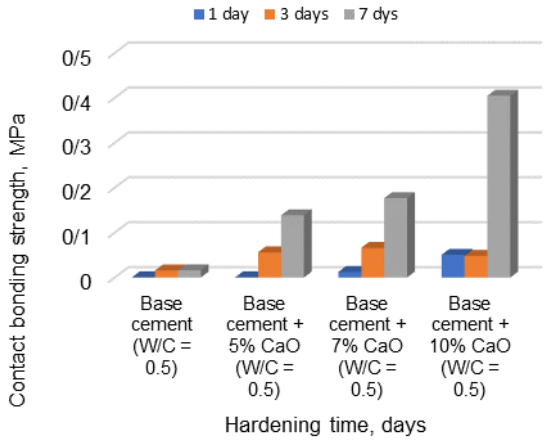

Figure 7. Influence of CaO in the developed composition on bonding strength at salt-cement interface

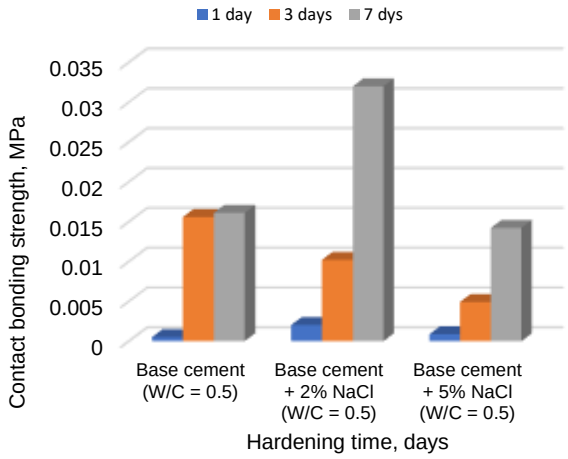

Figure 8. Influence of NaCl in the developed composition on bonding strength at salt-cement interface

during its crystallization leads to not only destruction of the internal cement structure, but also to the destruction of contacts with external objects, in particular, with salt rock sample.

Based on the experimental result following final cement composition (W/C = 0.45) was developed and its bonding strength with salt sample was calculated (Figure 9):

- Portland cement;
- PVP plasticizer-0.25% (wt.);
- Expanding additive Cao-5% (wt.);
- Mineral additive NaCl-2% (wt.)

The results of the study showed that the decrease in W/C to 0.45, by addition of the mixture of water 0.25% PVP, 2% NaCl and 5% Cao contribute to an increase of

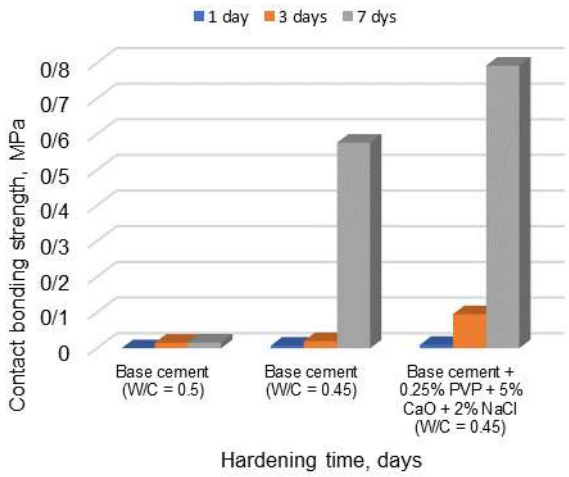

Figure 9. Bonding strength of final developed composition with salt rock sample

contact bonding strength of cement with the salt in 6-7 times compared to the base cement composition.

Also it is notable that increase in contact bonding strength in all systems with time from 1 to 7 days, has not a linear trend, which is reasonable output as the cement hardening process and it's strength development is inherently a complex phenomenon.

4. CONCLUSION

Analyzing the obtained results, we can draw the following conclusions about the contact bonding strength at the cement slurry-salt rock and cement rock-salt rock interfaces:

- Base cement composition at a standard W/C=0.5 practically does not have contact strength with salt rocks so it cannot provide integrity of the well annular space in the intervals of evaporate salt deposition.
- Maintaining a good-quality contact of cement and salt at all stages of their interaction can be provided by reducing excess water in the cement slurry, increasing the volumetric expansion of the cement composition and preparation of cement slurry with an aqueous solution of a similar salt.
- When the water content in the cement solution is low, the solubility of the salt rock on the surface of the sample is minimized during its initial contact with the cement slurry (this can be the case during slurry movement through the annular space).
- Furthermore, addition of NaCl to the water during cement mixing leads to reduction in setting time of cement slurry, which reduces the interaction time of free water with salt rock. It also contributes to the formation of salt-saturated hydrate neoplasms in the adhesive layer at the subsequent stages of coagulation of the cement and crystallization of the cement rock.
- CaO presence as an expandable agent, provides volumetric expansion of the cement, which in turn leads to increased pressure at salt-cement interface and consequently increased bonging strength.

6. REFERENCES

1. Amer, A., Dearing, H., Jones, R. and Sergiacomo, M., "Drilling trough salt formations: A drilling fluids review", in SPE Deepwater Drilling and Completions Conference, Texas, USA, 14-15 September, (2016). DOI: https://doi.org/10.2118/180326-MS
2. Hunter, B., Tahmourpour, F. and Faul, R., "Cementing casing strings across salt zones: An overview of global best practices", ***SPE Drilling & Completion***, Vol. 25, (2010), 426-437. DOI: https://doi.org/10.2118/122079-PA

3. Taheri, S. R., Pak, A., Shad, S., Mehrgini, B. and Razifar, M., "Investigation of rock salt layer creep and its effects on casing collapse", ***International Journal of Mining Science and Technology***, Vol. 30, (2020), 357-365. DOI: https://doi.org/10.1016/j.ijmst.2020.02.001
4. Wang, X., Qu, Z., Dou, Y. and Ma, W., "Loads of casing and cement sheath in the compressive viscoelastic salt rock", ***Journal of Petroleum Science and Engineering***, Vol. 135, (2015), 146-151. DOI: http://dx.doi.org/10.1016/j.petrol.2015.08.020
5. Jandhyala, S., Barhate, Y. R., Anjos, J., Fonseca, C. E. and Ravi, K., "Cement sheath integrity in fast creeping salts: Effect of well operations", in SPE Offshore Europe Oil and Gas Conference and Exhibition, Aberdeen, UK, 3-6 September, (2013). DOI: https://doi.org/10.2118/166622-MS
6. Islam, S., Islam, M. and Chandra Mondal, B., "Deterioration of Concrete in Ambient Marine Environment", ***International Journal of Engineering, Transactions B: Applications***, Vol. 25, No. 4, (2012), 289-301. DOI: 10.5829/idosi.ije.2012.25.04b.05
7. Teodoriu, C. and Asamba, P., "Experimental study of salt content effect on class G cement properties with application to well integrity", ***Journal of Natural Gas Science and Engineering***, Vol. 24, (2015), 324-329. DOI: http://dx.doi.org/10.1016/j.jngse.2015.03.039
8. Lago, F. R., Gonçalves, J. P., Dweck, J. and Cherem da Cunha, A. L., "Evaluation of Influence of Salt in the Cement Hydration to Oil Wells", ***Materials Research***, Vol. 20, (2017), 743-747. DOI: http://dx.doi.org/10.1590/1980-5373-MR-2017-0049
9. Simao, C. A., Miranda, C. R., Vargas, A. A., Pereira, R. F. L., Santos, R. L. L., Soares, M. A. S. and Conceicao, A. C. F., "Cementing in front of soluble salt zones", in SPE Deepwater Drilling and Completion, Texas, USA, 20-21 June, (2012). DOI: https://doi.org/10.2118/145719-MS
10. Bu, Y., Du, J., Guo, S., Liu, H., Liang, Y., Su, Z. and Li, Y., "Effects of formation water influx on the bonding strength between oil well cement and the formation", ***Construction and Building Materials***, Vol. 251, 118989, (2020). DOI: https://doi.org/10.1016/j.conbuildmat.2020.118989
11. Vrålstad, T., Saasen, A., Fjær, E., Øia, T., Ytrehus, J. D. and Khalifeh, M., "Plug & abandonment of offshore wells: Ensuring long-term well integrity and cost-efficiency", ***Journal of Petroleum Science and Engineering***, Vol. 173, (2019), 478-491. DOI: https://doi.org/10.1016/j.petrol.2018.10.049

APPENDIX 1. Experimental data of bonding strength at salt-cement interface

No.	Composition	W/C	Bonding strength at salt-cement interface, MPa		
			After 1 day	After 3days	After 7 days
1	**Base composition:** Portland cement, water	0.5	0.00051969	0.015590688	0.016110378
2	**Base composition:** Portland cement, water	0.45	0.00750951	0.02050176	0.57636176
3	Portland cement, water, CaO (5 wt%)	0.5	0.00051969	0.05623042	0.13839334
4	Portland cement, water, CaO (7 wt %)	0.5	0.01247255	0.06620846	0.17674644
5	Portland cement, water, CaO (10 wt %)	0.5	0.05035792	0.0482021	0.4046823
6	Portland cement, water, NaCl (2 wt%)	0.5	0.00202679	0.0102119	0.0319869
7	Portland cement, water, NaCl (5 wt %)	0.5	0.00088347	0.00491107	0.01421351
8	**Final composition:** Portland cement, PVP (0.25 wt %), Cao (5 wt %), NaCl (2 wt %)	0.45	0.00956	0.09564	0.792546

Persian Abstract

چکیده

سیمان برای دهه ها به منظور انجام وظایف مختلف و مهم درون چاه های نفت و گاز در صنعت مورد استفاده قرار گرفته است. به دلیل پیچیدگی ها و تفاوت ها در شرایط زمین شناسی و فنی یک چاه، ترکیبات مختلف سیمان، طراحی و در مناطق مختلف جهان مورد استفاده قرار گرفته اند. بسیاری از مخازن هیدروکربنی به وسیله لایه های ضخیم نمکی پوشانده شده اند که حفاری و سیمان کاری آن ها مشکل زا و هزینه بر می باشد. دوغاب سیمان به عنوان یک سیال پایه آبی با سنگ های نمک وارد واکنش می شود که در نتیجه آن ویژگی های سیمان تغییر می کند که این امر نهایتاً می تواند باعث به خطر افتادن یکپارچگی چاه در مقابل لایه های نمکی و استخراج موثر مخازن هیدروکربنی زیرین شود. در این مطالعه، بر اساس تجربیات آزمایشگاهی و صنعتی، یک ترکیب سیمان که شرایط سیمان کاری در لایه های نمکی را داشته باشد، طراحی شده است. آزمایشات بر روی استحکام پیوند بین نمک و سیمان انجام شده است چرا که استحکام پیوند به عنوان یکی از عواملی در نظر گرفته می شود که به طور قابل توجهی بهره وری سیمان در فراهم کردن یکپارچگی چاه را تحت تاثیر قرار می دهد. نتایج، موثر بودن ترکیب طراحی شده در سیمان کاری لایه های نمکی را تایید می کند.

AIMS AND SCOPE

The objective of the International Journal of Engineering is to provide a forum for communication of information among the world's scientific and technological community and Iranian scientists and engineers. This journal intends to be of interest and utility to researchers and practitioners in the academic, industrial and governmental sectors. All original research contributions of significant value focused on basics, applications and aspects areas of engineering discipline are welcome.

This journal is published in three quarterly transactions: Transactions A (Basics) deal with the engineering fundamentals, Transactions B (Applications) are concerned with the application of the engineering knowledge in the daily life of the human being and Transactions C (Aspects) - starting from January 2012 - emphasize on the main engineering aspects whose elaboration can yield knowledge and expertise that can equally serve all branches of engineering discipline.

This journal will publish authoritative papers on theoretical and experimental researches and advanced applications embodying the results of extensive field, plant, laboratory or theoretical investigation or new interpretations of existing problems. It may also feature - when appropriate - research notes, technical notes, state-of-the-art survey type papers, short communications, letters to the editor, meeting schedules and conference announcements. The language of publication is English. Each paper should contain an abstract both in English and in Persian. However, for the authors who are not familiar with Persian, the publisher will prepare the latter. The abstracts should not exceed 250 words.

All manuscripts will be peer-reviewed by qualified reviewers. The material should be presented clearly and concisely:

- *Full papers* must be based on completed original works of significant novelty. The papers are not strictly limited in length. However, lengthy contributions may be delayed due to limited space. It is advised to keep papers limited to 7500 words.
- *Research* notes are considered as short items that include theoretical or experimental results of immediate current interest.
- *Technical notes* are also considered as short items of enough technical acceptability with more rapid publication appeal. The length of a research or technical note is recommended not to exceed 2500 words or 4 journal pages (including figures and tables).

Review papers are only considered from highly qualified well-known authors generally assigned by the editorial board or editor in chief. Short communications and letters to the editor should contain a text of about 1000 words and whatever figures and tables that may be required to support the text. They include discussion of full papers and short items and should contribute to the original article by providing confirmation or additional interpretation. Discussion of papers will be referred to author(s) for reply and will concurrently be published with reply of author(s).

INSTRUCTIONS FOR AUTHORS

Submission of a manuscript represents that it has neither been published nor submitted for publication elsewhere and is result of research carried out by author(s). Presentation in a conference and appearance in a symposium proceeding is not considered prior publication.

Authors are required to include a list describing all the symbols and abbreviations in the paper. Use of the international system of measurement units is mandatory.

- On-line submission of manuscripts results in faster publication process and is recommended. Instructions are given in the IJE web sites: www.ije.ir-www.ijeir.info
- Hardcopy submissions must include MS Word and jpg files.
- Manuscripts should be typewritten on one side of A4 paper, double-spaced, with adequate margins.
- References should be numbered in brackets and appear in sequence through the text. List of references should be given at the end of the paper.
- Figure captions are to be indicated under the illustrations. They should sufficiently explain the figures.
- Illustrations should appear in their appropriate places in the text.
- Tables and diagrams should be submitted in a form suitable for reproduction.
- Photographs should be of high quality saved as jpg files.
- Tables, Illustrations, Figures and Diagrams will be normally printed in single column width (8cm). Exceptionally large ones may be printed across two columns (17cm).

PAGE CHARGES AND REPRINTS

The papers are strictly limited in length, maximum 6 journal pages (including figures and tables). For the additional to 6 journal pages, there will be page charges. It is advised to keep papers limited to 3500 words.

Page Charges for Papers More Than 6 Pages (Including Abstract)	
For International Author ***	**$55 / per page**
For Local Author	**100,000 Toman / per page**

AUTHOR CHECKLIST

- Author(s), bio-data including affiliation(s) and mail and e-mail addresses).
- Manuscript including abstracts, key words, illustrations, tables, figures with figure captions and list of references.
- MS Word files of the paper.

International **J**ournal of **E**ngineering, P.O. Box 13145-1659, Tehran, I.R. Iran
Materials and Energy Research Center, 5 Ahuramazda St., Alvand Ave., Argentina Sq., Tehran, Islamic Republic of Iran
www.merc.ac.ir - www.emerc.ac.ir

THOMSON REUTERS

WEB OF SCIENCE

Scopus®

CAS®
A DIVISION OF THE
AMERICAN CHEMICAL SOCIETY

Google
Scholar